UNIVERSITÀ DI PARMA

UNIVERSITA' DEGLI STUDI DI PARMA

DOTTORATO DI RICERCA IN

"*INGEGNERIA INDUSTRIALE*"

CICLO XXXV

Additive Manufacturing of Lightweight Al-Si-Mg and Ti-Al-V Alloys via Laser-Powder Bed Fusion: Post-Heat Treatment Optimization on Microstructure and Mechanical Properties

Coordinatore:

Chiar.mo Prof. Gianni Royer Carfagni

Tutore:

Chiar.ma Prof.ssa Emanuela Cerri

Dottorando:

Ing. Emanuele Ghio

Anni Accademici 2019/2020 – 2021/2022

[*This page intentionally left blank*]

Firma Coordinatore

_____

Firma Tutor

_____

[*This page intentionally left blank*]

"That's all"

[*The Devil wears Prada*]

[*This page intentionally left blank*]

ABSTRACT

AlSi7Mg, AlSi10Mg and Ti6Al4V lightweight alloys are widely used within automotive, aerospace, and biomedical fields where high mechanical performance and safety factors are required. In fact, the age-hardening aluminium alloys are characterized by high specific tensile strengths and good corrosion resistance, as well as the titanium alloy that show higher tensile strengths, corrosion resistance and cell biocompatibility. Adding the advantages conferred by the Laser-Powder Bed Fusion manufacturing technology, the application of these alloys can significantly increase. The present doctoral thesis analyses the effects induced by different heat treatments to evaluate their optimization on AlSi7Mg, AlSi10Mg and Ti6Al4V samples manufactured via Laser-Powder Bed Fusion. Both the AlSi7Mg and AlSi10Mg were firstly studied in the as-built conditions; in which the effects induced by the build platform pre-heated at 150 °C were carefully investigated along the total height (300 mm) of the samples. At the same time, the microstructural effects and the resultant mechanical properties obtained by the layer thickness (+ 40 μm) and hatch spacing (– 150 μm) variations were also investigated on the AlSi10Mg samples. Secondly, the effects induced by direct aging at 175 °C, 200 °C and 225 °C were also examined in order to homogenize the mechanical properties and HV microhardness from the bottom to the top regions of the manufactured samples. After just the 1–2 h treatment at 175 °C and 200 °C for the AlSi7Mg and AlSi10Mg alloys, respectively, the mechanical properties were already homogenized and optimized. The homogenization in mechanical properties was also evaluated after the solution heat treatment at 505 °C and artificial aging at 175 °C for both aluminium alloys. Even considering the samples in peak-aging conditions, the yield and ultimate tensile strength were always lower than those obtained by samples heat-treated in optimized direct aging conditions. These worsening effects were also reflected on the ductility, whose values were lowered of 11 %.

Abstract

Ti6Al4V samples manufactured via Laser-Powder Bed Fusion in different build orientations were analysed in as-built and heat-treated conditions. In order to reduce the anisotropy of the mechanical properties, the effects of two different annealing heat treatments at 704 °C and 740 °C were carefully investigated through SEM, XRD and EBSD measurements. Despite the different cooling pathways between both annealing heat treatments, and the consequent coarsening effects of the α-phase laths (+ 23 %), no variation in terms of yield and ultimate tensile strengths were obtained. EBSD and SEM investigations did not show a preferential orientation of the α-phase, but highlighted that the same α-laths maintained the same α'-martensite orientations during the $\alpha \rightarrow \alpha + \beta$. The effective decrease of the tensile strengths was obtained after the solubilization heat treatment at 1050 °C × 60 min, due to the recrystallized microstructure. In fact, the ultimate tensile strength and the yield strength decreased to 925 and 825 MPa, respectively. At the same time, elongation values did not significantly due to the formation of an α-case layer on account of the oxygen diffusion, on the sample surface, during the solubilization heat treatment. Moreover, the different thickness of the samples promoted several cooling pathways and, consequently, the formation of different microstructures at room temperature, despite the same fast cooling in argon gas (60 min). Lastly, the sand-blasting process decreased the surface roughness (– 50 %) but increases the plastic strain thanks to the impact of glass spheres on the sample surface. No variations in terms of tensile strengths were detected.

In relation to the AlSi10Mg alloys in as-built and heat-treated conditions, the correlation between the HV microhardness and tensile strengths can be good approximated by Cahoon's equations. From the comparison of the theoretical and experimental Vickers microhardness values, and those calculated by the yield strength, a correction factor of 0.891 was obtained to adjust Cahoon's equation. On the other hand, Ti6Al4V samples heat-treated at 704 °C and 740 °C show a discrepancy between the real and calculated HV values of 21–22 %. Therefore, the α-phase increase of about 21–22 % the HV values compared to those calculated with the Cahoon equation.

SOMMARIO

Le leghe leggere AlSi7Mg, AlSi10Mg e Ti6Al4V sono leghe ampiamente utilizzate in differenti settori industriali, quali *automotive*, *aerospace* e *biomedico* dove sono richieste elevate proprietà meccaniche e, conseguentemente, elevati coefficienti di sicurezza. Infatti, le leghe di alluminio rafforzabili tramite processi di invecchiamento sono caratterizzate da elevate proprietà meccaniche specifiche. Parallelamente, le leghe di titanio mostrano proprietà tensili più elevate rispetto a quelle dell'alluminio così come la resistenza a corrosione e la biocompatibilità cellulare. Se si aggiungono tutti i vantaggi conferiti dal processo *Laser-Powder Bed Fusion*, le applicazioni di queste leghe possono aumentare significativamente. In tal contest, la presente tesi di dottorato analizza gli effetti indotti da differenti trattamenti termici per poterne valutare una loro ottimizzazione. In primo luogo, sia la lega AlSi7Mg che la lega AlSi10Mg sono state analizzate in condizioni *as-built*, dove sono stati analizzati, lungo l'intera altezza degli stessi campioni (300 mm), gli effetti indotti dalla piattaforma pre-riscaldata alla temperature di 150 °C. Nello stesso tempo, sono stati esaminati gli effetti indotti da un incrementato di + 40 μm del *layer thickness* e un decremento di – 150 μm dell'*hatch spacing* sulla microstruttura di campioni in AlSi10Mg. In secondo luogo, gli effetti indotti da trattamenti termici di invecchiamento diretto alle temperature di 175 °C, 200 °C e 225 °C sono stati analizzati anche nell'ottica di omogeneizzare le proprietà meccaniche e le durezze tra le regioni *top* e *bottom* dei campioni stampati. Già dopo 1–2 h di trattamento termico di invecchiamento diretto a 175 °C, per la lega AlSi7Mg, e 200 °C, per la lega AlSi10Mg, le proprietà meccaniche sono state omogeneizzate e, contemporaneamente, ottimizzate. Queste condizioni sono state anche valutate dopo solubilizzazione a 505 °C ed invecchiamento artificiale a 175 °C per entrambe le leghe. Anche considerando i campioni in condizioni di *peak-aging*, lo snervamento e la resistenza ultima a trazione sono sempre rimaste inferiori a quelle ottenute da campioni trattati termicamente con ottimizzate condizioni di invecchiamento diretto. Questi effetti negativi sono anche riflessi sui valori di duttilità che sono risulti essere inferiori a l'11 %. Le analisi di microscopia ottica ed elettronica, con correlate misure XRD, sono state eseguite sui

campioni *as-built* e trattati termicamente per valutarne variazioni in termini microstrutturali. Contestualmente, sono state studiati sia la variazione di densità, sia fenomeni di precipitazione promossi, in primo luogo, dalla piattaforma pre-riscaldata e, in secondo luogo, dai trattamenti termici eseguiti sui campioni *as-built*.

Differenti campioni in Ti6Al4V stampati tramite la tecnologia *Laser-Powder Bed Fusion* in differenti orientazioni sono stati analogamente analizzati sia in condizioni *as-built* sia dopo trattamenti termici. Nell'ottica di omogeneizzare l'anisotropia delle proprietà meccaniche, due differenti trattamenti termici di ricottura, rispettivamente alle temperature di 704 °C e 740 °C sono stati investigati per mezzo di analisi di microscopia elettronica, EBSD e XRD. Nonostante I differenti raffreddamenti tra i due trattamenti termici di ricottura, e il conseguente effetto di *coarsening* delle fasi α (+ 23 %), non è stata rilevata nessuna variazione in termini di proprietà meccaniche. Analisi SEM ed EBSD non hanno evidenziato orientazioni preferenziali delle stesse fasi α, ma ha messo in luce che la stessa fase α segue le stesse orientazioni descritte dalla martensite da cui si trasforma durante il trattamento. Un effettivo decremento delle proprietà tensili è avvenuto dopo il trattamento termico di solubilizzazione a 1050 °C × 60 min, dove la microstruttura ricristallizzata decrementa la resistenza ultima a trazione sino a 925 MPa e lo snervamento sino a 825 MPa. D'altro canto, non è stato mostrato un significativo aumento dei valori di duttilità molto probabilmente per la formazione dell'α-*case layer*, il quale si è formato grazie alla diffusione di ossigeno nella superficie esterna dei campioni durante solubilizzazione. Nello stesso tempo, nonostante il medesimo raffreddamento in argon (60 min), i differenti spessori dei campioni hanno indotto differenti velocità di raffreddamento e, conseguentemente, differenti morfologie microstrutturali a temperatura ambiente. Infine, il processo di sabbiatura ha diminuito i valori di rugosità superficiale (– 50 %), ma ha aumentato la deformazione plastica nella superficie esterna dei campioni grazie all'impatto delle spere in vetro sulla stessa superficie. Nessuna variazione in termini di proprietà tensili è stato rilevato dopo il processo di sabbiatura.

In relazione alla lega AlSi10Mg in condizioni *as-built* e post trattamento termico, le correlazioni tra la microdurezza Vickers e le proprietà tensili possono essere ben approssimante con le equazioni di Cahoon. Dalla comparazione dei valori reali e di quelli calcolati considerando i valori di snervamento, è stato ottenuto un fattore di correzione di 0.891 da inserire nell'equazione di Cahoon. D'altro canto, i campioni in Ti6Al4V, trattati termicamente a 704 °C e 740 °C, hanno mostrato una discrepanza tra gli stessi valori di durezza reali e quelli calcolati di circa il 21–22 %. Quindi, le differenti orientazioni delle fasi α incrementano del 21–22 % le durezze che possono essere ottenute utilizzando l'equazione di Cahoon.

ACKNOWLEDGEMENTS

I would like to express sincere gratitude to my estimated supervisor, professor Emanuela Cerri, for her support and advice during my PhD study and research activities. Her guidance and teaching skills helped me in my personal and professional growth as a PhD student and, secondly, as a postdoctoral researcher.

My sincere thank also goes to professor Giovanni Bolelli who has helped with my PhD thesis through SEM and XRD measurements. I also would like to thank Beam-it for providing the material.

Additionally, I would like to extend my sincere thanks to Federico for his constant encouragement and unwavering support during my PhD course. He also helped me in my personal and professional growth solving many of my doubts, anxieties, and fears.

I would like to express my gratitude to my parents and especially to my sweet sister for always helping me every step of the way and for their keen interest in my academic achievements.

I am highly thankful to my friend Alessandro for the English revision of the present PhD thesis. Lastly, my special thanks to Giulia who directly or indirectly supported me every step of the way.

[*This page intentionally left blank*]

PUBLICATIONS

- Ghio, E.; Cerri, E. Aging response in Selective Laser Melted AlSi10Mg alloy as function of distance from substrate plate. *Mater. Sci. Forum.* **2021**, *1016*, 476–480. https://doi.org/10.4028/www.scientific.net/MSF.1016.476
- Cerri, E.; Di Giovanni, M.T.; Ghio, E. A study of intermetallic phase stability in Al-Si-Mg foundry alloy: the role of Cu additions. *Metall. Ita.* **2020**, *7–8*, 37–47.
- Cerri, E.; Ghio, E. Effect of distance along the build axis on mechanical properties and microstructure in AlSi10Mg SLM alloy. *Mater. Sci. Forum.* **2021**, *1016*, 309–314. https://doi.org/10.4028/www.scientific.net/MSF.1016.309
- Cerri, E.; Ghio, E. AlSi10Mg alloy produced by Selective Laser melting: relationships between Vickers microhardness, Rockwell hardness and mechanical properties. *Metall. Ita.* **2020**, *7–8*, 5–17.
- Cerri, E.; Ghio, E.; Bolelli, G. AlSi10Mg alloy manufactured by single and multi-laser Selective Laser Melting: effect of the distance from the build platform on mechanical properties and microstructure. *J. Mater. Eng. Perform.* **2021**, *30*, 4981–4992. https://doi.org/10.1007/s11665-021-05577-8
- Cerri, E.; Ghio, E. Effect of friction stir processing at high rotation rate on aging of a HPDC Mg9Al1Zn. *Metals.* **2021**, *10(8)*, 1014. https://doi.org/10.3390/met10081014
- Paoletti, C.; Cerri, E.; Ghio, E.; Santecchia, E.; Cabibbo, M.; Spigarelli, S. Effect of low-temperature annealing on creep properties of AlSi10Mg alloy produced by Additive Manufacturing: experiments and modelling. *Metals.* **2021**, *11(2)*, 179. https://doi.org/10.3390/met11020179
- Cerri, E.; Ghio, E. Work hardening in heat-treated AlSi10Mg alloy manufactured by single and double laser selective laser melting: effects of layer thickness and hatch spacing. *Materials*. **2021**, *14(17)*, 4901. https://doi.org/10.3390/ma14174901

Publications

- Ghio, E.; Cerri, E. Additive manufacturing of AlSi10Mg and Ti6Al4V lightweight alloys via laser powder bed fusion: A review of heat treatments effects. *Materials*. **2022**, *15(6)*, 2047. https://doi.org/10.3390/ma15062047
- Cerri, E.; Ghio, E. Aging Profiles of AlSi7Mg0.6 and AlSi10Mg0.3 Alloys Manufactured via Laser-Powder Bed Fusion: Direct Aging *versus* T6. *Materials.* **2022**, *15(17)*, 6126. https://doi.org/10.3390/ma15176126
- Cerri, E.; Ghio, E. Defect-correlated mechanical properties of selective laser melted Al-Si-Mg alloy with post process heat treatments. *J. Mater. Eng. Perform.* **2022**, *31*, 8047–8067. https://doi.org/10.1007/s11665-022-06874-6
- Cerri, E.; Ghio, E.; Bolelli, G. Effect of surface roughness and industrial heat treatments on the microstructure and mechanical properties of Ti6Al4V alloy manufactured by laser powder bed fusion in different built orientations. **2022**, *851C*, 143635. https://doi.org/10.1016/j.msea.2022.143635
- Ghio, E.; Cerri, E.; Riccio, M.; Sisti, J. Mechanical properties and microstructure of Ti6Al4V Extra Low Interstitial alloy produced via laser and electron additive manufacturing processes. *Metall. Ita.* **2022**, *10*, 69–83.
- Cerri, E.; Ghio, E.; Bolelli, G. Ti6Al4V-ELI Alloy Manufactured via Laser Powder-Bed Fusion and Heat-Treated below and above the β-Transus: Effects of Sample Thickness and Sandblasting Post-Process. *Appl. Sci.* **2022**, *12(11)*, 5359. https://doi.org/10.3390/app12115359

In international conferences proceedings:

- Ghio, E.; Cerri, E. Aging response in Selective Laser Melted AlSi10Mg alloy as function of distance from substrate plate. *Mater. Sci. Forum*. **2021**, *1016*, 476–480. https://doi.org/10.4028/www.scientific.net/MSF.1016.476
  Accepted for the International conference on Processing & Manufacturing of advanced materials (Thermec'2021).
- Cerri, E.; Ghio, E. Effect of distance along the build axis on mechanical properties and microstructure in AlSi10Mg SLM alloy. *Mater. Sci. Forum.* **2021**, *1016*, 309–314. https://doi.org/10.4028/www.scientific.net/MSF.1016.476
  Accepted for the International conference on Processing & Manufacturing of advanced materials (Thermec'2021).

In national conferences proceedings:

- Ghio, E.; Di Giovanni, M.T.; Rimoldi, T.; Cerri, E. Stabilità delle fasi intermetalliche di alluminio commerciale da fonderia Al-Si-Mg: il ruolo della percentuale di Cu. Poster accepted for 37th AIM conference.
- Cerri, E.; Ghio, E. Durezze Vickers, Rockwell e proprietà meccaniche: correlazioni per una lega AlSi10Mg prodotta per Selective Laser Melting. Accepted for 38th AIM conference.
- Cerri, E.; Ghio. E. Ottimizzazione di trattamenti termici non-convenzionali per campioni di AlSi10Mg prodotti per Selective Laser Melting. Accepted for 38th AIM conference.
- Ghio, E.; Cerri, E. Revisione degli effetti di differenti trattamenti termici sulla lega AlSi10Mg prodotta per Laser Powder Bed Fusion. Accepted for 39th AIM conference.
- Cerri, E.; Ghio, E. Effetto della sabbiatura e del trattamento termico *over* β-transus su campioni in Ti6Al4V-ELI prodotti tramite *Laser Powder Bed Fusion*. Accepted for 39th AIM conference.

[*This page intentionally left blank*]

INDEX

ABSTRACT VII
SOMMARIO IX
ACKNOWLEDGEMENTS XI
PUBLICATIONS XIII
INDEX XVII
PART 1 23
CHAPTER 1 Introduction 25
1.1. The Aims and Novelty of this Thesis 25
1.2. Thesis Structure 26
1.3. Metallurgical Aspects and Heat Treatments of Al-Si-Mg 29
1.4. Metallurgical Aspects and Heat Treatments of Ti-Al-V 34
1.5. The Additive Manufacturing Process 40
Process Parameters 42
1.6. Experimental Procedure 50
1.6.1. Al and Ti Alloys Manufactured via L-PBF 50
1.6.2. The Microstructural Characterization 53
1.6.3. The Mechanical Properties Characterization 55
CHAPTER 2 Summary of Results and Discussion from the Articles 59
2.1. Microstructural Analysis 59
2.1.1. AlSi7Mg and AlSi10Mg L-PBFed Alloys 59
2.1.2. Ti6Al4V-ELI L-PBFed Alloy 66
2.2. Mechanical Properties Optimization 71

INDEX

2.2.1. AlSi7Mg and AlSi10Mg L-PBFed Alloys 71
2.2.2. Ti6Al4V-ELI L-PBFed Alloy 80
2.3. Relationships between Vickers Microhardness and Tensile Strength .. 86
2.3.1. Theoretical Background 86
2.3.2. Empirical Correlations: (HV-UTS), (HV-YS) and (HV-HRF)..... 88
CHAPTER 3 Main Conclusions from the Articles 91
3.1. As-Built and Heat-Treated AlSi7Mg and AlSi10Mg Alloys..... 91
3.2. As-Built and Heat-Treated Ti6Al4V Alloys..... 93
3.3. Relationships between HV Microhardness, UTS, YS and HRF. 94
3.4. Future Works 95
LIST OF FIGURES..... 97
LIST OF TABLES..... 101
ACRONYMS..... 103
PART 2 105
ARTICLE 1 107
Effect of the Distance from Build Platform and Post-Heat Treatment of AlSi10Mg Alloy Manufactured by Single- and Multi-Laser Selective Laser Melting 109
Abstract 109
1. Introduction..... 109
2. Materials and Methods 111
3. Results and Discussion 113
3.1. Microstructure and Mechanical Properties of As-Built AlSi10Mg Samples 113
3.2. Microstructure and Mechanical Properties of Treated AlSi10Mg Samples 121
4. Conclusions 126
ARTICLE 2 129
Aging Profiles of AlSi7Mg0.6 and AlSi10Mg0.3 Alloys Manufactured via Laser-Powder Bed Fusion: Direct Aging versus T6 131
Abstract 131

1. Introduction 131
2. Materials and Methods 134
3. Results 138
3.1. Density Analysis 138
3.2. Microstructural Analysis 140
3.3. Microhardness Profiles in As-Built and Direct Aged Conditions 143
3.4. Microhardness Profiles After Solubilization and T6 Heat-Treatments 146
3.5. Mechanical Properties 147
4. Discussion 149
4.1. Density Analysis 149
4.2. Effects of Direct Aging Heat Treatments 149
4.3. Effects of Solubilization and T6 Heat Treatments 153
5. Conclusions 156
ARTICLE 3 159
Aging Response in Selective Laser Melted AlSi10Mg Alloy as Function of Distance from the Substrate Plate 161
Abstract 161
ARTICLE 4 163
Work Hardening of Heat-Treated AlSi10Mg alloy Manufactured by Single and Double Laser Selective Laser Melting: Effects of Layer Thickness and Hatch Spacing 165
Abstract 165
1. Introduction 165
2. Materials and Methods 168
3. Results and Discussion 170
3.1. Microstructure 170
3.2. Mechanical Properties 175
4. Conclusions 189
ARTICLE 5 191
Defect-Correlated Vickers Microhardness of Al-Si-Mg Alloy Manufactured by Laser Powder Bed Fusion with Post process Heat Treatments 193
Abstract 193
1. Introduction 194
2. Materials and Methods 196

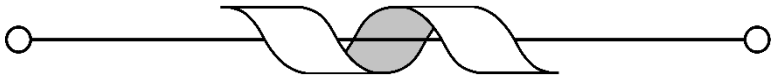
INDEX

3. Results 199
3.1. Microstructure and Porosities Before and After Heat Treatments 199
3.2. Analysis of Vickers Microhardness and Mechanical Properties 211
4. Conclusions 217
Appendix A 218
ARTICLE 6 221
Effect of Surface Roughness and Industrial Heat Treatments on the Microstructure and Mechanical Properties of Ti6Al4V Alloy Manufactured by Laser Powder Bed Fusion in Different Built Orientations 223
Abstract 223
ARTICLE 7 225
Ti6Al4V-ELI Alloy Manufactured via Laser Powder-Bed Fusion and Heat-Treated below and above the β-Transus: Effects of Sample Thickness and Sandblasting Post-Process 227
Abstract 227
1. Introduction 227
2. Materials and Methods 230
3. Results 233
3.1. Microstructure and Surface Roughness 233
3.2. Mechanical Properties 239
4. Discussion 243
5. Conclusions 248
ARTICLE 8 251
Effect of Low-Temperature Annealing on Creep Properties of AlSi10Mg Alloy Produced by Additive Manufacturing: Experiments and Modelling 253
Abstract 253
1. Introduction 253
1.1. AlSi10Mg Alloy Produced by Additive Manufacturing: Main Structural Features 253
1.2. AlSi10Mg Alloy Produced by Additive Manufacturing: Effect of Stress Relieving/Low Temperature Annealing 254
1.3. AlSi10Mg Alloy Produced by Additive Manufacturing: Creep Response 258
2. Materials and Methods 260

3. Results 260
4. Discussion 262
4.1. Analysis of the Effect of Low-Temperature Annealing on Creep Response 262
4.2. Modelling the Effect of Low-Temperature Annealing on Creep Response 263
5. Conclusions 266
Appendix A 267
Appendix B 269
ARTICLE 9 271
AlSi10Mg Alloy Produced by Selective Laser Melting: Relationship between Vickers Microhardness, Rockwell Hardness and Mechanical Properties 273
Abstract 273
1. Introduction 273
2. Material and Methods 276
3. Results and Discussions 277
3.1. Relationship between HV and HRF 277
3.2. Relationship between Strength and Hardness 281
4. Conclusions 286
REFERENCES 287

[*This page intentionally left blank*]

PART 1



[*This page intentionally left blank*]

CHAPTER 1

Introduction

1.1. The Aims and Novelty of this Thesis

The present thesis aims to evaluate the optimizations of different heat treatments (HTs) to obtain the best and more homogenized mechanical properties of AlSi7Mg, AlSi10Mg and Ti6Al4V alloys manufactured via Laser-Powder Bed Fusion (L-PBF). *Table 1* carefully summarizes the objectives and methodologies for each lightweight alloy considered.

The objectives related to aluminium alloys are:

- Evaluating the effects induced on both the microstructure and mechanical properties by the distance from the build platform (BP) pre-heated at 150 °C (ARTICLE 1, ARTICLE 2, ARTICLE 3, ARTICLE 4 and ARTICLE 5)
- Study of the impact induced, firstly, by the single and multi-laser machine set-up and, secondly, by the process parameters variation on AlSi10Mg (ARTICLE 1, ARTICLE 2 and ARTICLE 4)
- Analysis of different direct aging heat treatments to obtain an optimization and homogenization of the mechanical properties after the L-PBF process (ARTICLE 1, ARTICLE 2, ARTICLE 3 and ARTICLE 4)
- Analysis of T6 heat treatments characterized by different time-temperature conditions to evaluate the minimum worsening effects on the mechanical properties (ARTICLE 2 and ARTICLE 4).
- Creep properties evaluation of the AlSi10Mg at the direct aging temperature (ARTICLE 8).
- Analysis of the relationships between the Vickers microhardness and the tensile properties (ARTICLE 9).

The thesis objectives related to titanium alloy are (ARTICLE 6 and ARTICLE 7):

- Evaluating the microstructure and mechanical properties related to different build orientations (0°, 45°, 90°) and in different heat-treated conditions.
- Analysis of the sample surface before and after a sandblasting process and its effects induced on the mechanical properties.
- Evaluation of the effects induced on microstructure and mechanical properties by different aging heat treatments.
- Determining the sample thickness impact on the microstructure after different heat treatments performed above and below the β-transus.

The importance of the present thesis lies within the need to develop heat treatments to optimize the mechanical performance of AlSi7Mg, AlSi10Mg and Ti6Al4V samples manufactured via L-PBF. In relation to the aluminium alloys, the crucial problem is linked to the effects induced by the pre-heated BP during the manufacturing process and the consequent optimization of the tensile and creep properties. Direct aging and T6 heat treatments will be analysed and compared to each other. Finally, new correlations between HV microhardness and yield and ultimate tensile strength will be proposed. In the same context, the fundamental and empirical relationships between the HV and tensile strength will also be studied considering the α-phase orientation in the heat-treated Ti6Al4V samples. As regards this $\alpha + \beta$ Ti alloy, heat treatments below (704 °C and 740 °C) and above (1050 °C) the β-transus temperature will be evaluated to satisfy the current standard specification within the automotive and aerospace industries. The effects induced by different heat build orientations (90°, 45°, $0°_{xz}$, $0°_{xy}$) and a sand-blasting process performed on heat-treated Ti6Al4V extra low interstitial (ELI) samples were also carefully studied.

1.2. Thesis Structure

With the purpose of building up, firstly, a comprehensive background of the L-PBF process and the metallurgical aspect of AlSi7Mg, AlSi10Mg and Ti6Al4V alloys and, secondly, the results obtained during the doctoral course, the present thesis will be organized as shown in *Figure 1*.

Table 1. Mapping of thesis aims, objectives and technologies.

Aims: *the present thesis aims to evaluate the optimizations of different heat treatments to obtain the best and more homogenized mechanical properties of AlSi10Mg, AlSi7Mg and Ti6Al4V alloys manufactured via Laser-Powder Bed Fusion.*			
Materials:	***AlSi10Mg***	***AlSi7Mg***	***Ti6Al4V-ELI***
Objectives:	• Microstructural analysis • Mechanical characterization of as-built and heat-treated samples in relation to: **1.** single and double-laser machine set up, **2.** distance from the pre-heated BP, **3.** process parameters variation • Pore's analysis • Optimization of direct aging and T6 HTs	• Microstructural analysis • Mechanical characterization of as-built and heat-treated samples in relation to: **1.** single and double-laser machine set up, **2.** distance from the pre-heated BP • Optimization of direct aging and T6 heat treatments	• Microstructural analysis • Mechanical characterization of heat-treated samples in relation to: **1.** build orientations, **2.** sand-blasting process. • Analysis of industrial heat treatments.
Methodologies:	• Optical and scanning electron microscopy with image analysis. • XRD analysis. • Tensile test at room temperature. • Microhardness and hardness measurements. • Creep test.	• Optical and scanning electron microscopy with image analysis. • XRD analysis. • Tensile test at room temperature. • Microhardness measurements.	• Optical and scanning electron microscopy with image analysis. • XRD and EBSD analysis. • Tensile test at room temperature. • Microhardness and surface roughness measurements. • Creep test.

Chapter 1: Introduction

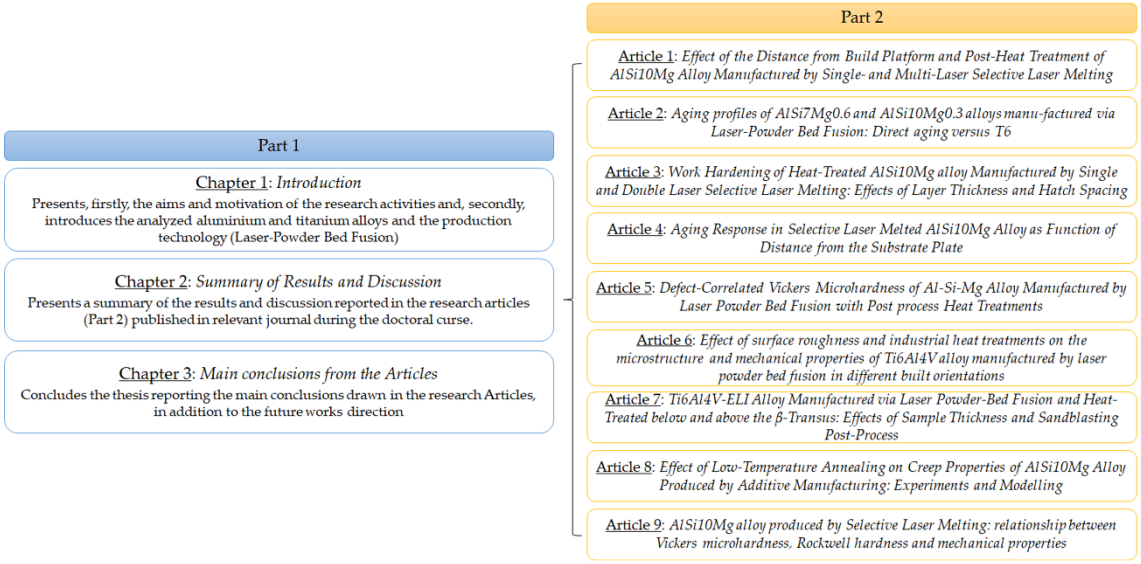


Figure 1. Thesis structure.

The present Part 1 is composed of the "Introduction" (Chapter 1), "A summary of the Results and discussion" (Chapter 2), and "Main Conclusions from the Articles" (Chapter 3).

The first chapter aims to focus on the purposes and novelty of the present doctoral thesis, and to build a basis better to understand the research activities performed on AlSi7Mg, AlSi10Mg and Ti6Al4V alloys. It also presents a brief description regarding the Additive Manufacturing (AM) technology and Laser-Powder Bed Fusion process. This section was extracted by:

Ghio, E.; Cerri, E. Additive Manufacturing of AlSi10Mg and Ti6Al4V lightweight Alloys via Laser Powder Bed Fusion: A Review of Heat Treatment Effects. *Materials*. **2022**, *15(6)*, 2047. https://doi.org/10.3390/ma15062047

The second chapter presents the most significant results obtained by the research activities performed during the doctoral course and published in relevant journals, which are focused on subject areas of material science and metallurgy.

The third chapter summarizes the conclusions from the published research articles related to the aims of the present thesis, and it presents possible future works.

Part 2 exhibits the research articles that support and demonstrate the results discussed in Chapter 2. Only the manuscripts licensed under the CC-BY 4.0 (https://creativecommons.org/licenses/by/4.0) are completely included.

1.3. Metallurgical Aspects and Heat Treatments of Al-Si-Mg

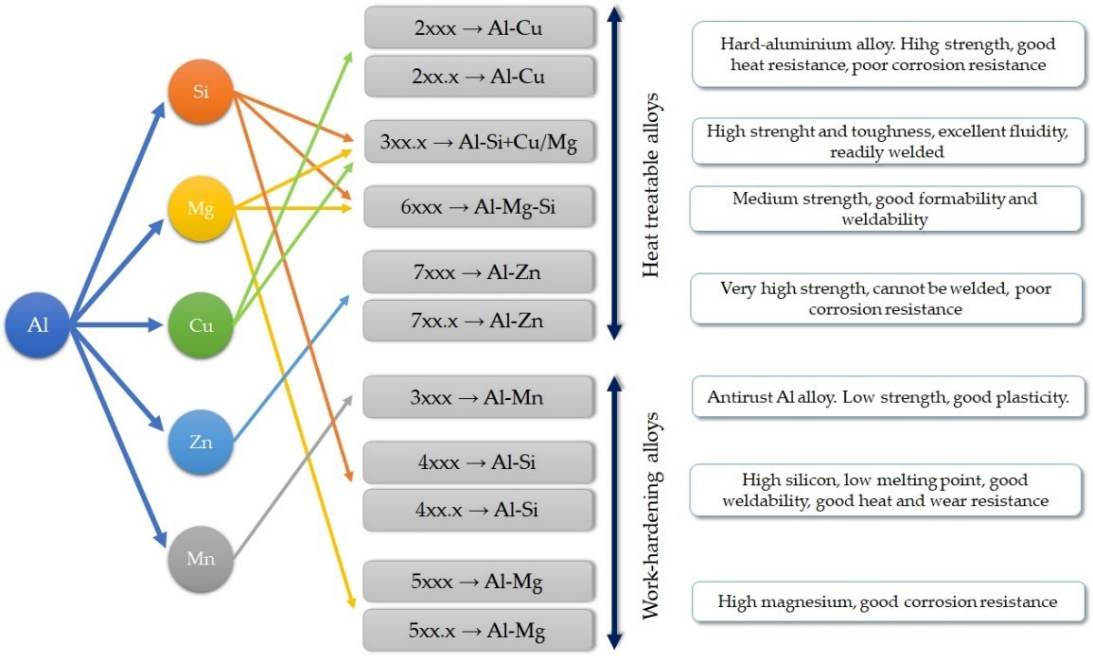
Aluminium (Al) is a soft material characterized by high specific strength, excellent formability, high corrosion resistance, and high electrical and thermal conductivity [1,2]. It is the world's most abundant metal (~ 8 %) and it can be extracted from bauxite mineral through the Bayer and Hall-Heròult processes [2,3]. Focusing on pure aluminium, its high specific strength is only conferred by its low density (ρ = 2.7 g/cm^3); in fact, the tensile strength varies from 70 to 175 MPa after cold work strengthening mechanism [1].

In order to increase the industrial applications of the pure Al, its tensile strength, fatigue resistance, fracture toughness and corrosion resistance must be improved. The first step is to enrich the chemical composition of the pure Al, the second one is to perform different HTs where possible. As a matter of fact, the different chemical elements allow to separate the cast (1–8xx.x) and wrought (1–8xxx) Al alloys (*Figure 2*) in heat-treatable and work-hardening alloys. In the first case, Cu, Mg+Si, Li and Zn increase the heat treatment capability thanks to their enlargement effects on the solid solution region. In fact, these alloys show a high response to the precipitation phenomena during the aging HT. In the second case, Mn, Si and Mg, with Si and Mg not combined, allow to increase the mechanical properties only through the strain hardening mechanisms. In this case, the applicable HTs do not confer a strengthening contribution [2].

The AlSi7Mg and AlSi10Mg[50,90] alloys, which are discussed in the present thesis, basically belong to the heat-treatable Al-Si+(Mg) ternary system where the Si content can vary from 0.8–1.2 % of 4006 to 18.5–21.5 % of 4019 [4,5].

Generally, the phase diagram of the Al-Si system, drawn in *Figure 3*, adequately describes the Al-Si+(Mg) ternary system. As all phase diagrams of two metals only partially soluble in the solid state, it presents a eutectic point, which is placed at (12.6 %, 577 °C). The 12.6 % amount of Si separates the hypoeutectic (AlSi7Mg and AlSi10Mg) to the hypereutectic alloys, while the 577 °C value describes the minimum temperature at which this binary system melts. Following the liquidus curve, the eutectic temperature can increase up to ~ 660 °C, temperature at which the pure Al starts the solidification process by crystallizing in face-centred cubic (fcc) lattice structure (12 of coordination number and 0.74 of APF) [2,6–8].

The same phase diagram is also characterized by a close solid solution region (yellow zone in *Figure 3*) in which the maximum Si solubility into α-Al matrix is 1.65 %.



Cast	Alloying elements	Wrought	Alloying elements
1xx.x	Pure aluminium (99.xx%)	1xxx	Pure aluminium (99.xx%)
2xx.x	Cu	2xxx	Cu
3xx.x	Mg+Si+(Cu and/or Mg)	3xxx	Mn
4xx.x	Si	4xxx	Si
5xx.x	Mg	5xxx	Mg
6xx.x	- - - Not used - - -	6xxx	Mg+Si
7xx.x	Zn1	7xxx	Zn
8xx.x	Tin	8xxx	Others

Figure 2. Wrought and cast Al alloys families classified through their principal alloying elements.

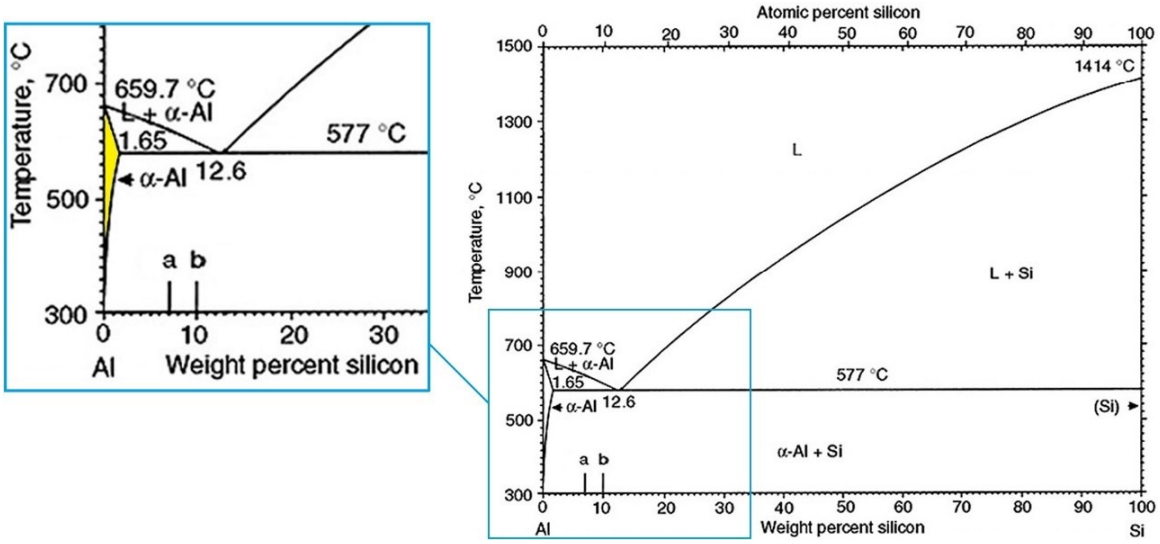


Figure 3. Phase diagram of Al-Si binary system (Adapted from Reference [6]).

For this reason, Si phase with diamond cubic crystal structure can precipitate with a polygonal or a plate-like morphology during the high-temperature or low-temperature reactions, respectively (*Figure 4*) [9].

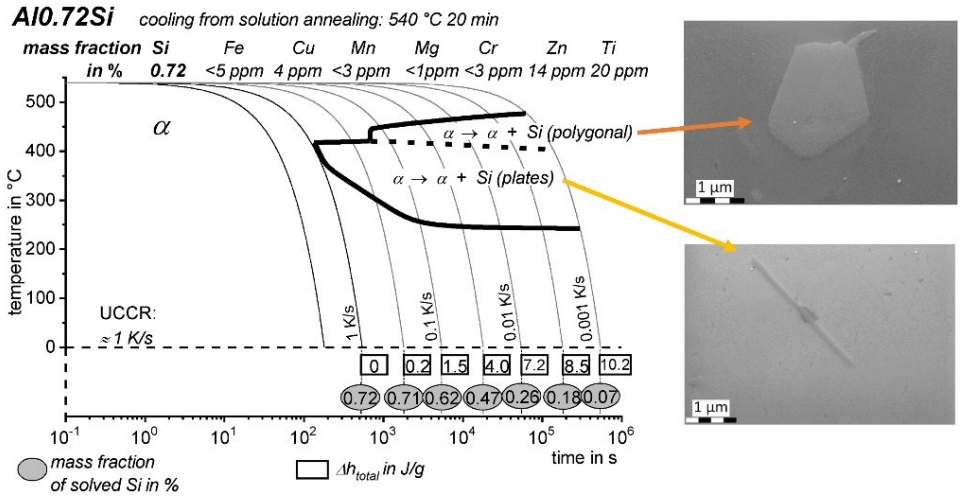


Figure 4. CCT curves of Al0.72Si alloy with SEM micrographs highlighting the Si precipitates with polygonal and plate-like morphologies (Adapted from Reference [9]).

Despite this precipitation during the cooling paths from the solubilization temperature, the biggest disadvantage of the Al-Si alloys is the lack of heat treatable capability. As a matter of fact, the highest contributions to improve the mechanical properties are conferred, firstly, by the cold working through the strengthening induced by the plastic deformation and, secondly, by the presence of dispersoid particles [2,10]. Lastly, the size and morphology of Si eutectic affect control the mechanical properties especially in the case of the cast alloys, in which the strain hardening is not generally applied [11,12].

In order to improve the heat treatment capability, the chemical composition of the Al-Si alloys must be enriched with a low (< 0.6 %) percentage of Mg. In this case, the Al-Si-Mg ternary system always belongs to 4xxx for the wrought alloy, but to 3xx.x for the cast alloy (*Figure 2*). Owing to the added Mg, the tensile strength increases thanks to the following precipitation sequence [13] promoted by the direct or artificial aging:

SSS of α-Al → GP zones → cluster → metastable ε'' → metastable ε' → stable ε-Mg_2Si

where the SSS forms different Guinier-Preston (GP) zones, which promote the lower strengthening contribution. The following metastable ε'' precipitates induce an increment in terms of the mechanical properties, and they can show the following chemical compositions: Mg_5Si (*Figure 5a*), $Mg_4Al_3Si_4$ (*Figure 5b*), $Mg_5Al_2Si_4$ (*Figure 5c*), Mg_6AlSi_4 (*Figure 5d*) [14–17].

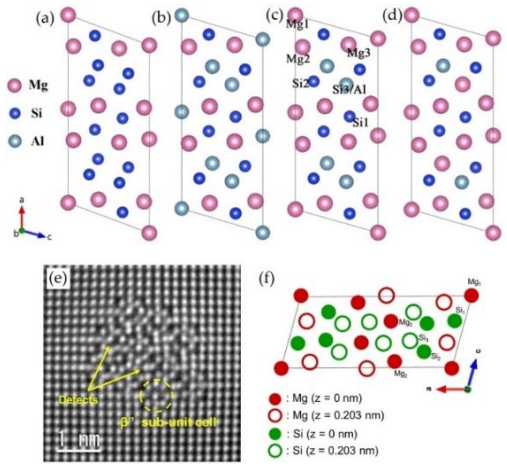


*Figure 5. Atomic models of ε'' precipitate:(**a**) Mg5Si, (**b**) Mg4Al3Si4, (**c**) Mg5Al2Si4, (**d**) Mg6AlSi4 (**f**) Mg5Si6. (**e**) Atomically-resolved STEM image of ε'' precipitate (Adapted from References [16,17]).*

Other authors also proposed the monoclinic Mg_5Si_6 (*Figure 5e,f*) which, firstly, transforms in hexagonal semi-coherent ε' rod and, secondly, in a cubic incoherent ε-Mg_2Si (*Figure 6*) [17].

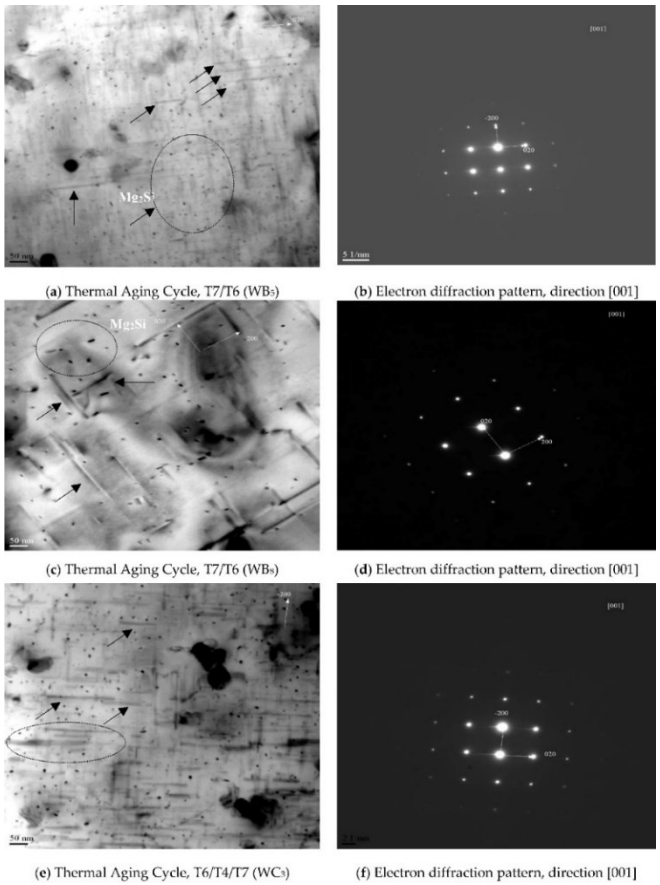


*Figure 6. TEM images showing the formation of different Mg_2Si precipitates (**a**,**c**,**e**) with correlated diffraction patterns, direction [001] (**b**,**d**,**f**) (Reprinted from Reference [17]).*

In this scenario, the highest mechanical properties were reached at the peak aging, in which case semi-coherent ε' precipitates are finely dispersed in α-Al matrix. This metallurgical condition can be achieved during the third step of the following T6 HT (*Figure 7*), which is composed by:

1. Solution heat treatment (SHT) that dissolves the soluble phases and increases the amount of Si and Mg in solid solution. For Al-Si-Mg ternary alloys, the SHT temperature range varies from 500 to 540 °C [2].
2. Quenching that allows to keep the supersaturated solid solution at room temperature.
3. Artificial Aging (AA) treatment (150–200 °C) that controls and promotes the precipitation sequence previously mentioned.

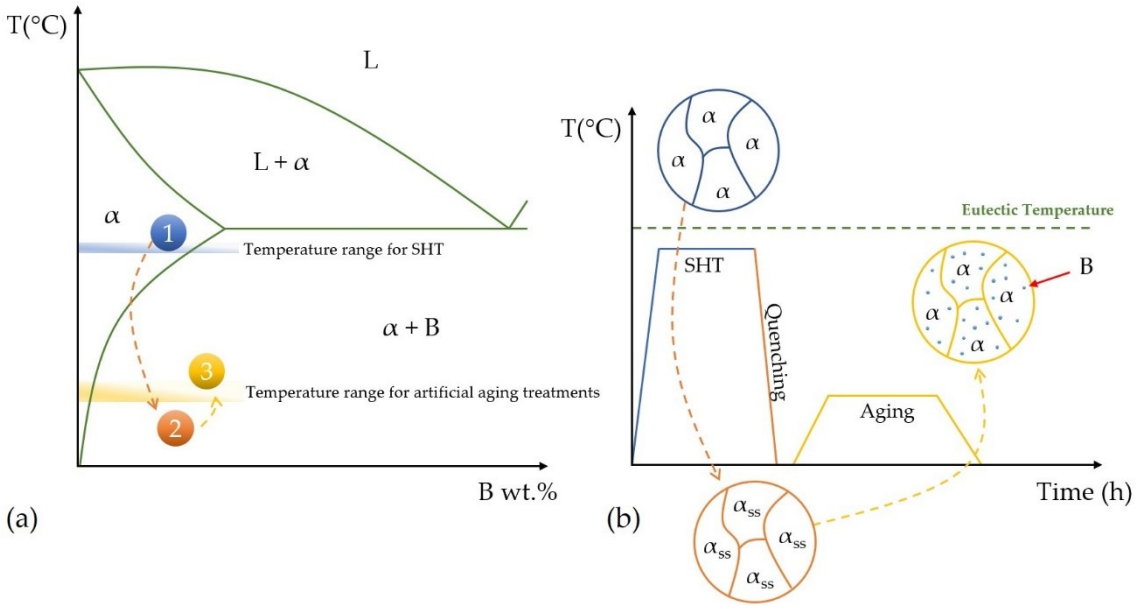


*Figure 7. Precipitation hardening sequence drown in: (**a**) a phase diagram with partial solubility where the temperature ranges of the SHT and artificial aging are illustrated, (**b**) time-temperature diagram of T6 heat treatment.*

Similarly, T4 HT follows the thermic path shown in *Figure 7b*, but the aging occurs at room temperature (natural aging) for long time periods (6–40 days). For this reason, the obtained mechanical properties will be lower than those conferred by the artificial aging (AA) [18].

Other HTs are formed by a partial solubilization + natural aging with (T2) or without (T1) cold working, SHT + cold work + natural aging (T3), partial solution + artificial aging (T5), SHT + stabilizing (T7), SHT + cold work + artificial aging (T8), SHT + artificial aging + cold work (T9), partial solubilization + cold work + artificial aging (T10) [2,19].

From an industrial perspective, Al-Si-Mg alloys can be used not only in automotive and aerospace industry for shipbuilding, mechanical engineering, etc …, but also in biomedical and electrical applications thanks to their reported metallurgical aspects [20,21]

The present thesis will consider the effects of the direct aging (DA, ~ T5) and T6 HTs on the AlSi7Mg and AlSi10Mg alloys. Both belong to 3xx.x series as confirmed by their nominal chemical compositions listed in *Table 2*.

Table 2. Nominal chemical composition (wt.%) of AlSi7Mg and AlSi10Mg alloys.

Alloys	Al	Si	Mg	Fe	Cu	Mn	Ni	Zn	Pb	Sn
AlSi7Mg	Bal.	6.5–7.5	0.45–0.70	≤ 0.19	≤ 0.05	≤ 0.10	-	≤ 0.07	-	-
AlSi10Mg		9.0–11.0	0.20–0.45	≤ 0.55	≤ 0.10	≤ 0.35	≤ 0.05	≤ 0.10	≤ 0.05	≤ 0.05

1.4. Metallurgical Aspects and Heat Treatments of Ti-Al-V

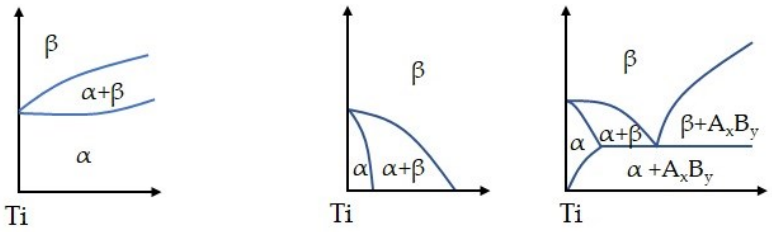
Titanium (Ti) is a lightweight metal (ρ = 4.5 g/cm^3) characterized by excellent corrosion resistance, excellent formability (ductility) and *high* tensile strength if compared to pure aluminium. In fact, yield strength varies from 170 to 500 MPa, while the ultimate tensile strength can also reach 550 MPa. These tensile strengths characterize the commercially pure titanium (CP-Ti) that can be classified with four different grades (1–4) regarding the amount of N (0.03–0.05 %), Fe (0.00–0.50 %) and O (0.18–0.40 %) in addition to C and H that are always constant at 0.08 and 0.015 %, respectively [22,23].

In order to increase and optimize the mechanical properties of pure Ti, its chemical composition can be enriched with different α- and β-stabilizer alloying elements, which generate several Ti alloys (*Figure 8*). The former (Al, N, O, C) expand the α region and increase the creep resistance and the weldability of pure Ti by stabilizing the α-phase at room temperature. On the other hand, the latter (V, Mo, Fe, Cr, Ni, …) stabilize, instead, the β-phase and improve the heat-treatment capability, ductility and the strain rate sensitivity. These properties increase when the amount of alloying elements characterized by β-stabilizer behaviour increases as well. In fact, the amount of β-phase at room temperature increases. To define these effects, the following aluminium and molybdenum equivalent (wt.%) relationships can be considered [24,25]:

$$Al_{eq} = Al + \frac{1}{3}\,Sn + \frac{1}{6}\,Zr + 10\,(O + N) \quad (1)$$

$$Mo_{eq} = Mo + 0.67\,V + 2.9\,Fe + 1.6\,Cr - Al + 0.44\,W + 0.28\,Nb + 0.22\,Ta + 1.25\,Ni + 1.7\,Mn + 1.70\,Co \quad (2)$$

where the alloying elements are grouped in relation to their α- or β-stabilizer behaviour. As a matter of fact, the near-α, α+β, near-β and β alloys can be defined by increasing the Mo_{eq} starting from the unalloyed α-Ti (*Figure 8*).



α	Near-α	α+β	Near-β	β
Unalloyed Ti	Ti-5Al-6Sn-2Zr-1Mo-0.2Si	Ti-6Al-4V Grade 5	Ti-6Al-2Sn-4Zr-6Mo	Ti-8Mo-8V-2Fe-3Al
Grades 1-4	Ti-6Al-2Sn-4Zr-2Mo	Ti-6Al-V-ELI Grade 23	Ti-8Mn	Ti-11.5Mo-6Zr-4.5Sn
Ti-5Al-2.5Sn	Ti-8Al-1Mo-1V	Ti-6Al-4V-2Sn	Ti-35V-15Cr	Ti-13V-11Cr-3Al

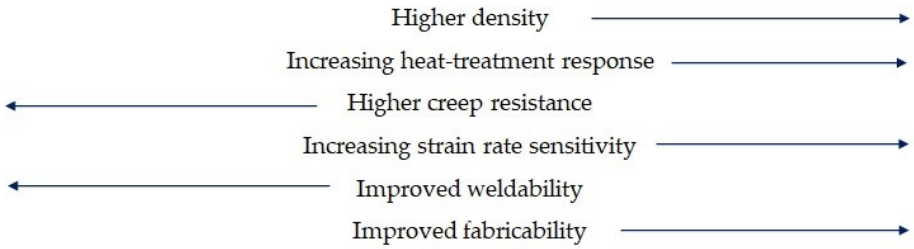


Figure 8. Schematic representation of the effects induced by the α- and β-stabilizer alloying elements on Ti mechanical properties. Some Ti alloys are listed in all categories: α, near α, α+β, near-β and β.

In addition, the percentage of Al_{eq} and Mo_{eq} provides an estimation of the ultimate tensile strength of a considered Ti alloy, as follows [26]:

$$\sigma_u = 235 + 60[Al]_{eq} + 50[Mo]_{eq} \quad (3)$$

where 235 is taken as the ultimate tensile strength of the pure Ti, whereas 60 and 50 are the MPa/wt. % contributions of Al_{eq} and Mo_{eq}, respectively.

A graphical representation of the strengthening effects of the main Ti alloys, using the Eq. (3), is illustrated in *Figure 9*. The orange symbol indicates the Ti6Al4V alloy [26].

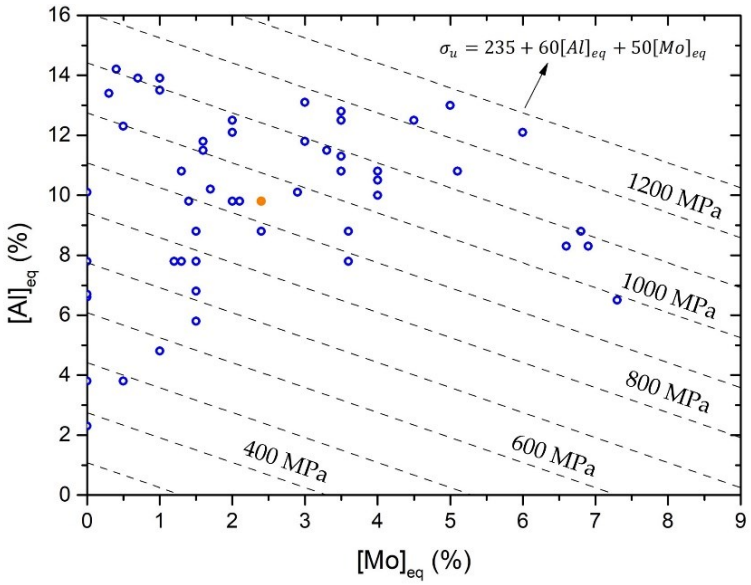


Figure 9. Strengthening diagram of Ti alloys reported in [26] in relation to the Al_{eq} and Mo_{eq} percentage. The orange symbol indicates the α+β Ti6Al4V alloys that is analysed in the present doctoral thesis.

Ti6Al4V (~ 10 % of Al_{eq} and ~ 2.5 % Mo_{eq}) belongs to the Ti-Al-V ternary system and combines the α-stabilizing Al and the β-stabilizing V that confer a α+β microstructure at room temperature (red arrow in *Figure 10*) [22,25]. Ti6Al4V alloy is characterized by a higher quantity of hexagonal closed packed (hcp) α-phase than the face-centred cubic β-phase. In additive manufactured Ti6Al4V alloy, the β-phase even tends even to 0 % at room temperature and in as-built conditions [27].

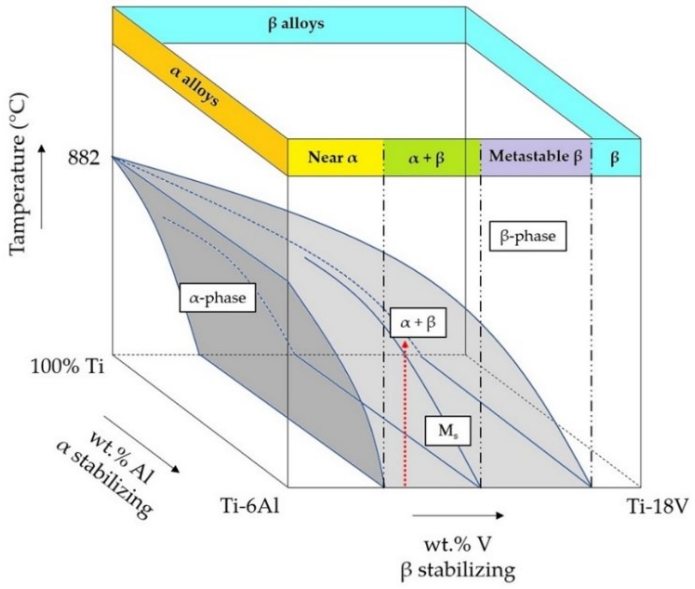


Figure 10. Three-dimensional Ti-6Al-V phase diagram where V varies from 0 to 18 wt.%.

The amount of α-phase remains constant from room temperature to ~ 600 °C, starting from which it decreases in favour of β-phase up to the β-transus temperature, beyond which the α-phase is totally transformed. This transition temperature can be determined through the following equation [28]:

$$T_{\beta_{Tr}} = 882 + 21.1[Al] - 9.5[Mo] + 4.2[Sn] - 6.9[Zr] - 11.8[V] - 12.1[Cr] - 15.4[Fe] + 23.3[Si] + 123[O] \quad (4)$$

where [*alloy element symbols*] represents the wt.% of each alloying element in the chemical composition of the considered Ti alloy [29]. As regards Ti6Al4V, its β-transus temperature is in a range between 977 and 1032 °C which decreases considering the Ti6Al4V-ELI [30–32]. Moreover, the presence of α- and β-stabilizer alloying elements also influences the M_s temperature and, consequently, the formation of both hexagonal α'-martensite and orthorhombic α''-martensite during a fast cooling. In this scenario, the mechanical properties of Ti6Al4V alloy can be still improved through both the strain hardening and different heat treatments like SHT + aging (STA, Solution Treatment and Aging) thanks to its ability to produce an age-hardening response. As a matter of fact, the strengthening takes place through the precipitation of secondary hcp (hexagonal closed packed) α-phase and/or α_2-Ti_3Al [25,33–35].

In order to obtain an aging hardening response, the STA must follow the heat-treatment profile shown in *Figure 11* where the SHT can be performed above (super-transus solubilization) or below (sub-transus solubilization) the β-transus, while the subsequent aging can be performed in the temperature range between 400 and 700 °C [33].

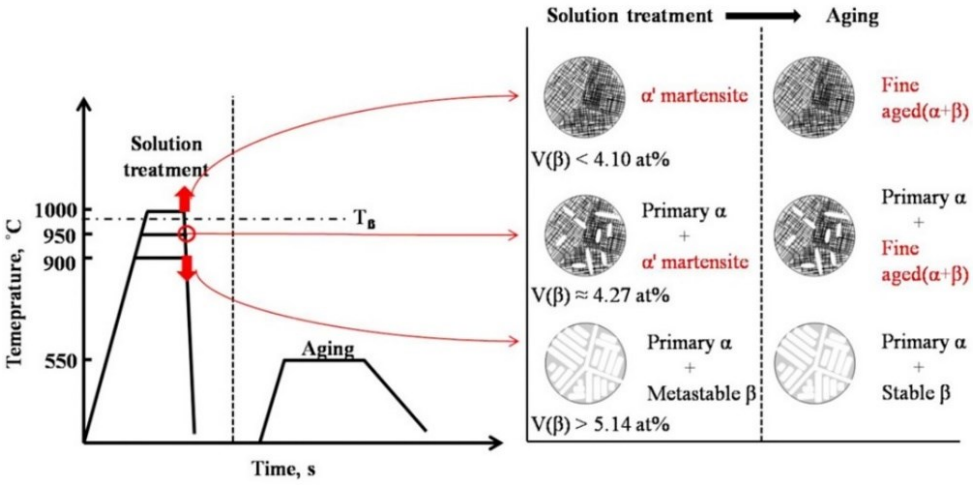


Figure 11. Time-temperature diagram of STA (Reprinted from Reference [36]).

During the SHT, the $\alpha \rightarrow \beta$ transformation starts to take place from 600 °C during the heating, as previously reported, and it only ends when it reaches the β-region, namely by exceeding the β-transus temperature. In fact, only the super-transus solubilization can promote the full transformation in β-phase. In addition to the temperature reached, the main difference between these SHTs is based on the microstructural transformation that occurs during the quenching. The super-transus causes a complete $\beta \rightarrow \alpha'$ martensite transformation (cooling rate < 410 °C/s, [33]), whereas the sub-transus promotes a microstructure formed by primary α-phase, which is not transformed in β-phase during heating, and α' martensite arising from transformed β-phase. If the SHT temperature is too low, the obtained microstructure is composed by primary α-phase and metastable β-phase. Therefore, the following aging treatment does not induce significant effects. In fact, the SSS at room temperature is not guaranteed at low SHT temperatures. Finally, the mechanical properties obtained after the aging HT are strongly influenced by the super- or sub-transus SHT. Firstly, the coarsening effects of the β-grains can occur by increasing the holding time at high SHT temperature; secondly, the untransformed α' martensite makes the ductility behaviour worse. In this scenario, slower cooling rate can be used after SHT to prevent the $\beta \rightarrow \alpha'$ martensite transformation. At the same time, the SSS at room temperature is not guaranteed.

During the aging HT, secondary α-phase precipitates in β-matrix inducing an improvement of the mechanical properties because it hinders the movements of the dislocations [29,37]. Generally, the aging treatments are subdivided into 4 categories: single step at high or at low temperatures, duplex and direct aging heat treatments as exhaustively described by Yumak et al. [38]. In addition, an aging heat treatment performed in the temperature range between 500 and 600 °C promotes the precipitation of α_2-Ti_3Al in the α-laths (*Figure 12*) [33].

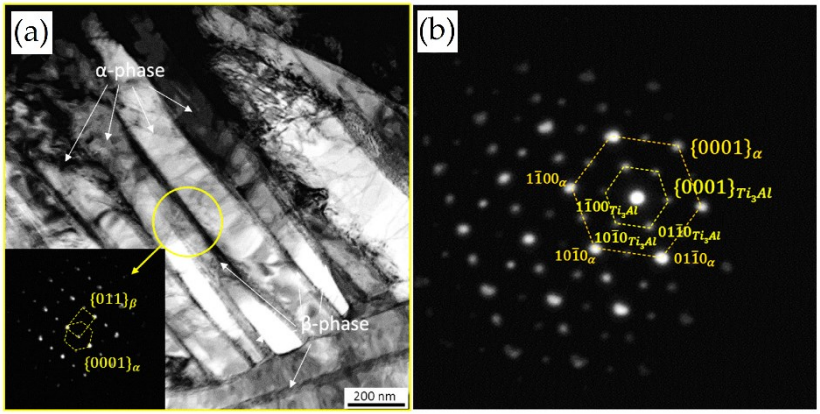


*Figure 12. (**a**) BFTEM (Bright-Field Transmission Electron Microscopy) image shows the α+β ultrafine microstructure, (**b**) SAED patter showing the α_2-Ti3Al precipitate within the α-lath (Reprinted from Reference [33]).*

From an industrial point of view, Ti alloys were widely used not only into aerospace and biomedical fields thanks to their cell biocompatibility; but also in automotive and chemical industries (*Table 3*).

Table 3. Principal uses of the Ti alloys within automotive, aerospace, biomedical and chemical sectors.

Industry sector	Uses	References
Aerospace	Gas turbine engine (components and sheet form for after-burner structures), wings, fuselage as bulkheads/frame, upper shins, helicopter rotors	[22,39]
Automotive	Body panels, connecting rods, valves, rocker arms, suspension turbocharger rotors	
Biomedical	Bone plates, artificial joint prostheses, dental implants, pacemakers, heart valves, surgical instruments, wheelchairs, …	[22,40]
Chemical	Pressure and reaction valves, piping, pumps, tubing, condensers, agitators, filters, …	[22,39]
Marine	Deep-sea submersibles, racing yacht components, fire pumps, ducting, water jet propulsor systems, ship propellers, …	[22,41]

The present thesis will consider the Ti6Al4V-ELI alloy which is characterized by a different nominal chemical composition with respect to the Ti6Al4V (*Table 4*). Lower interstitial contents provide improved ductility and fracture toughness.

Table 4. Nominal chemical composition (wt.%) of Ti6Al4V and Ti6Al4V-ELI alloys.

Alloys	Ti	Al	V	Fe	O	C	N	H
Ti6Al4V	Bal.	5.50–6.50	3.50–4.50	≤ 0.40	≤ 0.20	≤ 0.08	≤ 0.05	≤ 0.015
Ti6Al4V-ELI				≤ 0.25	≤ 0.08			≤ 0.012

1.5. The Additive Manufacturing Process

AM technology is a process opposed to the subtractive manufacturing methodologies because it joins materials to make components from a 3D model, as defined through the ASTM 52900:2015 standard specification [42]. If low-volume and high-value objects (e.g., in aerospace and biomedical fields) are considered, the manufacturing processes belonging to the AM scenario present different advantages as opposed to the conventional subtractive manufacturing (as mentioned in Section 1 – see [33]) [43–48]. In this scenario, another advantage is the ability to print lightweight objects thanks to a complex software system that minimizes the part geometry after a careful engineering analysis. In parallel with the metallurgical sector, other research fields focus their attention on the sample design and the surface geometry to improve the mechanical properties of the manufactured object and the consequent advantages induced by AM [49,50].

Focusing on these processes, the building of 3D metal physical objects takes place through the fusion or bond (e.g., melting, sintering) of the material feedstock, which is in the form of powder and/or filament/wire, joined layer by layer [42]. The different form of the material feedstock subdivides the processes in powder bed fusion (PBF) and direct energy deposition (DED). In the former printing method, a laser or electron beam energy source melts and fuses the powder following the 3D project of the component (*Figure 13a*), while, in the latter method, a nozzle deposits the material feedstock, as shown in *Figure 13b* [42,51–53]

The present review is based on the L-PBF AM process (*Figure 13a*), a technology where the powder bed, deposited on the BP (BP) by a recoater roller or blade, is scanned and melted through a laser beam characterized by a laser power P [W], and generated by one of the following energy sources: Yb:YAG fiber, Nd:YAG, CO_2 laser, infrared, etc. [54]. The moving mirror, controlled by a computer system, deflects the laser source according to the 3D project. Only when a layer is totally scanned and melted, the BP lowers by a quantity equal to the layer thickness (t, [mm]) and the recoater roller or blade spreads a new powder layer. This procedure is repeated until the complete 3D physical object is manufactured [55–57].

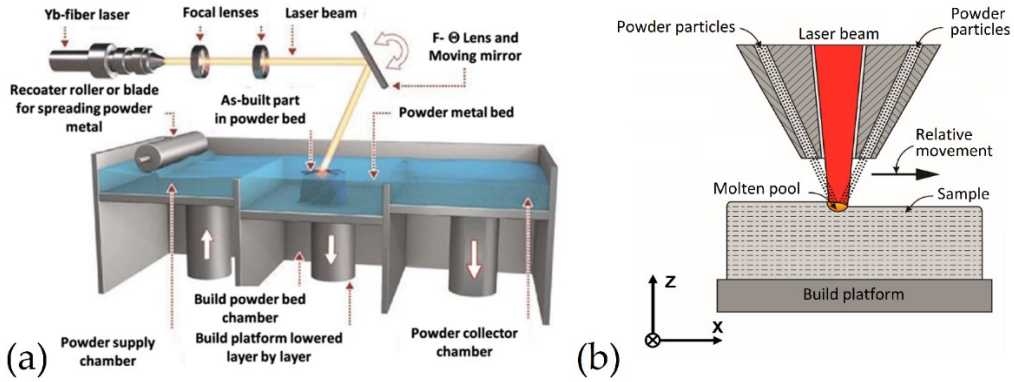


*Figure 13. (**a**) laser powder bed fusion (L-PBF) process; (**b**) direct energy deposition (DED) process (Adapted from References [53,58]).*

During the L-PBF process, the laser beam transmits enough energy to melt the entire layer depth and a portion of the previously solidified layer, guaranteeing the adhesion between them [59]. The molten pool (MP) depth is key to obtaining this adhesion and the absence of defects. Tang et al. [60] illustrated the following criterion to have a full melting:

$$\left(\frac{h}{W}\right)^2 + \left(\frac{t}{D}\right)^2 \leq 1 \tag{5}$$

where h is the hatch spacing [mm], which is the distance between the centre of one laser scan track and the consecutive one (*Figure 14*) [59], W is the width [mm], D is the total depth of the MP [mm], and t is the layer thickness [mm]. The full melting is obtained only if Eq. (5) is satisfied. As a matter of fact, the MP overlaps and the consequent yellow zone shown in *Figure 14* are guaranteed.

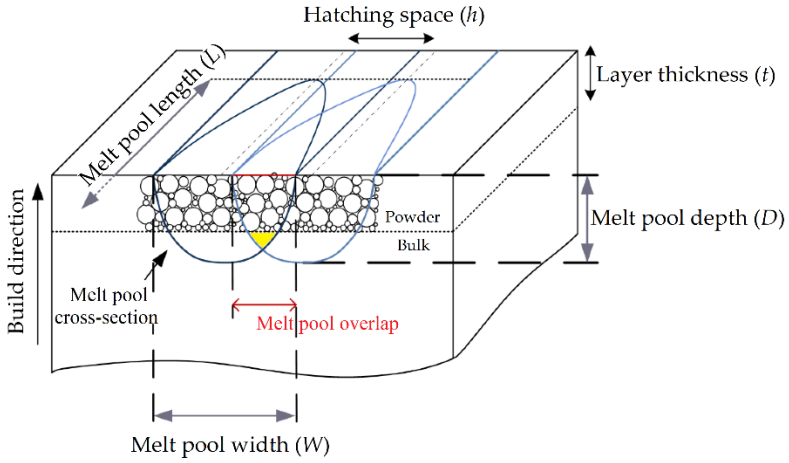


Figure 14. Schematic representation of the interaction between the laser beam source and the powder bed during the L-PBF process highlighting the overlap area between two adjacent laser scan tracks where the principal dimensions are labelled (Reprinted from Reference [61]).

Another important process parameter, in addition to P [W], h [mm] and t [mm] is the scan speed (v, [mm/s]) at which the laser source moves. Combining these parameters, the energy density function (ED, [J/mm^3]) can be defined as follows:

$$ED = \frac{P}{vht} \tag{6}$$

According to the manufacturing requirements, the ED function determines the sample's density and, therefore, characterizes the as-built mechanical properties. *Table 5* shows a wide range of process parameters used to manufacture both AlSi10Mg and Ti6Al4V alloys, highlighting whether the obtained samples are fully dense ($\delta \geq 99.0$ %), or dense ($99.0 < \delta \leq 85$ %) or porous ($\delta < 85.0$ %).

In this scenario, the porous Ti6Al4V samples were often manufactured for biocompatibility requirements into biomedical fields because the cell adhesion and proliferation were increased [62–64].

Process Parameters

The principal process parameters (P, v, h, t), which define the ED function (Eq. (6)), influence microstructure and mechanical properties of AlSi10Mg and Ti6Al4V as-built samples manufactured via L-PBF process [65–67]. As shown in *Figure 15*, they are the only parameters that can be fully controlled, together with the laser source parameters, to obtain a high-quality sample. On the other hand, the other parameters such as environment, material characteristics and parameters of the 3D model can compromise its quality due to their partial controllability.



Figure 15. Factors correlated to the selective laser melting (or L-PBF) and subdivided into controlled and partially controlled (Reprinted from Reference [70]).

Table 5. Principal process parameters values used to manufacture AlSi10Mg and Ti6Al4V samples via L-PBF process.

Materials	*P*, [W]	*v*, [mm/s]	*h*, [µm]	*t*, [µm]	*ED*, [J/mm³]	Fully Dense, Dense, Porous	BR [1], [cm³/h]	References
AlSi10Mg	350	1050	170	50	39	Fully dense	32	[65]
	788	1099	300	60	40	Fully dense	71	[68]
	463, 625, 788, 950	500, 800, 1099, 1400, 1700, 2000	300, 350, 400		17–75	Dense	38–174	
	300, 463, 788	800, 1400, 1700, 2300	300, 350, 400			Porous		
	100	250, 500, 750, 1000	50, 100	40	25–200	Dense	2–14	[69]
	320, 360, 400	600, 750, 900	70.90–116.40	30	145–200	Dense	25–28	[70]
	370	1300	190	30	50	Dense	27	[71]
	240, 260, 320, 360, 400	1200, 1400, 1600, 1800, 2000	36, 40, 45, 51.4, 60	30	111	Fully dense	8–13	[72]
	400, 440	1350, 1500	105	50	38–56	Fully dense	25–28	[73]
	300	1230	105	50	68	Dense	23	
	150	500, 1500, 2500	45, 75, 105	30	74, 95, 222	Fully dense	2–28	[74]
	250	1500	75	30	74	Dense	12	
	150	2500	105, 150	30, 60	9, 13	Porous	28–81	
Ti6Al4V	250	1600	60	30	87	Fully dense	10	[75]
	170	1250	100	30	45	Dense	13	[76]
	200	200	180	50	111	Dense	6	[77]
	157	225	100	50	14	Dense	4	[78]
	100	700	75	30	6	Dense	6	[79]
	260, 280, 300	1000, 1200, 1400	140	30	44–67	Dense	15–21	[80]
	55–95	150–1000	49.5–99	25	148–269	Fully dense	1–11	[81]
	240, 300, 360	800, 1000, 1200	80, 100, 120	40	62.5–94	Dense	9–21	[82]
	200	800	80	30	10	Porous	7	[83]
	240	240	50	30	67	Porous	1	[64]
	100	400	70	50	7	Porous	5	[63]
	90	600	90	30	6	Porous	6	[62]

Table 6 illustrates the type of defects that affect the sample's quality.

Table 6. Defects present into L-PBFed samples: cause, remedy, and effects.

Type of Defect	Cause	Remedy	Effects	References
Lack-of-fusion (LOF)	Inhomogeneous distribution of the powder bed Non-optimization of the *ED* function Lack of material or low energy inducing no complete adherence of the melt to the surrounding material	Reduction in the layer thickness and increase of energy penetration	Decrease in mechanical properties and fatigue resistance	[69,78,84–86]
Keyhole pore	MP instability Non-optimized process parameters	Increase in energy depth penetration and laser power	Decrease in mechanical properties and fatigue resistance	[60,87]
Gas pores	Gas dissolution within the melt material Gas wrapped into the gas atomized particles Entrapment of the gas present into the build chamber Gas flow within the build chamber	Reduction in the layer thickness, and the pressure into the chamber Reduction in the O_2 Re-melting	Loss density, decrease in tensile strength and fatigue resistance. Gas pores are less critical in crack propagation than the LOF	[69,88–93]]
Anisotropy	Build orientation	HTs	Tensile properties correlated to the orientations	[78,94,95]
Preferential evaporation	Temperature-dependent vapor pressure	Reduction in linear energy density rather than the hatch spacing	Alloying elements loss and pore's formation	[96–98]
Residual stress and distortion	High thermal gradient during the L-PBF process	Pre-heated BP Post-process HTs Opportune scan strategy and re-melting Sacrificial material and support structures	Sample distortion if residual stress is higher than the YS Alloying elements loss and pore's formation Loss of tolerance requirement Reduction in fatigue resistance and tensile properties	[99–102]
Balling	Low viscosity of melt material Excess of melt material MP instability: capillarity, Marangoni's effect Splashing of MP due to its high surface temperature	Reduction in *ED* value	Porosity Stress Concentration point Surface quality and roughness Intralayer connection	[81,103–107]

The main types of defects present within a sample manufactured via L-PBF process are lack-of-fusion (LOF), keyhole, and gas pores; each one of these is characterized by a distinct formation mechanism and growth [69,89,98]. Focusing on LOF pores, it can be classified as a defect with partially melted powders (*Figure 16a*) or poor binding defect due to the insufficient melt material during solidification (*Figure 16b*) [108]. De facto, LOF is derived from an improper melting of the powder particles or from the MP instability (as discussed later) due to the inadequate value of the *ED* function.

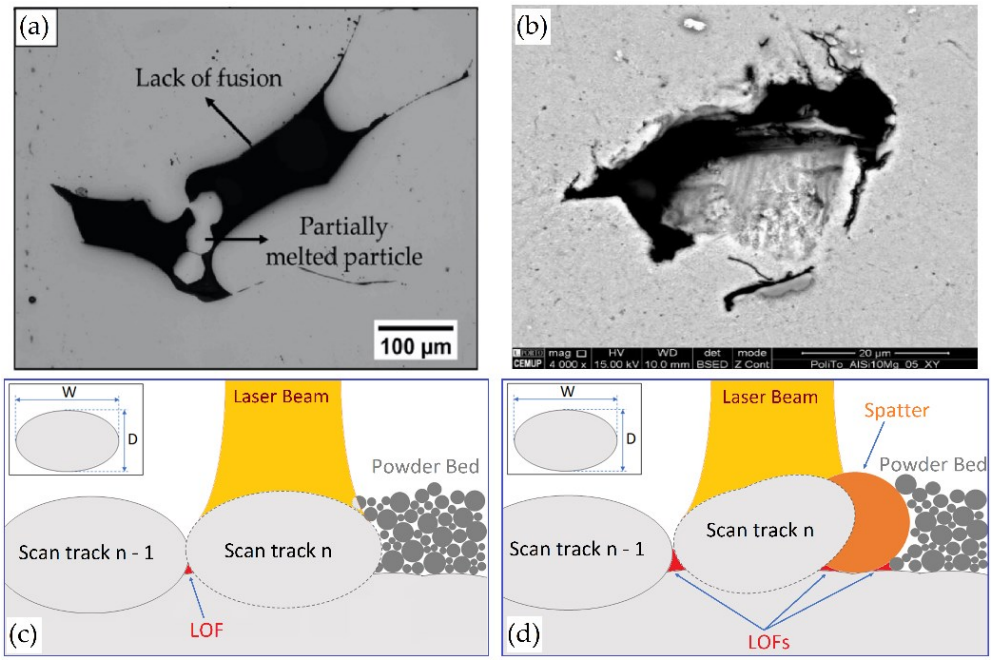


*Figure 16. Lack of Fusion (LOF) pores classifying as pores: (**a**) with un-melted particles, (**b**) poor bonding defects (Adapted from References [109,110]). Schematic representation of the LOF formation during the L-PBF process: (**c**) lack of adequate laser scan tracks overlap; (**d**) presence of defects such as spatter.*

Tang et al. [60] illustrated the typical trend of sample porosity in relation to the *ED* and the variation of the scan speed maintaining the laser power constant (*Figure 17*). In detail, the LOF pores are formed with low *ED* and high scan speed, while high *ED* and low scan speed induce a keyhole pore formation.

Darvish et al. [111], however, showed that the LOF formations are also caused by the imperfect overlap of the laser scan tracks (*Figure 16c*) or by the presence of spatter on the layer surface (*Figure 16d*).

On the other hand, the keyhole and LOF formation mechanisms are very difficult to determine due to the interaction of different physical phenomena (e.g., Maragoni effect, vaporization, recoil pressure, laser reflection) that take place within micron

seconds during the rapid solidification of the MP [87]. In this scenario, Bayat et al. [87] added capillarity pressure as a physical phenomenon to determine the MP instability and the consequent keyhole formation. Thus, the presence of different cold zones characterized by high surface tension and negligible pressure recoil causes the pore's formation. The same results were obtained by [112].

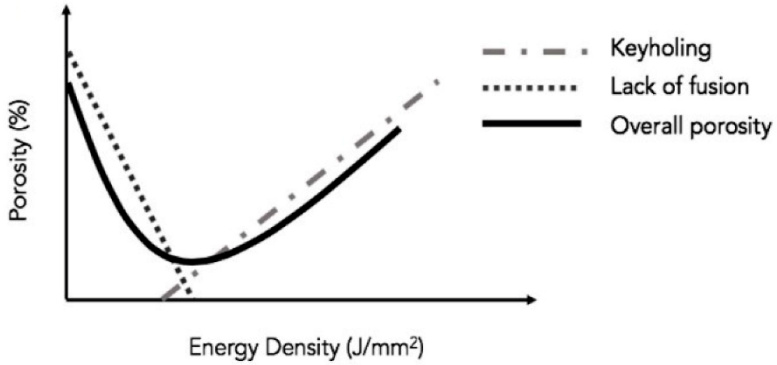


Figure 17. Porosity trend in relation to the ED and scan speed variations (Adapted from Reference [113]).

Finally, the LOF and keyhole are grouped under the name melting-related defects due to their irregular shape (*Figure 16a,b*), while gas pores are considered separately due to their spherical morphology (<100 μm) [69,108]. The main causes of gas pore formation (*Table 6*) are the presence of gas wrapped into the gas atomized powder, or the dissolution/entrapment of gas present within the build chamber [69,88–93]. Focusing on AlSi10Mg samples, the gas pores can also be caused by the H_2O reduction during the L-PBF process due to the thermal cycles induced by the printing methodology [114]. De facto, the water follows the subsequent chemical reactions:

$$2H_2O \rightarrow 2H_2 + O_2$$

$$3H_2O + 2Al \rightarrow Al_2O_3 + 3H_2$$

producing diatomic hydrogen that dissolves into monoatomic hydrogen atoms ($H_2 \rightarrow 2H_{absorbed}$). Subsequently, the H atoms diffuse within the liquid aluminium due to their high solubility in this metallic material [115]. Considering that the partition coefficient depends on the solidification rate, the L-PBF is characterized by a greater solubility of hydrogen than the cast process because the AM process is a rapid solidification process [116]. Weingarten et al. [89] summarized that the formation of pores decreases where the hydrogen contamination of the powder is lower (< 50 % of pores after the drying of the powder at 200 °C) or where optimized management is used. In relation to the mechanical properties, Gong et al. [117] concluded that the tensile strength and fatigue resistance of as-built Ti6Al4V samples are not influenced by 1 vol% of gas pores but are considerably

degraded with a volume fraction of 5 vol%. The same conclusions can be rewritten for AlSi10Mg as-built samples [65,118]. In this scenario, the hot isostatic pressing (HIP) HT can be used not only to densify the material but also to reduce the residual stress [119,120]. At the same time, if the fatigue resistance is increased due to the pore's reduction, the tensile properties of Ti6Al4V samples decrease, as can be observed in *Figure 18* [121–125]. In contrast, the ductility increases. More details and microstructural analysis will also be discussed in Sections 3, 4, 6 and 7 for AlSi10Mg samples (see [33]).

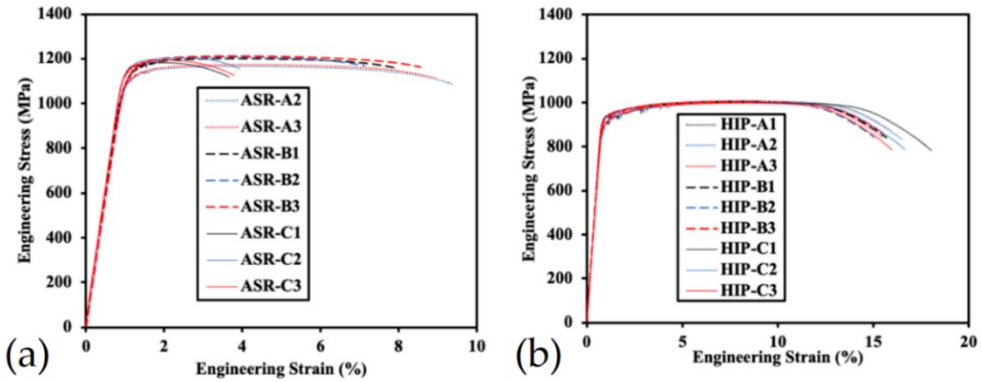


*Figure 18. Tensile properties of heat-treated Ti6Al4V samples after stress relief (**a**) and hot isostatic pressing HTs (**b**) (Reprinted from Reference [125]).*

The best mechanical properties of the as-built sample, which are necessary to obtain excellent mechanical properties after the HT, can be reached by printing with optimized process parameters. In other words, working in the operating window shown in *Figure 19* must be necessary [102]. On the other hand, this generalization neglects other important phenomena (*Table 6*, *Figure 15*) that must be considered during the L-PBF process.

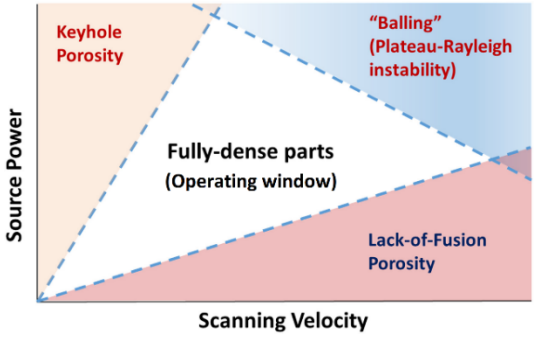


Figure 19. Operating window of the L-PBF process in relation to the laser beam source and scanning speed (Reprinted from Reference [102]).

Focusing on the balling phenomena and preferential evaporation defects, the main causes are strictly related to the thermal gradient and the instability of the MP

[81,103–107]. Kruth et al. [126] suggested that the balling phenomenon takes place when the material underlying the MP does not wet due to the surface tension. As a matter of fact, the balling phenomenon occurs when the MP surface becomes larger than the surface of a sphere that contains the same volume. This situation can be prevented if the process parameters are contained in the operating window (*Figure 19*).

On the other hand, if the temperature of the exposed powder exceeds the temperature melting point, the evaporation phenomena occur, inducing a loss in mechanical properties of the as-built samples [96,126]. Juechther et al. [96] affirmed that the evaporation effects decrease linearly with the *ED* transferred to the MP. Masmoudi et al. [127], analyzing the build chamber atmosphere, concluded that the evaporated volume during the L-PBF process can be controlled. Generally, the inert environment (continuous Ar or Ar + He or N gas flow, [128,129]) is used to avoid metal oxidation during the laser-powder process, particularly for Ti6Al4V and AlSi10Mg alloys that are characterized by high oxygen affinity. The build chamber environment is already high-oxidizing for the spatter particles and MP, considering an oxygen level of 1000 ppm [128,129]. On the other hand, an opportune gas flow stabilizes the depth of the MP and reduces the spatter phenomena and, consequently, oxidation [130,131]. Last but not least, the inert gas environment is an essential factor to obtain a better quality of the samples due to the pores and surface roughness reduction [132,133].

The principal process parameters (*P*, *h*, *v*, *t*) also influence the MP temperature and dimension, melt lifetime and the build rate [104,134]. De facto, the MP characterized by a typical semi-ellipsoidal shape is described by a thermal gradient decreasing from the centre to its boundaries (*Figure 20a*) [135].

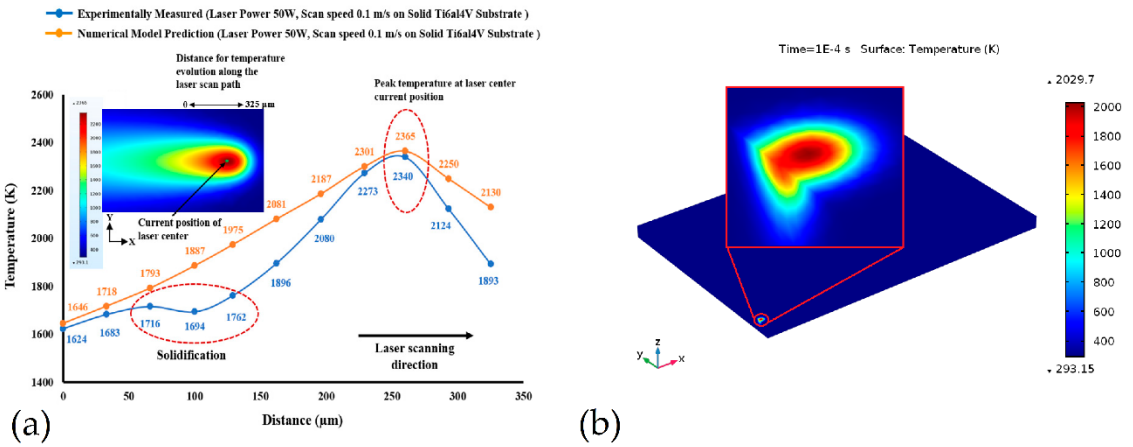


*Figure 20. (**a**) temperature trends of a molten pool (MP) measured and calculated along the xy plane; (**b**) distribution of temperature along the xy and xz planes (Adapted from Reference [135]).*

Due to the conduction heat transfer, the solidified material around the MP is also invested by a thermal gradient distribution (*Figure 20b*), causing a heat affected zone (HAZ) and consequent microstructural effects in AlSi10Mg and Ti6Al4V samples [65,135,136]. In addition, these thermal gradients and the MP dimensions are affected by the process variation induced by the optimization of sample quality (*Figure 21*) [137,138].

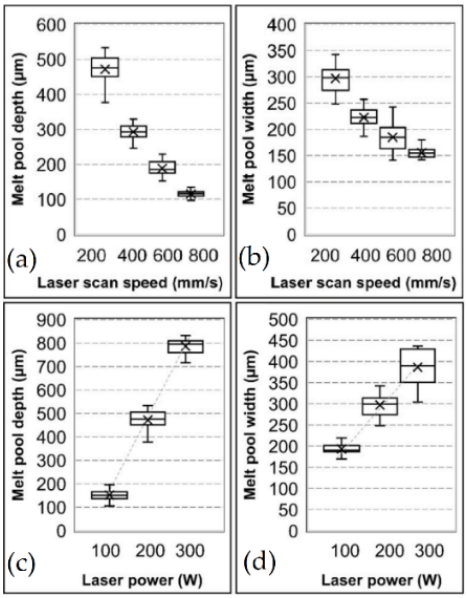


*Figure 21. MP depth (**a**,**c**) and width (**b**,**d**) related to the: (**a**,**b**) laser scan speed (mm/s) and (**c**,**d**) laser powder (W) (Adapted from Reference [137]).*

Lastly, the v, h, and t variation in L-PBF process cause a variation of the build rate (*BR*, [cm³/h], [134]) and the consequent productivity because it is defined as follows:

$$BR = vht \tag{7}$$

where v, h and t are the scan speed [mm/s], hatch spacing [mm] and layer thickness [mm], respectively. Thus, being that the *BR* equation is the denominator of Eq. (6), the *ED* function is strictly related to industrial productivity. Generally, a build rate of 5–20 cm³/h characterizes the L-PBF systems, but new AM machines (e.g., XLine 1000) also reach 100 cm³/h [139,140]. *Table 6* shows some BR values referred to in the literature analyzed and the samples' density reached. Shi et al. [141] showed an increase of layer thickness up to 200 µm, maintaining a Ti6Al4V sample density $\delta > 99.73$ % (fully dense). On the other hand, varying the layer thickness of AlSi10Mg and Ti6Al4V samples manufactured via L-PBF changes the mechanical properties obtained [67,75,117,141]. The use of double or quadruple lasers, which work in parallel on the same layer powder bed, or the use of skin-core scan strategy are other examples concerning the increase in the *BR* [134,142].

1.6. Experimental Procedure

As Chapter 2 will contain a summary of results and a brief discussion, the present section will show the materials on which the research activities were based, and the methodologies used.

1.6.1. Al and Ti Alloys Manufactured via L-PBF

Gas atomized powders, whose chemical compositions are shown in *Table 7*, were used to manufacture the AlSi7Mg, AlSi10Mg and Ti6Al4V-ELI samples represented through the Solidworks (Dassault Systèmes, Waltham, Québec, Canada) projects in *Figure 22a,b*. The powders were also characterized by a granulometry in the range from 20 to 60–70 μm, and by an apparent density higher than 1.53–1.54 and 2.2 g/cm^3 for AlSi7Mg-AlSi10Mg and Ti6Al4V-ELI, respectively.

Table 7. Chemical composition (wt.%) of gas atomized powders.

Alloys	Al	Si	Fe	Cu	Mn	Mg	C	O	N	H	V	Ti
AlSi7Mg	Bal.	7.04	0.06	<0.005	0.006	0.59	0.007	0.030	<0.002	0.002	-	0.12
AlSi10Mg		10.0	0.12	0.001	0.005	0.31	<0.005	0.028	<0.002	0.002	-	0.040
Ti6Al4V	6.47	-	0.21	-	-	-	0.01	0.09	0.01	0.001	4.06	Bal.

The representative projects related to AlSi7Mg and AlSi10Mg (*Figure 22a*) exhibits the geometries of bars (10 × 10 × 300 mm^3) and billets (10 × 100 × 300 mm^3) that are manufactured on a BP pre-heated at 150 °C and formed by different zones. In the first yellow zone, only one laser scans the powder bed; while two lasers work in parallel in the second red zone. Consequently, the bars and billets will be designated in single-laser (SL) and double laser (DL) regardless of the SLM machine used. As a matter of fact, the first batch of AlSi10Mg (job 1) was manufactured using the quad-laser SLM®500 machine; while the second (job 2) and the third (job 3) batches of AlSi10Mg and AlSi7Mg, respectively, were printed with a double-laser SLM®280 machine. In job 1, creep samples were also manufactured together with the bars and billets. Besides, their growth direction was parallel to the build direction (z-axis).

Figure 22b shows, however, the batch designed to analyse the Ti6Al4V-ELI alloy. It is composed of 24 tensile samples with a dog-bone geometry according to ASTM E8/E8M standard specification [143], and these samples are disposed in different build directions (90°, 45°, 0°$_{xz}$, 0°$_{xy}$) as well as the 4 bars (cross-section of 15 × 15 mm^2). Creep samples (cross-section of 6 × 6 mm^2) were also manufactured along z-axis. The dimensions of dog-bone tensile samples agree with the ASTM E8/E8M [143]. In order to analyse the effects of different heat treatments, as will be discussed later, three identical

batches (*Figure 22b*) were manufactured using SLM®280 machine. In this case, single and double-laser zones were not considered.

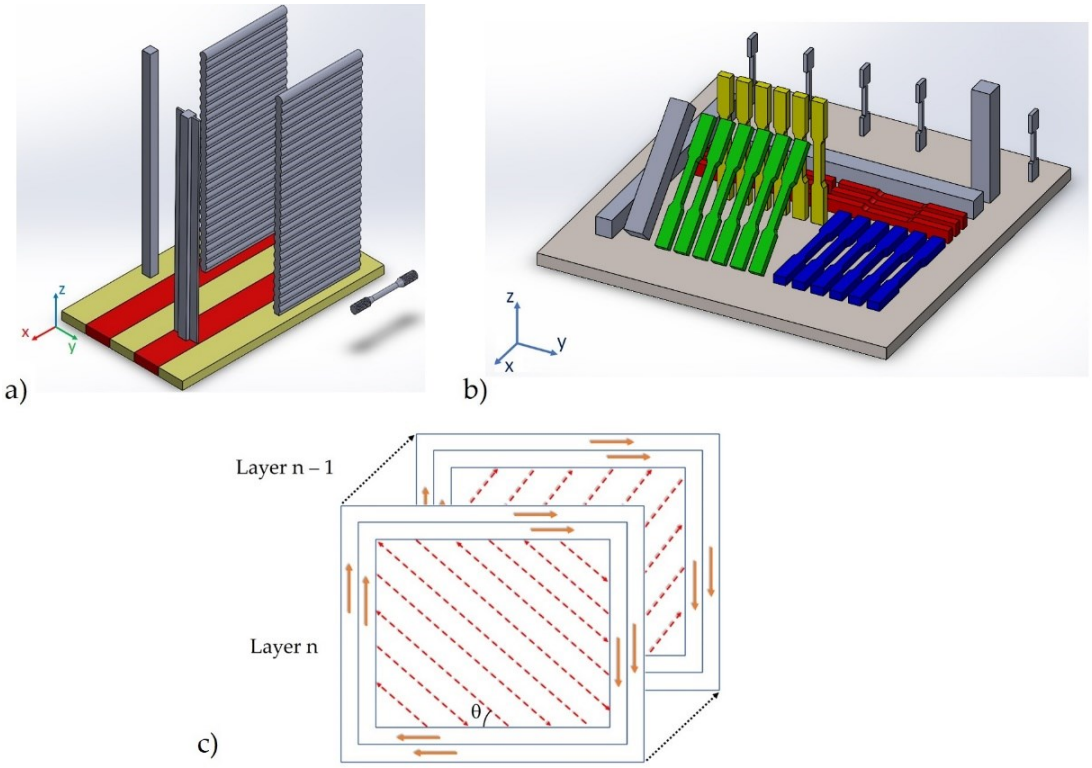


*Figure 22. Representative Solidworks projects of: (**a**) AlSi7Mg and AlSi10Mg alloys and (**b**) Ti6Al4V-ELI alloys which were manufactured following the skin-core scanning strategy (**c**). Dog-bone tensile samples were printed along different orientations: z (90°, yellow), 45° (green), xz (0°, red) and xy (0°, blue) (Reprinted and adapted from References [144,145]).*

In order to manufacture jobs 1–3 (*Figure 22a*) and the Ti6Al4V-ELI samples (*Figure 22b*), the skin-core scan strategy was used (*Figure 22c*). Generally, the laser firstly scans the external frame (skin) and, secondly, it scans the area (core) contained in the solidified skin. Here the laser scan tracks are in parallel to each other and inclined at 56.5° (θ in *Figure 22c*) with respect to the base of the skin. This procedure is repeated for each deposited layer up to the complete manufacturing of the 3D component. Each layer (n) was rotated by 67° with respect to the previously solidified layer (n–1).

Table 8 shows the process parameters used to manufacture jobs 1–3 and the Ti6Al4V-ELI batches. The superscript 50 (AlSi10Mg^{50}) and 90 (AlSi10Mg^{90}) will be used to identify the alloy manufactured with 50 and 90 μm of layer thickness, respectively.

Table 8. Process parameters used to print the batches of AlSi7Mg, AlSi10Mg and Ti6Al4V-ELI samples.

Alloys	Zone	P [W]	V [mm/s]	h [µm]	t [µm]	ED [J/mm³]	Build platform T [°C]
AlSi7Mg	Skin	330	600	70	90	87.3	150
AlSi10Mg [1]	Core	370	1400			42.0	
AlSi10Mg [2]	Skin	330	600	170	50	64.7	
	Core	350	1150			35.8	
Ti6Al4V	Skin [3]	-	-	120	60	-	80
	Core	340	1250			37.8	

[1] job 2 manufacturing with SLM®280, [2] job 1 manufacturing with SLM®500, [3] process parameters unavailable.

In order to evaluate the effects of the heat treatments and to choose the best temperature-time conditions, the AlSi7Mg and AlSi10Mg bars were cut into small blocks (10 × 10 × 15 mm³). Due to the effects induced by the pre-heated BP along the build direction (z-axis) the bars, and therefore the blocks, were subdivided into three different regions: bottom (0–100 mm), middle (100–200 mm) and top (200–300 mm). On each block, direct aging and T6 heat treatments were performed as illustrated through the process flow in *Figure 23a*. Consequently, the billets were heat-treated only following the best temperature-time parameters obtained.

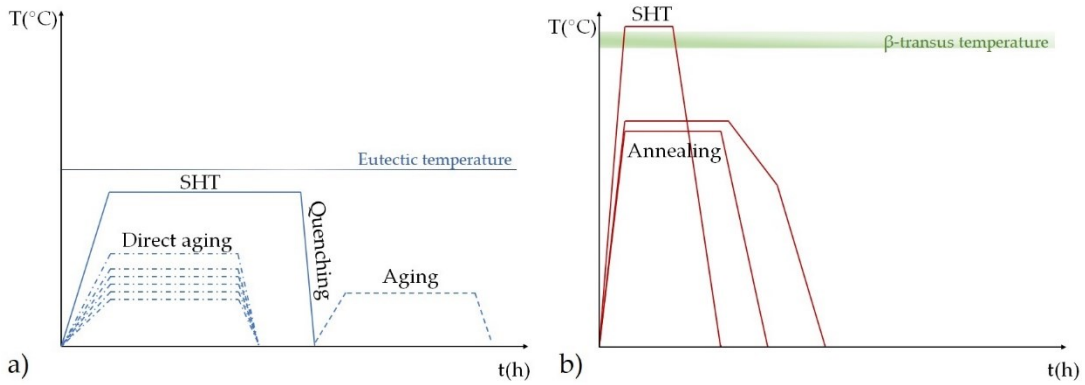


*Figure 23. Diagrams of the heat treatment processes performed on (**a**) AlSi7Mg and AlSi10Mg, and (**b**) Ti6Al4V-ELI samples.*

In relation to the Ti6Al4V-ELI samples, the three batches were heat-treated at 704 °C × 120 min, 740 °C × 130 min and 1050°C × 60 min and cooled in Argon gas for 1 h, as shown in *Figure 23b*. Only in the case of the annealing at 740 °C, the cooling in Argon gas was preceded by a furnace cooling up to 530 °C × 90 min in order to homogenize the mechanical properties and to improve the ductility.

Table 9 shows the analysed heat treatments and highlights the best temperature-time conditions.

Table 9. Heat treatments performed on AlSi7Mg, AlSi10Mg and Ti6Al4V-ELI samples.

Alloy	Heat treatment	Temperatures [°C]	Times [h]
Job 1	Direct aging	150	0.5, 4, 6, 12, 18, 22, 30
		175, ***200***, 225, 250	0.5, 1, 2, ***4***, 6, 10, 14, 30
		300	0.5, 1, 2, 4, 6, 10, 30
	T6	505 + 175	4 + 4
	Direct aging	NA [3] + 150, 175, 200, 225, 250, 300	0.5, 1, 2, 4, 6, 12, 18, 24
Job 2	Direct aging	175, ***200***, 225	***4***
	T6	505 + 175	4 + 4
	SHT	505	0.04, 0.08, 0.17, 0.33, 0.50, 0.67, 0.83, 2, 4
	T6	505 + 175	4 + 0.5, 1, 2, 4, 8, 16, 32
Job 3	Direct aging	150, 175	0.5, 1, 2, 4, 8, 16
		200, 225	0.5, 1, 2, 4, 8
	SHT	505	0.04, 0.08, 0.17, 0.33, 0.50, 0.67, 0.83, 2, 4
	T6	505 + 175	4 + 0.5, 1, 2, 4, 8, 16, 32
Ti6Al4V-ELI	Annealing	704, 740	2, 2.17
	SHT	1050	1
	Aging	450, 500, 600, 650	0.5, 1, 2, 4, 8, 16, 32, 64, 128

[3] NA means Natural Aged (room temperature).

Aluminium samples were heat-treated with an electric muffle furnace (Nabertherm GmbH, Lilienthal, Germany) where the temperature was controlled through a K-type thermocouple. As regards the Ti6Al4V-ELI samples, the heat treatments were carried out with a vacuum furnace by Beam-IT company.

1.6.2. The Microstructural Characterization

The microstructural characterization was performed, firstly, through the DMi8 (Leica, Wetzlar, Germany) inverse optical microscope (OM) and, secondly, by using the Nova NanoSEM 450 (ThermoFisher, Hillsboro, Oregon, USA) equipped with a field emission gun source.

Both the Al and Ti alloy samples were mechanically grinded with SiC papers and polished with colloidal silica suspension. Some Ti6Al4V-ELI samples were etched by Kroll's reagent (100 mL of H_20 + 2 mL of HF + 4 mL of HNO_3) for OM and SEM investigations. Other Ti6Al4V-ELI samples were further polished with ~ 60 nm-sized colloidal silica for electron backscattered diffraction (EBSD) measurements. The EBSD maps were acquired using e⁻Flash 1000 (Bruker Nano, GmbH, Berlin, Germany) detector.

Phase analysis was carried out through an X'Pert PRO PANanalytical (Malvern Panalytical, Malvern, UK) diffraction system which is equipped with a Cu-Kα radiation source working at 40 mA and 40 kV. The same method was used to evaluate the effects

induced by the sand-blasting process on the outer surface of the Ti6Al4V-ELI tensile samples. For each XRD result obtained and mentioned in Chapter 2, see the parameters used in ARTICLE 1, ARTICLE 6 and ARTICLE 7.

In relation to the statistical analysis of pores before and after the heat treatments performed on AlSi10Mg (job 2), six OM micrographs at a magnification of 1000× were studied according to ISO 13322-1:2014. Consequently, the density values were calculated considering that the value of 2.68 g/cm^3 was associated with an AlSi10Mg characterized by 0 % of porosity [68]. As regards the statistical analysis of the area and thickness of the Si-eutectic particles, three different OM and SEM micrographs were used. The former for the solubilized samples for a holding time longer than 1 h; while the latter for the other heat-treated conditions. For further information see the experimental procedure or materials and method sections of ARTICLE 1, ARTICLE 2 and ARTICLE 5.

In order to obtain the cooling rate $(\dot{T})$ related to the AlSi10Mg samples of jobs 1 and 2, the following equation was considered:

$$SDAS = k\dot{T}^{-n} \tag{8}$$

where *SDAS* is the secondary dendritic arm spacing (here considered as α-Al cells), k and n the pre-exponential (43.2) and exponential (0.324) constant as illustrated by Motyka et al. [146]. The SDAS values were obtained through the intercept method; namely counting the intersections between different lines of known length and the α-Al cells, as illustrated in *Figure 24a*.

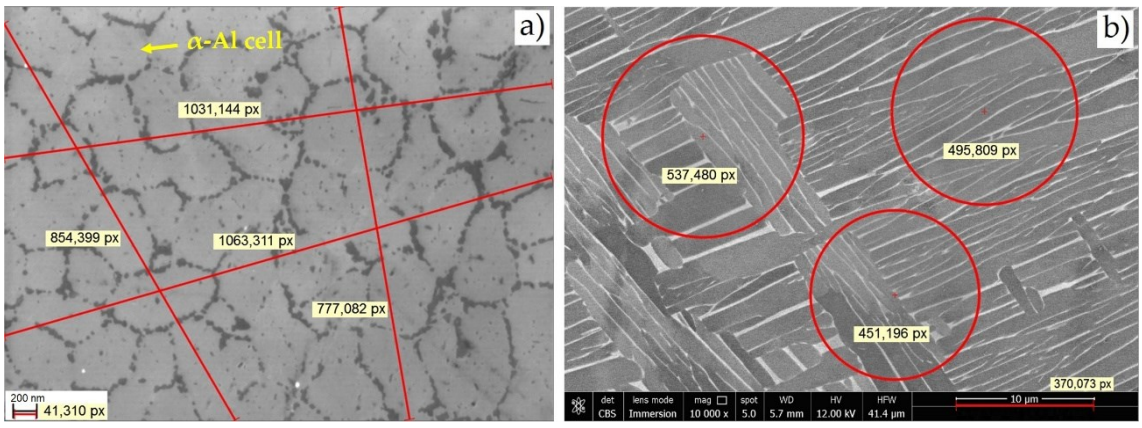


*Figure 24. Intercept method used to calculate: (**a**) the SDAS values of as-built AlSi10Mg samples, (**b**) the α-laths width of the heat-treated Ti6Al4V-ELI samples.*

In relation to the measurements of the α-lath size, the used methodology was proposed by Van der Voort et al. [147], who drew a circumference of known radius (R)

and calculated its intersections with the α-lamellae (*Figure 24b*). The α-lath width (N_α) can be obtained through the following equation:

$$N_\alpha = \frac{2\pi R}{M} \quad (9)$$

where M is the number of intersections. The same intersection method illustrated in *Figure 24a* was used to calculate the number of grains and their average size of the solubilized and Solution Treated and Aged Ti6Al4V-ELI samples.

1.6.3. The Mechanical Properties Characterization

All Vickers microhardness (HV) values shown in this work were measured using a VMHT Leica (Leica, Wetzlar, Germany) tester equipped with a set of loads from 1 to 2000 gf. Firstly, 500 gf of load (HV0.5) and 15 s of indentation time were used to evaluate the effects induced by the different heat treatments and to analyse the samples in as-built conditions. Secondly, 100 gf (HV0.1) and 15 gf (HV0.015) of loads were used to analyse the contributions conferred by the several microstructural morphologies in Ti6Al4V-ELI and Al samples, respectively. All Vickers microhardness measurements were performed in accordance with the UNI EN ISO 6507-1:2018.

In relation to the Ti6Al4V-ELI samples, the HV0.5 measurements related to the xy and xz planes of the as-built bar and the heat-treated samples were the average values of a matrix of 3×3 indentations (*Figure 25a*).

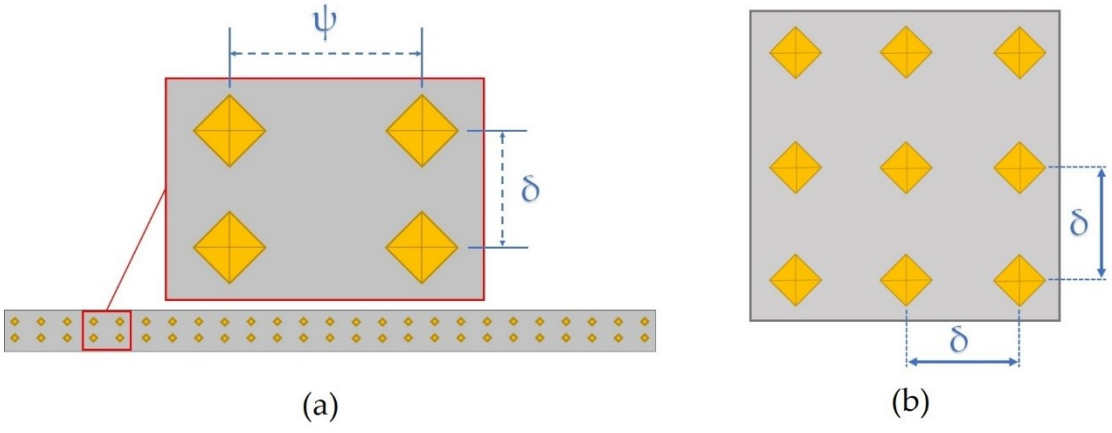


*Figure 25. Schematic representation of the: (**a**) 3×3 matrix used to evaluate the HV0.5 values of Ti6Al4V-ELI samples, and AlSi7Mg and AlSi10Mg samples on xy plane, (**b**) HV0.5 profiles performed on the SL and DL AlSi10Mg and AlSi7Mg bars in as-built conditions (Adapted from References [145,148]).*

The same matrixes were used to evaluate the HV0.5 values of the Al samples in as-built and heat-treated conditions on the xy plane. Generally, all indentations forming

the matrix are spaced a quantity δ apart from each other to avoid the effects induced by the plastic deformation. This quantity is defined as follows:

$$\delta > 2.5 d_m \tag{10}$$

where d_m is the average value of the two diagonals of an indentation.

In relation to the as-built AlSi7Mg and AlSi10Mg[50,90] bars, the Vickers microhardness profiles were obtained as an average of two profiles performed in parallel to each other, and arranged along the build direction as reported in the schematic illustration in *Figure 25b*. Each profile was composed of 60 measurements which had a space ψ equal to 5 mm, apart. The couple of HV0.5 profiles were spaced a higher quantity than $2.5d_m$ apart, as shown through the Eq. (10).

After the direct aging and T6 HTs (*Table 9*) on jobs 1–3, as well as after the STA on Ti6Al4V-ELI samples, the aging curves were built through the HV0.5 average values obtained by the matrix 3×3 (*Figure 25a*) carried out on each sample analysed.

The effects induced by the sand-blasting process were also analysed through HV0.5 profiles performed on the cross-section of the Ti6Al4V-ELI tensile samples. Each profile discussed in Chapter 2 was obtained by the average of the three profiles as schematically illustrated in *Figure 26*. Profiles 1, 2 and 3 were formed by 15 indentations 500 μm apart, except for the 2nd and 14th that were taken at a distance of 250 μm from the 1st and 3rd and from the 13th and 15th, respectively. For further details, see the materials and methods section of the ARTICLE 7.

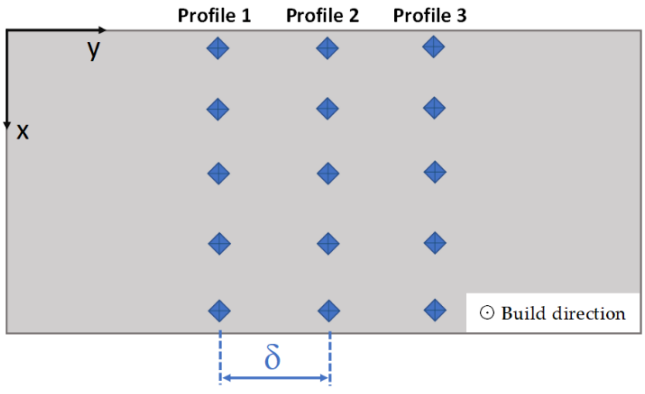


Figure 26. HV profiles carried out on cross-section of the heat-treated Ti6Al4V-ELI tensile samples after and before the sand-blasting process (Reprinted from Reference [145]).

Tensile tests were performed at room temperature using a Z100 servo-hydraulic machine (Zwick/Roell, Ulm, Germany) for both aluminium and titanium alloys. The cylindrical AlSi7Mg and AlSi10Mg samples (*Figure 27a*) were tested with a strain rate of 0.008 s^{-1}; while the 0.0167 s^{-1} rate was applied to test the dog-bone Ti6Al4V-ELI samples

(*Figure 27b*). In the first case, the cylindrical samples were mechanically obtained from the billets shown in *Figure 22a* and, consequently, their major axis of symmetry was always maintained parallel to the BP. In the second case, the dog-bone Ti6Al4V-ELI samples were directly manufactured following the dimensions reported in *Figure 22b*.

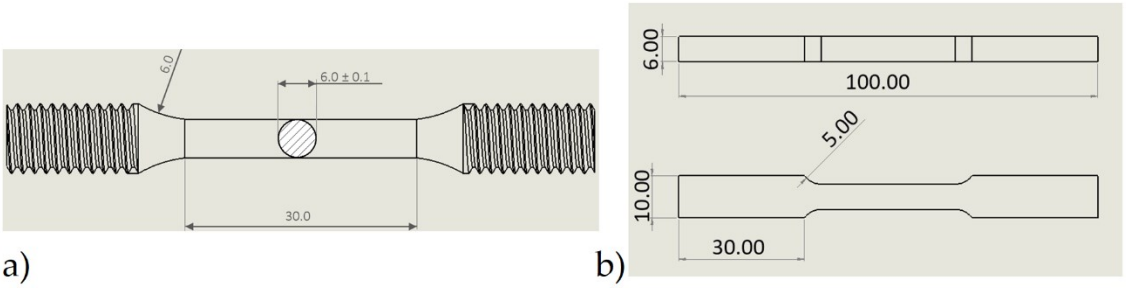


*Figure 27. Schematical representation of the (**a**) cylindrical AlSi7Mg and AlSi10Mg tensile samples and (**b**) dog-bone Ti6Al4V-ELI samples (Reprinted form References [144,145]).*

Generally, the AlSi7Mg and AlSi10Mg were tested in as-built and heat-treated conditions (direct aging, SHT and T6), while the Ti6Al4V-ELI samples were only tested in heat-treated conditions before and after the sand-blasting process. For further information see ARTICLE 1, ARTICLE 2, ARTICLE 3, ARTICLE 4, ARTICLE 6 and ARTICLE 7.

Creep properties of AlSi10Mg alloys were investigated using a constant load. The tensile creep experiments were carried out in air on the as-built samples at 150 °C, 175 °C and 225 °C (see ARTICLE 8).

In order to evaluate the best correlation between the Vickers microhardness and Rockwell hardness, the measures of the latter were performed on the same xy plane of both the as-built and direct aged AlSi10Mg samples considered for the HV measurements. Due to the obtained Vickers microhardness values, a load of 60 kgf and the ball indenter (diameter of 1.588 mm) were used to measure the HRF hardness. Consequently, the HV – HRF correlations are analysed and validated.

[*This page intentionally left blank*]

CHAPTER 2

Summary of Results and Discussion from the Articles

As widely discussed in Chapter 1, the scope of the present section is to provide a summary of the main findings obtained during the research activities. The results shown in the following subchapters and the related discussion are an extract of the main published articles, which are collected in Part 2. Therefore, for further information about the presented and discussed results, directly see the research articles. They were designed as ARTICLE 1, ARTICLE 2, ARTICLE 3, ARTICLE 4, ARTICLE 5, ARTICLE 6, ARTICLE 7, ARTICLE 8 and ARTICLE 9.

Firstly, the microstructures of both aluminium and titanium alloys were illustrated by discussing the effects induced by different heat treatments. Secondly, the variation of mechanical properties variation, in terms of Vickers microhardness and tensile strengths, between the as-built and heat-treated conditions were reported. At the same time, the optimal temperature-time conditions were highlighted. Lastly, the empirical correlation between the tensile strengths and Vickers microhardness were presented for AlSi10Mg and Ti6Al4V samples.

2.1. Microstructural Analysis

In the following sub-chapter, the as-built microstructures of the AlSi7Mg, AlSi10Mg[50,90] and Ti6Al4V alloys will be discussed, as well as the effects induced by different HTs.

2.1.1. AlSi7Mg and AlSi10Mg L-PBFed Alloys

The fine and inhomogeneous microstructure of the AlSi10Mg[50] and AlSi7Mg alloys is reported in *Figure 28* in which xy (*Figure 28a,b*) and xz (*Figure 28c,d*) planes are investigated.

As widely reported in the literature, xy planes show the typical ellipsoidal shape of the MPs and different laser scan tracks arranged according to the scanning strategy (*Figure 22c*) used during the L-PBF process. The typical "fish-scale" structure, where the cross-section of the laser scan tracks are partially overlapped, is observable on the xz plane for both the AlSi10Mg^{50} (*Figure 28c*) and AlSi7Mg (*Figure 28d*) alloys (ARTICLE 1, ARTICLE 2, ARTICLE 3 and ARTICLE 4). Moreover, the as-built AlSi10Mg^{90} samples are characterized by the same microstructure morphology (see ARTICLE 4) while, however, the MP depth is comparable to that shown in *Figure 28d* due to the same layer thickness of 90 µm (*Table 8*). In both cases, the chosen process parameters satisfy the full melting criterion shown in Eq. (5).

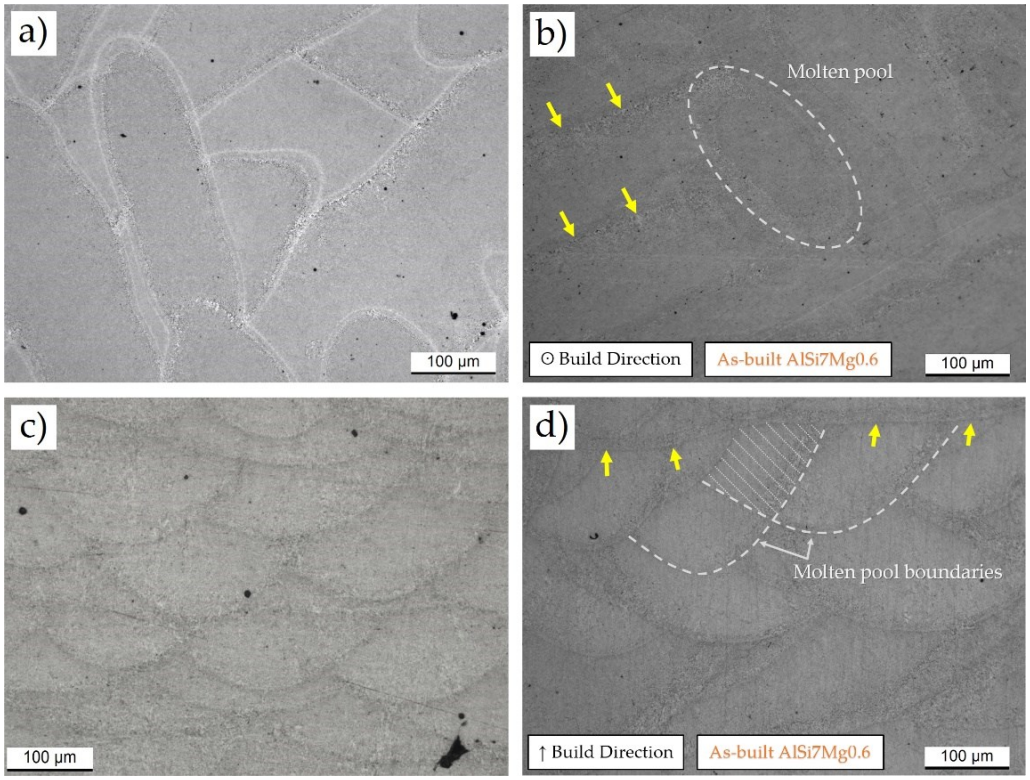


*Figure 28. OM micrographs performed on the xy (**a**,**b**) and xz (**c**,**d**) planes of the AlSi10Mg^{50} (**a**,**c**) and AlSi7Mg (**b**,**d**) alloys in as-built conditions (Reprinted from ARTICLE 1 and ARTICLE 2).*

The layer thickness variation of 40 µm between the AlSi10Mg^{50} and AlSi10Mg^{90} causes a microstructural variation in terms of grains morphology, as widely discussed in ARTICLE 4. In fact, the different undercooling characterizing the solidification process of the MP influences the columnar-to-equiaxed transition (CET), leading to a greater quantity of equiaxed grains compared to columnar grains in AlSi10Mg^{90} samples. For these reasons, the HV0.015 profiles of the as built AlSi10Mg^{90} (ARTICLE 4) show higher values than the same profiles measured on the AlSi10Mg^{50} bars. The grain

morphology differences are also present within the external frame (skin, *Figure 22c*) of the AlSi10Mg[90] as reported in *Figure 29a*. In this case, the xz plane presents a layer-packing rather than the "fish-scale" structure due to the skin-core scanning strategy adopted during the L-PBF process. At higher magnification, the equiaxed grains are observable within the centre of the laser scan track (*Figure 29b,c*), while the columnar grains form the overlapped area between two overlaid layers (*Figure 29b,d*) (ARTICLE 5).

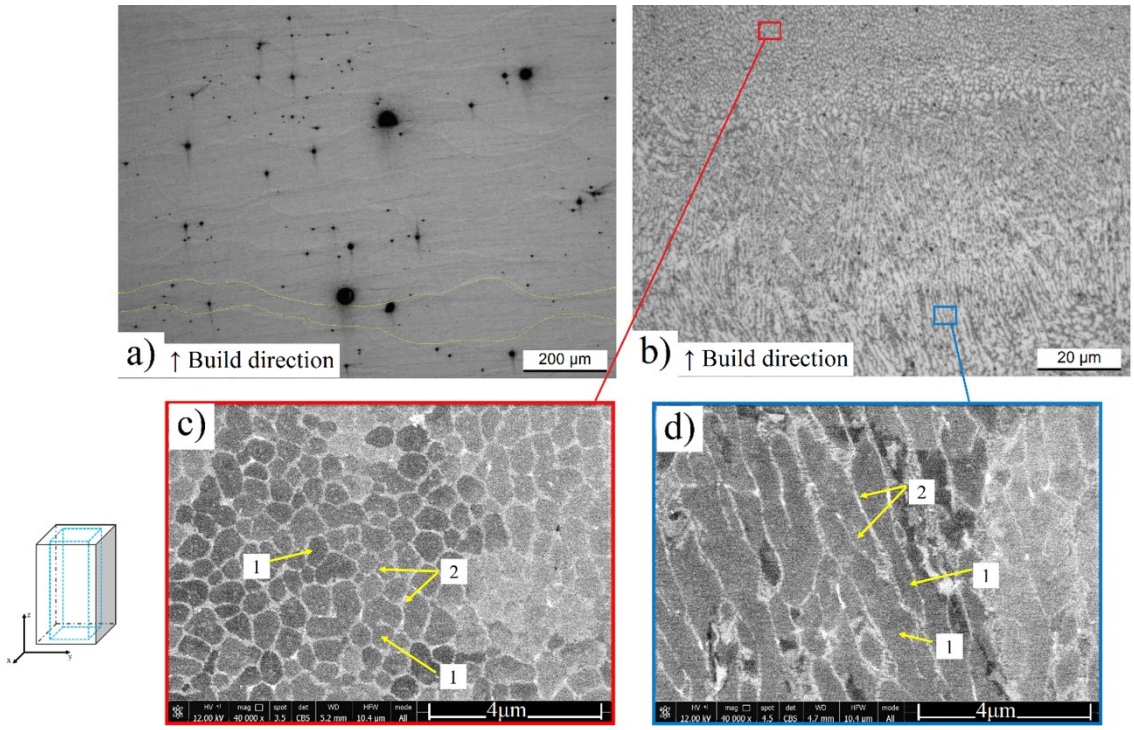


*Figure 29. OM (**a**,**b**) and SEM (**c**,**d**) micrographs of the external frame (skin) of the as-built AlSi10Mg[90] samples (Reprinted from ARTICLE 5).*

As also indicated by panels 1 and 2 in *Figure 29c,d*, the as-built AlSi10Mg[90] samples are formed by Si-eutectic particles, confirmed by the EDS maps discussed in Article 3, and these particles surround the α-Al matrix, as better highlighted in *Figure 30*. Generally, the centre of the MP or the laser scan track is composed of Si-eutectic particles arranged in a network. From a three-dimensional point of view, this network constitutes a tubular structure [33]. The central zone, marked with the number 3 in *Figure 30a*, is also highlighted in *Figure 30b* where the α-Al matrix is subdivided by a continuous network of Si-eutectic. Due to the thermal gradient and heat fluxes affecting the laser scans tracks and MP boundaries, the Si-eutectic network is destroyed, and the Si-particles grow (*Figure 30c,d*), leading to the formation of the HAZ (see ARTICLE 1 and ARTICLE 4). For these reasons, the HV0.015 measurements pointed out lower values on

the MP or laser scan tracks boundaries compared to those on their centre. At the same time, the microstructure of the HAZ strongly influences the crack propagation (ARTICLE 4). At the same time, as-built AlSi7Mg samples show the same microstructure morphology of the AlSi10Mg[50,90] samples [149,150].

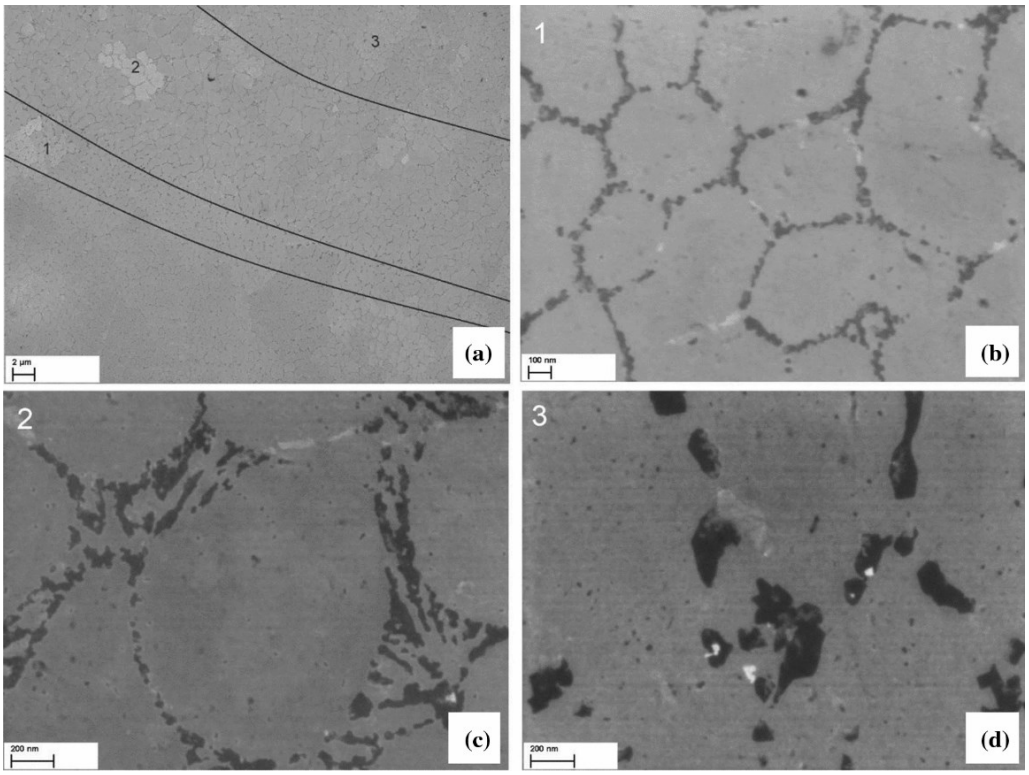


*Figure 30. SEM micrographs of as-built AlSi10Mg[50] samples investigating the Si-eutectic network transformation (**a**) from the MP centre (zone 3) to its boundary (zone 1). (**c**–**d**) SEM micrographs at higher magnification (160k×) of zones 1, 2 and 3 (Reprinted from the ARTICLE 1).*

The impact of the BP pre-heated at 150 °C is not observable on the Si-eutectic network morphology and size (ARTICLE 1), but it is evident within the α-Al cells where the β-Mg_2Si phase and Si nanoparticles are precipitated (ARTICLE 1, ARTICLE 4 and ARTICLE 5). Obviously, these phenomena are more marked when the manufacturing time is increased; namely from the top regions to the bottom ones of the as-built bars. On the other hand, the damaging effects of the Si-eutectic network were observed by Macías et al. [100] and Martins et al. [151], who discussed the effects of a BP pre-heated at 200 °C. As a matter of fact, the same worsening effects are obtained after the DA at 200 °C × 6 h (*Figure 31b*); while the DA up to 175 °C only promotes the precipitation phenomena and the coarsening phenomena of the precipitates already formed during the manufacturing process (*Figure 31a*). The DA at 225 °C × 6 h obviously induces greater worsening effects and coarsening phenomena than the DA at 200 °C (*Figure 31c*). Lastly,

the SHT at 505 °C followed by the AA at 175 °C fully deletes the Si-eutectic network and induces recrystallization phenomena of the nano-size grains which formed the as-built microstructure. This is identifiable through the channelling contrast of the microstructure in *Figure 31d*.

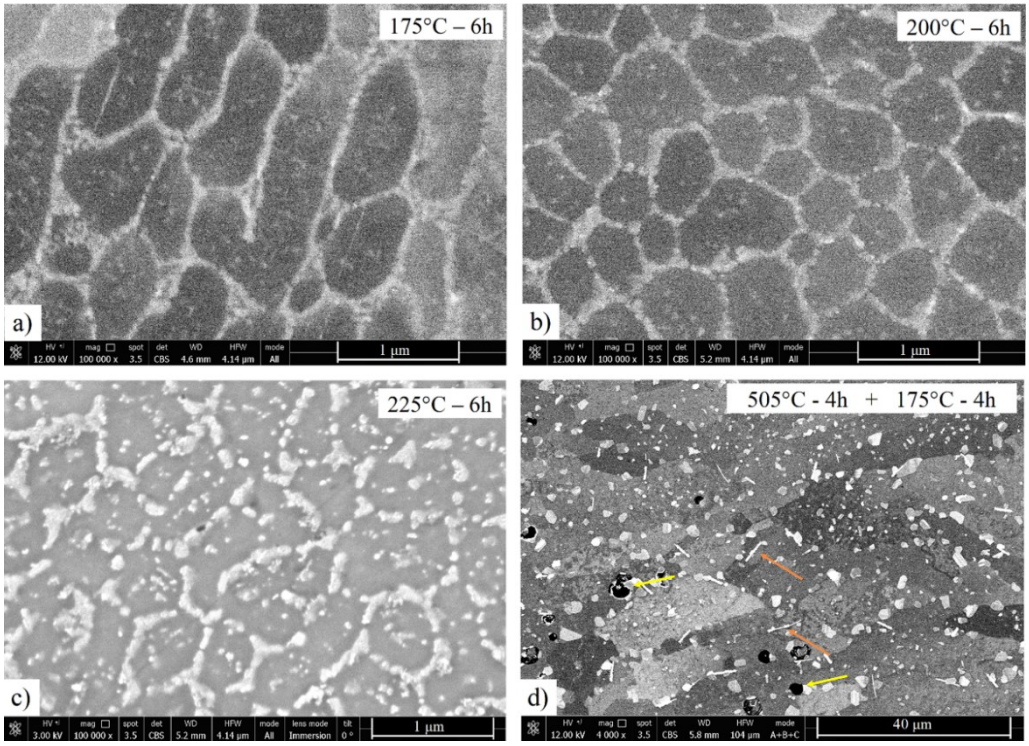


*Figure 31. SEM micrographs of AlSi10Mg[90] samples heat-treated at: (**a**) 175 °C, (**b**) 200 °C and (**c**) 225 °C × 6 h and (**d**) 505 °C × 4 h + 175 °C × 4 h (Reprinted from ARTICLE 5).*

In addition to the microstructural rearrangement promoted by the SHT, the Si-eutectic particles are affected by coarsening phenomena (comparing the scale bars of the T6 heat-treated and direct aged SEM micrographs) (ARTICLE 1, ARTICLE 2, ARTICLE 4 and ARTICLE 5). In fact, the equivalent diameter of these particles increases from 0.05 ± 0.01 μm in as-built cases to 0.2–5.4 μm after the SHT at 505 °C × 4 h (ARTICLE 1 and ARTICLE 2). Obviously, decreasing the SHT time, the reached equivalent diameter range is lower than 0.2–5.4 μm (ARTICLE 2) as it is possible to observe in *Figure 32*. The Si-eutectic network is completely destroyed and the Si particles become distinguishable at a magnification of 1000× (*Figure 29b* vs. *Figure 32a,b*), after just 5 min of SHT. Increasing the SHT time up to 4h (*Figure 32c,d*) the Si-particles per unit area clearly decrease and their size consequently increase for both AlSi7Mg and AlSi10Mg[90]. ARTICLE 2 also reported that the Si-particles per unit area decrease from 0.076 to 0.043 μm^{-2} and 0.092 to 0.054 μm^{-2} for AlSi7Mg and AlSi10Mg[90], respectively. In addition, the average equivalent

diameters increase from 0.81 μm and 0.82 μm to 1.32 μm and 1.23 μm, respectively. Lastly, the SHT promotes the formation of different precipitates like the brittle and acicular β-Al_5FeSi and more spherical Fe-Si-Mg precipitates (orange arrows in *Figure 32c,d*). More details related to the HTs effects on the microstructure are mainly discussed in ARTICLE 1, ARTICLE 2 and ARTICLE 4.

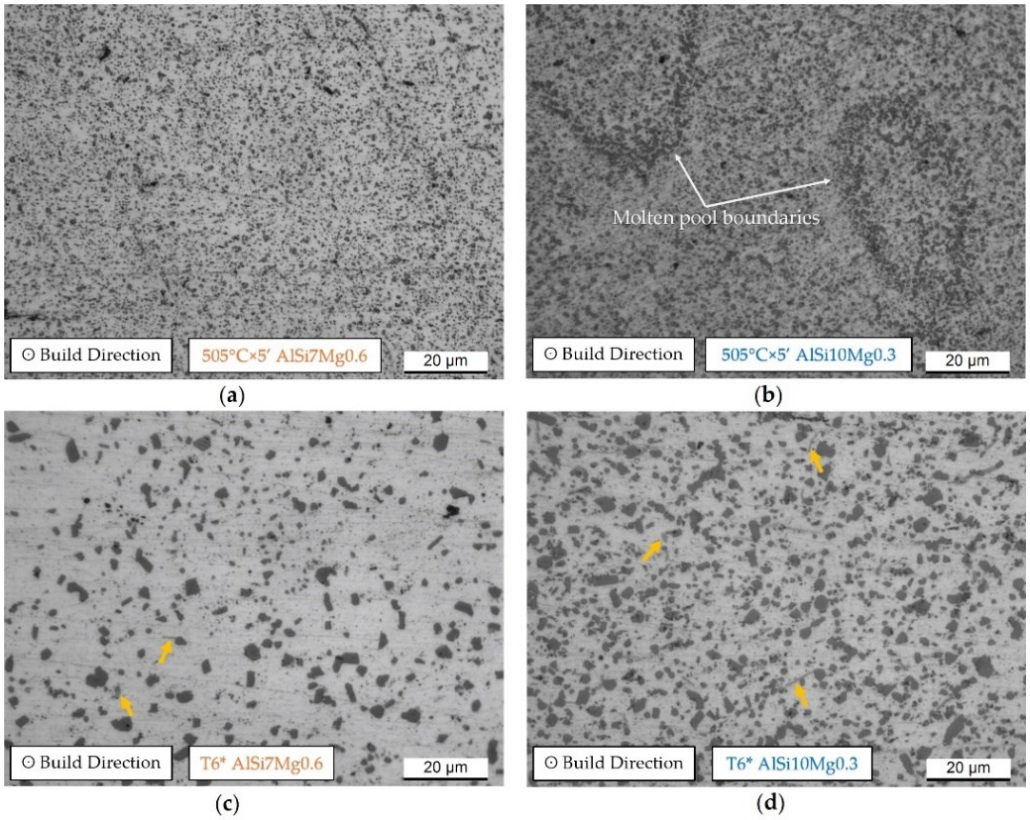


*Figure 32. OM micrographs of solution heat treated AlSi7Mg (**a**,**c**) and AlSi10Mg (**b**,**d**) for 5 min (**a**,**b**) and 4 h (**c**,**d**) at 505 °C (Reprinted from ARTICLE 2).*

Another crucial effect induced by the HT at high temperatures (i.e., SHT at 500 °C) is the decrease in density of the heat-treated Al-Si-Mg alloys (see ARTICLE 2 and ARTICLE 5). As a matter of fact, the T6 heat-treated samples generally show a higher quantity of big pores compared to the as-built ones (*Figure 33*).

As carefully discussed in ARTICLE 5 the high temperatures reached during the HT increase, firstly, the area of pores thanks to the contained gases and, secondly, the number of pores due to the same concept describing the movement of vacancies during the permanence at high temperatures.

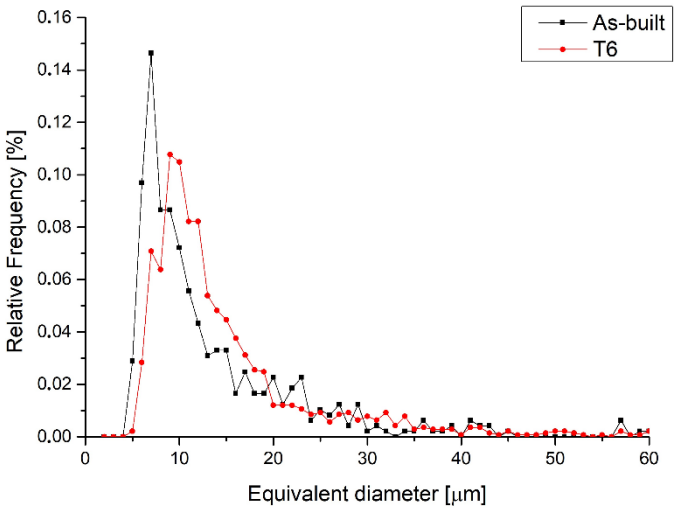


Figure 33. Statistical analysis of the pore equivalent diameters before and after the SHT 505 °C + aging 175 °C (Reprinted from ARTICLE 5).

Furthermore, the DA at 225 °C promotes a decrease in density for both the AlSi7Mg and AlSi10Mg[90] alloys, as highlighted in *Figure 34a*. For further information see ARTICLE 2. On the other hand, the BP pre-heated at 150 °C does not seem to affect the pore number and their area because the as-built density values of the regions from top to bottom are fully comparable. Moreover, it is possible to underline that the hot BP promotes the coarsening effects of the pores by focusing on *Figure 34b*. In fact, the bottom regions of the bars are characterized by a lower number of pores compared to the top ones which have higher dimensions. Therefore, the pore dimension compensates for their number, and vice versa, in the density calculation.

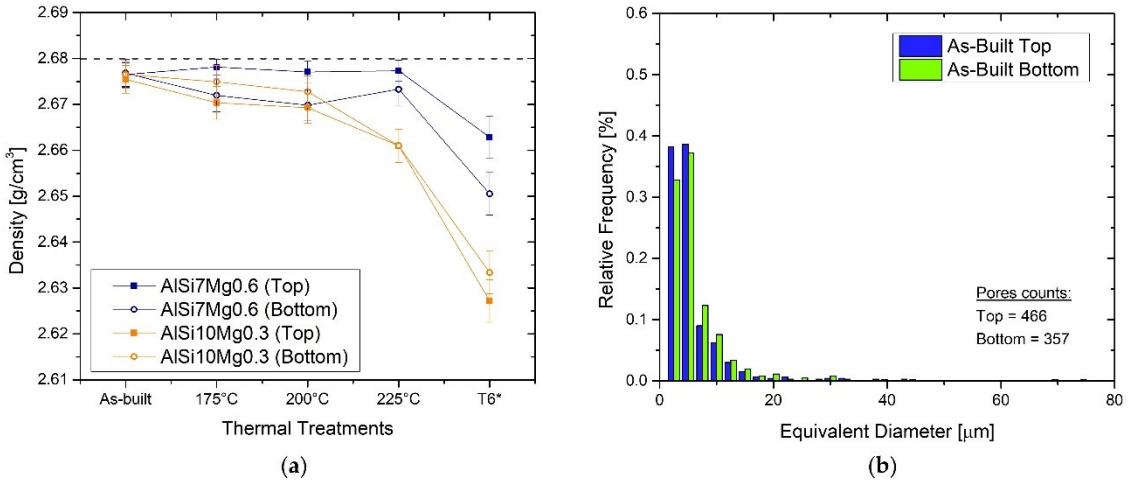


Figure 34. Trend of density values of the as-built, direct aged and solution heat-treated AlSi7Mg and AlSi10Mg[90] samples (Reprinted from ARTICLE 2).

The density variation during the HT is substantially controlled by metallurgical pores rather than the lack-of-fusion (LOF) pores thanks to the different formation mechanisms. In the first case, pores are formed by different gases (e.g., oxygen, argon, nitrogen, etc) that are trapped during the solidification of the MP (ARTICLE 5) and, consequently, characterized by a spherical shape with a diameter lower than 100 μm. On the other hand, the latter are formed by unoptimized process parameters and/or by the MP instability (ARTICLE 5). LOF pores are generally characterized by an elongated morphology, where their major axis is longer than 100 μm and placed along the xy plane. Therefore, their minor axis is observable on the xz plane (ARTICLE 2 and ARTICLE 5). From these premises, the density variations are generally controlled by the metallurgical pores because the high HT temperatures increase the pressure of the gas contained within the pore and, at the same time, they decrease the yield strength of the material around the pore. Thanks to this synergetic effect, the gas pressure can deform the weakened material by increasing the pore volume. On the other hand, only the high holding time at SHT temperatures can confer spheroidization phenomena to LOF (ARTICLE 5).

2.1.2. Ti6Al4V-ELI L-PBFed Alloy

The as-built Ti6Al4V-ELI sample (*Figure 35*) also shows the MP on the xz plane (*Figure 35a*) and the laser scan tracks on the xy plane (*Figure 35b*). Unlike the as-built L-PBFed Al-Si-Mg alloys, the columnar β-grains grow perpendicularly to the BP and pass through each deposited layer, from the bottom regions to the top ones of the samples (*Figure 35a*). In fact, the columnar β-grains are arranged in parallel with respect to the build direction. Focusing on the xz plane, the OM micrographs highlight the typical nearly equiaxed cross-section of the columnar grains (dashed contour in *Figure 35b*). As widely discussed in ARTICLE 6, the different build orientations do not affect the arrangement of these columnar β-grains, which remains visible after the HTs at 704 °C and 740 °C (ARTICLE 6). The high magnification OM micrograph in *Figure 35c* exhibits the acicular α'-martensite phase that completely fills the columnar β-grains thanks to the $\beta \rightarrow \alpha'$-martensite transformation during the solidification process of the MP (> 410 °C/s). Generally, the α'martensite laths nucleate on the columnar β-grain boundaries and then grow along directions that are inclined by 45° with respect to the same boundaries. Within the centre zone of the columnar grains, the α'-martensite laths form a crosshead structure where primary, secondary, tertiary and quartic grades of the α'-martensites intersect each other [152]. Also in this case, the BP pre-heated at 80 °C does not influence

the as-built microstructure, unlike the heating at 400 °C [153], in which case the $\alpha' \rightarrow \alpha + \beta$ decomposition takes place.

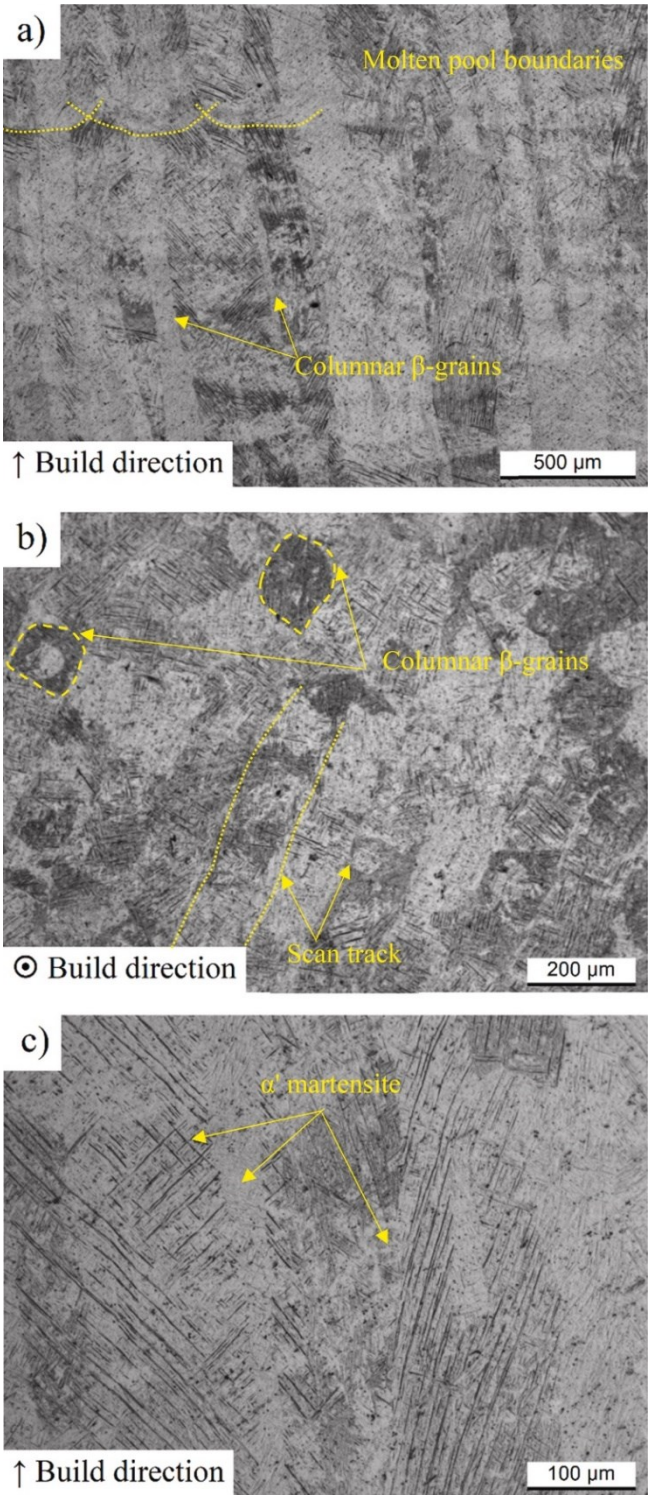


*Figure 35. OM micrographs performed on xy (**a**) and xz (**b**,**c**) planes of the as-built Ti6Al4V sample (Reprinted from Reference [155]).*

Greater decomposition effects were obtained after the HTs at 704 °C × 120 min and, clearly, at 740 °C × 130 min, but Spigarelli et al. [154] demonstrated that the $\alpha' \rightarrow \alpha + \beta$ transformation was not completed because different colonies of α'-martensite were observed through TEM observations. At the same time, *Figure 36* shows that the cross-head structure of the α-phase still remains visible after both the HTs at 704 °C (*Figure 36b*) and 740 °C (*Figure 36d*), respectively. In particular, the primary, secondary and tertiary α'-martensites transform into primary, secondary and tertiary α-phases, respectively, while the quartic α'-martensite transforms into β-phase [33]. The EDS spectra related to points A and B in *Figure 36b* confirm that the dark phase is the α-phase, while the brighter zones are related to the β-phases thanks to the quantity of Al, Fe and V alloying elements (*Table 10*) (ARTICLE 6 and ARTICLE 7).

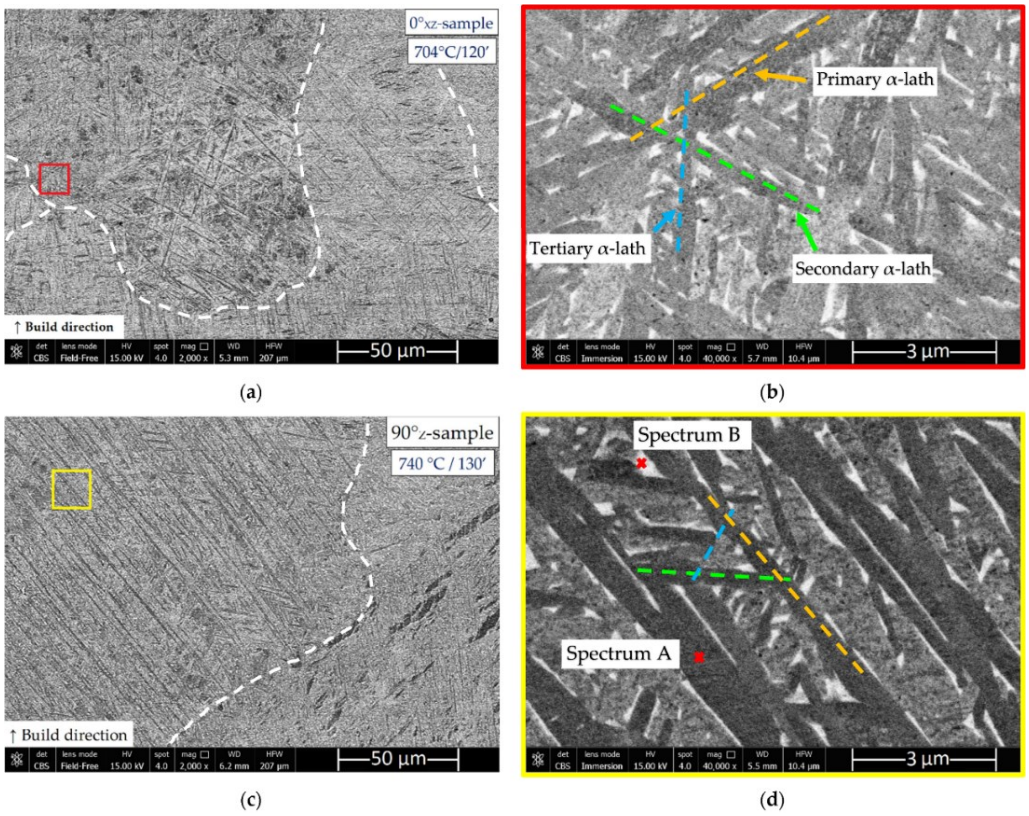


*Figure 36. SEM micrographs of Ti6Al4V-ELI samples heat-treated at 704 °C × 120 min (**a**,**b**) and 740 °C × 130 min (**c**,**d**) where (**b**,**d**) represent the magnification of the red and yellow square area (Reprinted from ARTICLE 7).*

Table 10. Chemical composition (EDS) of spectra A and B (wt.%) (see ARTICLE 7).

Spectrum	Ti	Al	V	Fe	Phase
A	91.6	7.2	1.2	-	α
B	89.9	2.0	7.9	0.2	β

Considering the EDS spectra (ARTICLE 6) and the β-phase location (*Figure 36b,d*), the β-stabilizer alloying elements diffuse from the hcp lattice of the α'-martensite and promote the β-phase formation along its boundaries. At the same time, the supersaturated α'-laths become α-laths stabilized by the α-stabilizer alloying elements that remain within the hcp lattice.

The EBSD maps reported in *Figure 37* detected a 2–3 % of β-phase in both the heat-treated conditions. Therefore, the increase in HT temperature and the different cooling method do not influence the quantity of transformed β-phase.

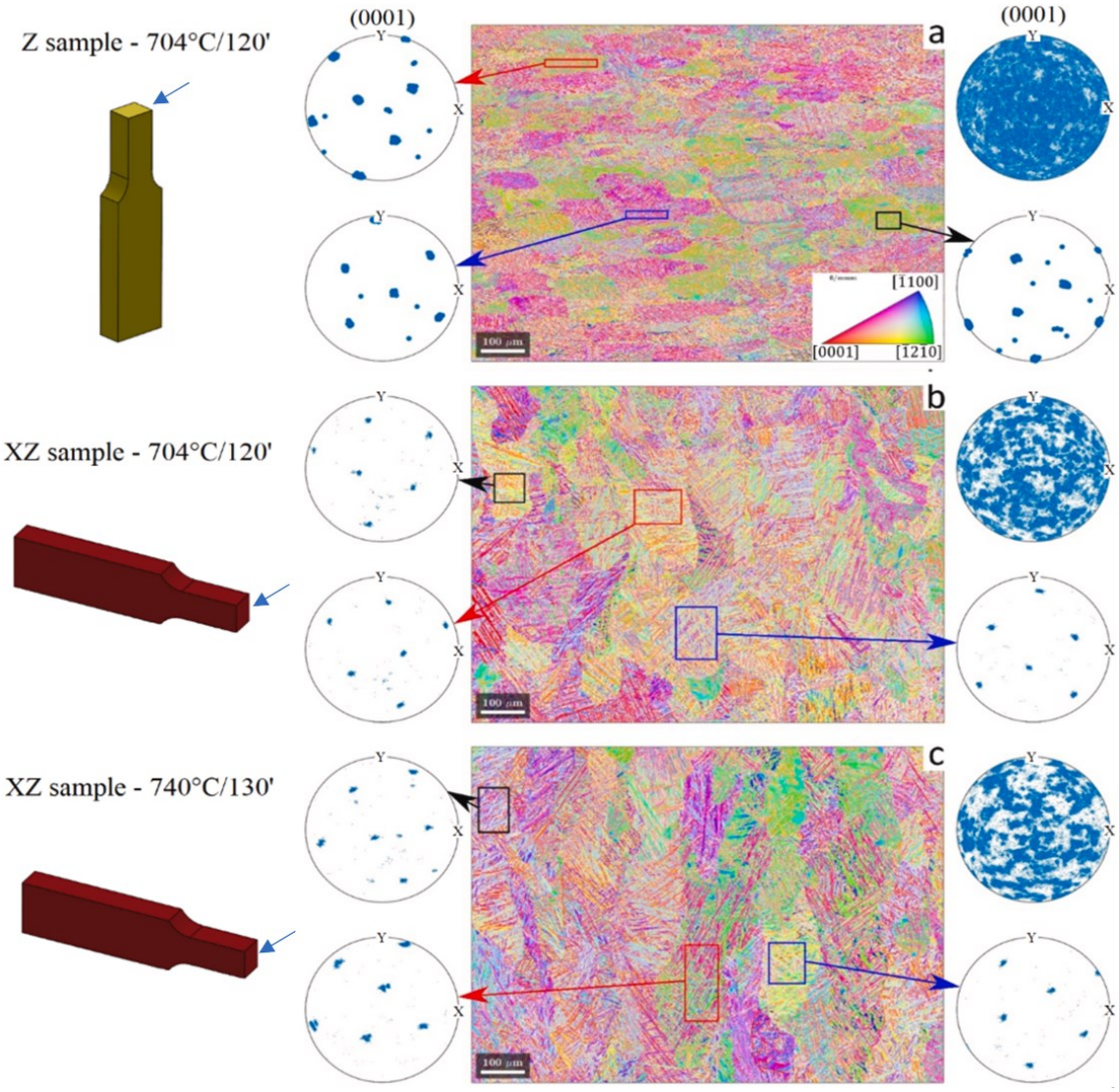


*Figure 37. EBSD maps acquired on (**a**) xy planes of the Ti6Al4V sample heat-treated at 704 °C × 120 min, (**b**) xz plane of Ti6Al4V sample heat-treated at 704 °C × 120 min, (**c**) xz plane of the Ti6Al4V sample heat-treated at 740 °C × 130 min. Scalebar length is 100 μm in all planes and the pole figures report <0001> direction of the α-phase (Reprinted form Reference [155]).*

At the same time, the EBSD measurements reveal different orientations of the α-phase within the columnar β-grains, in contrast with the literature results previously reported and discussed. On the other hand, the following orientational relationships between the α and β phases can be drawn as $(100)_\beta \parallel (0001)_{\alpha'}$ and $[11\bar{1}]_\beta \parallel [2110]_{\alpha'}$. At the same time, these Burger's relationships are the same describing the α'-martensites in as-built conditions. As a matter of fact, the $\alpha' \rightarrow \alpha + \beta$ decomposition only takes place through the Al and V alloying elements diffusion, as previously discussed. For further information see ARTICLE 6.

In all cases, the SHT at 1050 °C × 60 min promoted the recrystallization process of the columnar β-grains in equiaxed ones (*Figure 38*). On the other hand, the $\alpha + \beta$ microstructure formed within the recrystallized equiaxed β-grains is influenced by the differences in sample thickness (*Figure 38a,c* vs *Figure 38b,d*) which affect the cooling rate during the same furnace cooling in argon gas for 60 min.

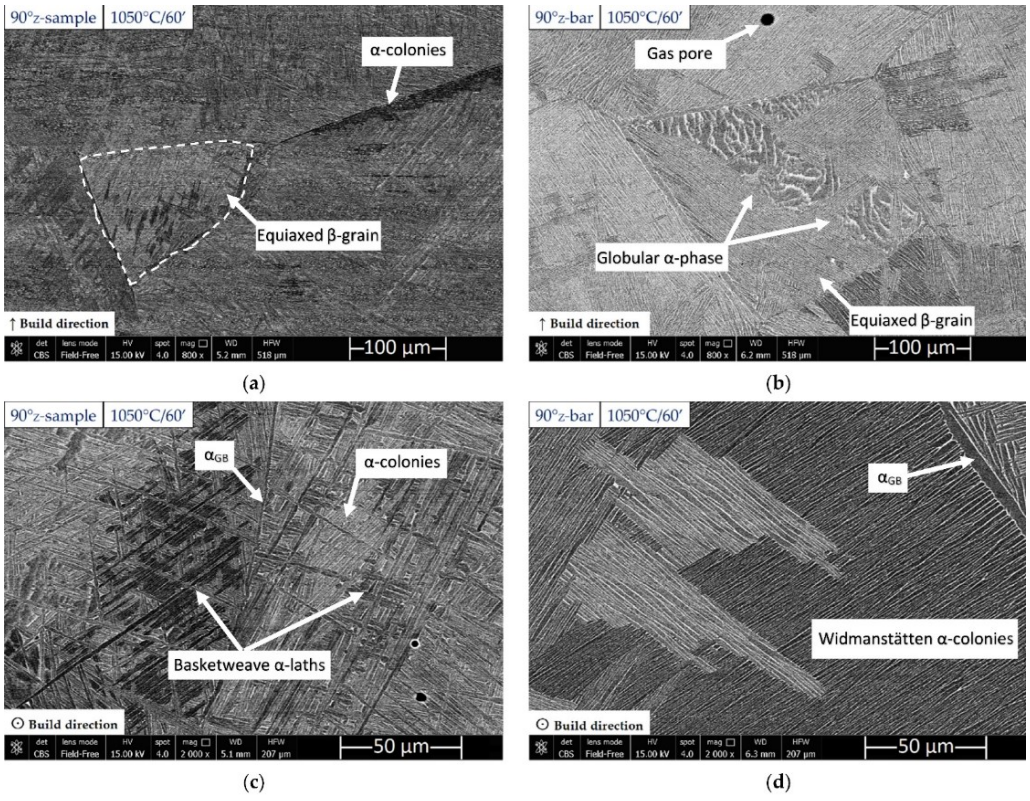


*Figure 38. SEM micrographs of Ti6Al4V-ELI tensile samples heat-treated at 1050°C × 60 min (**a**,**b**) and bars heat-treated at 1050 °C × 60 min (Reprinted from ARTICLE 7).*

Creep and tensile samples are formed by α-laths in a basketweave structure and by fine α-colonies which nucleate on the α_{GB} (α Grain Boundary) and grow to the centre of the equiaxed grains (*Figure 38c*). On the contrary, bars show α-colonies in a

basketweave structure (Widmanstätten) and globular α-phases (*Figure 38b*) despite the same furnace cooling for 1h with argon gas (see ARTICLE 7). As a matter of fact, Ahmed et al. [156] affirmed that the α-laths in a basketweave (*Figure 38a,c*) structure are formed by cooling rates < 15 °C s^{-1}, unlike the cooling rates < 1.5 °C s^{-1} necessary to promote the α-colonies (*Figure 38b,d*) in a basketweave structure (ARTICLE 7).

2.2. Mechanical Properties Optimization

In the following sub-chapters, Vickers microhardness was measured to evaluate the optimization of the HTs and the correlated tensile properties of the as-built and heat-treated samples were discussed. The effects induced by DA HTs performed in the range between 175 and 225 °C, SHT and T6 were examined for the AlSi7Mg and AlSi10Mg[50,90] alloys. At the same time, two HTs at 704 °C and 740 °C and one at 1050 °C (below and above the β-transus, respectively) were discussed for Ti6Al4V samples manufactured in different build orientations.

2.2.1. AlSi7Mg and AlSi10Mg L-PBFed Alloys

The as-built AlSi7Mg (*Figure 39a*) and AlSi10Mg[90] (*Figure 39b*) SL and DL bars show a decreasing trend of the HV0.5 measurements from the bottom regions to the top ones due to the precipitation phenomena (sub-chapter 2.1.1.). If the perfect overlap between the SL and DL profiles is also considered, as well as the microstructure morphologies (*Figure 28*, see ARTICLE 1, ARTICLE 2 and ARTICLE 4), the heat-treated samples will not be distinguished in relation to the machine set-up (i.e., between SL and DL). Focusing on the AlSi7Mg bars, the HV profiles (*Figure 39a*) are almost constant at around 120 ± 4 HV0.5 both in the bottom and middle regions, respectively; while they decrease to 110 ± 4 HV0.5 in the top region (200–300 mm). In this case, the high manufacturing time (~ 75 h) may induce over-aging phenomena on the bottom region as confirmed by the following aging curves. On the contrary, the AlSi10Mg[90] bars already show the same decreasing trends from the bottom (132 ± 2 HV0.5) to the top (110 ± 2 HV0.5) regions (*Figure 39b*) thanks to the lower manufacturing time. In relation to the AlSi10Mg[50] bars, the HV measurements follow the trends characterizing the AlSi10Mg[90] but at lower values: 120 ± 5 HV0.5 and 106 ± 5 HV0.5 for bottom and top regions, respectively, due to the differences in terms of grain morphologies (see sub-chapter 2.1.1.).

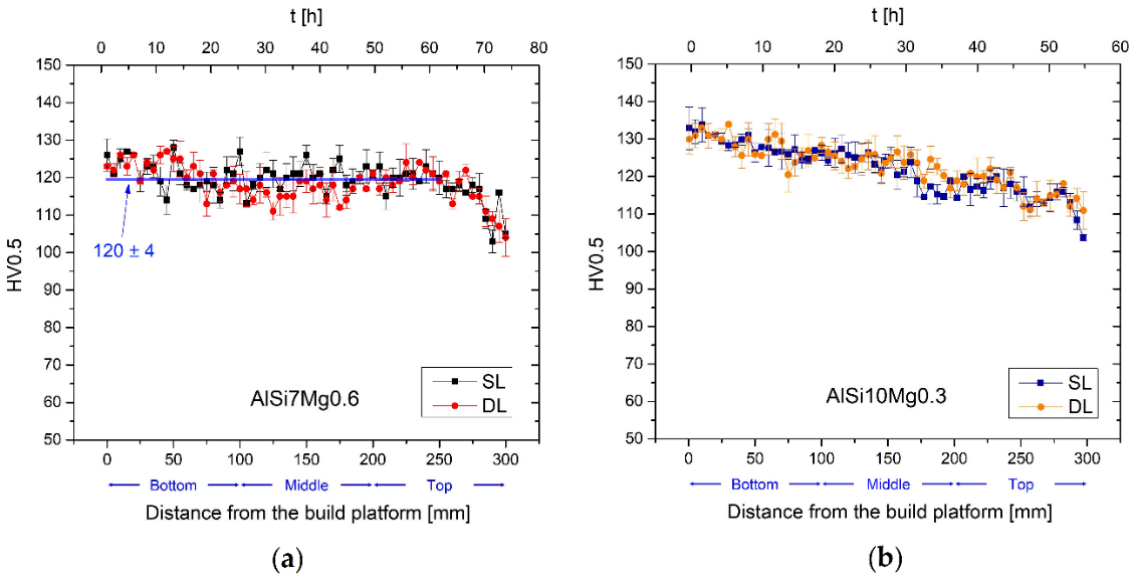


*Figure 39. HV profiles obtained by the microhardness measured on the as-built SL and DL: (**a**) AlSi7Mg and (**b**) AlSi10Mg[90] bars, respectively (Reprinted from ARTICLE 2).*

The microhardness variation between the bottom and top regions in all the analysed aluminium bars is conferred by the differences in terms of precipitates within the α-Al matrix (*Figure 40*), as previously mentioned. In fact, the amount of nano Si-particles and β-Mg_2Si (XRD analysis in ARTICLE 1) confers a contribution of the material strengthening, as will be discussed in the last part of the present sub-chapter.

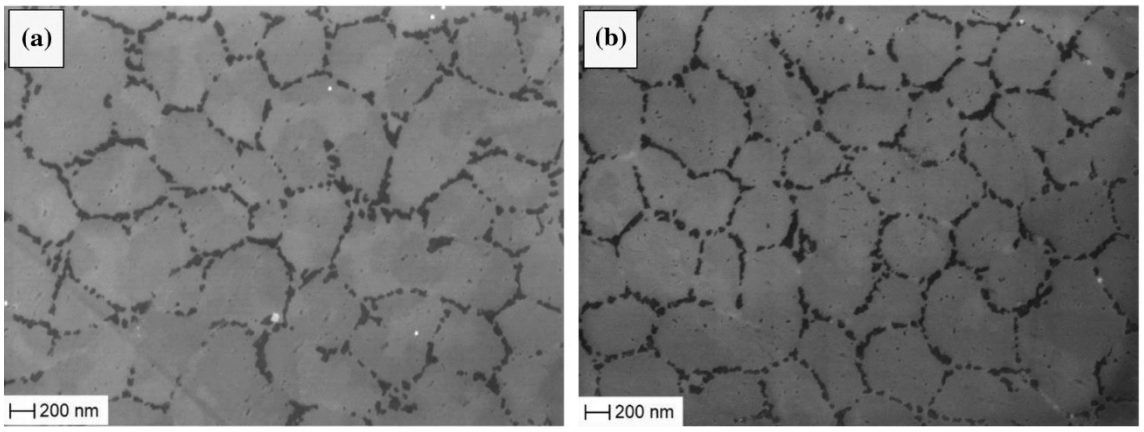


*Figure 40. SEM micrographs of the (**a**) top and (**b**) bottom regions of AlSi10Mg bars in as-built conditions (Reprinted from ARTICLE 1).*

Due to these variations, DA HTs were performed on the bars to evaluate a possible homogenization of the mechanical properties between the opposite regions of the bars retaining the good performance conferred by the L-PBF process. As a matter of fact, different aging responses obtained by unoptimized HT parameters can generally

confer worsening effects in mechanical components characterized by a higher height than 10 mm.

Figure 41 illustrates the aging curves of the AlSi7Mg (*Figure 41a,b*) and AlSi10Mg^{90} (*Figure 41c,d*) samples direct aged at 175 °C, 200 °C and 225 °C. Generally, the homogenization of the HV values between the AlSi7Mg top (*Figure 41a*) and bottom (*Figure 41b*) samples is obtained at 175 °C × 2 h. For the top samples, already the DA at the 175 °C × 1 h confers a peak-aging condition (128 ± 3 HV0.5), in which the as-built microhardness increases of about + 13.4 %. *Figure 42* validates the presence of a higher precipitate amount than the as-built samples (*Figure 40*), and the consequent increase in hardness. On the contrary, the monotonical decrease of the HV profile of the bottom samples supports their over-aging conditions given that the undamaged Si-eutectic network (*Figure 31*) cannot confer detrimental effects on the mechanical properties. In addition, the XRD analysis (ARTICLE 1) confirms the coarsening effects of the precipitates within the α-Al matrix. After the DA at 200 °C, the HV measurements were, in contrast, homogenised after the 1h of treatment. In relation to the DA at 225 °C, the as-built bottom and top samples already present the homogenised HV values due to the effects induced by the hot BP (*Figure 39*). In summary, the as-built blocks, which are taken to consideration to evaluate the HF effects, were obtained from a different distance with respect to the BP. For the top samples, their distance decreases with the increase in HT temperature, and vice versa for the bottom ones. This choice has been dictated by the results obtained in other research activities (ARTICLE 1, ARTICLE 2 and ARTICLE 4). For more information, see ARTICLE 2. Considering the AlSi10Mg^{90} samples, the microhardness measured on the bottom and top samples are already homogenised after 1h of all the DA temperatures considered (*Figure 41c,d*). For both the AlSi7Mg and AlSi10Mg^{90} samples, the DA at higher temperatures also causes damaging effects on the Si-eutectic network (*Figure 31c,d*) in addition to the precipitation phenomena (see ARTICLE 1, ARTICLE 2, ARTICLE 4 and ARTICLE 5). In fact, the constant trend of the aging curve of the AlSi7Mg top samples DA at 200 °C is explained by these synergetic effects; namely, the precipitation phenomena balance the decrease in HV values conferred by the damaged Si-eutectic network. The lower microhardness values were measured on the bottom and top samples solution heat-treated at 505 °C × 2.5 min – 4 h. In fact, the HV values significantly decrease from 120 ± 4 HV0.5 and 132 ± 2 HV0.5 (as-built conditions) to 81 ± 1HV0.5 and 76 ± 1HV0.5 for the AlSi7Mg and AlSi10Mg^{90} samples, respectively, already after the SHT at 505 °C × 2.5 min. Subsequently, both trends slowly decrease to 64 ± 2 HV0.5 and 59 ± 1 HV0.5 after 4 h of treatment, respectively. This primary severe hardness reductions are conferred by the significant variation of the microstructural morphology (*Figure 31* and *Figure 32*) both in terms of

Si-eutectic particles and grain size as discussed in sub-chapter 2.1.1. The continuous increase of the grain size induces the secondary decrease of HV measurements [33]. On the other hand, the double content of Mg present in AlSi7Mg alloy rather than in AlSi10Mg (*Table 7*) alloy provides better effects both in SHT and T6 heat-treated conditions. In the first case, the higher strengthening of the AlSi7Mg samples is conferred by a solid solution characterized by higher Mg content. In the second case, the 0.6 % of Mg allows to obtain a higher amount of β-Mg_2Si hardening precipitates, namely a higher aging response as highlighted by the peak-aging of both the AlSi7Mg (111 ± 2 HV0.5) and AlSi10Mg[90] (97 ± 2 HV0.5) reached after 8 h and 4 h at 175 °C, respectively (see ARTICLE 2).

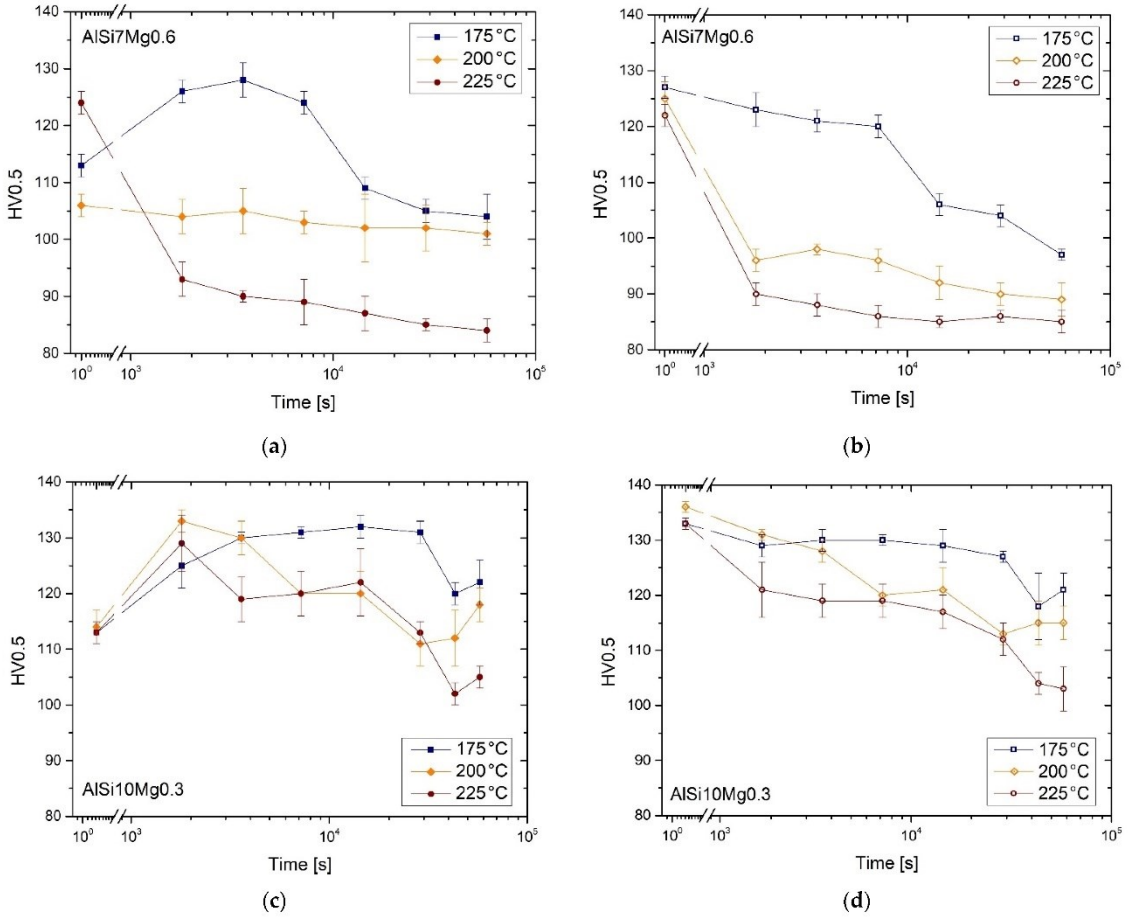


*Figure 41. Aging curves obtained after the DA at 175 °C, 200 °C and 225 °C analyzing the top (**a**,**c**) and bottom (**b**,**d**) samples of the AlSi7Mg (**a**,**b**) and AlSi10Mg[90] (**c**,**d**) samples (Reprinted from ARTICLE 2).*

Despite the different process parameters between the AlSi10Mg[50] and AlSi10Mg[90] samples (*Table 8*), the former also reached 96 ± 2 HV0.5 at the same peak-aging conditions (SHT at 505 °C× 4 h + AA at 175 °C × 4 h).

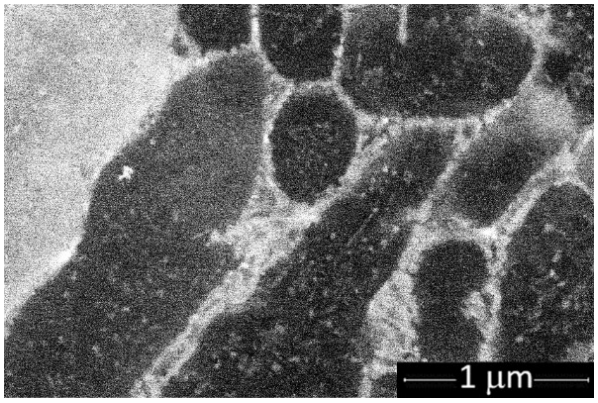


Figure 42. SEM micrographs of top AlSi10Mg samples DA at 175 °C (Reprinted from ARTICLE 1).

In relation to the as-built mechanical properties, all the AlSi7Mg and AlSi10Mg[50,90] samples follow the trends described by the HV profiles (*Figure 39*) thanks to the higher UTS and YS values of the bottom tensile samples compared to those of the top ones (ARTICLE 1, ARTICLE 2 and ARTICLE 4) as shown in *Table 11*.

Table 11. Mechanical properties of the as-built AlSi7Mg, AlSi10Mg[50] and AlSi10Mg[90] tensile samples (ARTICLE 1, ARTICLE 2 and ARTICLE 4).

Samples	AlSi7Mg			AlSi10Mg[50]			AlSi10Mg[90]		
	UTS [MPa]	YS [MPa]	ε [%]	UTS [MPa]	YS [MPa]	ε [%]	UTS [MPa]	YS [MPa]	ε [%]
Bottom	423 ± 6	292 ± 4	11.4 ± 0.4	425 ± 13	282 ± 12	7.1 ± 0.5	438 ± 13	283 ± 10	6.7 ± 0.7
Top	419 ± 6	278 ± 10	11.9 ± 0.5	364 ± 6	222 ± 2	7.2 ± 0.2	410 ± 7	239 ± 6	6.8 ± 1.2

Figure 43 exhibits the mechanical properties of the optimized HT conditions (temperature-time) obtained by the analysis of the HV measurements. For the AlSi10Mg alloys (*Figure 43a*), also the tensile samples DA at 175 °C (U-HT1, ARTICLE 1) shows the effects induced by the aging phenomena both on the UTS and YS values which increase of about + 7.3 % and + 3.0 %, respectively. Increasing the DA temperatures at 200 °C (U-HT2, ARTICLE 1) and 225 °C (U-HT3, ARTICLE 1), the tensile strengths show a decreasing trend, reaching ~ 336 ± 5 MPa and ~ 192 ± 7 MPa for the UTS and YS, respectively. On the other hand, the elongation obviously increases from 7.1 ± 1.0 % to 14.5 ± 1.0 %. The AlSi7Mg tensile samples show the same trends (*Figure 43b*) when the DA temperatures are increased, also in terms of reached UTS and YS values (see ARTICLE 2). In this case, the tensile samples DA at 225 °C are characterized by lower ductility values (~ 11 ± 1.0 %) than the previously mentioned AlSi10Mg (*Figure 43a*). The highest elongation values (~ 22 %) are obtained only after the SHT at 505 °C × 4 h, in which case the AlSi7Mg samples are characterized by the microstructure illustrated in *Figure 32c*. At the same time, the UTS and YS decrease to 250 ± 7 MPa and 137 ± 5 MPa, respectively. These worsening effects are recovered by the AA at 175°C × 4h and × 8h,

peak-aging conditions of the AlSi10Mg and AlSi7Mg alloys, respectively. Firstly, the highest reached values are 284 ± 7 MPa for the UTS and 234 ± 6 MPa for the YS of the AlSi10Mg[90]. Secondly, the AlSi7Mg (*Figure 43b*) is characterized by higher strength values: 297 ± 11 MPa for the UTS and 253 ± 8 MPa for the YS. As regards the tensile strengths of the AlSi10Mg[50], the obtained values (284 ± 5 MPa for UTS and 235 ± 4 MPa for YS) also confirm no dependence between the process parameters and the mechanical properties after the T6 HT. The exhibited elongations after the T6 HT do not show any improvements from the as-built conditions. As a matter of fact, only a few AlSi10Mg samples are characterized by higher ductility values than 12 %, values for which the tensile samples reached the necking formation. Therefore, a perfectly ductile failure is not show by all tensile samples as also confirmed by the Considère criterion in ARTICLE 4. No direct aging samples shown the necking after the failure.

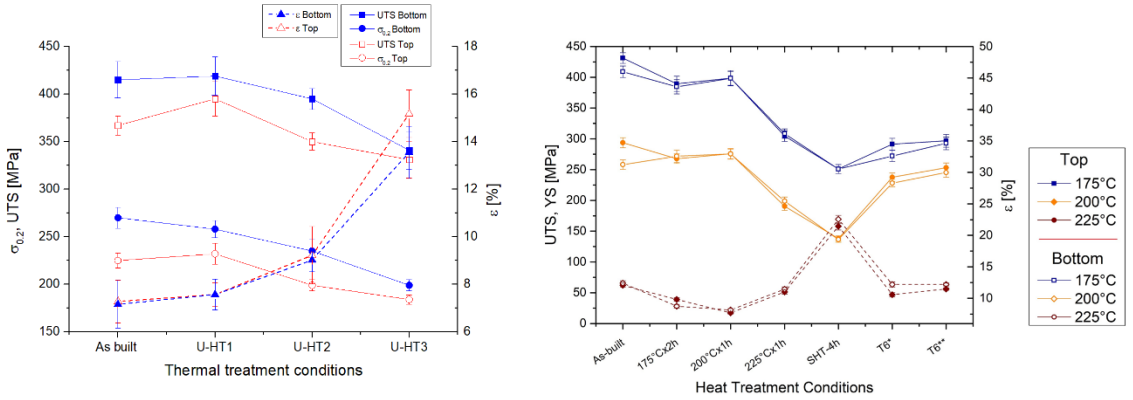


*Figure 43. Mechanical properties of top and bottom (**a**) AlSi10Mg and (**b**) AlSi7Mg samples in as-built and heat-treated conditions (Reprinted from ARTICLE 1 and ARTICLE 2).*

In relation to the fracture mechanisms, not only the as-built and direct aged tensile samples exhibited a crack propagation generally along the HAZ (ARTICLE 4), but also the T6 heat-treated samples showed the same conditions where the MP or laser scan track boundaries are present. As regards the as-built samples, the HAZs facilitate the crack propagation due to their microstructural morphology (*Figure 30*). As a matter of fact, the little amount of Si-eutectic particles confers a lower resistance than that shown by the full cellular structure. The same explanation can be adapted for the direct aged samples (ARTICLE 4), in which case the HAZ is affected by the coarsening phenomenon. On the other hand, the T6 heat-treated samples exhibited a deflection of the crack path in correspondence with the MP boundaries, as previously mentioned. In these samples, however, the crack propagates by interconnecting the voids formed thanks to the

decohesion phenomena between the same aluminium matrix and the Si-eutectic particles (ARTICLE 4).

The described and discussed variations in terms of Vickers microhardness and tensile strength for both aluminium alloys can also be described through the following strengthening sum:

$$\sigma_{0.2} = \sigma_f + \sigma_{ss} + \sigma_{HP} + \sigma_{Or} + \sigma_\rho + \sigma_{pre} \quad (11)$$

where σ_f is the friction lattice stress [MPa], σ_{ss} is the stress contribution related to the solid solution (chemical concentration of Mg and Si within the lattice) [MPa], σ_{HP} and σ_{Or} are the stresses related to the Hall-Patch and Orowan mechanisms, respectively, σ_ρ is the stress conferred by the dislocation density and σ_{pre} is the stress related to the precipitates and the consequent dislocations [33]. In as-built conditions, the high values of HV, YS and UTS are mainly conferred by the third, fourth and fifth terms of the Eq. (11). Firstly, the nanometric grain size provides a contribution of around 89 MPa calculated through the following Hall-Petch equation:

$$\sigma_{HP} = \frac{K}{\sqrt{d}} \quad (12)$$

where K is a material constant (~ 0.04 MPa $m^{-1/2}$) and d is the average grain size. Secondly, the Orowan mechanisms (*Figure 44*) trigger a significant increase of the material strengthening during the deformation thanks to both the full-cellular structure of the aluminium samples and the presence of the nano Si-particles. For further information see [33]. As a results of this, the dislocation density (ρ) increases by leading a proportional rise in material strengthening, as follows:

$$\sigma_\rho = MbG\beta\sqrt{\rho} \quad (13)$$

where M, b, G and β are the Taylor factor, the Burger's vector, the shear modulus and the material constant, respectively.

On the contrary, the differences between top and bottom samples are related to the σ_{pre} strengthening contribution only due to the variation in terms of precipitates (*Figure 40*), as well as for AlSi7Mg and AlSi10Mg samples DA at 175 °C, in which case, however, the over-aging conditions decrease the σ_{ss} and σ_{Or} contributions. On the other hand, the damaged Si-eutectic network continues to reduce the σ_{Or} contribution owing to the rise in DA temperatures. Reaching the T6 heat-treated conditions, only the σ_{Or}, σ_{pre} and σ_ρ control the strengthening mechanisms. In fact, the σ_{ss} term becomes negligible and the σ_{HP} reaches lower values than 15 MPa [33,157–159].

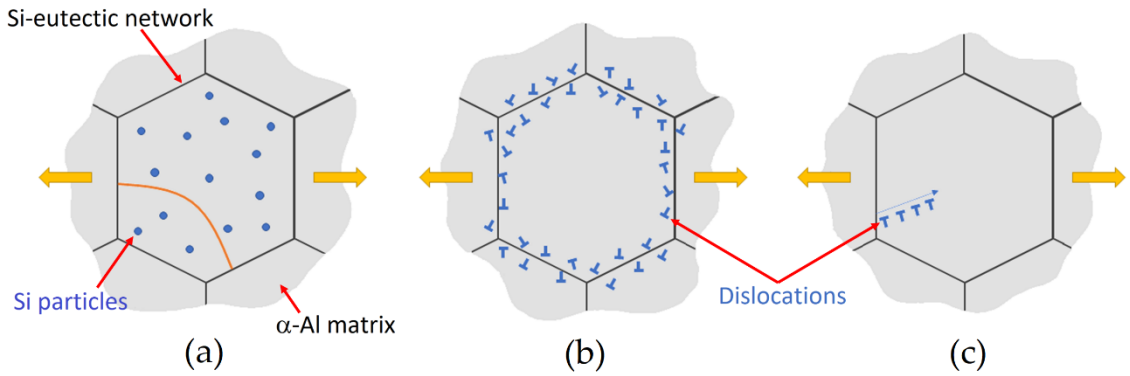


*Figure 44. Schematic representation of plastic deformation mechanisms related to the full cellular structure: (**a**) dislocation de-pinning from the atoms dispersed into SSS α-Al matrix; (**b**) deformation by cutting dislocation "forests"; (**c**) emission of dislocation from the interface between the Al and Si (Reprinted from Reference [33]).*

The effects of Si-particle ripening conferred by the DA HTs or obtained during the creep test at 150 °C, 175 °C and 225 °C also induce a decrease in terms of creep resistance as shown in *Figure 45a*. The amount of decrease in stress is shown in *Figure 45b* where the following equation is reported for the 150 °C and 175 °C testing temperatures:

$$\Delta\sigma = \sigma^{ad} - \sigma^{ht} \tag{14}$$

where σ^{ad} and σ^{ht} represent the stress applied to obtain a given value of the minimum strain rate in as-built and heat-treated conditions, respectively.

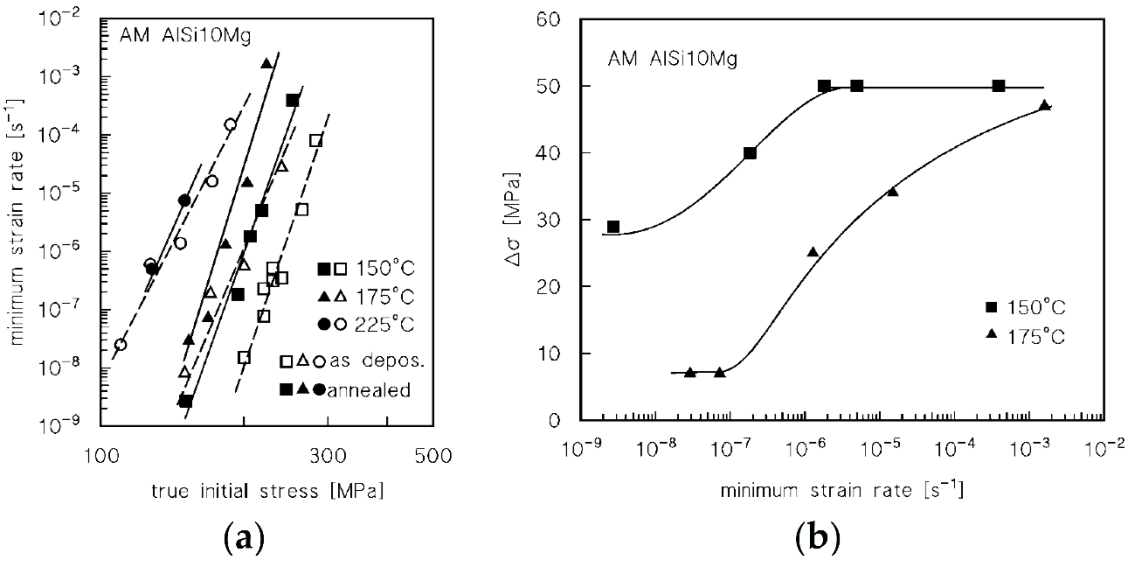


*Figure 45. (**a**) Minimum creep rate dependence on applied stress for as-built and heat-treated AlSi10Mg samples. (**b**) Stress variation (Δσ) as a function of the minimum creep rate (Reprinted from ARTICLE 8).*

In the same figure, the curve related to 225 °C is omitted because it overlaps with to the as-built case. At low testing temperatures (150 °C), the creep strengthening is maintained due to lower coarsening effects of Si-particles compared to in the case at 175 °C, in which the $\Delta\sigma$ monotonically decreases (from 47 to 7 MPa). For further information and the model-based validation see ARTICLE 8.

In order to quantify the quality of the analysed aluminium samples in as-built and heat-treated conditions, the following quality index (QI) equation was considered:

$$QI = UTS_T + \hat{d}\, log(\varepsilon_T) \tag{15}$$

where the UTS_T is the true ultimate tensile strength ($UTS_T = UTS(1+\varepsilon)$), the ε_T is the true elongation ($\varepsilon_T = \ln(1+\varepsilon)$) and $\hat{d}$ is an empirical parameter making QI values independent of the YS. The calculated quality indices for as-built, DA and T6 heat-treated conditions were then plotted in QI-graphs as shown in *Figure 46*. Generally, the highest quality indices were shown by the as-built bottom AlSi10Mg (525–585 MPa) and AlSi7Mg (570–595 MPa) tensile samples. In relation to the top AlSi10Mg samples, the lower QI (475–525 MPa) is conferred by the low UTS values than those obtained by the bottom samples. Focusing on the DA HTs, the best QI values are instead exhibited by the lower testing temperatures (175 °C and 200 °C). In fact, the AlSi7Mg direct aged at 225 °C shows the same QI values of the T6 heat-treated AlSi7Mg and AlSi10Mg samples manufactured with both the L-PBF process and casting technique. Despite the low UTS values reached by the solution heat-treated AlSi7Mg samples, their QI is comparable to the T6 heat-treated samples (ARTICLE 2 and ARTICLE 4).

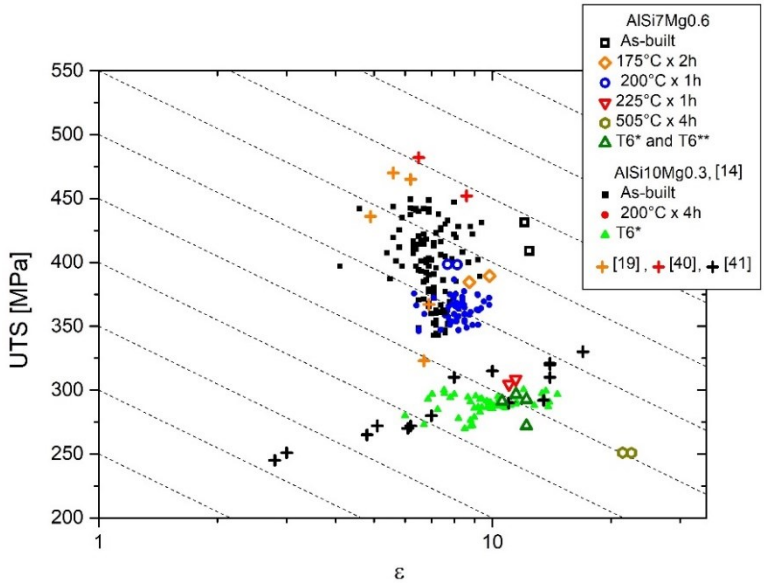


Figure 46. QI-graphs of as-built, DA and T6 heat-treated AlSi10Mg and AlSi7Mg samples. References [14,19,40,41] are the following new References [67,71,160,161] (Reprinted from ARTICLE 2).

2.2.2. Ti6Al4V-ELI L-PBFed Alloy

Due to the fully martensitic microstructure, the as-built Ti6Al4V-ELI samples are characterized by high values of UTS (~ 1200 MPa) and YS (~ 1050 MPa), while the elongations are lower than 7 % [33,79,86,162,163]. After the HTs at 704 °C and 740 °C, both the UTS and YS values decrease to 1050 ± 20 MPa and 950 ± 25 MPa, respectively, due to the $\alpha' \rightarrow \alpha + \beta$ decomposition discussed in sub-chapter 2.1.2. On the contrary, the elongations increase at higher values than 8.5 %. As widely discussed in ARTICLE 6, the different build orientations (90°, 45°, $0°_{xz}$, $0°_{xy}$ in *Figure 22b*) do not confer significant effects on the mechanical performance (*Figure 47*). In fact, the only UTS and YS variations of 40 and 50 MPa, respectively, between the XZ/XY and the Z/45° samples are observable after the HT at 704 °C × 120 min.

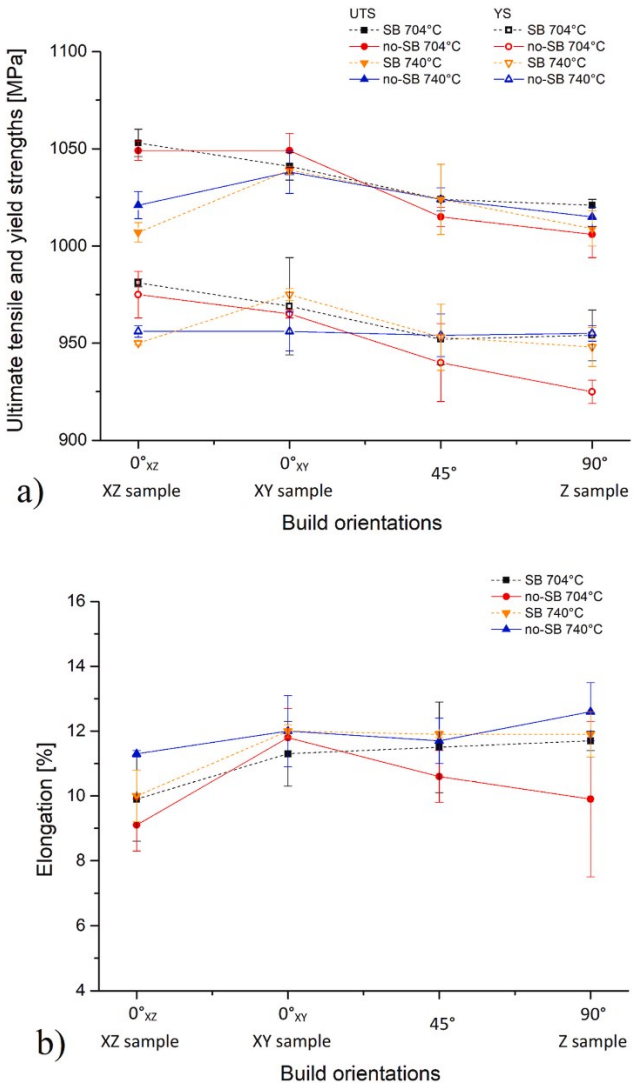


*Figure 47. Mechanical properties of Ti6Al4V-ELI samples of different build orientations and surface finishing: (**a**) UTS and YS, (**b**) elongations (Reprinted from Reference [155]).*

Considering the lack of preferential orientations of the α-phases highlighted in *Figure 37*, the possible source of anisotropy can be inferred, as follows:

1. the elongation of the columnar β-grains along the build direction (i.e., z-axis);
2. the presence of lack-of-fusion pores on the xy/xz planes;
3. a different amount, also in terms of dimensions, of the α_2-Ti_3Al and $TiAl_3$ precipitates.

Firstly, the presence of the columnar β-grains even after the HT at 704 °C (*Figure 36*, *Figure 37*) controls the crack propagation during the tensile test. Generally, the horizontal samples (H-samples) show higher tensile strengths and ductility than the vertical samples (V-samples) due to the correlation between the directions of the tensile load and the major axis of the columnar grains [33].

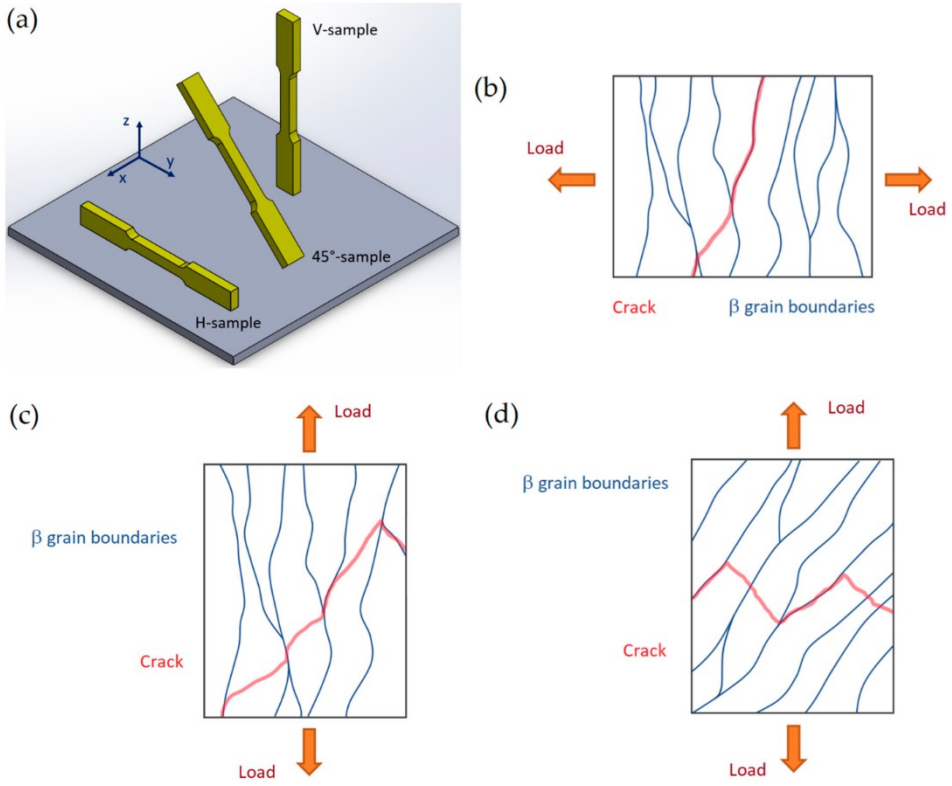


*Figure 48. Schematic representation of different Ti6Al4V samples: (**a**) H-, 45°- and V-samples, (**b**–**d**) under the same load conditions but with different orientation between the load axis and the columnar β-grains (Reprinted from Reference [33]).*

As a matter of fact, the V-samples (*Figure 48a,c*) promote a more tortuous crack path thanks to its intergranular propagation along the α-phase grain boundaries compared to the other build orientations, as shown in *Figure 48b,d*. *Figure 48b* illustrates a crack propagation, which characterizes the H-samples, essentially along the β-grain

boundaries where the slip of the crack along the α-phase grain boundary interconnects two adjacent β-grain boundaries. On the other hand, *Figure 48d* shows a trans-granular crack propagation that confers a fluctuating path through the columnar grains [33]. Considering that the columnar β-grains remain even after the HT at 740 °C, this cannot be the origin and the main cause of the anisotropy behaviour.

Secondly, during a tensile test, the LOF pores can influence the premature failure of the samples if the load direction is perpendicularly arranged to the LOF major-axis (xy plane, *Figure 49a,b*). At the same time, if the tensile load is in parallel with the same major axis, the LOF pore tend to close, and the premature failure can be avoided (*Figure 49c*). In the first case of load condition, the one that characterizes the V-samples, the perpendicular position between the load and major axis always promotes a premature failure due to the opening effects of the LOFs (*Figure 49d*). In the second load condition, the premature failure state increase with increasing the angle (θ) between the same load direction and the major axis of LOFs (*Figure 49d*). The maximum effect is highlighted when θ is equal to 90°, namely when the load direction is also perpendicular to the major axis (condition that always characterizes the V-samples).

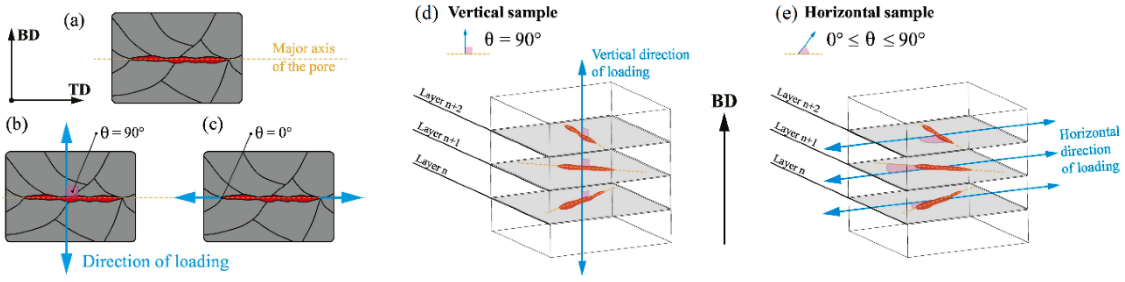


*Figure 49. Schematic representation of the load direction and the LOF major axis during a tensile test in V-samples (**b**,**d**) and H-sample (**c**,**e**); (**d**,**e**) Schematic representation of the load direction and the different orientation of LOF major axis within the same sample and correlated to the different layers (Reprinted from Reference [33]).*

Thirdly, the anisotropy behaviour can be conferred by the different precipitation phenomena related to the α_2-Ti_3Al and $TiAl_3$ intermetallics. As a matter of fact, the XRD measurements, shown in ARTICLE 6 and ARTICLE 7, highlight the diffraction peaks of both precipitates only in some heat-treated samples at 704 °C and 740 °C, respectively. In this context, the aging effects induced by these HTs on the other samples cannot be excluded because the precipitate dimensions can be less than the detectable limit of the XRD measurement. Further microstructural analysis will be carried out in future works. From these premises, the identified α_2-Ti_3Al and $TiAl_3$ through the XRD analysis can be affected by coarsening phenomena because they can already be formed during the L-PBF process [33].

Always from a mechanical point of view, the sand-blasting process does not influence the mechanical properties of the heat-treated Ti6Al4V-ELI samples (*Figure 47*). As discussed in ARTICLE 6 and ARTICLE 7, the sand-blasting effects are only detected on the outer surface of the samples where, firstly, the surface roughness decreases from S_a > 17 μm to S_a < 17 μm and, secondly, the plastic strain is accumulated. In fact, the broadening diffraction peaks of the α-phase in *Figure 50* confirm the lattice distortion as a consequence of the deformation induced by the impact of the glass spheres. At the same time, the penetration depth of the plastic strain can be approximately estimated as the X-Ray penetration depth because both the SEM investigations (ARTICLE 6) and the HV0.5 profiles (*Figure 51*), performed on the cross-section of the tensile samples, do not reveal any inhomogeneity.

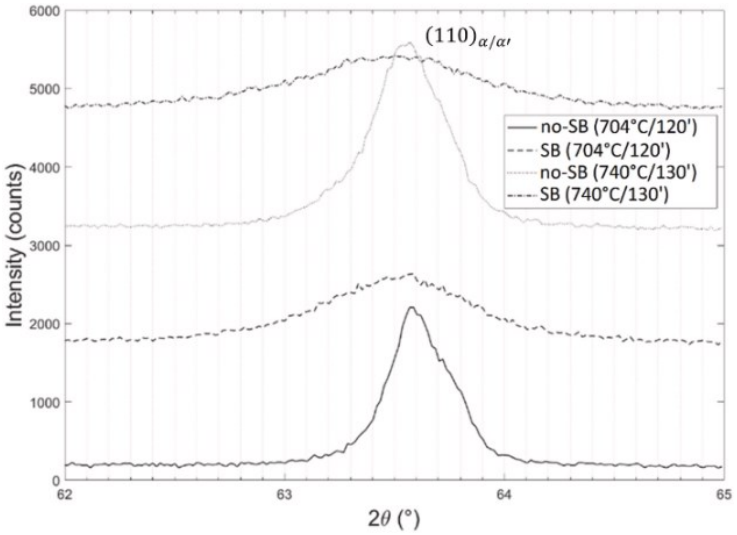


Figure 50. XRD patterns related to the no-SB (no Sand Blasted) and SB Ti6Al4V-ELI samples for both heat-treated conditions (Reprinted from Reference [155]).

Figure 51a,b shows the HV0.5 profiles performed on the tensile samples cross-section both in SB (circle symbols) and no-SB (square symbols) conditions. All pairs of profiles do not reveal any variation from the centre (381 ± 5 HV0.5 and 383 ± HV0.5) to the outer edge (383 ± 9 HV0.5 and 388 ± 8 HV0.5), form which the indentation is placed at 100 μm. The only increase in HV measurements (*Figure 51c*) was found on the cross-section of the tensile samples that were heat-treated at 1050 °C × 60 min because the outermost part of the cross-section presents an α-case layer as shown in *Figure 52*.

The HT temperature over β-transus triggers the formation of the α-case layer due to the diffusion of the oxygen alloying element in the interstitial position of the hcp lattice of the α-phase. The presence of a higher content of oxygen atoms increases the β-transus temperature locally and, therefore, the $\alpha \rightarrow \beta$ transformation during the heating

and holding time at high temperatures (e.g., 1050 °C) is prevented. In fact, the following cooling in argon gas does not modify the microstructure, differently from as in the equiaxed β-grains (*Figure 38*) in which the $\alpha \rightarrow \beta$ occurs.

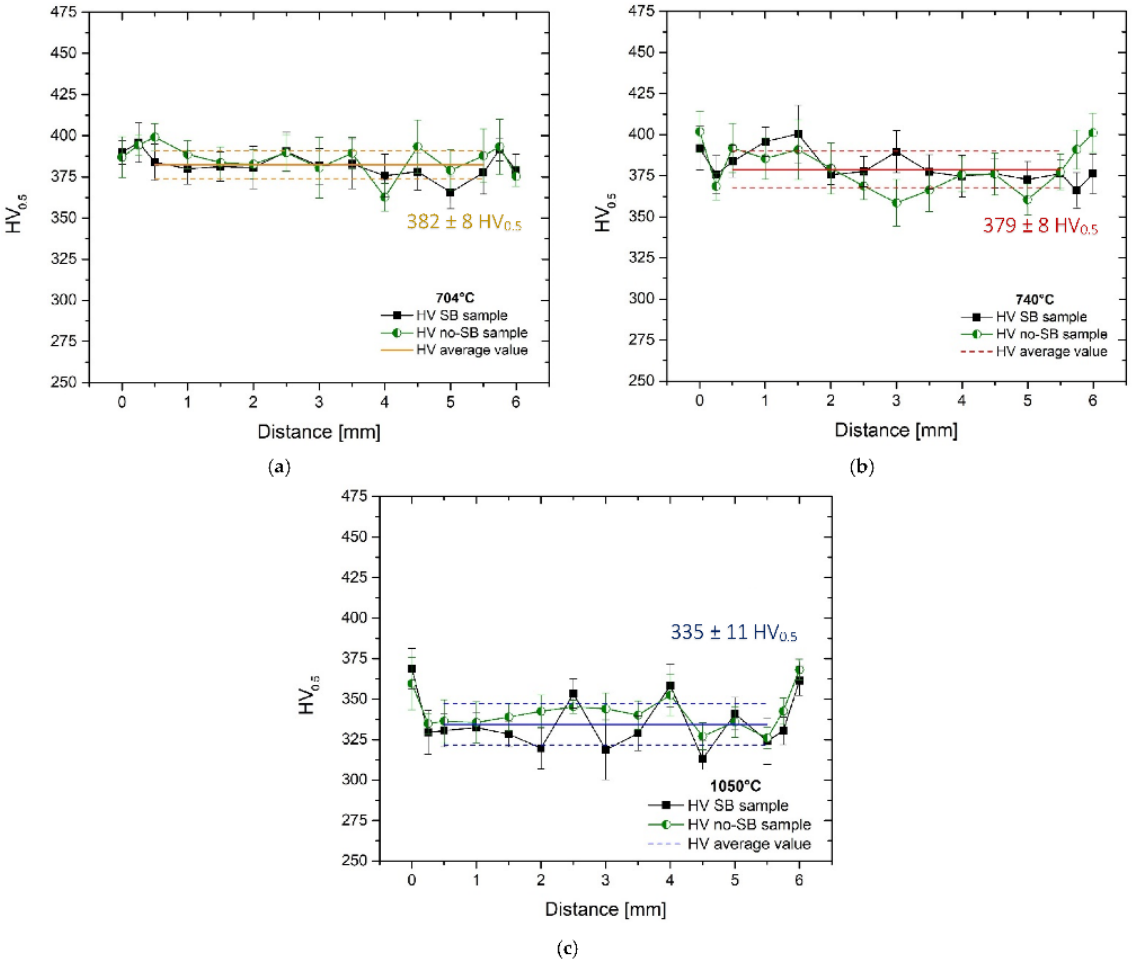


*Figure 51. HV profiles related to the cross-section of SB and no-SB samples heat-treated at 704 °C (**a**), 740 °C (**b**) and 1050 °C (**c**) (Reprinted from ARTICLE 7).*

At the same time, the presence of the interstitial atoms of oxygen, which form an interstitial solid solution, confers an increase in hardness of about 12 %, as highlighted in ARTICLE 7. In the same article, the presence of oxygen was also confirmed by the XRD pattern performed on the sample surface which highlighted different peaks related to titanium oxides.

In relation to the mechanical properties of the Ti6Al4V-ELI samples heat-treated at 1050 °C × 60 min, the average UTS and YS decrease to 918 ± 7 MPa and 818 ± 7 MPa (*Figure 53*), respectively, due to the microstructural morphology variation discussed in *Figure 38*. On the other hand, the elongation values reach 12.7 ± 1.0 %, which satisfy the

current standard specification. At the same time, the presence of the α-case layer could have promoted the premature failure of the tensile sample, thus explaining the contained elongation values. In addition, the sand-blasting process does not compromise the mechanical performance of these heat-treated samples despite their lower plastic deformation resistance, as widely discussed in ARTICLE 7.

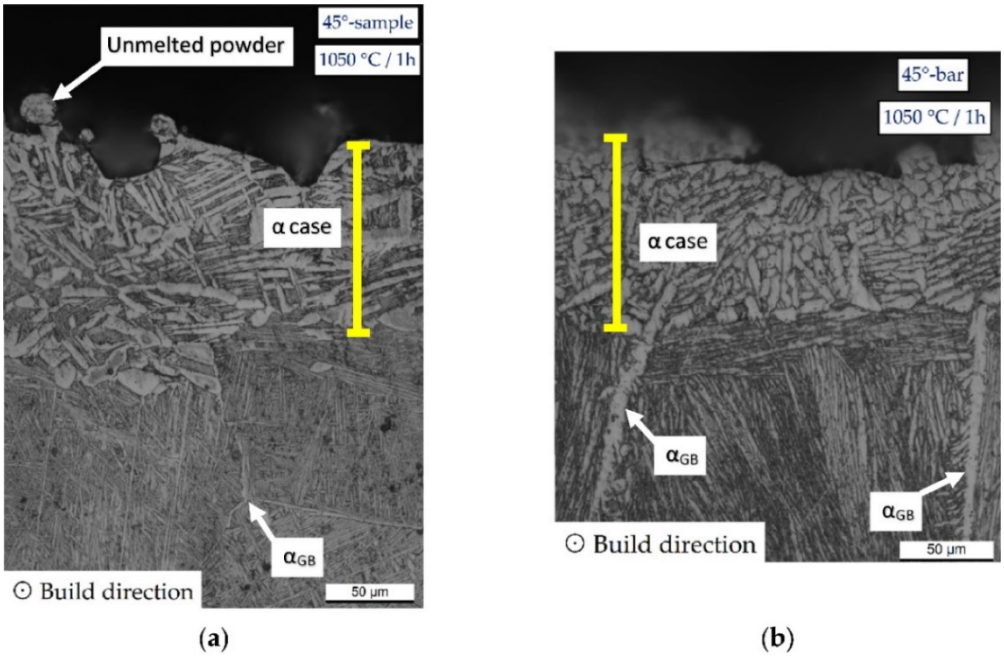


*Figure 52. OM micrographs of the Ti6Al4V sample (**a**) and bar (**b**) performed on the xy plane. Both samples are heat-treated at 1050 °C × 60 min (Reprinted from ARTICLE 7).*

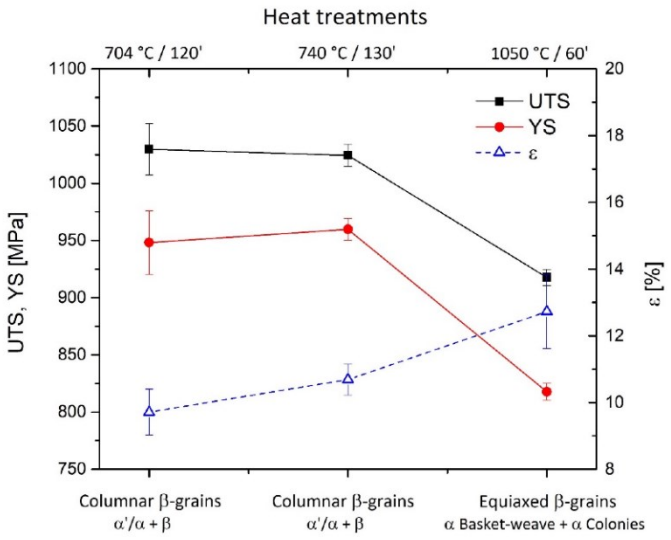


Figure 53. Average mechanical properties of Ti6Al4V samples heat-treated at 704 °C, 740 °C and 1050 °C (Reprinted from ARTICLE 7).

2.3. Relationships between Vickers Microhardness and Tensile Strength

In the following sub-chapter, the correlations between the HV microhardness and the tensile strengths were analysed for both AlSi10Mg and Ti6Al4V samples in as-built and heat-treated conditions. At the same time, the HV-HRF correlations were discussed for the as-built and direct aged AlSi10Mg samples.

2.3.1. Theoretical Background

The correlations between the HV microhardness and the UTS and/or YS can represent a fast and effective method to have a first evaluation of the mechanical properties of the heat-treated samples, and the consequent HT optimization. As a matter of fact, the "quasi-non-destructive" hardness test allows to obtain faster responses by the different effects induced by several HTs on the as-built samples. Also in terms of testing time, the only requirement dictated by the Vickers microhardness test is the minimum sample thickness that must be 1.5 times the average diagonal length of the indentation [164]. On the contrary, the destructive tensile test dictates major requirements in relation to sample geometry and dimensions as listed in [143]. In this scenario, more materials and research time are required to obtain a first evaluation of the HT effects if only the tensile test is taken into consideration. At the same time, the Vickers microhardness test cannot totally replace the results through the tensile test.

In this framework, Tabor et al. [165] first showed a correlation between the HV microhardness and the plastic strain obtained during the indentations. The same authors suggested that the stress correlated stress values are well defined by HV/3 and HV/2.9 ratio for copper and steel, respectively. Secondly, Cahoon et al. [166] proposed the following correlations that are based on the power-law strain hardening, in which the stress is a function of the true strain (σ_T), strain hardening (n) and strength coefficient (K):

$$UTS = \left(\frac{HV}{2.9}\right)\left(\frac{n}{0.217}\right)^n \tag{16}$$

$$YS = \left(\frac{HV}{3}\right)(0.1)^n \tag{17}$$

where UTS, YS and HV are the ultimate tensile strength, yield strength and Vickers microhardness. As widely reported in the literature, the previously mentioned correlations are focused on different alloys like AISI 304, AISI 316L, AISI 1020, aluminium and titanium alloys produced via casting or forging techniques. At the

present, no results are correlated to the same alloys produced via L-PBF process as also expressed in Articles 6 and 9. For these reasons, the strain hardening (n) and the strength coefficient (K), also known as Hollomon's parameters, were determined for both L-PBFed AlSi10Mg and Ti6Al4V samples through the method proposed by Dieter et al. [167].

In addition, new simple correlations between the HV and HRF hardness were analysed for AlSi10Mg alloys in as-built and direct aged samples. It is useful to know that the HV and HRF hardness scales are not directly connected due to their different test methodologies. In the former case, the HV values can be considered as a pressure (force × area); in the latter one, the Rockwell hardness values are related to the penetration depth of the ball or cone indenters. In the present thesis, the proposed HV-HRF correlations are validated through a pre-existing equation, which has already been confirmed for the casting alloys and which correlates the Vickers microhardness and the Rockwell hardness through the force used during the test, the indenter geometries, Young's modulus E and the yield strength. In fact, this equation is described as follows:

$$HV = \frac{\varphi_1 \varphi_2^n \left(F_t^{1/m} - F_0^{1/m}\right)}{\left(\varphi_3 \varphi_4 (1+m)\right)^{1/m} (k - HR)} \left(\frac{\left(E/_{YS}\right)^n YS}{1+n} \right)^{m-1/m} \quad (18)$$

where F_t and F_0 are the pre-load and load, E is Young's modulus, YS the yield strength and k is a constant (*Table 12*).

Table 12. Parameters used to validate the HV-HRF values through the Eq. (18) (Reprinted from ARTICLE 9).

Vickers microhardness		Rockwell hardness	
α_1	32.45	α_1	8.142
α_2	2	α_2	1.104
α_3	0.05753	α_3	0.1578
α_4	0	α_4	0.433
χ	136°	D_R	1.588 [4]
η	0.102	k	130 [4]
s	0.002		

[4] Both the D_R and k values are related to the F scale.

The φ_1, φ_2, φ_3 and φ_4 coefficients, which are related to the indenter geometry, and the loading exponent (m) are defined as follows:

$$\begin{cases} \varphi_1 = \dfrac{2\eta\gamma_1 D_R \sin\left(\frac{\chi}{2}\right)}{s} \\ \varphi_2 = \gamma_2 \\ \varphi_3 = \alpha_1 D_R \\ \varphi_4 = \alpha_3 \\ m = n\alpha_4 + \alpha_2 \end{cases} \quad (19)$$

where α_1, α_2, α_3 and α_4 are constant reported by [167] and shown in *Table 12*. Lastly, the terms γ_1 and γ_2 are defined as follows:

$$\begin{cases} \gamma_1 = \dfrac{3\alpha_1}{8\,tan^2\left(\frac{\chi}{2}\right)} \\ \gamma_2 = \alpha_3 \end{cases} \tag{20}$$

2.3.2. Empirical Correlations: (HV-UTS), (HV-YS) and (HV-HRF)

Figure 54 shows the distribution of values of the UTS vs. HV (*Figure 54a*) and YS vs. HV (*Figure 54b*) where the dotted lines represent the linear fits which are described by the following equations:

$$UTS = 3.20\,HV_{0.5} + 8.58 \tag{21}$$

$$YS = 2.54\,HV_{0.5} - 49.62 \tag{22}$$

where the slope of Eq. (21) is comparable with that of equations reported in the previous sub-chapter. In relation to the YS, the obtained linear fit (Eq. (22)) can be compared to the Petty equation obtained by [169] for cast aluminium alloys:

$$YS = 0.148\,HV_{0.5} - 1.59 \tag{23}$$

where the values are expressed in ton/in^2. On the contrary, Cahoon's equation (Eq. (17)) underestimates the YS values, since it considers the HV0.5 in the range 95–130 HV0.5. Therefore, a correction factor (ζ) can be considered to better approximate Eq. (17), as follows:

$$YS = \left(\frac{HV}{3\,\zeta}\right)(0.1)^n \tag{24}$$

where its value was estimated to be equal to 0.891 regarding the as-built and direct aged AlSi10Mg samples. For further information see ARTICLE 9.

On the other hand, the same factor (ζ) was used for the Ti6Al4V samples (ARTICLE 6) to evaluate the effects induced by the α-phase orientation [170]. As a matter of fact, only the orientations of the hcp α-phase within the columnar β-grains influence the HV measurements as widely discussed in ARTICLE 6.

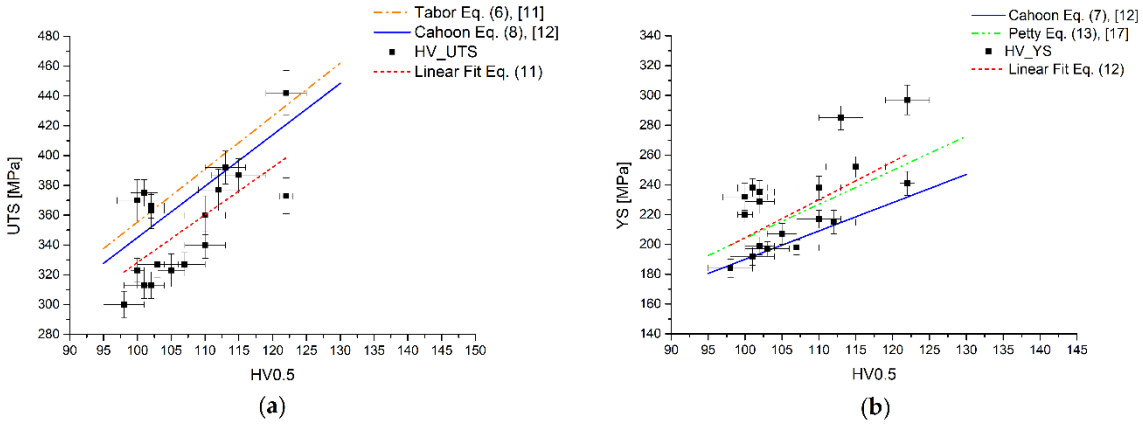


*Figure 54. Distribution of values of HV vs. UTS (**a**) and HV vs. YS (**b**) where the dotted red lines are the fits (Reprinted from ARTICLE 9).*

In this scenario, the impact factor (A or ζ) highlights that the α-phase orientation discussed in *Figure 37* confers a discrepancy of 21–22 % between the actual tensile strengths and those predicted through Cahoon's equation as confirmed by the graphical representation in *Figure 55*.

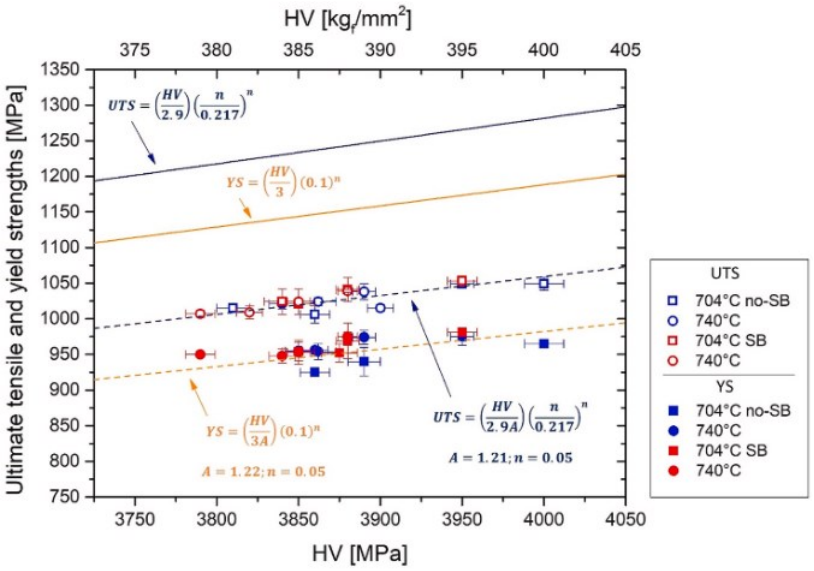


Figure 55. HV microhardness as a function of UTS and YS measured on Ti6Al4V samples heat-treated at 704 °C and 740 °C. The black lines are related to the models indicated by Cahoon et al. [166] (Reprinted from Reference [155]).

In relation to the HV-HRF correlations obtained for the as-built and direct aged AlSi10Mg samples, the distribution of values shown in *Figure 56* was firstly validated through the Eq. (18) which defined a domain of existence. Secondly, the same distribution of values was analysed through the best fit.

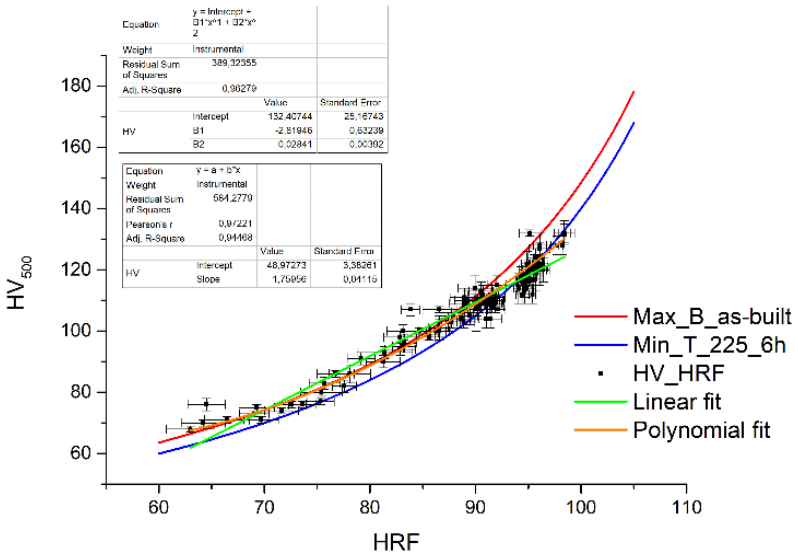


Figure 56. Distribution of HV-HRF values overlaps to the domain of existence calculated through Eq. (18). Orange and green curves indicate the polynomial and linear fits, respectively (Reprinted from ARTICLE 9).

In the first case, the domain of existence (bordered by the red and blue curves) contains the distribution of HV-HRF values and, therefore, validates the accuracy of the following analysed fits. In fact, the HV values calculated through the Eq. (18) show a maximum overestimation and underestimation of 19 % and 4 %, respectively, with respect to the real measured HV values. In this scenario, the polynomial fit has the following equation:

$$HV_{0.5} = 0.0284\, HRF^2 - 2.8195\, HRF + 132.4074 \tag{25}$$

where the associated R^2 is equal to 0.96, and it is the best fit because it is fully contained in the same domain. At the same time, the following linear fit shows an excellent R^2 of 0.94, but the curve is not totally contained in the same domain (*Figure 56*).

The linear fit has the following equation:

$$HV_{0.5} = 1.7596\, HRF - 48.9727 \tag{26}$$

For further information see ARTICLE 9.

CHAPTER 3

Main Conclusions from the Articles

The present thesis aims to evaluate the optimizations of different heat treatments to obtain the best and more homogenized mechanical properties of AlSi7Mg, AlSi10Mg[50,90] and Ti6Al4V alloy manufactured via Laser-Powder Bed Fusion. It analyses both the as-built microstructure and the effects induced by low and high temperatures and the consequent mechanical properties.

For a better understanding of the main findings presented and discussed in Chapter 2, they will be grouped and listed in two different sub-chapters.

3.1. As-Built and Heat-Treated AlSi7Mg and AlSi10Mg Alloys

The principal conclusions from ARTICLE 1, ARTICLE 2, ARTICLE 3, ARTICLE 4, ARTICLE 5, ARTICLE 8 and ARTICLE 9 are the following:

1. The high cooling rate characterizing the L-PBF process generates an ultrafine and inhomogeneous microstructure where the α-Al matrix, which contained nano Si-particle, is surrounded by a network of Si-eutectic. The AlSi7Mg and AlSi10Mg[50,90] show the same microstructures both in single laser and double laser samples. The only microstructural change was detected by comparing the AlSi10Mg[90] and AlSi10Mg50, since in the former the different layer thickness and hatch spacing promote a higher quantity of the equiaxed grains compared to that of the columnar grains, something that does not happen in the latter.
2. The build platform pre-heated at 150 °C promotes precipitation phenomena related to the β-Mg_2Si phase which are also influenced by the time (height) of exposure. The quantity of nano Si-particles decreases while their dimensions increase by increasing the exposure time.

The precipitation sequence simultaneously proceeds from the SSS of the α-Al matrix to the incoherent β-Mg_2Si; namely towards over-aging conditions as highlighted by the bottom AlSi7Mg samples in as-built conditions.

3. The pre-heated build platform induces coarsening phenomena of the pores in the bottom regions of the manufactured samples. In fact, the top ones show a higher amount of small metallurgical pores. Generally, all analysed as-built samples only show 0.01 % of lack-of-fusion pores.
4. The DA at 175 °C causes a progressive increase of precipitation phenomena both in top samples where the HV initially increases and in bottom ones where the over-aging occurs. Increasing the DA temperatures (≥ 200 °C), the HV improvements conferred by the precipitation phenomena in top samples are balanced (AlSi7Mg DA at 200 °C) or reduced (other ones), firstly, by the coarsening phenomena of the Si-particles and, secondly, by the damaging effects of the Si-eutectic network. In this scenario, the DA at 225 °C confers the highest worsening effects with a view to maintain a fine cellular structure.
5. The direct aged AlSi10Mg shows lower creep resistance than the same as-built samples. Generally, the creep response of the as-built and direct aged samples became more and more similar as the applied stress decreased and/or temperature increased. The mathematical model presented in Article 8 was successfully validated considering the L-PBFed AlSi10Mg alloy as a composite material.
6. The SHT at 505 °C completely deletes the Si-eutectic network and promotes a formation of Si-eutectic particles both in AlSi7Mg and AlSi10Mg[50,90] samples. In fact, the Si-eutectic particle thickness increases from 0.05 ± 0.01 μm in as-built samples to 5–5.4 μm after the solubilization at 505 °C × 4 h. In addition to the microstructural changes and grain recrystallization, the SHT confers a decrease in density due to both the formation of new pores and the spheroidization and coalescence of the ones formed during the L-PBF.
7. Due to the microstructural differences between the bottom and top regions, the tensile strengths and the Vickers microhardness decrease linearly with the increase in sample height (0–300 mm). The AlSi10Mg[50,90] alloys show a decreasing trend from ~ 130 to ~ 110 HV0.5, whereas the AlSi7Mg shows a constant HV profile at around 120 ± 4 HV0.5 both in the bottom and middle regions, and this value highlights the over-aging phenomena in the bottom ones. In the same bars, the decreasing trend in HV values is emphasized only in the top region (200–300 mm). In addition, the low-density characterizing the external frame (skin) of the

as-built AlSi10Mg[90] bars ($\Delta\rho$ = 0.3 g/cm^3) balances the age-hardening phenomena conferred by the precipitates.

8. The elongation values of the as-built samples do not show significant variation between the top and bottom regions. On the other hand, the AlSi7Mg samples show higher ductility values (~ 10 %) than the AlSi10Mg[50,90] ones (~ 7.5 %) due to the lower Si content.
9. The DA at 175 °C homogenizes the HV measurements and tensile strength between bottom and top samples only after 2h and 4h of treatments for both AlSi7Mg and AlSi10Mg[50,90] samples, respectively. The DA time decreases at around 1h for both alloys and DA at higher temperatures than 200°C. At the same time, the UTS and YS values decrease, more for the bottom samples than the top ones, with the increase in DA temperatures and time.
10. The SHT induces the worst effects on both the UTS and YS which decrease from ~ 425 MPa and ~ 275 MPa to ~ 250 MPa and ~ 130 MPa, respectively. Only by reaching the peak-aging conditions, (175 °C × 2 h and × 4 h for AlSi7Mg and AlSi10Mg samples, respectively) both the tensile strengths are recovered. The elongation values follow a decreasing trend from ~ 22 % to ~12 %. Therefore, the T6 HTs do not confer improving effects on the mechanical properties of the as-built and direct aged (up to 200 °C) samples.
11. The cracks generally propagate along both the laser scan tracks and molten pool boundaries both in as-built and heat-treated samples. In fact, the molten pool boundaries, which remained even after the SHT, also control the crack path during the plastic deformation. In addition, the cracks interconnect the coarsened Si-particles due to the decohesion phenomena between the same Si-particles and the α-Al matrix.

3.2. As-Built and Heat-Treated Ti6Al4V Alloys

The principal conclusions from the ARTICLE 6 and ARTICLE 7 are the following:

1. The as-built microstructure of the Ti6Al4V-ELI samples shows columnar β-grains arranged in parallel to the build direction and formed by α'-martensite. After just the HT at 704 °C × 120 min, the α'-martensite → α + β transformation partially occurs while the columnar β-grains remain visible. They recrystallize in equiaxed grains after the HT at 740 °C × 130 min, while recrystallize during the HT at 1050 °C × 60 min. During the following cooling with argon gas, the sample thickness influences the obtained structures within the equiaxed β-grains. Increasing the thickness from 6 to 15 mm, the basketweave formed only α-lath

develops into a basketweave structure composed of α-colonies. At the same time, the samples characterized by the highest thickness also show both finer α-colonies at the α_{GB} and globular α-phase. The HT at 1050 °C also promotes the formation of an α-case layer due to the diffusion of oxygen atoms from the outer surface of the sample to its centre.

2. During the transformation at 704 °C and 740 °C, the α-phase maintains the same lattice orientation of the α'-martensite laths which do not show any preferential orientations. At the same time, the different build orientations of the manufactured samples do not influence the microstructural morphology.
3. After the sand-blasting process, the surface roughness is reduced to lower values than 17 μm and the titanium oxides, which are formed during the HT at 1050 °C, are removed. The impact of glass spheres promotes a plastic strain on the outer sample surface up to a depth comparable to the X-Ray penetration depth. In fact, the HV0.5 profiles performed on the cross-section of the samples do not reveal any variation produced by the plastic strain.
4. Both the UTS and YS decrease from ~ 1030 MPa and ~ 950 MPa, which are the values of the samples heat-treated at 740 °C to ~ 925 MPa and ~ 825 MPa, respectively, after the HT at 1050 °C. On the other hand, the elongations increase from ~ 10 % to ~ 13 %. The continuous increasing trend can be restricted by the presence of the α-case layer.

3.3. Relationships between HV Microhardness, UTS, YS and HRF.

The principal conclusions from the ARTICLE 6 and ARTICLE 9 are the following:

1. A linear relationship between the Vickers microhardness and tensile strengths can be applied with good approximation. Cahoon and Petty equations can be used, respectively, to evaluate the UTS and YS values from the HV values.
2. The range suggested for strain hardening is 0.19–0.25, while for the strength coefficient is 589–890 MPa for as-built and direct aged AlSi10Mg samples.
3. The HV-HRF correlation can be approximated by a second order equation.
4. The same Cahoon equation related to the YS does not approximate the yield strengths of the Ti6Al4V samples heat-treated at 704 °C and 740 °C. A discrepancy of 21–22 % between the reals values and those obtained by Cahoon's equation is only conferred by the α-phase orientations.

5. For these reasons, the impact factors ζ (0.891) and A (1.21–1.22) must be considered in Cahoon's equation to evaluate the YS depending on the HV measurements for the AlSi10Mg and Ti6Al4V samples, respectively.

3.4. Future Works

From the results summarized and discussed in the present thesis, different future works will be able, firstly, to better delineate the microstructural effects induced by the optimized heat treatments and, secondly, to improve the additive manufacturing industrial sector.

In relation to aluminium alloys, further microstructural analysis will be performed through TEM measurements to thoroughly understand the effects of the pre-heated build platform on the bars. In addition, the effects on ductility and on the fracture mechanisms will be studied because the elongation values do not follow the same decreasing trend of the UTS and YS. In order to reduce the manufacturing time, other heat treatments will be defined to optimize the mechanical properties of the Al and Ti alloys manufactured through different process parameters.

As regards the Ti6Al4V-ELI samples, different post-process aging heat-treatments will be analysed to improve the tensile strength after the solubilization at 1050 °C.

In addition, the deposition process of other metallic materials on both Al and Ti alloys through the L-PBF process will be considered. In this scenario, the several mechanical, physical, and chemical properties can be improved and adapted to different industrial applications. Subsequently, other new heat treatments will be necessarily defined.

[*This page intentionally left blank*]

LIST OF FIGURES

Figure 1. Thesis structure. 28
Figure 2. Wrought and cast Al alloys families classified through their principal alloying elements. 30
Figure 3. Phase diagram of Al-Si binary system (Adapted from Reference [6]). 30
Figure 4. CCT curves of Al0.72Si alloy with SEM micrographs highlighting the Si precipitates with polygonal and plate-like morphologies (Adapted from Reference [9]). 31
*Figure 5. Atomic models of ε'' precipitate:(**a**) Mg5Si, (**b**) Mg4Al3Si4, (**c**) Mg5Al2Si4, (**d**) Mg6AlSi4 (**f**) Mg5Si6. (**e**) Atomically-resolved STEM image of ε'' precipitate (Adapted from References [16,17]).* 32
*Figure 6. TEM images showing the formation of different Mg_2Si precipitates (**a**, **c**, **e**) with correlated diffraction patterns, direction [001] (**b**, **d**, **f**) (Reprinted from Reference [17]).* 32
*Figure 7. Precipitation hardening sequence drown in: (**a**) a phase diagram with partial solubility where the temperature ranges of the SHT and artificial aging are illustrated, (**b**) time-temperature diagram of T6 heat treatment.* 33
Figure 8. Schematic representation of the effects induced by the α- and β-stabilizer alloying elements on Ti mechanical properties. Some Ti alloys are listed in all categories: α, near α, α+β, near-β and β. 35
Figure 9. Strengthening diagram of Ti alloys reported in [26] in relation to the Al_{eq} and Mo_{eq} percentage. The orange symbol indicates the α+β Ti6Al4V alloys that is analysed in the present doctoral thesis. 36
Figure 10. Three-dimensional Ti-6Al-V phase diagram where V varies from 0 to 18 wt.%. 36
Figure 11. Time-temperature diagram of STA (Reprinted from Reference [36]). 37
*Figure 12. (**a**) BFTEM (Bright-Field Transmission Electron Microscopy) image shows the α+β ultrafine microstructure, (**b**) SAED patter showing the α_2-Ti3Al precipitate within the α-lath (Reprinted from Reference [33]).* 39
*Figure 13. (**a**) laser powder bed fusion (L-PBF) process; (**b**) direct energy deposition (DED) process (Adapted from References [53,58]).* 41
Figure 14. Schematic representation of the interaction between the laser beam source and the powder bed during the L-PBF process highlighting the overlap area between two adjacent laser scan tracks where the principal dimensions are labelled (Reprinted from Reference [61]). 41

LIST OF FIGURES

Figure 15. Factors correlated to the selective laser melting (or L-PBF) and subdivided into controlled and partially controlled (Reprinted from Reference [70]). 42

*Figure 16. Lack of Fusion (LOF) pores classifying as pores: (**a**) with un-melted particles, (**b**) poor bonding defects (Adapted from References [109,110]). Schematic representation of the LOF formation during the L-PBF process: (**c**) lack of adequate laser scan tracks overlap; (**d**) presence of defects such as spatter.....45*

Figure 17. Porosity trend in relation to the ED and scan speed variations (Adapted from Reference [113]).....46

*Figure 18. Tensile properties of heat-treated Ti6Al4V samples after stress relief (**a**) and hot isostatic pressing HTs (**b**) (Reprinted from Reference [125]).....47*

Figure 19. Operating window of the L-PBF process in relation to the laser beam source and scanning speed (Reprinted from Reference [102]).....47

*Figure 20. (**a**) temperature trends of a molten pool (MP) measured and calculated along the xy plane; (**b**) distribution of temperature along the xy and xz planes (Adapted from Reference [135]). 48*

*Figure 21. MP depth (**a**,**c**) and width (**b**,**d**) related to the: (**a**,**b**) laser scan speed (mm/s) and (**c**,**d**) laser powder (W) (Adapted from Reference [137]).....49*

*Figure 22. Representative Solidworks projects of: (**a**) AlSi7Mg and AlSi10Mg alloys and (**b**) Ti6Al4V-ELI alloys which were manufactured following the skin-core scanning strategy (**c**). Dog-bone tensile samples were printed along different orientations: z (90°, yellow), 45° (green), xz (0°, red) and xy (0°, blue) (Reprinted and adapted from References [144,145]). 51*

*Figure 23. Diagrams of the heat treatment processes performed on (**a**) AlSi7Mg and AlSi10Mg, and (**b**) Ti6Al4V-ELI samples. 52*

*Figure 24. Intercept method used to calculate: (**a**) the SDAS values of as-built AlSi10Mg samples, (**b**) the α-laths width of the heat-treated Ti6Al4V-ELI samples.....54*

*Figure 25. Schematic representation of the: (**a**) 3×3 matrix used to evaluate the HV0.5 values of Ti6Al4V-ELI samples, and AlSi7Mg and AlSi10Mg samples on xy plane, (**b**) HV0.5 profiles performed on the SL and DL AlSi10Mg and AlSi7Mg bars in as-built conditions (Adapted from References [145,148]). 55*

Figure 26. HV profiles carried out on cross-section of the heat-treated Ti6Al4V-ELI tensile samples after and before the sand-blasting process (Reprinted from Reference [145]).....56

*Figure 27. Schematical representation of the (**a**) cylindrical AlSi7Mg and AlSi10Mg tensile samples and (**b**) dog-bone Ti6Al4V-ELI samples (Reprinted form References [144,145]).....57*

*Figure 28. OM micrographs performed on the xy (**a**,**b**) and xz (**c**,**d**) planes of the AlSi10Mg^{50} (**a**,**c**) and AlSi7Mg (**b**,**d**) alloys in as-built conditions (Reprinted from ARTICLE 1 and ARTICLE 2)...60*

*Figure 29. OM (**a**,**b**) and SEM (**c**,**d**) micrographs of the external frame (skin) of the as-built AlSi10Mg^{90} samples (Reprinted from ARTICLE 5). 61*

*Figure 30. SEM micrographs of as-built AlSi10Mg^{50} samples investigating the Si-eutectic network transformation (**a**) from the MP centre (zone 3) to its boundary (zone 1). (**c**–**d**) SEM micrographs at higher magnification (160k×) of zones 1, 2 and 3 (Reprinted from the ARTICLE 1). 62*

*Figure 31. SEM micrographs of AlSi10Mg^{90} samples heat-treated at: (**a**) 175 °C, (**b**) 200 °C and (**c**) 225 °C × 6 h and (**d**) 505 °C × 4 h + 175 °C × 4 h (Reprinted from ARTICLE 5).....63*

*Figure 32. OM micrographs of solution heat treated AlSi7Mg (**a**,**c**) and AlSi10Mg (**b**,**d**) for 5 min (**a**,**b**) and 4 h (**c**,**d**) at 505 °C (Reprinted from ARTICLE 2). 64*

Figure 33. Statistical analysis of the pore equivalent diameters before and after the SHT 505 °C + aging 175 °C (Reprinted from ARTICLE 5). 65

Figure 34. Trend of density values of the as-built, direct aged and solution heat-treated AlSi7Mg and AlSi10Mg^{90} samples (Reprinted from ARTICLE 2). 65

*Figure 35. OM micrographs performed on xy (**a**) and xz (**b**,**c**) planes of the as-built Ti6Al4V sample (Reprinted from Reference [155]). 67*

*Figure 36. SEM micrographs of Ti6Al4V-ELI samples heat-treated at 704 °C × 120 min (**a**,**b**) and 740 °C × 130 min (**c**,**d**) where (**b**,**d**) represent the magnification of the red and yellow square area (Reprinted from ARTICLE 7). 68*

*Figure 37. EBSD maps acquired on (**a**) xy planes of the Ti6Al4V sample heat-treated at 704 °C × 120 min, (**b**) xz plane of Ti6Al4V sample heat-treated at 704 °C × 120 min, (**c**) xz plane of the Ti6Al4V sample heat-treated at 740 °C × 130 min. Scalebar length is 100 μm in all planes and the pole figures report <0001> direction of the α-phase (Reprinted form Reference [155]). 69*

*Figure 38. SEM micrographs of Ti6Al4V-ELI tensile samples heat-treated at 1050°C × 60 min (**a**,**b**) and bars heat-treated at 1050 °C × 60 min (Reprinted from ARTICLE 7). 70*

*Figure 39. HV profiles obtained by the microhardness measured on the as-built SL and DL: (**a**) AlSi7Mg and (**b**) AlSi10Mg^{90} bars, respectively (Reprinted from ARTICLE 2). 72*

*Figure 40. SEM micrographs of the (**a**) top and (**b**) bottom regions of AlSi10Mg bars in as-built conditions (Reprinted from ARTICLE 1). 72*

*Figure 41. Aging curves obtained after the DA at 175 °C, 200 °C and 225 °C analyzing the top (**a**,**c**) and bottom (**b**,**d**) samples of the AlSi7Mg (**a**,**b**) and AlSi10Mg^{90} (**c**,**d**) samples (Reprinted from ARTICLE 2). 74*

Figure 42. SEM micrographs of top AlSi10Mg samples DA at 175 °C (Reprinted from ARTICLE 1). 75

*Figure 43. Mechanical properties of top and bottom (**a**) AlSi10Mg and (**b**) AlSi7Mg samples in as-built and heat-treated conditions (Reprinted from ARTICLE 1 and ARTICLE 2). 76*

*Figure 44. Schematic representation of plastic deformation mechanisms related to the full cellular structure: (**a**) dislocation de-pinning from the atoms dispersed into SSS α-Al matrix; (**b**) deformation by cutting dislocation "forests"; (**c**) emission of dislocation from the interface between the Al and Si (Reprinted from Reference [33]). 78*

*Figure 45. (**a**) Minimum creep rate dependence on applied stress for as-built and heat-treated AlSi10Mg samples. (**b**) Stress variation (Δσ) as a function of the minimum creep rate (Reprinted from ARTICLE 8). 78*

Figure 46. QI-graphs of as-built, DA and T6 heat-treated AlSi10Mg and AlSi7Mg samples. References [14,19,40,41] are the following new References [67,71,160,161] (Reprinted from ARTICLE 2). 79

*Figure 47. Mechanical properties of Ti6Al4V-ELI samples of different build orientations and surface finishing: (**a**) UTS and YS, (**b**) elongations (Reprinted from Reference [155]). 80*

LIST OF FIGURES

*Figure 48. Schematic representation of different Ti6Al4V samples: (**a**) H-, 45°- and V-samples, (**b**–**d**) under the same load conditions but with different orientation between the load axis and the columnar β-grains (Reprinted from Reference [33]).* *81*

*Figure 49. Schematic representation of the load direction and the LOF major axis during a tensile test in V-samples (**b**,**d**) and H-sample (**c**,**e**); (**d**,**e**) Schematic representation of the load direction and the different orientation of LOF major axis within the same sample and correlated to the different layers (Reprinted from Reference [33]).* *82*

Figure 50. XRD patterns related to the no-SB (no Sand Blasted) and SB Ti6Al4V-ELI samples for both heat-treated conditions (Reprinted from Reference [155]). *83*

*Figure 51. HV profiles related to the cross-section of SB and no-SB samples heat-treated at 704 °C (**a**), 740 °C (**b**) and 1050 °C (**c**) (Reprinted from ARTICLE 7).* *84*

*Figure 52. OM micrographs of the Ti6Al4V sample (**a**) and bar (**b**) performed on the xy plane. Both samples are heat-treated at 1050 °C × 60 min (Reprinted from ARTICLE 7).* *85*

Figure 53. Average mechanical properties of Ti6Al4V samples heat-treated at 704 °C, 740 °C and 1050 °C (Reprinted from ARTICLE 7). *85*

*Figure 54. Distribution of values of HV vs. UTS (**a**) and HV vs. YS (**b**) where the dotted red lines are the fits (Reprinted from ARTICLE 9)* *89*

Figure 55. HV microhardness as a function of UTS and YS measured on Ti6Al4V samples heat-treated at 704 °C and 740 °C. The black lines are related to the models indicated by Cahoon et al. [166] (Reprinted from Reference [155]). *89*

Figure 56. Distribution of HV-HRF values overlaps to the domain of existence calculated through Eq. (18). Orange and green curves indicate the polynomial and linear fits, respectively (Reprinted from ARTICLE 9). *90*

LIST OF TABLES

Table 1. Mapping of thesis aims, objectives and technologies. *27*
Table 2. Nominal chemical composition (wt.%) of AlSi7Mg and AlSi10Mg alloys. *34*
Table 3. Principal uses of the Ti alloys within automotive, aerospace, biomedical and chemical sectors. *39*
Table 4. Nominal chemical composition (wt.%) of Ti6Al4V and Ti6Al4V-ELI alloys. *39*
Table 5. Principal process parameters values used to manufacture AlSi10Mg and Ti6Al4V samples via L-PBF process. *43*
Table 6. Defects present into L-PBFed samples: cause, remedy and effects. *44*
Table 7. Chemical composition (wt.%) of gas atomized powders. *50*
Table 8. Process parameters used to print the batches of AlSi7Mg, AlSi10Mg and Ti6Al4V-ELI samples. *52*
Table 9. Heat treatments performed on AlSi7Mg, AlSi10Mg and Ti6Al4V-ELI samples. *53*
Table 10. Chemical composition (EDS) of spectra A and B (wt.%) (see ARTICLE 7). *68*
Table 11. Mechanical properties of the as-built AlSi7Mg, AlSi10Mg^{50} and AlSi10Mg^{90} tensile samples (ARTICLE 1, ARTICLE 2 and ARTICLE 4). *75*
Table 12. Parameters used to validate the HV-HRF values through the Eq. (18) (Reprinted from ARTICLE 9). *87*
Table 13. Acronyms and their definitions *103*

[*This page intentionally left blank*]

ACRONYMS

Table 13 lists the acronyms used in the present thesis, and their definitions.

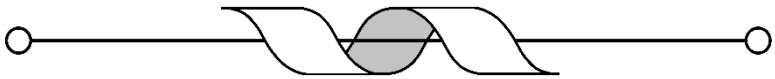
Table 13. Acronyms and their definitions

Acronyms	Meanings
AA	Artificial Aging
AM	Additive Manufacturing
APF	Atomic Packing Factor
bcc	body-centred cubic
BP	Build Platform
BR	Build Rate
CCT	Continuous Cooling Transformation
DA	Direct Aging
DED	Direct Energy Deposition
DL	Double Laser
EBSD	Electron Backscattered Diffraction
ED	Energy Density
EDS	Energy Dispersive X-ray Spectroscopy
ELI	Extra Low Interstitial
fcc	face-centred cubic
GP	Guinier Preston
HAZ	Heat Affected Zone
hcp	hexagonal closed packed
HV	Vickers Microhardness
HT	Heat Treatment
HRF	Rockwell hardness scale F
LOF	Lack-Of-Fusion
L-PBF(ed)	Laser-Powder Bed Fusion(Fused)
MP	Molten or melt pool
OM	Optical Microscope
PBF	Powder Bed Fusion
QI	Quality Index
SB	Sand Blasted
SDAS	Secondary Dendrite Arm Spacing
SEM	Scanning Electron Microscope
SHT	Solution Heat Treatment
SL	Single Laser

Table 13. Cont.

Acronyms	Meanings
SLM	Selective Laser Melting
SSS	Supersaturated Solid Solution
STA	Solution Treatment and Aging
TEM	Transmission Electron Microscope
U-HT	Unconventional Heat Treatment
UTS	Ultimate Tensile Strength
XRD	X-Ray Diffraction
YS	Yield Strength

PART 2



[*This page intentionally left blank*]

ARTICLE 1

Effect of the Distance from Build Platform and Post-Heat Treatment of AlSi10Mg Alloy Manufactured by Single- and Multi-Laser Selective Laser Melting

---

Emanuela Cerri, Emanuele Ghio & Giovanni Bolelli

Journal of Material Engineering and Performance, *30* (**2021**) 4981–4992

https://doi.org/10.1007/s11665-021-05577-8

“The following version of the manuscript is made available under the CC-BY-NC-ND 4.0 license”

https://creativecommons.org/licenses/by-nc-nd/4.0/

Effect of the Distance from Build Platform and Post-Heat Treatment of AlSi10Mg Alloy Manufactured by Single- and Multi-Laser Selective Laser Melting

Emanuela Cerri [1], Emanuele Ghio [1], Giovanni Bolelli [2].

[1] Department of Engineering and Architecture, University of Parma, Via G. Usberti 181/A, 43124, Parma, Italy.

[2] Department of Engineering "Enzo Ferrari", University of Modena e Reggio Emilia, Via P. Vivarelli 10/1, 41125, Modena, Italy.

Abstract

In the present study, AlSi10Mg samples produced by Selective Laser Melting (SLM) were studied. Samples were machined from two types of bars obtained through different methods: either single laser (SL) or multiple laser (ML) machine set up. The bars were built perpendicular to the platform, which was pre-heated at 150 °C (working temperature), up to a height of 300 mm. The effect of the distance from the platform on the mechanical properties was investigated through tensile samples in as-built condition and after unconventional heat treatments (U-HT). Tensile strength changed by 80 MPa along the Z-axis (build direction) for SL case and by 100 MPa for ML case in the as-built samples. Vickers microhardness revealed an analogous gradient. This was correlated to a gradient in intra-granular precipitates' distribution along the Z-axis, as revealed by scanning electron microscopy (SEM). An unconventional heat treatment at 175 °C for 6 h slightly improves the mechanical strength; higher temperature treatments at 200 and 225 °C for the same duration cause a progressive decrease in strength with an increase in elongation. The amount and size of the precipitates and the thickness of eutectic Si change with the heat treatment temperature, justifying the mechanical behavior.

Keywords: AlSi10Mg, build axis, mechanical properties, selective laser melting

1. Introduction

Selective Laser Melting (SLM) is a particular Additive Manufacturing (AM) process that allows producing metal components of complex geometry. The most frequently used materials, known for returning excellent properties after SLM processing, are aluminum alloys, titanium alloys, steel, Inconel [171,172]. Usually, SLMed alloys exhibit higher tensile strength and microhardness than their as-cast counterparts due to the optimization of laser scan speed, scan strategy, build direction and new heat treatments [173,174]. In this context, improve not only the efficiency of aluminium alloy, but also the build rate compared to single laser [134,175]. As reported

by A.H. Maamoun et al. [176] and K.G. Prashanth et al. [177], the eutectic unstable microstructure of AlSi10Mg produced by SLM affects their mechanical properties. Specifically, the SML technology kinetically promotes a cellular microstructure: the part of liquid remaining after α-Al solidification generates the formation of eutectic Si along the cellular boundaries during the molten pool solidification. Considering the scan strategy of SLM, it is possible to observe that various laser passes induce a microstructural variation: in fact, a heat-affected zone is generated at the edge of any part of the material that has been melted [176–178]. The same morphological inhomogeneity is also present along the Z-axis as reported by [173,177,178], and in the case of overlapping lasers there is a condition of inhomogeneity within molten pools [176,179]. However, a variation of mechanical properties is also present along the Z-axis or build axis [172,174,180,181].

Moreover, the conditions of molten pool solidification such as the high cooling rate (10^6 K/s) and the variation of solubility of Si in the Al matrix [177] make the cellular microstructure very sensitive to a limited increase of temperature, for example through an ageing heat treatment at low temperature (~ 200 °C) [177,182,183].

Due to this sensitivity, the pre-heated build platform may influence the detectable gradient of mechanical properties as a function of distance from the surface. As reported by Brandl et al. [179], the presence of a pre-heated platform induces an increase of mechanical properties. As a matter of fact, the permanence of the samples in the temperature range between 150 °C and 200 °C causes the precipitation of an extremely fine Mg_2Si phase along the boundary of cellular α-Al. Several studies have shown the coexistence of Mg and Si in the same region around the α-Al grains [176–178].

Interesting results are also obtained by aging the AlSi10Mg alloy; in fact, the applied heat treatments induced a coarsening of eutectic Si and the precipitation of Mg_2Si phase, in addition to a homogenization of the microstructure, a reduction of porosity and an increase of ductility [172,173,184–186]. Takata et al. [186] demonstrated the greater presence of Mg_2Si at temperatures below 400 °C. On the other hand, Lam et al. [178] and Li et al. [185] showed the presence of Mg_2Si precipitates even within as-built samples. The thermal cycles induced by SLM technology led to diffusion of Mg and Si atoms through quenched in vacancies within the α-Al supersaturated matrix and consequently to the formation of Mg_2Si phase on preferential sites [187] such as dislocations [188]. If a solution heat treatment (SHT) is applied [173,176], a significant coarsening of the microstructure and a destruction of eutectic Si network are induced, causing a decrease of UTS and σ_y.

In the same scenario, an unconventional heat treatment without SHT can be considered with the aim to prevent an excessive decrease in strength whilst increasing the ductility as reported by Montero et al. [189]. In conclusion, Fiocchi et al. [183] used low ageing temperatures and demonstrated a significant decrease in mechanical properties already at 294 °C.

In the current scenario, this paper aims to investigate the mechanical properties and microstructure of the AlSi10Mg SLM alloy as function of the distance along the build axis in as-built and in unconventional heat treatment conditions. The samples printed with single laser and multi-laser are analyzed in as-built condition. The obtained results show a slight different between single laser and multi-laser, so the only single laser samples are studied for the different heat treatment conditions.

2. Materials and Methods

Bulk specimens of AlSi10Mg aluminum alloy were produced by SLM from spherical gas-atomized powder with nominal composition as shown in *Table 1.1*.

Table 1.1. AlSi10Mg chemical composition (wt.%).

Al	Si	Fe	Mg	Cu	Mn	Zn	Ti	Pb	Sn
Bal.	9.60	0.10	0.38	< 0.05	< 0.01	< 0.01	< 0.01	< 0.01	< 0.01

SLM processing was carried out at 150 °C using an SLM500 device (quad laser SLM solutions) equipped with an Yb:YAG laser. The parameters used for preparing the samples are as follows: scanning speed 1500 mm/s, power 350 W, layer thickness 50 μm, hatch spacing 0.17 mm. High purity argon gas was used during SLM processing in order to avoid oxygen contamination. Two different bars (300x100x10 mm) are manufactured by single laser (SL) and multi-laser (ML), respectively, in zones D and AB of pre-heated build platform (*Figure 1.1a*). In agreement of ASTM E804 standard (*Figure 1.1b*), 26 tensile samples have been machined to machine tools for each bar printed. Moreover, the axis of symmetry of these samples was kept parallel to build platform as reported in (*Figure 1a*).

The build pre-heated platform is divided in two different zones: the first bar (D) is produced by single laser, while the second, bar (AB), is produced by quadruple laser delivered though specific algorithms created by the SLM500 machine manufacturer. Moreover, “top” was used to designate samples cut at bar height > 150 mm and “bottom” for samples extracted at bar height < 150 mm.

The AlSi10Mg samples were subjected to different unconventional heat treatments at 175 °C (U-HT1), 200 °C (U-HT2) and 225 °C (U-HT3) up to 6 h, performed in a muffle furnace (Nabertherm) with the K-thermocouple placed in contact to samples.

For tensile tests, samples in as-built and unconventional heat-treated conditions were cut and machined from the solid geometries (*Figure 1.1b*), according to ASTM E804. Tensile tests were performed at room temperature using a Zwick Z100 servo hydraulic device, at a strain rate of 0.008 s^{-1}.

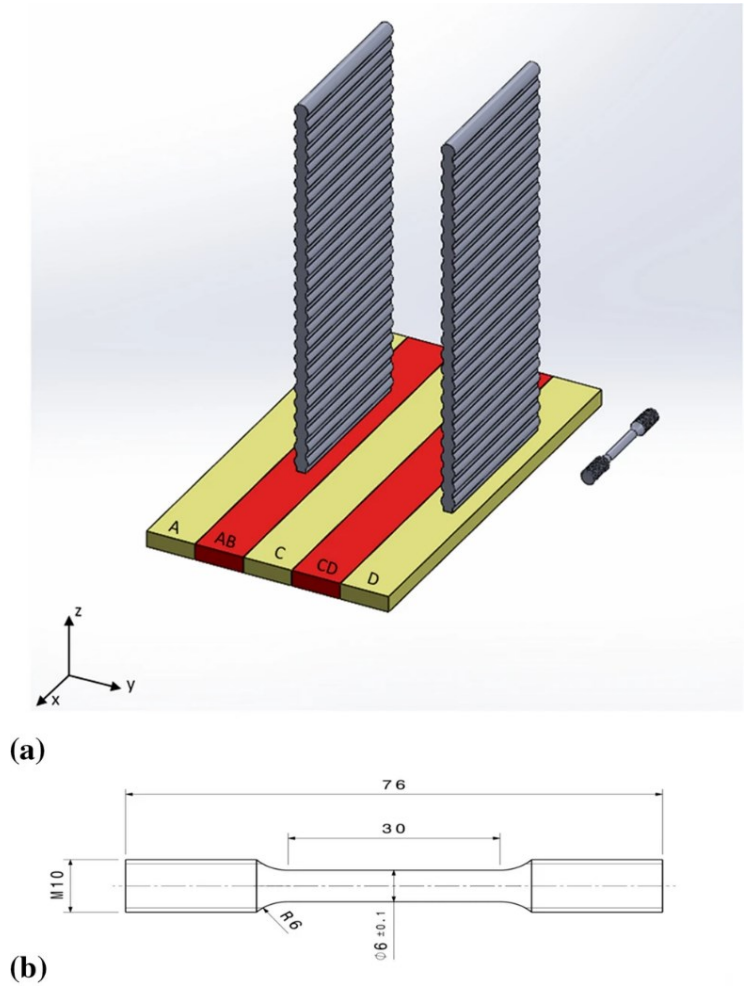


*Figure 1.1. (**a**) Bar AB (ML) and bar D (SL) produced by SLM. Tensile sample machined by bars with axis of symmetry parallel to build platform; (**b**) tensile sample according to ASTM E804.*

Vickers microhardness was measured at different heights (in the vertical bars shown in *Figure 1.1a*) and in all different thermal treatment conditions by 500 gf load and a dwell time of 15 s.

For microstructure investigations, samples were mechanically ground with SiC papers and polished using colloidal silica suspension (≈ 60 nm size). Microstructure was characterized by optical microscope (OM) (Leica DMi8) and scanning electron microscopy (SEM: Nova NanoSEM 450 equipped with a field emission gun source, FEI Thermo Fisher Scientific, Hillsboro, Oregon, USA). Phase composition was assessed by x-ray diffraction (XRD: X'Pert PRO, PANAlytical, Almelo, NL) using Cu-Kα radiation emitted from a conventional source operated at 40 kV, 40 mA and detected through a 1D array of solid-state detectors (XCelerator, PANAlytical) with a Ni filter.

Finally, statistical analysis of porosity dimension and eutectic Si band thickness was performed on polished sample sections by image analysis (LAS image software equipped with the OM).

3. Results and Discussion

3.1. Microstructure and Mechanical Properties of As-Built AlSi10Mg Samples

Figure 1.2 shows the fine and inhomogeneous microstructure of SLM samples analyzed in the XY plane and in the XZ plane. As widely reported in the literature, the first plane mentioned is characterized by the characteristic ellipsoidal shapes of molten pool, elongated in the scanning direction; the second shows a "fish scale" structure along build direction. In the next layer, the laser scanning direction is rotated by 90°, as confirmed by the transversal line perpendicular to melt pools. *Figure 1.2a* and *b* shows the differences between the single laser case (*Figure 1.2a*, D bar) and the multi-laser case (*Figure 1.2b*, AB bar) in XY plane: it is possible to observe the greater number of different scan track directions in *Figure 1.2b*. In addition, all micrographs (*Figure 1.2*) are characterized by the random presence of spherical pores that will be discussed later, but in *Figure 1.2c* a keyhole pore is showed and it is located between two scan tracks at the edge of molten pool. The microstructure of molten pool (*Figure 1.3*) is characterized by an increase in cell size from the center to the boundary, as widely reported in the literature. Considering the three SEM pictures showing the *Figure 1.3b,c,d* (areas 1, 2 and 3 in *Figure 1.3*), the eutectic Si network is gradually destroyed from the center to the coarse and heat-affected zones (HAZ) [69,190].

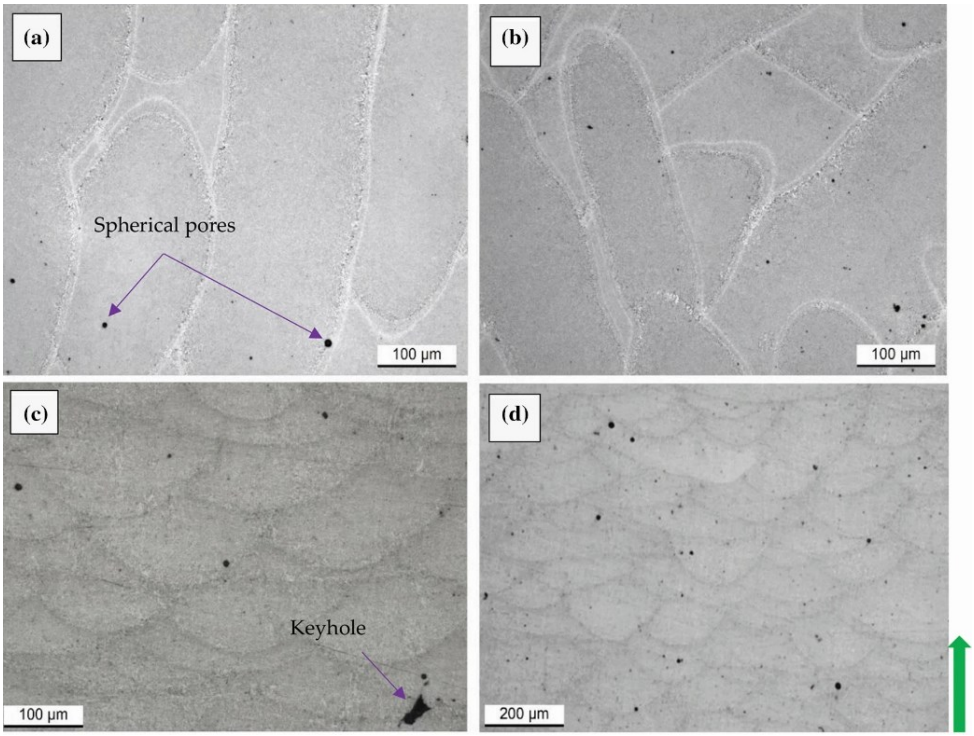


*Figure 1.2. Light microscopy of SLMed samples showing melt pools, scan tracks and porosity for SL samples (**a**, **c**) and ML samples (**b**, **d**) respectively in XY and XZ planes. The green arrow shows the build direction in the XZ plane.*

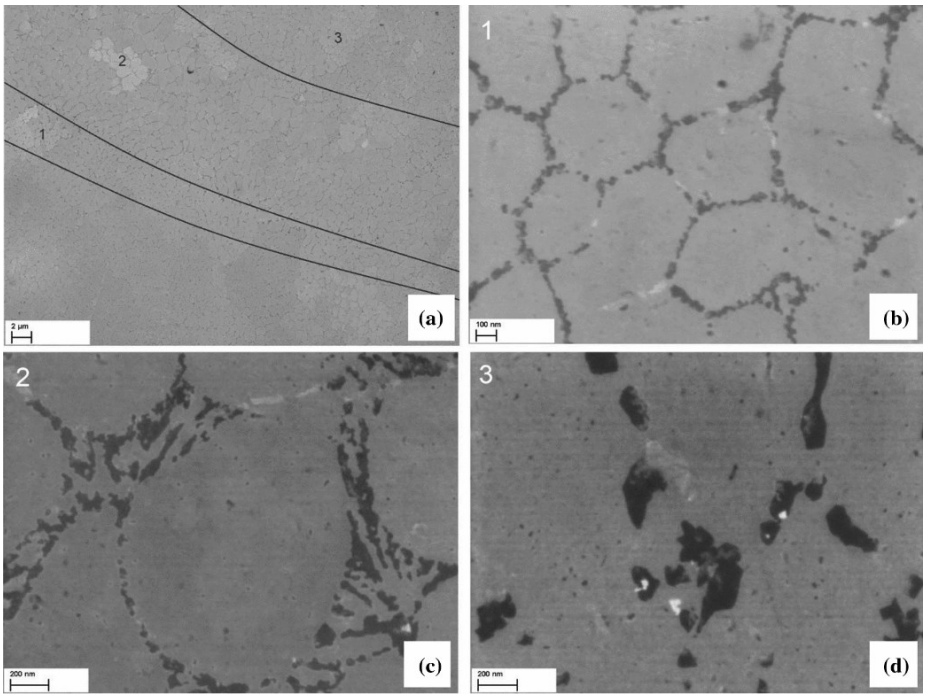


*Figure 1.3. SEM micrographs of AlSi10Mg sample in as-built condition: (**a**) molten pool at low magnification (8k×); (**b**) center of molten pool; (**c**) coarse zone; (**d**) HAZ zone.*

Figure 1.4 shows the molten pool boundary and the overlap region among two adjacent track scans, which increases if the hatch distance decreases [69,191]. In this case of study, the sample was scanned with long bidirectional vectors in one layer with a hatch distance of 170 μm. On the other hand, considering the high magnification micrograph shown in *Figure 1.4b*, it can be emphasized the effect of temperature gradient (G) and the crystal growth rate (R) within the molten pool: the grains growth takes place along the thermal gradient and their orientations change within the molten pool because the G direction varies [134,184,192–194]. As a matter of fact, from the bottom of molten pool, the G direction remains perpendicular to its boundary; on the contrary, the G direction will be deflected toward the center of the melt pool from the side of the same boundary [193]. In fact, the cross section of molten pool is mainly composed of columnar grains and by small equiaxed grains near melt pool boundary. In the same context, considering a melt pool in the last scanned layer n, the grains direction can change from 0° to 90° compared to that which characterized the melt pool in the layer n–1 (*Figure 1.4b*), as reported by D. Kong et al. [194].

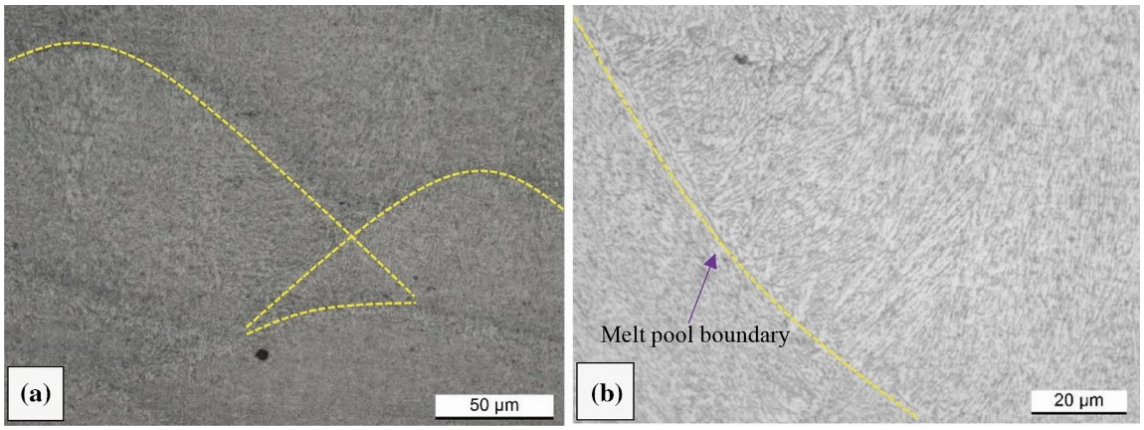


*Figure 1.4. High magnification micrographs (500×, 1000×) of SLMed samples in as-built condition along the XZ plane: (**a**) edges of the molten pools (yellow dotted lines) and overlap zone between two track scans; (**b**) region near fusion line, showing cellular growth.*

Finally, the characterization of this cellular structure can be done considering the G/R ratio and the product of G and R: the morphology and the size of solidification structure were described by the first and the second values, respectively, as reported by [193–196].

Image analysis results in *Figure 1.5a* shows that the bottom part of the multi-laser case (AB-bottom) has 60 % of its porosity characterized by an equivalent diameter smaller than 1 μm, about 17 % has a size ranging between 1 and 2 μm and about 7 % is between 2 and 3 μm, decreasing to zero for larger areas. The overall density is 99.9 % on overage. At the top of the same bar (i.e., approximately at the maximum distance from

the pre-heated platform surface), porosity presents a similar size distribution: 40 % of the porosity has an area smaller than 1 μm, about 20 % between 1 and 2 μm and 15 % ranges between 2 and 3 μm. The density is 99.2 %.

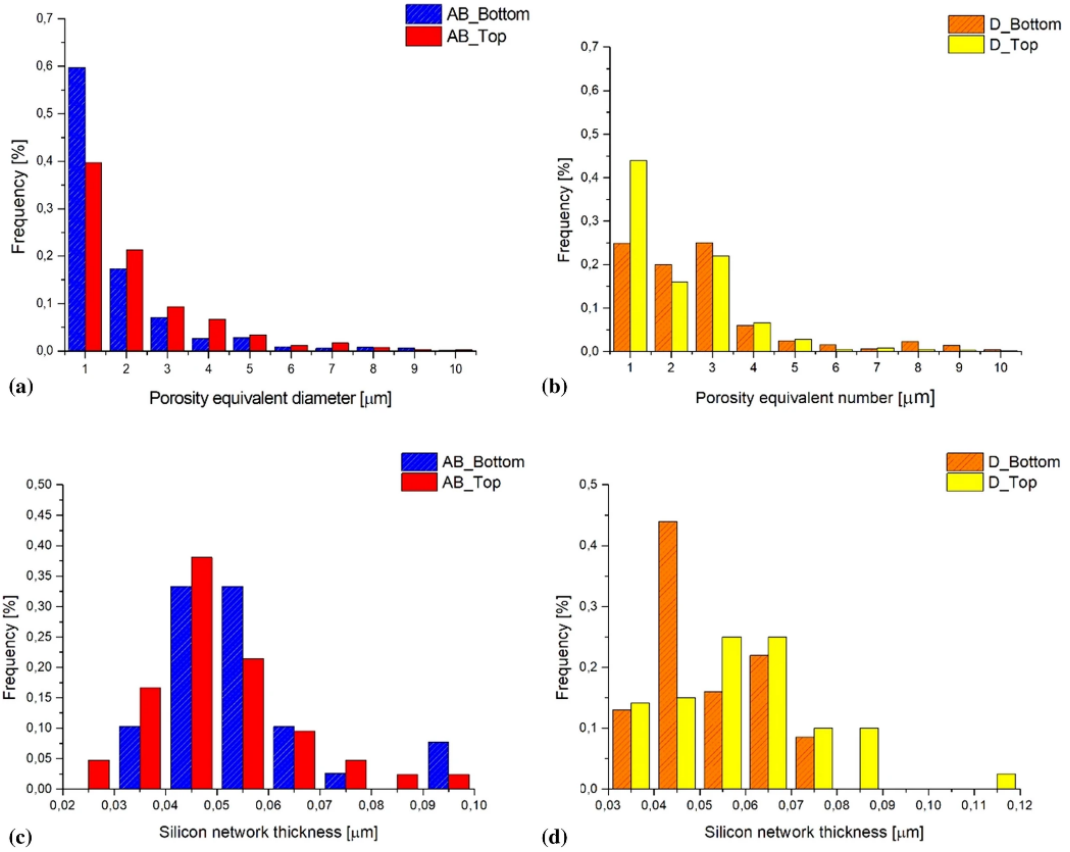


*Figure 1.5. Statistical distribution of porosity (**a**, **b**) and eutectic Silicon network thickness (**c**, **d**). (**a**) Distribution of porosity for AB samples, top and bottom; (**b**) Distribution of porosity for D samples, top and bottom; (**c**) Distribution of Si eutectic for AB samples; (**d**) Distribution of Si eutectic for D samples.*

Considering the single laser case (D-bottom) in *Figure 1.5b*, the bottom samples are characterized by 25 % of porosity with equivalent diameter smaller than 1 μm, whereas 20 % of the pores have diameter in the 1–2 μm range and 25 % have a diameter between 2 and 3 μm. The density is 99.0 %. As regards the top samples, pores with an equivalent diameter lower than 1 μm account for 45 % of the overall porosity; this decreases to 17 % and increases again to 22% for the diameter ranges 1–2 μm and 2–3 μm, respectively. The density is 98.5 %.

The frequency of pores with equivalent diameter greater than 3 μm tends to 0 both for single and overlapping samples. However, it is possible to observe that the multi-laser case has the highest frequency of smaller pores, as also reported by Li et al. [175]. Moreover, bottom samples show slightly lower porosity than top samples as also

reported by [197]; at the same time, in the bottom section there is a higher frequency of small pores (equivalent diameter < 1 μm) than at the top one. As regards the reported values, Aboulkhair et al. [69] and Buchbinder et al. [134] suggested a modification of scan strategy and an increase in laser power up to 1 kW, respectively, to increase density. Moreover, the density of as-built AlSi10Mg SLMed samples was between 95.3 % and 99.9 %, as reported by Lam et al. [178].

In the as-built conditions, very fine eutectic silicon is found at the border of α-grains, as shown in high magnification SEM micrographs of *Figure 1.3*. In detail, the average eutectic thickness ranges from 0.045 to 0.065 μm in both kinds of samples (SL and ML) with a standard deviation of 0.020 μm as shown in *Figure 1.5c* and *d*. Considering such small thickness and the error associated with the measurements, the statistical distributions are similar at the top and bottom in the single and overlapping laser samples. So, in terms of eutectic Si distributions, there are no great microstructural variations in relation to machine setup (single or multi-laser) comparing AB and D bars, as also reported by Zhang et al. [192]. It is inferred that pre-heating the platform at 150 °C does not induce a significant coarsening of eutectic Si. A higher platform temperature, on the other hand, could have caused coarsening of eutectic Si, as reported by Fiegl et al. [140] and Buchbinder et al. [198] through experiments with a platform heated at 200 and 250 °C.

Analysis of XRD patterns performed on top and bottom SL samples (*Figure 1.6*) confirms that there are no significant differences in terms of structure. The Mg_2Si phase was detected through a weak peak at an angle (2θ) of 40.4° in both patterns as reported by [176,178].

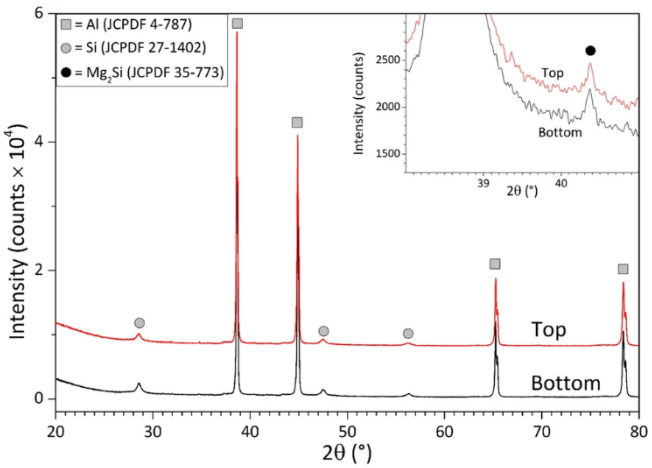


Figure 1.6. XRD patterns of the AlSI10Mg top and bottom samples in as-built condition. The inset shows a high-definition pattern acquired around the main peak of Mg_2Si.

Figure 1.7 illustrates the microstructural differences inside the α-grains of top (*Figure 1.7a* and *b*) and bottom regions (*Figure 1.7c* and *d*) of the billets, in single (left column) and multi-laser samples (right column). There are small precipitates phase inside α-Al grains at the bottom (*Figure 1.7c* and *d*), while precipitates are not visible at the top section (*Figure 1.7a* and *b*) at the magnification of 80 k×. Higher-resolution views (*Figure 1.8*) at 100 k× clarify that fine, sub-micrometer precipitates (arrows) do exist in both bottom (a) and top (b) samples, but they are more numerous in the former (*Figure 1.8a*). However, it should be remarked that the amount of precipitates is not fully homogeneous: in both areas, the amount of precipitates varies among different grains, probably because of slight differences in thermal history, e.g., among center, coarse zone and HAZ as discussed previously.

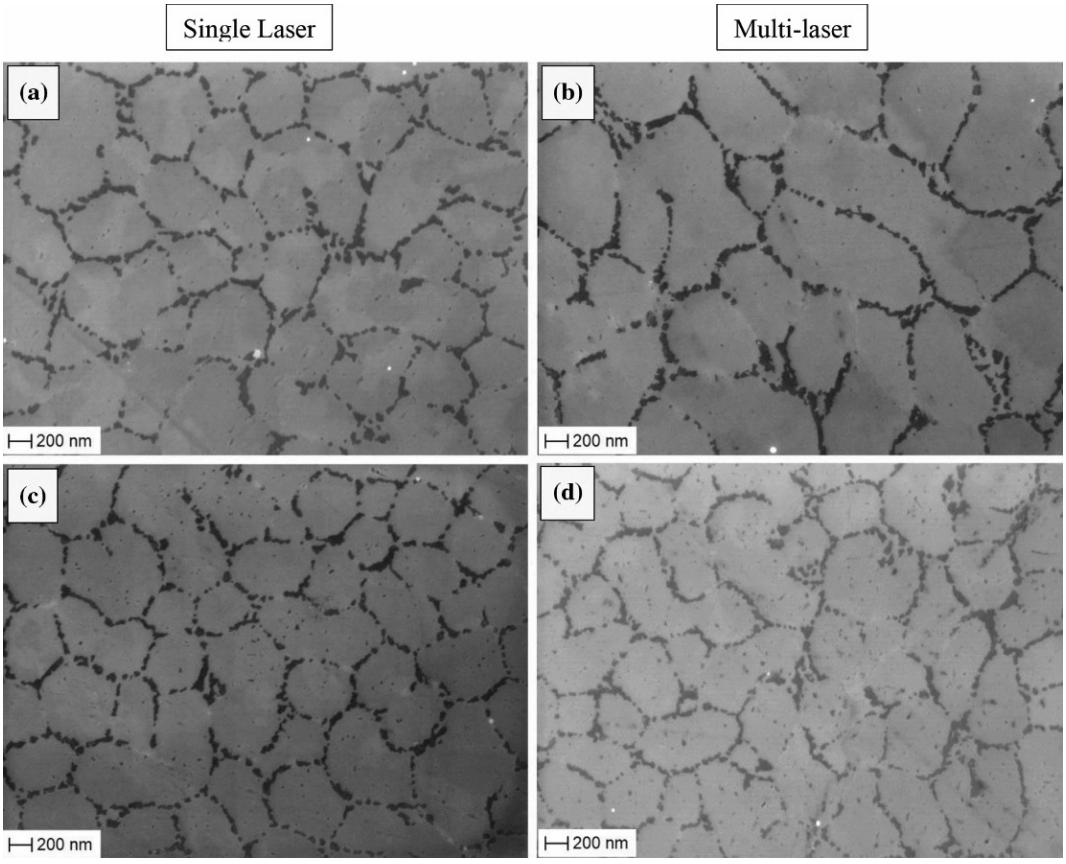


*Figure 1.7. SEM micrographs of the top regions (**a**, **b**) and bottom regions (**c**, **d**) of the bars for single laser (**a**, **c**) and multi-laser (**b**, **d**) samples, respectively.*

Considering two different studies of Kim et al. [199] and Hadadzadeh et al. [187], the fine precipitates visible within the α-Al grains can be both Si precipitates and Mg_2Si phases; so, this condition represents an additional strengthening of the matrix. All of these are also in agreement with the researchers reported by Casati et al. [184] and Li et

al. [185]. In this context, Ji et al. [200] have demonstrated that the SLM process creates a supersaturated solid solution (SSS) of Si in α-Al matrix due to the solidification process of molten pool. As a matter of fact, the high cooling rate (10^6–10^8 K/s) reduces quantity of Si rejected into the liquid. With the successive scanned layers, the Si particles precipitate and grow in the previous solidified layer due to the high temperature that is generated [200–202]. Kimura et al. [201] reported the same scenario with a SSS formed by Si and Mg solvents.

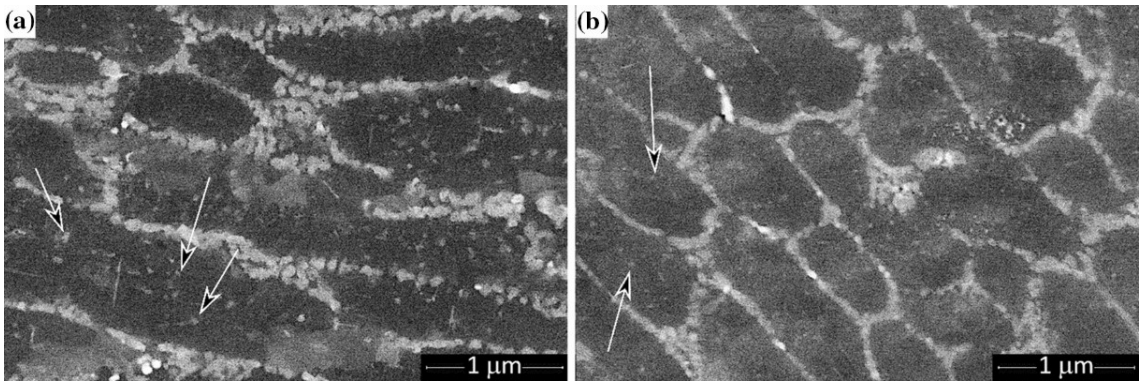


*Figure 1.8. High-resolution SEM micrographs of the bottom (**a**) and top (**b**) regions of the single laser sample. Arrows indicate some nanosized Si within the α-Al grains.*

Figure 1.9 shows the Vickers microhardness measured along the build axis (or Z-axis) of the two bars. Vickers microhardness is higher at the bottom of the bar (~ 125 HV at 0–30 mm distance from the bottom for both bars), but at the maximum height (300 mm), it decreases to 110 HV and 103 HV, respectively, for AB and D bars. In terms of time and according to HV values reported in *Figure 1.9*, HV decreases by 12 % and 16 % for the single and multi-laser samples, respectively, in 40 h (i.e., the job duration time) during exposure at 150 °C (platform temperature).

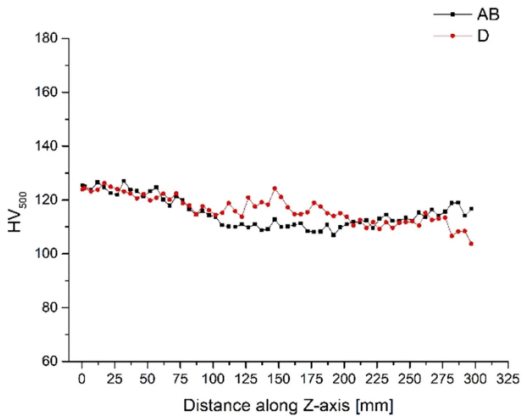


Figure 1.9. Microhardness measured along the build (Z) axis for single laser samples (D) and multi-laser samples (AB).

The tensile properties measured in samples machined at different heights of the bar (according to *Figure 1.1a*) are illustrated in *Figure 1.10a* and *Figure 1.10b*, as a function of the distance from the platform (distance along Z-axis). The yield strength and the UTS decrease in samples extracted at higher Z, ranging from 290 to 220 MPa and from 440 to 360 MPa, respectively, for the Single laser case. For the multi-laser case, both $\sigma_{0.02}$ and UTS vary from 300 to 190 MPa and from 445 to 345 MPa, respectively. The greatest variation was, therefore, obtained in multi-laser samples (+ 110 MPa for yield strength and + 100 MPa for UTS), compared to the variations obtained for single laser samples, as reported in *Table 1.2*. The % engineering elongation, ε, shows average values of (7 ± 1) % in both kinds of samples and over the entire 300 mm-long investigation region along the Z-axis (*Figure 1.10*). Unlike tensile strength, ductility is not affected by increasing distance along the build axis.

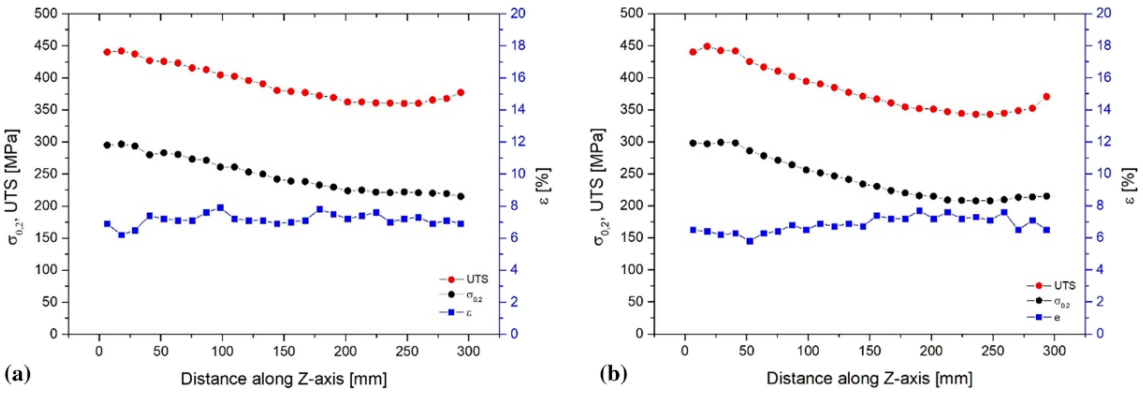


*Figure 1.10. Tensile properties measured as a function of the distance from the bottom region for (**a**) multi-laser laser samples and (**b**) single laser samples.*

Table 1.2. Variation of the mechanical properties of AlSi10Mg samples for the single laser case and multi-laser case.

	Variation from bottom to top					
	Absolute differences			**Relative change**		
	$\Delta\sigma_{0.2}$	**ΔUTS**	**Δε**	**$\Delta\sigma_{0.2}$**	**ΔUTS**	**Δε**
Sample AB: Multi-laser	110 MPa	100 MPa	– 0.9 %	– 37 %	– 22 %	+ 14 %
Sample D: Single laser	70 MPa	80 MPa	– 0.8 %	– 24 %	– 18 %	+ 12 %

Hardness and tensile strength values are closely related to precipitation strengthening phenomena depending on distance from the heated platform as reported in *Figure 1.7* and *Figure 1.8* and by [176–178]. In fact, there is a difference between the top and bottom samples in terms of intra-granular precipitates (Si or Mg_2Si phase), as explained previously. This can be regarded as an aging effect due to prolonged exposure to 150 °C. Yang et al. [158] confirmed that Mg_2Si phase induces a little strengthening at

160 °C for 8 h. At the top of Z-axis, i.e., farther away from the heated platform, tensile strength and HV are lower because the matrix contains fewer precipitates. Therefore, it is mainly hardened by solid solution, which is a less effective mechanism than precipitation strengthening. The slight increase in strength (+17 MPa for SL case and +27 MPa for ML case) of the last top samples (*Figure 1.10*) can be attributable to lattice distortion due to Si dispersed in α-Al matrix during SLM process as previously reported [184,192,203]. In fact, these samples are not affected by build platform which induces a stress relaxation and/or an overaging, as reported by [176,184,185].

The smaller decline of strengths along the Z-axis in the SL samples compared to ML samples could perhaps be also attributable to lower coarsening of the microstructure due to lower heat input. Anyway, the effect is barely visible by SEM (*Figure 1.7*). In fact, mechanical properties and microstructure are largely comparable between SL and ML samples. In this context, the ML samples are affected by a greater amount of thermal energy than SL samples due to re-melting or partial re-melting of solidified tracks [184,204]. This situation induces a decrease in anisotropy that characterized the as-built samples; in fact, the thermal gradient induces a <100> texture orientation of microstructure along build direction, as reported by Dai et al. [202] and Guan et al. [204]. Similarly, Zhang et al. [192] show a greater isotropy for the overlap samples (18.3 % of the area) than single laser samples (12.6 %). So, also considering the effect of build platform as previously reported, it can be explained how ML samples have a greater loss in strength than SL samples in the middle part of two bars printed. Therefore, in the following paragraphs, only the results of single laser samples will be considered.

3.2. Microstructure and Mechanical Properties of Treated AlSi10Mg Samples

Figure 1.11 presents the trend of tensile strengths and elongations for the AlSi10Mg samples subjected to unconventional treatments at 175, 200 and 225 °C for 6 h, designated as U-HT1, U-HT2 and U-HT3, respectively, for samples at the top and at the bottom. Values of mechanical properties are also listed in *Table 1.3*.

Table 1.3. Mechanical properties and their variations of top and bottom AlSi10Mg samples depending different heat treatment conditions.

HT Conditions	UTS [MPa]		$\sigma_{0.02}$ [MPa]		ε [%]	
	Top	Bottom	Top	Bottom	Top	Bottom
As-built	367 ± 10	415 ± 19	225 ± 8	270 ± 11	7.3 ± 0.7	7.2 ± 0.6
U-HT1	396 ± 18	419 ± 16	232 ± 11	258 ± 9	7.6 ± 0.6	7.6 ± 0.4
U-HT2	350 ± 9	395 ± 11	199 ± 6	235 ± 12	9.2 ± 0.5	9.0 ± 1.0
U-HT3	331 ± 19	341 ± 15	184 ± 5	199 ± 6	15.2 ± 1.0	13.6 ± 1.1

From *Figure 1.11*, the gap reduction of tensile properties between the top and bottom samples is achieved by the U-HT3. In the bottom samples, which had already been aged at 150 °C during the build process itself (as explained previously), additional aging due to the treatment at 175 °C has a barely perceivable effect. In the top samples, which were less affected by the pre-heated platform, the aging effect is comparatively more significant. In fact, after the U-HT1 treatment, the top and bottom samples develop comparable microstructures.

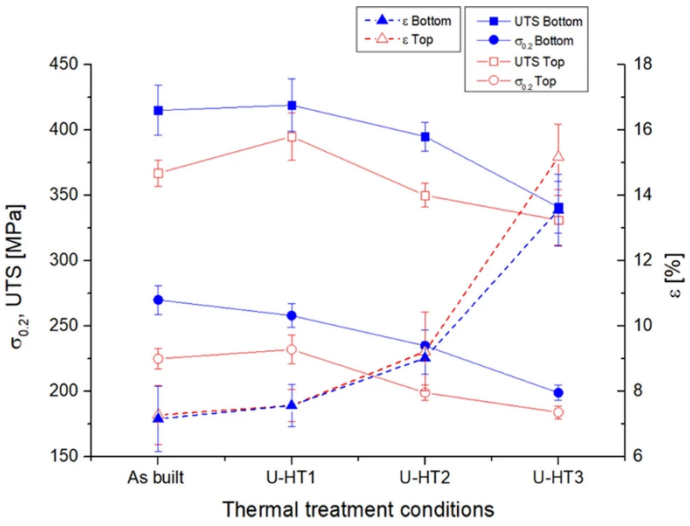


Figure 1.11. UTS, yield strength and elongation values of top and bottom AlSi10Mg samples in as-built, U-HT1, U-HT2 and U-HT3 conditions.

Both are rich of fine precipitates within the α-Al matrix (*Figure 1.12a,b*). A comparison between *Figure 1.8b* and *Figure 1.12b* particularly highlights the increased amount of fine, intra-granular precipitates in the top sample. The aging condition of both the top and bottom samples has thus become comparable after this heat treatment. On the other hand, the treatment seems not to affect the network of eutectic Si, which remains comparable to the one seen in as-built condition (compare *Figure 1.12* to *Figure 1.8*).

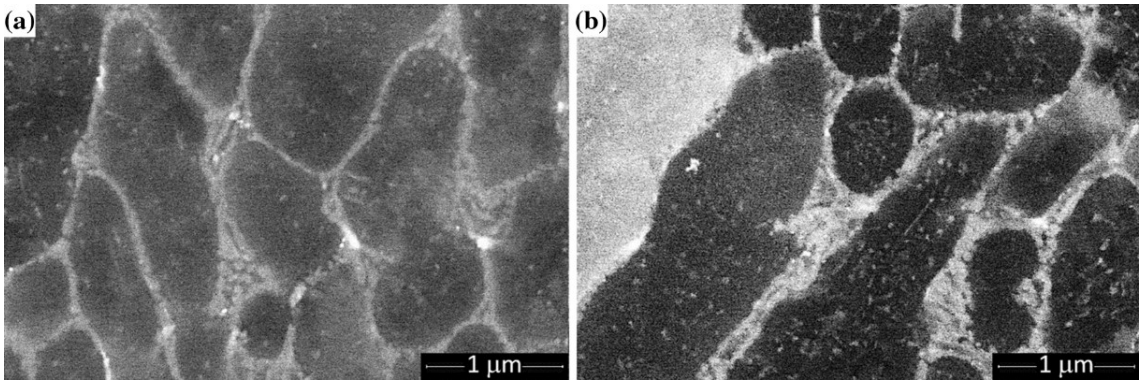


*Figure 1.12. High-resolution SEM micrographs of the bottom (**a**) and top (**b**) AlSi10Mg samples in U-HT1 condition.*

Figure 1.13 shows that U-HT3 induces an increase in the size of eutectic Si compared to as-built condition. SEM micrographs shown in *Figure 1.14a* and *Figure 1.14b* highlight the incipient destruction of the Si eutectic network and confirm the coarsening of Si particles compared to *Figure 1.8* and *Figure 1.12*. After the aging treatment at 225 °C (U-HT3), the UTS and yield strengths have a maximum decrease compared to as-built AlSi10Mg samples for top and bottom regions, while ductility has a maximum increase. In detail, the largest variations occur for the bottom samples and are 24 % and 26 %, respectively, for UTS and $\sigma_{0.02}$. Fiocchi et al. [183] and Mertens et al. [205] reported comparable results.

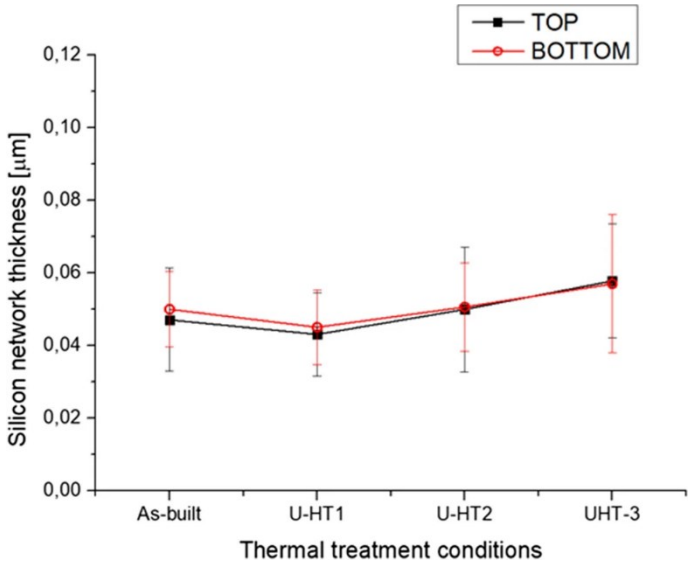


Figure 1.13. Average values of Si eutectic thickness measured in as-built condition and different heat treatments.

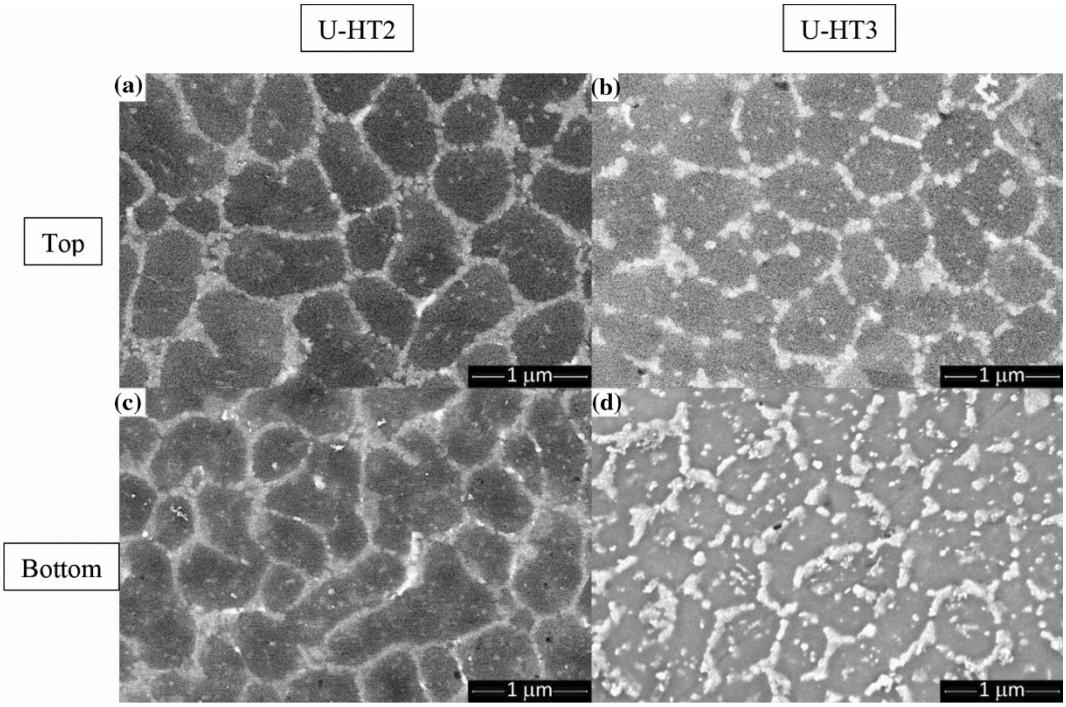


*Figure 1.14. High-resolution SEM micrographs of the top regions (**a**,**b**) and bottom regions (**c**,**d**) of the bars, respectively, for U-HT2 (**a**,**c**) and U-HT3 (**b**,**d**) conditions.*

Consistently, XRD patterns in *Figure 1.15a*, *Figure 1.15b* and *Figure 1.15c* show that the Si peaks become somewhat more intense and narrower after U-HT3 treatment, compared to the as-built condition, which confirms the coarsening of Si.

Further, the relative intensity of the different diffraction peaks of α-Al changes after the U-HT3 treatment: the (200) peak at 44.7° becomes more intense than the (111) peak at 38.5°. This indicates that the α-Al phase is undergoing a change in crystal orientation.

The greatest UTS loss of 74 MPa is, therefore, explained by the combined effects of coarsening of the Si precipitates and interruption of Si eutectic network. The latter phenomenon allows easier movement of dislocations through the neighboring α-Al grains: dislocations are less likely to interact with coarser eutectic Si. Consequently, the strength needed to break the tensile specimen is also reduced; in fact, the required energy for plastic deformation must not be dissipated in the deformation of eutectic Si as reported by [199].

Due to such major microstructural re-arrangement, the values of tensile strengths become completely comparable between top and bottom samples. Any difference between the aging conditions of top and bottom after the build process is indeed lost through the alterations caused by the U-HT3 treatment. As regards the

ductility, the results obtained on the U-HT3 samples can be regarded as optimal values, when compared both to the other samples tested within the present work (as shown in *Table 1.3*) and to literature data pertaining to analogous thermal treatment conditions [140,175,183,206].

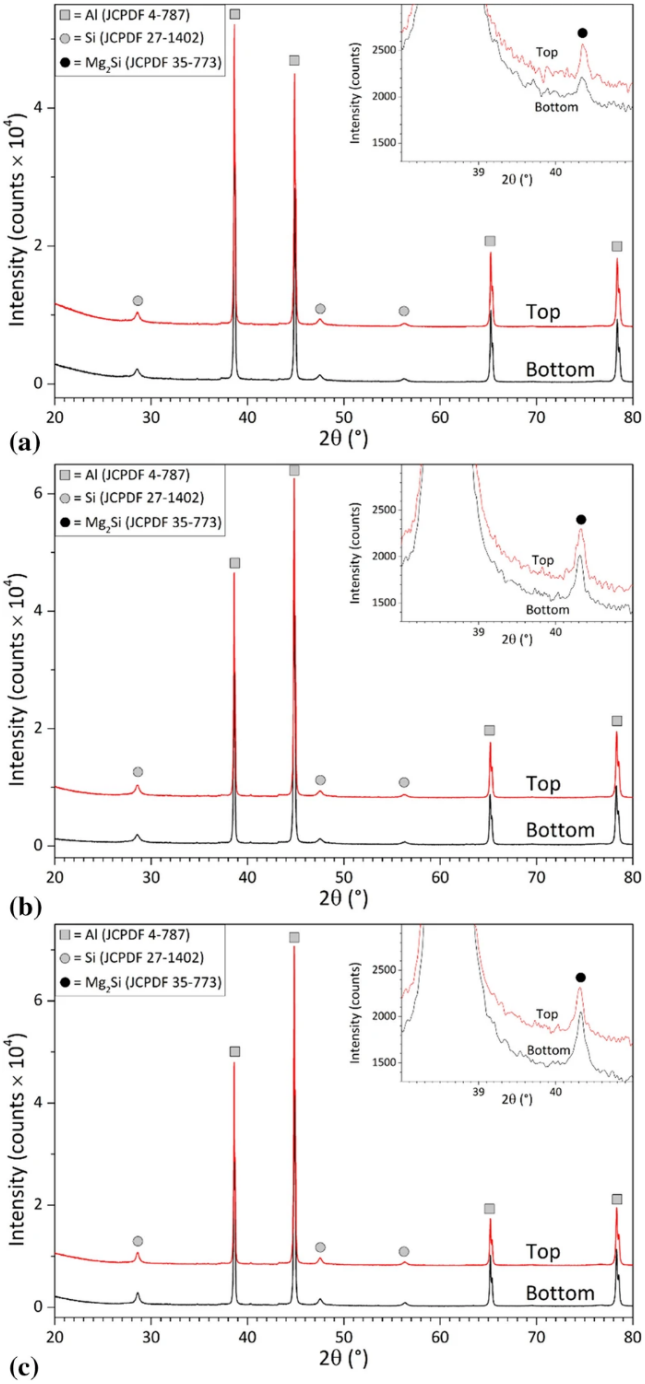


*Figure 1.15. XRD patterns for AlSi10Mg top and bottom samples in U-HT1 (**a**), U-HT2 (**b**) and U-HT3 (**c**) conditions. Insets show high-definition patters acquired around the peak of Mg_2Si.*

The U-HT2 condition, on the other hand, seems to provide an optimum compromise between retaining the mechanical properties and providing acceptable values of elongation, although the effect of the distance from the build platform is retained.

This compromise is achieved as the unconventional heat treatment causes a slight increase in the size of eutectic Si (*Figure 1.13*), as well as a slight coarsening effect on the precipitates within α-Al grains (*Figure 1.14a* and *Figure 1.14c*), but it does not cause a destruction of the Si eutectic network (*Figure 1.14a,c*), compared to the as-built condition (compare to *Figure 1.8*).

4. Conclusions

In summary, the effects of distance from the pre-heated build platform on SLMed AlSi10Mg samples processed by single and multi-laser (SL, ML, respectively) scanning methods were studied. All of these were analyzed in as-built condition and after unconventional heat treatments (U-HTs). The following conclusions have been drawn:

1. An ultrafine and inhomogeneous microstructure was detected in as-built samples by SEM micrographs and XRD analysis. It is characterized by α-Al grains with a network of eutectic Si, and nanosized intra-granular precipitates that likely consist of Si and Mg_2Si phases. There is no substantial difference either between SL and ML or between top and bottom samples in terms of eutectic Si thickness. Proximity to the pre-heated build platform, therefore, does not induce coarsening of eutectic Si. In fact, the range is from 0.045 μm to 0.065 μm with a standard deviation of 0.020 μm. However, the SL samples show a lower density than ML samples; furthermore, the porosity decreases from top to bottom samples. Bottom samples also contain greater amounts of intra-granular precipitates.
2. Due to these microstructural differences, the tensile strength and Vickers microhardness decrease linearly as the height increases along the Z-axis for as-built samples. The greatest loss of mechanical properties was achieved for the ML samples. In detail, HV decreases by 12 % and 16 % for SL and ML samples, respectively. The yield strength and UTS decrease by about 25 % and 18 %, respectively, for the SL case, about 35 % and 22 %, respectively, for the ML case.
3. Unconventional heat treatments with suitably adjusted temperature can provide an optimal combination between strength and ductility. Starting from the highly metastable microstructure of the as-built samples, the aging

induced by such heat treatments causes a progressive re-arrangement of the Si network and further intra-granular precipitation. A treatment at 200 °C, in particular, causes slight rounding and coarsening of Si to yield improved ductility, but still it retains high mechanical strength.

4. The effect induced by the pre-heated platform along the Z-axis was reduced by unconventional heat treatments at 175 °C (U-HT1) and 225 °C (U-HT3). In the first case, this is due to the aging treatment induced on the "top" samples, which makes them similar to the "bottom" samples that had already been aged by prolonged proximity to the build platform during the SLM process. The second case is characterized by coarsening of both intra-granular precipitates and eutectic Si, and by destruction of the eutectic Si network, which levels out the properties in all areas of the sample. The treatment at 200 °C (U-HT2), on the other hand, retains the mechanical properties' gradient along the Z-axis.

[*This page intentionally left blank*]

ARTICLE 2

Aging Profiles of AlSi7Mg0.6 and AlSi10Mg0.3 Alloys Manufactured via Laser-Powder Bed Fusion: Direct Aging versus T6

Emanuela Cerri & Emanuele Ghio

Materials, 15(17) (**2022**) 6126

https://doi.org/10.3390/ma15176126

“The following version of the manuscript is made available under the CC-BY-NC-ND 4.0 license”

https://creativecommons.org/licenses/by-nc-nd/4.0/

Aging Profiles of AlSi7Mg0.6 and AlSi10Mg0.3 Alloys Manufactured via Laser-Powder Bed Fusion: Direct Aging versus T6

Emanuela Cerri [1], Emanuele Ghio [1]

[1] Department of Engineering and Architecture, University of Parma, Via G. Usberti 181/A, 43124, Parma, Italy.

Abstract

The artificial aging heat treatments performed directly on as-built and solubilized AlSi7Mg0.6 and AlSi10Mg0.3 samples were characterized and discussed. The analysed bars and billets (height of 300 mm) were manufactured via the Laser Powder-Bed Fusion process on a build platform heated at 150 °C. Therefore, its influence on the as-built samples was studied in terms of mechanical performance variations between the bottom and top regions. Vickers microhardness measurements were performed to obtain aging profiles after direct aging (175–225 °C) and T6 heat treatments and to highlight better time and temperature parameters to optimize the mechanical properties of both alloys. SEM observations were used to characterize the microstructure before and after the heat treatments and its influence on the fracture mechanisms. Generally, the direct aging heat treatments show the same effects on both aluminium alloys, unlike the solubilization at 505 °C followed by artificial aging at 175 °C. The strengths vs. elongation values obtained after the direct aging treatments are better than those exhibited by T6 as highlighted by the quality index.

Keywords: AlSi10Mg and AlSi7Mg alloys; aging profiles; direct aging heat-treatments; T6 heat-treatment; heat-treatment optimization; Laser Powder Bed Fusion

1. Introduction

Laser-Powder Bed Fusion (LPBF) is an Additive Manufacturing (AM) technology for metals and alloys, where one or more lasers scan a powder bed (layer) on a cold or hot build platform. This layer-by-layer process aims to manufacture geometrically complex components which can be also characterized by high customization. LPBF also minimizes the material waste and reduces the costs and time of production, namely the advantages conferred by the AM processes. At the same time, the complex software allows obtaining a weight reduction of the designed mechanical or structural components thanks to careful optimization of their geometry. In fact, the metal material will be distributed within specified design space in accordance with the

Finite Element Analysis (FEA) results [48,55,207]. For these reasons, the LPBF process is good for several industrial applications, e.g., automotive and aerospace thanks to the possible production of commercial and military vehicles and/or aircraft structures [20,43,207].

In this scenario, the hypo-eutectic AlSi7Mg0.6 and AlSi10Mg0.3 alloys find numerous uses owing to their high specific strength conferred by their low density (ρ = 2.68 g/cm^3) and to the good corrosion resistance due to the oxide film [1,208]. Both the cast A357 (AlSi7Mg0.6) and AlSi10Mg0.3 aluminium alloys belong to the age-hardening Al-Si-Mg ternary system where the 0.3 and 0.6 % of Mg promote the following precipitation phenomena [33]:

SSS → GP zone → β'' coherent precipitate → β' semi-coherent precipitate → β-Mg_2Si incoherent precipitate

Therefore, the age hardening response promotes firstly the formation of the GP (Guinier–Preston) zones, which are extremely fine-scaled solute enriched regions, from the SSS and, secondly, their evolution in coherent β" (Mg_5Si or $Mg_5Al_2Si_4$), semi-coherent β' ($Al_3Mg_9Si_7$) and incoherent β-Mg_2Si precipitates [13,33,209,210]. Focusing on Al-Si-Mg alloys manufactured via the LPBF process, the high cooling rate (~ 10^6 K/s) causes an initial Si concentration in α-Al matrix higher than the equilibrium content of 1.65 % [211,212]. Therefore, the mechanical performance of both aluminium alloys can be improved through both T5 and T6 heat treatments (HTs). In the former case, the ultimate tensile strength (UTS), yield strength (YS), and hardness are improved by performing artificial ageing (AA) at about 160 °C. In the latter case, the AA follows the solubilization heat treatment (SHT) at about 500–540 °C for different holding time, and makes it possible to obtain higher UTS, YS and hardness than the T5 as discussed by [213]. Perreira et al. [149] reported (321 ± 2) MPa and (271 ± 2) MPa of UTS and YS, respectively, and (118 ± 12) HV after a standard T6 (535 °C × 0.25 h + 160 °C × 10 h) performed on cast AlSi7Mg0.6. Van Cauwenbergh et al. [212] showed, however, (228 ± 16) MPa for UTS and (183 ± 33) MPa for YS of a cast AlSi10Mg0.3 alloy heat treated at (540 °C × 8 h + 160 °C × 6 h). The elongation reaches (1.50 ± 0.40) %, a very low value as for the previously mentioned A357-T6 showing (2.9 ± 0.3) %. The same mechanical properties were reported in [149,212]. Kempen et al. [214] reported an HV improvement form 95–105 HV in as-cast conditions to 130–133 HV after the T6 on AlSi10Mg0.3 cast alloy.

Focusing on the as-built AlSi7Mg0.6 and AlSi10Mg0.3 alloys, the conventional T6 HT generally confers detrimental effects for the UTS, YS and hardness values. As a matter of fact, the full-cellular structure where the α-Al matrix is surrounded by nano-size Si-eutectic particles distribution is completely destroyed by the high temperatures

reached during the SHT [67,215]. From a three-dimensional point of view, the eutectic particles formed a tubular structure arranged along with the build direction (i.e., parallel to the build platform) which confers UTS and YS higher than 360 MPa and 210 MPa, respectively, for the as-built AlSi10Mg0.3 alloy [33]. Comparable mechanical properties are shown by the as-built AlSi7Mg0.6 alloy [201,216]. As widely dis-cussed in [33,65], the pre-heated (hot) build platform plays fundamental roles on both the precipitation phenomena and the residual stress amount and, consequently, on the obtained mechanical performance. At the same time, the SSS formed thanks to the high cooling rate characterizing the LPBF process fails. As regards the ductility, the as-built values (< 9 %) do not satisfy the current standard specifications yet. The micro-structural changes induced by the T6 HT lead the UTS and YS at values lower than 300 MPa and 250 MPa, respectively, without a satisfactory improvement of the elongation values. In addition, the high temperatures reached during the SHT induces a pore size increment as widely reported by [18,71] and discussed in [144] for the AlSi10Mg0.3 alloy. Tonelli et al. [218] added that the T6 HT can reduce the microstructural anisotropy and the correlated mechanical properties, in addition to the completely relieve of the residual stress after 10 min at 540 °C in AlSi7Mg0.6 subjected to LPBF. To reduce the residual stress and nullify the sample distortions when it is separated from the build platform, the stress relief at 300 °C × 2 h is suggested instead of the T6 [33]. In fact, the former confers better mechanical performance than the latter.

In relation to the build platform temperature and the total height of the manufactured samples, direct aging (DA) HTs at temperatures lower than 250 °C can lead to greater optimized mechanical properties, also through a reduction of the processing time with respect to T6 HT. As a matter of fact, the SSS of the as-built AlSi7Mg0.6 and AlSi10Mg0.3 samples can trigger the precipitation phenomena already during the DA [209]. In addition, the full-cellular structure continues to preserve the mechanical properties of the heat-treated samples [33].

The present work aims to evaluate the effects induced by T6 HT on the AlSi7Mg0.6 subjected to LBPF in terms of microstructure, porosity and mechanical performance, and to compare them to the effects obtained by the L-PBFed AlSi10Mg0.3 alloy in the same heat-treated conditions. In addition, different time of SHT were also considered and analysed. At the same time, it presents the best impact conferred on the same aluminium alloys by different direct aging heat-treatments also considering the effects induced by the pre-heated build platform.

2. Materials and Methods

The set of powders used to manufacture the samples analyzed in the present work are AlSi7Mg0.6 and AlSi10Mg0.3. *Table 2.1* listed their nominal chemical compositions. In both cases, the particles diameter had a distribution of 20–63 μm and the apparent density is higher than the 1.52 g/cm^3.

Table 2.1. Nominal chemical composition (wt.%) of AlSi7Mg0.6 and AlSi10Mg0.3 gas-atomized powders.

Al	Si	Mg	Fe	Cu	Mn	Zn	Ti	C	H	N	O
Bal.	7.04	0.59	0.06	<0.005	0.006	0.011	0.12	0.03	0.002	< 0.002	0.03
	10	0.31	0.12	0.001	0.005	0.002	0.04	<0.005	0.002	<0.002	0.10

The L-PBF process was conducted on SLM®280 machine where two IPG fiber laser, characterized by a maximum power of 700 W, work in parallel manufacturing samples both in single laser (SL) and double laser (DL) zones, respectively. In the former zone, only one laser scans the powder bed; while in the latter one, the powder bed is scanned simultaneously by two lasers. The design of the printed samples, where the yellow and red areas of the build platform represent the SL and DL zones, is shown in [144]. For both aluminium alloys, bars (10 × 10 × 300 mm^3) and billets (10 × 100 × 300 mm^3) were manufactured with the same process parameters (*Table 2.2*) but in different processing time. AlSi10Mg0.3 billets and bars are manufactured in 54 h, while AlSi7Mg0.6 samples were printed in 75 h. This difference in manufacturing time was dictated by a slowdown in the powder bed deposition.

Table 2.2. Process parameters used to manufacture AlSi7Mg0.6 and AlSi10Mg0.3 bars and billets.

Zone	Laser Power (P, [W])	Scan speed (v, [mm/s])	Layer thickness (t, [μm])	Hatch spacing (h, [μm])	Energy density (ED, [J/mm^3])	Build Platform [°C]
Skin	330	600	90	70	87.3	150
Core	370	1400			42.0	

For a better understanding of the discussed results, all billets and bars are divided into three different groups in relation to their total height: bottom (0–100 mm), middle (100–200 mm) and top (200–300 mm). All samples were manufactured using the skin-score scan strategy represented in *Figure 2.1*. The dotted arrows, which indicate the laser scan tracks, are inclined of 56.5° with respect to the skin base. For each deposited layers, the scanning direction is rotated of 67° with respect to the previous scanned and solidified layer.

The aim of the present study is to analyze the effects induced by the DA and T6 HTs and to identify the optimal conditions on both AlSi7Mg0.6 and AlSi10Mg0.3 alloys. *Table 2.3* summarizes the studied HT conditions and the samples on which the HTs were

performed. T6* and T6** will represent the peak-aging conditions for the AlSi10Mg0.3 and AlSi7Mg0.6 alloys, respectively. The temperatures chosen for the DA, SHT and AA heat treatments were based on [65,67] where the AlSi10Mg0.3 alloy manufactured with a layer thickness of 50 μm were analyzed. The top and bottom samples listed in *Table 2.3* were cut by the bars (see *Figure 2.1* in [144]) and the different heights were chosen in relation to the both the HV measurements performed on the same bars in as-built conditions and to the results obtained in [65,67]. The T5 (i.e., DA) and T6 HTs were carried out following the conditions dictated by the standard specification of aluminium-alloy casting [219].

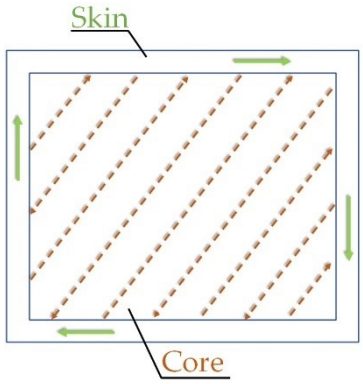


Figure 2.1. Skin-Core scan strategy used to manufacture AlSi7Mg0.6 and AlSi10Mg0.3 bars and billets. The skin thickness is 200 ± 10 μm.

Table 2.3. Heat treatment performed on AlSi7Mg0.6 and AlSi10Mg0.3 samples.

HT	Temperature	Time	Samples
DA	175 °C	30 min, 1 h, 2 h, 4 h, 8 h, 16 h	Top (280–300 mm) and Bottom (0–20 mm)
	200 °C		Top (260–280 mm) and Bottom (20–40 mm)
	225 °C		Top (240–260 mm) and Bottom (40–60 mm)
SHT	505 °C	2.5 min, 5 min, 10 min, 20 min, 30 min, 40 min, 50 min, 1 h, 2 h, 4 h	Other (60–260 mm)
T6	505 °C	4 h	
	175 °C	30 min, 1 h, 2 h, 4 h, 8 h, 16 h, 32 h	

The HV values were measured with a VMHT Leica (Leica, Wetzlar, Germany) microhardness tester using 500 gf of load and 15 s of indentation time in accordance with UNI EN ISO 6507-1:2018 standard specification. All indentations were performed on the mechanically ground and polished surface of the bars. For the as-built SL and DL bars, the HV measurements were performed on the xz (perpendicular to the build platform) and xy (parallel to the build platform) planes where two HV profiles and a 3 × 3 matrix were built, respectively. Each HV profile was formed by 60 measurements where the distance between two successive indentations was 5 mm (ψ in *Figure 2.2a*). A distance of 1 mm was used to also separate the two profiles to avoid the work-hardening effect. For

each couple of indentations at the same height, the 60 average values of HV were used to plot the HV profiles (*Figure 2.8*) for the SL and DL bars. Focusing on xy planes, the 3 × 3 matrices were always carried out on the center of the bar cross-section to avoid the contribution conferred by the skin part (*Figure 2.2*) as shown in [144]. The 9 indentations were spaced 1 mm from each other as highlighted by the δ in *Figure 2.2b*. The same 3 × 3 matrices were also used to evaluate the microhard-ness on xy planes of the direct aged, solution and T6 heat-treated samples (*Table 2.3*). All points forming the aging curves and the SHT profiles, and related to each HT conditions, were calculated as the average of the 9 indentations. The correlated standard deviations were used as error bands.

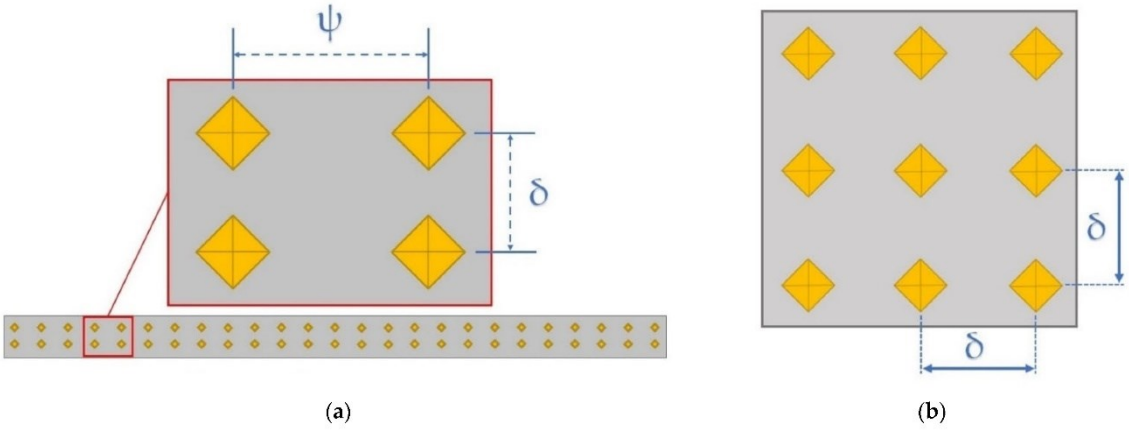


*Figure 2.2. Schematical representation of the HV profiles (**a**) and 3 × 3 matrix (**b**) performed on the xz and xy planes of the bars, respectively. The build directions are: (**a**) parallel to the longer side of the bar, (**b**) perpendicular to the xy plane (i.e., on which the HV is measured).*

The as-built and heat-treated microstructure was analyzed by the DMi8 optical microscope (OM) (Leica, Wetzlar, Germany) equipped with LAS-X software through which the image analysis of both the Si-eutectic particles in T6 heat-treated samples and pores was performed. Firstly, one OM micrograph at 500× and three at 1000× of magnification were considered to analyze the Si-eutectic on solution heat-treated samples at 1 h (SHT 1h), 2 h (SHT 2h) and 4 h (SHT 4h). Secondly, the pores analysis was carried out following the methodology used in [144] because the density values of the heat-treated AlSi7Mg0.6 samples will be compared to those discussed for the AlSi10Mg0.3 samples in the same research article. For this reason, the chosen HTs are: DA at 175 °C, 200 °C and 225 °C × 8 h, and T6*. Also in this case, a density of 2.68 g/cm^3 is considered for an AlSi7Mg0.6 sample having 0 % in vol. of pores, and all studied micrographs were taken on the xy plane. In summary, six different OM micrographs (magnification of 100×) were systematically analyzed to evaluate the relative density of the as-built and heat-treated AlSi7Mg0.6 samples. The micrographs were manually

analyzed through the LAS-X 2D software to determine the relative density (ρ_r) of each sample. And then, the following equation was considered:

$$\rho_r = 1 - \frac{\sum_i (A_p)_i}{\sum_{j=1}^{6} (\hat{A})_j} \tag{2.1}$$

where A_p is the area of a single analyzed pore and $\left[\sum_{j=1}^{6} (\hat{A})_j\right]$ is the total area of the considered six OM micrographs. Its value is 24,936.41 × 10^3 μm^2. The errors associated to the density values were calculated, as expressed and validated in the Appendix A of the [144], as follows:

$$e_a = \frac{\rho_r^{max} - \rho_r^{min}}{2} = \frac{\left[1 - \frac{\left[\sum_i (A_p)_i\right]_{min}}{\sum_{j=1}^{6} (\hat{A})_j}\right] - \left[1 - \frac{\left[\sum_i (A_p)_i\right]_{max}}{\sum_{j=1}^{6} (\hat{A})_j}\right]}{2} \tag{2.2}$$

where $\left[\sum_i (A_p)_i\right]_{min}$ and $\left[\sum_i (A_p)_i\right]_{max}$ are the underestimation and overestimation of the total pore area, respectively. Both contributions were obtained by combining the standard errors, listed in *Table 2.4*, with each value of the pore area. In details, these standard errors consider both the errors committed by the operator during the image analysis and the error related to the OM (see [144]).

Table 2.4. Standard errors that are associated to each pore area analyzed [144].

Areas	Standard errors
$A_p < 1\ \mu m^2$	10 %
$1\ \mu m^2 \leq A_p < 10\ \mu m^2$	7 %
$10\ \mu m^2 \leq A_p < 30\ \mu m^2$	6 %
$A_p \geq 30\ \mu m^2$	4 %

Tensile tests were conducted at room temperature using the Z100 Zwick/Roell (ZwickRoell, Einsingen, Germany) servo-hydraulic machine with a cross-head speed of 0.008 s^{-1}. The cylindrical tensile samples were mechanically obtained by the as-built billets, and their dimensions are illustrated in *Figure 2.3*. After the turning process, the tensile samples were heat-treated following the optimal conditions highlighted by the HV measurements to complete them with the tensile properties.

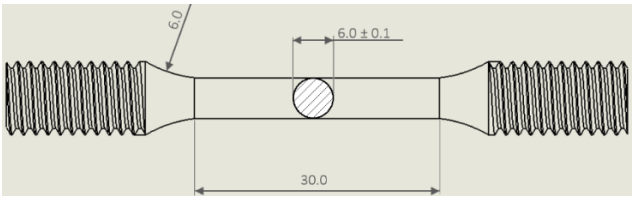


Figure 2.3. Graphical representation of a cylindrical tensile sample obtained from the as-built billets (Reprinted from Reference [144]).

Thanks to the machining process, the skin part (*Figure 2.1b*) was removed and, therefore, its possible detrimental effects on the mechanical performance, as widely demonstrated in [144].

3. Results

3.1. Density Analysis

The as-built AlSi7Mg0.6 samples are characterized by a density of 2.667 ± 0.003 g/cm^3 both in the bottom and top regions. The same density values characterize the as-built AlSi10Mg0.3 samples that show 2.675 ± 0.003 g/cm^3 and 2.676 ± 0.003 g/cm^3 for the top and bottom, respectively (*Figure 2.4*). Even after the DA at 175 °C × 8 h and 200 °C × 8 h, the density values of the AlSi7Mg0.6 and AlSi10Mg0.3 in top and bottom regions remain almost unchanged. The first step related to the decrease in density (up to 2.660 ± 0.004 g/cm^3) is shown by AlSi10Mg0.3 samples after the DA at 225 °C × 8 h; the second after the T6* where the density values reach 2.627 ± 0.005 g/cm^3 and 2.633 ± 0.005 g/cm^3 for the top and bottom samples, respectively. These latter values are consistent with those exhibited in [65,67,215].

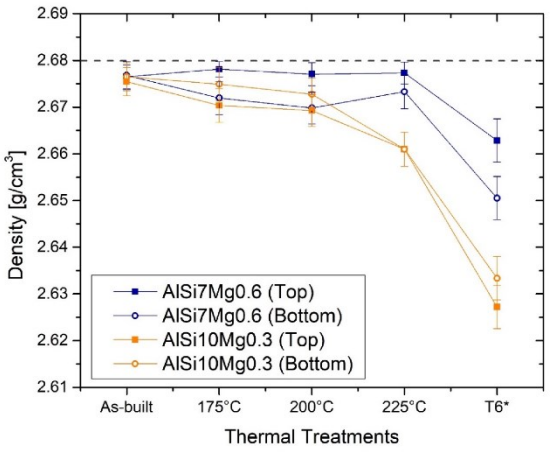


Figure 2.4. Trends of the density values related to top and bottom of the AlSi7Mg0.6 and AlSi10Mg0.3 samples before and after the direct aging at 175, 200, 225 °C for 8 h and the T6. The values related to the AlSi10Mg0.3 samples were presented and discussed in [67].*

Focusing on the top and bottom AlSi7Mg0.6 samples in as-built conditions and after the T6*, *Figure 2.5a,b* illustrates the relative frequencies of the equivalent diameters of all analyzed pores which are classified through the graphs drawn in *Figure 2.5c,d*. In this scenario, the as-built top and bottom samples (*Figure 2.5a*) approximatively show the same number of pores, 466 for the top and 357 for the bottom regions, characterized by the same equivalent diameters. In details, the top samples have 38 % and 39 % of pores with an equivalent diameter of 2.5 and 5 μm, respectively; the bottom samples

show 33 % and 37 %, respectively (*Figure 2.5a*). The frequencies decrease at 9 % and 12 % for the porosity having an equivalent diameter of 7.5 μm on top and bottom regions, respectively. The trend continues to decrease from the last-mentioned values down to zero for equivalent diameters of about 35 μm. Regarding the AlSi7Mg0.6 after the T6*, firstly, the total counted pores increase from the as built case, secondly, the maximum relative frequencies (44 % and 52 % for top and bottom samples, respectively) are concentrated on the equivalent diameter of 5 μm (*Figure 2.5b*) and not also distributed on lower values as in *Figure 2.5a*. The relative frequency trends strongly decrease to 7.5 μm (*Figure 2.5b*), and then decrease up to 0 % at around 40 μm. The relative density values of the top and bottom samples are 99.37 % and 98.92 %, respectively, i.e. (2.663 ± 0.005) g/cm^3 and (2.651 ± 0.005) g/cm^3 (see *Figure 2.4*). These lower density values of the bottom samples are dictated by the presence of a major quantity of larger pores than in the top samples (> 7.5 μm in *Figure 2.5a*, > 10 μm in *Figure 2.5b*).

Figures 2.5c,d correlate the maximum dimension of the analyzed pores, which is the greatest Feret diameter [144], and their roundness (R) that is defined as follows [219]:

$$R = \frac{4\pi A}{p^2} \tag{2.3}$$

where A and p are the area and perimeter of the object (pore in this context) analyzed through the image analysis. This object/pore tend to be a circle if $R \rightarrow 1$, while it becomes less round when $R \rightarrow 0$. At the same time, the orange and yellow areas group together the metallurgical (< 100 μm) and lack-of-fusion (> 100 μm) pores which are illustrated in the OM micrographs in *Figure 2.5c* and *Figure 2.5d*, respectively. From these premises, all analyzed pores in as-built samples (*Figure 2.5c*) can be considered as metallurgical pores and, therefore, formed by the gas dissolved within the molten pools.

After the T6* HT, the increase in pore quantity is also highlighted, as well as their tendency to hire a more circular shape (*Figure 2.5d*). In fact, the points distribution is shifted upwards. In addition, two LOF pores were found within the analyzed area. Considering their formation mechanisms, both of LOF pores are certainly generated during the L-PBF process. The SHT can only promote spheroidization phenomena [33,65].

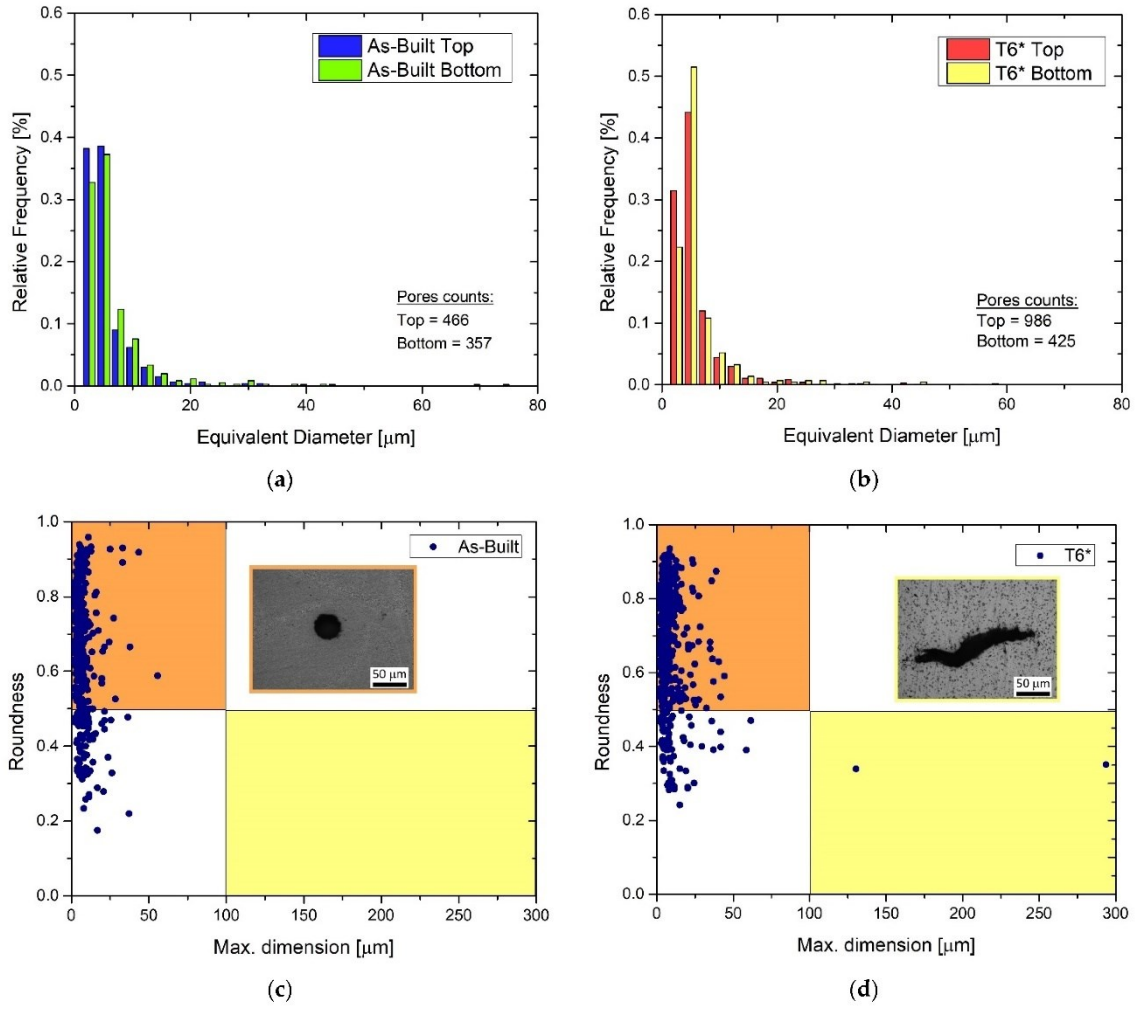


*Figure 2.5. (**a**,**b**) Statistical distribution of the equivalent diameter of the pores and (**c**,**d**) their roundness versus their maximum dimensions in: as-built (**a**,**c**) and heat-treated T6* samples (**b**,**d**).*

3.2.Microstructural Analysis

The OM micrographs shown in *Figure 2.6a* clearly show the typical "fish scale" structure which is formed by the cross-section of the laser scans. Due to the scanning strategy (*Figure 2.1*) used during the L-PBF, this fish-scale is longitudinally interrupted by a laser scan track (indicated in *Figure 2.6a* by yellow arrows). The same laser scan tracks are observable on the xy plane (*Figure 2.6b*), as well as the molten pool characterized by the typical ellipsoidal shape which is highlighted through the dotted ellipse. *Figures 2.6c,d* compare the microstructure of the AlSi7Mg0.6 and AlSi10Mg0.3 samples heat-treated at 175 °C × 8 h. No differences can be observed at the considered magnification. In addition, the SL (*Figure 2.6a*) and DL (*Figure 2.6c*) samples do not show any microstructural differences as widely discussed in [65] for the AlSi10Mg0.3 samples in as-built conditions. For this reason, only the SL samples will be considered in the

following parts related to the discussion of the heat-treated microstructures. At the same time, the same conclusions will be obviously drawn after the discussion of the HV values in as-built conditions.

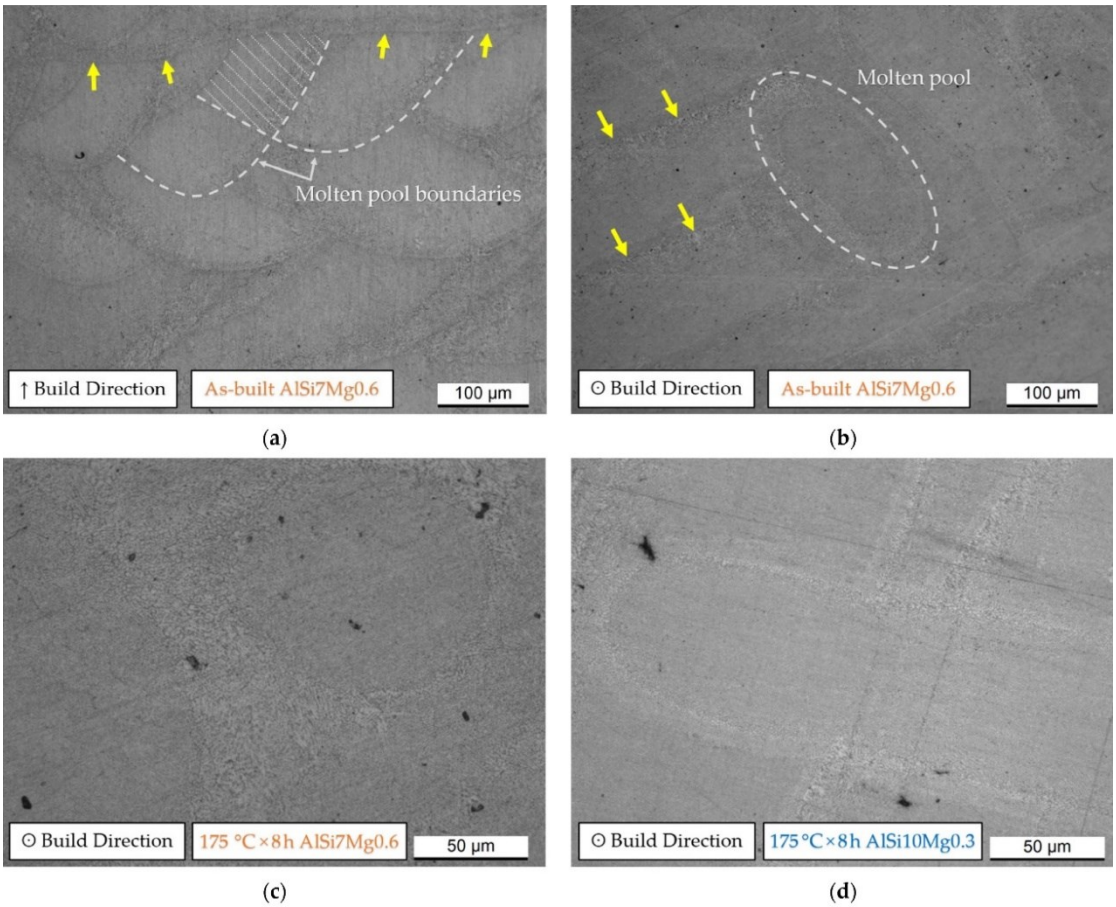


*Figure 2.6. OM micrographs showing the as-built AlSi7Mg0.6 microstructure on the xz (**a**) and xy (**b**) planes, namely on the planes parallel (↑ Build Direction) and perpendicular (⊙ Build Direction) to the build direction, respectively. (**c**,**d**) OM micrographs of the AlSi7Mg0.6 (**c**) and AlSi10Mg0.3 (**d**) after the direct aging at 175 °C × 8 h (⊙ Build Direction). The yellow arrows indicate the boundaries of the laser scan tracks.*

The microstructure obtained after the SHT (505 °C × 5 min) is clearly affected by coarsening of the Si-eutectic particles (*Figure 2.7a,b*) and it became more homogenized only after 505 °C × 4 h (*Figure 2.7c,d*). As a matter of fact, the molten pool boundaries exhibited by the AlSi10Mg0.3 heat-treated samples for 5 min (*Figure 2.7b*) disappear after 4 h (*Figure 2.7d*). In contrast, the solution heat-treated AlSi7Mg0.6 samples do not frequently exhibit structures related to the molten pool or laser scan tracks on the xy and/or xz planes already after 5 min. On the other hand, both aluminium alloys show clearly different precipitates which are indicated by orange arrows in *Figure 2.7c,d*. Surely, the further microstructural investigation will be performed in future works. At the same time, the precipitate having an elongated morphology can be associated with

the brittle iron intermetallics, while the more spherical precipitate present within the AlSi7Mg0.6 α-Al matrix can be classified as Fe-Si-Mg intermetallics (*Figure 2.6c*) [149,220,221].

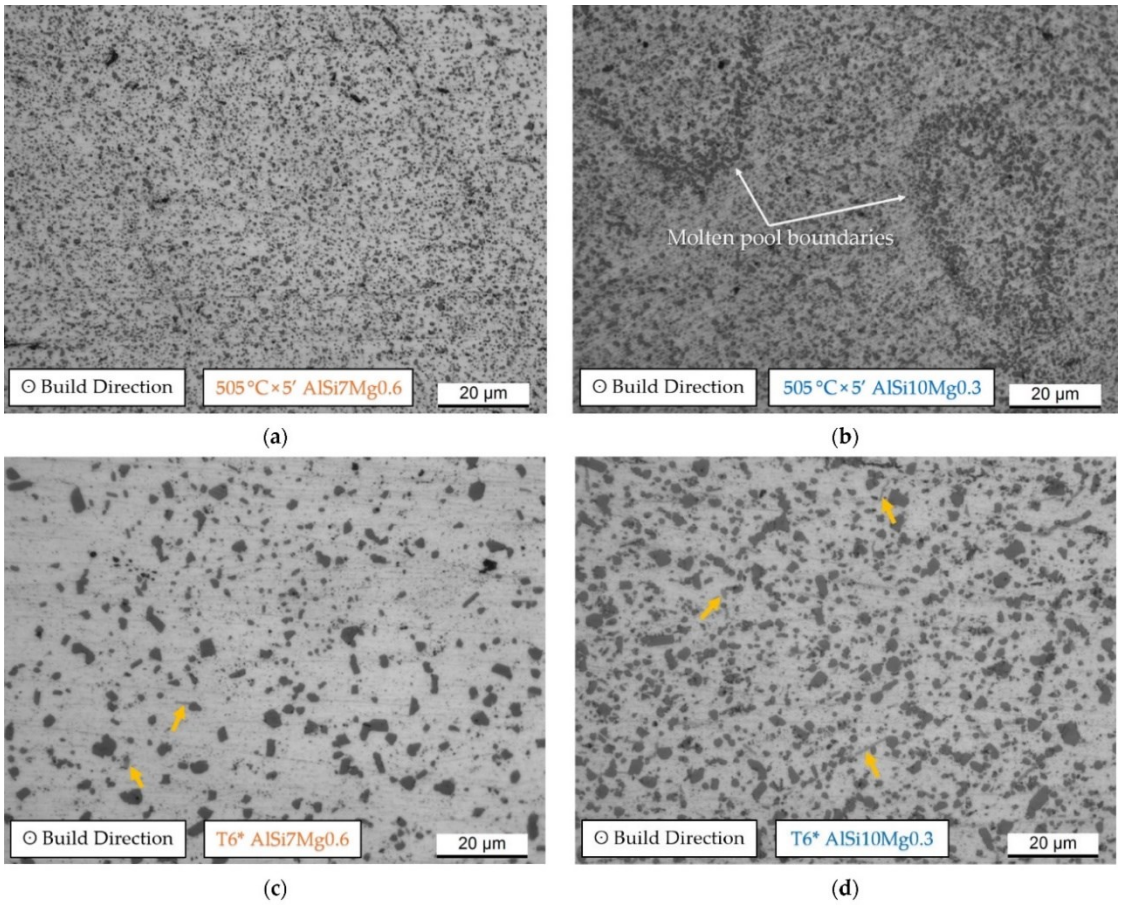


*Figure 2.7. OM micrographs of the AlSi7Mg0.6 (**a**,**c**) and AlSi10Mg0.3 (**b**,**d**) microstructure after both the SHT at 505 °C × 5 min (**a**,**b**) and T6* (**c**,**d**). Orange arrows indicate different precipitates.*

Si-eutectic particles were analyzed in both the AlSi7Mg0.6 (*Figures 2.8a,b*) and AlSi10Mg0.3 (*Figures 2.8c,d*) samples solution heat-treated at 505 °C × 1 h, × 2 h and × 4 h, respectively. The statistical analysis related to the AlSi7Mg0.6 (*Figure 2.8a*) shows a displacement of the equivalent diameters range from 0.2–3.4 μm (SHT 1h) to 0.2–5 μm and 5.4 μm for the SHT 2h and SHT 4h, respectively. At the same time, the Si particles per unit of area decreases from 0.076 to 0.043 (μm^{-2}) while the average equivalent diameter increases from 0.81 to 1.32 μm. Despite the difference in holding time of 2 h at 505 °C between the red (SHT 2h, *Figure 2.7b*) and yellow (SHT 4h, *Figure 2.8b*) trends remain almost comparable except for the SHT 4h samples which show higher frequencies of Si-eutectic particles having equivalent diameters between 4.2 and 5.4 μm. As a matter of fact, SHT 4h confers higher coarsening phenomena of Si-eutectic particles.

The same trends are described by the AlSi10Mg0.3 (*Figures 2.8c,d*) after the same HT conditions. In detail, the equivalent diameter range increases from 0.2–4 μm (SHT 1h) to 0.2–5 μm and 7.4 μm for SHT 2h and 4h, respectively. The Si particles per unit of area decrease simultaneously from 0.092 to 0.054 (μm^{-2}) while the average equivalent diameter increases from 0.82 to 1.23 μm. Comparing *Figure 2.8d* and *Figure 2.8b*, the AlSi10Mg0.3 samples heat-treated at 505 °C × 2 h and 4 h show the same trends illustrated by the AlSi7Mg0.6.

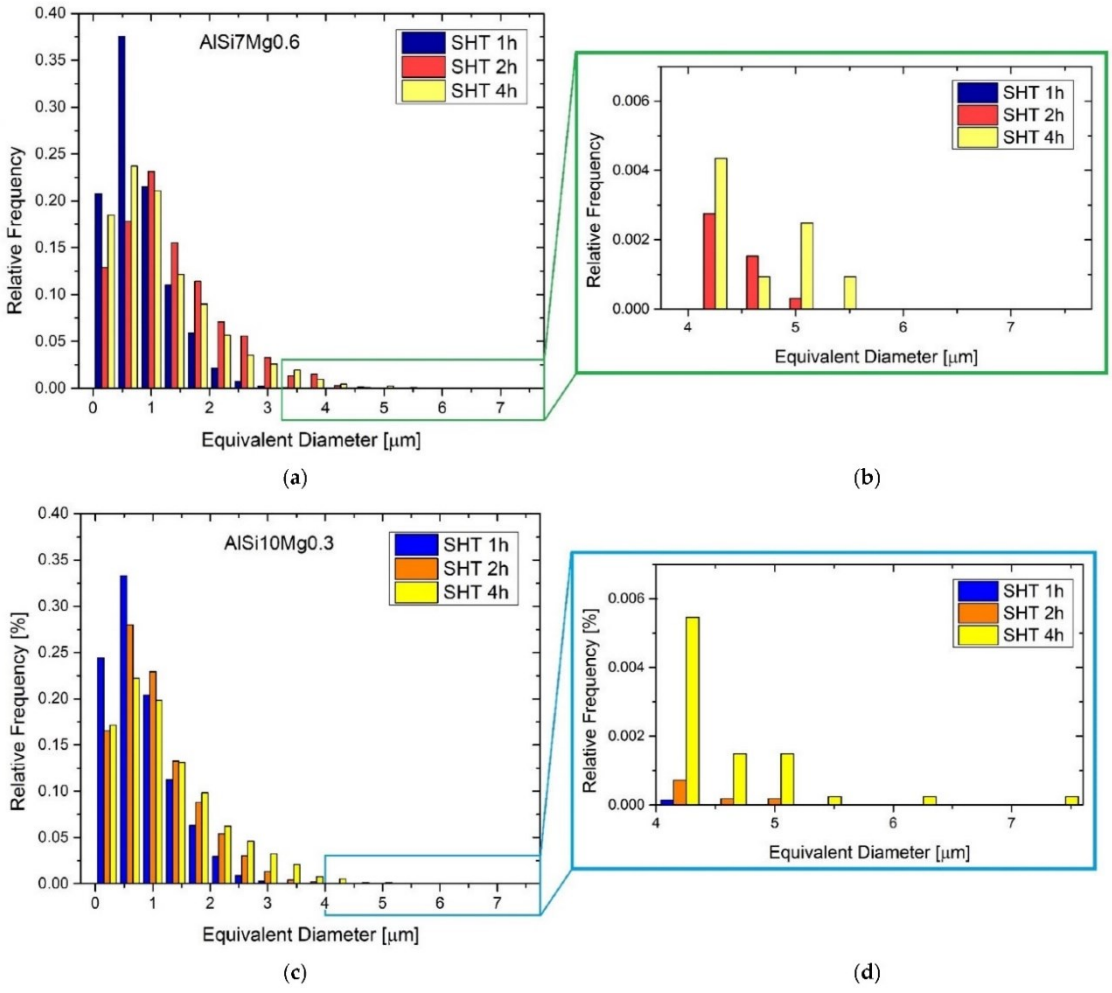


*Figure 2.8. Statistical analysis of the equivalent diameter of the Si-eutectic particles analyzed on: (**a**,**b**) AlSi7Mg0.6 and (**c**,**d**) AlSi10Mg0.3 samples solution heat treated at 505 °C × 1 h, 2 h and 4 h. The graphs in panels (**b**) and (**d**) are the magnifications of the same graphs in (**a**) and (**c**).*

3.3. Microhardness Profiles in As-Built and Direct Aged Conditions

Figure 2.9a illustrates the HV profiles of the SL and DL AlSi7Mg0.6 bars in as-built conditions. Both profiles were performed along the build direction (z-axis) and highlight the perfect overlap between the trends related to the SL and DL bars. As a

matter of fact, the bottom and middle regions are characterized by HV values remaining constant at around (120 ± 4) HV0.5 for both the SL and DL bars. Only considering the farthest region of the same bars from the build platform, namely the last 200–300 mm, the HV values decrease. AlSi10Mg0.3 SL and DL bars (*Figure 2.9b*) show the same decreasing trends, which are however extended from the bottom to the top regions. In this case, the HV measurements decrease from (133 ± 1) HV0.5 and (131 ± 2) HV0.5 to (108 ± 4) HV0.5 and (112 ± 3) HV0.5 for the SL and DL cases, respectively. Because both the SL and DL trends (*Figure 2.9*) perfectly overlap, only the SL samples will be considered in the following part related to the heat-treatments as also reported in Section 3.2. Finally, the top regions of the AlSi7Mg0.6 and AlSi10Mg0.3 HV profiles, respectively, can be perfectly overlapped. Considering the as-built top and bottom samples, the anisotropy in HV measurements between the xy (*Table 2.5*) and xz (*Figure 2.9a*) planes are not detectable.

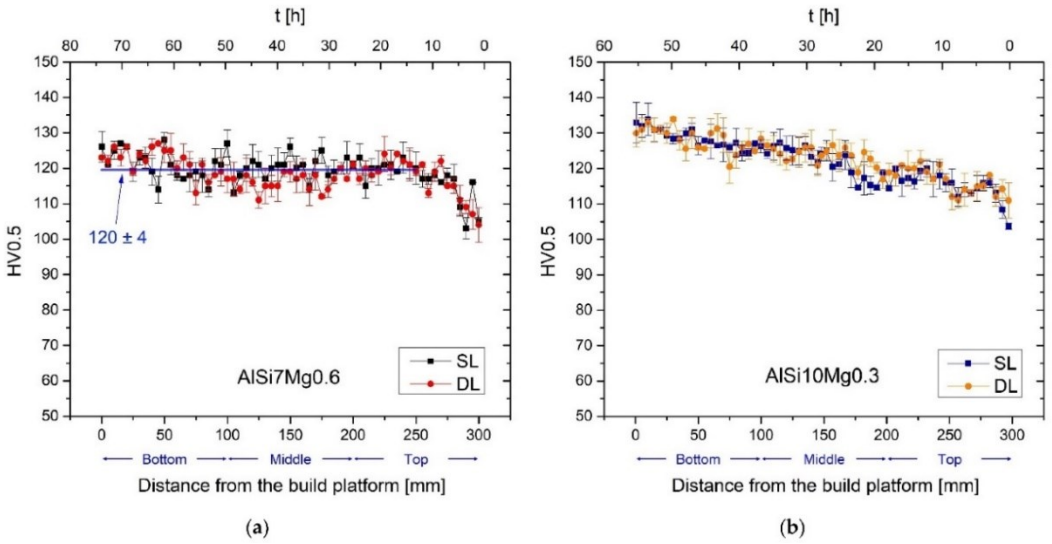


*Figure 2.9. HV profiles from bottom to top regions of the AlSi7Mg0.6 (**a**) and AlSi10Mg0.3 (**b**) SL and DL bars.*

Table 2.5. Vickers microhardness values, and their variation, measured on the as-built and direct aged AlSi7Mg0.6 and AlSi10Mg0.3 samples. For each DA at 175, 200 and 225 °C, the HV measured at the peak-aging and after 16 h of treatment were listed.

HT Conditions		AlSi7Mg0.6				AlSi10Mg0.3			
		Top		Bottom		Top		Bottom	
		HV0.5	Δ [%]	HV0.5	Δ [%]	HV0.5	Δ [%]	HV0.5	Δ [%]
175 °C	0 h	113 ± 2	-	127 ± 2	-	113 ± 2	-	133 ± 1	-
	Peak-Aging	128 ± 3	+ 13.4	-	-	132 ± 2	+ 16.8	-	-
	16 h	104 ± 4	– 18.8 [1]	97 ± 1	– 23.6	122 ± 4	– 7.58 [1]	121 ± 3	– 9.0
200 °C	0 h	106 ± 2		125 ± 3	-	114 ± 3	-	136 ± 1	-
	Peak-Aging	-	-	-	-	133 ± 2	+ 16.7	-	-
	16 h	101 ± 2	– 4.7	89 ± 3	– 32.0	118 ± 3	– 11.3 [1]	115 ± 3	– 15.4

Table 2.5. Cont.

HT Conditions		AlSi7Mg0.6				AlSi10Mg0.3			
		Top	**Bottom**	**Top**	**Bottom**				
		HV0.5	Δ [%]	HV0.5	Δ [%]	HV0.5	Δ [%]	HV0.5	Δ [%]
225 °C	0 h	124 ± 2	-	122 ± 2	-	113 ± 2	-	133 ± 1	-
	Peak-Aging	-	-	-	-	129 ± 5	+ 14.2	-	-
	16 h	84 ± 2	– 32.3	85 ± 2	– 30.3	105 ± 2	– 18.6 [1]	103 ± 4	– 22.6

[1] The HV variation (Δ[%]) is calculated between the Peak-Aging and the HV values after 16 h.

All aging curves related to both AlSi7Mg0.6 (*Figure 2.10a,b*) and AlSi10Mg0.3 (*Figures 2.10c,d*) are illustrated in *Figure 2.10*, where the filled and empty symbols are related to the top (*Figure 2.10a,c*) and bottom (*Figure 2.10b,d*) samples, respectively. Focusing on top AlSi7Mg0.6 samples, only those DA at 175 °C exhibits an increment in HV values up to the peak aging at a holding time of 2 h. After this, the HV measurements tend to decrease down to (104 ± 4) HV0.5, values less than (113 ± 2) HV0.5 of the as-built top sample. On the other side, the top sample DA at 225 °C immediately exhibits a fast decrease from (124 ± 2) HV0.5 to (84 ± 2) HV0.5 after 16 h because the considered top sample was far 240–260 mm from the hot build platform, unlike the top samples considered for the DA at 175 °C (260–280 mm) and 200 °C (280–300 mm). In the latter case, the DA does not induce any variation in terms of HV measurements except for a slight decrease in HV values from (106 ± 2) HV0.5 (as-built) to (101 ± 2) HV0.5 (200 °C × 16 h). Considering the aging profiles (*Figure 2.10b*) related to the bottom samples, no peak-aging can be observed. As a matter of fact, the as-built HV values decrease of about 24 %, 29 % and 30 % after the DA at 175 °C, 200 °C and 225 °C × 16 h, respectively.

Top AlSi10Mg0.3 samples (*Figure 2.10c*) DA at 175 °C, 200 °C and 225 °C × 0.5–16 h, respectively, exhibit different aging responses from the AlSi7Mg0.6 due to the different as-built HV values at the same distance from the hot build platform (*Figure 2.9*). The DA at 175 °C × 4 h confers a peak aging at (132 ± 2) HV0.5, where the DA at 200 and 225 °C induce the peak-aging conditions already after 0.5 h reaching (133 ± 2) HV0.5 and (129 ± 5) HV0.5, respectively. These results are consistent with [210,222]. Also in this case, the bottom AlSi10Mg0.3 samples show a decreasing trend for all DA temperatures considered. *Table 2.5* summarize the HV microhardness values, and their variations, in as-built, peak-aging conditions, and after 16 h of HT.

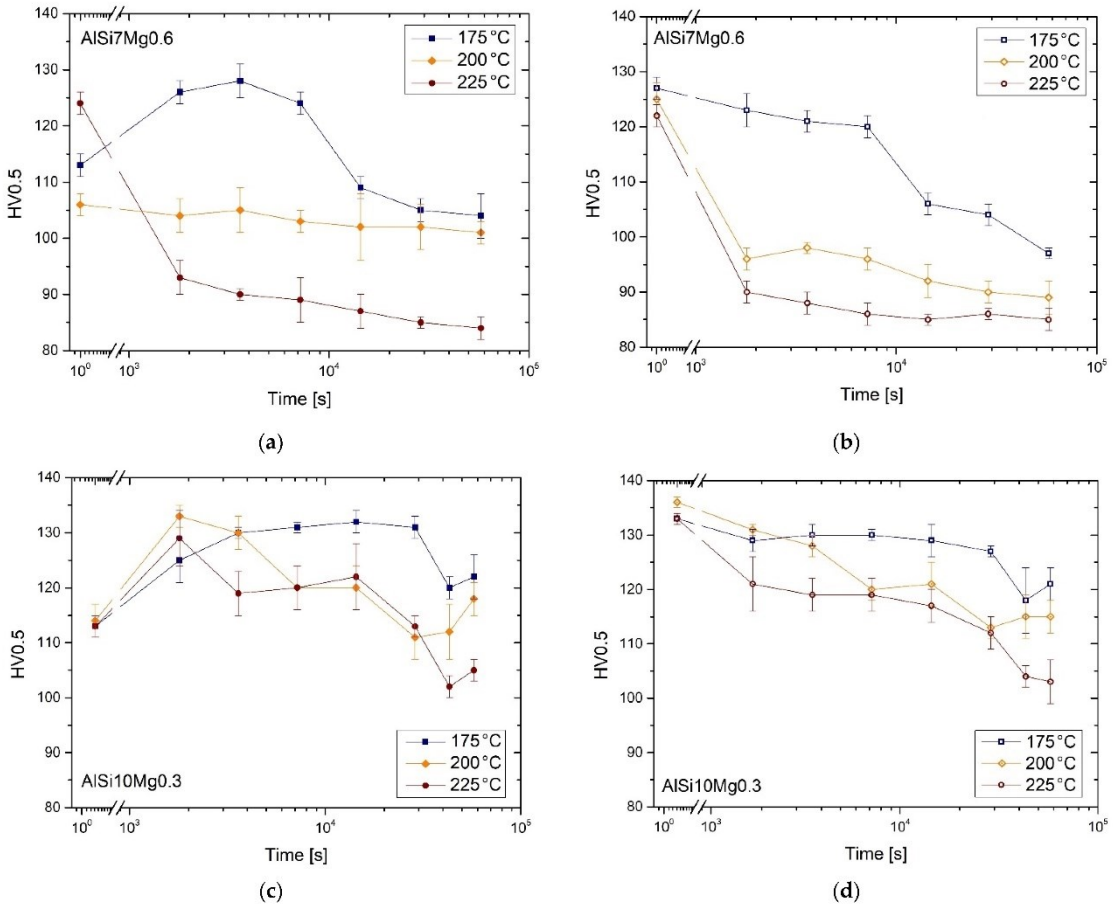


*Figure 2.10. Aging curves of the top (**a**,**c**) and bottom (**b**,**d**) samples of the AlSi7Mg0.6 (**a**,**b**) and AlSi10Mg0.3 (**c**,**d**) alloys direct aged at 175 °C, 200 °C and 225 °C. The as-built conditions are considered at time equal to 1, and not to 0, because the time-axes are in log scale.*

3.4. Microhardness Profiles After Solubilization and T6 Heat-Treatments

Figure 2.11a compares the HV profiles of the AlSi7Mg0.6 (black line-symbols) and AlSi10Mg0.3 (red line-symbols) alloys solution heat treated at 505 °C for 2.5 min–4 h. Already starting from 2.5 min of treatment-time, the HV values fall from (118 ± 6) HV0.5 and (122 ± 4) HV0.5 to (81 ± 1) HV0.5 and (76 ± 1) HV0.5 for AlSi7Mg0.6 and AlSi10Mg0.3, respectively. Increasing the SHT time up to 4 h, the continuous decreasing trends of the HV values reach (62 ± 2) HV0.5 and (59 ± 1) HV0.5 in the former and latter cases, respectively. In addition, both profiles remain basically parallel to each other at a distance of about (5.8 ± 2.6) HV0.5.

After the AA at 175 °C, the maximum reductions after the SHT 4h are partially recovered in 4 h and 8 h for AlSi10Mg0.3 and AlSi7Mg0.6 alloys as illustrated in *Figure 2.10b*. In the former case, the peak-aging reaches 97 ± 1 HV0.5 which is always below the as-built microhardness values reported in *Figure 2.9b*. In the latter one, the AA at 175 °C × 8 h confers a microhardness of about (111 ± 2) HV0.5 that is perfectly confrontable to

the top AlSi7Mg0.6 samples in as-built conditions (*Figure 2.9a*). Rao et al. [210] reported 64 HV and 58 HV after a SHT at 535 °C × 1 h and × 8 h, respectively. Both microhardness values are recovered after AA HTs at 165 °C × 6 h reaching the peak-aging at 120 HV, and at 180 °C × 2 h with 118 HV of peak-aging. After the same SHT at 535 °C × 1 h, Casati et al. [222] illustrated 78 HV increasing at 113 HV after an AA at 160 °C × 4 h. Higher HV values are discussed by Vanzetti et al. [216] who studied a SHT at 540 °C × 15 min (102 ± 5 HV) followed by an AA at 170 °C × 6 h (132 ± 3 HV).

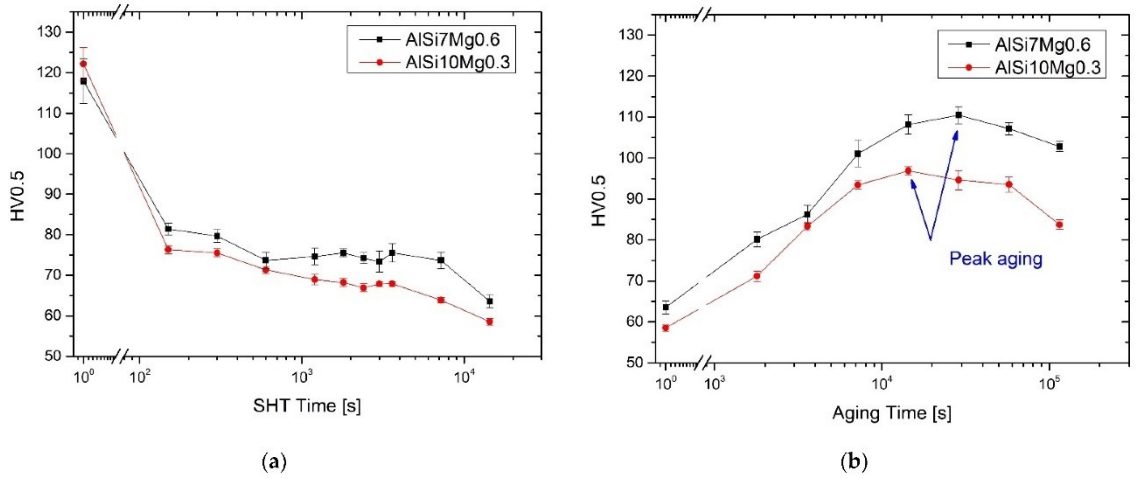


*Figure 2.11. HV measurements on AlSi7Mg0.6 and AlSi10Mg0.3 samples after the SHT at 505 °C × 2.5 min – 4 h (**a**) and after the artificial aging at 175 °C × 0–32 h (**b**). The as-built conditions are considered at time equal to 1, and not to 0, because the time-axes are in log scale.*

3.5. Mechanical Properties

To complete the mechanical characterization of the AlSi7Mg0.6 samples heat-treated at optimal conditions, *Figure 2.12* shows the obtained UTS, YS and elongation values from the tensile testing at room temperature.

Focusing on the as-built values, the HV variation between the bottom (full symbols) and top (empty symbols) samples is again confirmed by both the UTS and YS values. In fact, the bottom samples are characterized by a UTS of (431 ± 9) MPa and YS of (294 ± 8) MPa unlike the (409 ± 9) MPa and (258 ± 8) MPa shown by the top samples. As highlighted by the HV measurements performed on the DA samples, also the DA at 175 °C × 2 h, 200 °C × 1 h and 225 °C × 1 h homogenize the tensile strengths between the top and bottom samples. In addition, if the first and second HT conditions confer a maximum decrease of – 9.5 % and – 8.8 % of UTS and YS for the bottom samples, respectively; the third condition reduces them to about – 29.5 % and – 35.4 %. *Table 2.6* summarizes the other variations also in terms of elongations which follow the inverse trends of the UTS and YS.

Table 2.6. Variation of the mechanical properties between the as-built and heat-treated conditions for AlSi7Mg0.6 samples.

Samples	HTs	ΔUTS	ΔYS	HTs	ΔUTS	ΔYS
Top	175 °C	– 6.0%	+ 5.3%	SHT	– 38.7%	– 47.2%
Bottom		– 9.7%	– 8.8%		– 41.8%	– 53.1%
Top	200 °C	– 2.6%	+ 6.7%	T6*	– 33.5%	– 11.6%
Bottom		– 7.6%	– 6.1%		– 32.4%	– 19.1%
Top	225 °C	– 24.6%	– 23.0%	T6**	– 28.4%	– 4.9%
Bottom		– 29.4%	– 35.2%		– 31.2%	– 13.8%

The highest detrimental effects were conferred by the SHT (505 °C × 4 h) because the UTS and YS reach (251 ± 7) MPa and (138 ± 4) MPa, respectively. On the other hand, the elongation values exponentially increase up to 21.4 ± 0.6 % and 22.5 ± 0.6 % for the bottom (+ 77.7 %) and top (+ 81.6 %) samples, respectively. Focusing on the T6* (SHT + 175 °C × 4 h), the aging phenomena increase the UTS and YS at maximum values of (291 ± 10) MPa and (238 ± 7) MPa, respectively. The UTS reaches the YS of the as-built values, while the T6* YS shows an increment of + 100 MPa with respect to the SHT samples. On the other hand, the AlSi10Mg0.3 in the peak-aging conditions (T6*) (*Figure 2.11b*) shows the same UTS (288 ± 7 MPa) and YS (234 ± 7 MPa) values, as reported and discussed in [67]. As regards the AlSi7Mg0.6 samples in peak-aging conditions (T6**), the UTS and YS reach the maximum values of (297 ± 10) MPa and (253 ± 8) MPa, respectively. At the same time, in all considered cases, the AA confers detrimental effects on the elongations shown by the SHT samples. In fact, the ductility reaches the same as-built values.

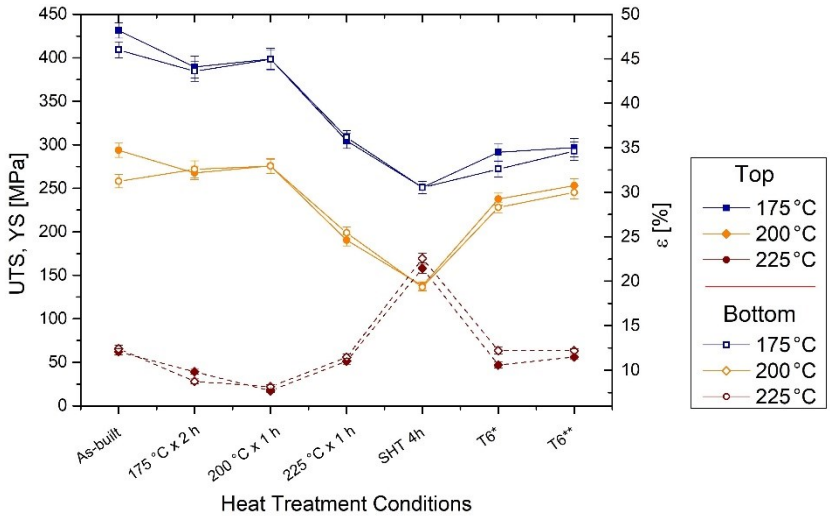


Figure 2.12. UTS, YS and elongation (ε) values of the AlSi7Mg0.6 samples in as-built conditions, and after the optimal conditions of the DA, solution, T6 (SHT + 175 °C × 4 h) and T6** (SHT + 175 °C × 8 h) heat treatments.*

4. Discussion

4.1. Density Analysis

Both AlSi7Mg0.6 and AlSi10Mg0.3 samples in as-built conditions are characterized by high values of density (> 2.676 g/cm^3), namely by a restrained vol.% of pores which correspond to a ρ_r higher than 99.83 %. For these reasons, the process parameters (*Table 2.2*) also used to manufacture the AlSi7Mg0.6 samples can be considered as optimized values to obtain high-quality samples. The results are consistent with those reported in [33] for the AlSi10Mg0.3 and in [99,201,223] for AlSi7Mg0.6. Increasing the HT temperatures, the density values tend to decrease due to the synergetic effects between the increase of the number of total pores (vol. %) (*Figure 2.5*) and the growth of the area of the pre-exiting pores formed during the L-PBF process. The analyzed pores in as-built AlSi7Mg0.6 bar are classifiable as metallurgical pores (equivalent diameter < 100 μm), namely as pores formed by the gas enclosed within the molten pool during the L-PBF process. Therefore, at high temperatures reached by an SHT, the material around a pore can be deformed due to the following synergetic effects: increase of the internal pressure and decrease of the yield strength of the material around the pore [144,158,224]. These effects are the same reported and discussed in [144] for the AlSi10Mg0.3 alloy. Therefore, the same research article can exactly explain the formation of pore during the AM process, and its variation during the HT in AlSi7Mg0.6 samples. In addition, already the build platform heated at 150 °C influences the dimensions of the pores as reported in (*Figure 2.5a*). The bottom region is characterized by a lower number of pores, characterized by higher dimensions, than the top regions, as also discussed in as-built AlSi10Mg0.3 bars in [144]. All of this, however, does not reflect a density variation between the bottom and top samples because the pores dimension compensates for their number, and vice versa.

Finally, all density values obtained for the AlSi7Mg0.6 do not influence the HV measurements thanks to the maximum $\Delta\rho_r$ = 0.05 g/cm^3. In fact, only a $\Delta\rho_r$ > 0.3 g/cm^3 can influence the indentations and the correlated HV values due to the high distribution of pores within the material, as carefully demonstrated in [144]. The presence of metallurgical and LOF pores generates worsening effects on the ductility values, as will be discussed in Section 4.3, and on the fatigue life [151,225]

4.2. Effects of Direct Aging Heat Treatments

The as-built AlSi7Mg0.6 and AlSi10Mg0.3 bars show comparable HV profiles that highlight the precipitation phenomenon induced by the build platform heated at 150 °C, as discussed in [65]. In fact, the AlSi10Mg0.3 exhibits a continuous decreasing

trend, where the HV values vary from (132 ± 4) HV0.5 to (110 ± 5) HV0.5, thanks to the precipitation phenomena related to both the β-Mg_2Si phase and nano Si-particles as also discussed in [65,144]. The same precipitation phenomena were shown in [33]. Di Egidio [215] and Yang et al. [158] showed the β-Mg_2Si phase and Si-particles already in AlSi7Mg0.6 samples direct aged at 160 °C × 4 h and 8 h, respectively.

Focusing on the as-built AlSi7Mg0.6 bars, the bottom region could be characterized by an over-aging phenomenon, unlike the top where the decreasing trend of the as-built HV values (*Figure 2.9a*) can confirm a lower precipitation phenomenon. This is also confirmed by the aging curves related to the bottom and top samples where the former shows a constantly decreasing trend (*Figures 2.10b,d*), while the latter shows peak-aging conditions (*Figures 2.10a,c*). The study on the effects induced by the hot build platform on the AlSi10Mg0.3 bar supports these considerations [65]. Finally, the increasing trend of the YS shown by the top AlSi7Mg0.6 (see *Figure 2.12* and *Table 2.5*) direct aged at 175 °C × 2 h (+ 5.3 %) and 200 °C × 1 h (+ 6.7 %) can confirm the precipitation effects. Considering the following sum [33]:

$$YS = \sigma_f + \sigma_{SS} + \sigma_{HP} + \sigma_{Or} + \sigma_\rho + \sigma_{Pre} \tag{2.4}$$

where the σ_f [MPa] is the friction stress of the lattice, σ_{SS} [MPa] is the SSS strengthening, σ_{HP} [MPa] is the strength obtained by the grains size (Hall-Patch equation), σ_{Or} [MPa] is the Orowan strengthening, σ_ρ is the dislocation hardening and σ_{Pre} is the contribution conferred by the precipitates and dislocations, the strengthening effects which contribute to YS improvement are attributable to the precipitation phenomenon. In relation to the first and second strengthening terms, DA cannot increase their contribution due to the reduction of the solid solution and the consequent decrease of the friction stress [226]. The reduction of Mg and Si chemical concentrations $\left(C^{Mg}_{\alpha-Al}; C^{Si}_{\alpha-Al}\right)$ in the α-Al matrix promotes the reduction of the σ_{SS} as described by the following equation:

$$\sigma_{SS} = k_{Mg}\left(C^{Mg}_{\alpha-Al}\right)^m + k_{Si}\left(C^{Si}_{\alpha-Al}\right)^m \tag{2.5}$$

where k and m are two constants related to Mg and Si alloying elements [33]. The decreasing in chemical concentration promotes a decrease in material strengthening [228]. In relation to the Hall-Petch equation, the low temperatures reach during the DA do not induce grain coarsening effects and, consequently, a strengthening variation [229]. The main causes of the YS improvement are related to the following sum:

$$\sigma_{Or} + \sigma_\rho + \sigma_{Pre} \tag{2.6}$$

where their enhancement is conferred by the increase of the precipitate volume fraction (σ_{Pre}) and their interactions with the dislocation movement (σ_{Or}) as widely described

in [33]. In relation to the σ_{Pre} contribution, its following mathematical model combines the volume fraction (f) of the precipitates and their dimensions (l_D, l_t), as follows:

$$\sigma_{Pre} = C\frac{Gb}{(l_D l_t)^{1/2}}\left[f^{1/2} + 0.70\left(\frac{l_D}{l_t}\right)^{1/2} + 0.12\left(\frac{l_D}{l_t}\right)f^{3/2}\right] \quad (2.7)$$

where C [-] is a material constant, G [GPa] is the shear modulus of Al ($G = 25.4\ GPa$, [229]), b is the Burger vector ($b = 0.286\ nm$, [33]), l_D and l_t are the diameter and thickness of the precipiates, respectively. Eq. (2.7) highlights an increase in material strengthening when the volume fraction (f) increases, as possible to detect in peak-aged samples [33,65,151,216,217]. The same results can be also obtained modifying the l_D and l_t values. Increasing consequently the number of obstacles, the dislocation-precipitate interactions rise during the plastic deformation. As a matter of fact, dislocations interact with the Si particles dispersed within the α-Al matrix (*Figure 2.13a*), and with the Si-eutectic network (*Figure 2.13b*), which can promote the emission of other dislocations (*Figure 2.13c*) [33]. Considering that the Si-eutectic network breaks in Al-Si-Mg samples DA at temperatures higher than 175 °C, the only increase in tensile strength and HV microhardness, with respect to the as-built conditions, can be conferred by the precipitation phenomena. In this scenario, the damaging effects of the Si-network previously discussed for the DA at 200 °C, and the precipitation phenomena, can confirm the constant trend of the Vickers measurements (*Figure 2.10a*). The extensive damaging effects of the Si-network and the coarsening phenomena conferred by the DA at 225 °C cannot promote an increase in Vickers microhardness and tensile strengths.

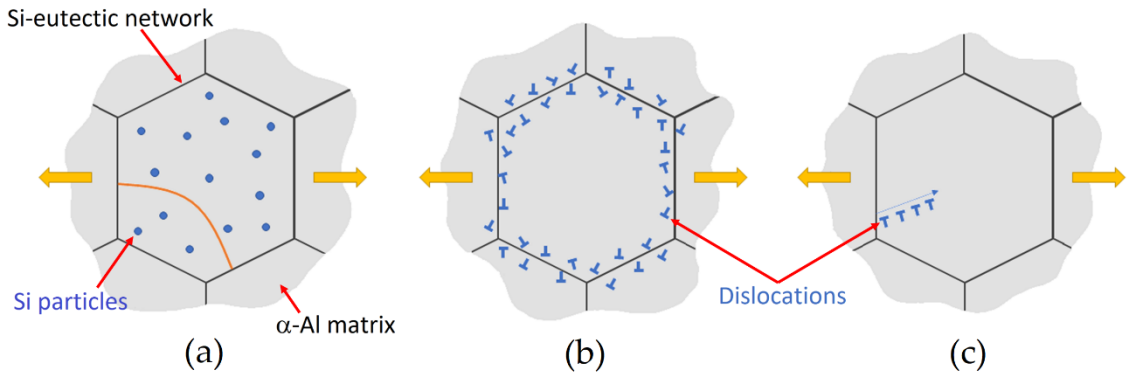


*Figure 2.13. Graphical representation of the interaction between the dislocations and: (**a**) the Si-particles within the α-Al matrix, and (**b**,**c**) the Si-eutectic network (Reprinted from Reference [33]).*

In this scenario, the Orowan mechanism explains the material strengthening where the interactions between a dislocation line and different impenetrable precipitates promote the formation of dislocation loops around the same particles, increasing

consequently the strengthening of material [33,230]. Considering the Si-precipitates, the Orowan contribution in Al-Si alloys can be estimated as proposed by [231], as follows:

$$\sigma_{Or}^{Si} = \frac{\varphi G b}{d_{Si}} \left(\frac{6 f_{Si}}{\pi}\right)^{\frac{1}{3}} \tag{2.8}$$

where φ [-] is a material constant, G [GPa] is a shear modulus, b is a Burger vector, d_{Si} is the diameter of Si-particle and f_{Si} is the volume fraction of the Si particles. Hadadzadeh et al. [187] affirmed that the β-Mg_2Si precipitates act a material strengthening similar to the Si precipitates that increases the results obtained through Eq. (2.4) of about ~ 13 MPa. Li et al. [232] obtained an increment of 27 ± 2 MPa. Because the β-Mg_2Si precipitates follow the Orowan looping, the obtained material strengthening contributions are given by:

$$\sigma_{Or}^{Mg_2Si} = M \frac{0.4 G b}{\sqrt{1-\vartheta}} \frac{ln\left(2\sqrt{\frac{2}{3}}R\right)}{\lambda} b \left(\frac{R}{b}\right)^{\left(\frac{3m}{2}-1\right)} \tag{2.9}$$

where M is the Taylor factor (M = 3.06, [33,232]), b is the Burger vector, G [GPa] is the shear modulus, ϑ is the lattice parameter mismatch at room temperature, λ is the distance between two adjacent particles, R is the average precipitate diameter and m is the Poisson's ratio of aluminium (m = 0.34–0.35, [232,233]). This confirms our hypothesis on the precipitation effects correlated to the variation of the YS in Eq. (2.4). Lastly, the terms (σ_ρ) related to the dislocation hardening (i.e., to the dislocation density [234]) is subjected to the following contrasting effects: the relieve of the internal residual stresses with the decrease in dislocation number, and its increase due to the dislocation motion and pile up around the precipitates [33,231,235–237].

A further microstructural investigation will be surely performed in future works to better characterize the microstructure before and after the HTs, and to detail their effects in relation to the discussion reported above.

Several DA HTs were performed to homogenize the differences between the bottom and top regions (*Figures 2.9*, *2.12*) while persevering the high mechanical performance conferred by the L-PBF process. Already after the DA at 175 °C × 2 h, the HV measurements for top and bottom AlSi7Mg0.6 samples are homogenized thanks to the intersection of both the over-aging conditions. In fact, if the bottom sample shows an over-aging phenomenon thanks to the absence of a peak-aging (*Figure 2.10b*), the top sample reaches it only after the peak-aging at 1 h. Focusing on the DA at 200 °C and 225 °C, 1 h of treatment can represent the optimal HT conditions for HV homogenization. Also the tensile test performed on this optimal HT conditions confirm the homogenization in terms of UTS, YS and elongation (*Figure 2.12*). At the same time, the

first and second DA do not confer detrimental effects on the as-built properties unlike the DA at 225 °C × 1 h where the coarsening phenomena of the Si-eutectic network occurs [65]. In a reduced way, the latter effect can be also characterized by the samples direct aged at 200 °C because the top samples do not show significant variations in terms of HV measurements. Therefore, the damaged Si-eutectic network can balance the hardening effects of the precipitation phenomena. Similar conditions were reported by the bottom and top AlSi10Mg0.3 samples which homogenized their HV values after 1 h of holding time at 175 °C, 200 °C and 225 °C.

4.3. Effects of Solubilization and T6 Heat Treatments

SHT deletes the fine as-built microstructure of both the L-PBFed AlSi7Mg0.6 and AlSi10Mg0.3 (*Figures 2.6, 2.7*) already after 2.5 min of treatment. Due to the high reached temperature (505 °C), initially, the Si-eutectic network begins to show different openings where the α-Al matrix interconnects two adjacent cells as shown in *Figure 2.14b*. Then, the Si particles grow on the remaining Si-eutectic network until the complete network destruction [33]. Increasing the SHT time, the growth of the globular Si-eutectic particles proceeds (*Figure 2.6*) and, consequently, the Si-particles per unit area decrease. As a matter of fact, the maximum equivalent diameters increase from 3 μm (SHT 1h) to 5.4 and 7.4 μm for the SHT 4h AlSi7Mg0.6 and AlSi10Mg0.3 alloys, respectively. Joining together this coarsening phenomenon to the recrystallization process of the nano-size grains of the as-built samples [228,236], the HV measurements are designed to decrease (*Figure 2.11a).* The same decreasing trend is exhibited by the tensile samples, where the UTS and YS decreased by – 48.8 % and – 53.1 %, respectively.

In addition to these detrimental effects, the SHT also promotes an increment of pore size and a formation of new pores as previously discussed and reported by [18,71]. In other words, it promotes a decrease in density from 2.675–2.677 g/cm^3, which defines the as-built samples as high-quality or fully-dense samples, to 2.663 g/cm^3 and 2.651 g/cm^3 for AlSi7Mg0.6 and AlSi10Mg0.3 samples, respectively. Despite these reached densities, the HV measurements were not influenced as discussed in Section 4.1. On the other hand, the presence of defects influences the ductility of both the as-built and heat-treated AlSi7Mg0.6 and AlSi10Mg0.3 samples [151,225,235]. Metallurgical and LOF pores were often revealed within both the fractured MP boundaries and laser scan segments of the as-built AlSi10Mg0.3 samples, as analyzed by [235], and they can be consequently considered as trigger points of the cracks. *Figure 2.14a* shows the same findings. After the crack initiation, it generally propagates and grew nearly the MP and/or laser scan tracks boundaries where the HAZ (Heat-Affected Zone) offers less resistant Si-eutectic network (*Figure 2.14b*). In this context, the occurrence of fracture in

the laser scan tracks was also observed in AlSi10Mg0.3 horizontal samples by [235]. Through SEM investigations, [235] also exhibited that the crack path extends along the α-Al cell boundaries where the Si-particles are easily connected. From a three-dimensional point of view, these crack paths lead to the layer-layer or intra-layer fracture [33] The analogous fracture mechanism described the direct aged AlSi7Mg0.6 and AlSi10Mg0.3 samples thanks to their microstructural morphology comparable with the as-built samples [67,215,217,238].

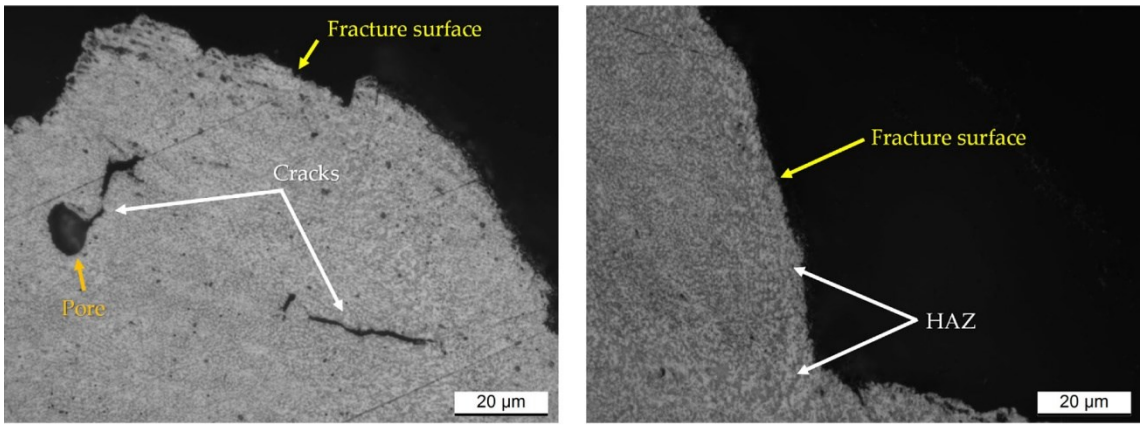


*Figure 2.14. Longitudinal sections of the as-built AlSi10Mg0.3 samples showing: (**a**) the crack initiation from a pore, (**b**) the crack propagation along the HAZ.*

Focusing on the T6 heat-treated samples, the cracks principally interconnect the coarse Si-particles due to their decohesion phenomena from the α-Al matrix. For these reasons, the Si-eutectic particles (indicated by white arrows in *Figure 2.15a*) remain often attached at fracture surface. At the same time, the ductile α-Al matrix seems to hinder the crack propagation. The same findings are shown by [215,235]. Also in T6 heat-treated Al-Si-Mg samples, the pores can promote the crack initiation as highlighted by [215], who exhibited the same fracture profile and structure shown in *Figure 2.15b*. In addition, the presence of MP and/or laser scan tracks boundaries (*Figure 2.7b*), remain even after the SHT, control the crack propagation as widely discussed in [67], where the T6** heat-treated AlSi10Mg0.3 samples were analyzed. In fact, the crack can easily interconnect the micro voids formed by the decohesion phenomena where the Si-eutectic particles are very close to each other. The MP or laser scan track boundaries satisfy this condition.

The AA at 175 °C recovers the HV measurements after the SHT 4h thanks to the precipitation phenomena correlated to the β-Mg_2Si. The T6** AlSi7Mg0.6 samples reach (111 ± 2) HV0.5, values that characterize the peak-aging (*Figure 2.10b*) and the top bar in as-built conditions (*Figure 2.9*). On the other hand, the peak-aging shown by the T6*

AlSi10Mg0.3 samples do not reach again the microhardness of the top as-built conditions (*Figure 2.9*). On the other hand, the peak-aging shown by the T6* AlSi10Mg0.3 samples do not reach again the microhardness of the top as-built samples with the (97 ± 1) HV0.5. Despite the differences in terms of the Si wt.%, the difference of about (14 ± 3) HV0.5 between both the peak-aging conditions is conferred by the different content of Mg which can promote several amounts of β-Mg_2Si phase during the AA. Always in relation to the Mg content, the SHT AlSi7Mg0.6 samples (*Figure 2.11*) show higher HV values than AlSi10Mg0.3 alloy in the same conditions due to the higher Mg percentage in solid solution, as confirmed by [239] and through the Eq. (2.4).

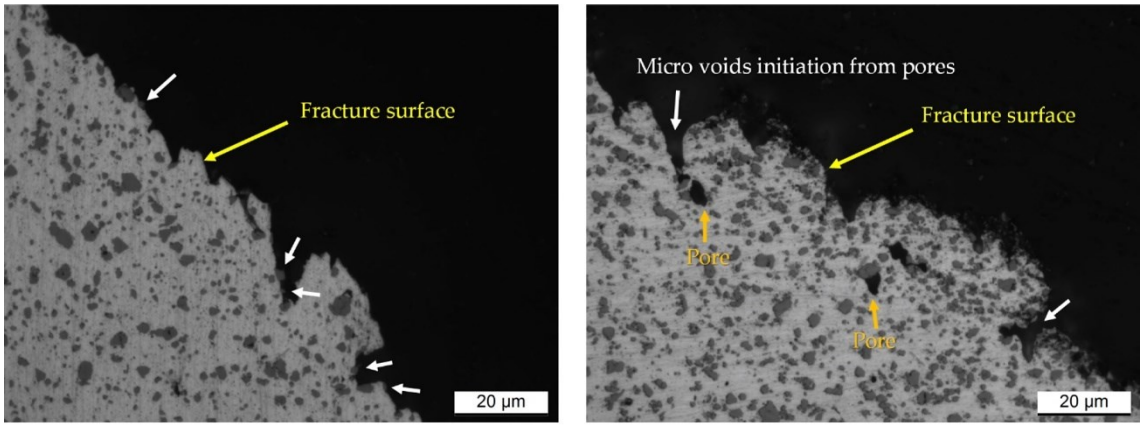


*Figure 2.15. Longitudinal sections of the T6** AlSi10Mg0.3 samples showing: (**a**) the Si-particles attached (white arrows) at the fracture surface, (**b**) the pores and the micro-voids initiation from pores.*

The AA at 175 °C recovers the HV measurements after the SHT 4h thanks to the precipitation phenomena correlated to the β-Mg_2Si. The T6** AlSi7Mg0.6 samples reach 111 ± 2HV0.5, values that characterize the peak-aging (*Figure 2.10b*) and the top bar in

In conclusion, although the improvement of HV values of the AlSi7Mg0.6 alloy in peak-aging conditions, the UTS (~ 280 ± 5 MPa) and the YS (~ 230 ± 5 MPa) remain lower than the UTS and YS values of the as-built, DA at 175 °C × 2 h and DA at 200 °C × 1 h top and bottom samples. In addition, the T6* heat-treated samples do not show any enhancement in terms of ductility, contrary to the expectations highlighted in the Introduction. As a matter of fact, the elongation values are fully comparable to those obtained for the as-built and DA samples (*Figure 2.12*).

To obtain an effective evaluation of the optimal HT conditions, the *UTS* and elongation (ε) values can be combined defining the *QI* (Quality Index), as follows:

$$QI = UTS + d\,log(\varepsilon) \tag{2.10}$$

where *d* (equal to 150) is an empirical parameter that makes the *QI* independent of the YS. The results obtained were plotted in the same QI-graph reported in [67] for the AlSi10Mg0.3 alloy (*Figure 2.16*). Also in this case, the as-built AlSi7Mg0.6 samples are characterized by higher QI values (570–595 MPa) than the DA samples at 175 °C × 2 h (526–538 MPa) and at 200 °C × 1 h (531–535 MPa). At the same time, these values are also higher than those discussed in [67] for AlSi10Mg0.3 samples and reported by Paul et al. [160]. On the other hand, the detrimental effects of the DA at 225 °C are highlighted by QI values (461–467 MPa) which are comparable with those referred to as the T6* and T6** HTs (435–456 MPa). These last values can be matched with the QI values of the T6 AlSi10Mg0.3 samples produced by casting [71,160,161] and L-PBF [67] techniques, respectively.

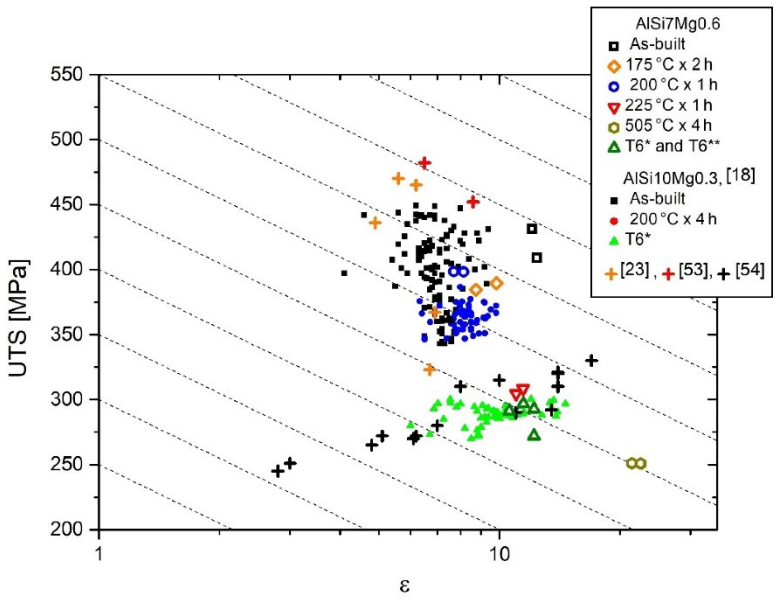


Figure 2.16. QI-graph where the elongation and the ultimate tensile strengths of as-built and heat-treated AlSi7Mg0.6 samples are compared to the results reported in [67]. The References [18,23,53,54] are replaced by [67,71,159,160] (Adapted from Reference [67]).

5. Conclusions

The present research article aims to evaluate the effects induced by different DA and T6 heat treatments on AlSi7Mg0.6 and AlSi10Mg0.3 alloys manufactured via Laser-Powder Bed Fusion process. In this scenario, the following conclusions can be drawn:

1. The as-built HV values of AlSi7Mg0.6 do not greatly differ from those shown by AlSi10Mg0.3. Both couples of profiles perfectly overlap from a 200 mm bar height despite the differences in Si and Mg content.

2. There are no substantial differences between the SL and DL AlSi7Mg0.6 samples both in terms of as-built microstructure and mechanical properties. The proximity to the hot build platform induces an increment of HV values in the bottom rather than in the top regions thanks to the precipitation phenomena of Si particles and β-Mg_2Si phase in AlSi10Mg0.3 bars. The same HV profile was, however, obtained for AlSi7Mg0.6 bars. In addition, the bottom regions are characterized by a lower number of pores, but having larger dimensions, than the top regions.
3. The differences in the mechanical performance between the bottom and top AlSi7Mg0.6 samples are levelled out by the DA at 175 °C × 2 h, which does not in-fluence the ultimate tensile and yield strengths such as the DA at 200 °C × 1 h. The same results are obtained for AlSi10Mg0.3 samples after 1 h of the same direct aging heat treatments.
4. The SHT certainly confers high elongation values to AlSi7Mg0.6 samples, thus satisfying the current standard specifications ($\varepsilon \gg 10$ %). The worsening effects on UTS and YS are recovered through the subsequent artificial aging, but the elongations return again at the direct aged values. For these reasons, and considering the QI values, the direct aging heat treatments at the peak aging conditions confer better mechanical performance.

[*This page intentionally left blank*]

ARTICLE 3

Aging Response in Selective Laser Melted AlSi10Mg Alloy as Function of Distance from the Substrate Plate

---

Emanuele Ghio & Emanuela Cerri

Materials Science Forum, *1016* (**2021**) 476–480

https://doi.org/10.4028/www.scientific.net/MSF.1016.476

“Due to copyright license, full article can be found at the following DOI link:
https://doi.org/10.4028/www.scientific.net/MSF.1016.476”

Aging Response in Selective Laser Melted AlSi10Mg Alloy as Function of Distance from the Substrate Plate

Emanuele Ghio [1], Emanuela Cerri [1]

[1] Department of Engineering and Architecture, University of Parma, Via G. Usberti 181/A, 43124, Parma, Italy.

Abstract

Selective Laser Melting (SLM) builds a metallic part in a layer-by-layer mode with growth occurring along the vertical axis. Metallic powder layers are melted by a laser beam by programmed scan sequences inducing specific mechanical properties in the as-built samples according to process parameters. Post heat treatments are usually performed to optimise the mechanical behaviour. In this work, the effects induced by heat treatments at 175°, 200° and 225°C on SLMed bars of Al10SiMg were investigated as function of distance from the substrate plate. The bars were 300 mm height and in the as-built condition, Vickers microhardness and tensile strength decreased along the built direction, while the elongation increased from the bottom to the top of the billet. After heat treatments, Vickers microhardness resulted lower of 10HV at the top of the bar compared to its bottom in contact with the hot substrate; microhardness decreased with time at constant temperature compared to the as-built. Tensile properties showed variations of 50 MPa and 1% elongation between the top and the bottom of the billet when aging was performed at 175°C for 4h; the strength and ductility gradients were reduced to 20 MPa and 0,5% respectively by increasing the aging time to 6h. Microstructure investigations performed by scanning electron microscopy confirmed the different evolution of Silicon particles and precipitated particles at different height of the bars.

Keywords: AlSi10Mg, Heat Treatment, Selective Laser Melting

[*This page intentionally left blank*]

ARTICLE 4

Work Hardening of Heat-Treated AlSi10Mg alloy Manufactured by Single and Double Laser Selective Laser Melting: Effects of Layer Thickness and Hatch Spacing

---

Emanuele Ghio & Emanuela Cerri

Materials, 14(17) (**2021**) 4901

https://doi.org/10.3390/ma14174901

“The following version of the manuscript is made available under the CC-BY-NC-ND 4.0 license”

https://creativecommons.org/licenses/by-nc-nd/4.0/

Work Hardening of Heat-Treated AlSi10Mg alloy Manufactured by Single and Double Laser Selective Laser Melting: Effects of Layer Thickness and Hatch Spacing

Emanuele Ghio [1], Emanuela Cerri [1]

[1] Department of Engineering and Architecture, University of Parma, Via G. Usberti 181/A, 43124, Parma, Italy.

Abstract

The present study analyzed the microstructure and the mechanical properties of AlSi10Mg SLMed bars (10 × 10 × 300 mm) and billets (10 × 100 × 300 mm) before and after the direct aging at 200 °C for 4 h and the T6 heat treatment. The discussed results are compared to those obtained by the AlSi10Mg samples manufactured with the same geometry but using different process parameters (layer thickness higher than 40 μm and a hatch spacing lower than 100 μm) and also through the Quality Index (QI). These work conditions allow the obtaining of a microstructural variation and different tensile properties in as-built top samples. In both batches, the cycle time was 45 h and together with the preheated build platform at 150 °C, induced an increase of UTS (Ultimate Tensile Strength) and yield strength on the bottom rather than the top samples due to the aging phenomena. Upon completion of the direct aging heat treatment, the effects induced by the platform were cancelled, keeping a full cellular microstructure that characterized the as-built SLMed (Selective Laser Melted) samples. Moreover, the Considère criterion and the work hardening analysis showed that the failure occurs after the necking formation in some of the T6 heat-treated samples. In this last case, the Si eutectic network globularized into Si particles, causing a decrease of UTS (from around 400 MPa to 290 MPa) in favor of an increase of ductility up to 15 % and reaching a QI in the range 400–450 MPa. These values place these samples between the high-quality aluminium cast alloy and T6 heat-treated ones.

Keywords: work hardening, layer thickness, AlSi10Mg, Selective Laser Melting, mechanical properties.

1. Introduction

The Selective Laser Melting (SLM) process allows for the obtaining of a 3D physical object, with complex geometry, built by a layer-by-layer method. Due to this machine set-up, the process takes place in the powder bed fusion category within the additive manufacturing field. During the print process, a laser beam scans a single layer (thickness in the range between 20 and 100 μm) according to the CAD (computer-aided

design) project [240]. In this context, the great customization capabilities that characterize this process, and the good performance obtained by fabricated parts compared to the conventional manufacturing process, are controlled by the optimization of different process parameters [69,241,242]. In other words, through the perfect combination between the scan strategy and the energy density (φ, [J/(mm^3)]), which can be defined as follows:

$$\varphi = \frac{P}{vht} \tag{4.1}$$

where P is the laser power [W], v is the scan speed [mm/s], h is the hatch distance [mm] and the t is the layer thickness [mm]; moreover, the denominator of the fraction is defined as build rate ($BR = vht$, [(mm^3)/s]) [128,134,243]. On the other hand, using a higher hatch distance or a combination of low laser power with high scan speed, or powder containing gas, the density and the consequent mechanical properties of the manufactured part are compromised [69,89,242,244].

Considering instead the layer thickness (t) and focusing on the influence on mechanical properties induced by its variation, many studies of this nature cannot be found in the literature. The research of Yastroitsev et al. [245] places the layer thickness as the second parameter in terms of importance after laser power. In fact, the process parameters of the SLM process should be recalibrated after the layer thickness variation. First, the deposition process, the packing density and the homogeneity of a bed powder layer can be compromised [246]. Second, with an increase of t the increase in depth of penetration is necessary to ensure the adhesion between the new scanned layer and the previously solidified layer. Sufiiarov et al. [247] and Nguyen et al. [248] studied the Inconel 718 alloy and a decrease in tensile strength combined with in-creasing layer thickness from 20 to 50 μm resulted. The other outcome was the variation in terms of *BR* (Build Rate); in fact, the volume of powder bed scanned increases with an increase of *t* decreasing the process time.

In this context, a reduction in the processing time can also be obtained by a multi-laser machine setup, and in this scenario a few types of research can be found in the literature [192]. As a matter of fact, Liu et al. [249] showed that the mechanical properties of Ti6Al4V alloy are uniform between the samples produced by a single and a multi-laser. Moreover, the use of a multi-laser influences the molten pool, the HAZ (heat-affected zone) and the thermal gradient, as reported by Masoomi et al. [250] and Liu et al. [251] for the Ti6Al4V and AlSi10Mg alloys, respectively. As concerns the aluminium alloy, Zhang et al. [192] demonstrated slight microstructure differences and the consequent slight decrease of UTS between 481 ± 2 MPa for single laser samples and 471 ± 7 MPa for multi-laser samples. Finally, focusing on the AlSi10Mg, the alloy selected in

the present paper, there are many studies concerning only the influence on the mechanical properties and the density caused by the variation of scan speed, hatch distance, laser power and scan strategy [69,89,214,242,252].

The AlSi10Mg alloy is widely used in the SLM process and its near-eutectic composition of Al and Si make the process possible by laser beam [214]. Considering the optimization of previous process parameters and the high cooling rate (10^6–10^7 K/s) that characterizes the SLM process, both a very fine microstructure and a fully dense part can be obtained. Moreover, the full-cellular structure of the Si eutectic network in the α-Al matrix that is formed, in addition to the Orowan looping behaviour, make the mechanical properties of the AlSi10Mg SLMed higher than the same casting alloy. As a matter of fact, the SLMed samples show YS between 250 and 300 MPa, UTS ≤ 400 MPa and strain at failure ≤ 7 % rather than YS between 90 and 110 MPa and UTS between 190 and 210 MPa of casting alloy [65,69,71,190,214,224,244,253]. Additionally, the use of a preheated build platform usually in the range between 150 and 200 °C can increase the mechanical properties of as-built samples due to the aging phenomena [184]. This range of temperature causes the precipitation of Mg_2Si along the boundary of α-Al due to SSS (super-saturated solid solution) that is generated during the solidification of the molten pool [65,184,172,255]. Casati et al. [184] analyzed the effects induced by the preheated build plat-form on AlSi10Mg samples SLMed. The authors show that the DSC scan profiles highlighting that the precipitation phenomena occurred during the "hot-stage" manufacturing process.

Therefore, starting from an excellent manufactured part, it is possible to perform different post-processing heat treatments for an improvement of compromise between tensile strength and elongation at break. This Al-Si-Mg alloy is mostly used in automotive and aerospace industries, and the optimization of post-process heat treatments can implement the areas of use. For example, the SLM process induces high residual stress due to the thermal effects in as-built samples. Therefore, stress relief or new heat treatment are needed to reduce this possible cause of failure during use. In this context, it is possible to emphasize that the improvement of ductility is the main aim in the AM field. Substantially, the scope is an increase of the elongation at break without decreasing the ultimate tensile strength (UTS) and yield strength (YS). In this context, the T6 heat treatment (solution heat treatment "SHT" + water quenching "WQ" + artificial aging "AG") causes a good improvement in ductility (≈ 20 %) and a drastic decrease of the UTS [173,185]. The SHT allows obtaining a dissolution of soluble phases or traces of other elements, but the high temperature induces a globularization of Si particles, which is the main cause of loss in terms of UTS and YS, as previously reported [185]. Subsequently, only after the water quenching the microstructure is stabilized at

room temperature. In fact, considering the AlSi10Mg phase diagram, the solubilization of the element within the α-Al matrix would decrease with a slow decrease in temperature. Finally, a recovery in terms of mechanical properties is caused by the precipitation (GP zones → β'' → β' → β) of the β-Mg_2Si phases during artificial aging [13,256]. At the same time, the good compromise between the tensile strengths and the strain at break can be obtained by direct aging (DA), i.e., by heat treatment performed directly in as-built samples without the SHT. The DA is normally carried out at a temperature lower than 200 °C and can maintain the full-cellular structure that characterized the as-built samples SLMed [65,184,228,257]. Cerri et al. [65], analyzing the AlSi10Mg samples, showed a gradual destruction of the Si eutectic network after the DA was at 225 °C for 6 h. Nevertheless, the obtained mechanical properties were satisfactory (UTS of 350 ± 10 MPa, YS of 200 ± 8 MPa and ε of 14 ± 1 %).

This paper aims to highlight the effects induced by the variation of the layer thickness (t) and of the hatch spacing (h) in the AlSi10Mg alloy manufactured by single and multi-laser selective laser melting. The work was conducted through optical microscopy analysis. Vickers microhardness and tensile tests following the Considère's criterion on samples before and after the DA (200 °C/4 h) and the T6 HT were undertaken. Finally, the quality indexes have been used to evaluate the best compromise between the UTS and the elongation at break values.

2. Materials and Methods

AlSi10Mg gas-atomized powder with normal distribution between 20 μm and 60 μm was used and its chemical composition is shown in *Table 4.1*.

Table 4.1. Chemical composition of AlSi10Mg samples (wt.%).

Elements	Al	Si	Fe	Mg	Cu	Mn	Zn	Ti	Pb	Sn
wt.%	Bal.	10.0	0.12	0.31	0.001	0.005	0.002	0.042	0.001	<0.01

Figure 4.1 shows the bars (300 × 10 × 10 mm) and the billets (300 × 100 × 10 mm) manufactured by SLM280 equipped with 400W IPG fibre laser. The yellow and red parts of the preheated build platform at 150 °C are the single laser (SL) and double laser (DL) zones. For clarity, all samples and bars were be divided into "bottom" (height < 150 mm) and "top" (height > 150 mm) regions. Moreover, both the tensile samples and the bars were designated with "SL-90 and DL-90" rather than "SL-50 and DL-50" of those analyzed [65] and considered in the present study. In this context, 90 and 50 referred to the different layer thicknesses adopted during the SLM process, while the other process parameters are shown in *Table 4.2*.

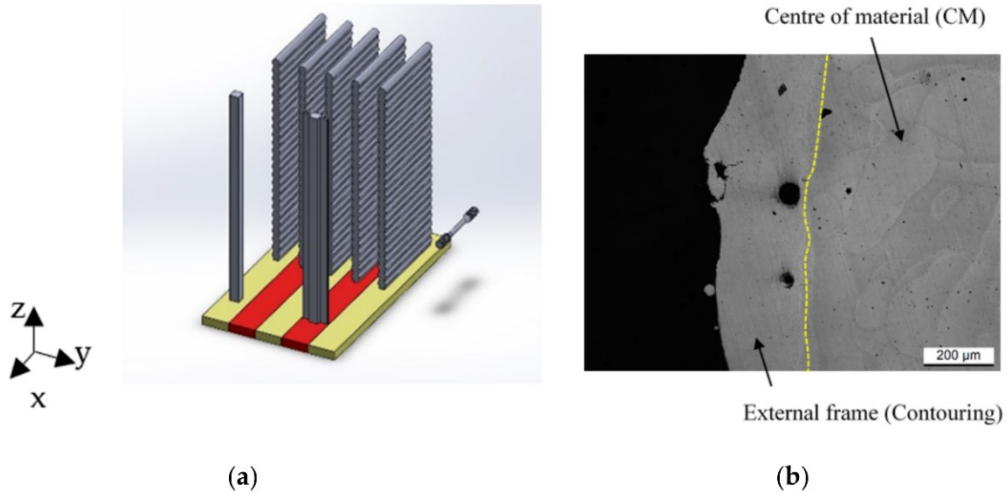


*Figure 4.1. (**a**) Job of SL (yellow region) and DL (red region) AlSi10Mg 90-samples; (**b**) Optical microscope micrograph which shows the bar cross-section (⊙ Build direction).*

According to the ASTM E804 standard, 26 tensile samples (from 1 at the bottom to 26 at the top region) have been machined into machine tools for each billet. Their symmetry axis was either perpendicular to the build direction (Z-axis) or parallel to the build platform, as shown in *Figure 4.1a*.

The AlSi10Mg samples were analyzed in as-built condition and after two different heat treatments. The first was the direct aging at 200 °C/4 h; the second was the T6 heat treatment (HT) (505 °C/4 h + 175 °C/4 h) as shown in *Table 4.2*.

Table 4.2. Process parameters used for 50 and 90 AlSi10Mg samples.

Process Parameters	90-Samples	50-Samples
Layer thickness [µm]	90	50
Scan speed [mm/s]	1400	1150
Hatch spacing [µm]	70	170
Laser power [W]	370	350
Energy density [J/mm^3]	42	36
Temperature of build platform [°C]	150	
Heat treatments	DA: 200 °C/4 h	
	T6: 505 °C/4 h + 175 °C/4 h	

The tensile tests were performed at room temperature using a Z100 Zwick/Roell servo-hydraulic device and at a strain rate of 0.008 s^{-1} in accordance with ASTM E804.

The Vickers microhardness was measured along both the XZ plane and the XY plane in all heat treatment conditions using a 500 gf load and a dwell time of 15 s. The profiles along the XZ plane were performed both on the external frame and the centre of

the material. In both cases, they were developed along different lines parallel to the edges of the bars, and each of these was formed by 60 indentations spaced 5 mm apart. The Leica VMHT microhardness tester (Leica, Wetzlar, Germany), which is equipped with a standard pyramidal indenter, was used for all measurements discussed in the present study.

The microstructure was analyzed by the DMi8 optical microscope (OM) (Leica, Wetzlar, Germany), and by different Vickers microhardness profiles with 15 gf of load in as-built condition.

The density of all samples was obtained through the 2D analysis of pores performed on the samples' surface, which was mechanically ground by SiC paper and then polished with colloidal suspension. The analysis was carried out with the Leica OM equipped with LAS-X 2D software (LAS AF V4.0, Leica Microsystems, Mannheim, Germany). According to ISO 13322-1:2014, six micrographs (at a magnification of 100×) were acquired and, subsequently, analyzed to determine the total pores area. Therefore, using the image analysis method, the density (ϱ) was calculated as follows:

$$\rho = 1 - \frac{\sum_i (A_p)_i}{\sum_{j=1}^{6} (\tilde{A})_j} = 1 - \frac{\sum_i (A_p)_i}{24936.41\ \mu m^2} \quad (4.2)$$

where $\sum_i (A_p)_i / \sum_{j=1}^{6} (\tilde{A})_j$ is the ratio between the total area of pores and the total area analyzed was 24,936.41 μm².

3. Results and Discussion

3.1. Microstructure

Figure 4.2 shows the characteristic microstructure of SL-90 and SL-50 AlSi10Mg SLMed samples considering the XZ (first row *Figure 4.2a,c,e*) and the XY (second row *Figure 4.2b,d,f*) planes, respectively. Considering *Figure 4.2a*, the typical fish-scale structure formed by the molten pools' cross-sections can be seen. This particular structure is located in the build direction due to the laser handling during the layer (n) scanning, which also remelts a part of the previously solidified layer (n − 1). On the other hand, the depth of the cross-section and the overlap area are controlled by density energy (φ) and by hatch spacing, respectively [92]. Only after the analysis of the XY plane can the characteristic ellipsoidal shape of the molten pool be observed (*Figure 4.2b*).

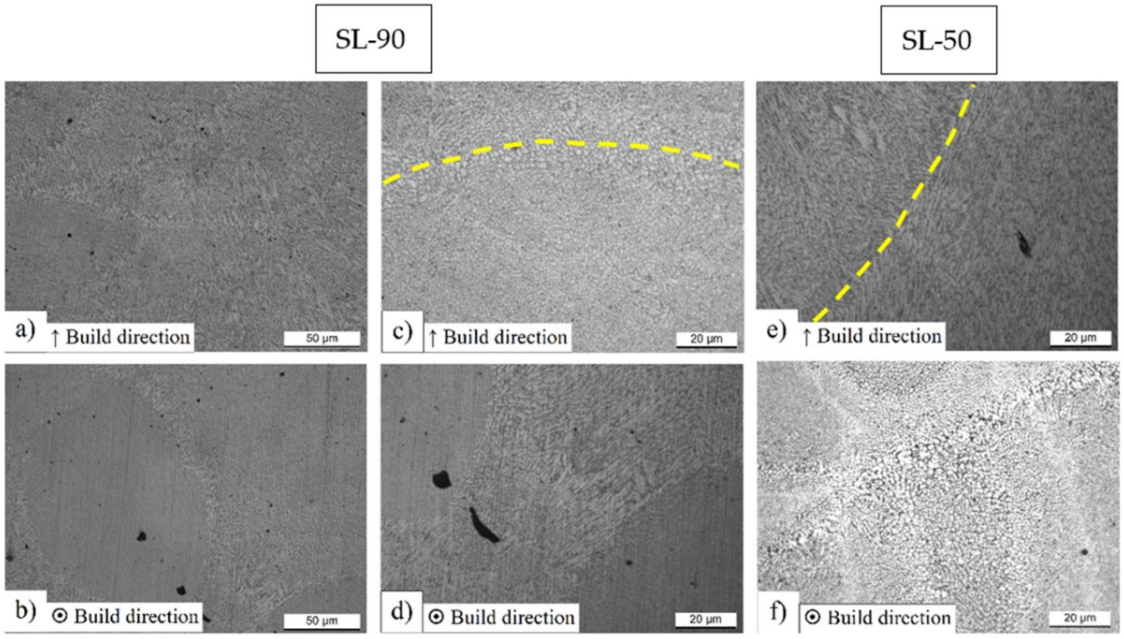


*Figure 4.2. High magnification micrographs of as-built AlSi10Mg 90-samples in XZ plane (**a**, **c**) and XY plane (**b**, **d**), and of as-built AlSi10Mg 50-samples in XZ plane (**e**) and XY plane (**f**).*

Focusing on *Figure 4.2c,d*, it is possible to highlight the complex thermal history which characterized the samples manufactured through the SLM process. As a matter of fact, the high cooling rate (10^6–10^7 K/s), various heat fluxes, and the different thermal gradients induce a variation in grain dimensions and morphology [184,251,258]. In this context, the molten pools' cross-sections are often formed by columnar grains that are arranged along the thermal gradient [193]; however, focusing on *Figure 4.2a*, it is possible to observe the presence of both the columnar and equiaxed grains into different molten pools. *Figure 4.2c* shows a high magnification micrograph of the molten pool cross-section (XZ plane) where the yellow dotted line highlights its boundary. The only presence of equiaxed grains that dominate the entire microstructure can be observed. Pham et al. [193] and Guan et al. [204] showed the same microstructural configuration through the EBDS analysis carried out on AlSi10Mg SLMed samples. On the other hand, the SL-50 samples show the molten pool cross-sections (*Figure 4.2e*) that are only dominated by columnar grains arranged along the thermal gradient, as studied and reported in [65]. Lingda et al. [259] show how the solidification process is described by a planar growth followed by a competitive grain growth between the equiaxed and columnar grains within the molten pool due to the differences in undercooling, which generates an instability at the interface between liquid and solid. With an increase of the undercooling, the molten pool cross-section is totally formed by equiaxed grains, which show a decrease in size from the fusion line to the center of the molten pool. A. Hadadzadeh et al. [260] demonstrated that the CET (columnar-to-equiaxed transition) is

strictly related to the thermal gradient (G) and the solidification rate (R) ratio; in fact, if the G/R decreases the CET is promoted. Moreover, as reported by the same authors, the crystallographic orientation is the other important parameter that influences the CET due to the correlation between the undercooling and the angle between the growth rate and <hkl> direction of the growing dendrite. Finally, it can be emphasized that the analyzed 90-samples are characterized by an inhomogeneous solidification process along the different planes considered, as shown in *Figure 4.2d*, where a magnification of *Figure 4.2b* highlights the area between the molten pool and the laser scan tracks. In this case, the columnar grains characterize the microstructure along the XY plane, unlike the SL-50 sample (*Figure 4.2f*) where the microstructure is only formed by the equiaxed grains as analyzed in [65], and as reported by [260]. Normally, the XY plane shows the equiaxed grains within the laser scan tracks or the molten pool where their dimensions increase from the center to the edges due to the heat input produced during the SLM process [199,261,262]. In this context, the process parameters have a considerable influence on the heat input; in fact, as reported by Paul et al. [160], the number of columnar grains increase with increasing the layer thickness or the hatch spacing; while the quantity of equiaxed grains increases and their dimensions decrease with decreasing the hatch spacing. As demonstrated by the same authors, the decrease of hatch spacing (≈ − 53 %) induces a greater influence on microstructure than an increase of the layer thickness (≈ + 50 %).

Figure 4.3 shows the microhardness profile performed along with the different directions and considering the different kinds of microstructure previously discussed. *Figure 4.3a,c,b,d* shows the XZ plane and XY plane of SL-90, respectively; while *Figure 4.3e,f* show the same planes referred to SL-50 samples. Generally, the microhardness values decrease in correspondence to the molten pool (about 15 and 22 HV_{15}) and scan tracks boundaries (about 36 HV_{15}) focusing on *Figures 4.3a,b,d*, respectively, due to the effects induced by HAZ, i.e., the destruction of the Si network and the presence of coarse zone [65,262,263]. As reported by Chen et al. [237], this microstructural configuration is less effective at hindering the dislocation movements; in fact, it shows a greater plastic deformation than the other zones formed by a full-cellular structure. On the other hand, the microhardness profile shown in *Figure 4.3c* does not show a great variation between the center and the molten pool boundary. Considering the average HV_{15} trend, this is lower than those related to the equiaxed grains (*Figure 4.3a,b,d*) because the columnar grains are characterized by a lower deformation resistance under load than the equiaxed grains [264–266]. As a matter of fact, the molten pool cross-section characterized by equiaxed grains (*Figure 4.3a*) shows 133 ± 10 HV_{15} rather than 107 ± 4 HV_{15} of the cross-section characterized by columnar grains (*Figure 4.3c*). These values are the average of

the microhardness obtained in each profile discussed. Finally, comparing the microhardness profile shown in *Figure 4.3a–d* to that shown in *Figure 4.3e,f*, the SL-90 are characterized by higher HV_{15} values than the SL-50 due to the different micro-structures, which is caused by the increase of layer thickness and the decrease of hatch spacing that have influenced the cooling rates of 1.62×10^7 K/s and 9.57×10^6 K/s, respectively. These values are evaluated after the analysis of the secondary dendrite arms spacing (*SDAS*) and through the following equation:

$$SDAS = k\dot{T}^{-n} \tag{4.3}$$

where k and n are the pre-exponential ($k = 43.2$) and exponential ($n = 0.324$) constant, and $\dot{T}$ is the cooling rate expressed in (K/s), as reported by Matyjia et al. [267]. All of these confirmed by Liu et al. [268] justified the increase of hardness between 50 and 90-samples by the fine grains formed due to the increase of overlap regions. In other words, this was due to the decrease of the hatch spacing. Hyer et al. [269] analyzed the characteristics induced by the variation of different process parameters in AlSi10Mg SLMed samples, and through this showed a decrease in cell size with the increase of scan speed (from 800 to 1800 mm/s) and of the layer thickness (from 30 to 90 μm).

Figure 4.4 shows the microstructure obtained after the DA at 200 °C/4 h and T6 for AlSi10Mg DL-90 samples. In this context, it is necessary to highlight the perfect comparison between the SL-90 and DL-90 in terms of microstructure. As reported by Cerri et al. [65], there is no microstructure variation between the microstructure of SL-50 and DL-50 both in the as-built case and after the DA at 200 °C/4 h. In this context, it is possible to observe the same result comparing the microstructure shown in *Figure 4.4a,b* to those reported in *Figure 4.2*. On the other hand, the T6 heat-treated samples show a greater microstructure variation. The as-built AlSi10Mg samples are characterized by a solid supersaturated solution of Si in the α-Al matrix due to the high cooling rate and the Si eutectic that forms a fibrous structure which will be destroyed after the SHT. Only after the SHT and artificial aging process is the Si rejected from the α-Al matrix and the Si particles precipitate along the Al-Si boundaries.

Increasing the SHT temperature causes the Si particles to grow, and their number decrease as a consequence [259]. Simultaneously, the Mg_2Si-phase precipitates and the elongated and brittle β-Al_5FeSi phase grows in α-Al matrix as reported by [261,270].

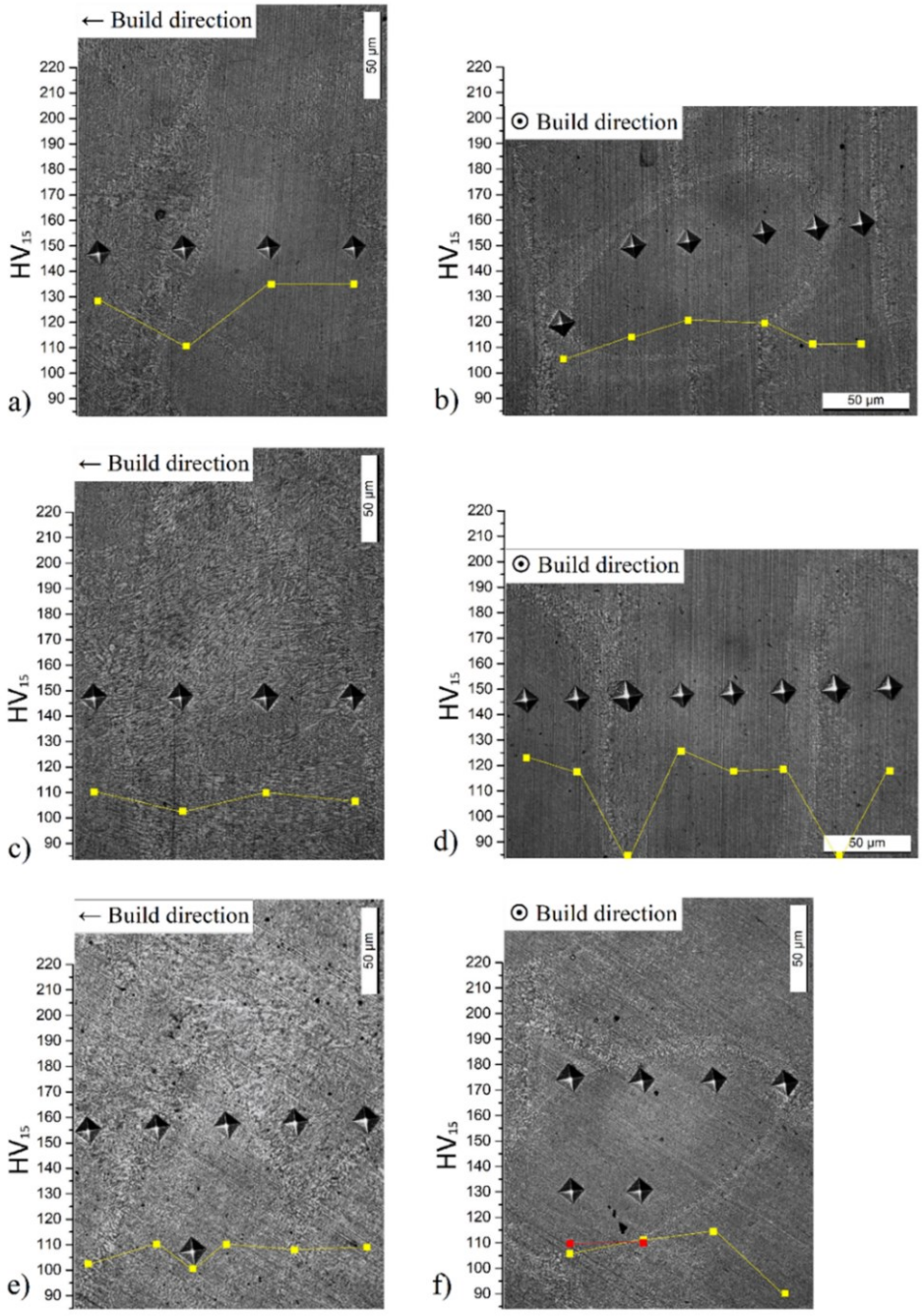


*Figure 4.3. Vickers microhardness profiles (yellow and red curves) of as-built AlSi10Mg 90-samples (**a**– **d**) and 50-samples (**e**, **f**) performed in XZ (**a**, **c**, **e**) plane and XY plane (**b**, **d**, **f**).*

In terms of Si eutectic (*Figure 4.4d*), the microstructure of the SL-50 samples after the T6 heat treatment is shown in *Figure 4.4d*, and it is possible to observe the same microstructural conditions of the DL-90. Finally, the ellipsoidal shape of the molten pool is still visible in the XY plane (*Figure 4.4d*) due to the particle accumulation effect along the edges of scan tracks rather than at their centre, as reported by Li et al. [258].

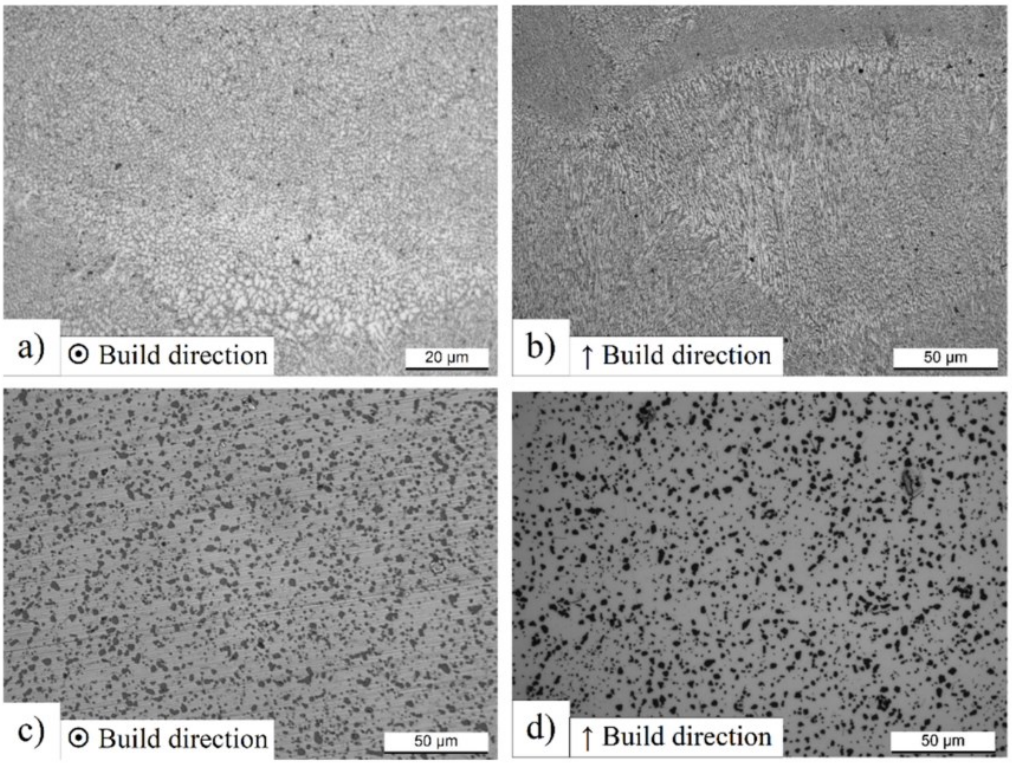


*Figure 4.4. High magnification micrographs of SL AlSi10Mg DL-90 (**a**– **c**) and SL-50 (**d**) microstructure after 200 °C/4 h (**a**, **b**) and T6 (505 °C/4 h + 175 °C/4 h) HT (**c**, **d**). The first and second columns are referred to XY plane and XZ plane, respectively.*

3.2. Mechanical Properties

Figure 4.5a,b shows the Vickers microhardness profiles performed along the Z-axis on the external frame (red profiles) and the CM (orange profiles) of the SL-90 and DL-90 bars in as-built condition, respectively. Instead, the two blue curves represent the microhardness profiles of as-built SL-50 and DL-50 measured along the build di-rection in the CM. Considering the orange and blue microhardness profiles in *Figure 4.5a*, both the SL-90 and the SL-50 show the same effects of aging phenomena induced by the preheated build in the bottom region rather than in the top region, which is strengthened only by solid solution, as reported by [65,255]. In fact, the HV_{500} values decrease from 124 ± 3 HV_{500} to 109 ± 3 HV_{500} and from 130 ± 2 HV_{500} to 114 ± 4 HV_{500} for SL-50 and SL-90, respectively. The average difference of the microhardness values (~ 6 HV_{500}) between the SL-90 and SL-50 can be attributed to the difference in grain size dimension as previously discussed in Section 3.1. On the other hand, the variation between the CM (orange profile) and the external frame (red profile) is caused by the difference in terms of density as reported in *Table 4.3*. Comparing the bottom and top values, it is possible to observe that the variation of density remains constant (1.88 % and 2.04 %,

respectively). *Figure 4.5b* shows the same trend previously discussed for CM SL-90; in fact, the microhardness values decrease from 130 ± 2 HV_{500} to 117 ± 3 HV_{500}. Focusing on the microhardness profile of the DL-90 external frame, the effects induced by the aging phenomena are reduced by the high density of the pores, as illustrated by the density values shown in *Table 4.3*.

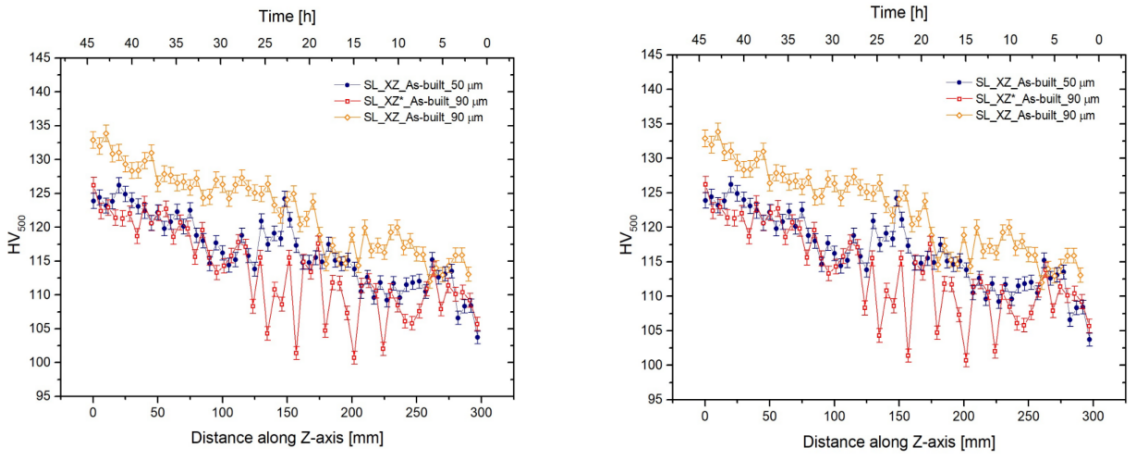


*Figure 4.5. Microhardness profile of as-built SL (**a**) and DL (**b**) 90-samples carried out along the build direction (Z-axis). The blue and orange curves are related to the centre of 50-bars and 90-bars, respectively. The red curve represents the microhardness profile of the external frame of 90-samples.*

In fact, the difference in density in the bottom region between the CM and the external frame is around 12.20 %. In the same context, as reported in [65], the as-built DL-90 shows lower values than the as-built SL-90.

Table 4.3. Density values of AlSi10Mg 90-samples and 50-samples in as-built condition and after the heat treatments.

HT	Planes	SL		DL	
		Bottom	Top	Bottom	Top
As-built	XZ-90	99.62 ± 0.01%	99.76 ± 0.04%	99.20 ± 0.05%	99.33 ± 0.02%
	XZ-90 [1]	97.74 ± 0.09%	97.72 ± 0.11%	86.99 ± 0.22%	95.50 ± 0.09%
	XZ-50	99.00 ± 0.01%	98.5 ± 0.03%	99.9 ± 0.01	99.2 ± 0.05%
200 °C/4 h	XZ-90	99.73 ± 0.02%	99.60 ± 0.01%	-	-
T6	XZ-90	98.15 ± 0.06%	97.95 ± 0.01%	97.58 ± 0.01%	98.12 ± 0.01%

[1] These density values are referred to the external frame.

Moreover, if the density of SL samples decreases along the build direction, the inverse behaviour characterizes the DL samples. Andani et al. [271] attribute the density decrease of DL samples to the unmelted spatters phenomena, which is less present in SL samples. Moreover, it can be highlighted that porosity behaviour is not controllable due

to the high number of parameters that can influence the density [272]. Chen et al. [273] show the influence of the energy density (φ) on the large pores rather than the small; also, the wrong optimization of all parameters contained in (φ) can induce a high number of defects. The same undesirable results are obtained due to the presence of gas within the gas atomized powder and due to the hydrogen solubility into the melt pool. In this context, the pores nucleation takes place only when the maximum hydrogen solubility is reached in these points. Weingarten et al. [89] demonstrated an increase in pores if they nucleate at the solidification front rather than at the melting front due to the combination between the solidification time and the terminal velocity of pores. The former depends on the ratio between the molten pool length and the scan speed, the later on gravity acceleration, kinematic viscosity and pore radius. Finally, the density can be affected by the scan strategy despite the optimization of (φ) and by Marangoni flow, as reported by [93,71]. Finally, comparing the variation between the maximum 99.87 ± 0.01 % and the minimum 98.50 ± 0.06 % density values of CM as-built samples with those reported in the literature, the process parameters have been effectively optimized. In this context, it is necessary to observe that only the CM will be subject to the uniaxial tensile load due to the removal of the external frame by machining tools (see Materials and methods). Therefore, the high quantity of pores present in the external frame will not contribute to the causes of the failure of the sample.

After the T6 heat treatment, the densities decrease (see *Table 4.3*) due to the pore variation, which can be caused by the variation in grain structure [70,71,274]. Other authors have shown that with the increase of SHT temperature the gas pressure increases and, if the temperature is able to reduce the yield strength of the material around the pore, it can deform it [71,89]. It is certainly possible to say that the pores may spheroidize to minimize the free surface energy as expressed by the Young-Laplace equation [224]. On the other hand, some other authors do not highlight the variation in density after the T6 HT [275,276]. Ultimately, the DA at 200 °C/4 h does not induce any variation in density, as can be seen in *Table 4.3*. As concerns the XY plane, the Vickers microhardness shows a slight difference between SL-90 and DL-90 both in the bottom (132 ± 3 HV_{500} and 131 ± 3 HV_{500}) and in the top regions (115 ± 5 HV_{500} and 110 ± 2 HV_{500}). Comparing these HV_{500} values with those obtained along the XZ plane, it can emphasize the microstructure homogeneity along the different planes as supported by the optical microscope analysis (*Figure 4.2*). The same results are shown by Maamoun et al. [261] which analyzed the effects induced by the process parameters on the AlSi10Mg SLMed samples.

Figure 4.6 presents the tensile properties of AlSi10Mg samples in as-built condition (*Figure 4.6a,b*) after the DA at 200 °C/4 h (*Figure 4.6c*) and the T6 HT (*Figure*

4.6d) were analyzed along the build direction. *Figure 4.6a* shows the mechanical properties of the as-built SL-90 and DL-90, which do not present marked differences in terms of strengths and elongation at break, as also reported by Cerri et al. [65]. For these reasons, in the following discussion of heat treatment, only SL-90 and the SL-50 will be considered. The average UTS values decrease from 438 ± 13 MPa and 418 ± 9 MPa to 411 ± 8 MPa and 392 ± 11 MPa for SL-90 and DL-90, respectively. Simultaneously, the yield strengths decrease from 284 ± 10 MPa and 281 ± 9 MPa to 237 ± 6 MPa to 232 ± 4 MPa for the same analyzed samples. The ductility remains constant at around 6.9 ± 1.0 %. *Figure 4.6b* shows the same decreasing trends of mechanical properties of as-built SL-50 and DL-50 samples that were studied in Cerri et al. [65]; but, comparing these to the *Figure 4.6a*, it is possible to observe the greater decrease of all tensile strengths along the build direction (Z-axis), as also shown in *Table 4.4*, which illustrates the absolute differences. If the bottom samples are characterized by the same tensile strength values, the top SL-90 and DL-90 show higher UTS and yield strength values than the SL-50 and DL-50.

Table 4.4. Variation of the mechanical properties from bottom to top of SL-90 and 50, DL-90 and 50 AlSi10Mg samples in as-built and heat-treated conditions.

HT	Samples	Absolute Differences		Relative Change			
		$\Delta\sigma_{0.2}$	ΔUTS	$\Delta\sigma_{0.2}$	ΔUTS	$\Delta\sigma_{0.2}$	ΔUTS
As-built	SL-90	46 MPa	28 MPa	− 0.4%	− 16%	− 6%	+ 6%
	DL-90	50 MPa	36 MPa	− 0.6%	− 18%	− 8%	+ 8%
	SL-50 [65]	70 MPa	80 MPa	− 0.8%	− 24%	− 18%	+ 12%
	DL-50 [65]	110 MPa	100 MPa	− 0.9%	− 37%	− 22%	+ 14%
200 °C/4 h	SL-90	11 MPa	10 MPa	− 0.5%	− 5%	− 3%	+ 6%
	SL-50	19 MPa	22 MPa	+ 0.8%	− 8%	− 6%	− 10%
T6	SL-90	3 MPa	3 MPa	+ 1.8%	− 1%	− 1%	+ 16%
	DL-90	− 11 MPa	− 15 MPa	− 1.6%	+ 5%	+ 5%	+ 20%

As also reported by [65], the microstructure between the top and bottom regions does not show a variation except for the precipitation phenomena induced by the preheated build platform. This behaviour is also confirmed by Casati et al. [184]. In the same context, the temperature used for heating the substrate (150 °C) may have induced a reduction of the residual stress as reported by L. Wang et al. [277]. Therefore, the top region can be affected by higher values of residual stress than the bottom region due to the different residence time within the build chamber during the SLM process, as shown by the top-X axis (Time [h]). Moreover, the variation of tensile strengths between the top 90-samples (*Figure 4.6a*) and the 50-samples (*Figure 4.6b*) can be justified through the different process parameters used, which induce different residual stress, i.e., differences in terms of dislocation density due to the high cooling rates and the complex thermal cycling, as reported by Tomus et al. [278]. In the same context, as reported by Yakout et

al. [279] the increase of residual stress with decreasing of hatch distance and increasing energy density is shown, i.e., the same conditions that differentiate the manufacturing process between the 90-samples and the 50-samples (see Materials and methods). *Figure 4.6c* shows the tensile properties of SL-90 and SL-50 after the DA at 200 °C/4 h. The DA induces a greater homogenization between the bottom and top regions for the SL-90 than the SL-50 considering the absolute variation shown in *Table 4.3*. In this context, the average UTS values decrease from 373 ± 3 MPa and 369 ± 8 MPa to 363 ± 7 MPa and 348 ± 2 MPa for SL-90 and SL-50, respectively. Simultaneously, the yield strengths decrease from 230 ± 3 MPa and 229 ± 6 MPa to 219 ± 6 MPa to 210 ± 2 MPa for the same analyzed samples. The ductility remains constant at around 8.3 ± 0.9 %, which is comparable to that shown by the as-built samples.

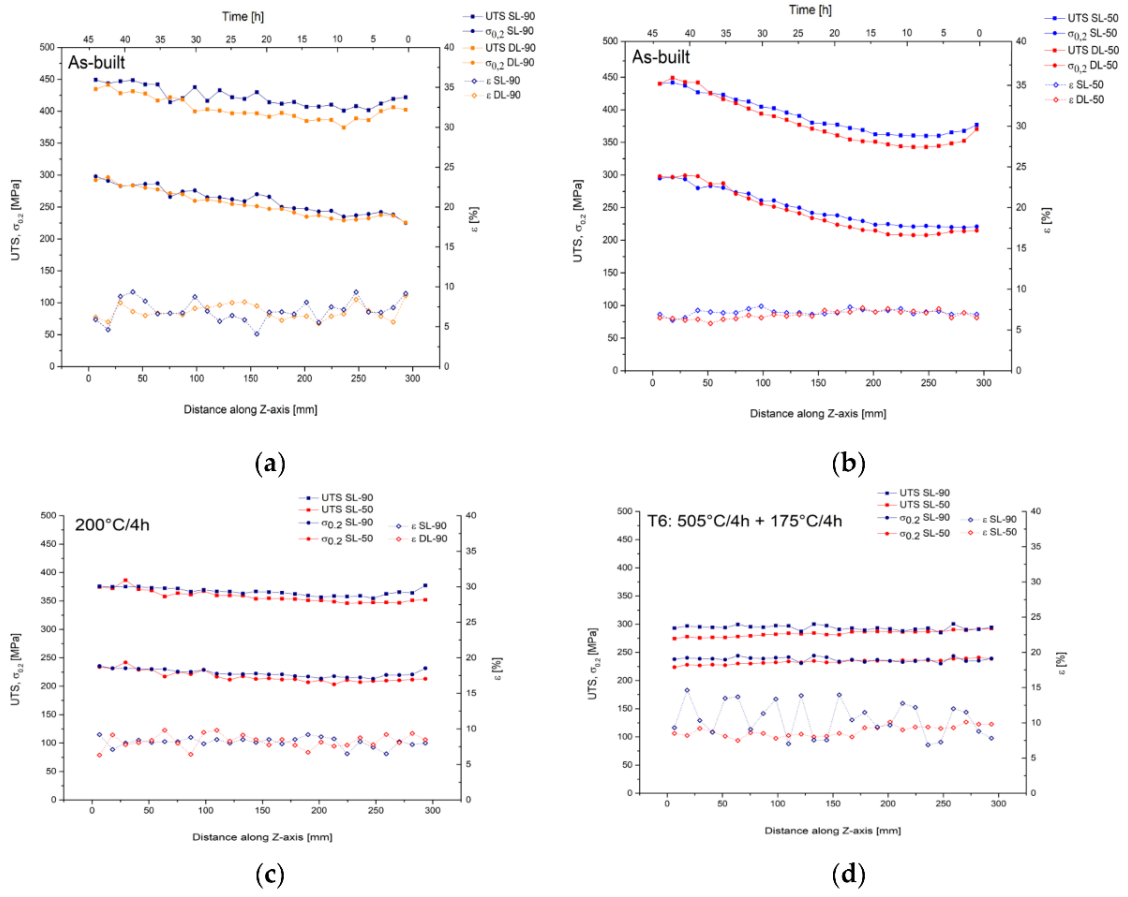


*Figure 4.6. ensile properties of AlSi10Mg samples: (**a**) as-built SL-90 and DL-90; (**b**) as-built SL-50 and DL-50; (**c**) SL-90 and SL-50 after 200 °C/4 h; (**d**) SL-90 and SL-50 after T6 heat treatment. The blue arrows indicate the samples will be considered in Figure 4.7.*

In addition, the top regions of SL-90 were characterized by higher strength values than the SL-50. This behaviour can justify the argument about the residual stress

because the DA at 200 °C/4 h can tend to reduce it like a preheated build platform; moreover, it does not influence the microstructure (*Figure 4.2* and *Figure 4.4*), as also reported in [65,228]. On the other hand, the T6 heat treatment induces a significant decrease of the UTS values (≈ 280 MPa), despite the YS values remaining constant to those shown after the DA heat treatment. Moreover, the absolute differences of the tensile properties be-tween bottom and top samples are substantially knocked down for the SL-90; while for SL-50 the UTS and YS values show a slight increase from the bottom to the top regions. Finally, the average elongations at break increase up to 9.5 ± 1.2 % and 10.6 ± 2.4 % for SL-50 and SL-90, respectively. All of this is attributable to the microstructural variation shown in *Figure 4.4*.

As widely reported in the literature, the strengthening mechanisms of AlSi10Mg samples change before and after the various heat treatments affecting the mechanical properties, as previously discussed. This behavior is described by all contributions of the following equation [280,281]:

$$\sigma_y = \sigma_f + \sigma_{ss} + \sigma_{HP} + \sigma_{Or} + \sigma_p + \sigma_{pre} \tag{4.4}$$

where σ_f is the lattice friction stress, σ_{ss} is the solid solution strengthening, σ_{HP} is the strengthening related to the grain size (Hall-Petch relationship), σ_{Or} is the Orowan strengthening related to the Si particles, σ_p is the dislocation hardening, σ_{pre} is the contribute of the dislocations and precipitates. As reported by Li et al. [282], the first parameter can be neglected due to its small value (5.5 MPa) as compared with the other contributions, while this change significantly after the different heat treatments are undertaken. In the as-built conditions, without the precipitation phenomena induced by the preheated build platform, the strengthening mechanisms are described by the following parameters σ_{ss}, σ_{HP} and σ_p. Increasing the amount of Si particles and the Mg_2Si-phases by the precipitation phenomena (preheated build platform and/or DA at 200 °C/4 h), the σ_{Or} increases due to the Orowan looping mechanisms [237]. Hadadzadeh et al. [280] concluded that the Si particles are not shared by the dislocation, so, therefore, these contribute to a reinforcing phase. In the same context, after the DA at 200 °C/4 h, the strength decreases due to the decrease of solid solution strengthening and because of the dislocation density.

Firstly, Yang et al. [158] analyzed the following equation:

$$\sigma_{ss} = k_{Mg}\left(C_\alpha^{Mg}\right)^m + k_{Si}\left(C_\alpha^{Si}\right)^m \tag{4.5}$$

where k_{Mg} and k_{Si} are 17 and 11 MPa wt%$^{-1}$, m is 1 and *C* is the chemical concentration of Mg and Si [158,159]. They suggest that, after the DA and/or stress relief, Si and Fe will still be in solid solution as opposed to Mg, which will be present in a lower concentration

due to its high diffusion rate. Finally, the σ_{ss} contribution can be considered negligible after the T6 heat treatment [158,159]. As m is 1, this suggests that this contribution can be neglected after the T6 HT. Secondly, Baek et al. [157] showed a high dislocation density in AlSi10Mg as-built samples than in the same samples after the direct aging at 180 °C for 6 h. Initially, the rapid cooling induced by SLM process creates a high dislocation density which is partially eliminated by the DA. The same authors suggest that the direct aging heat treatment induces a uniform distribution of dislocation within the Al-matrix due to the precipitation phenomena. Finally, in the T6 heat-treated samples, the same authors highlighted the localization of density only around the coarse Si particles, and it is possible to conclude that the σ_p decreases. Moreover, after this heat treatment the decrease of strength is also induced by the increase of grains size as described by the following Hall-Patch equation:

$$\Delta\sigma_{HP} = \frac{K}{\sqrt{d}} \tag{4.6}$$

where *K* is the material constant, which is approximatively 0.04 MPa $m^{1/2}$ [283], and *d* is the average grains size. As reported by Baek et al. [157], the σ_{HP} value decreases from 89 MPa in as-built condition to 12 MPa after the T6 HT.

The dislocation hardening can be estimated through the following equation [65]:

$$\sigma_p = \beta M G b \sqrt{\rho_p} \tag{4.7}$$

where β is a constant of the material, *M* is the Taylor factor, *G* is the shear modulus of Al matrix, *b* is Burgers vector of Al and ρ_p is the density of dislocation.

Starink et al. [284], who analyzed a model for predicting strength in overaged Al-Zn-Mg-Cu casting alloys, suggested a detailed relationship to determine the contribution of dislocation and precipitates:

$$\sigma_{pre} = C_4 \frac{Gb}{(l_D l_t)^{1/2}} \left[f^{1/2} + 0.70 \left(\frac{l_D}{l_t}\right)^{1/2} f + 0.12 \left(\frac{l_D}{l_t}\right) f^{3/2} \right] \tag{4.8}$$

where C_4 is a constant, l_D is the diameter of the discs of the precipitate, l_t its thickness, and f is the volume fraction.

Figure 4.7a,c,e show the strain hardening rate (θ) as a function of true strain (ε) and the true stress-strain curves of all samples characterized by minimum and maximum elongation at break in as-built condition (*Figure 4.7a*, samples 4 and 14), after DA (*Figure 4.7c*, samples 1 and 21) and T6 HT (*Figure 4.7e*, samples 2 and 10). In this scenario, it is useful to highlight the Considère's criterion, which defines the onset of necking through the intersection between the strain hardening rate and the true stress-strain curves [167]. The strain hardening rate (θ) is defined as the derivative of σ with respect to ε:

$$\theta = \frac{d\sigma}{d\varepsilon} \tag{4.9}$$

where σ and ε are the true stress and true strain, respectively. *Figure 4.7b,d* show the fracture surfaces of SL-90 sample in as-built condition and after the DA at 200 °C/4 h; while *Figure 4.7f* the fracture surface of SL-90 samples after the T6 HT. According to Considère's criterion, the failure occurs before the necking formation for SL-90 samples in as-built condition and after the direct aging. In fact, the θ values are around 1800 and 1600 MPa, respectively. Chen et al. [237] show the same results considering only the as-built samples highlighting the strict correlation between the strain hardening rate and the Orowan strengthening mechanism, as previously mentioned. Focusing on *Figure 4.7e*, sample 10, which shows the minimum elongation at break value (*Figure 4.6d*), achieves the failure just before the necking formation, at θ of 335 MPa. Sample 2, however, shows the intersection between the true stress-strain and the strain hardening rate curves at 320 MPa and 0.101 of true stress and true strain, respectively. Considering the fracture surfaces shown in *Figure 4.7b,d* and that which was previously discussed, it is possible to observe the absence of necking and a fracture behaviour less ductile than sample 2 after the T6 HT (*Figure 4.7f*). Finally, the T6 heat-treated samples characterized by a ductility value over 12 % (*Figure 4.6d*) show a failure that occurs after the necking formation rather than before.

Strain-hardening exponents (n) were calculated according to the ASTM standard E464 [285], and all obtained results are also confirmed by [160]. In this context, it is possible to emphasize that the n value calculated for the samples (2) is exactly 0.101 as previously reported (*Figure 4.7e*).

The strain hardening is an important value to understand concerning the material strengthening; in fact, it gives information about the plastic behaviour after the yield strength point. As widely reported in the literature, the n strain hardening exponent always assumes values between 0 and 1.

More specifically, n is equal to 0 when the material is a perfectly plastic solid which shows the same value between the yield strength and the UTS, while the material is a perfectly elastic material when n = 1.

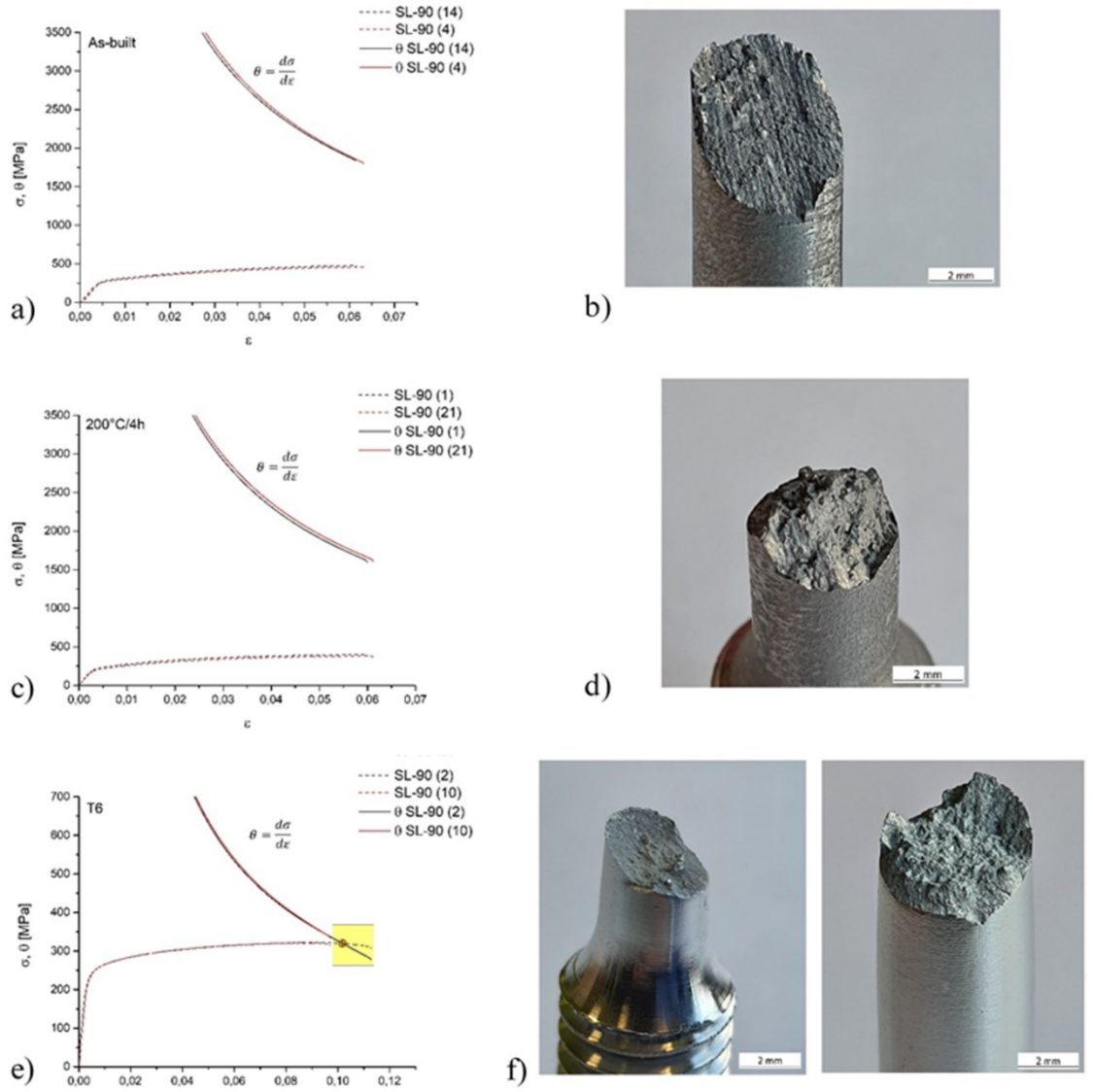


*Figure 4.7. True tensile stress-strain curves and strain hardening rate θ (**a**,**c**,**e**) of SL-90 AlSi10Mg samples in as-built condition (**a**,**b**), after the direct aging (**c**,**d**) and the T6 heat treatment (**e**,**f**). Fracture surfaces of: (**b**) sample (4) in as-built condition, (**d**) sample (21) heat-treated at 200 °C/4 h, (**f**) samples (10) and (2) T6 heat-treated, respectively.*

Figure 4.8a shows the strain hardening trends in function of the Z-axis considering the as built and the heat-treated 90-samples and 50-samples. Generally, the as-built samples are characterized by an increase of n values with increasing distance from the preheated build platform. This behaviour can be explained through the possible increase of high-density defects or dislocations as previously reported by the argumentation of the residuals stress [286]. Sjögren et al. [287] study the effective correlation between the dislocation movements and the strain hardening exponent (n), which increases with the increase of the multiplication and entanglement of dislocations.

Moreover, the 90-samples show higher strain hardening exponents than the 50-samples, which tends to homogenize only after the DA at 200 °C/4 h. Also considering the top and the bottom region, the n values tend to stabilize due to the possible loss of the effects induced by the preheated build platform as reported in [65]. In detail, the DA can be induced by an increment of the precipitation phenomena both in top and bottom regions, and it can be considered as a stress relief HT for the top regions. In fact, the n values decrease with the possible decreasing of the dislocation density, as also reported by [288]. Finally, the n values decrease in all samples which were T6 heat-treated according to a decrease in the variation between the yield strength and the UTS values for each analyzed sample [289].

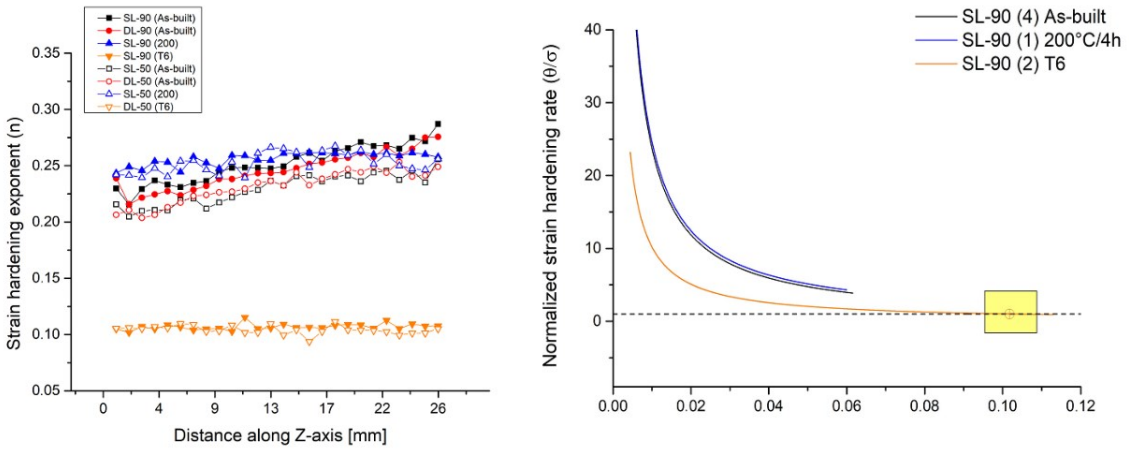


*Figure 4.8. (**a**) Strain hardening values of as-built and heat-treated 90-samples and 50-samples in function of the distance from the build platform. (**b**) Normalized strain hardening rate $\theta=d\sigma/d\varepsilon$ of as-built, direct aged and T6 heat-treated samples. The black dashed line indicates the points that satisfy the Considère's criterion, in other words, where the strain hardening rate and the true stress coincide.*

All of these can be justified by the microstructural variation (*Figure 4.2* and *Figures 4.4*) such as by the grain size, second-phase particles, dislocation density and the SDAS [287,290]. As reported by Li et al. [282], there is a strict relationship between the work strain hardening and the density mobile dislocation, which depends on the full-cellular and non-cellular structure. Moreover, the work hardening can assume a high value due to the high density of pre-existing dislocation, i.e., defects generated by the SLM process. In the full-cellular case, there are three possible scenarios: (1) dislocation de-penning from the supersaturated α-Al matrix; (2) a network of cutting dislocations at the interface Al-Si; and (3) dislocation emission from the interface Al-Si that moves through the grain. The same authors emphasize that the combination between the first and the second scenarios determine the hardening mechanisms. On the other hand, the

mobile dislocation easily traverses the grains if the microstructure presents the fragmented and coarsened Si eutectic (non-cellular structure) as obtained after the T6 HT (*Figure 4.4*). *Figure 4.8b* reports the strain hardening rate normalized with the true stress [286] of the samples (4), (1) and (2) as representative of the as-built, direct aged and T6 heat-treated conditions, respectively. Focusing on as-built and direct aged samples, it is worth repeating that the failures occur before the necking formation, and these can be considered as premature failures caused by the mechanisms previously discussed. On the other hand, the T6 heat-treated sample shows a lower strain hardening rate than the other samples due to its microstructure. Moreover, sample (2) intersects the black dashed line, i.e., the value 1, which represents the points where the Considère's criterion is satisfied. In fact, these values represent the equality between the true stress and the strain hardening rate.

Figure 4.9a shows the fracture profile of the sample (1) after DA at 200 °C/4 h, where it is possible to observe the non-linear course of the crack, in other words, a tortuous crack propagation through the microstructure. As a matter of fact, the fracture profile shows some zones where the crack propagates in a straight line and other zones where it propagates following other geometries due to the propagation along the HAZs and coarse zones, as shown in *Figure 4.9b,c*. These zones, as discussed in Microstructure's section, are generated along the boundaries of molten pools and laser scan tracks. Therefore, knowing that the laser scan tracks' distribution and orientation are closely related to the scan strategy, this process parameter can affect the fracture mechanisms of samples characterized by a full-cellular microstructure.

The same results are obtained by Paul et al. [160] through the analysis of AlSi10Mg SLMed samples manufactured using different scan strategies. Focusing on *Figure 4.9c*, the white dotted line highlights a semi-ellipsoidal shape of the fracture profile, and observing the presence of the heat-affected zone, it can assume the presence of a laser scan track before failure of the sample. On the other hand, the cracks also propagated within both the molten pool (*Figure 4.9d*) and the laser scan tracks (*Figure 4.9e*), but the heat-affected zones remain the preferential areas of propagation.

In the same context, Delahaye et al. [262] show that the void initiation becomes more favorable along with the interface between the Al-matrix and coarsened Si particles in HAZs. As a matter of fact, considering the following equation, which describes the work (W) necessary to create a crack, it is possible to describe these fracture mechanisms as:

$$W \propto \gamma_{Al} + \gamma_{Si} - \gamma_{AlSi} \tag{4.10}$$

where γ_{Al} and γ_{Si} are the surface energy of the Al-matrix and of the Si precipitates, respectively, while γ_{AlSi} is the interface energy. So, an increase of γ_{AlSi} due to the increase of Si eutectic and due to the tendency of decohesion between the particles and the matrix, the work to initiate a void (W) decreases, for example, from the center of the molten pool to the HAZ.

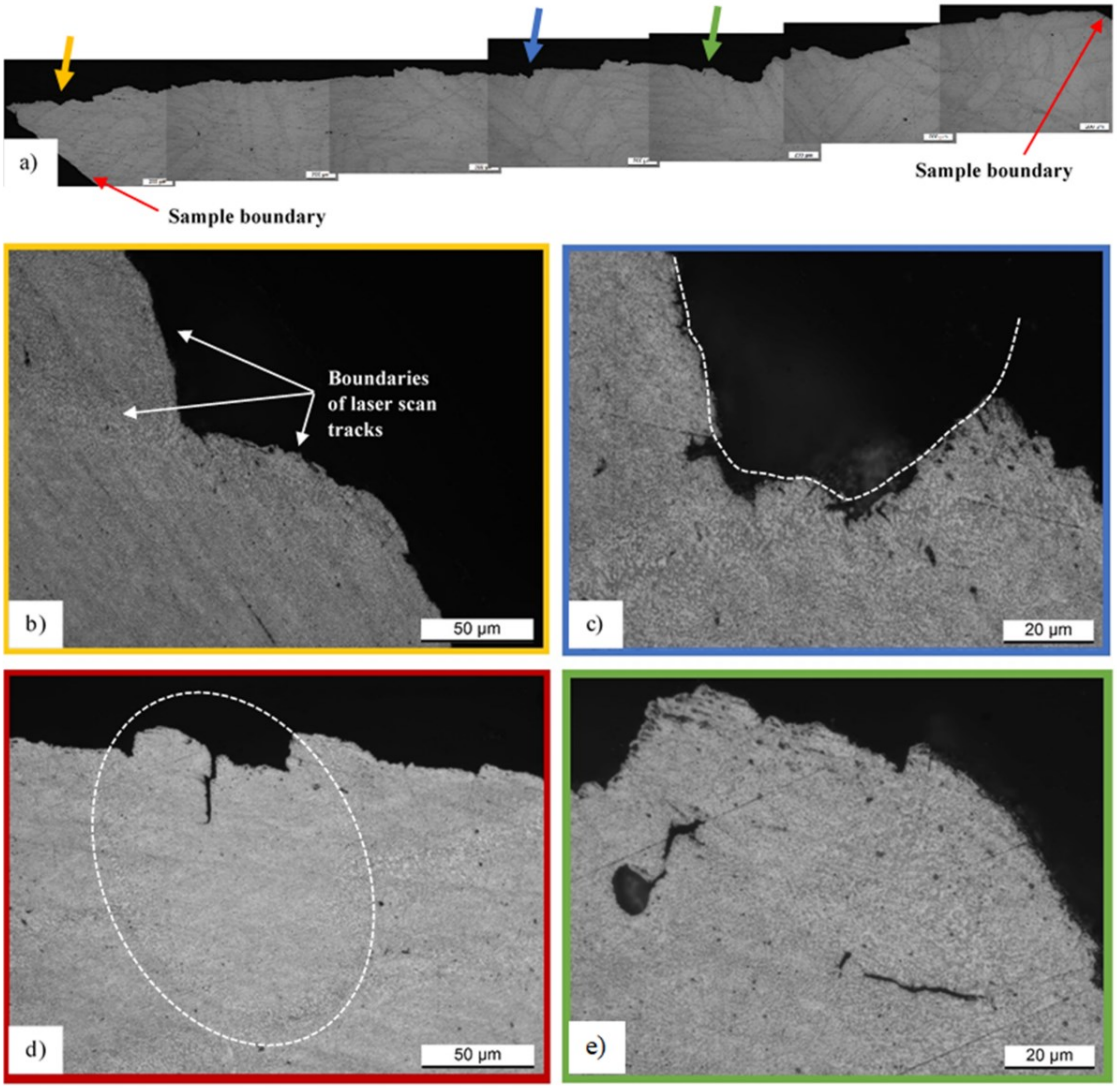


*Figure 4.9. Fracture profile (**a**) of SL-90 (1) sample direct aged where the yellow, blue, red and green arrows indicate four different zones shown in (**b**–**e**) panels. The white dotted line (**c**) indicates a hypothetic laser scan track, while that in (**d**) indicates a molten pool.*

On the other hand, the presence of pores can be the last, but not the least, cause of crack initiation, as shown in *Figure 4.9e*, where it is also possible to observe the cracked HAZ. As widely reported in the literature, depending on the quantity of defects present in AlSi10Mg SLMed samples, a competition between the brittle and the ductile fracture can

be observed; namely, a crack propagation both within the molten pool or laser scan tracks and within the HAZs. As reported and discussed by Delahaye et al. [262], in the absence of defects, the crack propagation tends to occur along the HAZ, i.e., in the weakest zones of the microstructure.

The fracture profile of the T6 heat-treated sample (2) is shown in *Figure 4.10a*, where the orange arrow indicates a piece of fracture surface incorporated in epoxy resin (black areas). Also for this sample, the voids nucleate at the Si particles through the decohesion with the Al-matrix (Si particles show in *Figure 4.10b*); consequently, the void coalescence can occur as highlighted by the dotted circumference in *Figure 4.10b*, and the crack can propagate, as observed by Aboulkhair et al. [173]. During the tensile test, the crack propagation occurs, interconnecting the voids previously mentioned. In other words, it advances among the Si particles (*Figure 4.10c*). At the same time, the cracked Al-matrix is also observed in *Figure 4.10c*. Focusing on the optical microscope, the micrograph in *Figure 4.10d* shows the white dotted ellipse highlighting the possible presence of a molten pool before the T6 HT (see *Figure 4.4c*). In this context, it is possible to observe that the molten pool and the laser scan tracks, which remain after the HT as discussed in Microstructure section, can influence the fracture mechanisms. In fact, at their boundaries there is a greater presence of Si particles than at their center, so there are more possibilities that all voids can be interconnected by a crack, as reported by Zhao et al. [261].

In conclusion, to obtain an effective comparison between all analyzed samples, it is possible to use the Quality Index (QI) as well as the AlSi10Mg SMLed alloy as reported by Tang et al. [292]. This numerical parameter was defined by Drouzy et al. [293] for expressing the mechanical "quality" of the aluminium alloys, and it can be calculated through the following equation:

$$QI = UTS + d\,log(\varepsilon) \tag{4.11}$$

where UTS is the ultimate tensile strength and d is an empirical parameter which is determined, as suggested by Drouzy et al. [294], to make QI independent of the yield strength, and ε is the engineering elongation to fracture. In this context, it is possible to observe that the as-built 90-samples and 50-samples are characterized by higher QI values (between 480–580 MPa) than the direct aged at 200 °C/4 h (between 460–525 MPa) as shown in *Figure 4.11*.

The same as-built QI values were calculated focusing on the studies carried out by Paul et al. [160] and Girelli et al. [71]. Both the bottom 90- and 50-samples show higher QI values than the top samples due to the highest ultimate tensile strengths, as reported in *Figures 4.6a,b*.

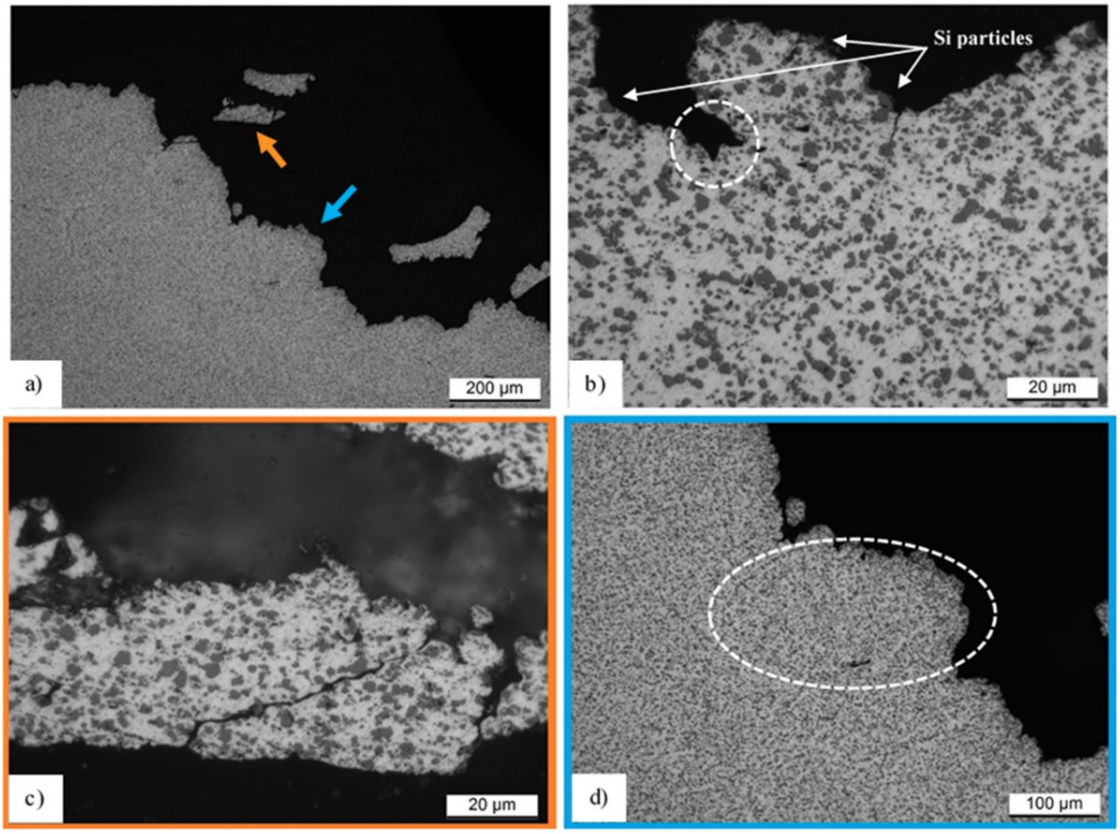


*Figure 4.10. Fracture profile (**a**) of the T6 heat-treated sample (2) where the orange and light-blue arrows indicate two different zones shown in (**c**,**d**). The micrograph (**b**) shows another area of the same sample.*

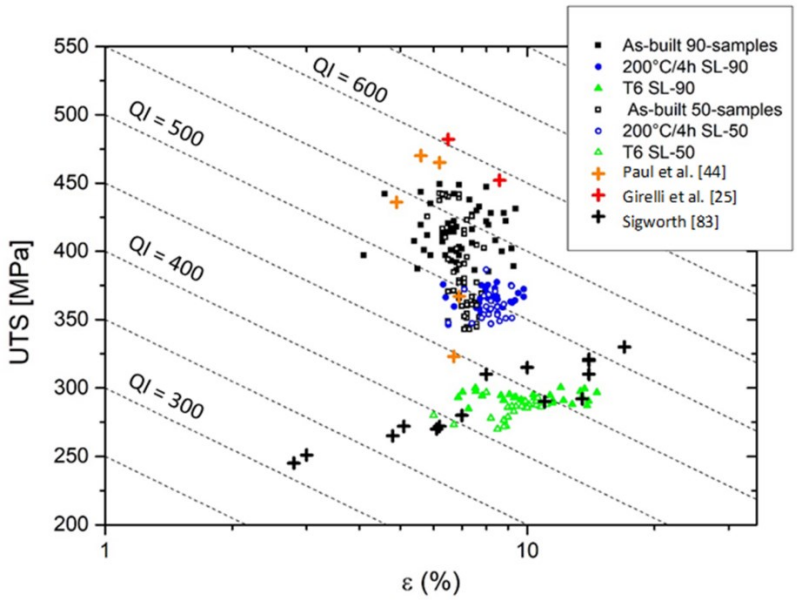


Figure 4.11. Comparison of mechanical properties of AlSi10Mg SLM in as-built and heat-treated conditions through the Quality Index (QI) with the results shown in the literature. The References [25,44,83] are replaced by [71,160,161].

On the other hand, the top 50-samples are characterized by the same quality indexes obtained after the DA at 200 °C/ 4 h. Furthermore, it can be concluded that this direct aging homogenized the mechanical properties along the build direction, and it may be a good compromise focusing on the QI values (460–540 MPa).

Finally, the T6 HT show the largest decrease of the QI range (415–470 MPa), and a higher homogenization than the other considered samples due to the marked microstructural variation (*Figure 4.4*). Considering the QI values analyzed by G. Sigworth [161], who studied the quality in aluminium casting, it possible to observe that the T6 heat-treated AlSi10Mg SLMed samples are perfectly comparable to the high-quality SS aluminum casting alloy.

4. Conclusions

In the study, AlSi10Mg samples manufactured by single e double laser selective laser melting using a layer thickness of 90 μm and a hatch spacing of 70 μm were analyzed before and after the direct aging (200 °C/4 h) and the T6 heat treatment (505 °C/4 h + 175 °C/4 h). In addition, these SL and DL samples have been compared to other AlSi10Mg selective laser melted samples, in the same heat-treated conditions, manufactured with a layer thickness lower than 40 μm and a hatch spacing higher than 100 μm. The main conclusions are as follows:

1. The microstructure does not show any variation before and after heat treatments (direct aging 200 °C/4 h, T6) between the 50 and 90-samples in the same conditions, but the decrease of hatch spacing induces higher effects than the increase in layer thickness. In fact, the 90-samples are characterized by a finer microstructure formed by a mixture of columnar and equiaxed grains than the 50-samples despite the similar energy density values ($\Delta\varphi = 6$ J/(mm^3)).
2. The microstructure shows a great variation only after the T6 HT, where the Si eutectic network is destroyed and coarsened Si eutectic particles are formed. How-ever, the ellipsoidal shape of the molten pools remains visible in the XY plane, and these could still influence the fracture mechanisms as well as in the samples directly aged. In the T6 heat-treated samples the crack propagates among the Si coarsened particles. Within the full-cellular structure, the crack propagation occurs along with the heat-affected zones and coarse zones.
3. In as-built condition, the HV500 microhardness profile decreases along the build direction (Z-axis) from 130 ± 2 HV_{500} to 114 ± 4 HV_{500} and from 130 ± 2 HV_{500} to 117 ± 3 HV_{500} for SL-90 and DL-90, respectively, due to the precipitation hardening phenomena induced in the bottom region by the preheated build

platform. In the same region, the high-density variation (12.20 %) between the CM and the external frame of DL-90 induces a decrease of about 15 HV_{500}, thus nullifying the precipitation hardening effects.

4. The direct aging tends to homogenize the mechanical properties between top and bottom top, while at the same time inducing a small increase of ductility (from 6.9 ± 1.0 % to 8.3 ± 0.9 %). Only after the T6 HT did some samples show the elongation at break of 12–15%; while if the UTS values decreased approximately 294 ± 4 MPa, the yield strength values would remain constant with those obtained after direct aging (≈ 230 MPa). For these reasons, the strain hardening exponents decrease by approximately 0.24 for as-built and direct aged samples to 0.10 for T6 heat-treated samples.
5. The Considère's criterion shows that the failure occurs after the necking formation only in the samples characterized by a ductility higher than 12 %. Moreover, the strain hardening rate was about 1800 MPa and 1600 MPa at the fracture point for the as-built and the direct aged samples, respectively.

ARTICLE 5

Defect-Correlated Vickers Microhardness of Al-Si-Mg Alloy Manufactured by Laser Powder Bed Fusion with Post process Heat Treatments

---

Emanuela Cerri, Emanuele Ghio & Giovanni Bolelli

Journal of Materials Engineering and Performance, *31* (**2022**) 8047–8067

https://doi.org/10.1007/s11665-022-06874-6

“The following version of the manuscript is made available under the CC-BY-NC-ND 4.0 license”

https://creativecommons.org/licenses/by-nc-nd/4.0/

Defect-Correlated Vickers Microhardness of Al-Si-Mg Alloy Manufactured by Laser Powder Bed Fusion with Post process Heat Treatments

Emanuela Cerri [1], Emanuele Ghio [1], Giovanni Bolelli [2].

[1] Department of Engineering and Architecture, University of Parma, Via G. Usberti 181/A, 43124, Parma, Italy.

[2] Department of Engineering "Enzo Ferrari", University of Modena e Reggio Emilia, Via P. Vivarelli 10/1, 41125, Modena, Italy.

Abstract

Laser Powder Ped Fusion is an Additive Manufacturing process characterized by different advantages like the manufacture of samples with complex geometry without the use of tools and/or molds. Generally, the manufactured samples are characterized by high tensile strengths which, however, can be affected by the presence of defects due to the unoptimized process parameters. In a large applications field, a low density of the as built AlSi10Mg samples is a very important parameter to considered, e.g. due to both the loss of the tensile strengths correlated to a premature failure of the samples and the increase of time and costs associated with the manufacturing process. In addition, different post-process heat treatments can increase these effects leading to an ineffective manufacturing process. In this scenario, the present work shows the analysis of spherical and lack-of-fusion pores induced by the laser powder bed fusion process on the AlSi10Mg samples, and their variations after different heat treatments (direct aging and T6). At the same time, the influence of pores on the Vickers microhardness and the tensile properties has been studied in the same AlSi10Mg samples (bars and billets), that were printed with single and double laser machine set-up. Different process parameters were also analyzed and compared. The study was supported by the microstructural and pore analysis performed by optical microscopy along the XZ plane (build direction) and the XY plane. Finally, the greatest effects of pores were observed on the Vickers microhardness values; in fact, two different relationships between microhardness and density variation are discussed. The T6 heat treatment lead to a rounding of the pores already formed in the as built samples, and to a formation of new small pores.

Keywords: AlSi10Mg, Laser Powder Bed Fusion, gas pores, Vickers microhardness, heat treatments, process parameters.

1. Introduction

AlSi10Mg alloy is a hypoeutectic aluminium alloy based on Al-Si-Mg ternary system, characterized by low density, low thermal expansion and excellent mechanical properties, which make it optimal for aerospace and automotive fields. The production of high-quality metallic powders allows the use of the AlSi10Mg alloy in Additive Manufacturing (AM) processes obtaining good quality samples. The as built samples show a very fine microstructure where the α-Al matrix is surrounded by the network of eutectic silicon that make the AlSi10Mg much resistant, but less ductile [185,294]. Cabrini et al. [295], who analyzed the selective laser melted AlSi10Mg alloy, highlighted the presence of brittle and acicular β-Al_5FeSi phases in the as built samples and ε-Mg_2Si precipitates after heat treatments at temperatures between 200 °C and 500 °C. Cao et al. [296] showed that the brittle and acicular β phases are responsible for the decrease of mechanical properties in Al-Si alloy. On the other hand, Cerri et al. [65] emphasized the effects of the Mg_2Si phases in increasing the UTS and the yield strength. In that study, the precipitation hardening phenomena were induced in as-built samples by the pre-heated build platform. Despite the metallurgical aspect, the mechanical behaviour can be conditioned by the process parameters optimization for the AM technology due to the defects generated within the manufactured parts.

In Selective Laser Melting (SLM), also known as a L-PBF (Laser Powder Bed Fusion) process, samples are manufactured by scanning metallic powder layers with a laser beam, which is characterized by a specific laser power (P, [W]), depending on the type of machine. During the printing process, the physical object is built layer-by-layer on the build platform to its maximum height following a CAD (Computer-Aided Design) project [241]. L-PBF is characterized by four main process parameters: laser power, scan speed $\left(\overrightarrow{v_s}, \left[\frac{mm}{s}\right]\right)$, layer thickness (t, [mm]), and hatch spacing (h, [mm]) that define the energy density function $\left(\psi = \frac{P}{v_s h t}, \left[\frac{J}{mm^3}\right]\right)$. As widely discussed in the literature, process parameters may explain variations in UTS (Ultimate Tensile Strength), σ_y (Yield strength), and ductility through their influence on both the microstructure and the presence of pores. As reported in the study of Wang et al. [297], the increase of energy density from 25 to 60 $\frac{J}{mm^3}$, the relative sample density tends to increase from 92.0 to 93.0 %; while at $\psi = 10$ $\frac{J}{mm^3}$ it settles around 97.5 %. Consequent to these variations, UTS and σ_y increase. Similar results were obtained by Heyr et al. [269]: relative material density increased when energy density was in the range between 25 and 60 $\frac{J}{mm^3}$, while it decreased from 99.5 % to 93 % for energy density up to 100 $\frac{J}{mm^3}$.

In this scenario, Aboulkhair et al. [69] showed how the process parameters' variation can affect the pores' formation in SLMed AlSi10Mg. They affirmed that one of the most effective parameters is the hatch spacing *h* because a lack of overlap between two adjacent laser tracks is generated on the XY plane if *h* increases. Moreover, another problem is related to the layer thickness *t* that must be reduced (if the hatch spacing is increased) to satisfy the intra-layer cohesion. Tang et al. [298] proposed the following equation (Eq. (5.1)) to verify whether the overlap between adjacent molten pools is sufficient:

$$\left(\frac{h}{W}\right)^2 + \left(\frac{t}{D}\right)^2 \leq 1 \tag{5.1}$$

where *h* and *t* are hatch spacing and layer thickness [mm], as defined above, while *W* is the melt pool width [mm] and the *D* the melt pool depth [mm]. In the same context, different combination of the scan speed and the laser power can decrease the density due to the lack of a perfect fusion and the consequent non-adherence between the new layer and the previously scanned layer. Bai et al. [68] show the decrease in density using a combination of high scan speed and low laser power due to the inability of the laser beam to provide adequate melting energy.

Other authors focused their attention on the defects generated in as built samples manufactured by L-PBF process. Anderson et al. [299] showed how the presence of different amounts of trapped gas within the gas atomized powder and the satellites on the particles' surface is related to the density. In the latter case, the presence of satellites can induce flowability problems during powder deposition causing a density decrease in the manufactured sample. Instead, Shi et al. [300] highlighted the effects induced by the pre-heated build platform on the density of AlSi10Mg samples manufactured with different energy density values. The results show a slight increase of density with increasing the build platform temperature from 35 °C to 200 °C and using an energy density of 77 $\frac{J}{mm^3}$. On the other hand, the same authors concluded that the variation of the energy density function induces a greater effect on pores' formation than the pre-heating temperature of the build platform. Focusing on the mechanical properties, an interesting study about pores and their effects was conducted by Tiwari et al. [301]. The authors showed a decrease of UTS and yield strength of about 46 % and 17 %, respectively, due to the relative density decrease from 99.2 % to 95.5 %. The maximum effect was shown on elongation, which decreased by 80 %. On the other hand, pores are critical defects that dominate the fracture mechanism and, consequently, the fatigue life, during a fatigue test [302]. Xu et al. [303] highlighted that pores generate a stress/strain concentration in the material around their surface, this effect increases with pore size. In addition, the stress/strain concentrations increase if the distance between two pores is

lower than their radius by considering the perpendicular direction to the load axis. Furthermore, pores with an irregular shape are characterized by higher stress concentration than spherical ones as analyzed by [304].

In this scenario, the aim of the present manuscript is to study the 2D statistical distribution of pores within different 300 mm-high AlSi10Mg bars and billets manufactured via L-PBF, before and after different post-process heat treatments. In addition, the effects induced by pores and heat treatments on Vickers microhardness were studied. Finally, the results were also compared to those by Cerri et al. [65], who analyzed AlSi10Mg SLMed bars characterized by a lower layer thickness than was used in the present work and a hatch spacing of 170 μm.

2. Materials and Methods

Pre-alloyed gas atomized AlSi10Mg powder, with a size distribution between 20 and 60 μm, was used for the L-PBF process. The chemical composition of the powder is reported in *Table 5.1*.

Table 5.1. Chemical composition of SLM AlSi10Mg powder (wt.%).

Al	Si	Fe	Mg	Cu	Mn	Ti	Other
Bal.	10.0	0.12	0.31	0.03	0.005	0.040	< 0.01

Six bars and three billets, from which the tensile samples were obtained, were manufactured using an SLM280™® (SLM Solutions Group AG, Lübeck, Germany) machine equipped with 2×400 W IPG fiber lasers and a build platform of 280×280 mm^2. This machine set-up allows to obtain two different zones as shown in *Figure 5.1a* where a schematic representation of the manufactured samples was illustrated. The red zones characterized by a single laser (SL) process, while the yellow zones by two lasers (DL) that work in parallel. During the printing process, argon was used to reduce the oxygen content below 0.2 %. The bars (10×10×300 mm^3) and billets (10×100×300 mm^3) were printed according to the scan strategy shown in *Figure 5.1b* where the layer "n+1" was rotated by 67° compared to the previous layer "n".

The L-PBF process used the skin-core strategy for printing where each layer was formed by the external frame (EF), which is scanned first, and the area inside the frame or center zone (CM) represented by the dotted arrows in *Figure 5.1b* and scanned then to the EF. Each arrow that schematically represents a laser scan track is inclined by 56.5° (α angle) and all are arranged parallel to each other. For better characterization, all bars were divided along the height into two parts, namely the top (heights from 150 to 300

mm) and the bottom (from 0 to 150 mm). In addition, the EF and the CM zones were analyzed along the XZ plane (EF_{XZ}, CM_{XZ}) and the XY plane (EF_{XY}, CM_{XY}) as highlighted through the different planes in *Figure 5.1c*.

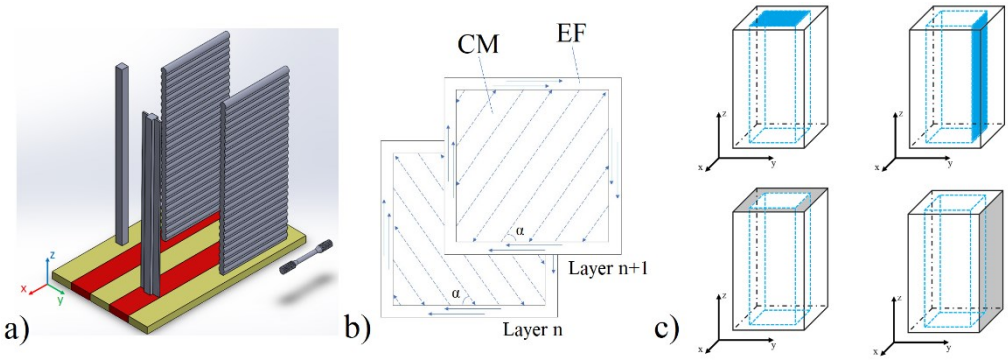


*Figure 5.1. (**a**) AlSi10Mg bars (10x10x300 mm) printed by a single (blue zones, grey bars) and by double lasers (yellow zone, white bars); (**b**) Scan strategy with α = 56.5° and contour thickness of 200μm; (**c**) Graphical representation of the different analyzed zones: the CM (light-blue) and the EF (grey).*

The other process parameters used for producing the bars are illustrated in *Table 5.2*.

Table 5.2. Process parameters used for producing AlSi10Mg bars and billets: external frame (EF) and center zone (CM).

Process parameters	Values for the CM	Values for the EF
Laser power	$370\ W$	$330\ W$
Scanning speed	$1400\frac{mm}{s}$	$600\frac{mm}{s}$
Layer thickness	$90\ \mu m$	
Hatch spacing	$70\ \mu m$	
Pre-heated build platform	$150\ °C$	
Laser beam diameter	$100\ \mu m$	
Energy density	$41.9\frac{J}{mm^3}$	$87.3\frac{J}{mm^3}$

The same process conditions were used to manufacture the billets which were mechanically processed to obtain 26 cylindrical samples having the dimensions illustrate in *Figure 5.2* according to ASTM E8/E8M – 13a standard specification. Due to the cutting, facing and contour touring operations performed on all tensile samples, the EF was removed and, therefore, all microstructural and pores analysis were related to the CM. For a better understanding of the results, the analysed tensile samples cross-section (*Figure 5.2*) can be considered as the CM_{XZ} (*Figures 5.1a*) thanks to the position of mutual parallelism between the tensile sample axis of symmetry and the xy plane of the build platform (*Figure 5.1a*).

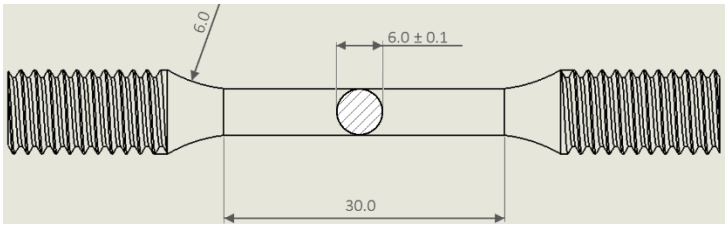


Figure 5.2. Graphical representation of a tensile sample obtained through turning operations from the billets. The green arrow indicates the build orientation, while the white circle the tensile sample cross-section.

Pores' analysis was performed with a DMi8 Leica© optical inverted microscope (OM) equipped with LAS-X 2D image analysis software. All samples were mechanically ground by SiC papers and subsequently polished with colloidal suspension. According to ISO 13322-1:2014, a measurement area has been systematically defined by considering 6 micrographs at a magnification of 100×. The relative density was calculated on the same polished surfaces where the Vickers microhardness tests were carried out. Focusing on the tensile samples, it was calculated (Appendix A) on their cross-section (*Figure 5.2*). A density of 2.68 $\frac{g}{cm^3}$ was considered for AlSi10Mg samples characterized by 0 % porosity as reported by [68].

In the present manuscript, bars were studied in the as built condition and after different heat treatments. Direct aging was performed at 175, 200 and 225 °C for 6 h, 8 h and 16 h while, for the T6 treatment, bars and billets were solution treated at 505 °C for 4 h, water quenched, and aged at 175 °C for 4 h. The temperature in the electric muffle furnace was controlled by a digital K-type thermocouple in contact with the samples. The microstructure of as built and heat-treated SL-90 bars was analyzed through optical and scanning electron microscopies (SEM: Nova NanoSEM, FEI thermo Fisher Scientific, Hillsboro, OR, USA); while the microstructural analysis of the DL-90 bars was omitted according to the study performed in [65]. For a better understanding, SL-90 and DL-90 indicate the single and double laser zones (*Figure 5.1a*), respectively, where the bars analyzed in this work were manufactured.

Vickers microhardness profiles were performed both on XZ and XY planes at the top and bottom regions, and distinguishing the CM and EF zones, in the as built and heat-treated bars. Three microhardness profiles, from the bottom to the top regions, were performed on each XZ plane (EF_{XZ}, CM_{XZ}), each consisting of 54 measures. On the CM_{XY} area, however, ten random measurements were performed. All HV measures were carried out with a load of 500 gf for an indentation time of 15 s according to UNI EN ISO 6507. Finally, Vickers microhardness values were also compared to as built and T6 heat-treated bars printed with a layer thickness of 50 μm analyzed in [65]. Whenever the results of this study are compared to those in [65], the present samples are referred to as

SL-90 (single-laser) and DL-90 (double-laser) whilst those from [65] are designated as SL-50 DL-50, referring to their different layer thickness of 90 μm (this work) and 50 μm [65], respectively.

Tensile tests were performed at room temperature with Z100 Zwick/Roell servo-hydraulic machine according to ASTM E8/E8M – 13a standard specification.

3. Results

3.1. Microstructure and Porosities Before and After Heat Treatments

The as built microstructure of EF_{XZ} is reported in *Figures 5.3a,b* where the cross-section of the laser scan tracks can be observed. Their geometry is conferred by the scan strategy reported in *Figure 5.1b*. Focusing on the high magnification micrograph (*Figure 5.3b*) of the EF_{XZ} zone (*Figure 5.3a*), the microstructure shows the presence of columnar grains between two overlapped laser scan tracks, while the equiaxed grains within the layer as discussed in [67] through the CET (columnar-to-equiaxed transition). Higher magnification SEM micrographs show (*Figures 5.3c,d*) the α-Al matrix (yellow arrows, panel 1) surrounded by the Si-eutectic particles (yellow arrows, panel 2). *Figure 5.3d* is a SEM micrograph emphasizing the cellular structures that are formed during the SLM process of the AlSi10Mg alloy, as also reported by [237]. In *Figure 5.3b*, it is possible to observe the progressive refinement of the microstructure from the layer boundary to the center due to the heat fluxes generated during the SLM process. In fact, the boundaries of the laser scan tracks and of the molten pool are characterized by a coarse zone and heat affected zone (HAZ) [69,192].

The high magnification SEM micrograph shown in *Figure 5.4* illustrates the Si particles that precipitate within the α-Al matrix due to the L-PBF process [202,212]. At the same time, their amount increases from the bottom to the top regions due to the pre-heated build platform which influences the Si atoms diffusion from the SSS α-Al [65,184,212]. As discussed and analysed in [65], the pre-heated build platform induces not only an increase of Si particle amount but also the precipitation phenomena of the ε-Mg_2Si phase [184].

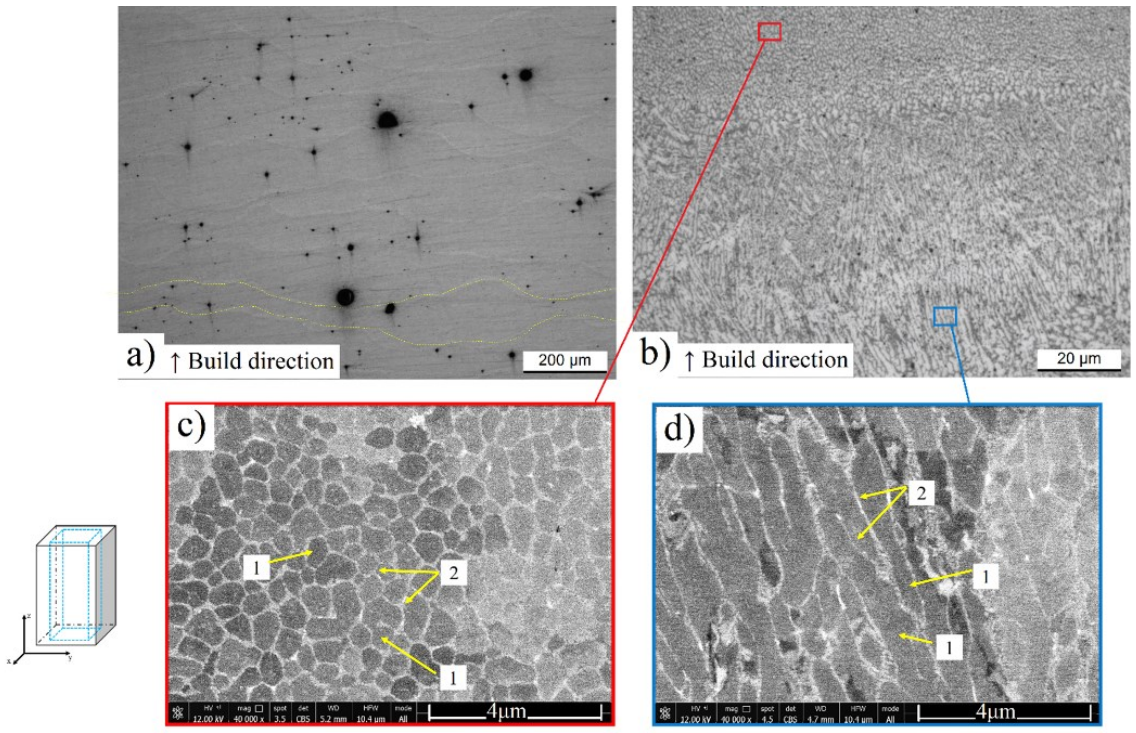


*Figure 5.3. (**a**) OM micrograph showing the microstructure of EFXZ in the as-built case. (**b**) High magnification micrograph of the microstructure shown in the panel. The dotted yellow lines indicate the boundaries of the scan tracks. The blue and red panels show SEM micrographs of the equiaxed (**c**) and the columnar (**d**) grains.*

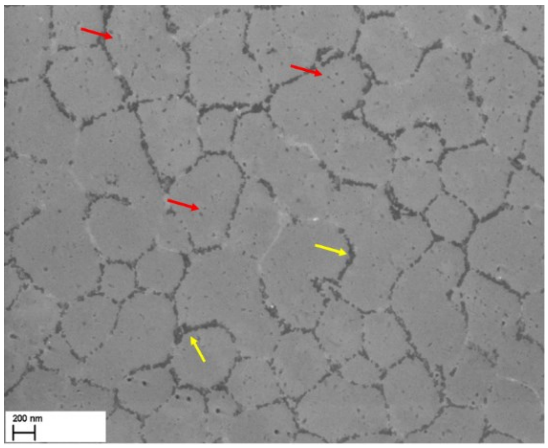


Figure 5.4. SEM micrograph of the as built AlSi10Mg samples where the yellow arrows indicate the Si eutectic network, while the red ones the Si particles that precipitate within the α-Al matrix.

Figure 5.5a is a micrograph of the CM_{XY} area showing the laser scan tracks' intersections. It is thus possible to observe different molten pools, characterized by the typical ellipsoidal shape. Their cross-sections along the XZ plane are shown in *Figure 5.5b* with the yellow dotted lines revealing their boundaries. The same optical micrograph reveals the two typical kind of pores: 1) spherical pores (< 100 µm) with a

circular geometry; 2) lack-of-fusion pores or LOF (> 100 μm) characterized by an irregular shape with their major axis direct on the XY plane [69]. The random pores' distribution, which is predominately formed by spherical pores, is visible in *Figures 5.5a,b* for the CM_{XY}, CM_{XZ} areas and in *Figures 5.5c,d* for EF_{XY}, EF_{XZ} zones, respectively. Usually, the LOF pores are localized between two adjacent molten pools due to an improper optimization of process parameters, or an inhomogeneous powder bed, or a material discontinuity arising from weak inter-particle bonding [69,72,305]. Spherical pores are instead generated by different gases present within the build chamber or trapped into the gas atomized powder (e.g Ar or N) due to its radial pressure distribution within molten Al [297,300,306].

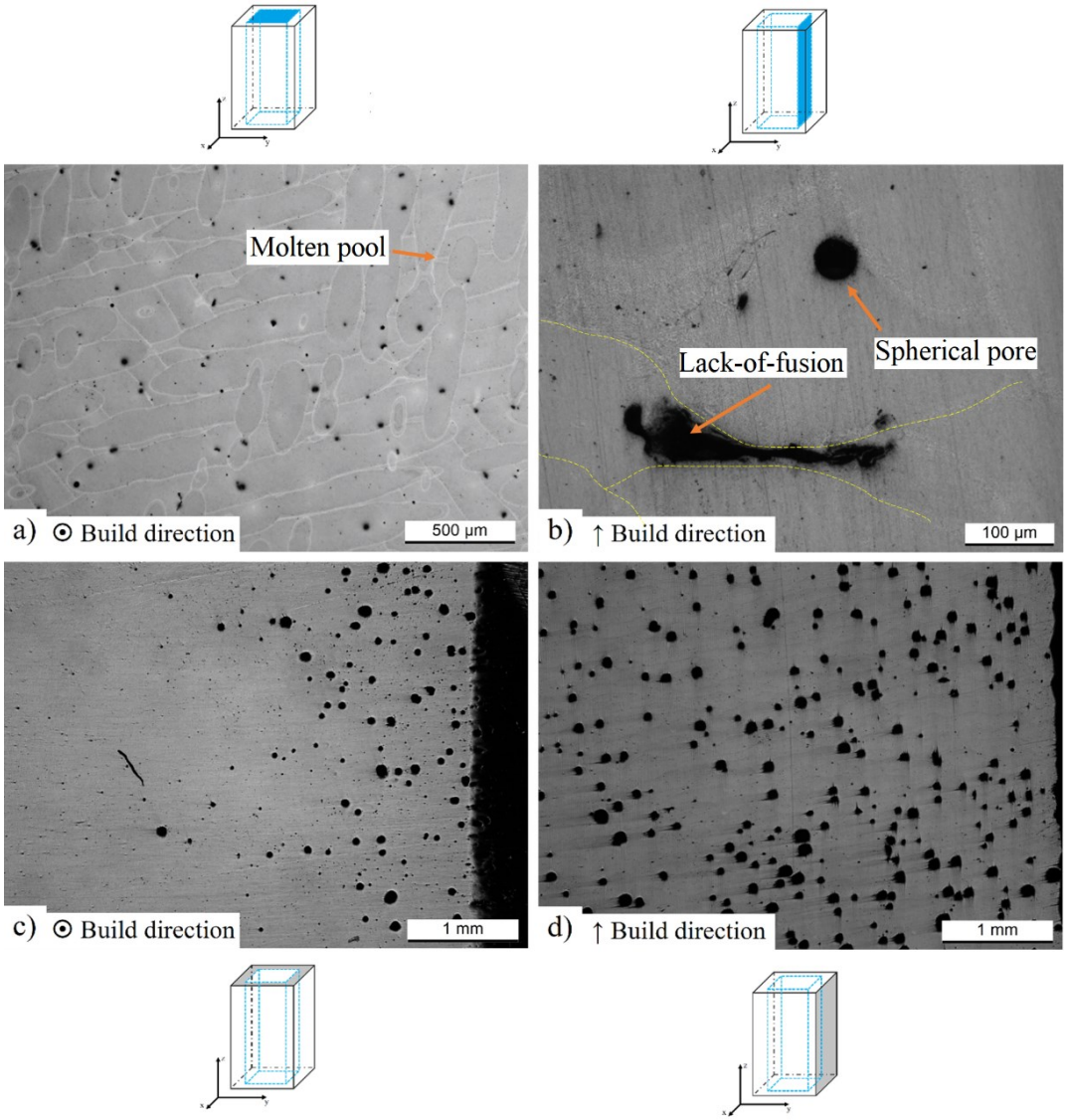


*Figure 5.5. OM micrographs acquired on CM_{XY} (**a**), CM_{XZ} (**b**), EF_{XY} (**c**) and EF_{XZ} (**d**). The yellow dotted lines indicate the molten pool boundaries.*

On the other hand, hydrogen is the only gas soluble in molten aluminium. Its absorption is caused by the decomposition of moisture in air ($2H_2O \rightarrow 2H_2 + O_2$) and/or by aluminium oxidation ($3H_2O + 2Al \rightarrow Al_2O_3 + H_2$) as reported by [115].

From an analytical point of view, the hydrogen pores can be formed during the L-PBF process of the AlSi10Mg alloy due to the combination between the short time (t_M) from melting to solidification of the molten pool and the terminal velocity (v_T) for the pores [89]. These quantities are expressed through the following Eq. (5.2) and Eq. (5.3):

$$t_M = \frac{l_M}{v_s} \tag{5.2}$$

$$v_T = \left(\frac{2g}{9\eta}\right) r_p^2 \tag{5.3}$$

where l_M is the molten pool length [m], v_s is the scan speed $\left[\frac{m}{s}\right]$, g is the acceleration of gravity $\left[\frac{m}{s^2}\right]$, η is the kinematic viscosity [St] of aluminium and r_p is the pore radius [m]. Pores nucleated at the melting front can escape easier from the pool than those nucleated on the solidification front (*Figure 5.6*) due to the position with respect to the interface between the molten pool and the atmosphere of the build chamber.

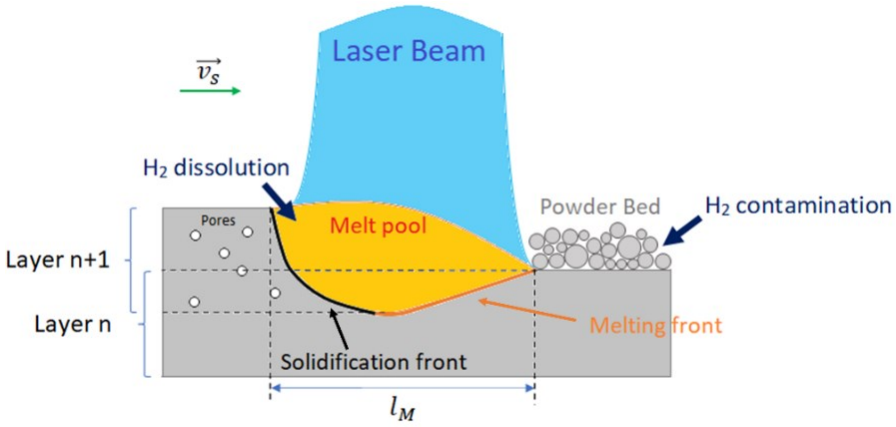


Figure 5.6. Schematic representation of gas pores formation during the SLM process.

Figure 5.7 shows the microstructure at low magnification after thermal treatments. *Figures 5.7a,b,c* illustrate the microstructure on the CM_{XY} surface after direct aging for 16 h at 175 °C, 200 °C and 225 °C, respectively. At the investigated magnification, only for the T6 heat treatment a coarsening of the Si particles is shown in *Figure 5.7d*. This is probably due to the rejection of Si from the supersaturated α-Al matrix during the SHT (Solution Heat Treatment), as reported by Li et al. [185]. The microstructural configuration that characterizes the L-PBF process remains partially visible even after the T6 heat treatment due to the accumulation of Si particles along the scan tracks or molten pool boundaries rather than at their center [258] as shown in *Figure*

5.7d. On the other hand, SEM observations illustrate that the eutectic silicon forming the network structure in the as built samples coarsens at 225 °C, as shown by the comparison of *Figure 5.8c* with *Figure 5.8a* (175 °C – 4 h) and *Figure 5.8b* (200 °C – 6 h).

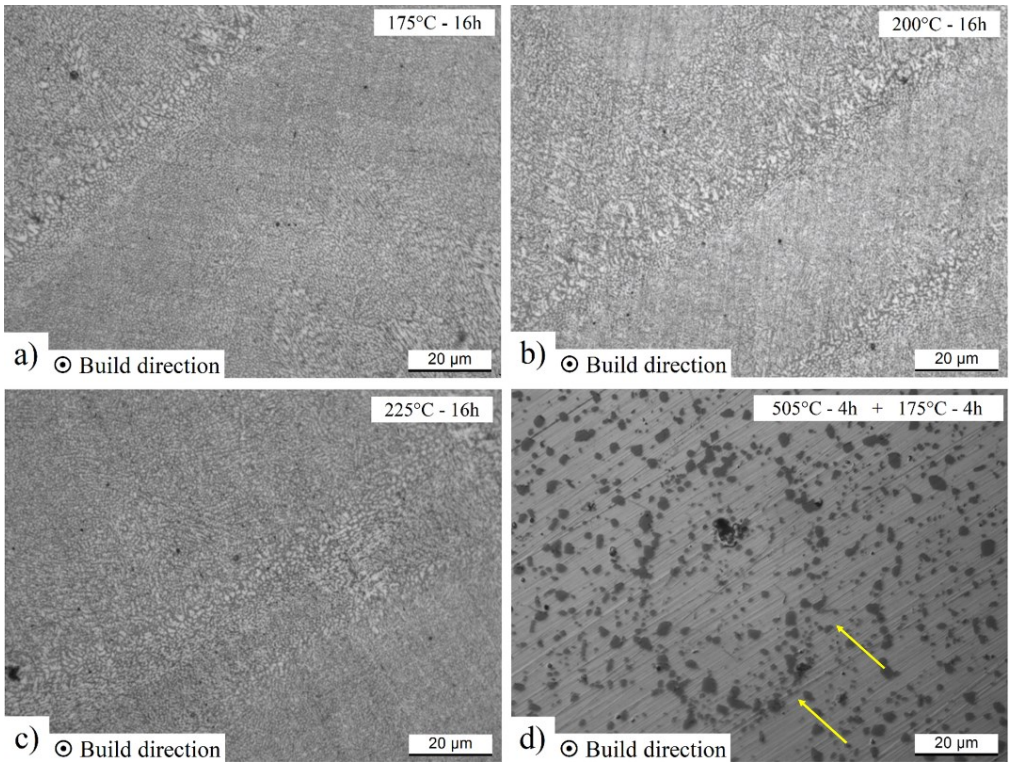


*Figure 5.7. Microstructure of the CMXY surface of AlSi10Mg bars after direct aging for 16 h at 175 °C (**a**), 200 °C (**b**) and 225 °C (**c**), and after the T6 heat treatment (**d**). The yellow arrows indicate a molten pool that remained visible after the T6 heat treatment.*

SEM micrographs (*Figure 5.8d*) also confirm the significant microstructural re-arrangement produced by the T6 heat treatment, with much coarser (note the different scale needed in *Figure 5.8d* to visualize the microstructure, compared to *Figures 5.8a,b,c*), re-crystallized α-Al grains, identifiable through their channelling contrast. Larger, polygonal Si particles are more randomly distributed and do not form a network surrounding extremely fine, cellular α-Al grains as it happened in the as-built and directly aged samples. Pores (indicated by yellow arrows) and acicular Fe-rich intermetallic (indicated by orange arrows) are also visible in this sample.

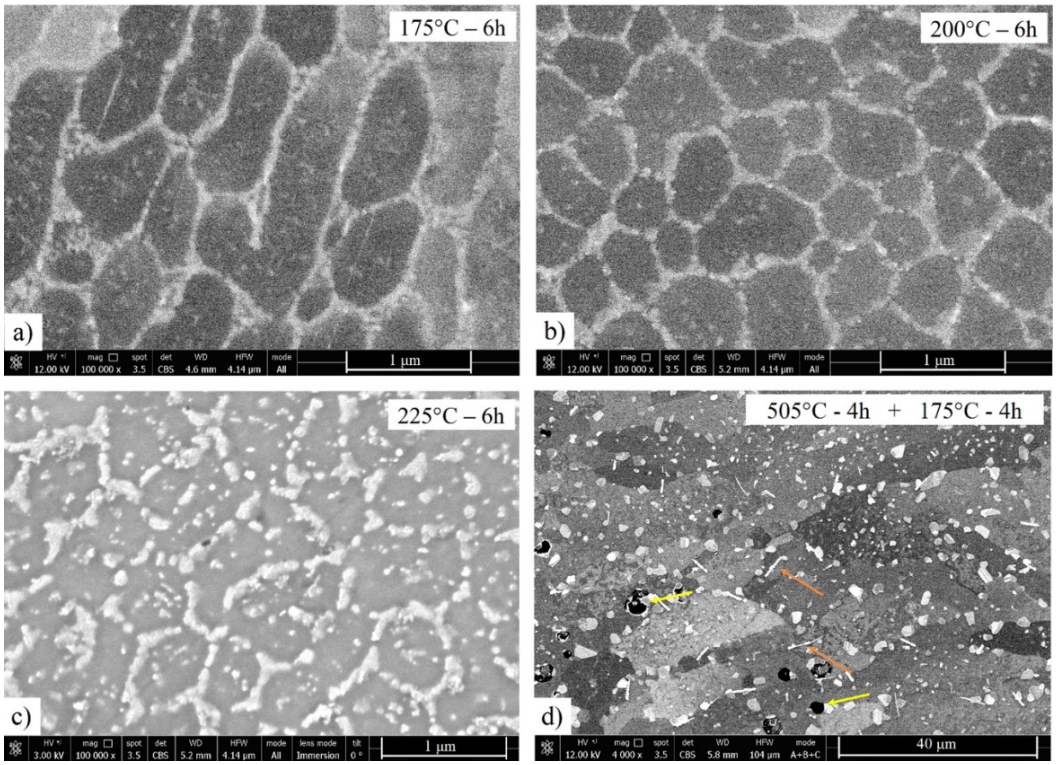


*Figure 5.8. SEM micrographs of AlSi10Mg microstructure after direct aging for 6h at 175 °C (**a**), 200 °C (**b**) and 225 °C (**c**), and after T6 heat treatment (**d**).*

The statistical results of image analysis of pores in as built bars are reported in *Figure 5.9*, for the SL-90 (*Figures 5.9a,b*) and DL-90 samples (*Figures 5.9c,d*) measured in the CMxz and the EFxz of the same bar. The analysis was performed at the bottom (*Figures 5.9a,c*) and top regions (*Figures 5.9b,d*) analyzing the relative frequency of the equivalent diameter of the pores (Appendix A). Focusing on the SL-90 case (*Figures 5.9a,b*), the CMxz surfaces on the bottom and top bars show analogous distributions of equivalent pore diameters (≤ 25 µm) with maximum frequency of 10 µm (about 40 % of all pores). So, the densities at the bottom and top samples are 99.62 ± 0.01 % $\left(2.67\ \frac{g}{cm^3}\right)$ and 99.76 ± 0.01 % $\left(2.67\ \frac{g}{cm^3}\right)$, respectively. On the other hand, the EFxz surfaces are characterized by several pores with a larger diameter (up to 125 µm); it can be emphasized that the statistical distribution of the EFxz in *Figure 5.9b* shows a homogeneous frequency of pores up to 80 µm. The densities of the bottom and top EFxz samples are lower than those related to CMxz surfaces being 97.74 ± 0.09 % $\left(2.62\ \frac{g}{cm^3}\right)$ and 97.22 ± 0.11 % $\left(2.61\ \frac{g}{cm^3}\right)$, respectively. This slight variation in density between top and bottom regions was obtained due to the almost similar ratio between the total pore area and the total analyzed area $\left(\sum_{j=1}^{6}\widehat{A}_j\right)$: 0.023 and 0.028, respectively. In more details, the top region is characterized by higher big pores than the bottom for the fact that the former shows 316

pores with a total area of $6.92 \cdot 10^5\ \mu m^2$ ($2190.4\ \mu m^2/pore$) and the latter 630 pores with a total area of $5.94 \cdot 10^5\ \mu m^2$ ($895.1\ \mu m^2/pore$). In this case, further investigations will be performed to understand what process conditions can influence the difference between these top and bottom regions in terms of pores dimension and quantity. The correlations between the SL-90 machine set-up and the energy density values, or between the bar position within the build chamber and the printing process may be taken as the main causes to analyze. Considering the DL 90 bars, all statistical distributions are narrower show higher values of relative frequencies (45–60 % for equivalent diameters of 10 μm) than the SL-90 bars, as also analyzed in Cerri et al. [65]. Similar to SL-90 bars, the distribution related to the EFXZ surface reveals the presence of a few very large pores (up to 150 μm) as shown in *Figure 5.5d*. The densities are 99.20 ± 0.06 % $\left(2.66\ \frac{g}{cm^3}\right)$ and 99.33 ± 0.02 % $\left(2.66\ \frac{g}{cm^3}\right)$ in the core (i.e. calculated from the CMXZ data) and 86.99 ± 0.22 % $\left(2.33\ \frac{g}{cm^3}\right)$ and 95.50 ± 0.09 % $\left(2.56\ \frac{g}{cm^3}\right)$ in the skin (i.e. calculated from the EFXZ data). *Figures 5.9e,f* show the statistical distribution of pore sizes on the CMXY surfaces of the SL-90 and DL-90 bars in as built conditions, comparing the bottom regions (black profile) to the top regions (red profile). In both graphs, a magnification of the equivalent diameter axis was considered comparing the *Figure 5.9e,f* with *Figures 5.9a–c*, for the following reasons: 1) the relative frequency tends to zero for sizes higher than 15 μm; 2) only the shape of the gas pores can be influenced by the low temperature of the pre-heated build platform. In this context, it is possible to observe that the build platform induces a slight difference between the bottom region and the top region in terms of quantity of small pores. In fact, the pores with an equivalent diameter lower than 5 and 7 μm for SL-90 and DL-90 bars, respectively, are characterized by a higher relative frequency considering the top region rather than the bottom region. The same results are obtained by [300]. On the other hand, comparing the results shown in *Table 5.3*, the bottom regions are characterized by larger pores than the top regions for all analyzed CM zones.

Table 5.3. Average values of the are per pore (μm²/pore).

	Bottom		**Top**	
	CMXZ	**CMXY**	**CMXZ**	**CMXY**
SL-90	149 ± 6	100 ± 3	85 ± 3	64 ± 3
DL-90	645 ± 25	640 ± 25	293 ± 12	246 ± 10

As noted in the Introduction, the energy density values affect the as-built material density more than does the pre-heating temperature of the platform.

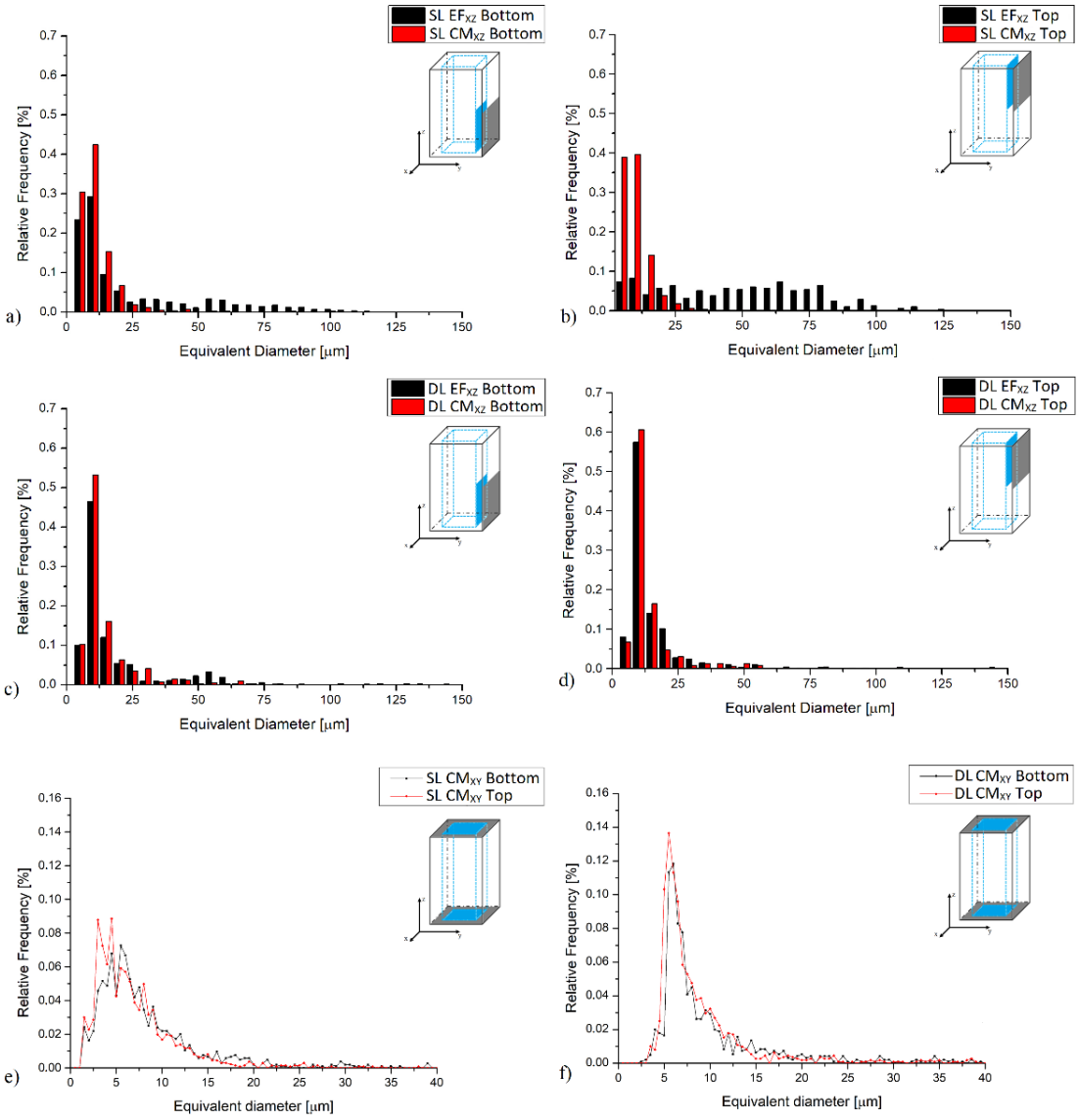


*Figure 5.9. Statistical distribution of porosity for SL-90 (**a**, **b**, **e**) and DL-90 (**c**, **d**, **f**) samples analyzed along EF_{XZ}, CM_{XZ} and CM_{XY} of the bars. The graphs (**a**, **c**) and (**b**, **d**) are referred to the bottom and top regions, respectively. (**e**, **f**) compare the bottom region to the top region.*

De facto, plotting the results (*Figure 5.10*) reported by other authors [68,69,134,173,179,184,214,253,307–309] a consistent trend emerges showing very low density (porosity) values at ED lower than 30 $\frac{J}{mm^3}$, while the maximum (~ 2.68 g/cm^3) at energy densities roughly comprised between 35 $\frac{J}{mm^3}$ and 60 $\frac{J}{mm^3}$, which includes the CM regions from the present work (35.8 $\frac{J}{mm^3}$; red points in *Figure 5.10*) and the L-PBFed AlSi10Mg bars analyzed in [65] (41.9 $\frac{J}{mm^3}$, blue point in *Figure 5.10*). The lower density

of the EF zones of the SL and DL AlSi10Mg bars studied in this manuscript (87.3 $\frac{J}{mm^3}$) is also consistent with the generally decreasing density at the highest energy densities.

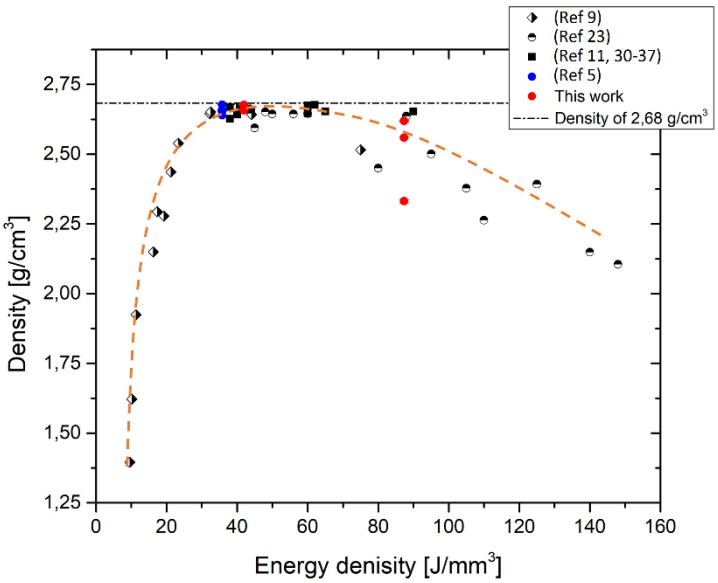


Figure 5.10. Density values as function of energy density obtained in the present study and reported in [5,9,11,30–37] which are replaced by [65,68,69,134,173,179,214,253,307–309].

Table 5.4 reports the density of the AlSi10Mg bars before and after heat treatments.

Table 5.4. Density values of SL and DL AlSi10Mg bars before and after heat treatments along the build direction and XY plane. The results from this work are also compared to the SL-50 and DL-50 samples previously characterized in [65].

Planes	HT conditions	SL		DL	
		Bottom	Top	Bottom	Top
CMXY - 90	As-built	99.87 ± 0.01 %	99.83 ± 0.01 %	99.15 ± 0.03 %	99.36 ± 0.02 %
	175°C/8h	99.81 ± 0.02 %	99.64 ± 0.02 %	-	-
	175°C/16h	99.72 ± 0.01 %	99.78 ± 0.01 %	-	-
CMXY - 90	200°C/8h	99.73 ± 0.02 %	99.60 ± 0.02 %	-	-
	200°C/16h	99.67 ± 0.02 %	99.66 ± 0.01 %	-	-
	225°C/8h	99.29 ± 0.02 %	99.29 ± 0.02 %	-	-
	225°C/16h	98.92 ± 0.02 %	99.19 ± 0.02 %	-	-
	T6	98.26 ± 0.08 %	98.03 ± 0.02 %	97.08 ± 0.12 %	98.07 ± 0.02 %
CMXZ - 90	As-built	99.62 ± 0.01 %	99.76 ± 0.01 %	99.20 ± 0.05 %	99.33 ± 0.02 %
	T6	98.15 ± 0.06 %	97.95 ± 0.04 %	97.58 ± 0.10 %	98.12 ± 0.08 %
CMXZ–50 [65]	As-built	99.00 ± 0.01 %	98.5 ± 0.03 %	99.9 ± 0.01 %	99.2 ± 0.05 %
EFXZ - 90	As-built	97.74 ± 0.09 %	97.72 ± 0.11 %	86.99 ± 0.22 %	95.50 ± 0.09 %

The percentage volume of pores increases with temperature. As a consequence, after the T6 heat treatment the density decreases from 99.87 ± 0.01 % $\left(2.68\ \frac{g}{cm^3}\right)$ to 98.26

± 0.08 % $\left(2.63\ \frac{g}{cm^3}\right)$ and from 99.83 ± 0.01 % $\left(2.68\ \frac{g}{cm^3}\right)$ to 98.03 ± 0.02 % $\left(2.63\ \frac{g}{cm^3}\right)$ at the bottom and top regions, respectively, in the SL-90 bar. The same density (porosity) trend occurs in the DL-90 samples, except for the difference between the bottom $\left(97.08 \pm 0.12\ \%, 2.60\ \frac{g}{cm^3}\right)$ and the top $\left(98.07 \pm 0.12\ \%, 2.63\ \frac{g}{cm^3}\right)$ regions. This trend is also reported by Majeed et al. [70], who analyzed the influence of T6 and T4 heat treatments on relative density and porosity of SLMed AlSi10Mg samples. Similarly, Girelli et al. [71] reported that SHTs at 510 °C and 540 °C reduce the relative density by 1.5 % and 3.7 %, respectively. *Figures 5.11a–d* illustrate the relationship between the maximum and the minimum dimensions of all pores (Appendix A) analyzed in the present paper (the black and red points are referred to pores in as-built and T6 heat-treated bars, respectively). Both *Figures 5.11a,b* (SL-90 bars) and *Figures 5.11c,d* (DL-90 bars) show an increase of the aspect ratio (AR) from the as built to the T6 heat-treated cases (Appendix A). In fact, the red linear fits (T6 samples) shown in *Figure 5.11* tend to get closer to the blue dashed lines (AR = 1) than the black linear fits (as-built samples). So, the T6 heat treatment induces a moderate spheroidization of the pores in the SL-90 and DL-90 bars. This is also directly illustrated by *Figure 5.12*, which does confirm a moderate rounding (Appendix A) of some pores (e.g. see the circled pore) when the same area (on the CM_{XY} surface) is imaged in the as built condition (*Figure 5.12a*) and after the T6 heat treatment (*Figure 5.12b*). Due to the exposure to the high temperature, the pressure variation at the interface between the gas and the material around it causes a variation of surface energy according to the Young-Laplace equation [224]:

$$\Delta p = \gamma\left(\frac{1}{R_1} + \frac{1}{R_2}\right) \tag{5.4}$$

where Δp is the pressure variation [Pa], γ is the interfacial tension [N/m] and R_1, R_2 are the principal radii of the sharp edges [mm]. Girelli et al. [71] explain the density variation through the increment of gas pressure within the pores consequently to the increase in temperature. If the temperature is sufficient to reduce the yield strength of the material around the pore, then the gas pressure can deform it.

On the other hand, Chaijaruwanich et al. [310] suggested the activation of inter-pores Ostwald ripening. Gu et al. [311] show the same tendency to reduce the pore surface energy after the solution heat treatments in the range between 530 and 540 °C.

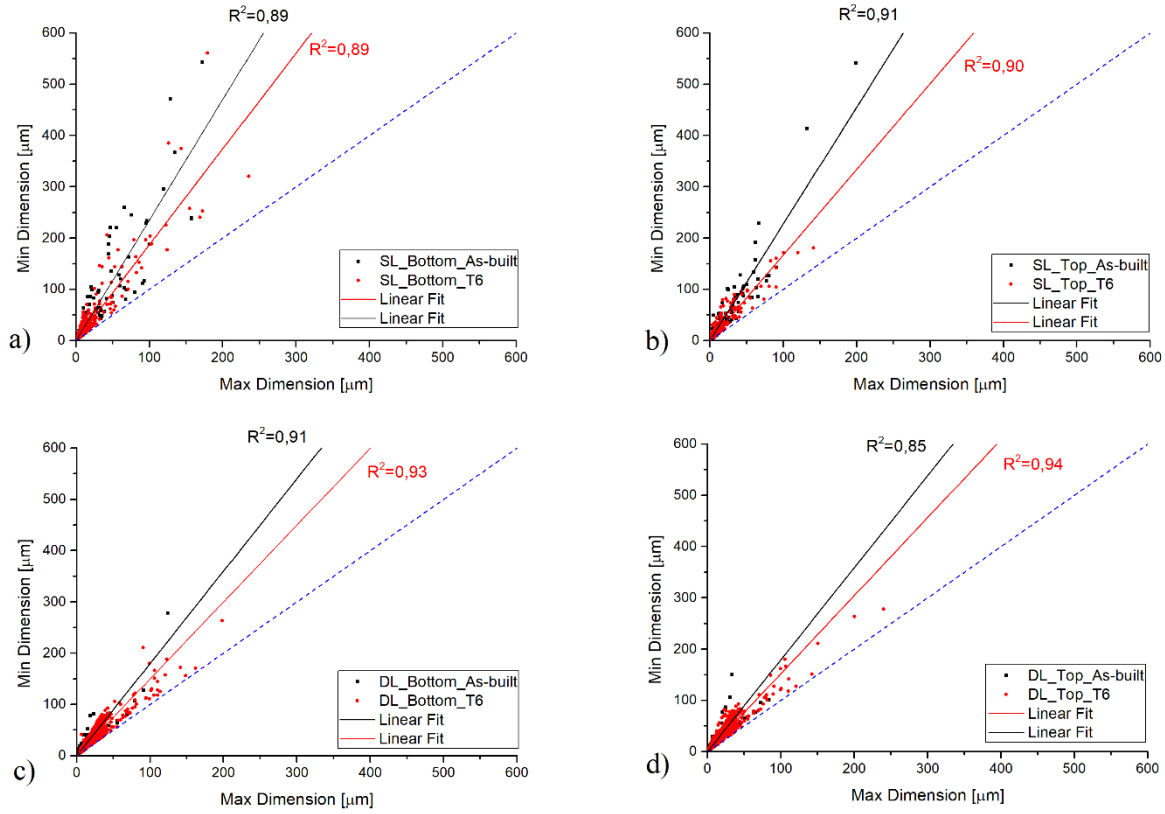


*Figure 5.11. Graphs show the maximum and minimum dimension of all pores analyzed before and after the T6 heat treatment for SL-90 (**a**,**b**) and DL-90 (**c**,**d**) bars. The dashed blue line represents the pore's aspect ratio equal to 1.*

Finally, the same authors [311] show the formation of small new pores during the T6 heat treatment as also shown in *Figure 5.12* (the arrow points out to a small pore formed after the T6 treatment, panel b, at a location where none was present in as-built condition, panel a).

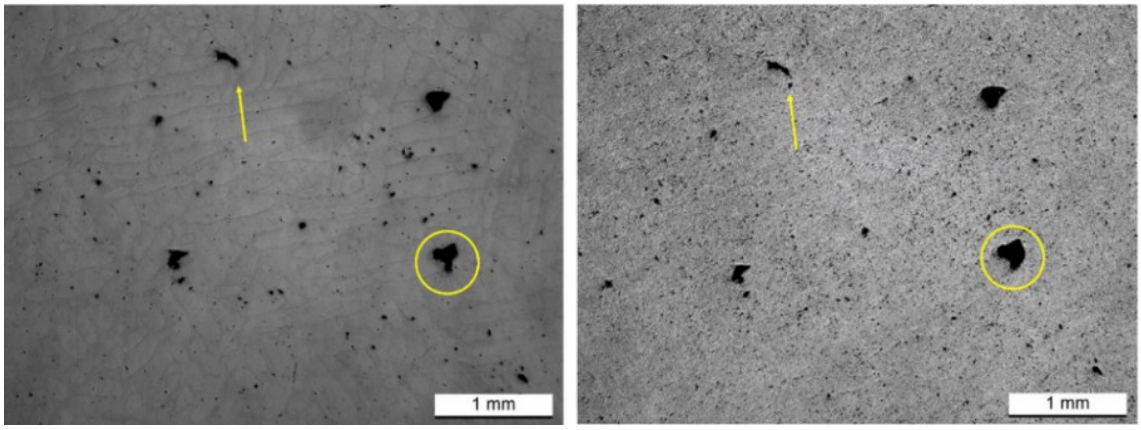


Figure 5.12. OM micrographs acquired at the same location on the CM_{XY} surface before and after the T6 heat treatment.

Figure 5.13 reports the roundness and the maximum dimension (length) of all analyzed pores, before (*Figure 5.13a*) and after the T6 heat treatment (*Figure 5.13b*). As previously reported, gas and LOF pores are characterized by a spherical shape with smaller (< 100 μm) size, and an irregular shape with bigger (> 100 μm) size, respectively. The orange (roundness > 0.5, length < 100 μm) and the yellow (roundness < 0.5, length > 100 μm) regions in *Figure 5.13* represent these different kinds of porosity. According to *Figure 5.13a* where 99.9 % of pores represent the spherical pores, the bars are characterized by a greater quantity of gas pores than LOF pores confirming the discussion about the graphs shown in *Figures 5.8e,f*. After the T6 heat treatment (*Figure 5.13b*) the pores' population piled even more toward roundness values close to 1. Accordingly, changes to the pores' distribution after the T6 heat treatment mainly concerned the pores with an equivalent diameter < 20 μm, as shown in *Figure 5.14a*. The red profile (T6 heat treatment) has lower relative frequencies for small pores (< 10 μm) than the black one (as built), and higher relative frequencies for pores with an equivalent diameter > 10 μm. The density variation after the T6 heat treatment can caused by the previously discussed phenomena [71,224,311].

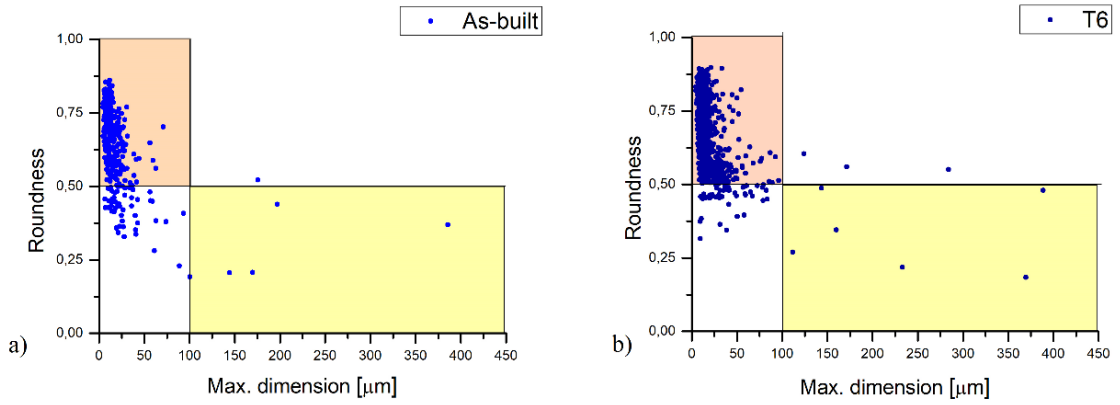


*Figure 5.13. Roundness and maximum dimension (length) of pores analyzed on the AlSi10Mg samples (XZ plane) in as-built (**a**) and after the T6 heat treatment (**b**).*

In addition, this variation can also occur due to the microstructural variation taking place during the SHT (*Figure 5.8*) and due to the precipitation phenomena induced by the artificial aging [70,275]. *Figure 5.14b* shows the same results obtained after the analysis of the tensile samples cross-section before and after the T6 heat treatment.

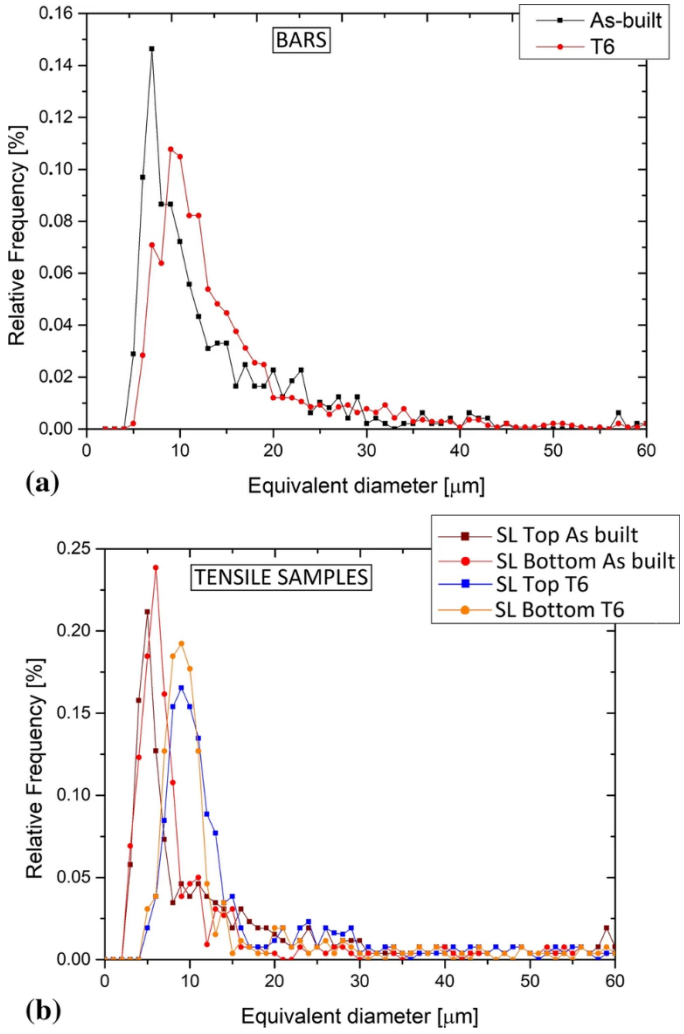


*Figure 5.14. Statistical distribution of pores before and after T6 heat treatment to the bars (**a**) and tensile samples (**b**).*

3.2. Analysis of Vickers Microhardness and Mechanical Properties

Figures 5.15a,b shows the Vickers microhardness profile (columns) of the bars along the build direction, over their entire 300 mm-length, together with the trends of density values (dashed-dotted lines) according to *Table 5.3*, for the SL-90 (*Figure 5.15a*) and DL-90 as built bars (*Figure 5.15b*). *Figure 5.15a* shows that, going from the bottom surface of the bar (z = 0) to the top surface (z = 300 mm), HV profiles measured along the z-axis exhibit a decreasing trend in both CMxz and EFxz planes, while the density values remain constant at 2.68 g/cm^3 and 2.62 g/cm^3, respectively. So, it is reasonable to assume that the decrease in HV depends on aging induced, in the L-PBFed AlSi10Mg bars, by the temperature of the SLM building platform, set at 150 °C. At this temperature, the Si and Mg-supersaturated Al matrix gives rise to the precipitation of very fine Si and Mg_2Si particles as illustrated in *Figure 5.4* [65]. Precipitation hardening is stronger at the bottom

of the bar than at the height of 300 mm due to the longer exposure time of the bottom region during the SLM process. The same decreasing trend of the SL EF_{XZ} profile along the z-axis is also found in SL CM_{XZ} values. The latter are approximately 10 HV higher due to the higher density in the CM region (a difference of 0.06 g/cm^3). A decreasing trend is analogously found in *Figure 5.15b* for the DL bar on both EF_{XZ} and CM_{XZ} surfaces, again due to aging effects. Notably, the HV profile on the DL EF_{XZ} surface shows a plateau in the bottom region, unlike all other measurements. This is probably due to the higher porosity: indeed, density changes by about 0.33 g/ cm^3 between the CM_{XZ} (2.66 g/cm^3) and the EF_{XZ} zones (2.33 g/ cm^3). The material is obviously weakened by higher porosity, counteracting the aging effects generated by the pre-heated build platform: the porous material indeed tends to collapse under the load transmitted by the pyramidal diamond Vickers indenter as reported by Tiwari et al. [301]. *Figure 5.14c* shows the Vickers microhardness profile measured on the XY plane (perpendicular to the build direction) of SL-90 bottom (orange columns) and top (brown columns) samples before and after the heat treatments. In the as-built conditions, the hardness difference between bottom and top samples is confirmed. After aging at 175 °C for 8 h, the hardness of the top samples increases (from 115 ± 5 HV to 132 ± 2 HV) due to precipitation phenomena, as demonstrated by Casati et al. [72] through DSC analysis. The bottom samples, on the other hand, might have faced an overaging process, and their microhardness decreases from 132 ± 3 HV to 127 ± 1 HV. As a result, the microhardness difference between the two regions is largely levelled out. After 16 h at 175 °C, HV values between top and bottom samples are fully homogenized, and the same is true for all the other direct aging heat treatments performed. The decreasing trend of the HV values with increasing treatment temperature is a combined effects of microstructural coarsening (*Figure 5.8*) and density variation [65].

The lowest HV values are found in the T6 samples, due to the complete microstructural change as reported in *Figure 5.8* as well as the increased porosity, as shown by the dashed curves. Whereas, however, the microstructural configuration of the bottom and top regions is completely homogenized after the T6 heat treatment, the ΔHV between the bottom and top regions (*Tables 5.5, 5.6 Figure 5.15*) is caused by the variation in density. For example, considering the DL bar (orange and yellow columns), the variation between bottom region (81 ± 2 HV) and the top region (86 ± 1 HV) is accompanied by a density variation of + 1 %. The same results are obtained with the SL-50 and the DL-50 AlSi10Mg bars analyzed in Cerri et al. [65]. The ΔHV between the top and bottom regions is confirmed by the mechanical properties variation in terms of ultimate tensile strength and yield strength as analyzed in [67].

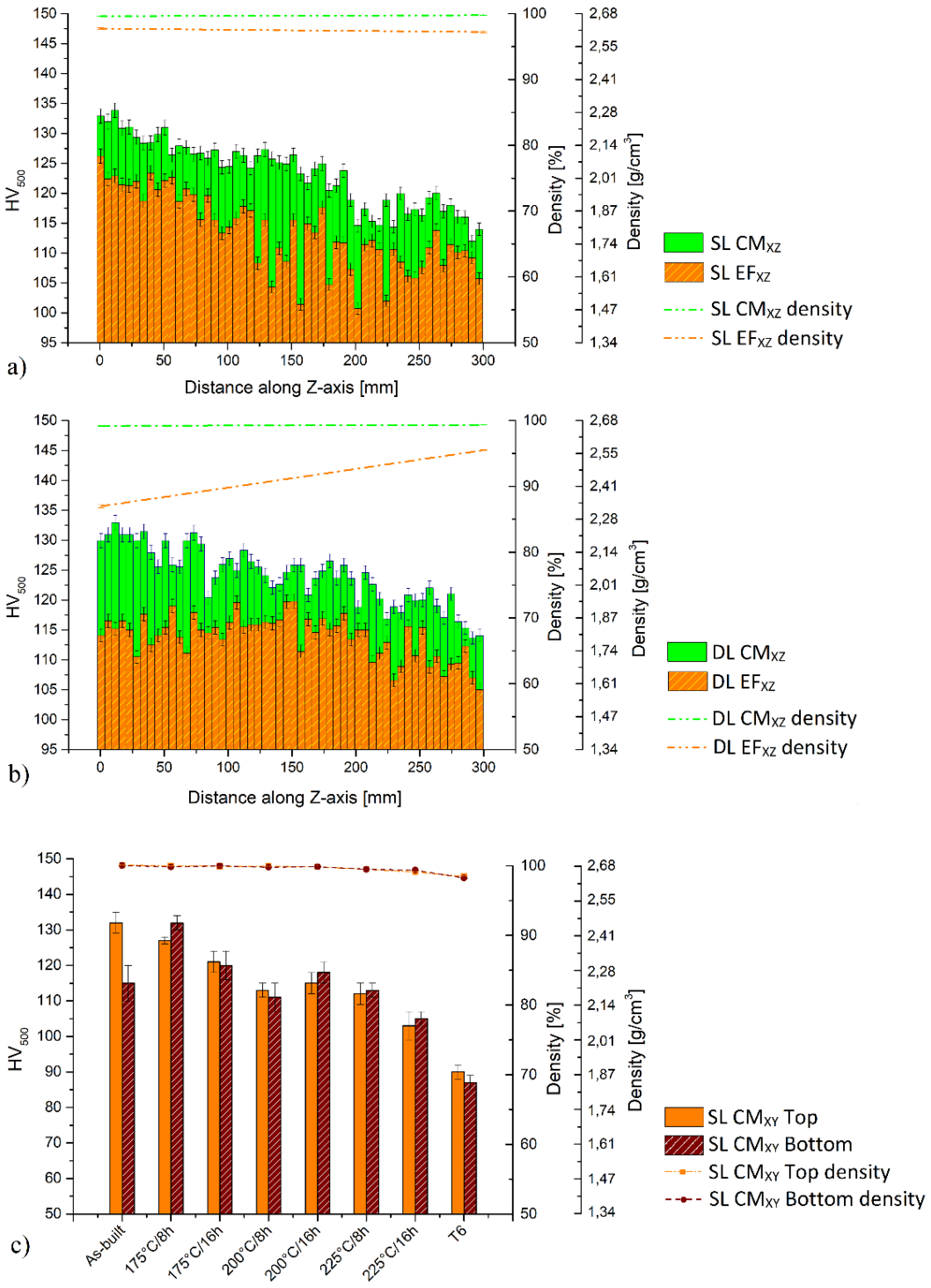


*Figure 5.15. Vickers microhardness profiles of as-built SL (**a**) and DL (**b**) AlSi10Mg bars performed along the EFXZ (orange columns) and the CMXZ (green columns) surfaces. (**c**) Vickers microhardness values of SL-90 AlSi10Mg bars measured on the XY plane before and after the T6 heat treatment. The dashed lines are referred to the density values.*

Table 5.5. Vickers microhardness and density values of the as-built and T6 AlSi10Mg bars.

AlSi10Mg bars		As built		T6	
		HV	Density [%]	HV	Density [%]
SL-90	Bottom	129 ± 3	99.87 ± 0.01	90 ± 2	98.26 ± 0.02
	Top	122 ± 4	99.83 ± 0.03	88 ± 3	98.03 ± 0.01
SL-50 [65]	Bottom	128 ± 3	99.00 ± 0.02	81 ± 2	97.17 ± 0.03
	Top	121 ± 4	98.50 ± 0.04	95 ± 2	98.06 ± 0.02
DL-90	Bottom	115 ± 5	99.15 ± 0.02	87 ± 2	96.30 ± 0.01
	Top	110 ± 3	98.07 ± 0.06	93 ± 3	97.20 ± 0.03
DL-50 [65]	Bottom	110 ± 2	99.90 ± 0.01	86 ± 1	98.03 ± 0.02
	Top	111 ± 5	99.2 ± 0.02	91 ± 2	97.08 ± 0.01

Table 5.6. Standard errors associated with the pore area.

	Areas	Standard error, [%]
1	$A_p < 1\ \mu m^2$	10
2	$1\mu m^2 \leq A_p < 10\ \mu m^2$	7
3	$10\mu m^2 \leq A_p < 30\ \mu m^2$	6
4	$A_p \geq 30\ \mu m^2$	4

The Vickers microhardness is directly correlated to and affected by the porosity [176] as illustrated in *Figure 5.16a*, where the effect of density on HV values is reported. In this graph, HV and density values analyzed in the present manuscript (orange, red and white symbols) were compared to those obtained in the literature (black square symbols) and [312]. Focusing on the same graph, the HV values related the top regions of the as built bars (orange symbols) show a behaviour fully comparable to that reported by [312]. Instead, the HV values associated to the bottom regions (red symbols) show higher microhardness values than those reported by [312] for the same densities, due to the higher permanence time on the build platform pre-heated at 150 °C than it occurred with the cubic samples in [312]. Finally, the T6 heat-treated bars show the same trend, namely a decrease in microhardness with decreasing density, but the curve is almost rigidly shifted toward lower HV values due to the microstructural changes as previously discussed (Section 3.1).

The correlation between the variation in density ($\Delta\rho$) and the microhardness variation (ΔHV) is also analyzed considering the same regions in as built condition and after the heat treatment. This experimental procedure nullifies the microstructural and precipitation contributions on the Vickers microhardness. Through the results obtained in this work (black symbols) the microhardness variation becomes larger as the increase of density grows larger, too. The largest density variations (0.25 g/cm^3 ÷ 0.35 g/cm^3), which are highlighted through the dotted yellow ellipse, were obtained considering the density values of the EF$_{XZ}$, CM$_{XZ}$ and CM$_{XY}$ bottom zones of the DL bar. In fact, as previously discussed through *Figure 5.4* and *Table 5.3*, the high $\Delta\rho$ between these zones

causes a strong decrease in the hardening effects induced by the precipitation phenomena. The changes in Vickers microhardness were correlated to the density variation through a linear fit (Eq. (5.5)) and a second-order polynomial fit (Eq. (5.6)):

$$\Delta\rho = 17.94\,\Delta HV - 18.58 \tag{5.5}$$

$$\Delta\rho' = 1.45\,\Delta HV^2 - 2.29\Delta HV + 15.43 \tag{5.6}$$

The second-order polynomial fit (blue curve in *Figure 5.16b* – Adjusted $R^2 = 0.90$) provides a better match to the data than the linear fit (red line – Adjusted $R^2 = 0.77$). In the same *Figure 5.16b*, the ΔHV and the $\Delta\rho$ values obtained from the results shown and discussed in [176] were plotted through the green symbols: their trend is also consistent with the polynomial fit. Moreover, it is possible to conclude that, even with the different L-PBF process parameters and the different heat treatment conditions employed in [176], the correlation between changes in Vickers microhardness and changes in sample density was unaffected.

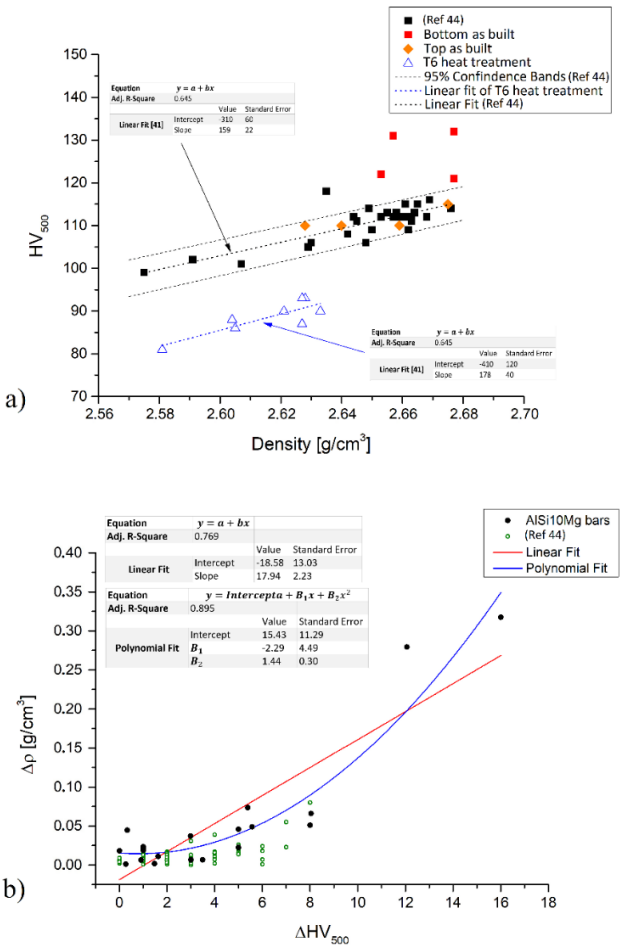


*Figure 5.16. **(a)** Effect of density on Vickers microhardness, **(b)** linear and polynomial fits between the microhardness and the density variation.*

Figure 5.17 illustrates the mechanical properties of the as built and T6 AlSi10Mg tensile samples in relation to the distance from the build platform. As previously discussed for the HV values (*Figures 5.14a,b*), also the UTS and YS values are characterized by decreasing trends from 0 to 300 mm due to the precipitation phenomena. The ductility values, instead, does not show the same trend most likely because the Si-eutectic network, which dominated the fracture mechanism of the as built samples, does not vary from bottom to top regions [65,237,282,291]. At the same time, the pores can be considered as a secondary contribution on the fracture mechanism due to the high-density values of the tensile test samples cross-section (*Table 5.4*) [117,313]. After the T6 heat treatment, the UTS and YS values were homogenized between the bottom and top regions due to the microstructural variation obtained after the SHT (*Figures 5.7, 5.8*). As concern the elongation values, which were analyzed in [237], part of the T6 heat-treated samples is characterized by a ductile fracture (also reaching 15 %), while another by a more fragile behaviour (reaching 7–9 %). Also in this scenario, the elongation values may be not significatively affected by the pores thanks to the high values shown in *Table 5.5*.

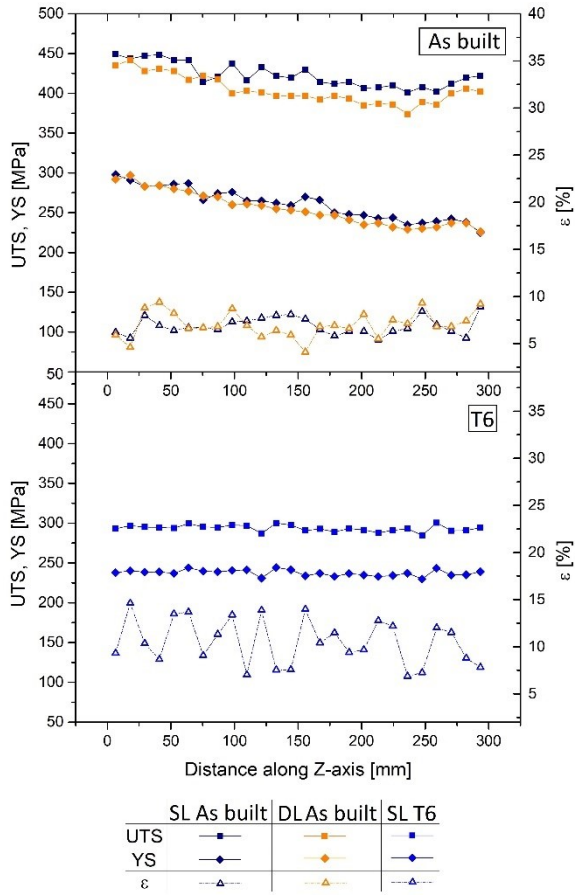


Figure 5.17. Tensile properties of the SL-90 and DL-90 as-built samples and of the T6 SL-90 AlSi10Mg samples.

4. Conclusions

The present paper studied the porosity in a laser powder bed fused Al-Si-Mg alloy and its relation to Vickers microhardness and mechanical properties. Direct aging and T6 heat treatments were also analyzed in terms of their effects on microstructure, pores and Vickers microhardness. Only the mechanical properties of the as built and T6 heat-treated samples were discussed due to their high-density values characterizing the CM of the direct aging samples. The following conclusions could be determined:

1. Lack-of-fusion pores (>100 μm, roundness < 0.5) and spherical pores (< 100 μm, roundness > 0.5) were found in all samples; but only the 0.01% of all pores consists of LOF pores.
2. As the build platform was pre-heated to 150 °C, the bottom regions of the CM zones are characterized by larger pores than the top regions. However, the greatest differences in density can be attributable to the energy density variation from 41.9 to 87.3 $\frac{J}{mm^3}$ between the center (CM) and external frame (EF) of the samples, respectively.
3. The as built bars are always characterized by a decrease in microhardness values along the total height (300 mm) in both CM and EF regions, due to the aging phenomena induced by the pre-heated build platform in the bottom region. In the bars built with a dual-laser scan, high porosity in the bottom layer ($\Delta\rho \approx 0.3$ g/cm^3) between the bottom and the top parts of the bar) partially offsets the effects of ageing. The same decreasing trend was observed even for the mechanical properties for both the single and dual-laser. In these cases, the amount of small pores and the high-density values do not take part significantly on ductility variation.
4. The T6 heat treatment induces moderate spheroidization and coalescence of the smallest pores (< 15–20 μm), as well as the formation of new pores. The complete destruction of the cellular structure that characterized the as built and directly aged bars and the reduction in density caused a remarkable decrease (– 30 %) of the Vickers microhardness in the T6 samples. This microstructural variation removes the effects induced by the pre-heated build platform.
5. Considering all samples in both as built and heat-treated conditions, the best fit between the relative density and microhardness variations is $\Delta\rho' = 1.45\ \Delta HV^2 - 2.29\ \Delta HV + 15.43$.

Appendix A

The pores' analysis was conducted according to ISO 46655-1:2014, and the measurements has been systematically performed on 6 micrographs at a magnification of 100× (*Figure 5.18a*) analyzing a total area of 24,936.41·10^3 μm² for each sample studied. The maximum and minimum dimension of each pore and its roundness were considered to evaluate the effect of T6 heat treatment. In the first case, the maximum and minimum dimensions (*Figure 5.18b*) represent the greatest (maximum Feret diameter) and the shortest (minimum Feret diameter) distance between parallel lines drawn through 2 points on a feature's boundary regardless of orientation, as textually reported in [219].

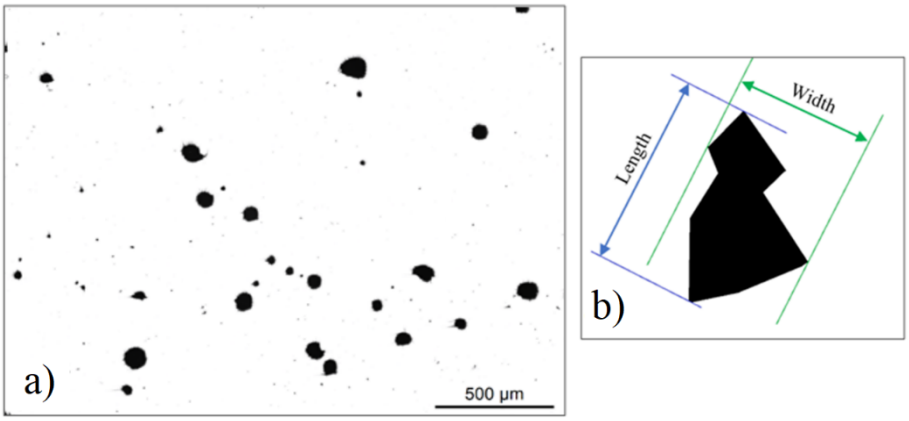


*Figure 5.18. (**a**) Binarized optical microscope image for image analysis and (**b**) graphical representation of length and width and pores according to [219].*

The ratio between the minimum and maximum Feret diameters defines the aspect ratio (AR) of the object analyzed. *Figure 5.10* illustrates the aspect ratio variation of all pores before and after the T6 heat treatment performed on bars manufactured via single and dual-laser machine set-up. In all graphs shown, the y- and x-axes represent the minimum and maximum dimensions, respectively, of all pores, while black and red lines the Linear Fits obtained by selecting all points and applying the automatic analysis of OriginPro 9.0.0 software. The same method was used to determine the square of the Pearson correlation coefficient (R^2). At the same time, the blue, green, and orange dotted lines were drawn considering the aspect ratios of 1, 0.5, and 0.1, respectively. For the three different lines, the following equations were considered:

$$y = x \tag{5.A1}$$

where y and x represent the minimum and maximum dimensions, respectively. *Figure 5.19* clarifies the interpretation of the plots reported in *Figure 5.10* showing a graphic schematization of the typical morphology in relation to the aspect ratio (AR) of pores [219]. The blue dotted line is referred to the AR equal to 1 (maximum dimension

coinciding with the minimum dimension), while the green and orange dotted lines to AR are equal to 0.5 and 0.1, respectively. These last functions are described by the following Eq. (5.A2) and Eq. (5.A3):

$$y = 2x \tag{5.A2}$$

$$y = 10x \tag{5.A3}$$

In the second case, the roundness (R) is defined as follows:

$$R = \frac{4\pi A}{p^2} \tag{5.A4}$$

where A and p are the are and the perimeter of the objects analyzed through the image analysis. The object is a circle if the R → 1, while it becomes less round of R → 0 [219]. The another considered parameter is the equivalent diameter defined as the diameter of a circle that is characterized by the same area of the object analyzed [219].

The average values of the pore per area [μm²/pore] were obtained as:

$$a = \frac{\sum_i (A_p)_i}{M} \tag{5.A5}$$

where A_p is the area of a single analyzed pore and M is the total pore's number.

The sample relative density was defined as follows:

$$a = \frac{\sum_i (A_p)_i}{M} \tag{5.A6}$$

where $\sum_{j=1}^{6} \widehat{A_j}$ is the area of the 6 micrographs analyzed for each sample, i.e. 24,936.41·10³ μm².

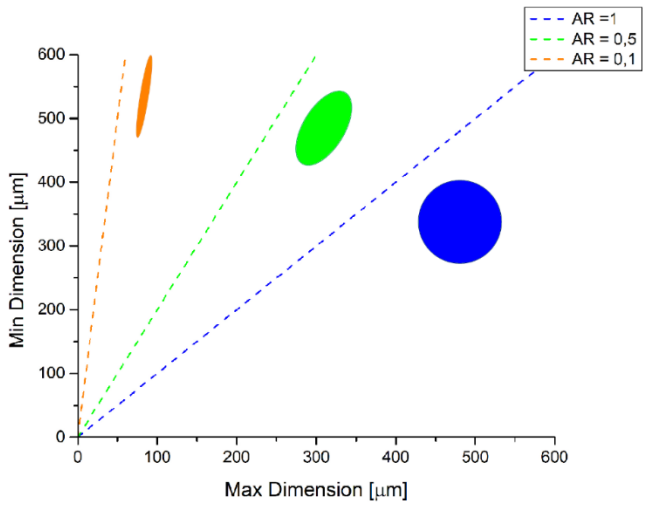


Figure 5.19. Graphical representation of the aspect ratio equal to 1 (blue line), 0.5 (green line) and 0.1 (orange line) to clarify Figure 5.12.

The standard errors ($\sigma_{\bar{x}}$) associated to pore area and consequently to the sample density were calculated by adding two contributions: one related to the operator and one to the OM device. The first contribution was calculated by comparing the objects' areas contained into two images shown in *Figures 5.20c, d*. The first image (*Figure 5.20c*) was drawn through GIMP-Image Manipulation Program to represent a micrograph with different kinds of pores (black objects) in terms of size, morphology, and area which was calculated through the automatic image analysis. These real areal values are obtained by selecting the only black pixels given that there is a perfect distinction between the central and external area of the black object (orange panel in *Figure 5.20c*). The second one (*Figure 5.20d*) shows the same image in *Figure 5.20c* but with pore boundaries that were artificially blurred to represent the real work conditions found during the manual image analysis. As a matter of fact, analyzing the high magnification optical micrographs, the pore boundaries appear blurred as represented in the orange panel in *Figure 5.20d*.

For evaluating the standard errors associated with each pore area, the automatic image analysis was carried out on *Figure 5.20c*, while the manual image analysis was performed on *Figure 5.18d* to evaluate the areas of the blurred black objects. This image was analyzed 20 times to obtain a good statistical population. So, the standard errors ($\sigma_{\bar{x}} = \sigma/\sqrt{N}$) were calculated through the standard deviation (σ) and the N observations and, subsequently, associated to the pore area as shown in *Table 5.6*.

By the fact that the standard errors were associated to the pore areas, it is necessary calculated an error (e_a) that will be associated with the density values, as follows:

$$e_a = \frac{\rho_{max} - \rho_{min}}{2} = \frac{\left[\left(1 - \frac{\left[\sum_i (A_p)_i\right]_{min}}{\sum_{j=1}^{6} \widehat{A_j}}\right) - \left(1 - \frac{\left[\sum_i (A_p)_i\right]_{max}}{\sum_{j=1}^{6} \widehat{A_j}}\right)\right]}{2} \quad (5.A7)$$

where ϱ is the relative density, and $\widehat{A_j}$ is the micrograph area (μm²). $\left(\left[\sum_i (A_p)_i\right]_{max}\right)$ and $\left(\left[\sum_i (A_p)_i\right]_{min}\right)$ are the overestimation and the underestimation of the total pore areas calculated applying the standard errors shown in *Table 5.6*.

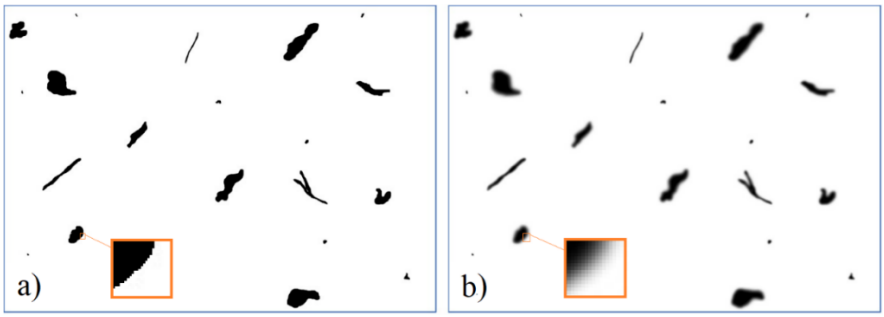


*Figure 5.20. Drawn image to evaluate the error contribution that can be caused by the operator during the image analysis: (**a**) clear image, (**b**) blurred image.*

ARTICLE 6

Effect of Surface Roughness and Industrial Heat Treatments on the Microstructure and Mechanical Properties of Ti6Al4V Alloy Manufactured by Laser Powder Bed Fusion in Different Built Orientations

---

Emanuela Cerri, Emanuele Ghio & Giovanni Bolelli

Materials Science and Engineering A, 851C (**2022**) 143635

https://doi.org/10.1016/j.msea.2022.143635

"The published Elsevier article is under the embargo period, so it is only available at the following DOI link: https://doi.org/10.1016/j.msea.2022.143635"

Effect of Surface Roughness and Industrial Heat Treatments on the Microstructure and Mechanical Properties of Ti6Al4V Alloy Manufactured by Laser Powder Bed Fusion in Different Built Orientations

Emanuela Cerri [1], Emanuele Ghio [1], Giovanni Bolelli [2].

[1] Department of Engineering and Architecture, University of Parma, Via G. Usberti 181/A, 43124, Parma, Italy.

[2] Department of Engineering "Enzo Ferrari", University of Modena e Reggio Emilia, Via P. Vivarelli 10/1, 41125, Modena, Italy.

Abstract

The emergence of powder bed fusion in recent years has made it one of the most demanded additive manufacturing technologies for Ti6Al4V alloys in the biomedical and aerospace industries due to its ease of part fabrication with complex geometry. However, Ti6Al4V components require a post-processing treatment to optimize their mechanical properties for engineering applications. The present study offers an analysis of the effects of different industrial heat treatments (704 °C for 120 min, 740 °C for 130 min) on the microstructure and tensile properties of Ti6Al4V samples manufactured by laser powder bed fusion in different orientations (Z, 45°, XY and XZ). These heat treatments were selected to improve the mechanical properties of the as-built material and to obtain samples representative of real industrial applications. SEM observations illustrated that the α' martensite grown in the columnar parent β-grains was converted into an α+β mixture after both heat treatments. EBSD showed that the newly formed α phase maintained, inside the parent β grains, the same orientation relationship as the as-built α' martensite. However, on a macroscopic scale, the α phase exhibited no preferential orientation. The heat-treated samples, which exhibited approximately 10 % lower ultimate tensile strength and yield strength than the as built samples but a 10–13 % higher elongation, were practically isotropic in their mechanical response. What little anisotropy was left was mainly attributed to few elongated interlamellar pores. The sandblasting process was also investigated; it did not affect the static mechanical properties of the samples but it reduced the Ra values by 25 %. Finally, Vickers microhardness vs. strength relationships were studied by considering the α-phase orientation.

Keywords: Ti6Al4V-ELI alloy; Laser Powder Bed Fusion; mechanical properties; crystallographic texture; hardness.

[*This page intentionally left blank*]

ARTICLE 7

Ti6Al4V-ELI Alloy Manufactured via Laser Powder-Bed Fusion and Heat-Treated below and above the β-Transus: Effects of Sample Thickness and Sandblasting Post-Process

---

Emanuela Cerri, Emanuele Ghio & Giovanni Bolelli

Applied Science, *12(11)* (**2022**) 5359

https://doi.org/10.3390/app12115359

“The following version of the manuscript is made available under the CC-BY-NC-ND 4.0 license”

https://creativecommons.org/licenses/by-nc-nd/4.0/

Ti6Al4V-ELI Alloy Manufactured via Laser Powder-Bed Fusion and Heat-Treated below and above the β-Transus: Effects of Sample Thickness and Sandblasting Post-Process

Emanuela Cerri [1], Emanuele Ghio [1], Giovanni Bolelli [2].

[1] Department of Engineering and Architecture, University of Parma, Via G. Usberti 181/A, 43124, Parma, Italy.

[2] Department of Engineering "Enzo Ferrari", University of Modena e Reggio Emilia, Via P. Vivarelli 10/1, 41125, Modena, Italy.

Abstract

Ti6Al4V-ELI is the most-used lightweight alloy in the aerospace industrial sector thanks to its high mechanical strength and corrosion resistance. The present paper aims, firstly, to evaluate the effects induced by different heat treatments, which were performed above and below the β-transus temperature on Ti6Al4V-ELI samples manufactured via Laser Powder-Bed Fusion in different orientations (XZ, XY, Z and 45°). The first set of tensile samples and bars were heat-treated at 1050 °C × 1 h, while the second and third set were heat-treated at 704 °C × 120 min following the AMS2801 standard specification, and at 740 °C × 130 min. These heat treatments were chosen to improve the as-built mechanical properties according to the ASTM F3001 and also ASTM F2924-14 standard specifications. Optical and SEM measurements reveal primary, secondary and tertiary α-laths below the β-transus, while above this temperature, the microstructure varies in relation to the sample's thickness. Secondly, this work analyzed the results obtained after a sandblasting process, which was performed on half of all the available heat-treated tensile samples, through XRD and Vickers microhardness measurements. XRD analysis also highlighted the presence of α_2-Ti_3Al and $TiAl_3$ precipitates and the microstructural change in terms of the α-phase.

Keywords: Ti6Al4V-ELI; α-colonies; Widmanstätten microstructure; sample thickness; Laser Powder-Bed Fusion; mechanical properties optimization; heat treatments; sandblasting process; α-case.

1. Introduction

Metallic materials for aerospace applications must be characterized by high mechanical strength, toughness and corrosion resistance at high and low temperatures [314–317]. Commercially, pure titanium and its alloys are widely used in this application field; 155,000 kg of these materials were used in 2020 alone [318]) as inter-tank structures (also in the cryogenic stage of launch vehicles), cockpit window frames, wing boxes,

fasteners, turbo engine parts, and for the aircraft fuselage, thanks to their low density (~ − 60 % of steel) [52,315,319]. In addition to the light-in-weight requirement, Singh et al. [316] add good durability (generally 4k–8k h and 30k–60k h for military and commercial airlines, respectively), low costs (initial cost for purchasing and maintenance) and good fabricability as desirable features for aeronautical parts. Additive Manufacturing (AM) technologies meet these latter requirements in addition to reducing the design and manufacturing time with respect to the conventional manufacturing processes [314,320]. Moreover, considering the "buy-to-fly" ratio, which is the ratio between the weight of the raw material used to manufacture the mechanical component and the weight of the final component, it reaches 10:1–20:1 for wrought-based conventional manufacturing. In opposition, "buy-to-fly" of AM of metals approaches a ratio of 1:1 due to its high material utilization in AM, the short production cycle and minimal use of tool machines [321–323]. As a matter of fact, AM technologies allow researchers to obtain a 3D physical object through the successive addition of material (layer-by-layer) following a CAD (Computer-Aided Design) project, which is converted into an .stl file before the manufacturing process [33,42]. Despite these advantages, Froes et al. [314] affirmed that only 8.2 % of the aerospace industry has adopted rapid-prototyping technology, while Gibbons et al. [324] underlined that the certification and qualification of the Laser Powder-Bed Fusion (L-PBF) process, which is an AM technology, do not differ from the conventional manufacturing process in the aerospace field.

L-PBF is a technology wherein a laser source scans and melts a powder bed that is deposited by a roller or recoater on the build platform [33]. To obtain a fully dense and high-quality sample, the following full melting criterion proposed by Tang et al. [60] must be satisfied:

$$\left(\frac{h}{W}\right)^2 + \left(\frac{t}{D}\right)^2 \leq 1 \tag{7.1}$$

where h [μm] and t [μm] are the hatch spacing and the layer thickness, respectively, while W [μm] and D [μm] are the width and the depth of the molten pool, respectively. In other words, the main process parameters that characterize the L-PBF process (laser power P [W], scanning speed v [mm/s], hatch spacing h [mm] and the layer thickness t [mm], and influence the molten pool dimensions, need to be optimized [137,325,326].

Ti6Al4V-ELI (Extra-Low Interstitial) is an α + β alloy at room temperature that contains Al and V elements as α- and β-stabilizers, respectively. In addition, the O, N and C atoms (in a small amount) stabilize the hcp (hexagonal closed packed) α-phase, while Fe stabilizes the bcc (body-centered cubic) β-phase [33,327,328]. Due to the high cooling rate (up to 10^8 K/s, [33]) that characterizes the L-PBF technology, the as-built microstructure of the Ti6Al4V-ELI sample is totally or partially formed by α'-martensite

contained within columnar β-grains arranged parallel to the build direction [329,330]. Generally, the UTS (Ultimate Tensile Strength) and YS (Yield Strength) values of as-built Ti6Al4V-ELI samples reach values higher 1.1 and 1.0 GPa, respectively, which decrease when the temperature of the pre-heated build platform or the percentage of decomposed α'-martensite are increased [33,153,331,332]. As a matter of fact, there is $\alpha' \rightarrow \alpha$ decomposition and a subsequent loss in mechanical properties of the as-built sample if the build platform is kept at high temperature (T > 400 °C, the temperature at which the martensite decomposes [333–335]) and/or due to the different values of energy density used $\left(E = {}^{P}/_{vht}, \left[\frac{J}{mm^3}\right]\right)$. At the same time, the ductility is often lower than 9 % and, consequently, the minimum tensile properties required by the F3001-14 standard specification are not satisfied [328]. In this scenario, optimized heat treatments can be necessary to obtain an improved balance in mechanical properties. Due to the chemical composition of the Ti6Al4V-ELI alloy and the phase transformations that can take place during different cooling pathways, its mechanical properties can be improved and/or tailored through different heat treatments performed below or above the β-transus temperature [33,336–338]. In particular, the as-built UTS and YS always decrease for each heat treatment performed on the as-built samples [33]. As a matter of fact, also considering a fully martensitic microstructure obtained in solution heat-treated and water-quenched samples, the UTS and YS are lower than 1.0 GPa and 950 MPa, respectively, due to the presence of recrystallized equiaxed β-grains [339–341]. At the same time, the elongation values do not show continuous growth with increasing heat-treating temperatures and time due to the following reasons: firstly, the presence of columnar β-grains, which significantly influence the fracture mechanisms, remains even after the heat treatments performed below the β-transus; secondly, defects generated during the L-PBF process play a fundamental role in the premature failure of samples [33,342]. On the other hand, the best balance between tensile strength and good elongation values (16–18 %, [33]) was obtained through the bimodal microstructure achieved after cyclic annealing heat treatments [329,343].

As previously discussed, the Ti6Al4V-ELI alloy is characterized by lower contents of oxygen (max 0.13 %), nitrogen, carbon and iron than the similar Ti6Al4V alloy. This difference in chemical composition confers improved values of ductility and fracture toughness, which are required in the aerospace sector. At the same time, the surface finishing of the Ti6Al4V-ELI sample is often correlated with air/gas flow problems correlated with the aerospace applications, but there are other reasons why aerospace engineering components require suitably low roughness. In fact, this is correlated with improved corrosion and wear resistance and with reduced friction during sliding contacts; moreover, it allows the uniform coverage of a component with

a thin film coating [344–346]. Surface roughness also has a huge impact on the fatigue life of a component, which is another important factor within the space and aerospace fields [347,348]. Möller et al. [349] correlated the surface roughness with fracture toughness, but no research concerning the effects on mechanical properties of Ti6Al4V-ELI samples was found in the literature.

The present paper aims to evaluate the microstructural effects induced by different heat treatments and the resulting mechanical properties, which are compared to the current standard specifications. Firstly, it analyzes the effects of two heat treatments performed below the β-transus temperature at 704 and 740 °C following the aeronautical standard specification (AMS 2801B); secondly, it analyzes the effects of the solution heat treatment at 1050 °C, which will be the starting point of future aging heat treatments. In addition, the present work studies the impact of the different heat treatments on samples characterized by different thicknesses. As a matter of fact, distinct aerospace components can possess widely different thicknesses, which can have an effect on their microstructures. Finally, the effects induced by the sandblasting process on the heat-treated samples are evaluated in terms of mechanical properties and surface characteristics.

2. Materials and Methods

Ti6Al4V-ELI powder (Tekna, Sherbrooke, QC, Canada) was used to manufacture tensile samples and bars via laser powder-bed fusion technology. The powder used was characterized by a granulometry between 20 and 60 μm and by an apparent density higher than 2.2 g/cm^3. Its chemical composition is reported in *Table 7.1*.

Table 7.1. Nominal chemical composition of Ti6Al4V-ELI in wt%.

Elements	Ti	Al	V	C	Fe	O	N	H	Y
wt.%	Bal.	6.47	4.06	0.01	0.21	0.09	0.01	0.001	< 0.001

Figure 7.1a shows a representative batch formed by 24 tensile samples and four bars directed along different directions, i.e., 0°$_{XZ}$ (blue), 0°$_{XY}$ (red), 45° (green) and 90°$_Z$ (yellow), considering their major axis of symmetry. For a better understanding of the results, the tensile samples and bars were designated as reported in *Table 7.2*, where their dimensions are also listed. Three batches (*Figure 7.1a*) were manufactured through the SLM®280 (SLM solutions, Lübeck, Germany) machine following the skin-core scan strategy reported in *Figure 7.1b*, wherein the red dotted arrows indicate the laser directions. The laser scan tracks were parallel to each other and inclined by 56.5° with respect to the base of the external frame. Each layer (n) was rotated by 67° with respect

to the previously solidified layer (n − 1). To manufacture all tensile samples and bars, the following process parameters were used: scanning speed of 1250 mm/s, laser power of 340 W, hatch spacing of 120 μm and layer thickness of 60 μm. The build platform was heated at 80 °C.

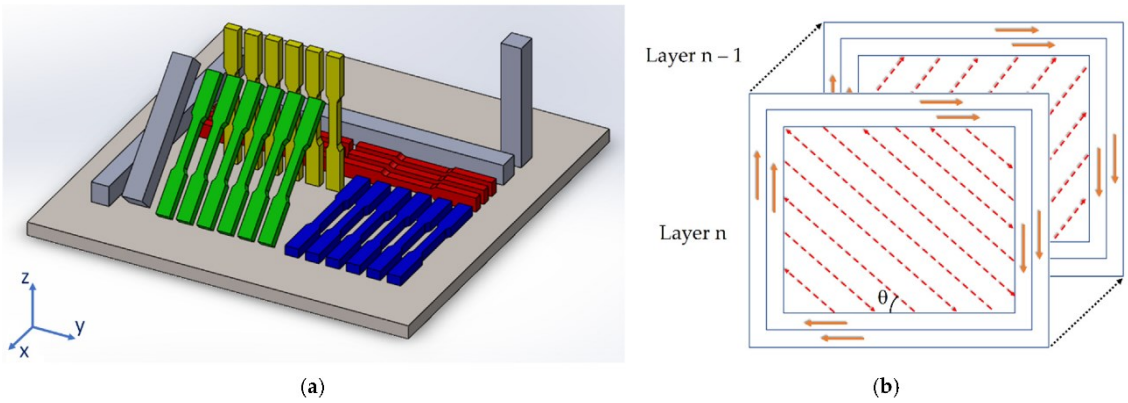


Figure 7.1. ***(a)*** *Solidworks (Dassault Systèmes, Waltham, Québec, Canada) drawing of tensile samples manufactured along the 0°XZ (blue), 0°XY (red), 45° (green) and 90°Z (yellow) directions and of bars grown along the same directions;* ***(b)*** *skin-core scan strategy where θ is 56.5° and the orange and red arrows indicate the laser scans directions.*

Table 7.2. Nomenclature used in the present paper for all tensile samples and bars and their dimensions.

Samples	Nomenclature	Colour	Length [mm]	Width [mm]	Thickness [mm]	Cross-Section Area [mm²]
Tensile samples	0°XZ-sample	Blue	10.0 [1]	6.0 ± 0.1 [1]	6.0 [1]	36
	0°XY-sample	Red				
	45°-sample	Green				
	90°Z-sample	Yellow				
Bars	0°XZ-bar	Grey	25	10	10	100
	0°XY-bar					
	45°-bar		10			
	90°Z-bar					

[1] Dimensions in agreement with the E8/E8M-16a standard specification.

All batches were heat-treated at three different temperatures below (704 and 740 °C) and above (1050 °C) the β-transus following the time–temperature curves reported in *Figure 7.2*. All treatments were performed in a vacuum furnace where the samples were cooled in argon gas for 1 h. The first batch was heat-treated at 704 °C for 2 h (704 °C/120′) following the ASM2801 standard specification, the second at 740 °C for 130 min (740 °C/130′) and the third at 1050 °C for 60 min (1050 °C/60′). The latter two heat treatments were performed to obtain a possible balance between strength and ductility to satisfy the ASTM F3001 standard specification. Focusing on the 740 °C/130′, the cooling pathway (red curve) was formed by the first step down to 520 °C in 90 min and the second down to room temperature in argon gas.

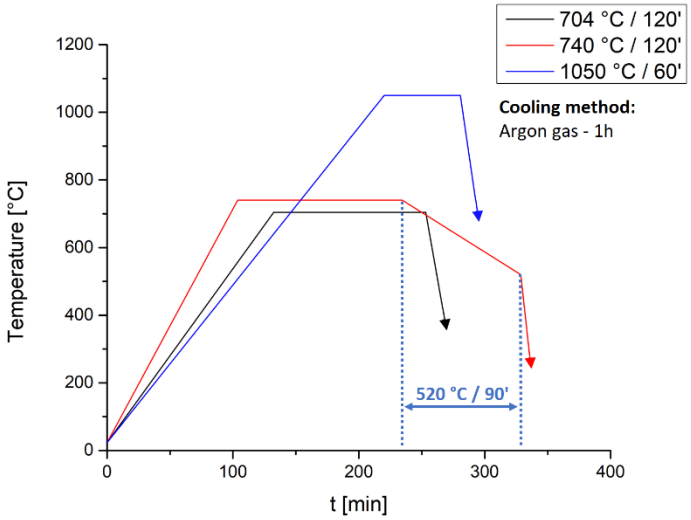


Figure 7.2. Temperature–time curves related to the heat treatment (704 °C/120 min, 740 °C/130 min and 1050 °C/60 min) studied in the present work.

After the heat treatments, a set of samples for each batch (*Figure 7.1a*) was sandblasted (SB) through a glass micro-sphere characterized by diameters between 200 and 300 μm. The process was performed manually with a distance of 300 mm from the sample surface and a pressure of 7 MPa. For a better understanding, all sandblasted samples will be called SB, while those characterized by an "as fabricated" surface will be called no-SB. Before and after the sandblasting process, the surface roughness was measured through an optical 3D profilometer (Taylor Hobson, Leicester, England).

To evaluate the mechanical properties of the both SB and no-SB samples after the different heat treatments, the tensile tests were performed at room temperature with a Zwick/Roell Z100 (ZwickRoell, Einsingen, Germany) machine using a strain rate of 0.0167 s^{-1}. Three tensile samples were tested for each direction in SB and no-SB conditions, respectively.

Vickers microhardness measurements were performed using both 500 gf ($HV_{0.5}$) and 100 gf ($HV_{0.1}$) loads and a 15 s indentation time according to the UNI EN ISO 6507-1:2018 standard specification. In the first case, 500 gf was used to evaluate the Vickers microhardness of all samples and bars. Each $HV_{0.5}$ value was obtained as an average of nine measurements arranged within a 3 × 3 matrix where indentations were spaced 1 mm from one another (*Figure 7.3a*). On the other hand, 100 gf of load was used to evaluate the microhardness of the α-colonies, α-laths arranged in a basketweave structure, and α_{GB} (Grain Boundary). Finally, three microhardness profiles (*Figure 7.3b*) were performed along on the cross-sections of the 90°$_Z$-samples heat-treated at 704, 740 and 1050 °C to analyze the effects induced by the sandblasting process on the surface of

the SB samples. Each profile was formed by 15 indentations that were 500 μm apart, except for the 2nd from the 1st and 3rd and the 14th from the 13th and 15th, which were spaced 250 μm apart. These chosen distances satisfy the following relationship: $\delta > 2d_m$, where δ and d are the distance between two successive indentations and the average value of the indentation's diagonal, respectively.

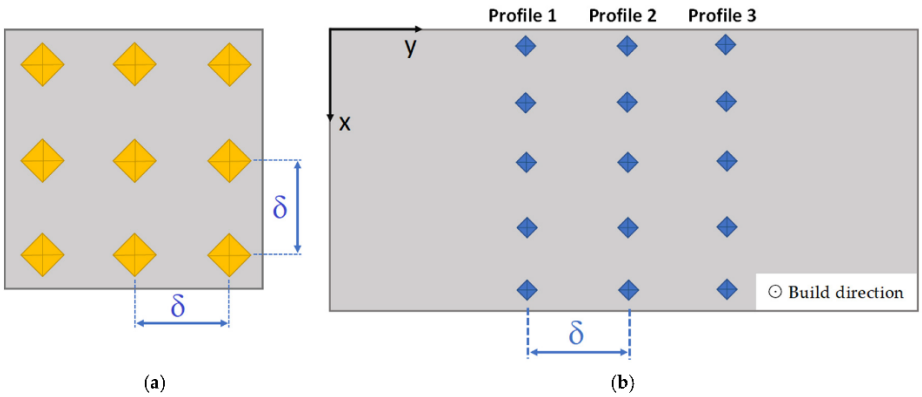


*Figure 7.3. (**a**) Matrix of 3 × 3 indentations where d is 1 mm of space between two adjacent indentations; (**b**) Vickers microhardness profiles performed on cross-section of the heat-treated 90°z-samples after and before the sandblasting process. Each profile is separated by δ.*

The heat-treated microstructures and the effects induced by the sandblasting process on the sample surface were analyzed through the DMi8 Leica optical microscope (Leica, Wetzlar, Germany) and the SEM Nova NanoSEM 450-FEI (ThermoFisher, Hillsboro, OR, USA) in parallel (xy plane, "⊙ Build direction") and perpendicular (xz plane, "↑ Build direction") directions to the build platform for 0°xz-, 0°xy-, 45°- and 90°z-samples. The thickness of α-laths and columnar β-grains was measured as reported by Gallaraga et al. [350] and Tiley et al. [351], respectively. In addition, energy-dispersive X-ray (EDX) spectroscopy (Quantax-200, Bruker Nano GmbH, Berlin, Germany) was used to evaluate both the α'/α and β phases and the effects induced by the sandblasting process on the sample surface.

3. Results

3.1. Microstructure and Surface Roughness

Figure 7.4 shows two OM micrographs illustrating the microstructure of as-built Ti6Al4V-ELI 45°-samples on the perpendicular (*Figure 7.4a*) and the parallel (*Figure 7.4b*) planes to the build platform. *Figure 7.4a* illustrates the presence of different columnar β-grains with the white dotted lines marking their boundaries. Prior columnar β-grains

are usually disposed perpendicularly to the molten pool, marked through the yellow dotted line, and totally formed by α'-martensite laths. *Figure 7.4b* shows the cross-sections of the columnar β-grains, characterized by a typical rectangular shape. In addition, they are generally contained within the laser scan tracks (marked with dotted yellow lines). Similar results are obtained on the same types of planes of the $0°_{XZ}$-, $0°_{XY}$- and $90°_{Z}$-samples, respectively.

Figure 7.5 shows the microstructure of both the $0°_{XZ}$-sample heat-treated at 704 °C/120 min (*Figure 7.5a,b*) and the $90°_{Z}$-sample treated at 740 °C/130 min (*Figure 7.5c,d*) where the columnar β-grains are always arranged alongside the build direction. The same microstructures are shown by the $0°_{XY}$-, $0°_{XZ}$-, 45°- and $90°_{Z}$-bars and they are consistent with those reported in [344,352,353].

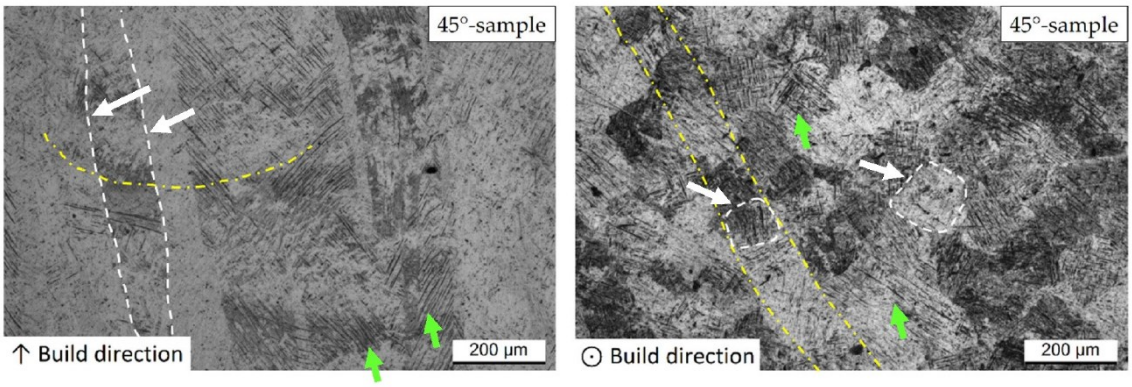


*Figure 7.4. OM micrographs of the microstructure of as-built Ti6Al4V-ELI 45°-sample observed: (**a**) on the plane perpendicular to the build platform, and (**b**) and on the plane parallel to the build platform. White and green arrows indicate the boundaries of the columnar β-grains (white dotted lines) and the laths of α′-martensite, respectively. The yellow dotted lines represent the molten pool boundary (**a**), and the laser scan tracks (**b**).*

As widely reported in the literature, the $\alpha' \rightarrow \alpha + \beta$ decomposition generates a microstructure where the primary, secondary and tertiary α-laths form a hierarchical structure such as the former α'-martensite laths. *Figure 7.5b* and *7.5c* illustrate the presence of this hierarchical structure where orange, green and light-blue dotted lines indicate the primary, secondary and tertiary α-laths, respectively. The EDS spectra of *Table 7.3* confirm that the laths are the α-phase (spectrum A) and lighter zones are the β-phase (spectrum B) [354]. The former is characterized by a higher content of the α-stabilizer alloying element (Al), while the latter are richer in the β-stabilizing alloy elements (V and Fe) [327]. Huang et al. [339] affirmed that the microstructure shown in *Figure 7.5b,d* was strictly related, firstly, to the self-accommodation of the α'-martensite and, secondly, to the Burgers relationships between the α and β phases.

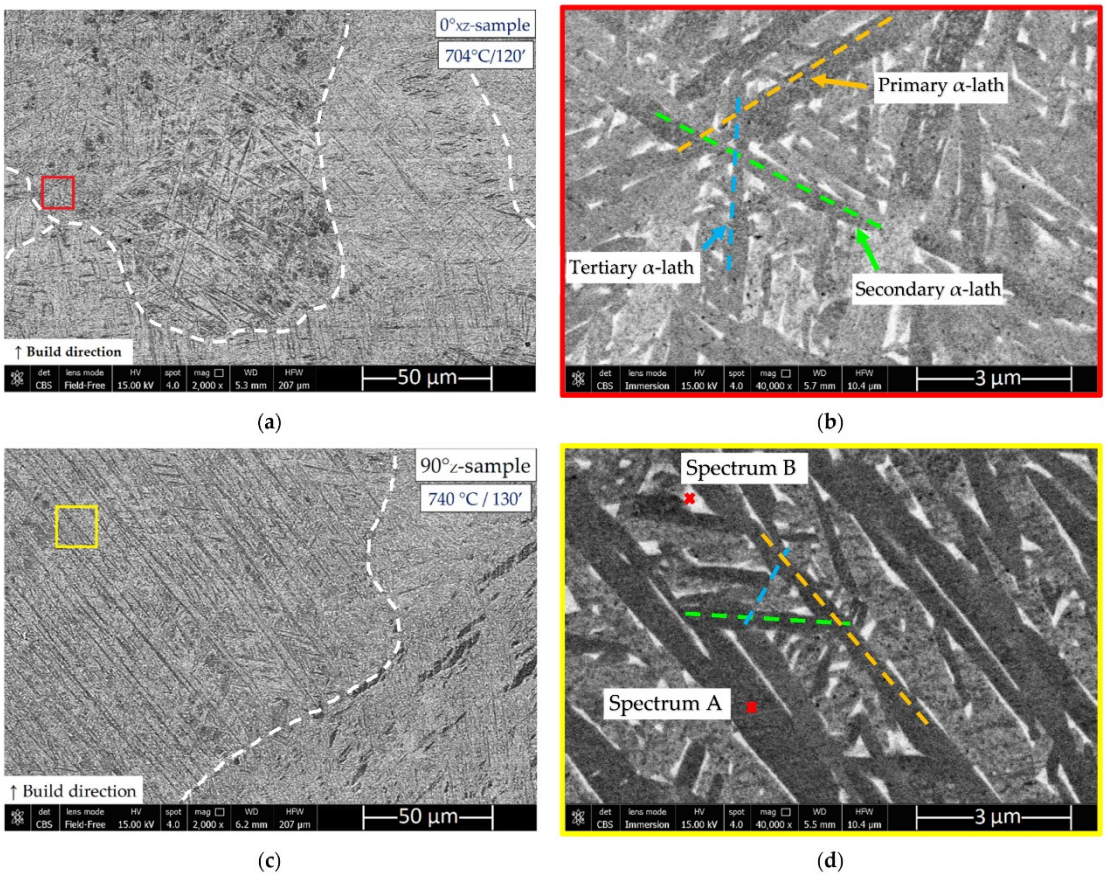


*Figure 7.5. SEM micrographs of the 0°xz-sample (**a**,**b**) after 704 °C/120′ and 90°z-sample (**c**,**d**) after 740 °C/130′. All images were acquired on the plane perpendicular to the build platform. Panel (**b**) illustrates the magnification (40k×) of the red square area in panel (**a**) (2k×), while panel (**d**) shows the magnification (40k×) of the yellow square area in panel (**c**) (2k×). Orange, green and light-blue dotted lines indicate primary, secondary and tertiary α-laths.*

Table 7.3. Chemical composition (EDS) of spectra A and B in wt%.

Spectrum	Ti	Al	V	Fe	Phase
A	91.6	7.2	1.2	-	α
B	89.9	2.0	7.9	0.2	β

In order to characterize the coarsening of the α-phase, its thickness was measured as a function of the heat-treatment conditions, and it increases from (540 ± 60) nm at 704 °C/120 min to (700 ± 10) nm at 740 °C/130 min due to the different temperatures and the furnace cooling from 740 to 520 °C in 90 min. The same results were obtained in [336,355,356]. For example, Haar et al. [336] discussed the same phenomenon during the heat treatments in the low-SSTR (Solid Solution Temperature Region), i.e., at temperatures below 800 °C.

Increasing the heat-treatment temperature above the β-transus (T = 1050 °C), the columnar β-grains recrystallize into equiaxed grains, as shown in *Figure 7.6a,b*, where the microstructures of the 90°z-sample (*Figure 7.6a,c*) and 90°z-bar (*Figure 7.6b,d*) are

shown. *Figure 7.6c,d* highlight the β-grain boundary formed by the α_{GB} (Grain Boundary) phase due to $\beta \rightarrow \alpha_{GB}$ transformation during the cooling, and from which the α-colonies and α-laths nucleate and grow. Tensile samples are formed by α-laths and small α-colonies that form a typical basketweave structure within the equiaxed β-grains (*Figure 7.6a,c*). On the other hand, the bar is formed by the Widmanstätten microstructure (*Figure 7.6b,d*) where wider α-colonies are arranged in a basketweave structure. In addition, *Figure 6b* shows a granular/globular α-phase, as also shown in [357]. Ahmed et al. [156] suggested that different cooling rates induce these microstructural differences between the basketweave of α-laths (< 15 °C s^{-1}) and the classical "basketweave" Widmanstätten morphology (< 1.5 °C s^{-1}). In the present work, the different cooling rates can be correlated to the different sample thicknesses between the tensile sample (6 mm) and the bar (10 mm) because both are simultaneously cooled with Argon gas for 1 h. Heat treatment at 1050 °C/60′ also induces the formation of an α-case surface layer with a thickness of 100–150 μm and hardness of (400 ± 10) $HV_{0.1}$ in both the tensile sample (*Figure 7.7a*) and bar (*Figure 7.7b*). Similar results are shown in [356,358] for the cross-sections of the 45°-sample and 45°$_Z$-bar.

Figure 7.8a shows the results of the XRD analysis performed on the cross-sections of the heat-treated 90°$_Z$-samples after the 704 °C/120 min, 740 °C/130 min and 1050 °C/60 min heat treatments. The different patterns show a reorientation and a possible recrystallization of the α-phase after the 1050 °C/60 min, as previously reported and illustrated in *Figures 7.5* and *6*. Due to the exact overlap between the peaks of the α and α' phases (as widely discussed in [33], it is not possible to discern which of the two phases exists in each sample through XRD patterns alone.

In this case, it is the microstructural observation in *Figure 7.6* which confirms that the diffraction peaks of the samples heat-treated at 1050 °C belong to the α-phase rather than the α'-martensite. Instead, the peaks appearing in the patterns of the 704 °C/120′ and 740 °C/130 min samples can be ascribed to the α'/α-phases.

The spectra also reveal peaks related to both the α_2-Ti_3Al and the $TiAl_3$ precipitates, which can be nucleated during the L-PBF process [33,331]. As a matter of fact, the heat treatments performed above 700 °C hardly cause precipitation phenomena in as-built Ti6Al4V-ELI samples because the precipitation temperatures of α_2-Ti_3Al and $TiAl_3$ are in the range of 500–600 °C and 460–515 °C, respectively [33,359]. In addition, the heat-treating temperature at 1050 °C did not induce the decomposition of these precipitates due to their higher decomposition temperature [33,360].

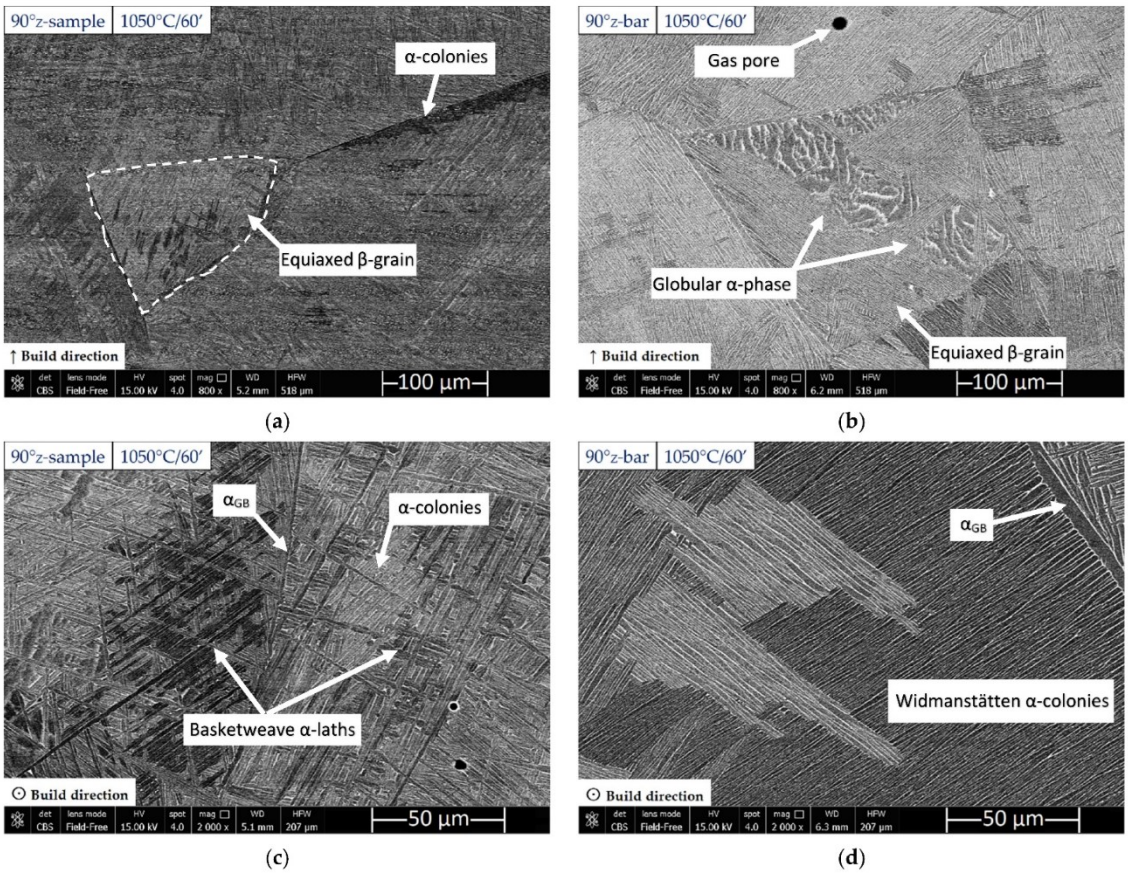


*Figure 7.6. SEM micrographs of the 90°z-sample (**a**,**c**) and the 90°z-bar (**b**,**d**) acquired on the perpendicular (**a**,**b**) and parallel (**b**,**c**) planes to the build platform after 1050 °C/60 min.*

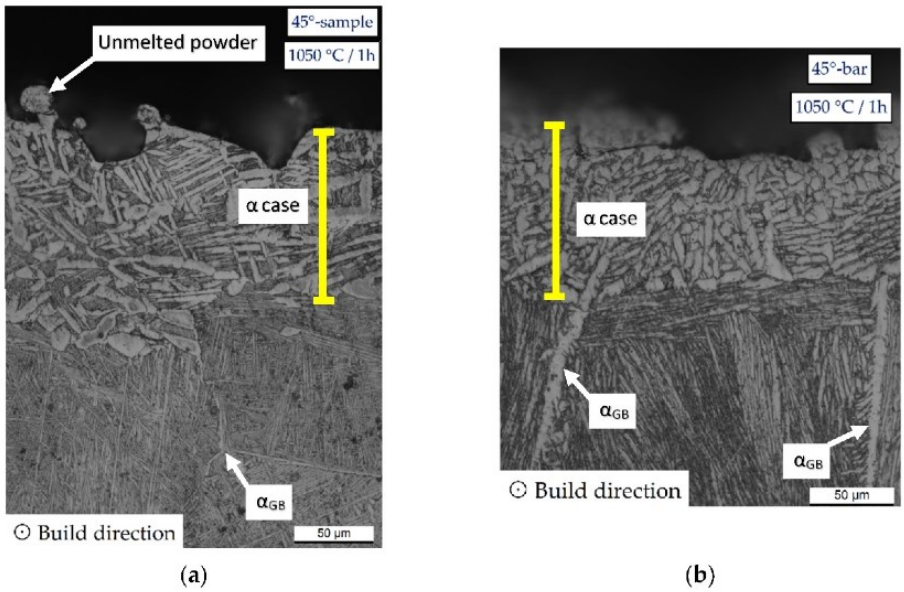


*Figure 7.7. OM micrograph of the cross-section of the 45°-sample (**a**) and 45°-bar (**b**) after heat treatment at 1050 °C/60 min.*

Figure 7.8b also highlights the effects induced by the sandblasting process on the surface of the heat-treated 90°z-samples. Firstly, it exhibits the broadening of the diffraction peaks related to the α-phase due to the accumulation of plastic strain in the near-surface area. Secondly, the patterns related to the 1050 °C/60 min samples confirm that the sandblasting process removes the oxide formed during the heat treatment despite the inert gas atmosphere.

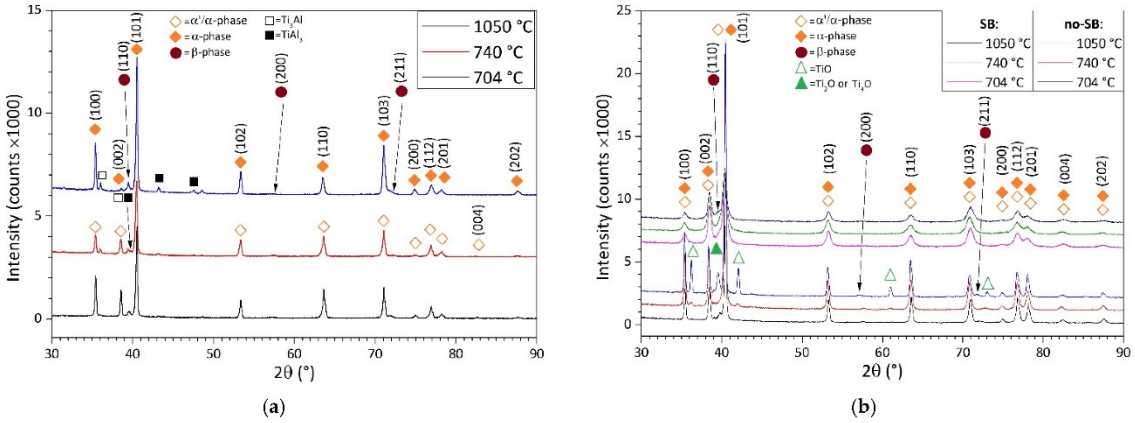


*Figure 7.8. XRD patterns of heat-treated 90°Z-samples at 704 °C/120 min, 740 °C/130 min and 1050 °C/60 min performed on sand-blasted cross-sections (**a**), and on the external surface (**b**) before and after the sandblasting process.*

Figure 7.9 illustrates the outer surface of the 45°-sample heat-treated at 704 °C/120 min before the sandblasting process. The S_a value was (26 ± 2) µm. This illustration can be considered representative of the surfaces of all samples analyzed in the present manuscript. Indeed, the surface analyses performed on the 0°xy-, 0°xz- and 90°z-samples exhibits the same scanned layers on which different powder particles are partially melted, which are shown in *Figure 7.9*.

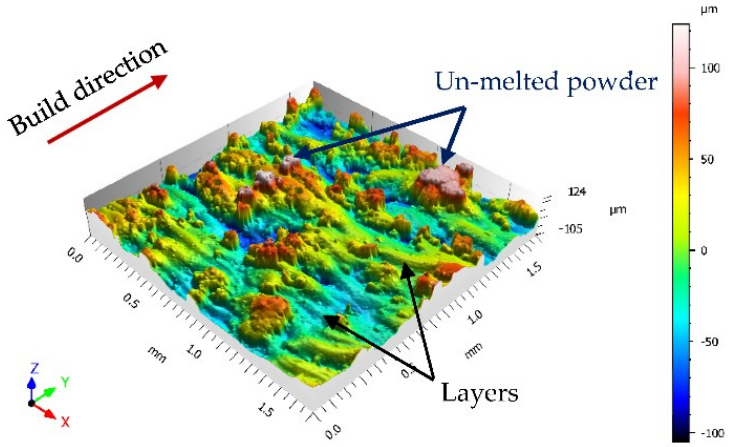


Figure 7.9. Topographical map of the 45°-sample heat-treated at 704 °C/120 min before the SB process.

After the sandblasting process, the surface roughness of the 45°-sample heat-treated at 704 °C/120 min decreases to 12 ± 1 μm. In fact, *Figure 7.10* shows a more uniform surface wherein the peak-to-valley distance is in the range of − 80–50 μm and not in the − 100–120 μm one. In particular, the sandblasting process smoothed down the properties of the as built surface: the outer surface does not show the un-melted particles seen in *Figure 7.9*. Additionally, in this case, all SB samples are characterized by a S_a in the range from 10 to 15 μm. At the same time, the R_z values decrease from 170–250 μm to 111–160 μm in the no-SB and SB samples, respectively.

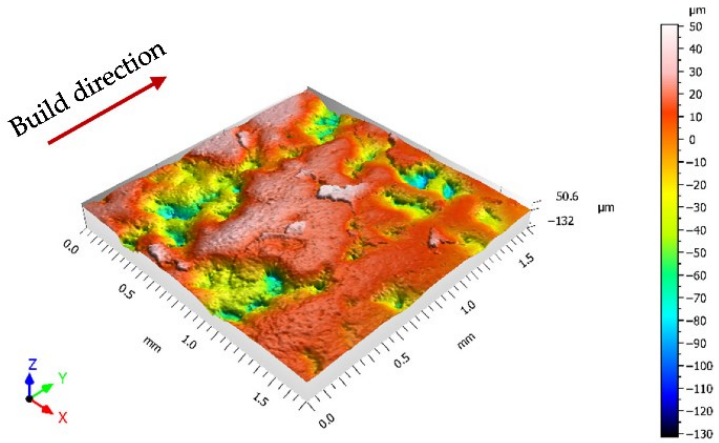


Figure 7.10. Topographical map of the 45°-sample heat-treated at 704 °C/120 min after the SB process.

3.2. Mechanical Properties

The mechanical properties of no-SB and SB 0°$_{XZ}$-, 0°$_{XY}$-, 45°-, 90°$_Z$-samples under all heat-treating conditions are shown in *Figure 7.11*. Focusing on the no-SB section of the graph, the samples heat-treated at 704 °C exhibit similar UTS, YS and elongation average values to the samples heat-treated at 740 °C (*Table 7.4*). On the other hand, the UTS and YS decrease up to 918 ± 7 MPa and 817 ± 6 MPa, respectively, after the treatment at 1050 °C/60 min. The mechanical properties of the SB 0°$_{XZ}$-, 0°$_{XY}$-, 45°-, 90°$_Z$-samples show the same trends, except for the elongation values at 1050 °C/60 min. In this case, the average value decreases from 12.75 ± 1.01 % in the no-SB case to 10.65 ± 0.21 % in SB condition.

The effects induced by the sandblasting process are also analyzed on the cross-section of the 90°$_Z$-sample through Vickers microhardness profiles (*Figure 7.3b*). *Figure 7.12* correlates the $HV_{0.5}$ microhardness profiles of no-SB and SB samples for each heat-treatment temperature within the same graph. In addition, the orange, red and blue lines indicate the $HV_{0.5}$ average values of the 3rd–13th indentations, namely the $HV_{0.5}$ values obtained by excluding the possible effects induced by the sandblasting process.

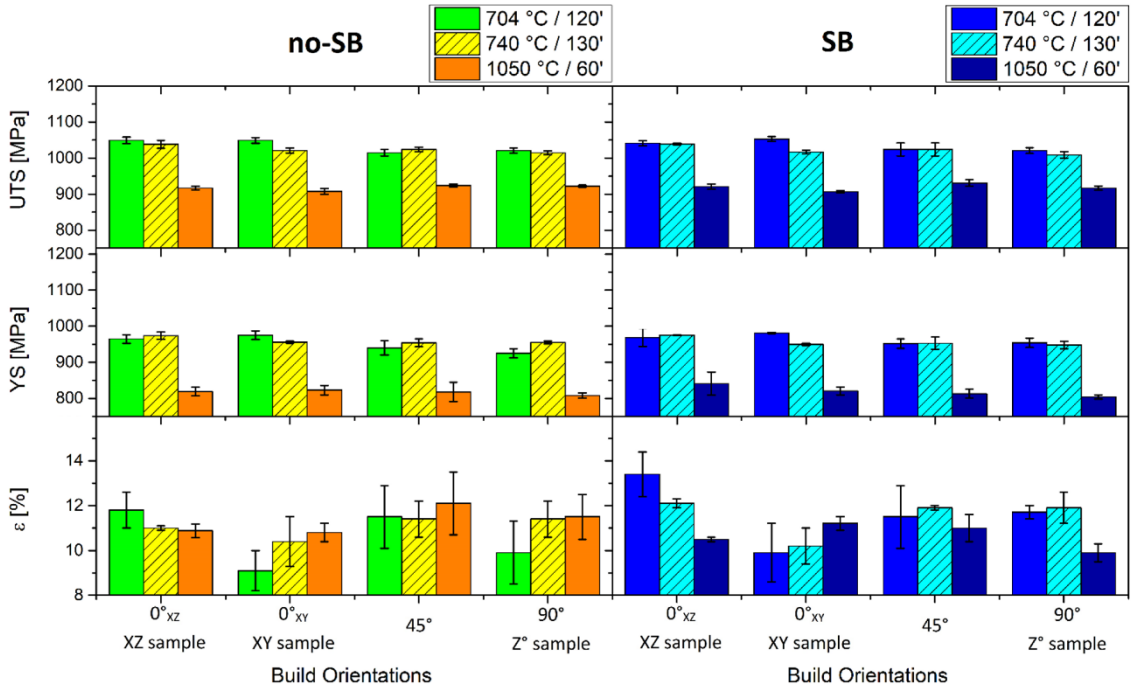


*Figure 7.11. Mechanical properties of 0°XZ-, 0°XY-, 45°-, 90°Z-samples heat-treated at 704 °C/120 min, 740 °C/130 min and 1050 °C/60 min in no-SB (**right section**) and SB (**left section**) conditions.*

These values agree with those reported in *Table 7.5*, which illustrates the $HV_{0.5}$ values of the heat-treated 0°XZ-, 0°XZ-, 45°-, 90°Z-bars and samples. The hardness values measured on bars heat-treated at 704 °C/120 min and 740 °C/130 min agree with those obtained on the heat-treated tensile samples (*Figure 7.12*). As a matter of fact, the 704 °C/120 min and 740 °C/130 min bars show the same microstructure of the tensile samples. Instead, considering the effects induced by the SHT at 1050 °C, the average $HV_{0.5}$ values of the bars are slightly higher than those obtained on the tensile sample due to the different microstructures (*Figures 7.5* and *7.6*).

Table 7.4. Average values of the mechanical properties of no-SB and SB samples heat-treated at 704 °C/120 min, 740 °C/130 min and 1050 °C/60 min.

Heat Treatments	No-SB		SB			
	UTS [MPa]	YS [MPa]	UTS [MPa]	YS [MPa]	UTS [MPa]	YS [MPa]
704 °C/120′	1034 ± 18	948 ± 28	10.58 ± 0.69	1035 ± 5	964 ± 9	11.85 ± 0.5
740 °C/120′	1025 ± 10	960 ± 10	11.05 ± 0.49	1022 ± 7	957 ± 7	11.53 ± 0.35
1050 °C/60′	918 ± 7	818 ± 7	12.75 ± 1.01	919 ± 3	820 ± 11	10.65 ± 0.21

Table 7.5. $HV_{0.5}$ measurements performed on heat-treated 0°$_{XZ}$-, 0°$_{XZ}$-, 45°-, 90°$_{Z}$-bars (xz and xy planes) and samples (xz plane) at 704 °C/120 min, 740 °C/130 min and 1050 °C/60 min.

Heat Treatments	0°$_{XZ}$-			0°$_{XY}$-			45°-			90°$_{Z}$-		
	Sample	Bar		Sample	Bar		Sample	Bar		Sample	Bar	
	xz Plane	xy Plane		xz Plane	xy Plane		Xz Plane	xy Plane		xz Plane	xy Plane	
704 °C/120′	387 ± 12	381 ± 15	374 ± 10	390 ± 10	379 ± 20	371 ± 19	381 ± 11	382 ± 10	368 ± 18	386 ± 6	381 ± 19	377 ± 15
740 °C/130′	375 ± 10	376 ± 17	361 ± 14	374 ± 6	370 ± 24	365 ± 21	372 ± 12	380 ± 12	370 ± 18	368 ± 10	374 ± 20	360 ± 18
1050 °C/60′	338 ± 5	341 ± 9	341 ± 8	336 ± 12	345 ± 8	343 ± 7	340 ± 9	339 ± 10	342 ± 8	339 ± 8	342 ± 5	348 ± 8

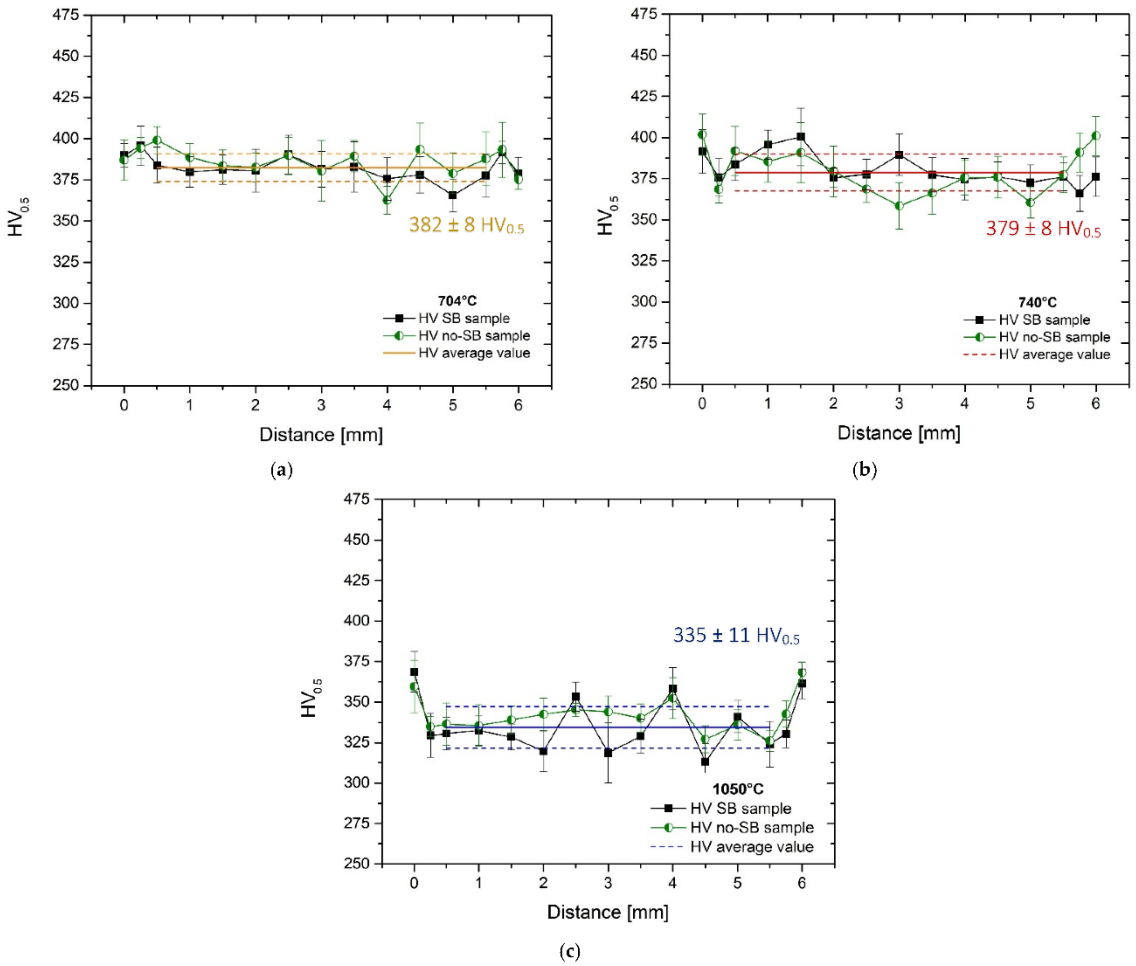


*Figure 7.12. Vickers microhardness profile measured on the cross-section of 90°z-samples heat-treated at: (**a**) 704 °C/120 min, (**b**) 740 °C/130 min and (**c**) 1050 °C/60 min. The orange, red and blue lines represent the HV0.5 average values of the 3rd–13th indentations of the Vickers profiles, while the dotted lines show the associated error ranges.*

Figure 7.13 shows the HV0.1 values of the different microstructures that form the 1050 °C/60 min heat-treated bars (*Figure 7.13a–d)* and tensile samples (*Figure 7.13e,f*). Increasing the thickness of α-laths that form the colonies (*Figure 7.13a,b*), the HV0.1 value decreases from 398 HV0.1 to 355 HV0.1, while the lowest value was obtained by the globular α-phase. Focusing on tensile samples, 332 HV0.1 was obtained for the basketweave α-laths in the center of the grain, while 392 HV0.1 was obtained for the fine α-phase within the colony in the zone adjacent to the grain boundary. On the other hand, the HV0.1 value of the α_{GB} decreases up to 335 HV0.1 when considering the bar's microstructure (*Figure 7.13d*).

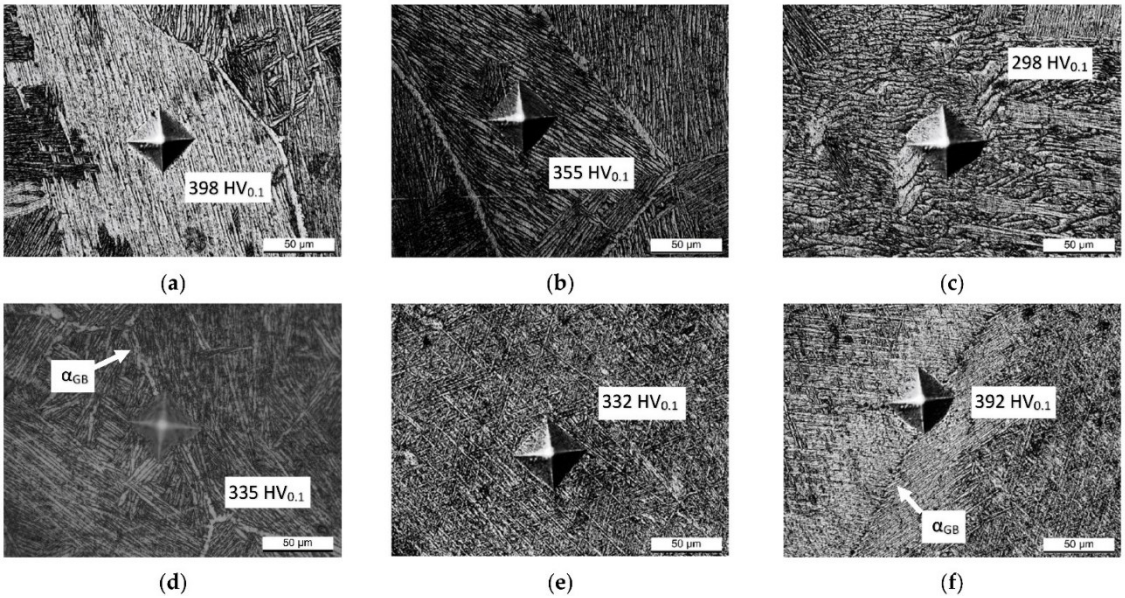


*Figure 7.13. $HV_{0.1}$ indentations performed on different microstructures of the heat-treated 1050 °C/60 min: (**a**–**d**) 90°$_z$-bar and (**e**,**f**) 90°$_z$-tensile sample.*

4. Discussion

The as-built microstructure of the L-PBF Ti6Al4V-ELI samples (*Figure 7.4*) is characterized by columnar β-grains that grow parallel to the *z*-axis, or perpendicular to the xy plane, following the heat fluxes developed during the L-PBF process [361,362]. The β-grains nucleate from the build platform and grow across each of the deposited layers along the <100> as shown in *Figure 7.4a* [363]. As a matter of fact, the columns are arranged perpendicular to the molten pools. At the same time, they are contained within the laser scan tracks on the xy plane, as shown in *Figure 7.4b*. This configuration of the columnar β-grains characterized all samples regardless of the build orientations (*Figures 7.4a* and *7.5*) [364]. The fully columnar structure is also confirmed by the relationships between the thermal gradient (G, [K/m]) and the solidification rate (R, [m/s]), which characterized the Ti6Al4V alloy during the L-PBF process [33]. In addition, the complex thermal history and the high cooling rate that characterized the L-PBF process induced the formation of α'-martensite, arranged in a hierarchical structure wherein the major axis of the primary α' formed an angle of 45° with respect to the β-grain boundary [33,112,152,365]. Yang et al. [152] also affirmed that the α'-martensite forms an angle of 30 or 60° or 30 to 60° with respect to the build orientation. In the same context, Huang et al. [339] showed angles of 30, 60 and 90° between different α'-laths. This hierarchical structure of the α'-martensite remains in the α-laths developed after the heat treatments at 704 and 740 °C. Likewise, the columnar shape of the prior β-grains is also retained

after those heat treatments. In particular, the α + β microstructure developed after the treatment below the β-transus presents primary, secondary and tertiary α-phase arranged along the same orientations as the progenitor α'-martensite laths. Haar et al. [336] confirmed the absence of quartic α-laths due to the $\alpha'_{quartic}$-martensite → β decomposition. The XRD spectra, shown in *Figure 8a*, confirm a possible partial α' → α + β transformation due to the presence of peaks related to the β phase, which are absent on the as-built XRD spectra [33]. TEM analysis discussed by Spigarelli et al. [154], which was performed on the same heat-treated samples, confirmed the presence of α'martensite and, therefore, the incomplete α' → α + β transformation. Therefore, this validates the α'/α-phase labels shown on the XRD patters related to the samples heat-treated at 704 °C/120 min and at 740 °C/130 min, respectively.

Because the α + β microstructure retains much of the features of the pristine α'-martensite, the mechanical properties of both the heat-treated samples at 704 and 740 °C do not vary significantly (*Figure 7.11* and *Table 7.5*). Therefore, the increase in the average thickness of the α-laths from (540 ± 60) to (700 ± 10) nm, which can be caused by both the higher heat-treatment temperature and the first step of cooling up to 520 °C in 90 min, does not influence the mechanical performance. Focusing on the error bars (*Figure 7.14*), which are obtained considering the tensile results of each build orientation (*Figure 7.11*), the samples heat-treated at 704 °C are characterized by a more pronounced anisotropy (ΔUTS = 4.75 %, ΔYS = 7.40 %) than those heat-treated at 740 °C (ΔUTS = 3.86 %, ΔYS = 4.30 %). These variations are calculated considering the maximum and minimum values of all build directions for each temperature. Vilaro et al. [353] reported ΔUTS = 4.40 % and ΔYS = 6.74 % after 730 °C/2 h with air cooling, while Simonelli et al. [78] did not detect any differences after the same heat treatment. As a matter of fact, the anisotropy depends significantly on the correlation between the load direction and both the lack-of-fusion (LOF) defects and the columnar β-grains [78,137,353,366]. The presence of α_2 and/or $TiAl_3$ precipitates can be another possible contribution to the anisotropy, as will be later discussed. Therefore, future works related to the influence of LOF, grain boundaries and α phases may be necessary for the heat treatments analyzed in the present manuscript. The only influence of α-phase coarsening is observable on the $HV_{0.5}$ microhardness values shown in *Table 7.5*.

During the SHT at 1050 °C for 60 min, the recrystallization process of the columnar β-grains in equiaxed grains takes place (*Figures 7.5* and *7.6*), as also reported by [33,339,352,367]. The same results were obtained by Huang et al. [339] who suggested that the equiaxed grains form from the split of the progenitor columnar β-grains. Wu et al. [368], however, showed the recrystallization process already after 1000 °C/40 min, followed by water quenching. Due to this microstructural change, together with the α-

laths in a basketweave structure (*Figure 7.6*), the UTS and YS values decrease (*Figure 7.9*) up to 918 ± 7 MPa and 817 ± 6 MPa, respectively; meanwhile, the elongation increases only up to 12.75 ± 1.01 % due to both the α-laths rather than α-colonies in a basketweave structure (*Figure 7.6a,c*) and the possible detrimental effect of the α-case [33,328,356,369].

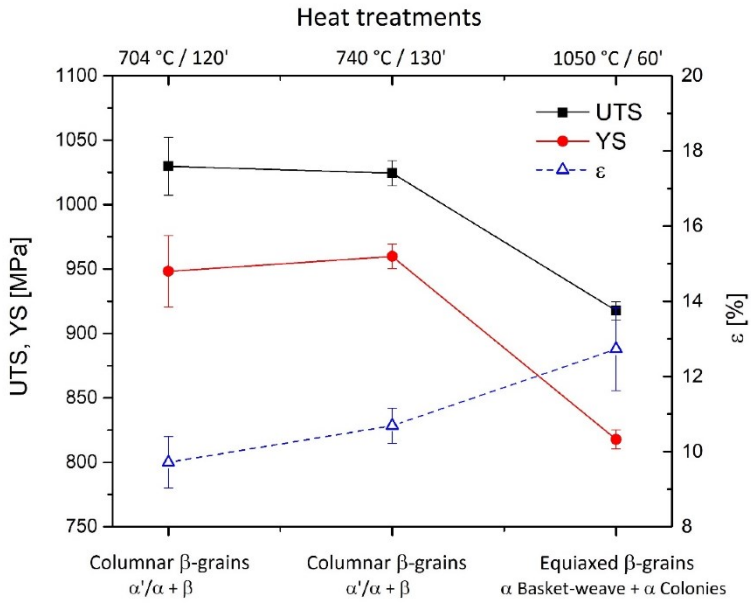


Figure 7.14. Average ultimate tensile strength, yield strength and elongation of the samples heat-treated at 704 °C/120 min, 740 °C/130 min and 1050 °C/60 min.

The same tensile properties are confirmed by [75,122,327,339]. In this scenario, the mechanical properties of all heat-treated samples satisfy the minimum requirements dictated by the ASTM F3001 (UTS of 860 MPa, YS of 795 MPa and ε of 8 %). However, in relation to the samples heat-treated at 1050 °C/60 min, the ASTM F3001-13a is not satisfied due to the presence of the α-case layer. In fact, post-processing operations are required to remove the α-case due to its worsening effects on fatigue life and ductility in aerospace components [315,356]. At the same time, the samples heat-treated at 704 and 740 °C, which are characterized by higher tensile properties than the solution heat-treated samples, also satisfy the F2924-14 standard specification (UTS of 895 MPa, YS of 825 MPa and ε of 10 %, [370]); this, however, is related to the Ti6Al4V alloy.

In relation to the cooling pathway, the Argon gas and the samples' thickness do not influence the microstructure of the samples heat-treated at 704 and 740 °C, as also reported in [75,336,340]. As a matter of fact, the cooling methods (water, air or gas, and furnace) have different effects in relation to the heat-treatment temperatures. In fact, the microstructure is not influenced by the cooling pathway if the cooling starts below ~800 °C [33,75,340]. By contrast, the $\beta \rightarrow \alpha'$-martensite transformation can take place when

cooling starts from above 800 °C, as the sample is converted to β-phase and cooled at a high cooling rate. Ji et al. [371] affirmed that the critical temperature is around 870 °C. As previously reported, Kaschel et al. [335] demonstrated that the α'-martensite starts to decompose at 400 °C and finishes at around 700 °C. Other authors, however, reported temperatures higher than 750 °C for $\alpha' \rightarrow \alpha + \beta$ decomposition [335,372,373]. Finally, the α-phase surely decomposes into β-phase following an exponential trend from ~ 800 °C to the β-transus temperature [336]. Focusing on the SHT treatment, the same cooling in Argon gas induces different microstructural morphologies (*Figure 7.6*) in relation to the sample thickness due to different cooling rates. Bars are characterized by α-colonies arranged in a basketweave (Widmanstätten) microstructure and globular α-phase (*Figure 7.6c,d*), while the tensile samples show α-laths in a basketweave structure within the equiaxed β-grain. At the same time, there are equiaxed grains formed by a mixture of α-laths at their center and α-colonies that nucleate and grow from the α_{GB} (*Figure 7.6b*). As previously reported, Ahmed et al. [156] confirmed that the Widmanstätten microstructure of α-laths and Widmanstätten microstructure of α-colonies form with cooling rates of 15 and 1.5 °C s^{-1}, respectively. Sieniawski et al. [374] showed that a rate of 9 °C s^{-1} forms a mixture of α-colonies and α-laths. Generally, different cooling pathways from the β-region can induce a diffusionless $\beta \rightarrow \alpha'$-martensite transformation with a rate > 20 °C s^{-1}, or a $\beta \rightarrow \alpha + \beta$ diffusional transformation whereby the microstructure can assume different morphology with a rate < 20 °C s^{-1} [33]. Gallaraga et al. [375] affirmed that the air cooling, which is characterized by a rate around 20 °C s^{-1} from 1000 to 500 °C, can induce the nucleation of the α'-martensite given that its M_s (Martensite start) temperature is $575 \leq T_{M_S} \leq 800$ °C [327].

Another important factor induced by the SHT at 1050 °C is the formation of the α-case layer as shown in *Figure 7.7*, both on tensile samples and bars. Seth et al. [356] affirmed that the α-case formation depends on the oxidizing capacity of the environment during heat-treating at high temperatures. As a matter of fact, the diffusion of oxygen atoms within the sample surface increases the β-transus temperature, as exhibited by the following equation:

$$T_{\beta-Tr} = 882 + 21.1[Al] - 9.5[Mo] + 4.2[Sn] - 6.9[Zr] - 11.8[V] - 12.1[Cr] - 15.4[Fe] + 23.3[Si] + 123.0[O] \quad (7.2)$$

where [*element*] represents the weight percentage of each element [376]. Kolachev et al. [377] proposed a similar linear relationship between the β-transus temperature and the chemical composition. Firstly, oxygen, as α-stabilizer alloying element [327], maintains a fraction of the α phase which does not undergo the $\alpha \rightarrow \beta$ transformation during the heat treatment. Secondly, it increases the $HV_{0.1}$ hardness, as shown in *Figure 7.15*, where

the globular α-phase within the samples is characterized by 360 $HV_{0.1}$, while the α-case has a hardness of 403 $HV_{0.1}$.

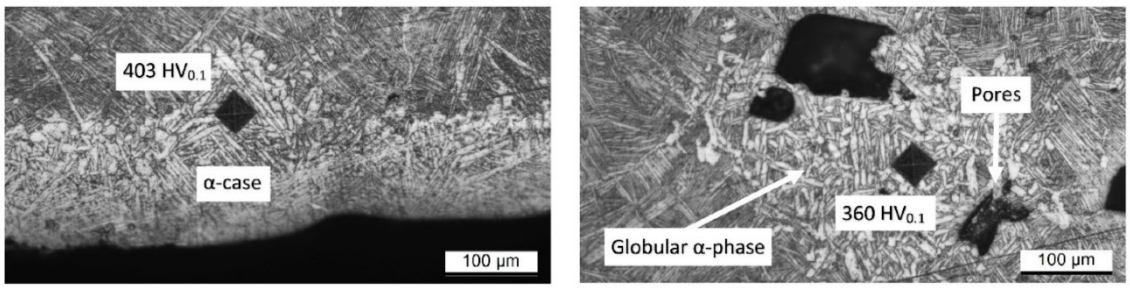


*Figure 7.15. Representative $HV_{0.1}$ indentations performed on the α-case layer (**a**) and on the globular α-phases in the center of the bar (**b**).*

The XRD analysis in *Figure 7.8* confirms the presence of different titanium oxides on the sample surface and, therefore, the possible diffusion of oxygen atoms within the sample. At the same time, these patterns show the presence of α_2-Ti_3Al and $TiAl_3$ precipitates in different heat-treated samples. On the other hand, the XRD pattern performed on the cross-section of the 90°$_Z$-sample (1) heat-treated at 740 °C (*Figure 7.16*) does not reveal any precipitate, despite it being manufactured and heat-treated in the same batch and direction as the 90°$_Z$-sample (2). This can confirm that the high heat inputs developed during the L-PBF process generate different zones, persisting for an adequate time in the precipitation temperature range [334]. Therefore, a more detailed analysis on these precipitates will be performed in future works. Moreover, the differences between the precipitation phenomena between two equal heat-treated samples can explain the variability in terms of mechanical properties and $HV_{0.5}$ (*Table 7.5*) and, therefore, their anisotropy.

Comparing the mechanical properties of the no-SB and the SB samples, the sandblasting process performed after the different heat treatments does not induce any variation, except for the ductility values between the no-SB and SB samples heat-treated at 1050 °C/60 min. The impact of the glass spheres on the sample surface induces plastic strain, as highlighted by the broadening of the α-peaks (*Figure 7.8*), and it can reduce the ductility. Future works on the effects of the sandblasting process on fracture mechanisms could be necessary. On the other hand, work-hardening was not detected by the Vickers hardness profiles on the cross-sections of all samples, as emphasized by the profiles in *Figure 12*. In particular, the average $HV_{0.5}$ values of the first and the last two points of each profile acquired on the 704 °C/120 min and 740 °C/130 min heat treatments (*Figure 7.12a,b*) do not significantly vary with respect to the hardness values measured at the

centre of the cross-section area; these are represented by the orange (*Figure 7.12a*) and red (*Figure 7.12b*) lines. In the 1050 °C/60 min samples, on the other hand, the $HV_{0.5}$ values next to the surface increase, but the same increase is seen for both the SB and no-SB samples (*Figure 7.12c*). This increase was, therefore, not a consequence of sandblasting; it was conferred by the presence of the α-case.

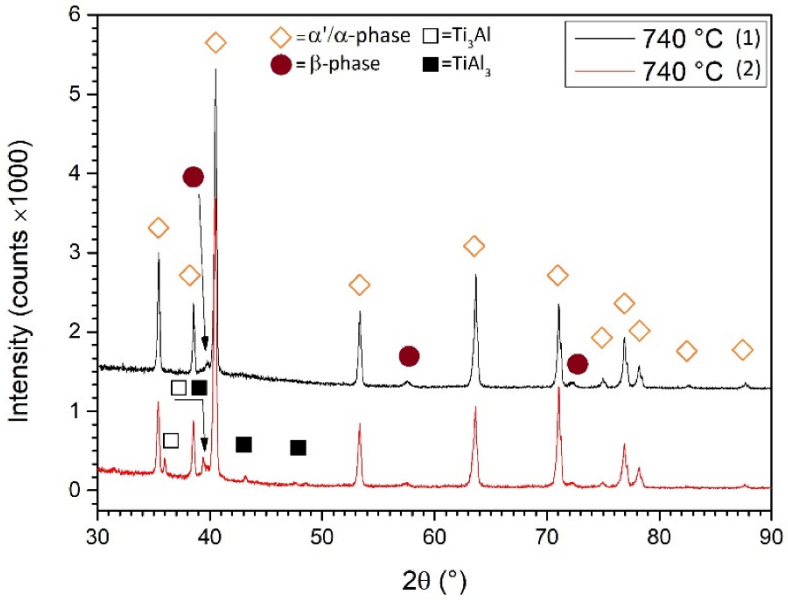


Figure 7.16. XRD patterns of two 90°Z-samples manufactured in the same batch and heat-treated at 740 °C/130 min. The black XRD pattern (1) is correlated to the red pattern (2) that is the same shown in Figure 7.8a.

The reduction in the surface's roughness was another consequence of the sandblasting process. Considering that 3.2 µm is the recommended surface roughness for aerospace applications [378], all values obtained in the present work are unsatisfactory because the R_a values decrease from 20–28 µm to 10–15 µm (*Figures 7.9* and *7.10*). On the other hand, the sandblasting post-process eliminates the presence of the un-melted particles on the surface and the oxides formed during the heat treatments (*Figure 7.8*).

5. Conclusions

The present paper aimed to evaluate the effects induced by different heat treatments (704 °C/120 min, 740 °C/130 min and 1050 °C/60 min), performed using an industrial furnace, on Ti6Al4V-ELI samples manufactured via Laser Powder-Bed Fusion in different build orientations. In addition, the effects of the sandblasting process were also analyzed. The main conclusions can be summarized as follows:

1. The microstructure of samples heat-treated at 704 and 740 °C is formed by columnar β-grains containing α'-martensite and α (primary, secondary and tertiary) + β phases. Some samples also showed α_2-Ti_3Al and $TiAl_3$ precipitates that are probably formed during the L-PBF process. These can cause the anisotropic behavior of the mechanical performance related to samples grown along the same direction.
2. The samples heat-treated at 704 °C show more anisotropic mechanical properties than the same tensile samples heat-treated at 740 °C. On the other hand, both satisfy ASTM F2924 and ASTM F3001 standard specifications. The increase in α-lath's thickness from 538 ± 66 to 704 ± 11 μm only influences the $HV_{0.1}$ microhardness measurements, but apparently has no effect on yield, ultimate tensile strength or elongation.
3. The microstructure of samples heat-treated at 1050 °C varies in relation to the sample's thickness. As a matter of fact, the tensile samples (6 mm) are formed by α-laths in a basketweave or Widmanstätten structure and small α-colonies within recrystallized equiaxed β-grains. Instead, bars (10 mm) are formed by wider α-colonies in a basketweave or Widmanstätten structure and globular α-phase within the same equiaxed β-grains. Moreover, in both cases, an α-case layer of about 100–150 μm is formed on the surface.
4. The samples heat-treated at 1050 °C show mechanical properties that satisfy only the ASTM F3001 standard specification. Despite the decrease in UTS and YS by about 10 % and 14 %, respectively, the elongation values do not show a significant increase with respect to the samples heat-treated at 704 and 740 °C, probably due to the presence of the α-case layer.
5. The sandblasting process does not induce effects on the mechanical properties, but increases the plastic strain in the near-surface area. The obtained surface roughness of the sandblasted tensile sample (12–16 μm) does not satisfy the requirements for aerospace applications.

[*This page intentionally left blank*]

ARTICLE 8

Effect of Low-Temperature Annealing on Creep Properties of AlSi10Mg Alloy Produced by Additive Manufacturing: Experiments and Modelling

---

Chiara Paoletti, Emanuela Cerri, Emanuele Ghio, Eleonora Santecchia, Marcello Cabibbo & Stefano Spigarelli

Metals, *11(12)* (**2021**) 179

https://doi.org/10.3390/met11020179

“The following version of the manuscript is made available under the CC-BY-NC-ND 4.0 license”

https://creativecommons.org/licenses/by-nc-nd/4.0/

Effect of Low-Temperature Annealing on Creep Properties of AlSi10Mg Alloy Produced by Additive Manufacturing: Experiments and Modelling

Chiara Paoletti [1], Emanuela Cerri [2], Emanuele Ghio [2], Eleonora Santecchia [1], Marcello Cabibbo [1], Stefano Spigarelli [1]

[1] Department of Industrial Engineering and Mathematical Science (DIISM), Università Politecnica delle Marche, Via B. Bianche, 60131, Ancona, Italy.

[2] Department of Engineering and Architecture, University of Parma, Via G. Usberti 181/A, 43124, Parma, Italy.

Abstract

The effects of postprocessing annealing at 225 °C for 2 h on the creep properties of AlSi10Mg alloy were investigated through constant load experiments carried out at 150 °C, 175 °C and 225 °C. In the range of the experimental conditions here considered, the annealing treatment resulted in an increase in minimum creep rate for a given stress. The reduction in creep strength was higher at the lowest temperature, while the effect progressively vanished as temperature increased and/or applied stress decreased. The minimum creep rate dependence on applied stress was modelled using a physically-based model which took into account the ripening of Si particles at high temperature and which had been previously applied to the as-deposited alloy. The model was successfully validated, since it gave an excellent description of the experimental data.

Keywords: creep, aluminium alloy, additive manufacturing, annealing, modeling.

1. Introduction

1.1. AlSi10Mg Alloy Produced by Additive Manufacturing: Main Structural Features

AlSi10Mg is an aluminum alloy which is extensively used in the production of parts by additive manufacturing (AM). Specifically, laser powder bed fusion (LPBF) is the most widespread AM technique for the production of components made of this alloy [379–381]. Starting from computer aided design (CAD) models, LPBF builds up new parts layer-upon-layer. Each layer is formed by small portions of powder (melt pools), which are selectively melted by the laser. The resulting very high cooling rates (~ 10^6 °C/s) and the sequence of passes, each of which acts as a thermal treatment on the lower and already solidified layers, produce an extremely fine structure with interesting

mechanical properties [253,382,383]. The complex structure typical of AlSi10Mg AM products can be schematically described as follows:

1. at a macroscopic level (100 μm–1 mm), the most noteworthy features are: (a) the high surface roughness resulting from the presence of melt pools; (b) the possible presence of porosities [384];
2. at a mesoscopic level (1–100 μm), the melt pool substructure is formed by columnar grains with diameters of several microns, which are subdivided into smaller long cells with diameters of a few hundreds of nm, separated by Si-Mg-rich eutectic regions [386–388];
3. at a microscopic level (10 nm–1 μm), the long cells are subdivided into equiaxed subcells, again with diameters of a few hundreds of nm, separated by a network of Si-rich eutectic regions. The eutectic regions are richer in Si [387] and contain densely spaced Si particles, the size and distribution of which can vary as a function of process parameters [384,385] or part size [386].

1.2. AlSi10Mg Alloy Produced by Additive Manufacturing: Effect of Stress Relieving/Low Temperature Annealing

As mentioned above, the mechanical properties of as-formed AM parts are indeed peculiar. The extreme thinness of the substructure gives the alloy very high yield and ultimate tensile strengths, which are roughly comparable with those typical of the T6 state, although at the expense of low ductility. Residual stresses and the presence of porosity can further decrease ductility and toughness. For this reason, postprocessing usually includes a stress-relieving or annealing treatment, which increases ductility but significantly reduces the tensile properties of the alloy. An example of the variation in tensile yield stress with annealing temperature for a fixed duration of 2 h is reported in *Figure 8.1* (data from [185,383,387–389]). The figure includes only the data for the low-temperature treatments, since at higher temperatures (400–550 °C) the meso- and microstructures undergo extensive variations that drastically change their very nature, which progressively approaches that of die-cast alloys. The first obvious evidence from *Figure 8.1* is the high variability in the mechanical properties of the alloy in the as-deposited state. This variation can be attributed to the differences in deposition conditions reflected in the different morphologies of the meso- and microstructures.

A point to be addressed is whether the complex trend of the yield strength can be somehow quantitatively described by a physically-based model. A simplified modelling approach [390] assumes that the mechanical properties of the alloy are mainly controlled by its microstructure, i.e., by the interaction between dislocations and obstacles at a submicron scale. The microstructural analysis carried out in [390]

confirmed that, in the as-deposited state, the microstructure of the alloy consists of 500 nm-wide cells, surrounded by a network of fine Si particles (Appendix A shows a representative micrograph of the microstructure).

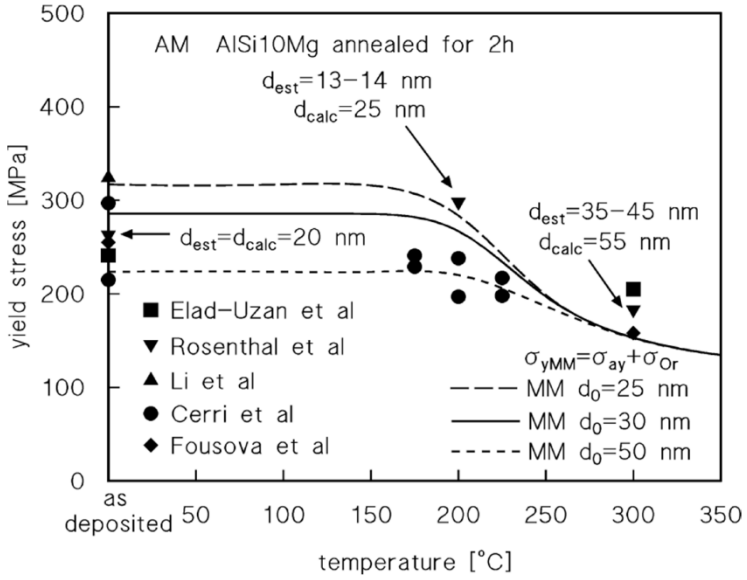


Figure 8.1. Effect of a 2-h postprocessing heat treatment on yield strength (on the left, the values for the as-deposited alloys) [185,383,387–389]. The figure also plots the roughly estimated value of the yield stress calculated by taking into account the effects of the Ostwald ripening of Si particles of different initial size (see Appendix A for details on the calculation of the Si particle size d_{calc}, and Table 8.1 for the meanings of symbols). In addition, data on the observed crystallite size, d_{est}, are reported [383].

Table 8.1 List of constitutive model parameters

Symbol	Meaning
σ	True applied stress [MPa]
$\dot{\varepsilon_m}$	Minimum creep rate [s^{-1}]
σ_0	Particle strengthening term (Orowan stress) [MPa]
α	Constant: 0.3
m	Taylor factor: 0.36
R	Gas constant: 8.314 J mol^{-1} K^{-1}
G	Shear modulus
b	Burgers vector: 2.47 × 10^{-10} m
ρ	Dislocation density [m^{-2}]
σ_p	Dislocation hardening term: $= \alpha m G b \rho^{1/2}$ [MPa]
τ_l	Dislocation line tension: $= 0.5\, Gb^2$ [N]
R_{max}	Maximum strength at the testing temperature [MPa]
k	Boltzmann constant: 1.38 × 10^{-23} J K^{-1}
D_{0L}	Pre-exponential factor in the Arrhenius equation describing the temperature dependence of the vacancy diffusion coefficient: 8.3 × 10^{-6} $m^2 s^{-1}$ [391]
Q_L	Activation energy in the Arrhenius equation describing the temperature dependence of the vacancy diffusion coefficient: 122 kJ mol^{-1} [391]

Table 8.1. Cont.

Symbol	Meaning
U_{SS}	Energy necessary for Si (and Mg) atoms still in solid solution to jump in and out of the atmosphere that spontaneously form around dislocations; previous calculations gave values close to 10–15 kJ mol^{-1} for Mg [392]. For the sake of simplicity, here U_{ss} is assumed to be 10 kJ mol^{-1}
R_{UTS^A}	Room temperature tensile strength of an alloy with the same impurity level, similar content of elements in solid solution and coarse intergranular intermetallics, in the absence of fine Si particle, here roughly estimate to be 115 MPa
L	Surface-to-surface interparticle spacing [m]
G_T, G_{RT}	Shear modulus at the testing temperature and at 25 °C, respectively [MPa]
M_{cg}	Temperature dependent dislocation mobility
d_0	Initial dimension of Si particles
d_{est}	Experimental estimate of the size of Si particles at time t
d_{calc}	Calculated value of the size of Si particles at time t
σ_{yi}	Yield stress
σ_a	Yield stress of an alloy containing 0.5 % Mg but no Si particles
σ_{Or^i}	Orowan stress in the i-region (I = H, S)

The interior of the observed cells, by contrast, contains few remote fine particles. This structure can be modelled as a combination of soft zones surrounded by hard regions. The cell interior can thus be seen as a soft zone which dislocations can easily pass through, while the eutectic region is a hard region which becomes a strong obstacle to dislocation motion. The resulting material model (MM) can be therefore used to attempt a description of the softening phenomena illustrated in *Figure 8.1*.

If hard (eutectic) and soft (cells) zones deform under similar strain rates, the strength of the "composite" material can be calculated as:

$$\sigma = f_H\sigma_H + (1 - f_H)\sigma_s \tag{8.1}$$

where σ_H and σ_s are the stresses acting on the hard and soft zones, respectively, and f_H is the volume fraction of the hard regions [395–397].

The yield stress of the alloy can then be estimated by assuming that the initial dislocation density is very low, thus showing that dislocation hardening does not significantly contribute to yielding. The stress necessary to start dislocation motion (yielding) in the hard and soft zones can therefore be tentatively calculated as:

$$\sigma_{yi} = \sigma_\alpha + \sigma_{Or^i} \tag{8.2}$$

where σ_α is the yield stress of an alloy containing 0.5 % Mg (60 MPa), which includes the solute hardening contribution of this alloying element, and σ_{Or^i} is the Orowan stress in the i-region (soft or hard). The Orowan stress, in turn, can be estimated by its simplest formulation [396], namely:

$$\sigma_{Or} = \frac{0.84mGb}{L} \quad (8.3)$$

where m = 3.05, G is the shear modulus, b is the Burgers vector and L is the surface-to-surface interparticle spacing. Following [390], it can be assumed that each cell has a size of 500 nm [385] and that the volume fraction of the eutectic portions is f_H = 0.25. Both cells and eutectic regions contain fine Si particles of initial size d_0. The initial surface-to-surface interparticle distance is assumed to be equivalent to d_0 in the hard zones and to 200 nm in cell interiors.

Once precipitation to the equilibrium volume fraction is complete, particle size evolves during annealing due to coarsening/ripening. Details about the equations used for the calculation of particle size (d_{calc}) and interparticle distance after annealing are presented in Appendix A. The calculated variations in yield stress Eqs. (8.2) and (8.3) obtained for MM with different d_0 values are presented in *Figure 8.1*. An analysis of the figure suggests that, in general terms, the combination of MM with the equations describing the Ostwald ripening phenomena of Si particles gives a reasonable description of the yield stress reduction after annealing. Nevertheless, at a closer look, some specific features emerge, namely:

1. in some cases (see, for example data from [389]), the yield stress monotonically decreases with increasing annealing temperature. The phenomenon is quite correctly described by the model curves;
2. in other cases (see data from [383] and evidence presented in [387]), precipitation of Si is not completed during the AM process. Thus, in the early stages of low-temperature annealing, an additional precipitation of fine Si particles results in an increase in yield stress. This secondary precipitation is not accounted for by the equations presented in Appendix A, since the model assumes that ripening starts immediately upon annealing. This fact is easily confirmed when comparing the estimated value of the Si crystallites (d_{est}) [383] and the calculated value of Si particle size (*Figure 8.1*). The secondary precipitation results in a finer particle size than the one predicted by the ripening equations.

The analysis above indicates that, also during stress relieving/low temperature annealing, AM AlSi10Mg alloy is affected by complex combinations of metallurgical phenomena (secondary precipitation, depletion of elements in solid solution, ripening). These phenomena occur on a microstructure the structural features of which (melt pool size, cell size, particle size, etc.) are strongly dependent upon processing conditions. On the other hand, both the temperature and duration of the postprocessing heat treatment need to be accurately selected in order to reduce brittleness and residual stresses, thus

avoiding an excessive softening of the alloy. It is therefore reasonable to select the highest temperature which does not result in a marked decrease in strength (200–300 °C). However, in cases in which Si precipitation only occurs during AM, a marked reduction in strength [387] can be observed for temperatures above 250 °C, presumably due to particle ripening, which is well described by the model curves. On these bases, a temperature of 225 °C/2 h appears to be an interesting candidate for stress relieving/low-temperature annealing treatment.

1.3. AlSi10Mg Alloy Produced by Additive Manufacturing: Creep Response

Although generally exhibiting poor creep resistance, aluminum alloys have attracted considerable attention as case-study materials (see [390,391] for detailed discussions). In addition, Al–Si alloys have been clearly demonstrated to behave as a sort of natural metal matrix composite in which an Al matrix is reinforced by Si particles [397]. In this sense, the creep response of these composites reinforced with nm-sized Si particles is an intriguing matter that deserves detailed investigation.

The creep behavior of AlSi10Mg produced by AM was first investigated in [253,398] and then more extensively addressed in [390], in the latter case by testing the as-deposited material. The experimental data, when described by the well-known phenomenological equation:

$$\dot{\varepsilon_m} = A(T)\sigma^n \tag{8.4}$$

where *A(T)* is a temperature dependent parameter, gave a stress exponent n that decreased with increasing temperature from 22 to 15. Such high values of the stress exponent are indeed frequently attributed to the strengthening effect of particle–dislocation [395,396]. On these bases, the MM described in Section 1.2 was successfully used in combination with the set of constitutive equations introduced in [390,391], namely:

$$\sigma = \sigma_0 + \sigma_p = \sigma_0 + \alpha m G b \rho^{1/2} \tag{8.5}$$

$$\dot{\varepsilon_m} = \frac{2M_{cg}\tau_l b L}{m}\left(\frac{\sigma_p}{\alpha m G b}\right)^4 \tag{8.6}$$

$$M_{cg} \cong \frac{D_{OL}b}{kT} exp\left(\frac{\sigma_p b^3}{kT}\right) exp\left\{-\frac{Q_L}{RT}\left[1-\left(\frac{\sigma_p}{R_{max}}\right)^2\right]\right\} exp\left(-\frac{U_{ss}}{RT}\right) \tag{8.7}$$

$$R_{max} = 1.5(R_{UTS^a} + \sigma_{Or})\frac{G_T}{G_{RT}} \tag{8.8}$$

The meanings of the different symbols are illustrated in *Table 8.1*, while the derivation of the model is reported in Appendix B. For a given value of the minimum strain rate, each of Eqs. (8.5)–(8.8) was applied in the hard and soft zones. The particle

strengthening term σ_0 was assumed to be equivalent to the Orowan stress and the particle size at the time corresponding to the minimum in creep rate was calculated using the equations in Appendix A, by assuming d_0 = 50 nm. The stress corresponding to the given strain rate was then expressed by Eq. (8.1). The resulting model curves are presented in *Figure 8.2*. The remarkable accuracy of the curves demonstrated that the basic assumption (creep response is mainly controlled by microstructure, i.e., by particle–dislocation interaction at a submicron scale, while, in this context, the mesostructured plays a minor role) was substantially correct.

The study presented here originated from the findings reported in the previous sections. As mentioned above, the creep response of Al10SiMg alloy has been dealt with by only a few studies and the subject is worth of deeper investigation. In addition, it has been recognized that annealing produces a softening of the microstructure but no quantitative models for this effect have been proposed. The aim of the study was thus twofold: i. to investigate the effect of low-temperature annealing (225 °C/2 h) on the creep response of heat-treated AM AlSi10Mg and compare the results with the as-deposited behavior; ii. to validate the quantitative predictions of the constitutive model that had already been successfully used for the as-deposited alloy.

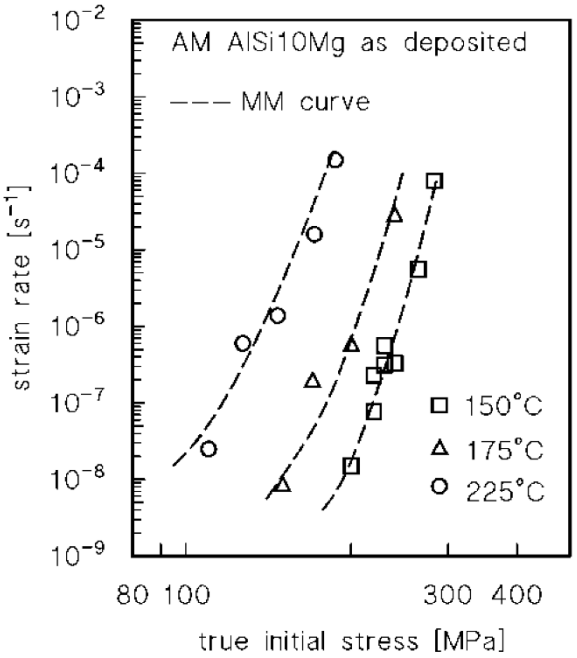


Figure 8.2. Experimental values of the minimum creep rate in as-deposited additive manufacturing (AM) AlSi10Mg and material model (MM) curves (see Appendixes A and B for the constitutive equations used in combination with the composite model, Eq. (8.1), with d_0 = 50 nm) [390].

2. Materials and Methods

Dogbone creep samples made of Al-9.6%Si-0.38% Mg alloy with a gauge length of 25 mm and a square section of 3 mm × 3 mm were produced by an SML500 machine (SLM Solutions, Lubecca, Germany) with the following deposition parameters: substrate temperature 150 °C, laser power 350 W, spot size 80 μm, scan speed 1.15 m/s, hatch spacing 170 μm, layer thickness 50 μm. The growth direction was parallel to the sample axis (loading direction). Stress relieving/low-temperature annealing at 225 °C for a duration of 2 h was applied to the as-built samples.

Constant load tensile creep experiments were carried out in air on the as-deposited samples at 150 °C, 175 °C and 225 °C. The samples were mostly strained up to rupture, although longer tests were interrupted after the end of the primary stage. The samples were heated in a three-zone furnace and both elongation, measured by LVDT, and temperature were continuously recorded during the test. Temperature was measured by four K-type thermocouples.

3. Results

After annealing, the microstructure of the alloy remained substantially similar to that shown in *Figure 8.A1* due the short annealing time, which, at maximum, could lead to an increase of a few nm in Si particle size.

Figure 8.3a shows typical examples of the strain vs. time creep curves. *Figure 8.3b* shows representative creep strain rate vs. strain curves.

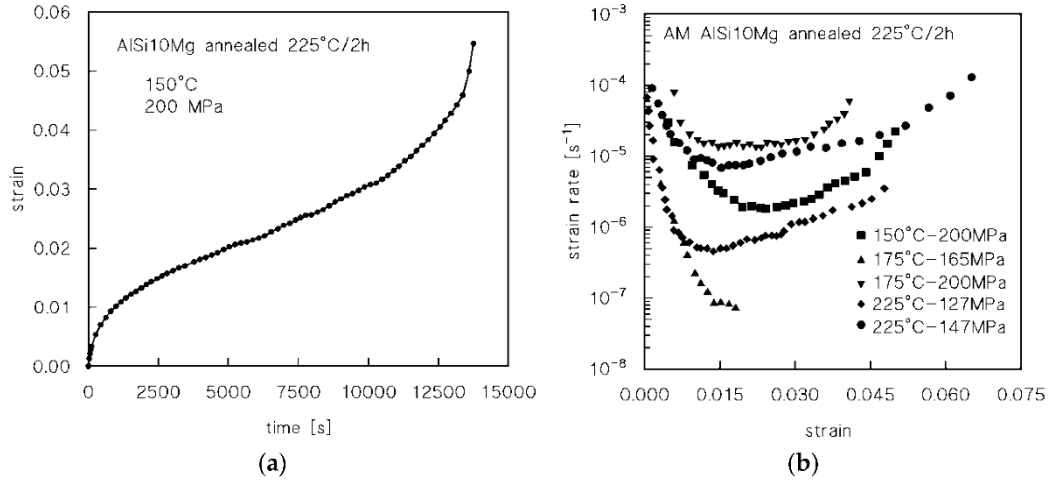


*Figure 8.3. Experimental creep curves: (**a**) example of strain vs. time curve; (**b**) strain rate vs. strain curves at different experimental conditions.*

The alloy exhibited the conventional three-stage behavior, with a well-defined primary region, a minimum creep rate range and a tertiary stage.

Figure 8.4 plots the minimum creep rate dependence on applied stress for the annealed alloy. The figure also plots the same data of *Figure 8.2*, obtained in [390], by testing the same material in the as-deposited condition. As in the case of the untreated alloy, the annealed material also exhibited high values for the stress exponent (n = 23, 29 and 17 at 150 °C, 175 °C and 225 °C respectively). The creep rates of the heat- treated alloy were higher than those of the as-deposited material, although the difference became smaller as the temperature and/or duration of the test increased. Within the range of experimental conditions investigated, the datasets for the as-deposited and the heat-treated materials align on almost parallel curves, i.e., indicating that the stress exponent was roughly equivalent, only at 150 °C. These findings indicate that, while at low temperatures the two materials behaved quite differently and heat treatment resulted in a marked worsening of the creep response, in the high temperature regime, in particular for long tests, i.e., low stresses, this effect progressively vanished and creep response became more and more similar.

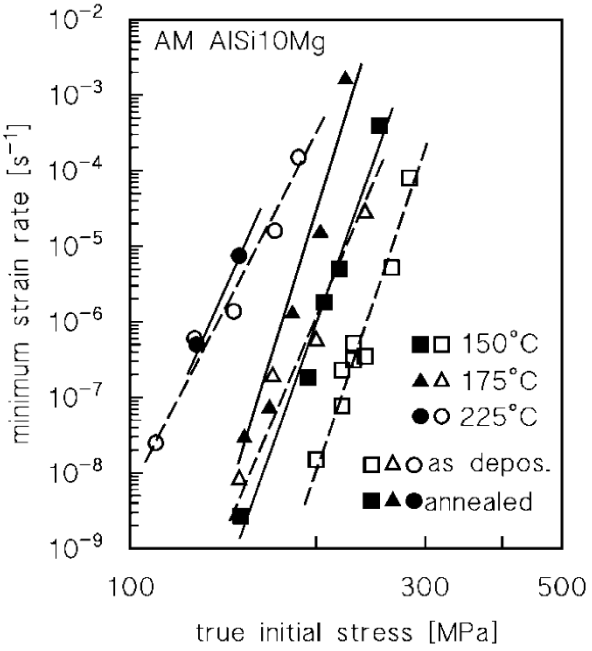


Figure 8.4. Minimum creep rate dependence on applied stress for the annealed and as-deposited [390] alloy.

Figure 8.5. plots the time to minimum creep rate (t_m) as a function of the minimum creep rate. The data align on a single line of slope − 1. The fact that the experimental data conform to the simple equation:

$$\dot{\varepsilon_m} t_m = c_m \tag{8.9}$$

implies that the same time-dependent mechanisms operate within the range of experimental conditions investigated.

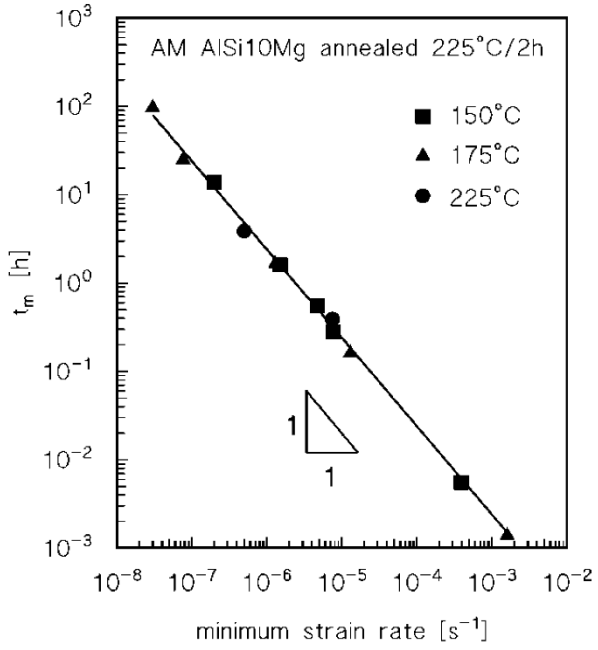


Figure 8.5. Time to minimum creep rate as a function of minimum creep rate for annealed alloy.

4. Discussion

4.1. Analysis of the Effect of Low-Temperature Annealing on Creep Response

Section 3 (*Figure 8.4*) unambiguously shows that even a low-temperature annealing at 225 °C for 2 h results in a marked decrease in creep properties, at least as long as the testing temperature does not exceed 150 °C. At higher temperatures, the reduction in creep response is more limited, because the as-deposited alloy also undergoes extensive softening during high-temperature exposure. In order to quantify the loss in creep resistance, the data in *Figure 8.4* were used to calculate Δσ, expressed as:

$$\Delta\sigma = \sigma^{ad} - \sigma^{ht} \tag{8.10}$$

where σ^{ad} and σ^{ht} are the stresses applied to obtain a given value of the minimum strain rate in as-deposited and heat-treated alloys, respectively (*Figure 8.6*). *Figure 8.6* only includes data for 150 and 175 °C, since at the higher temperature the experimental results for heat-treated and as-deposited alloys substantially overlap.

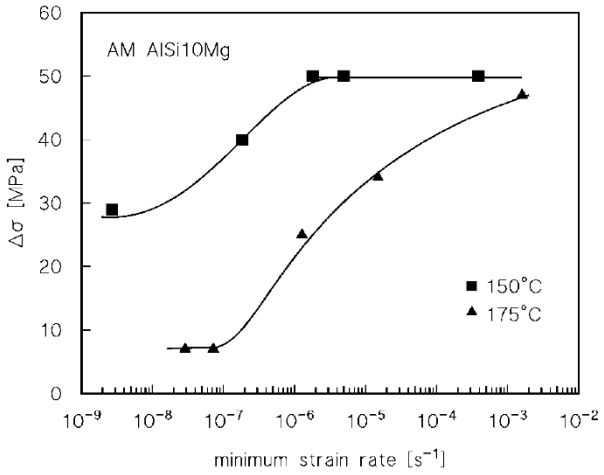


Figure 8.6. Δσ as a function of the minimum creep rate for 150 °C and 175 °C.

Figure 8.6 shows the as-deposited alloy creep tested at 150 °C maintained a 50 MPa advantage in strength until the minimum creep rate decreased below 10^{-6} s^{-1}. By contrast, at 175 °C, $\Delta\sigma$ monotonically decreased from 47 to 7 MPa with decreasing minimum creep rate. The softening obviously originates from the microstructural evolution during high-temperature exposure. Postprocessing annealing results in ripening/coarsening of the Si particles, which are the major sources of strengthening at high temperatures. At low testing temperatures, where ripening is a sluggish phenomenon, the advantage in creep strength is maintained until the time of exposure becomes so long that particles start to coarsen even in the as-deposited material. At 175 °C ripening is more rapid and the initial advantage of the as-deposited state, i.e., the presence of smaller particles in the microstructure, is rapidly lost and the two materials progressively become more and more similar. Although reasonable, this qualitative explanation needs to be supported by a more quantitative analysis of the relationship between creep response (the minimum creep rate) and the microstructural features (Si particle size and interparticle distance), which will be dealt with in the following section.

4.2. Modelling the Effect of Low-Temperature Annealing on Creep Response

Section 4.1 provides useful indications about the effect of annealing on creep response. Nevertheless, the combination of the constitutive equations illustrated in Appendixes A and B with the MM and Eq. (8.1) provides a useful tool for modelling creep response. All the parameters of the different equations are available, since the model was already successfully used to describe the as-deposited creep response (*Figure 8.2*). The only missing term is the time corresponding to the minimum creep rate, which, however, can be easily obtained from *Figure 8.5*. The annealing time was sufficiently short to not cause major variations in the microstructure, although a barely discernible

increase in size was nevertheless expected. Thus, Eq. (8.A6) in Appendix A can be used to estimate particle size after annealing. By taking d_0 = 50 nm, as in [390], after 2 h at 225 °C a particle size close to 59 nm can be obtained. Eq. (8.A6) and Eq. (8.9) can then be combined and used to estimate the size of the particles at tm for a given value of the minimum strain rate. Since the surface-to-surface interparticle spacing can be expressed as:

$$L = d\left(\frac{0.5}{\sqrt{6f/\pi}} - \sqrt{\frac{2}{3}}\right) \tag{8.11}$$

where f is the volume fraction of the particles (here assumed not to vary during the test, both in hard and soft zones), one obtains:

$$L = L_0 \frac{d}{d_0} \tag{8.12}$$

For the particles inside the cell only, particle distance was assumed to increase with time, due to ripening, until it reached half of the cell size (250 nm) and then to remain constant for longer durations. This assumption implied that, even for long time of exposure, at least one single particle remains in the cell interior. Once L has been determined, the equations in Appendix B can be used to calculate the model curves for the heat-treated material shown in *Figure 8.7*.

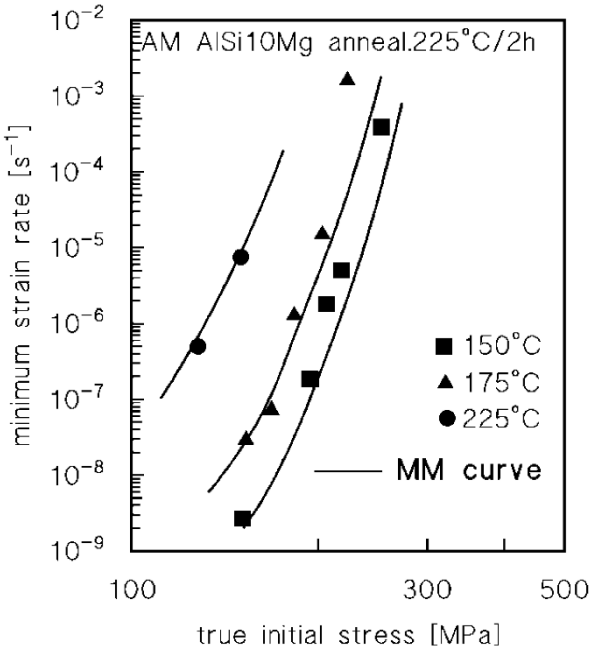


Figure 8.7. Model curves calculated for the material heat treated at 225 °C for 2 h. The only experimental datum used to calculate the curves is the relationship shown in Figure 8.4.

If one considers that all the parameters except the cm constant, which was, in fact, the only experimental value obtained from *Figure 8.4*, were calculated for the as-deposited alloy, the accuracy of the description is remarkable. The model significantly overestimates the material strength only in the very high strain rate region.

Figure 8.8a plots a comparison between the model curves obtained for the as-deposited and the heat-treated alloy; *Figure 8.8b* shows the experimental data available at 225 °C for the as-deposited alloy [390] and for the alloy annealed for 2 h at 225 °C (this study) and at 300 °C [398].

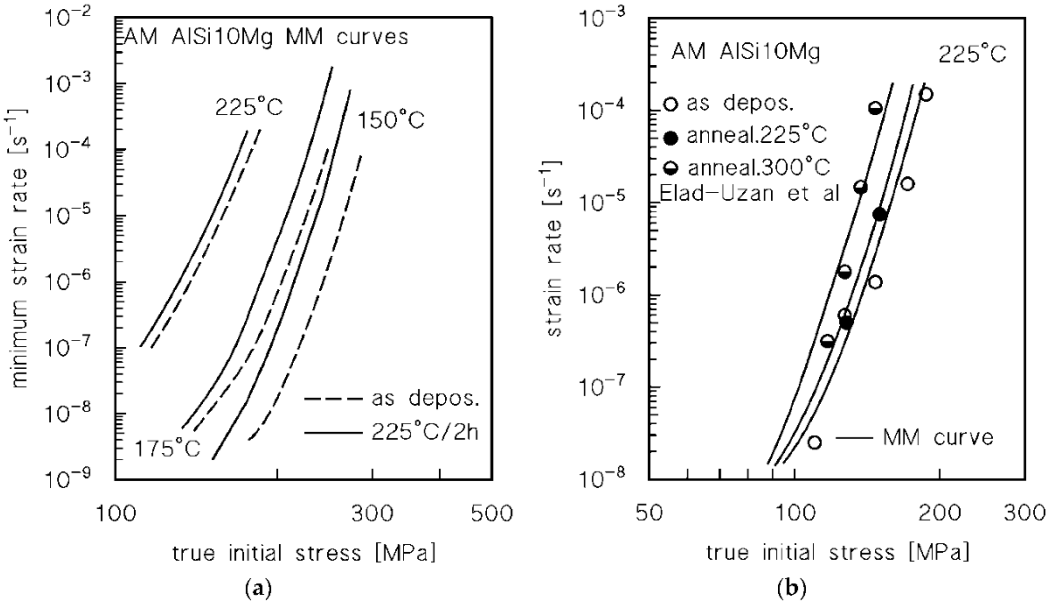


*Figure 8.8. (**a**) Model curves calculated for the as-deposited and the heat-treated (225 °C for 2 h) alloy; (**b**) minimum creep rate obtained at 225 °C for the as-deposited alloy [390] and for the alloy annealed for 2 h at 225 °C (this study) and at 300 °C [398]; (**b**) also includes the model curves calculated by combining the MM and the equations reported in Appendixes A and B.*

An interesting feature, which is qualitatively described in the previous subsection and well documented by *Figure 8.8b*, is the progressive convergence between the curves obtained for the different initial states as the strain rate decreases, i.e., the time of exposure increases. In addition, the advantage in creep response of the as-deposited alloy decreases as temperature increases (*Figure 8.8a*).

Both *Figure 8.7* and *Figure 8.8* validate the prediction of the model proposed in [392], which is sufficiently accurate to constitute a valid tool for the prediction of the creep response of the alloy investigated in different initial states.

The appropriateness of the basic assumption of the model, i.e., that the key factors controlling the creep response are the size and distribution of second-phase

particles, has thus been confirmed. Any annealing treatment causes ripening of the Si particles and, as a consequence, a reduction of the creep resistance of the alloy. The accuracy of the description implies that the model is a valid tool for the prediction of the creep response of Al–Si alloys, provided that sufficient data on the microstructural analysis and some information on the shape of the creep curve (the correlation between minimum creep rate and the time at which it is measured) are available. Ingot or rheo/thixocasting products actually exhibit microstructures which, after solution treatment, largely repeat the same morphology as that shown in Appendix A but at a larger scale, i.e., with much larger "cells" (the grains of Al) surrounded by a network of very coarse Si particles (see, for example, [399,400]). In this regard, the model presented here could in principle also be used for the analysis of the creep response of these conventionally produced materials.

5. Conclusions

The effect of low-temperature annealing at 225 °C on creep response was investigated by constant load experiments carried out at 150 °C, 175 °C and 225 °C. A comparison with the experimental data obtained by testing the as-deposited alloy demonstrated that annealing results in a loss of creep resistance that is more pronounced at lower temperatures. In general, the creep response of the as-deposited and of the heat-treated alloys became more and more similar as temperature increased and/or applied stress decreased. The alloy response was then compared with the prediction obtained from a physically-based model which took into account the effect of Si particle ripening. In order to apply the constitutive equations previously developed to describe pure aluminum and simpler Al alloys, the complex microstructure of AM AlSi10Mg was assimilated to that of a composite formed by soft zones (cell interiors) and hard zones (Si-rich eutectic regions). The constitutive equations were then used on the resulting simplified material model described by the rule of mixture. Since the values of all the parameters had been identified by studying the as-deposited material, only one datum was required for the physically-based model to work, namely the relationship between the time to minimum creep rate and minimum creep rate. The resulting description of the annealed material was excellent, as in the case of the as-deposited alloy, and the model was successfully validated. The straightforward conclusion is that the key factors which determine the creep response of the investigated material are the size and distribution of the second-phase particles. Annealing causes an increase in particle size and a parallel decrease in creep resistance that can be easily quantified by the proposed model.

Appendix A

Figure 8.A1 shows the microstructure of the alloy in the as-deposited state, with the cells surrounded by the fine Si particles.

During high-temperature exposure, once the precipitation process ends and the equilibrium volume fraction of the secondary phase (Si) is reached, the particles are thought to evolve by Ostwald ripening, which is described by an equation in the form:

$$d^3 = d_0^3 + \frac{64\gamma C_\infty V_m^2}{9RT} D_{eff}^t \quad (8.A1)$$

where d_0 is the initial particle size, d the particle size at time t, γ the interfacial energy, C_∞ the equilibrium concentration of the species that form the particles and V_m the molar volume of the particle.

The effective diffusion coefficient can be written as:

$$D_{eff} = D_{Ls} + A_{p2}\rho_m D_{ps} \quad (8.A2)$$

where $D_{Ls} = D_{0Ls}\exp(-Q_{Ls}/RT)$ is the lattice diffusion coefficient of the element forming the particle, $D_{ps} = D_{0ps}\exp(-Q_{ps}/RT)$ the corresponding pipe diffusion coefficient and ϱm the mobile dislocation density. A_{p2} is the effective sectional area for diffusion which takes into account the scavenging effect of solute atoms by moving dislocations. The mobile dislocation density can be obtained with the Orowan equation:

$$\dot{\varepsilon} = \frac{b}{m}\rho_m v_m \quad (8.A3)$$

where v_m is the dislocation velocity. Combined with Eq. (8.A1), Eq. (8.A2) gives:

$$D_{eff} = D_{Ls} + \frac{A_{p2}m}{bv_m}\dot{\varepsilon} D_{ps} \quad (8.A4)$$

If A_{p2} is indeed supposed to be proportional to the dislocation velocity v_m, then:

$$D_{eff} = D_{Ls}\left(1 + B'\dot{\varepsilon}\frac{D_{ps}}{D_{Ls}}\right) = D_{Ls}\left[1 + B\dot{\varepsilon}\, exp\left(\frac{Q_{Ls}-Q_{ps}}{RT}\right)\right] \quad (8.A5)$$

where $B = B'D_{0ps}/D_{0Ls}$ is a constant. Eq. (8.A5) is formally analogous to a similar equation proposed by Buffington et al. [401]. The Ostwald ripening equation thus becomes:

$$d^3 = d_0^3 + K_g D_{Ls} t + K_g D_{Ls} B\, exp\left(\frac{Q_{Ls}-Q_{ps}}{RT}\right)\dot{\varepsilon} t \quad (8.A6)$$

with:

$$K_g = \frac{64\gamma C_\infty V_m^2}{9RT} \quad (8.A7)$$

Since in the temperature range considered in this study the equilibrium solid solubility of Si in Al can be considered to be almost constant, the weak temperature

dependence of K_g was neglected. The activation energies in Eq. (8.A6) were considered to be Q_{Ls} = 124 kJ mol^{-1} and Q_{ps} = 0.6 Q_{Ls}; the calculation in [390] gave $D_{OLs}K_g$ = 2 × 10^{17} nm^3 h^{-1} and B = 10 s^{-1}.

In order to verify the accuracy of the model in predicting the effect of high-temperature exposure on particle size, the diameter of the Si particles after 30 h annealing (initial size 50 nm) was estimated and compared with the real microstructure in *Figure 8.A2*. At first glance, the model overestimates the size of the single particles; however, in the real microstructure, several agglomerates of these smaller Si precipitates can be observed. These agglomerates obviously behave as single larger particles. As a result, one can safely conclude that, although oversimplified, the description of the real microstructure of the alloy provided by the model is accurate.

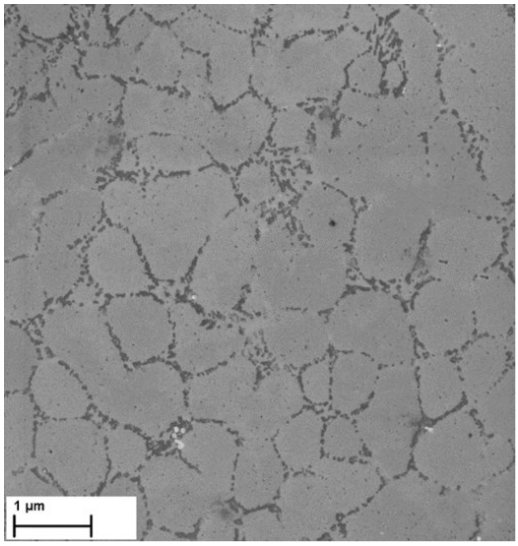


Figure 8.A1. Microstructure of the alloy in the as-deposited state.

Eq. (8.A6) was used to calculate the size of the particles in two conditions: i. after annealing, under the assumption that the precipitation process was completed during AM and ripening started just at the beginning of the postprocessing heat treatment; ii. during creep experiments, at the time corresponding to the minimum creep rate. In the latter case, since during primary creep the samples had experienced strain rates much higher than the minimum value, the value 10 $\dot{\varepsilon}$m was used for $\dot{\varepsilon}$ in Eq. (8.A6).

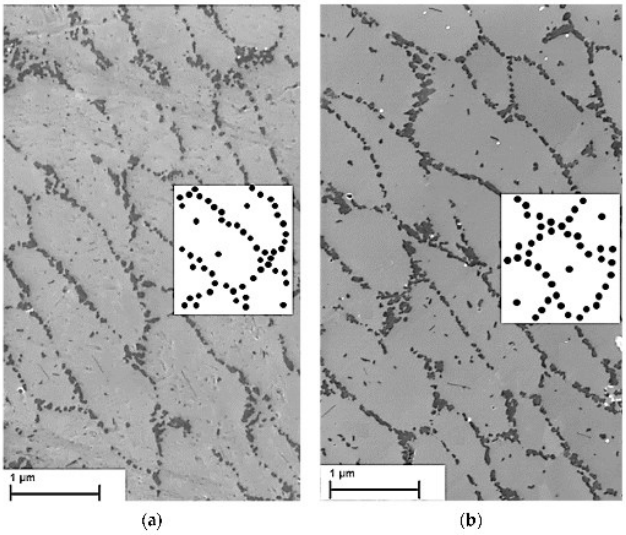


*Figure 8.A2. Comparison between the calculated particle size (the black circles in the insert, which qualitatively show the microstructure of the model material) and the real structure after annealing for 30 h. The diameter of the black circles in the inserts corresponds to the calculated particle size at the given magnification. (**a**) 175 °C, calculated size of Si particles = 53 nm; (**b**) 200 °C, calculated size of the particles = 63.*

Appendix B

The constitutive model was developed for Cu by [402–404] and was later modified to describe Al and its alloys [390,391]. The starting point is the well-known Taylor equation, here considered in a simplified form:

$$\sigma = \sigma_0 + \sigma_\rho = \sigma_0 + \alpha m G b \rho^{1/2} \tag{8.B1}$$

where ϱ is the dislocation density and $\sigma_\rho = \alpha m G b \rho^{1/2}$ is the dislocation hardening term. The stress σ_0 represents the strengthening contribution due to the interaction between fine particles and dislocations. This formulation of the Taylor equation does not take into account the stress required to move the dislocation in the absence of other dislocations nor the viscous drag stress due to solute atoms, since both these quantities, in a dilute solid solution reinforced by a fine dispersion of particles, are usually negligible when compared to the strengthening term due to particle–dislocation interaction.

The evolution of dislocation density during straining can be expressed as [402–404]:

$$\frac{d\rho}{d\varepsilon} = \frac{m}{bL^*} - \omega_p - \frac{2}{\dot{\varepsilon}} M_{cg} \tau_l \rho^2 \tag{8.B2}$$

where ω is a constant, τ_l is the dislocation line tension ($\tau_l = 0.5Gb^2$), M_{cg} is the dislocation mobility and L^* is the dislocation mean free path. At high temperatures, the equation can be simplified to:

$$\frac{d\rho}{d\varepsilon}=\frac{m}{bL^*}-\frac{2}{\dot{\varepsilon}}M_{cg}\tau_l\rho^2 \tag{8.B3}$$

The dislocation mean free path represents the distance travelled by a dislocation before it undergoes a reaction. In the presence of fine particles obstructing dislocation mobility, with L interparticle spacing, the dislocation mean free path can be expressed in the form [392]:

$$\frac{1}{L^*}=\frac{\sqrt{\rho}}{C_L}+\frac{1}{L} \tag{8.B4}$$

For alloys with densely spaced particles, Eq. (8.A11) becomes:

$$\frac{1}{L^*}\approx\frac{1}{L} \tag{8.B5}$$

At steady state, the combination of Eqs. (8.A8), (8.A10), and (8.A11) gives:

$$\dot{\varepsilon_m}=\frac{2M_{cg}\tau_l bL}{m}\left(\frac{\sigma_\rho}{\alpha mGb}\right)^4 \tag{8.B6}$$

Dislocation mobility in dilute Al-X solid solutions (where X is either Si or Mg) is [402–404]:

$$M_{cg}\cong\frac{D_0Lb}{kT}exp\left(\frac{\sigma_\rho b^3}{kT}\right)exp\left\{-\frac{Q_L}{RT}\left[1-\left(\frac{\sigma_\rho}{R_{max}}\right)^2\right]\right\}exp\left(-\frac{U_{ss}}{RT}\right) \tag{8.B7}$$

where R_{max} is the maximum strength of the alloy, tentatively quantified at room temperature as 1.5 times the ultimate tensile strength (R_{UTS}) of the alloy. The U_{ss} term describing the energy necessary for solute atoms to jump in and out of the clouds formed around dislocations has the form [403]:

$$U_{ss}=\frac{1}{3\pi}\frac{1+\nu}{1-\nu}\frac{G\Omega\delta R}{k} \tag{8.B8}$$

where ν is Poisson's ratio (= 0.3 in Al), Ω is the average Al atomic volume and δ is the volume atomic misfit.

ARTICLE 9

AlSi10Mg Alloy Produced by Selective Laser Melting: Relationship between Vickers Microhardness, Rockwell Hardness and Mechanical Properties

---

Emanuela Cerri & Emanuele Ghio

La Metallurgia Italiana, 7–8 (**2020**) 5–17

“The following version of the manuscript is made available under the CC-BY-NC-ND 4.0 license”

https://creativecommons.org/licenses/by-nc-nd/4.0/

AlSi10Mg Alloy Produced by Selective Laser Melting: Relationship between Vickers Microhardness, Rockwell Hardness and Mechanical Properties

Emanuela Cerri [1], Emanuele Ghio [1]

[1] Department of Engineering and Architecture, University of Parma, Via G. Usberti 181/A, 43124, Parma, Italy.

Abstract

Selective Laser Melted Al10SiMg samples were directly aged at different temperatures and times to establish the best mechanical properties for this alloy. The problem of finding meaningful relationships between hardness and tensile strengths has been addressed for materials produced by additive manufacturing technology. Relationships between hardness and yield and ultimate tensile strengths have been calculated by combining Hollomon parameters (the strain hardening exponent 'n' and the strength coefficient 'K') for the Selective Laser Melted Al10SiMg alloy. Firstly, the pre-existing relationships were considered and verified for AlSi10Mg SLMed alloy. Moreover, the relationship derived from ASTM standards and Hollomon parameters were calculated from the engineering stress-strain curves. Afterwards, the measured values of Rockwell hardness (HRF) and Vickers hardness (HV) were related to each other by a simple equation according to theory. The results showed the accuracy of this equation with respect to the theoretical one. Finally, the yield strength, UTS and ultimate strength (σ_b, in function of strain hardening exponent and natural base *e*) obtained by different condition of thermal treatments (175 °C, 200 °C and 225 °C for 2 h, 4 h and 6 h) were related to Vickers hardness values.

Keywords: Vickers microhardness, Rockwell hardness, Selective Laser Melting, AlSi10Mg, Yield strength, Ultimate tensile strength.

1. Introduction

Hardness and microhardness testing are fast and effective methods to determine the mechanical properties of metallic materials. In fact, they can be used and subsequently combined to have a first evaluation of mechanical properties such as yield and ultimate strength [405], playing an important role in the characterization of new alloys and production process. In this context, the "quasi-non-destructive" test as reported by Busby et al. [405] has to be considered too.

At present, Additive Manufacturing (AM) (as Selective Laser Melting (SLM)) is one of the prevalent technologies for metallic component production, but mechanical properties of those parts should be optimized [173,238,406] during post-process heat treatments. As the research of new thermal treatments to optimise mechanical properties requires a large quantity of material, the use of suitable correlations and equations starting from hardness measurements could solve the problem of optimization. In fact, the microstructure of SLMed components is thermodynamically unstable depending on temperature. Therefore, there is a great variation of yield strength, ultimate strength and elongation as function of treatment temperature and time duration [173,185,214,253].

Within this framework, the proposal of a new simple correlation between Vickers microhardness and Rockwell hardness, and the verification of pre-existing equations confirmed only for the traditional as-cast state are the objectives of this study [407]. As reported by Chen et al. [168], the conversion equations for hardness depend on yield strength (σ_y), Young's modulus (E), hardening exponent (n), strain coefficient (K) and different coefficients related to hardness test as indenter geometry (φ_1, φ_2, φ_3 and φ_4) and load (F_t and F_0). Eq. (9.1) reports the correlation between Vickers microhardness and Rockwell hardness as studied by [168]:

$$HV = \frac{\varphi_1 \varphi_2^n \left(F_t^{1/m} - F_0^{1/m}\right)}{\left(\varphi_3 \varphi_4^n (1+m)\right)^{1/m} (k - HR)} \left(\frac{\left(E/\sigma_y\right)^n \sigma_y}{1+n} \right)^{1-1/m} \tag{9.1}$$

$$\begin{cases} \varphi_1 = \dfrac{2\eta\gamma_1 D_R \sin\left(\theta/2\right)}{S} \\ \varphi_2 = \gamma_2 \\ \varphi_3 = \alpha_1 D_R^2 \\ \varphi_4 = \alpha_3 \\ m = n\alpha_4 + \alpha_2 \end{cases} \tag{9.2}$$

where m is the loading exponent, α_1, α_2, α_3, α_4 are constants as reported by Chen et al. [168] and shown in *Table 9.1*, D_R is the diameter of ball Rockwell indenter, γ_1 and γ_2 are coefficients reported in Eq. (9.3).

$$\begin{cases} \gamma_1 = \dfrac{3\alpha_1}{8\tan^2\left(\theta/2\right)} = 1.986 \\ \gamma_2 = 0.05753 \end{cases} \tag{9.3}$$

Table 9.1 also reports the angle θ of the Vickers indenter, the known constants η, S and k, the load and pre-load force induced by Rockwell hardness test.

Table 9.1. Parameters used in the Eq. (9.1) for hardness conversion [168]

Vickers microhardness		Rockwell hardness (HRF)	
α_1	32.45	α_1	8.142
α_2	2	α_2	1.104
α_3	0.05753	α_3	0.1578

Table 9.1. Cont.

Vickers microhardness		Rockwell hardness (HRF)	
α_4	0	α_4	0.4333
θ	136°	k	130 (for F scale)
η	0.102	-	
S	0.002		

Furthermore, the relationship between hardness and tensile strength and the equation of tensile strength (σ_b) are as follows [168,408]:

$$HV = \frac{2\eta\gamma_1(^{e\gamma_2}/_n)^n \sigma_b \sin\frac{\theta}{2}}{1+n} \quad (9.4)$$

$$\sigma_b = K\left(\frac{n}{e}\right)^n \quad (9.5)$$

where *e* is the Nepero's number and *n* and *K* are the Hollomon parameters as reported by *Table 9.2*. A very simple relationship is reported by Busby et al. [407] where the yield strength linearly depends on HV microhardness ($\sigma_y = 3.55$ HV). On the other hand, Tabor [165] and Cahoon [409] report other relationship between Vickers hardness and tensile strength, as follows:

$$UTS = \left(\frac{HV}{C}\right)(1-n)\left(\frac{12.5n}{1-n}\right)^n \quad (9.6)$$

$$\sigma_y = \left(\frac{HV}{3}\right)\left(\frac{1}{10}\right)^n \quad (9.7)$$

$$UTS = \frac{HV}{2.9}\left(\frac{n}{0.219}\right)^n \quad (9.8)$$

where *HV* is the Vickers hardness, *C* is a value between 2.9 and 3 as suggested by Tabor [165], n is the strain hardening and can be changed in Meyer's exponent as reported by [165,408]. Cahoon [408] suggested the range from 2.9 to 3.1 for the constant C. Finally, it is necessary to emphasize that the units of UTS and σ_y can be converted from kgf/mm^2 to MPa.

Table 9.2. Mechanical properties of AlSi10Mg dog-bone specimens obtained by tensile test (crosshead velocity: 0,02 mm/sec)

Temperature [°C]	HV	E [GPa]	σ_y [MPa]	UTS [MPa]	n	K [MPa]
T_as-built	112 ± 3	67 ± 3	215 ± 8	377 ± 14	0.255 ± 0.001	814 ± 1
B_as-built	122 ± 3	75 ± 5	297 ± 10	442 ± 15	0.204 ± 0.001	840 ± 1
T_175_2h	102 ± 2	74 ± 5	229 ± 8	363 ± 12	0.211 ± 0.001	712 ± 1
B_175_2h	122 ± 1	73 ± 5	241 ± 8	373 ± 12	0.201 ± 0.001	709 ± 1
T_175_4h	101 ± 2	73 ± 3	238 ± 6	375 ± 9	0.219 ± 0.001	754 ± 2
B_175_4h	115 ± 4	70 ± 5	252 ± 7	387 ± 11	0.213 ± 0.001	773 ± 2
T_175_6h	100 ± 3	73 ± 5	232 ± 9	370 ± 14	0.219 ± 0.001	748 ± 2
B_175_6h	113 ± 3	73 ± 3	285 ± 8	392 ± 11	0.200 ± 0.001	746 ± 2
T_200_2h	103 ± 3	72 ± 5	197 ± 5	327 ± 9	0.218 ± 0.001	741 ± 1

Table 9.2. Cont.

Temperature [°C]	HV	E [GPa]	σ_y [MPa]	UTS [MPa]	n	K [MPa]
B_200_2h	110 ± 3	73 ± 5	238 ± 8	360 ± 13	0.193 ± 0.001	671 ± 1
T_200_4h	101 ± 3	71 ± 2	216 ± 6	351 ± 10	0.236 ± 0.001	749 ± 2
B_200_4h	109 ± 3	80 ± 5	232 ± 5	372 ± 12	0.228 ± 0.001	784 ± 2
T_200_6h	100 ± 1	75 ± 5	220 ± 5	353 ± 8	0.204 ± 0.001	701 ± 1
B_200_6h	102 ± 2	74 ± 5	235 ± 8	323 ± 8	0.211 ± 0.001	631 ± 1
T_225_2h	107 ± 3	75 ± 4	198 ± 5	323 ± 8	0.209 ± 0.001	631 ± 1
B_225_2h	110 ± 3	73 ± 5	217 ± 6	340 ± 9	0.202 ± 0.001	652 ± 1
T_225_4h	101 ± 3	76 ± 5	192 ± 6	313 ± 9	0.209 ± 0.001	609 ± 1
B_225_4h	105 ± 2	72 ± 5	207 ± 7	323 ± 11	0.194 ± 0.001	601 ± 1
T_225_6h	98 ± 3	75 ± 5	184 ± 6	300 ± 9	0.198 ± 0.001	562 ± 1
B_225_6h	102 ± 2	73 ± 4	199 ± 6	313 ± 9	0.196 ± 0.001	589 ± 1

In this context, it is possible to observe that several studies and correlations are focused on steels such as AISI 304 [410], AISI 1020, AISI 316L [411] and on aluminium alloys like AA 6063-T5 and AA 1350 [411]. At present, no results are reported for AlSi10Mg produced by SLM. Therefore, this study aims to calculate and verify the correlations between the mentioned properties.

2. Material and Methods

Bulk specimens of AlSi10Mg aluminium alloy were produced by SLM from spherical gas-atomized powder with nominal composition shown in *Table 9.3*.

Table 9.3. Chemical composition of AlSi10Mg.

Al [%]	Si [%]	Fe [%]	Mg [%]	Cu [%]	Mn [%]	Zn [%]	Ti [%]	Pb [%]	Sn [%]
Bal.	9.60	0.10	0.38	< 0.05	< 0.01	<0 .01	< 0.01	< 0.01	< 0.01

SLM processing was carried out on a platform heated at 150 °C using an SLM500 device (SLM Solutions) equipped with an Yb-YAG laser. The parameters used for preparing the samples are as follows: scanning speed 1550 mm/s, power 350 W, layer thickness 50 mm, hatch spacing 0,17 mm. High purity argon gas was used during SLM processing in order to avoid oxygen contamination.

Solid geometries of 25 merged cylindrical bars with total length of 100 mm, total height of 300 mm and diameter of 10 mm were built. At the same time, bars with a 10x10 mm^2 area section were built in the same job with the same final height. Afterwards, tensile samples were cut and machined according to ASTM E804 from the solid geometries. Specimens were heat treated at 175°, 200° and 225 °C for 2, 4 and 6 h in an electric muffle-furnace. The same conditions were used for samples obtained by the billet. Tensile tests were performed at room temperature using a MTS810 machine in

according to ASTM E8 standard, at a strain rate of 0,008 s^{-1} on as-built and heat treated specimens.

Vickers microhardness (HV) was measured with a load of 500 g and a dwell time of 15 s according to UNI EN ISO 6507. The average HV values measured on dog bone samples have been related to their tensile properties (engineering stress strain curves). Rockwell hardness was measured, in according to UNI EN ISO 6508, with 10 kgf of pre-load and 60 kgf of load and ball indenter D_R of 1.588 mm diameter (HRF). HRF was evaluated on samples (nominated BS in this paper) cut from the bar.

Mathematical correlations were calculated by OriginPro 9.0 and the results compared to Eqs. (9.1) and (9.2). The analysis of engineering stress-strain curves obtained from tensile samples determined the calculation of Hollomon's parameters. In this case, the correlations have been evaluated according to Eqs. (9.4), (9.5), (9.6) and (9.13).

3. Results and Discussions

3.1. Relationship between HV and HRF

In this section, Vickers microhardness HV values and Rockwell HRF values are considered to determine the relationship between these two different hardness scales. All results obtained by hardness tests, performed on as-built 'BS' and on thermal treated 'BS' samples, are reported in *Figure 9.1*. *Figure 9.1* shows the trends that correlate HV microhardness to HRF hardness according to Eq. (9.1). In details, these plots were drawn considering data results from tensile tests (*Table 9.2*), the Eq. (9.2), the parameters reported in *Table 9.1* and the HRF values between 60 and 105. It is possible to observe that the upper and lower curves of *Figure 9.1* belong to the B_as-built state and T_225_6h, respectively. They create a domain for the included area where all the other heat treatment conditions are placed in. This region will be fundamental for comparison with test results. The aging at 225 °C for 6 h is the thermal treatment that induces the most significant decrease in hardness compared to the other heat treatments reported in *Table 9.2*. It should be noted that the Hollomon's parameters (*Table 9.2*), obtained plotting the true stress-strain curves in a Log-Log diagram as reported by [165,167,169,412], are also confirmed by I. Rosenthal et al. [406] working at the same heat treatment conditions and by [190,237].

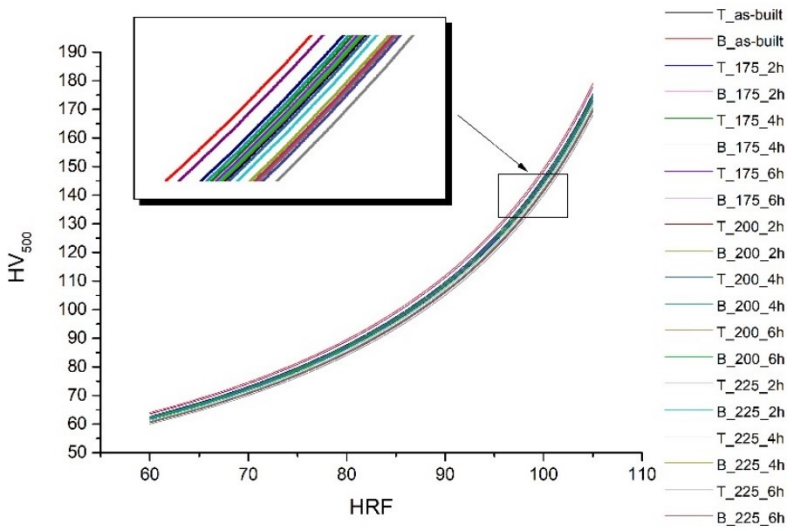


Figure 9.1. Curves obtained by Eq. (9.1) and parameters reported in Table 9.2.

As reported by Rometsch et al. [413], the strain hardening values of heat-treated aluminium casting alloys are much lower than those given in *Table 9.2*. This variation is attributable to the different microstructure between as-cast case and as-built case for AlSi10Mg alloy or heat treated with non-conventional treatments. In fact, as reported in *Figure 9.2a* [406], the size and morphology of microstructure and Si particles are greater than those reported in *Figure 9.2b*. As widely discussed in literature, the particular shapes and distribution of Si eutectic and precipitates induce high mechanical properties and consequently high Hollomon's parameters in the as-built cases and in non-conventional thermal treatment cases [173,185,214,237,253,406].

In general, the range of strain hardening exponent values suggests that the material could show a large uniform elongation. If there was a premature fracture, this would be due to the presence of defects within the microstructure [414].

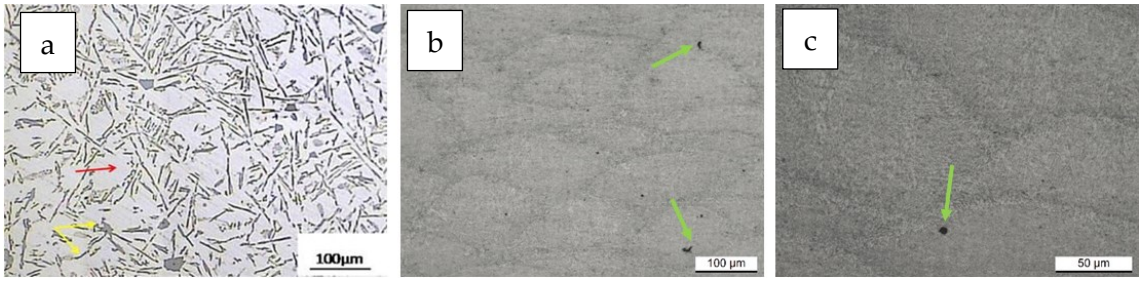


*Figure 9.2. OM images of (**a**) as-cast AlSi10Mg [408], (**b**) as-built AlSi10Mg SLMed (200×) and (**c**) as-built AlSi10Mg SLMed (500×). Red and yellow arrows mark Al matrix and Si eutectic, green arrows mark porosity.*

Finally, in *Figure 9.3* the true stress-strain curves and the trends of Hollomon's law ($\sigma = K\varepsilon^n$, [168]) are illustrated. All trends are comparable to those reported by [168].

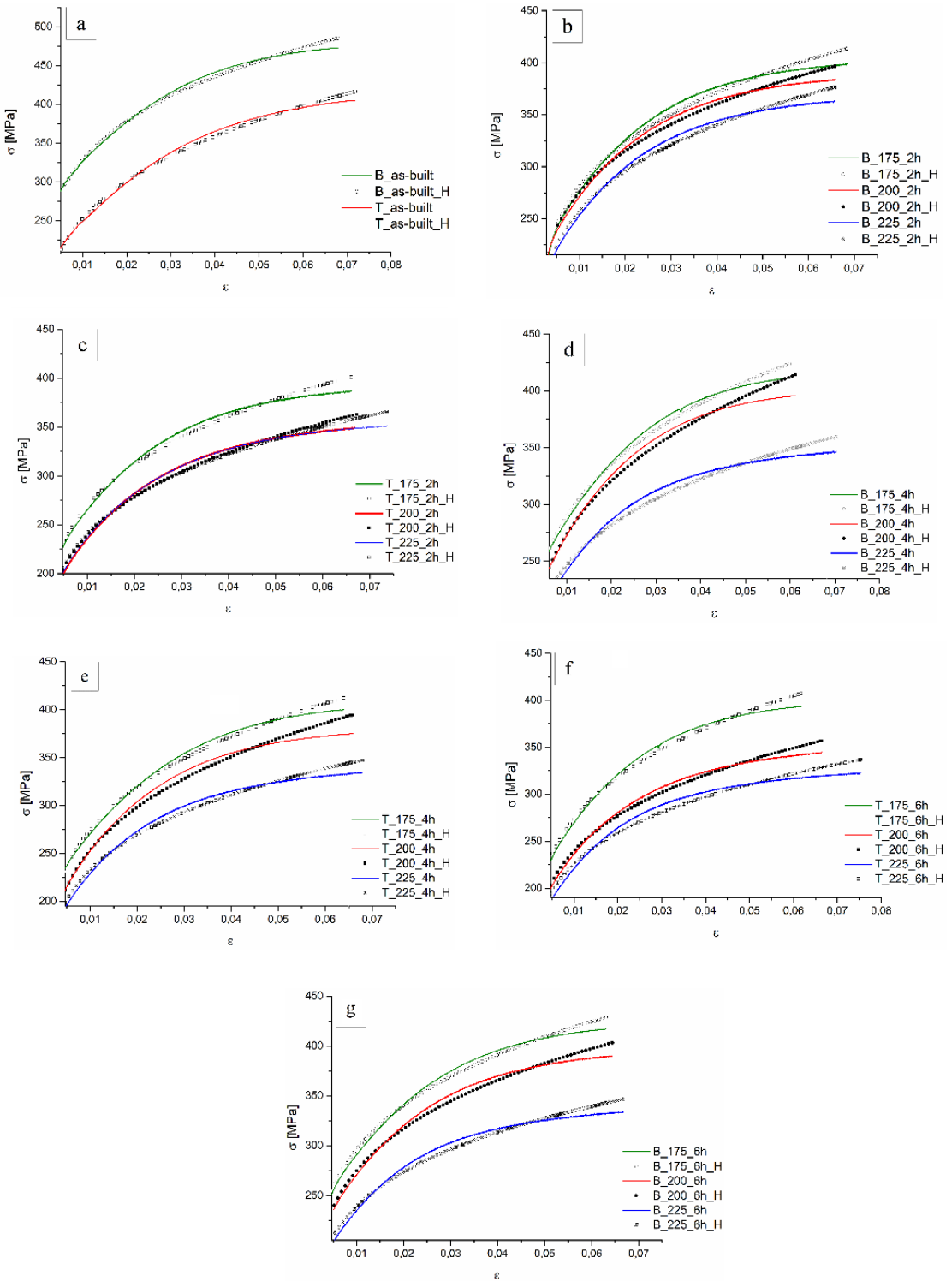


*Figure 9.3. True stress-strain curves Hollomon's law for different heat treatment conditions: (**a**) as-built, (**b**) and (**c**) 2 h at 175, 200, 225 °C, (**d**) and (**e**) 4 h at 175, 200, 225 °C, (**f**) and (**g**) 6 h at 175, 200, 225 °C.*

Figure 9.4 shows all the results obtained by hardness tests performed on as-built and on aged samples.

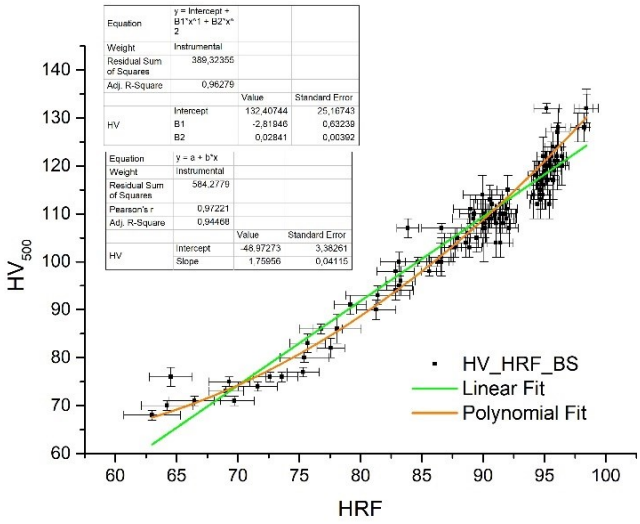


Figure 9.4. Vickers microhardness and Rockwell hardness values of as-built BS and thermal treated BS.

Moreover, in the same figure, the linear fit (green) and the polynomial fit (orange) are calculated in Eqs. (9.9) and (9.10) respectively:

$$HV_{500} = 1.7596\, HRF - 48.9727 \tag{9.9}$$

$$HV_{500} = 0.0284\, HRF^2 - 2.8195\, HRF + 132.4074 \tag{9.10}$$

The coefficients of determination (R^2) are 0.945 and 0.963 for Eq. (9.9) and Eq. (9.10), respectively. In *Figure 9.5*, the overlap of *Figure 9.4* and the domain of existence previously mentioned (upper and lower curve in *Figure 9.1*) are reported. It is possible to observe that comparing the linear and polynomial fit to domain derived from Eq. (9.1), the Eq. (9.10) correlates the two hardness scales with a better approximation than the Eq. (9.9). In other words, the polynomial function (orange line) has a greater range of existence contained within the domain (*Figure 9.1*) than the linear function (green function). Furthermore, both solutions have an intrinsic dependence on tensile properties as yield strength and Young's modulo due to their good approximation to Eq. (9.1).

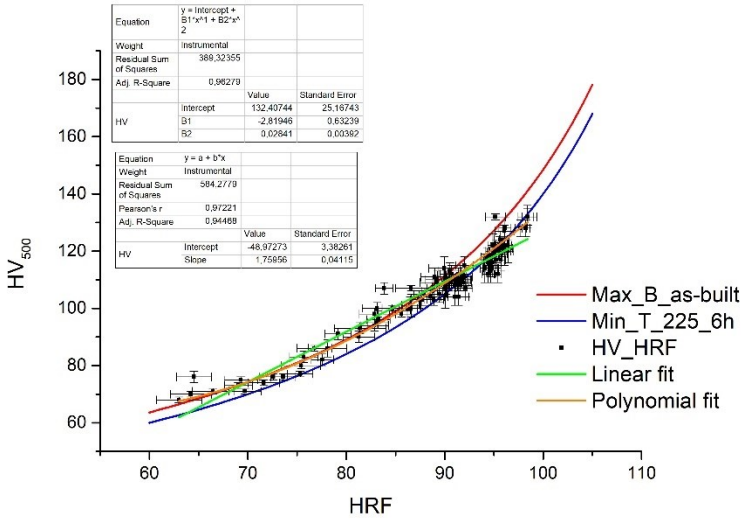


Figure 9.5. Overlap between the min and max curve obtained by Eq. (9.1) (red and blue curves) and the correlation reported by Eqs. (9.9) and (9.10).

In the same scenario, the equations described above make it possible to simplify the problem of correlation between hardness scales. In other words, HV microhardness and HRF hardness can be related by a polynomial fit equation without the necessary determination of mechanical properties of considered samples. This is also confirmed by the fact that R^2 has an excellent value for Eq. (9.10).

3.2. Relationship between Strength and Hardness

In this section, the focal point is the correlation of yield strength to HV and the dependence of UTS on HV (*Figure 9.6* and *Figure 9.7*, respectively). Many correlations found in literature depend on the strain hardening (n) and on various multiplication coefficients [165,168,408,409]; furthermore, it would be possible to list other simpler equations where hardness and tensile strengths have a direct proportionality [405,412]. *Figure 9.6* and *Figure 9.7* report the average value distributions obtained by microhardness and tensile tests. In addition, the red lines represent the linear fit between UTS and HV and between yield strength and HV as expressed in Eq. (9.11) and Eq. (9.12) respectively.

$$UTS = 3.20\ HV_{500} + 8.58 \tag{9.11}$$

$$\sigma_y = 2.54\ HV_{500} - 49.624 \tag{9.12}$$

So, looking at the Eq. (9.4) and comparing it to Eq. (9.11), it is necessary to consider Eqs. (9.3) and (9.5) and the parameters reported in *Table 9.1* and *Table 9.2*.

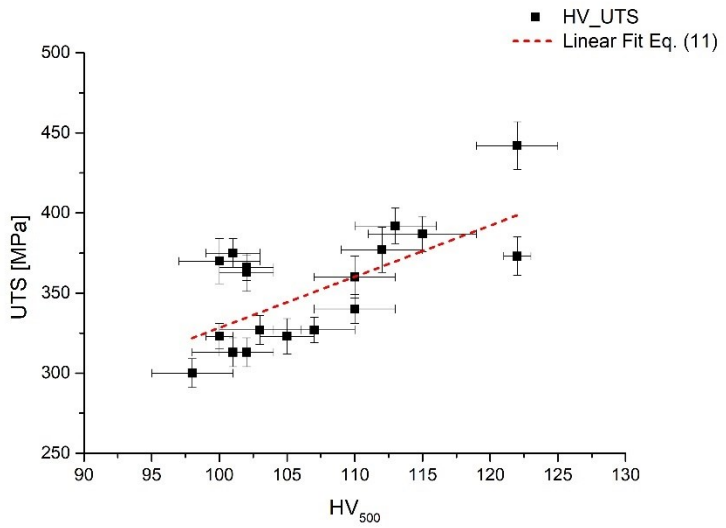


Figure 9.6. Linear fit between HV microhardness and UTS values reported in Table 9.2, where Eq. (11) is the new Eq. (9.11).

At this point it is possible to determine HV as function of σ_b [168,408] as predicted in Eq. (9.3). As reported by Li et al. [408], the σ_b is the maximum strength obtained in the engineering stress-strain curve. In other words, this strength is comparable to the UTS.

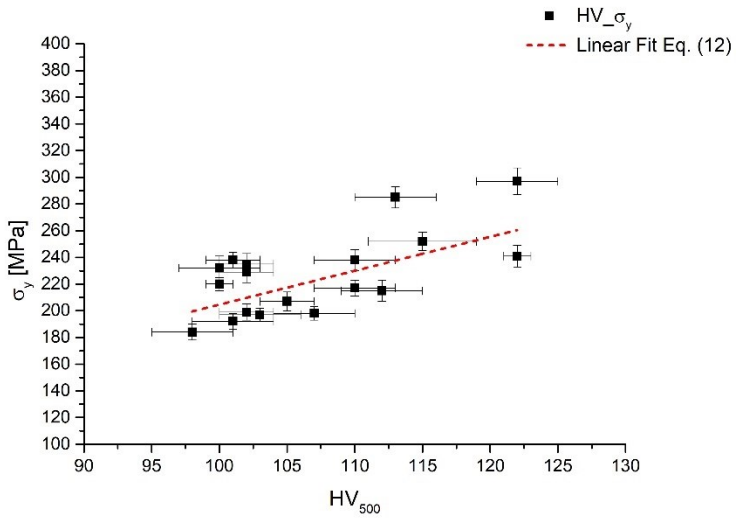


Figure 9.7. Linear fit between HV microhardness and σ_y values reported in Table 9.2 where Eq. (12) is the new Eq. (9.12).

With these premises, *Table 9.4* shows HV and σ_b values calculated through Eq. (9.3) and Eq. (9.5) respectively; it also reports the percentage errors calculated by comparing these values to HV and UTS as measured by microhardness and tensile tests. In the case of HV, an overestimation of 19 % and an underestimation of 4 % are obtained

comparing the values with HV, [168]. These error values are comparable to those reported by Kim et al. [415] and they depend on all strength values, σ_b, calculated by Eq. (9.5). In fact, as reported in *Figure 9.4*, the lower error of 10 % confirms the high overestimation of single HV hardness values (*Figure 9.8*). By considering the values of HV and UTS reported in the same table, and for the fact that σ_b is the UTS [408], it is possible to compare the linear fit (red line, Eq. (9.11)) of these values with the maximum and minimum of Eq. (9.4) in *Figure 9.8*. These curves, cyan and blue respectively, are calculated as expressed above and with the same method used in *Figure 9.1*. So, as already assessed in *Table 9.4* and shown in *Figure 9.8*, the max and min curve are shifted upwards compared to linear fit (Eq. (9.11)). This can be attributed to the percentage errors related to σ_b once again.

Table 9.4. Results of HV and tensile strength obtained by Eq. (9.1) and Eq. (9.3) and real values.

Temperature [°C]	HV [9]	HV	Error [%]	σ_b [MPa], [10]	UTS [MPa]	Error [%]
T_as-built	118	112 ± 3	5	445	377 ± 14	15
B_as-built	146	122 ± 3	17	495	442 ± 15	11
T_175_2h	121	102 ± 2	16	415	363 ± 12	13
B_175_2h	125	122 ± 1	2	420	373 ± 12	11
T_175_4h	124	101 ± 2	19	434	375 ± 9	13
B_175_4h	130	115 ± 4	12	449	387 ± 11	14
T_175_6h	124	100 ± 3	19	431	370 ± 14	14
B_175_6h	132	113 ± 3	14	442	392 ± 11	11
T_200_2h	123	103 ± 3	16	428	327 ± 9	15
B_200_2h	122	110 ± 3	10	403	360 ± 13	11
T_200_4h	116	101 ± 3	11	421	351 ± 6	16
B_200_4h	130	109 ± 3	16	445	372 ± 8	16
T_200_6h	121	100 ± 1	18	368	353 ± 8	12
B_200_6h	109	102 ± 2	6	417	323 ± 8	12
T_225_2h	113	107 ± 3	5	369	323 ± 8	11
B_225_2h	106	110 ± 3	– 4	386	340 ± 9	12
T_225_4h	105	101 ± 3	4	356	313 ± 9	12
B_225_4h	101	105 ± 2	– 4	361	323 ± 11	10
T_225_6h	105	98 ± 3	7	335	300 ± 9	10
B_225_6h	106	102 ± 2	4	332	313 ± 9	11

As the aim of this paper is the determination of a simple correlation between HV and UTS, it is opportune to start from the omission of σ_b. In fact, the use of UTS in the Eq. (9.6) and Eq. (9.8) leads to account for a lower overestimation of HV values than the use of the Eq. (9.4). In fact, this value decrease from 12 % to 9 %. *Figure 9.9* shows the trends of Tabor and Cahoon equations compared to linear fit (Eq. (9.11)) shown in *Figure 9.6*. It is possible to observe that the slopes are fully comparable (3.55 for Eq. (9.6) and 3.45 for Eq. (9.6) but using the Cahoon equation rather than the Tabor one it is possible

to get a better approximation of Eq. (9.11). For the reasons expressed and remembering the Tabor equation, the factor C calculated for AlSi10Mg SLMed is exactly 2.99. As reported by Cahoon [409], the suggested range value of C is from 2.9 to 3.1.

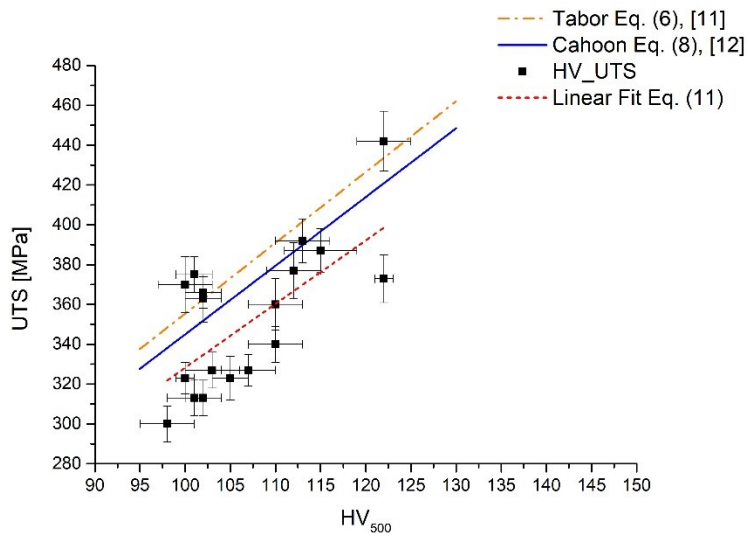


Figure 9.8. Correlation between Tabor (Eq. (9.6)) and Cahoon equation (Eq. (9.8)) and the linear fit reported in Figure 9.6. The References [11,12] are replaced by [165,409].

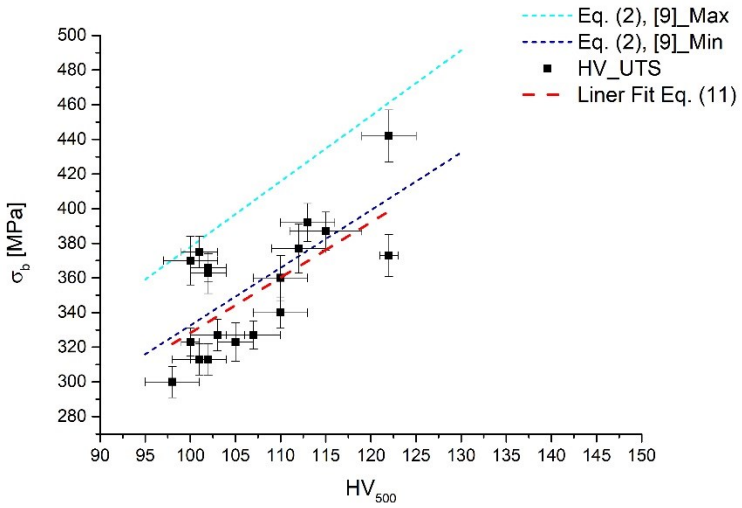


Figure 9.9 Results obtained by Eq. (9.2) (cyan line for the max and blu line for the min) and by linear interpolation reported in Figure 9.6. The Reference [9] is replaced by [168].

As regards the correlation between Vickers microhardness and yield strength, the considered equations are reported in *Figure 9.10*. All reported values of HV and σ_y are related through the following linear fit:

$$\sigma_y = 2.54\ HV_{500} - 49.62 \tag{9.12}$$

The standard error associated to the slope is 0.860. In this case, the best fit for aluminium alloys is represented by the Petty equation [169]:

$$\sigma_y = 0.148\ HV_{500} - 1.59 \tag{9.13}$$

It should be noted that the unit of measure of yield strength is in ton/in^2, so the conversion in MPa must be done multiplying for 15.4448. By applying this conversion factor, the slope of Petty equation is close to the slope reported in Eq. (9.12). In addition, the similar trend between this last equation and Eq. (9.13), [169] leads to suppose that the SLM process does not change the existing relationship between HV and the yield strength.

On the contrary, Eq. (9.7) underestimates the yield strength. So, the Eq. (9.14) introduces the coefficient ξ to better approximate the Cahoon equation to this study, as also performed by Keist et al. [170]. The value of ξ was estimated to be 0.891, average value of all cases reported in *Table 9.2*.

$$\sigma_y = \left(\frac{HV}{\xi \cdot 3}\right)\left(\frac{1}{10}\right)^n \tag{9.14}$$

Finally, as reported by Krishna et al. [412], it is possible to compare the linear fit with the ratio between UTS and yield strength: i) Low ratio (U-y < 1.20), ii) Medium ratio (1.20 < U-y < 1.52) and iii) High ratio (U-y > 1.52). In the present study, the average of all calculated ratios is 1.57. The results reported in *Table 9.5* show similar proportionality coefficient between present results and their correlations. It should be noted the proportionality coefficient can be compared if the linear interpolations have the coordinate zero as intercept. From this premise, the points reported in *Figure 9.5* and *Figure 9.6* are correlated with Eqs. (9.15) and (9.16) shown in *Table 9.5*.

Table 9.5. Equations (9.15) and (9.16) obtained by linear fit and reported by [412].

Data type	Equations	R^2	Valid range (HV)	Reference
High U-y ratio	UTS = 3.865 HV	0.845	50–142	[412]
	σ_y = 1.97 HV	0.665		
	UTS = 3.328 HV	0.995	95–125	Eq. (9.15)
	σ_y = 2.155 HV	0.987		Eq. (9.16)

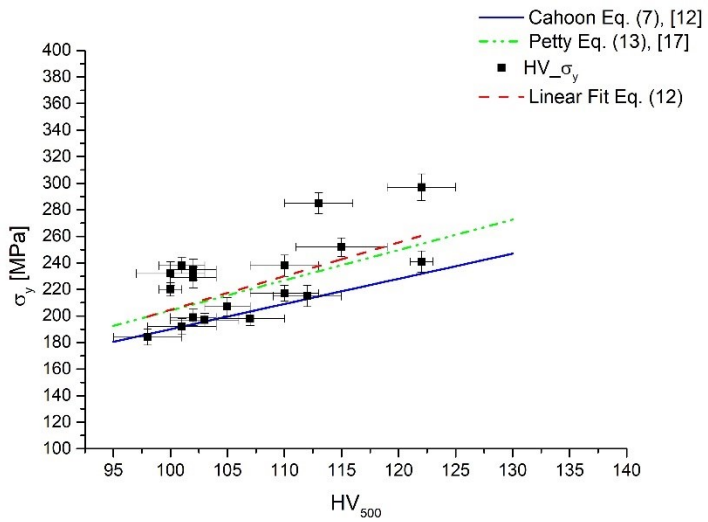


Figure 9.10. Correlation between microhardness and yield strength derived by Cahoon (Eq. (9.7)) and Petty equation (Eq. (9.13)) and linear fit reported in Figure 9.7. The References [12,17] are replaced by [169,409].

4. Conclusions

In the present paper, the relationships between HV and HRF hardness and HV and tensile strengths have been studied for AlSi10Mg alloy processed by SLM. Correlations were found for samples in the as built conditions and after aging treatments. The main conclusions can be summarised as follows:

1. The relationship between Vickers microhardness (HV) and Rockwell hardness (HRF) can be approximated by a second order equation. The dependence on mechanical properties and on geometry parameters of hardness tests are intrinsically expressed.
2. A linear relationship between Vickers microhardness and tensile properties can be applied with good approximation. The minimum overestimation of UTS values is obtained by Cahoon equation. For yield strength, the best approximation is obtained by Petty equation.
3. For this alloy the factor C considered in Tabor equation was calculated; the value obtained is 2.99.
4. The ranges suggest for strain hardening n is from 0.19 to 0.25 and for strength coefficient K is from 589 to 890 MPa for the case reported in this paper.

REFERENCES

[1] Davis, J.R. *ASM Specialty Handbook: Aluminium and Aluminium Alloys*, ASM International: Kinsman Rd, Novelty, OH, USA, **1993**.

[2] Polmear, I. *Light Alloys – From traditional Alloys to Nanocrystals*, Butterworth-Heinemann: Oxford, UK, vol. 4, pp. 97–235, **2005**.

[3] Raahaguem, B.; Williams, F. Introduction: Primary Aluminium-Alumina-Bauxite. *Smelter Grade Alumina from Bauxite*. Springer: Berlin, Germany, **2022**.

[4] Alloys, W.A. *International Alloys Designations and Chemical Composition Limits for Wrought Aluminium and Wrought Aluminium Alloys*, The Aluminium Association: Arligton, VA, **2005**.

[5] Kaufman, J. Applications for Aluminium Alloys and Tempers. *Introduction to Aluminium Alloys and Tempers*. ASM International: Kinsman Rd, Novelty, OH, USA, **2000**.

[6] Miao, Q.; Wu, D.; Chai, D.; Zhan, Y.; Bu, G.; Niu, F.; Ma, G. Comparative study of microstructure evaluation and mechanical properties of 4043 aluminum alloy fabricated by wire-based additive manufacturing. *Mater. Des.* **2020**, *186*, 108205. https://doi.org/10.1016/j.matdes.2019.108205

[7] Batukhtina, E.E.; Romanova, R.V.; Balokhonov, R.R.; Shakijanov, V.S. A crystal plasticity model for the deformation behavior of aluminum single crystals. *AIP Conf. Proced.* **2016**, *1785*, 040006. https://doi.org/10.1063/1.4967063

[8] Morinaga, M. Local Lattice Strains Around Alloying Elements in Metals. *A Quantum Approach to Alloy Design - An Exploration of Material Design and Development Based Upon Alloy Design Theory and Atomization Energy Method.* Elsevier: Amsterdam, The Netherlands, pp. 221–260, **2019**.

[9] Milkereit, B.; Starink, M.J.; Rometsch, P.A.; Schick, C.; Kessler, O. Review of the Quench Sensitivity of Aluminium Alloys: Analysis of the Kinetics and Nature of Quench-Induced Precipitation. *Materials*. **2019**, *12(14)*, 4083. https://doi.org/10.3390/ma12244083

[10] Wu, Y.; Liu, C.; Liao, H.; Jiang, G.; Ma, A. Joint effect of micro-sized Si particles and nano-sized dispersoids on the flow behavior and dynamic recrystallization of near-eutectic Al-Si based alloys during hot compression. *J. Alloys Compd.* **2021**, *856*, 158072. https://doi.org/10.1016/j.jallcom.2020.158072

[11] Joseph, S.; Kumar, S. A systematic investigation of fracture mechanisms in Al–Si based eutectic alloy—Effect of Si modification. *Mater. Sci. Eng. A.* **2013**, *588*, 111–124. https://doi.org/10.1016/j.msea.2013.09.019

[12] Zhou, X.; Xu, H.; Wu, Y.; Jiang, J.; Ma, A. Effect of eutectic Si size on the flow behavior and hot processing map of near eutectic Al–Si alloy. *J. Mater. Res. Technol.* **2021**, *15*, 5694–5705 https://doi.org/10.1016/j.jmrt.2021.11.015

[13] Edwards, G.A.; Stiller, K.; Dunlop, G.L.; Couper, M.J. The precipitation sequence in Al-Si-Mg alloys. *Acta Mater.* **1998**, *46(11)*, 3839–3904. https://doi.org/10.1016/S1359-6454(98)00059-7

[14] Andersen, J.S.; Sanderbergen, H.W.; Jansen, S.; TrÆholt, C.; Tundal, U.; Reiso, O. The crystal structure of the β'' phase in Al-Mg-Si alloys. *Acta Mater.* **1998**, *46(9)*, 3283–3298. https://doi.org/10.1016/S1359-6454(97)00493-x

[15] He, S.; Wang, J.; Zhang, D.; Wu, Q.; Kong, Y.; Du, Y. A First-Principles Study of the Cu-Containing β" Precipitates in Al-Mg-Si-Cu Alloy. *Materials*. **2021**, *14(24)*, 7879. https://doi.org/10.3390/ma14247879

REFERENCES

[16] Maeda, T.; Kaneko, K.; Namba, T.; Koshino, Y.; Sato, Y.; Teranishi, R.; Aruga, Y. Structural and compositional study of precipitates in under-aged Cu-added Al-Mg-Si alloy. *Sci. Rep.* **2018**, *8*, 16629. https://doi.org/10.1038/s41598-018-35134-8

[17] Ragab, K.A.; Bouazara, M.; Chen, X.G. Influence of Thermal Aging Parameters on the Characteristics of Aluminum Semi-Solid Alloys. *Metals*. **2018**, *8(10)*, 746. https://doi.org/10.3390/met8100746

[18] Singh, G.; Sharma, N. Study on the influence of T4 and T6 heat treatment on the wear behavior of coarse and fine WC particulate reinforced LM28 Aluminium cast composites. *JCOMC*. **2021**, *4*, 100106. https://doi.org/10.1016/j.jcomc.2021.100106

[19] Dahle, A. Heat Treatment of Aluminium Alloys. *Encyclopedia of Materials Science and Technology*. Elsevier: New York, vol. 3, pp. 1–3, **2001**.

[20] Kumar, M.S.; Javidrad, H.R.; Shanmugam, R.; Ramoni, M.; Adediran, A.A.; Pruncu, C.I. Impact of Print Orientation on Morphological and Mechanical Properties of L-PBF Based AlSi7Mg Parts for Aerospace Applications. *Silicon*. **2020**, *14*, 7083–7097. https://doi.org/10.1007/s12633-021-01474-w

[21] Sai Ganesh, M.R.; Reghunath, N.; Levin, M.J.; Prasad, A.; Doondi, S.; Shankar, K.V. Strontium in Al–Si–Mg Alloy: A Review. *Met. Mater. Int.* **2022**, *28*, 1–40. https://doi.org/10.1007/s12540-021-01054-y

[22] Donachie, M. *Titanium: A technical guide*, Materials Park, **2000**.

[23] Osman, R.B.; Swain, M.V. A Critical Review of Dental Implant Materials with an Emphasis on Titanium versus Zirconia. *Materials*. **2015**, *8(3)*, 932-958. https://doi.org/10.3390/ma8030932

[24] Bieler, T.; Trevino, R.; Zeng, L. *Encyclopedia of Condensed Matter Physics*. Chapter: Alloys: Titanium, pp. 66–76, **2005**.

[25] Kolli, R.P.; Devaraj, A. A Review of Metastable Beta Titanium Alloys. *Metals*. **2018**, *8(7)*, 506. https://doi.org/10.3390/met8070506

[26] Gorynin, I.; Ushkov, S. The strengthening molybdenum and aluminium equivalents of alloying elements in titanium alloys; in *Titanium'99: Science and Technology – Ninth Conference on Titanium*, **1999**.

[27] Takajo, S.; Tomida, T.; Caspi, E.N.; Pesach, A.; Tiferet, E.; Vogel, S.C. Property Improvement of Additively Manufactured Ti64 by Heat Treatment Characterized by In Situ High Temperature EBSD and Neutron Diffraction. *Metals*. **2021**, *10(11)*, 1661. https://doi.org/10.3390/met11101661

[28] Kumar, K.N.; Muneshwar, P.; Singh, S.K.; Jha, A.K.; Pant, B. Thermo Mechanical Working and Heat Treatment Studies on Meta-Stable Beta Titanium Alloy (Ti15V3Al3Sn3Cr) Plates. *Mater. Sci. Forum.* **2015**, *830–831*, 151–155. https://doi.org/10.4028/www.scientific.net/MSF.830-831.151

[29] Soundrarajan, S.; Vishnu, J.; Manuvasagam, G.; Muktinutalapati, N.R. Heat Treatment of Metastable Beta Titanium Alloys, Alfaro, S.C.A.; Borek, W.; Tomiczek, N. eds; IntechOpen: London, UK, **2020**.

[30] Tarin, P.; Gualo, A.; Simón, A.; Piris, N.M.; Badía, J.M. Study of Alpha-Beta Transformation in Ti-6Al-4V-ELI. Mechanical and Microstructural Characteristics. *Mater. Sci. Forum.* **2010**, *638–642*, 712–717. https://doi.org/10.4028/www.scientific.net/MSF.638-642.712

[31] Meyer, L.W.; Krüger, L.; Sommer, K.; Halle, T.; Hockauf, M. Dynamic strength and failure behavior of titanium alloys Ti-6Al-4V for a variation of heat treatments. *Mech. Time Depend. Mater.* **2008**, *12*, 237–247. https://doi.org/10.1007/s11043-008-9060-y

[32] Rogoff, E.; Antony, M.; Markle, P. Calculating Ti-6Al-4V β-Transus Through a Chemistry-Based Equation Derived from Combined Element Binary Phase Diagrams. *J. Mater. Eng. Perform.* **2018**, *27*, 5227–5235. https://doi.org/10.1007/s11665-018-3432-5

[33] Ghio, E.; Cerri, E. Additive Manufacturing of AlSi10Mg and Ti6Al4V Lightweight Alloys via Laser Powder Bed Fusion: A Review of Heat Treatments. *Materials*. **2022**, *15(6)*, 2047. https://doi.org/10.3390/ma15062047

[34] Morri, A. Trattamenti termici delle leghe α+β, correlazioni fra microstruttura a comportamento meccanico. *Metall. Ita.* **2008**, *11–12*, 1–10.

[35] Zherebstov, S.; Salishchev, G.; Łojkowski, W. Strengthening of a Ti-6Al-4V titanium alloy by means of hydrostatic extrusion and other methods. *Mater. Sci. Eng. A.* **2009**, *515(1–2)*, 43–48. https://doi.org/10.1016/j.msea.2009.03.005

[36] Oh, S.-T.; Woo, K.-D.; Kim, J.-H.; Kwak, S.-M. The Effect of Al and V on Microstructure and Transformation of β Phase during Solution Treatments of Cast Ti-6Al-4V Alloy. *Korean J. Mer. Mater.* **2017**, *55(3)*, 150–155. https://doi.org/10.3365/KJMM.2017.55.3.150

[37] Julien, R.; Velay, V.; Vidal, V.; Dahan, Y.; Forestier, R.; Rézaï-Aria, F. Characterization and modeling of forged Ti-6Al-4V Titanium alloy with microstructural considerations during quenching process. *Int. J. Mech. Sci.* **2018**, *142–143*, 456–467. https://doi.org/10.1016/j.ijmecsci.2018.05.023

[38] Yumak, N.; Aslantaş, K. A review on heat treatment efficiency in metastable β titanium alloys: the role of treatment process and parameters. *J. Mater. Res. Technol.* **2020**, *9(6)*, 15360–15380. https://doi.org/10.1016/j.jmrt.2020.10.088

[39] Veiga, C.; Davim, J.; Loureiro, A. Properties and applications of titanium alloys: A brief review. *Rev. Adv. Mater.* **2012**, *32*, 13–34.

[40] Rack, H.J.; Qazi, J.I. Titanium alloys for biomedical applications. *Mater. Sci. Eng. C.* **2006**, *26(8)*, 1267–1277. https://doi.org/10.1016/j.msec.2005.08.032

[41] Oryshchenko, A.S.; Gorynin, I.V.; Leonov, V.P.; Kudryavtsev, A.S.; Mikhailov, V.I.; Chudakov, E.V. Marine titanium alloys: Present and future. *Inorg. Mater. Appl. Res.* **2015**, *6*, 517-579. https://doi.org/10.1134/S2075113315060106

[42] ASTM *52900:2015*, *Additive Manufacturing – General Principles – Terminology*, West Conshohocken, PA, USA, **2015**.

[43] Martin, J.H.; Yahata, B.D.; Hundley, J.M.; Mayer, J.A.; Schadler, T.A.; Pollock, T.M. 3D printing of high-strength aluminium alloys. *Nature.* **2017**, *549*, 365–369. https://doi.org/10.1038/nature23894

[44] Williams, J.C.; Boyer, R.P. Opportunities and Issues in the Application of Titanium Alloys for Aerospace Components. *Metals*. **2020**, *10(6)*, 705–727. https://doi.org/10.3390/met10060705

[45] Vanmuster, L.; D'Haeyer, C.; Coucke, P.; Braem, A.; Van Hooreweder, B. Mechanical behavior of Ti6Al4V produced by laser powder bed fusion with engineered open porosity for dental applications. *J. Mech. Behav. Biomed. Mater.* **2022**, *126*, 104974. https://doi.org/10.1016/j.jmbbm.2021.104974

[46] Huang, R.; Riddle, M.; Graziano, D.; Warren, J.; Das, S.; Nimbalkar, S.; Cresko, J.; Masent, E. Energy and emissions saving potential of additive manufacturing: the case of lightweight aircraft components. *J. Clean. Prod.* **2016**, *135*, 1559–1570. https://doi.org/10.1016/j.jclepro.2015.04.109

[47] Duda, T.; Raghavan, L.V. 3D metal printing technology: the need to re-invent design practice. *AI & Soc.* **2021**, *33*, 241–252. https://doi.org/10.1007/s00146-018-0809-9

[48] Khorasani, M.; Ghasemi, A.; Rolfe, B.; Gibson, I. Additive manufacturing a powerful tool for aerospace industry. *Rapid. Prototyp. J.* **2022**, *28*, 87–100. https://doi.org/10.1108/RPJ-01-2021-0009

[49] Giganto, S.; Martínez-Pellitero, S.; Cuesta, E.; Zapico, P.; Barreiro, J. Proposal of design rules for improving the accuracy of selective laser melting (SLM) manufacturing using benchmarks parts. *Rapid Prototyp. J.* **2022**, *26(8)*, 1129–1143. https://doi.org/10.1108/RPJ-06-2021-0130

[50] Zhou, Y.; Abbara, E.M.; Fiang, D.; Azizi, A.; Poliks, M.D.; Ning, F. High-cycle fatigue properties of curved-surface AlSi10Mg parts fabricated by powder bed fusion additive manufacturing. *Rapid Prototyp. J.* **2022**, *28(7)*, 1346–1360. https://doi.org/10.1108/RPJ-09-2021-0253

[51] Babuska, T.F.; Krick, B.A.; Susan, D.F.; Kustas, A.B. Comparison of powder bed fusion and directed energy deposition for tailoring mechanical properties of traditionally brittle alloys. *Manuf. Letter.* **2021**, *28*, 30–34. https://doi.org/10.1016/j.mfglet.2021.02.003

[52] Dutta, B.; Froes, F.H.S. The Additive Manufacturing (AM) of titanium alloys. *Met. Powder Rep.* **2017**, *72(2)*, 96–106. https://doi.org/10.1016/j.mprp.2016.12.062

[53] Teixiera, Ó.; Silva, F.J.G.; Ferreira, L.P.; Atzeni, E. A Review of Heat Treatments on Improving the Quality and Residual Stresses of the Ti–6Al–4V Parts Produced by Additive Manufacturing. *Metals.* **2020**, *10(8)*, 1006. https://doi.org/10.3390/met10081006

[54] Lee, H.; Lim, C.H.J.; Low, M.J.; Tham, N.; Murukeshan, V.M.; Kim, Y.-J. Lasers in additive manufacturing: A review. *Int. J. Precis. Eng. Manuf.-Green Technol.* **2017**, *4*, 307–322. https://doi.org/10.1007/s40684-017-0037-7

[55] Galba, M.; Reischle, M. Additive manufacturing of metals using powder-based technology. *Additive Manufacturing*, 1st ed; Bandyopadhyay, A.; Bose, S.; Taylor&Francis Group: Boca Raton, Florida, p.46, **2016**. https://doi.org/10.1201/b18893

[56] Yang, L.; Hsu, K.; Baughman, B.; Godfrey, D.; Medine, F.; Menon, M.; Wiener, S. Additive Manufacturing of Petals: Technology, Materials, Design and Production. Springer: New York, USA, **2017**.

REFERENCES

[57] Sames, W.J.; List, F.A; Pannala, S.; Dehoff, R.R.; Babu, S.S. The metallurgy and processing science of metal additive manufacturing. *Int. Mater. Rev.* **2016**, *61*, 315–360. https://doi.org/10.1080/09506608.2015.1116649

[58] Arias-González, F.; Rodríguez-Contreras, A.; Punset, M.; Manero, J.M.; Barro, Ó.; et al. In-Situ Laser Directed Energy Deposition of Biomedical Ti-Nb and Ti-Zr-Nb Alloys from Elemental Powders. *Metals.* **2021**, *11(8)*, 1205. https://doi.org/10.3390/met11081205

[59] Kruth, J.-P.; Kumar, S. Statistical Analysis of Experimental Parameters in Selective Laser Sintering. *Adv. Eng. Mater.* **2005**, *7(8)*, 750–755. https://doi.org/10.1002/adem.200500030

[60] Tang, M.; Pistorius, P.C.; Beuth, J.L. Prediction of lack-of-fusion porosity for powder bed fusion. *Addit. Manuf.* **2017**, *14*, 39–48. https://doi.org/10.1016/j.addma.2016.12.001

[61] Letenneur, M.; Kreicberg, A.; Brailovski, V. Optimization of Laser Powder Bed Fusion Processing Using a Combination of Melt Pool Modeling and Design of Experiment Approaches: Density Control. *Manuf. Mater. Process.* **2019**, *3(1)*, 21–34. https://doi.org/10.3390/jmmp3010021

[62] Bartolomeu, F.; Costa, M.M.; Alves, N.; Miranda, G.; Silva, F.S. Selective Laser Melting of Ti6Al4V sub-millimetric cellular structures: Prediction of dimensional deviations and mechanical performance. *J. Mech. Behav. Biomed. Mater.* **202**, *113*, 104123. https://doi.org/10.1016/j.jmbbm.2020.104123

[63] Xiong, Y.-Z.; Gao, R.-N.; Zhang, H.; Dong, L.-L., Li, J.-T.; Li, X. Rationally designed functionally graded porous Ti6Al4V scaffolds with high strength and toughness built via selective laser melting for load-bearing orthopedic applications. *J. Mech. Behav. Biomed. Mater.* **2020**, *104*, 103673. https://doi.org/10.1016/j.jmbbm.2020.103673

[64] Yan, X.; You, S.; Chen, Z.; Jenkins, R.; Chen, C.; Wang, J.; Ma, W.; Bolot, R.; Lupoi, R.; Liao, H.; et al. Mechanical and *in vitro* study of anisotropic Ti6Al4V lattice structure fabricated using selective laser melting. *J. Alloys Compd.* **2019**, *782*, 209–223. https://doi.org/10.1016/j.jallcom.2018.12.220

[65] Cerri, E.; Ghio, E.; Bolelli, G. Effect of Distance from Build Platform and Post-Heat Treatment of AlS10Mg Alloy Manufactured by Single and Multi-Laser Selective Laser Melting. *J. Mater. Eng. Perform.* **2021**, *30*, 4981–4992. https://doi.org/10.1007/s11665-021-05577-8

[66] Olakanmi, E.O.; Cochrana, R.F.; Dalgrano, K.W. A review on selective laser sintering/melting (SLS/SLM) of aluminium powders: Processing, microstructure, and properties. *Prog. Mater. Sci.* **2015**, *74*, 401–477. https://doi.org/10.1016/j.pmatsci.2015.03.002

[67] Ghio, E.; Cerri, E. Work Hardening of Heat-Treated AlSi10Mg Alloy Manufactured by Single and Double Laser Selective Laser Melting: Effect of Layer Thickness and Hatch Spacing. *Materials.* **2021**, *14(17)*, 4901. https://doi.org/10.3390/ma14174901

[68] Bai, S.; Parevoshchikova, N.; Sha, Y.; Wu, X. The Effects of Selective Laser Melting Process Parameters on Relative Density of the AlSi10Mg Parts and Suitable Procedures of the Archimedes Method. *Appl. Sci.* **2019**, *9(3)*, 583. https://doi.org/10.3390/app9030583

[69] Aboulkhair, N.T.; Everitt, N.M.; Ashcroft, I.; Tuck, C. Reducing porosity in AlSi10Mg parts processed by selective laser melting. *Addit. Manuf.* **2014**, *1–4*, 77–86. https://doi.org/10.1016/j.addma.2014.08.001

[70] Majeed, A.; Zhang, Y.; Lv, J.; Peng, T.; Atta, Z.; Ahmed, A. Investigation of T4 and T6 heat treatment influences on relative density and porosity of AlSi10Mg alloy components manufactured by SLM. *Compt. Ind. Eng.* **2020**, *139*, 106194. https://doi.org/10.1016/j.cie.2019.106194

[71] Girelli, L.; Tocci, M.; Gelfi, M.; Pola, A. Study of heat treatment parameters for additively manufactured AlSi10Mg in comparison with corresponding cast alloy. *Mater. Sci. Eng. A.* **2019**, *739*, 317–328. https://doi.org/10.1016/j.msea.2018.10.026

[72] Yang, T.; Liu, T.; Liao, W.; MacDonald, E.; Wei, H.; Zhang, C.; Chen, X.; Zhang, K. Laser powder bed fusion AlSi10Mg: Influence of energy intensities on spatter and porosity evolution, microstructure and mechanical properties. *J. Alloys Compd.* **2020**, *849*, 156300. https://doi.org/10.1016/j.jallcom.2020.156300

[73] Riener, K.; Oswald, S.; Winkler, M.; Leichtfried, G.J. Influence of storage conditions and reconditioning of AlSi10Mg powder on the quality of parts produced by laser powder bed fusion (LPBF). *Addit. Manuf.* **2021**, *39*, 101896. https://doi.org/10.1016/j.addma.2021.101896

[74] Hastie, J.C.; Kartal, M.E.; Carter, L.N.; Attallah, M.M.; Mulvihill, D.M. Classifying shape of internal pores within AlSi10Mg alloy manufactured by laser powder bed fusion using 3D X-Ray micro computed tomography: Influence of processing parameters and heat treatment. *Mater. Charact.* **2020**, *163*, 110225. https://doi.org/10.1016/j.matchar.2020.110225

[75] Vrancken, B.; Thjis, L.; Kruth, J.-P.; Humbeeck, J.V. Heat treatment of Ti6Al4V produced by Selective Laser Melting: Microstructure and mechanical properties. *J. Alloys Compd.* **2012**, *541*, 177–185. https://doi.org/10.1016/j.jallcom.2012.07.022

[76] Wycisk, E.; Emmelmann, C.; Siddique, S.; Walther, F. High Cycle Fatigue (HCF) Performance of Ti-6Al-4V Alloy Processed by Selective Laser Melting. *Adv. Mater. Res.* **2013**, *816–817*, 134–139. https://doi.org/10.4028/www.scientific.net/AMR.816-817.134

[77] Edwards, P.; Ramulu, M. Fatigue performance evolution of selective laser melted Ti-6Al-4V. *Mater. Sci. Eng. A.* **2014**, *598*, 327–337. https://doi.org/10.1016/j.msea.2014.01.041

[78] Simonelli, M.; Tse, Y.Y.; Tuck, C. Effect of the build orientation on the mechanical properties and fracture modes of SLM Ti-6Al-4V. *Mater. Sci. Eng. A.* **2014**, *616*, 1–11. https://doi.org/10.1016/j.msea.2014.07.086

[79] Khorasani, A.; Gibson, I.; Goldberg, M.; Littlefair, G.L. On the role of different annealing heat treatments on mechanical properties and microstructure of selective laser melted and conventional wrought Ti-6Al-4V. *Rapid. Prototyp. J.* **2017**, *23(2)*, 295–304. https://doi.org/10.1108/RPJ-02-2016-0022

[80] Hu, Y.N.; Wu, S.C.; Withers, P.J.; Zhang, J.; Bao, H.Y.X.; Fu, Y.N.; Kang, G.Z. The effect of manufacturing defects of the fatigue life of selective laser melted Ti-6Al-4V structures. *Mater. Des.* **2020**, *192*, 108708. https://doi.org/10.1016/j.matdes.2020.108708

[81] Pal, S.; Lojen, G.; Hudak, E.; Rajtukova, V.; Brajlih, T.; Kokol, V.; Drstvenšek, I. As-fabricated surface morphologies of Ti-6Al-4V samples fabricated by different laser processing parameters in selective laser melting. *Addit. Manuf.* **2020**, *33*, 101147. https://doi.org/10.1016/j.addma.2020.101147

[82] Xiao, Z.; Chen, C.; Zhu, H.; Hu, Z.; Nagarajan, B.; Guo, L.; Zeng, X. Study of residual stress in selective laser melting of Ti6Al4V. *Mater. Des.* **2020**, *193*, 108846. https://doi.org/10.1016/j.matdes.2020.108846

[83] Zhang, M.; Yang, Y.; Wang, D.; Xiao, Z.; Song, C.; Weng, C. Effect of heat treatment on the microstructure and mechanical properties of Ti6Al4V gradient structures manufactured by selective laser melting. *Mater. Sci. Eng. A.* **2018**, *736*, 288–297. https://doi.org/10.1016/j.msea.2018.08.084

[84] Coeck, S.; Bisht, M.; Plas, J.; Verbist, F. Prediction of lack of fusion porosity in selective laser melting based on molten pool monitoring data. *Addit. Manuf.* **2019**, *25*, 347–356. https://doi.org/10.1016/j.addma.2018.11.015

[85] Xu, Z.W.; Wang, Q.; Wang, X.S.; Tang, C.H.; Guo, M.H.; Gao, P.B. High fatigue performance of AlSi10Mg alloy produced by selective laser melting. *Mech. Mater.* **2020**, *148*, 103499. https://doi.org/10.1016/j.mechmat.2020.103499

[86] Li, P.-H.; Guo, W.-G.; Huang, W.-D.; Su, Y.; Liu, X.; Yuan, K.-B. Thermomechanical response of 3D laser-deposited Ti-6Al-4V alloy over a wide range of strain rates and temperatures. *Mater. Sci. Eng. A.* **2015**, *647*, 34–42. https://doi.org/10.1016/j.msea.2015.08.043

[87] Bayat, M.; Thanki, A.; Mohanty, S.; Witvrouw, A.; Yang, S.; Thorborg, J.; Tiedje, N.S.; Hattle, J.H. Keyhole-induced porosities in Laser-based Powder Bed Fusion (L-PBF) of Ti6Al4V: High-fidelity modelling and experimental validation. *Addit. Manuf.* **2019**, *30*, 100835 https://doi.org/10.1016/j.addma.2019.100835

[88] Wirth, F.; Frauchiger, A.; Gutknecht, K.; Cloots, M. Influence of the Inter Gas Flow on the Laser Powder Bed Fusion (LPBF) Process. *Industrializing Additive Manufacturing*, 1st ed; Mebolt, M., Klahn, C. eds; Springer: New York, USA, pp. 109–204, **2020**. https://doi.org/10.1007/978-3-030-54334-1_14

[89] Weingarten, C.; Buchbinder, D.; Pirch, N.; Meiners, W.; Wissenbach, K.; Porawe, R. Formation and reduction of hydrogen porosity during selective laser melting of AlSi10Mg. *J. Mater. Process. Technol.* **2015**, *221*, 112–120. https://dx.doi.org/10.1016/j.jmatprotec.2015.02.013

[90] Emminghaus, N.; Paul, J.; Hoff, C.; Hermsford, J.; Kairle, S. Development of an empirical process model for adjusted porosity in laser-based powder bed fusion Ti-6Al-4V. *Int. J. Adv. Manuf. Technol.* **2021**, *118*, 1239-1254. https://doi.org/10.1007/s00170-021-07847-0

[91] Shiomi, M.; Osakada, K.; Nakamura, K.; Yamashita, T.; Abe, F. Residual Stress within Metallic Model Made by Selective Laser Melting Process. *CIRP Annals.* **2004**, *53*, 195–198. https://doi.org/10.1016/S0007-8506(07)60677-5

[92] Yu, G.; Gu, D.; Dai, D.; Xia, M.; Ma, C.; Chang, K. Influence of processing parameters on laser penetration depth and melting/re-melting densification during selective laser melting of aluminium alloy. *Appl. Phys. A.* **2016**, *891*, 122–134. https://doi.org/10.1007/s00339-016-0428-6

References

[93] Yu, W.; Sing, S.L.; Chua, C.K.; Tan, X. Influence of re-melting on surface roughness and porosity of AlSi10Mg parts fabricated by selective laser melting. *J. Alloys Compd.* **2019**, *792*, 574–581. https://doi.org/10.1016/j.jallcom.2019.04.017

[94] Maconiache, T.; Leary, M.; Lozanovsky, B.; Zhang, X.; Qian, M.; Faruque, O.; Brandt, M. SLM lattice structures: Properties, performance, applications and challenges. *Mater. Des.* **2019**, *183*, 108137. https://doi.org/10.1016/j.matdes.2019.108137

[95] Murchio, S.; Dallago, M.; Zanini, F.; Carmignato, S.; Zappini, G.; Berto, F.; Maniglio, D.; Benedetti, M. Additively manufactured Ti-6Al-4V thin strurs via laser powder bed fusion: Effect of building orientation on geometrical accuracy and mechanical properties. *J. Mech. Behav. Biomed. Mater.* **2021**, *119*, 104495. https://doi.org/10.1016/j.jmbbm.2021.104495

[96] Juechter, V.; Scharowsky, T.; Singer, R.F.; Körner, C. Processing window and evaporation phenomena for Ti-6Al-4V produced by selective electron beam melting. *Acta Mater.* **2014**, *76*, 252–258. https://doi.org/10.1016/j.actamat.2014.05.037

[97] King, W.E.; Barth, H.D.; Castillo, V.M.; Gallegos, G.F.; Gibbs, J.W.; Hahn, D.E.; Kamath, C.; et al. Observation of keyhole-mode laser melting in laser powder-bed fusion additive manufacturing. *J. Mater. Process. Technol.* **2014**, *214*, 2915–2925. https://doi.org/10.1016/j.jmatprotec.2014.06.005

[98] Martin, A.A.; Calta, N.P.; Khairallah, S.A.; Wang, J.; Depond, P.J.; Fong, A.Y.; Thampy, V.; et al. Dynamics of pore formation during laser powder bed fusion additive manufacturing. *Nature Commun.* **2019**, *10*, 1978. https://doi.org/10.1038/s41467-019-10009-2

[99] Wang, T.; Dai, S.; Liao, H.; Zhu, H. Pores and the formation mechanisms of SLMed AlSi10Mg. *Rapid Prototyp. J.* **2020**, *26/9*, 1657–1664. https://doi.org/10.1108/RPJ-02-2020-0036

[100] Macías, J.G.S.; Douillard, T.; Zhao, L.; Maire, E.; Pyka, G.; Simar, A. Influence of microstructure, strength and ductility of build platform temperature during laser powder bed fusion of AlSi10Mg. *Acta Mater.* **2020**, *201*, 231–243. https://doi.org/10.1016/j.actamat.2020.10.001

[101] Strano, G.; Hao, L.; Everson, R.M.; Evans, K.E. A new approach to the design and optimization of support structures in additive manufacturing. *Int. J. Adv. Manuf. Technol.* **2013**, *66*, 1247-1254. https://doi.org/10.1007/s00170-012-4403-x

[102] Oliviera, J.P.; LaLonde, A.D.; Ma, J. Processing parameters in laser powder bed fusion metal additive manufacturing. *Mater. Des.* **2020**, *193*, 108762. https://doi.org/10.1016/j.matdes.2020.108762

[103] Agarwala, M.; Bourell, D.; Beaman, J.; Marcus, H.; Barlaw, J. Direct selective laser sintering of metals. *Rapid. Prototyp. J.* **1995**, *1(1)*, 26–36. https://doi.org/10.1108/13552549510078113

[104] Sun, S.; Brandt, M.; Easton, M. Powder bed fusion processes: an overview. *Laser Additive Manufacturing: Materials, Design, Technologies, and Applications*; Brandt, M., ed; Elsevier: Amsterdam, The Netherlands, pp. 55–77, **2017**. https://dx.doi.org/10.1016/B978-0-08-100433-3.00002-6

[105] Liu, S.; Guo, H. Balling Behavior of Selective Laser Melting (SLM) Magnesium Alloy. *Materials.* **2020**, *13(16)*, 3632. https://doi.org/10.3390/ma13163632

[106] Yadroitsev, I.; Gusarov, A.; Yadroitsava, I.; Smurov, I. Single track formation in selective laser melting of metal powders. *J. Mater. Process. Technol.* **2010**, *210(10)*, 1624–1631. https://doi.org/10.1016/j.jmatprotec.2010.05.010

[107] Zhou, Y.; Wen, S.F.; Song, B.; Zhou, X.; Teng, Q.; Wei, Q.S.; Shi, Y.S. A novel titanium alloy manufactured by selective laser melting: Microstructure, high temperature oxidation resistance. *Mater. Des.* **2016**, *89*, 1199–1204. https://doi.org/10.1016/j.matdes.2015.10.092

[108] Zhang, B.; Li, Y.; Bai, Q. Defect Formation Mechanisms in Selective Laser Melting: A review. *Chin. J. Mech. Eng.* **2017**, *30*, 515–527. https://doi.org/10.1007/s10033-017-0121-5

[109] Gouveia, R.M.; Silva, F.J.G.; Atzeni, A.; Sormaz, D.; Alves, J.L.; Pereira, A.B. Effect of Scan Strategies and Use of Support Structures on Surface Quality and Hardness of L-PBF AlSi10Mg Parts. *Materials.* **2020**, *13(10)*, 2248. https://doi.org/10.3390/ma13102248

[110] Zafer, J.E.; Goel, S.; Ganvir, A.; Jansson, A.; Joshi, S. Encapsulation of Electron Beam Melting Produced Alloy 718 to Reduce Surface Connected Defects by Hot Isostatic Pressing. *Materials.* **2020**, *13(5)*, 1226. https://doi.org/10.3390/ma13051226

[111] Darvish, K.; Chen, Z.W.; Pasang, T. Reducing lac of fusion during selective laser melting of CoCrMo alloy: Effect of laser power on geometrical features of tracks. *Mater. Des.* **2016**, *112*, 357–366. https://doi.org/10.1016/j.matdes.2016.09.086

[112] Pantawane, M.V.; Ho, Y.-H.; Joshi, S.S.; Dahotre, N.B. Computational Assessment of Thermokinetics and Associated Microstructural Evolution in Laser Powder Bed Fusion in Manufacturing of Ti6Al4V Alloy. *Sci. Rep.* **2020**, *10*, 7579–7593. https://doi.org/10.1038/s41598-020-63281-4

[113] Dass, A.; Moridi, A. State of the Art in Direct Energy Deposition: From Additive Manufacturing to Materials Design. *Coatings.* **2019**, *9(7)*, 418–444. https://doi.org/10.3390/coatings9070418

[114] Mukerejee, T.; Wei, H.L.; De, A.; DebRoy, T. Heat and fluid flow in additive manufacturing – part II: Powder bed fusion of stainless steel, and titanium, nickel and aluminium base alloy. *Compt. Mater. Sci.* **2018**, *150*, 369–380. https://doi.org/10.1016/j.commatsci.2018.04.027

[115] Tiryakioğlu, M. The Effect of Hydrogen on Pore Formation in Aluminum Alloy Casting: Myth Versus Reality. *Metals.* **2020**, *10(3)*, 368. https://doi.org/10.3390/met10030368

[116] Huang, Y.; Long, M.; Liu, P.; Chen, D.; Gui, L.; Liu, T.; Yu, S. Effects of Partition Coefficients, Diffusion Coefficients, and Solidification Paths on Microsegregation in Fe-Based Multinary Alloy. *Metall. Mater. Trans. B.* **2017**, *48*, 2504–2515. https://doi.org/10.1007/s11663-017-1045-2

[117] Gong, H.; Rafi, K.; Gu, H.; Janaki Ram, G.D.; Starr, T.; Stucker, B. Influence of defects on mechanical properties of Ti-6Al-4V components produced by selective laser melting and electron beam melting. *Mater. Des.* **2015**, *86*, 545–554. https://doi.org/10.1016/j.matdes.2015.07.147

[118] Laursen, C.M.; DeJog, S.A.; Dickens, S.M.; Exil, A.N.; Susan, D.F.; Carrol, J.D. Relationship between ductility and the porosity of additively manufactured AlSi10Mg. *Mater. Sci. Eng. A.* **2020**, *795*, 139922. https://doi.org/10.1016/j.msea.2020.139922

[119] Plessis, A.D.; Yelamanchi, B.; Fischer, C.; Miller, J.; Beamer, C.; Rogers, K.; Cortes, P.; Els, J.; et al. Productivity enhancement of laser powder bed fusion using compensated shelled geometries and hot isostatic pressing. *Adv. Ind. Manuf. Eng.* **2021**, *2*, 100031. https://doi.org/10.1016/j.aime.2021.100031

[120] Masuo, H.; Tanaka, Y.; Morokoshi, A.; Yagura, H.; Uchida, T.; Yamamoto, Y.; Muramaki, Y. Influence of defects, surface roughness and HIP on the fatigue strength of Ti-6Al-4V manufactured by additive manufacturing. *Int. J. Fatigue.* **2018**, *117*, 163–179. https://doi.org/10.1016/j.ijfatigue.2018.07.020

[121] Ertuğrul, O.; Öter, Z.Ç.; Yilmaz, M.S.; Şahin, E.; Coşkun, Tarakçi, G.; Koç, E. Effect of HIP process and subsequent heat treatment on microstructure and mechanical properties of direct metal laser sintered AlSi10Mg alloy. *Rapid Prototyp. J.* **2020**, *26(8)*, 1421–1434. https://doi.org/10.1108/RPJ-07-2019-0180

[122] Leuders, S.; Lieneke, S.; Lammers, S.; Tröster, T.; Niendorf, T. On the fatigue properties on metals manufactured by selective laser melting – The role of ductility. *J. Mater. Res.* **2014**, *29*, 1911–1919. https://doi.org/10.1557/jmr.2014.157

[123] Romero, C.; Yang, F.; Bolzoni, I. Fatigue and fracture properties of Ti alloys from powder-based process – A review. *Int. J. Fatigue.* **2018**, *117*, 407–419. https://doi.org/10.1016/j.ijfatigue.2018.08.029

[124] Schneller, W.; Leitner, M.; Springer, S.; Grün, F.; Taschauer, M. Effect of HIP Treatment on Microstructure and Fatigue Strength of Selectively Laser Melted AlSi10Mg. *Manuf. Mater. Process.* **2019**, *3(1)*, 16. https://doi.org/10.3390/jmmp3010016

[125] Mahmud, A.; Huynh, T.; Zhou, L.; Hyer, H.; Mehta, A.; Imholte, D.D.; Woolstenhulme, N.E.; et al. Mechanical Behavior Assessment of Ti-6Al-4V ELI Alloy Produced by Laser Powder Bed Fusion. *Metals.* **2021**, *11(11)*, 1671. https://doi.org/10.3390/met11111671

[126] Kruth, J.-P.; Froyen, L.; Vaerenbergh, J.V.; Mercelis, P.; Rombouts, M.; Lauwers, B. Selective laser melting of iron-based powder. *J. Mater. Process. Technol.* **2004**, *149(1–3)*, 616–622. https://doi.org/10.1016/j.jmatprotec.2003.11.051

[127] Masmoudi, A.; Bolot, R.; Coddet, C. Investigation of the powder-laser-atmosphere interaction zone during the selective laser melting process. *J. Mater. Process. Technol.* **2015**, *225*, 122–132. https://doi.org/10.1016/j.jmatprotec.2015.05.008

[128] Santecchia, E.; Spigarelli, S.; Cabibbo, M. Material Reuse in Laser Powder Bed Fusion: Side Effects of the Laser—Metal Powder Interaction. *Metals.* **2020**, *10(30)*, 341. https://doi.org/10.3390/met10030341

REFERENCES

[129] Pauzon, C.; Forêt, P.; Hryha, E.; Arunprasad, T.; Nyborg, L. Argon-helium mixtures as Laser-Powder Bed Fusion atmospheres: Towards increased build rate of Ti-6Al-4V. *J. Mater. Process. Technol.* **2020**, *279*, 116555. https://doi.org/10.1016/j.jmatprotec.2019.116555

[130] Anwar, A.B.; Pham, Q.-C. Selective laser melting of AlSi10Mg: Effects of scan direction, part placement and inert gas flow velocity on tensile strength. *J. Mater. Process. Technol.* **2017**, *240*, 388–396. https://doi.org/10.1016/j.jmatprotec.2016.10.015

[131] Huang, H.-Y. Effects of shielding gas composition and activating flux of GTAW weldments. *Mater. Des.* **2009**, *30(7)*, 2404–2409. https://doi.org/10.1016/j.matdes.2008.10.024

[132] Vastola, G.; Pei, Q.X.; Zhang, Y.-W. Predictive model for porosity in powder-bed fusion additive manufacturing at high beam energy regime. *Addit. Manuf.* **2018**, *817*, 817–822. https://doi.org/10.1016/j.addma.2018.05.042

[133] Li, B.-Q.; Li, Z.; Bai, P.; Liu, B.; Kuai, Z. Research on Surface Roughness of AlSi10Mg Parts Fabricated by Laser Powder Bed Fusion. *Metals.* **2018**, *8(7)*, 524–534. https://doi.org/10.3390/met8070524

[134] Buchbinder, D.; Schleifenbaum, H.; Heidrick, S.; Meines, W.; Bültmann, J. High Power Selective Laser Melting (HP SLM) of Aluminium Parts. *Phys. Procedia.* **2011**, *12*, 271–278. https://doi.org/10.1016/j.phpro.2011.03.035

[135] Ansari, M.J.; Nguyen, D.S.; Park, H.S. Investigation of SLM Process in Terms of Temperature Distribution and Melting Pool Size: Modeling and Experimental Approaches. *Materials.* **2019**, *12(8)*, 1272. https://doi.org/10.3390/ma12081272

[136] Yang, J.; Sun, S.; Brandt, M.; Yan, W. Experimental investigation and 3D finite element prediction of the heat affected zone during laser assisted machining od Ti6Al4V alloy. *J. Mater. Process. Technol.* **2010**, *210*, 2215–2222. https://doi.org/10.1016/j.jmatprotec.2010.08.007

[137] Schwerz, C.; Nyborg, L. Linking In Situ Molten Pool Monitoring to Melt Size Distribution and Internal Flaws in Laser Powder Bed Fusion. *Metals.* **2021**, *11(11)*, 1856. https://doi.org/10.3390/met11111856

[138] Du, Y.; You, X.; Qiao, F.; Guo, L.; Liu, Z. A model for predicting the temperature field during selective laser melting. *Results Phys.* **2019**, *12*, 52–60. https://doi.org/10.1016/j.rinp.2018.11.031

[139] Bahavar, V.; Kattire, P.; Patil, V.; Khat, S.; Gujar, K.; Singh, R. A review on powder bed fusion technology of metal additive manufacturing; in *4th International conference and exhibition on Additive Manufacturing Technologies-AM-2014*, Banglore, India, **2014**.

[140] Fiegl, T.; Franke, M.; Körner, C. Impact of build envelope on the properties of additive manufactured parts from AlSi10Mg. *Opt. Laser Technol.* **2019**, *11*, 51–57. https://doi.org/10.1016/j.optlastec.2018.08.050

[141] Shi, X.; Ma, S.; Liu, C.; Chen, C.; Wu, Q.; Chen, X.; Lu, J. Performance of High Layer Thickness in Selective Laser Melting of Ti6Al4V. *Materials.* **2016**, *9(12)*, 975. https://doi.org/10.3390/ma9120975

[142] Bremen, S.; Meiners, W.; Diatlov, A. Selective laser melting – A manufacturing technology for the future? *Laser Technol. J.* **2012**, *9(2)*, 33–38. https://doi.org/10.1002/latj.201290018

[143] ASTM *E8/E8M-13a: Standard Test Method for Tension Testing of Metallic Materials*, West Conshohocken, PA, USA, **2013**.

[144] Cerri, E.; Ghio, E.; Bolelli, G. Defect-Correlated Vickers Microhardness of Al-Si-Mg Alloy Manufactured by Laser Powder Bed Fusion with Post-Process Heat Treatments. *J. Mater. Process. Technol.* **2022**, *31*, 8047–8067. https://doi.org/10.1007/s11665-022-06874-6

[145] Cerri, E.; Ghio, E.; Bolelli, G. Ti6Al4V-ELI Alloy Manufactured via Laser Powder-Bed Fusion and Heat-Treated Below and Above the β-Transus: Effects of Sample Thickness and Sandblasting Process. *Appl. Sci.* **2022**, *11(12)*, 5359. https://doi.org/10.3390/app12115359

[146] Motyka, M.; Kubiak, K.; Sieniawski, J.; Ziaja, W. Phase Transformation and Characterization of $\alpha + \beta$ Titanium Alloys. *Materials modelling and characterization*, Hashmi, S., ed; Elsevier: Amsterdam, The Netherlands, **2014**. https://doi.org/10.1016/B978-0-08-096532-1.00202-8

[147] Van der Voort, G.F.; Roósz, A. Measurement on the interlamellar spacing of pearlite. *Metallogr.* **1984**, *17*, 1–17. https://doi.org/10.1016/0026-0800(84)90002-8

[148] Cerri, E.; Ghio, E. Aging Profiles of AlSi7Mg0.6 and AlSi10Mg0.3 Alloys Manufactured via Laser-Powder Bed Fusion: Direct Aging versus T6. *Materials.* **2022**, *15(17)*, 6126. https://doi.org/10.3390/ma15176126

[149] Pereira, J.C.; Gil, E.; Solaberrieta, L.; Sebastián, M.S.; Bilbao, Y.; Rodríguez, P.P. Comparison of AlSi7Mg0.6 alloy obtained by selective laser melting and investment casting processes: Microstructure and mechanical

properties in as-built/as-cast and heat-treated conditions. *Mater. Sci. Eng. A.* **2020**, *778*, 139124. https://doi.org/10.1016/j.msea.2020.139124

[150] Huang, S.; Guo, S.-q.; Zhou, B.; Zhang, G.-h.; Zhang, X.-j. Microstructure and properties of AlSi7Mg alloy fabricated by selective laser melting. *China Found.* **2021**, *18*, 416–423. https://doi.org/10.1007/s41230-021-1004-z

[151] Martins, L.F.L.; Provenacher, P.R.; Brochu, M.; Brochu, M. Effect of Platform Temperature and Post-Processing Heat Treatment on the Fatigue Life of Additively Manufactured AlSi7Mg Alloy. *Metals.* **2021**, *11(5)*, 679. https://doi.org/10.3390/met11050679

[152] Yang, J.; Yu, H.; Yin, J.; Gao, M.; Wang, Z.; Zeng, X. Formation and control of martensite in Ti-6Al-4V alloy produced by selective laser melting. *Mater. Des.* **2016**, *108*, 308–318. https://doi.org/10.1016/j.matdes.2016.06.117

[153] Ali, H.; Ma, L.; Ghadbeigi, H.; Mumtaz, K. In-situ residual stress reduction, martensitic decomposition and mechanical properties enhancement through high temperature powder bed pre-heating of Selective Laser Melted Ti6Al4V. *Mater. Sci. Eng. A.* **2017**, *695*, 211–220. https://doi.org/10.1016/j.msea.2017.04.033

[154] Spigarelli, S.; Paoletti, C.; Cabibbo, M.; Cerri, E.; Santecchia, E. On the creep performance of the Ti-6Al-4V alloy processed by additive manufacturing. *Addit. Manuf.* **2022**, *49*, 102520. https://doi.org/10.1016/j.addma.2021.102520

[155] Cerri, E.; Ghio, E.; Bolelli, G. Effect of surface roughness and industrial heat treatments on the microstructure and mechanical properties of Ti6Al4V alloy manufactured by laser powder bed fusion in different built orientations. *Mater. Sci. Eng. A.* **2022**, *851*, 143635. https://doi.org/10.1016/j.msea.2022.143635

[156] Ahmed, T.; Rack, H.J. Phase transformation during cooling in α+β titanium alloys. *Mater. Sci. Eng. A.* **1998**, *243*, 206–211. https://doi.org/10.1016/S0921-5093(97)00802-2

[157] Baek, M.-S.; Kreethi, R.; Park, T.-H. Sohn, Y.; Lee, K.-A. Influence of heat treatment on the high-cycle fatigue properties and fatigue damage mechanism of selective laser melted AlSi10Mg alloy. *Mater. Sci. Eng. A.* **2021**, *819*, 141486. https://doi.org/10.1016/j.msea.2021.141486

[158] Yang, K.V.; Rometsch, P.; Davies, C.H.J.; Huang, A.; Wu, X. Effect of heat treatment on the microstructure and anisotropy in mechanical properties of A357 alloy produced by selective laser melting. *Mater. Des.* **2018**, *154*, 275–290. https://doi.org/10.1016/j.matdes.2018.05.026

[159] Sajadi, F.; Tiemann, J.-M.; Bandari, N.; Darabi, A.C.; Mola, J.; Schmauder, S. Fatigue Improvement of AlSi10Mg Fabricated by Laser-Based Powder Bed Fusion through Heat Treatment. *Metals.* **2021**, *11(5)*, 683. https://doi.org/10.3390/met11050683

[160] Paul, M.J.; Liu, Q.; Best, J.P.; Li, X.; Kruzic, J.J.; Ranamurty, U.; Gludovatz, B. Fracture resistance of AlSi10Mg fabricated by laser powder bed fusion. *Acta Mater.* **2021**, *211*, 116869. https://doi.org/10.1016/j.actamat.2021.116869

[161] Sigworth, G. Understanding Quality in Aluminium Castings. *Int. J. Metalcast.* **2011**, *5*, 7–22. https://doi.org/10.1007/BF03355504

[162] Zhang, X.-Y.; Fang, G.; Leeflang, S.; Böttger, A.J.; Zadpoor, A.A.; Zhou, J. Effect of subtransus heat treatment on the microstructure and mechanical properties of additively manufactured Ti-6Al-4V alloy. *J. Alloys Compd.* **2018**, *735*, 1562–1575. https://doi.org/10.1016/j.jallcom.2017.11.263

[163] Xu, W.; Sun, S.; Elambasseril, U.; Liu, Q.; Brandt, M.; Qian, M. Ti-6Al-4V Additively Manufactured by Selective Laser Melting with Superior Mechanical Properties. *JOM.* **2015**, *67*, 668–673. https://doi.org/10.1007/s11837-015-1297-8

[164] ISO *6507-2:2018, Metallic materials – Vickers hardness test – Part 1: Test method*, NSAI Irish Standard, **2018**.

[165] Tabor, D. The hardness and strength of metals. *J. Met.* **1951**, *79(7)*, 1–18.

[166] Cahoon, J.R.; Broughton, W.H.; Kutzak, A.R. The determination of yield strength from hardness measurements. *Metall. Trans.* **1971**, *2(7)*, 1979–1983. https://doi.org/10.1007/BF02913433

[167] Dieter, G.E.; Bacon, D. Mechanical Metallurgy: SI Metric Edition; Bever, M.B., Coply, S.M., Shank, M.E., Wert, C.A., Wickers, G.L., eds; McGrawh-Hill Book Company: New York, USA, **1989**.

[168] Chen, H.; Cai, L.-X. Theoretical Conversion of Different Hardness and Tensile Strength for Ductile Materials Based on Stress-Strain Curves. *Metall. Mater. Trans. A.* **2018**, *49*, 1090–1101. https://doi.org/10.1007/s11661-018-4468-8

References

[169] Bhaduri, A. Mechanical Properties and Work of Metals and Alloys; Springer: New York, USA, vol. 264, pp. 46–49, **2018**.

[170] Keist, J.S.; Palmer, T.A. Development of strength-hardness relationships in additively manufactured titanium alloys. *Mater. Sci. Eng. A.* **2017**, *693*, 214–224. https://doi.org/10.1016/j.msea.2017.03.102

[171] Kasperovich, G.; Hausmann, J. Improvement of fatigue resistance and ductility of Ti6Al4V processed by selective laser melting. *J. Mater. Process. Technol.* **2015**, *220*, 202–214. https://doi.org/10.1016/j.jmatprotec.2015.01.025

[172] Liu, Y.J.; Liu, Z.; Jiang, Y.; Wang, G.W.; Yang, Y.; Zhang, L.C. Gradient in microstructure and mechanical properties of selective laser melted AlSi10Mg. *J. Alloys Compd*. **2018**, *735*, 1414–1421. https://doi.org/10.1016/j.jallcom.2017.11.020

[173] Aboulkhair, N.T.; Maskery, I.; Tuck, C.; Ashcroft, I.; Everitt, N. The microstructure and mechanical properties of selective laser melted AlSi10Mg: The effect of conventional T6-Like heat treatment. *Mater. Sci. Eng. A.* **2016**, *667*, 139–143. https://doi.org/10.1016/j.msea.2016.04.092

[174] Tang, M.; Pistorius, P.C. Anisotropic Mechanical Behavior of AlSi10Mg Parts Produced by Selective Laser Melting. *JOM*. **2017**, *69*, 516–552. https://doi.org/10.1007/s11837-016-2230-5

[175] Li, Z.; Kuai, Z.; Bai, P.; Nie, Y.; Fu, G.; Liu, W.; Yang, S. Microstructure and Tensile Properties of AlSi10Mg Alloy Manufactured by Multi-Laser Beam Selective Laser Melting (SLM). *Metals*. **2019**, *9(12)*, 1337–1351. https://doi.org/10.3390/met9121337

[176] Maamoun, A.H.; Xue, Y.F.; Elbestawi, M.A.; Veldhuis, S.C. Thermal post-processing of AlSi10Mg parts produced by Selective Laser Melting using recycled powder. *Addit. Manuf.* **2018**, *21*, 234–247. https://doi.org/10.1016/j.addma.2018.03.014

[177] Prashanth, K.G.; Eckert, J. Formation of metastable cellular microstructures in selective laser melted alloys. *J. Alloys Compd.* **2016**, *707*, 26-34. https://doi.org/10.1016/j.jallcom.2016.12.209

[178] Lam, L.P.; Zhang, D.Q.; Liu, Z.H.; Chua, C.K. Phase analysis and microstructure characterization of AlSi10Mg parts produced by Selective Laser Melting. *Virtual Phys. Prototyp.* **2015**, *10(4)*, 207–215. https://doi.org/10.1080/17452759.2015.1110868

[179] Brandl, E.; Heckenberger, U.; Holzinger, V.; Buchbinder, D. Additive manufactured AlSi10Mg samples using Selective Laser Melting (SLM): Microstructure, high cycle fatigue, and fracture behavior. *Mater. Des.* **2012**, *34*, 159–169. https://doi.org/10.1016/j.matdes.2011.07.067

[180] Guan, K.; Wang, Z.; Gao, M.; Li, X.; Zeng, X. Effects of processing parameters on tensile properties of selective laser melted 304 stainless steel. *Mater. Des.* **2013**, *50*, 581–586. https://doi.org/10.1016/j.matdes.2013.03.056

[181] Popovich, A.; Sufiiarov, V.; Polozov, I.; Borisov, E.; Masaylo, D.; Orlov, A. Microstructure and mechanical properties of additive manufactured copper alloys. *Matter. Lett.* **2016**, *179*, 38–41. https://doi.org/10.1016/j.matlet.2016.05.064

[182] Prashanth, K.G.; Scudino, S.; Klauss, H.J.; Surreddi, K.B.; Löber, L.; Wang, Z.; Chaubey, A.K.; et al. Microstructure and mechanical properties of Al-12Si produced by selective laser melting: Effect of heat treatment. *Mater. Sci. Eng. A.* **2014**, *590*, 153–160. https://doi.org/10.1016/j.msea.2013.10.023

[183] Fiocchi, J.; Tuissi, A.; Bassani, P.; Biffi, C.A. Low temperature annealing dedicated to AlSi10Mg selective laser melting products. *J. Alloys Compd.* **2017**, *695*, 3402–3409. https://doi.org/10.1016/j.jallcom.2016.12.019

[184] Casati, R.; Nasab, M.H.; Coduri, M.; Tirelli, V.; Vedani, M. Effect of Platform Pre-Heating and Thermal-Treatment Strategies on Properties of AlSi10Mg Alloy Processed by Selective Laser Melting. *Metals.* **2018**, *8(11)*, 954. https://doi.org/10.3390/met8110954

[185] Li, W.; Li, S.; Liu, J.; Zhang, A.; Zhou, Y.; Wei, Q.; Yan, C.; Shi, Y. Effect of heat treatment on AlSi10Mg alloy fabricated by selective laser melting: Microstructure evolution, mechanical properties and fracture mechanism. *Mater. Sci. Eng. A.* **2016**, *663*, 116–125. https://doi.org/10.1016/j.msea.2016.03.088

[186] Takata, N.; Kodaira, H.; Sekizawa, K.; Suzuki, A.; Kobashi, M. Change in microstructure of selectively laser melted AlSi10Mg alloy with heat treatments. *Mater. Sci. Eng. A.* **2017**, *704*, 218–228. https://doi.org/10.1016/j.msea.2017.08.029

[187] Hadadzadeh, A.; Amirkhiz, B.S.; Mohammadi, M. Contribution of Mg_2Si precipitates to strength of direct metal laser sintered AlSi10Mg. *Mater. Sci. Eng. A.* **2019**, *739*, 295–300. https://doi.org/10.1016/j.msea.2018.10.055

[188] Fallah, V.; Korinek, A.; Ofori-Opoku, N.; Raeisinia, B.; Gallerneault, M.; Provatas, N.; Esmaeili, S. Atomic-scale pathway of early-stage precipitation in Al-Mg-Si alloys. *Acta. Mater.* **2015**, *82*, 457–467. https://doi.org/10.1016/j.actamat.2014.09.004

[189] Montero-Sistiaga, M.M.; Martens, R.; Vrancken, B.; Wang, X.; Van Hooreweder, B.; Kruth, J.-P.; et al. Changing the alloy composition of Al7075 for better processability by selective laser melting. *J. Mater. Process. Technol.* **2016**, *238*, 437–445. https://doi.org/10.1016/j.jmatprotec.2016.08.003

[190] Zhou, L.; Mehta, A.; Schulz, E.; McWilliams, B.; Cho, K.; Sohn, Y. Microstructure, precipitates and hardness of selectively laser melted AlSi10Mg alloy before and after the treatment. *Mater. Charact.* **2018**, *143*, 5–17. https://doi.org/10.1016/j.matchar.2018.04.022

[191] Pei, W.; Zhengying, W.; Zhen, C.; Junfeng, L.; Shuzhe, S.; Jun D. Numerical simulation and parametric analysis of selective laser melting process of AlSi10Mg powder. *Appl. Phys. A.* **2017**, *123*, 540. https://doi.org/10.1007/s00339-017-1143-7

[192] Zhang, C.; Zhu, H.; Hu, Z.; Zhang, L.; Zeng, X. A comparative study on single-laser and multi-laser selective laser melting AlSi10Mg: defects, microstructure and mechanical properties. *Mater. Sci. Eng. A.* **2019**, *746*, 416–423. https://doi.org/10.1016/j.msea.2019.01.024

[193] Pham, M.-S.; Dovgyy, B.; Hooper, P.A.; Gourlay, C.M.; Piglione, A. The role of side-branching in microstructure development in laser powder-bed fusion. *Nat. Com.* **2020**, *11*, 749. https://doi.org/10.1038/s41467-020-14453-3

[194] Kong, D.; Dong, C.; Wei, S.; Ni, X.; Zhang, L.; Li, R.; Wang, L.; Man, C.; Li, X. About metastable cellular structure in additively manufactured austenitic stainless steels. *Addit. Manuf.* **2021**, *38*, 101804. https://doi.org/10.1016/j.addma.2020.101804

[195] Yan, F.; Xiong, W.; Faierson, E.J. Grain Structure Control of Additively Manufactured Metallic Materials. *Materials.* **2017**, *10(11)*, 1260. https://doi.org/10.3390/ma10111260

[196] Wang, Y.; Yu, C.; Xing, L.; Li, K.; Chen, J.; Liu, W.; Ma, J.; Shen, Z. Grain structure and texture of SLM single laser. *J. Mater. Process. Technol.* **2020**, *281*, 116591. https://doi.org/10.1016/j.jmatprotec.2020.116591

[197] Liu, B.; Kuai, Z.; Li, Z.; Tong, J.; Bai, P.; Li, B.; Nie, Y. Performance Consistency of AlSi10Mg Alloy Manufactured by Simulating Multi Laser Beam Selective Laser Melting (SLM): Microstructures and Mechanical Properties. *Materials.* **2018**, *11(12)*, 2354. https://doi.org/10.3390/ma11122354

[198] Buchbinder, D.; Meiners, W.; Pirch, N.; Wissenbach, K. Investigation on reducing distortion by preheating during manufacture of aluminium components using selective laser melting. *J. Laser Appl.* **2014**, *26*, 012004. https://doi.org/10.2351/1.4828755

[199] Kim, D.-K.; Hwang, J.-H.; Kim, E.-Y.; Heo, Y.-U.; Woo, W.; Choi, S.-H. Evaluation of the stress-strain relationship of constituent phases in AlSi10Mg alloy produced by selective laser melting using crystal plasticity FEM. *J. Alloys Compd.* **2017**, *714*, 687–697. https://doi.org/10.1016/j.jallcom.2017.04.264

[200] Ji, Y.; Dong, C.; Kong, D.; Li, X. Design materials based on simulation results of silicon induced segregation at AlSi10Mg interface fabricated by selective laser melting. *J. Mater. Sci. Technol.* **2020**, *46*, 145–155. https://doi.org/10.1016/j.jmst.2020.01.037

[201] Kimura, T.; Nakamoto, T. Microstructures and mechanical properties of A356 (AlSi7Mg0.3) aluminium alloy fabricated by selective laser melting. *Mater. Des.* **2016**, *89*, 1294–1301. https://doi.org/10.1016/j.matdes.2015.10.065

[202] Dai, D.; Gu, D.; Poprawe, R.; Xia, M. Influence of additive multilayer feature on thermodynamics, stress and microstructure development during laser 3D printing of aluminium-based material. *Sci. Bull.* **2017**, *62*, 779–787. https://doi.org/10.1016/j.scib.2017.05.007

[203] Jägle, E.A.; Sheng, Z.; Wu, L.; Lu, L.; Risse, J.; Weisheit, A.; Raabe, D. Prediction Reactions in Age-Hardenable Alloys During Laser Additive Manufacturing. *JOM.* **2016**, *68*, 943–949. https://doi.org/10.1007/s11837-015-1764-2

[204] Guan, J.; Jiang, Y.; Zhang, X.; Chong, X. Microstructural evolution and EBSD analysis of AlSi10Mg alloy fabricated by selective laser remelting. *Mater. Charact.* **2020**, *161*, 110079. https://doi.org/10.1016/j.matchar.2019.110079

[205] Mertens, A.; Dedri, O.; Reuter, D.; Rigo, O.; Lecomte-Beckers, J. Thermal treatments of AlSi10Mg processed by laser beam melting, in *Proceedings of the 26th International Solid Freeform Fabrication Symposium*, vol. 1, **2015**.

References

[206] Zhang, C.; Zhu, H.; Qi, Y.; Zeng, X. The Effect of Annealing on Microstructure and Mechanical Properties of Selective Laser Melting AlSi10Mg, in *IOP Conference Series: Materials Science Engineering*. Vol. 538, p. 6, **2019**. https://doi.org/10.1088/1757-899X/538/1/012023

[207] Bertam, M.; Buxmann, K.; Furrer, P. Analysis of greenhouse gas emissions related to aluminium transport applications. *Int. J. Life Cycle Assess.* **2009**, *14*, 62–69. https://doi.org/10.1007/s11367-008-0058-0

[208] Leon, A.; Shirizly, A.; Aghion, E. Corrosion Behavior of AlSi10Mg Alloy Produced by Additive Manufacturing (AM) vs. Its Counterpart Gravity Cast Alloy. *Metals.* **2016**, *6(7)*, 148. https://doi.org/10.3390/met6070148

[209] Yaokawa, J.; Oh-ishi, K.; Dong, S.; Hara, M.; Musatani, T.; Sato, H. Dimensional changes induced by precipitation of supersaturated solid solution Si in selectively laser-melted AlSi10Mg during heat treatment. *Mater. Charact.* **2021**, *182*, 111533. https://doi.org/10.1016/j.matchar.2021.111533

[210] Rao, J.H.; Zhang, Y.; Zhang, K.; Huang, A.; Davies, C.H.J.; Wu, X. Multiple precipitation pathways in an Al-7Si-0.6Mg alloy fabricated by selective laser melting. *Scripta Mater.* **2019**, *160*, 66–69. https://doi.org/10.1016/j.scriptamat.2018.09.045

[211] Rao, J.H.; Zhang, Y.; Fang, X.; Chen, Y.; Wu, X.; Davis, C.H.J. The origins for tensile properties of selective laser melted aluminium alloy A357. *Addit. Manuf.* **2017**, *17*, 113–122. https://doi.org/10.1016/j.addma.2017.08.007

[212] Van Cauwenbergh, P.; Samaee, V.; This, L.; Nejezchlebová, J.; Sedlák, P.; Iveković, Schryvers, D.; et al. Unravelling the multi-scale structure-property relationship of laser powder bed fusion processed and heat-treated AlSi10Mg. *Sci. Rep.* **2021**, *11*, 6423. https://doi.org/10.1038/s41598-021-85047-2

[213] BoChao, L.; YoungKoo, P.; HongSheng, D. Effects of rheocasting and heat treatment on microstructure and mechanical properties of A356 alloy. *Mater. Sci. Eng. A.* **2011**, *528(3)*, 986–995. https://doi.org/10.1016/j.msea.2010.09.059

[214] Kempen, K.; This, L.; Humbeeck, J.V.; Kruth, J.-P. Processing AlSi10Mg by selective laser melting parameter: optimization and material characterization. *Mater. Sci. Technol.* **2015**, *31*, 917–923. https://doi.org/10.1179/1743284714Y.0000000702

[215] Di Egidio, G.; Ceschini, L.; Morri, A.; Martini, C.; Merlin, M. A Novel T6 Heat Treatment for AlSi10Mg Alloy Produced by Laser-Based Powder Bed Fusion: Comparison with T5 and Conventional T6 Heat Treatments. *Metall. Mater. Trans. B.* **2022**, *53B*, 284–303. https://doi.org/10.1007/s11663-021-02365-6

[216] Vanzetti, M.; Virgillito, E.; Aversa, A.; Manfredi, D.; Bondioli, F.; Lombardi, M.; Fino, P. Short Heat Treatments for the F357 Aluminium Alloy Processed by Laser Powder Bed Fusion. *Materials.* **2021**, *14(20)*, 6157. https://doi.org/10.3390/ma14206157

[217] Tonelli, L.; Liverani, E.; Morri, A; Ceschini, L. Role of Direct Aging and Solution Treatment on Hardness, Microstructure and Residual Stress of the A357 (AlSi10Mg0.6) Alloy Produced by Powder Bed Fusion. *Metall. Mater. Trans.* **2021**, *52*, 2484–2496. https://doi.org/10.1007/s11663-021-02179-6

[218] ASTM *Standard B917/B917M-12: Standard Practice for Heat Treatment of Aluminium-Alloy Casting from All Processes*; ADMET: West Conshohocken, PA, USA, **2012**.

[219] Mycrosystems, L. Measurement Parameter Description. In *Las AF 2D Analysis*, Mannheim, Germany, **2014**, pp. 113–116.

[220] Manente, A.; Timelli, G. Optimizing the Heat Treatment Process of Cast Aluminium Alloys. *Recent Trends in Processing and Degradation of Aluminium Alloys.* Ahmad, Z., ed.; **2011**, pp. 197–220. https://doi.org/10.5772/21659

[221] Lorusso, M.; Trevisan , F.; Calignano, F.; Lombardi, M.; Manfredi, D. A357 Alloy by LPBF for Industry Applications. *Materials*. **2020**, *13(7)*, 1488. https://doi.org/10.3390/ma13071488

[222] Casati, R.; Vedani, M. Aging Response of an A357 Al Alloy Processed by Selective Laser Melting. *Adv. Eng. Mater.* **2018**, *21(4)*, 1800406. https://doi.org/10.1002/adem.201800406

[223] Zou, T.; Chen, M.; Zhu, H.; Mei, S. Effect of Heat Treatments on Microstructure and Mechanical Properties of AlSi7Mg Fabricated by Selective Laser Melting. *J. Mater. Eng. Perform.* **2022**, *31*, 1791–1802. https://doi.org/10.1007/s11665-021-06324-9

[224] Zhang, B.; Meng, W.J.; Shao, S.; Phan, N.; Shamsaei, N. Effect of heat treatments on pore morphology and microstructure of laser additive manufactured parts. *Mat. Design Process. Comm.* **2019**, *1*, e29. https://doi.org/10.1002/mdp2.29

[225] Sausto, F.; Carrion, P.E.; Shamsei, N.; Beretta, S. Fatigue failure mechanisms for AlSi10Mg manufactured by L-PBF under axial and torsional loads: The role of defects and residual stresses. *Int. J. Fatigue.* **2022**, *162*, 106903. https://doi.org/10.1016/j.ijfatigue.2022.106903

[226] Zhao, Y.Y.; Lei, Z.F.; Lu, Z.P.; Huang, J.C.; Nieh, T.G. A simplified model connection lattice distortion with friction of Nb-based equiatomic high-entropy alloys. *Mater. Res. Lett.* **2019**, *7(8)*, 340–346. https://doi.org/10.1080/21663831.2019.1610105

[227] Ponzak, A.; Thole, V.; Sanders, P. The Natural Aging Effect on Hardenability in Al-Mg-Si: A Complex Interaction between Composition and Heat Treatment Parameters. *Metals.* **2018**, *8(5)*, 309. https://doi.org/10.3390/met8050309

[228] Park, T.-H.; Beak, M.-S.; Hyer, H.; Sohn, Y.; Lee, K.-A. Effect of direct aging on microstructure and tensile properties of AlSi10Mg alloy manufactured by selective laser melting. *Mater. Charact.* **2021**, *176*, 111113. https://doi.org/10.1016/j.matchar.2021.111113

[229] Kending, K.L.; Miracle, D.B. Strengthening mechanisms of an Al-Mg-Sc-Zr alloy. *Acta Mater.* **2002**, *50(16)*, 4165–4175. https://doi.org/10.1016/S1359-6454(02)00258-6

[230] Keyhani, A.; Roumina, R. Dislocation-precipitate interaction maps. *Comput. Mater. Sci.* **2018**, *141*, 153–161. https://doi.org/10.1016/j.commatsci.2017.09.036

[231] Li, X.P.; Ji, G.; Chen, Z.; Addad, A.; Wu, Y.; Wang, H.W.; Vleugels, J.; Van Humbeeck, J.; Kruth, J.-P. Selective laser melting of nano-TiB_2 decorated AlSi10Mg alloy with high fatigue strengths and ductility. *Acta Mater.* **2017**, *129*, 183–193. https://doi.org/10.1016/j.actamat.2017.02.062

[232] Li, R.; Wang, M.; Li, Z.; Cao, P.; Yuan, T.; Zhu, H. Developing a high-strength Al-Mg-Si-Sc-Zr alloy for selective laser melting: Crack-inhibiting and multiple strengthening mechanisms. *Acta Mater.* **2020**, *193*, 83–98. https://doi.org/10.1016/j.actamat.2020.03.060

[233] Motz, C.; Pippan, R. Deformation behaviour of closed-cell aluminium foams in tension. *Acta Mater.* **2001**, *49*, 2463–2470. https://doi.org/10.1016/S1359-6454(01)00152-5

[234] Rodriguez, P. Sixty years of dislocations. *Bull. Mater. Sci.* **1996**, *19*, 857–872. https://doi.org/10.1007/BF02744623

[235] Di Giovanni, M.T.; de Menezed, J.T.O.; Bolelli, G.; Cerri, E.; Castrodeza, E.M. Fatigue crack growth behavior of a selective laser melted AlSi10Mg. *Eng. Fract. Mech.* **2019**, 217, 106564. https://doi.org/10.1016/j.engfracmech.2019.106564

[236] Merino, J.; Ruvalcaba, B.; Varela, J.; Arrieta, E.; Murr, E.L.; Wicker, R.B.; Benedict, M.; Medina, F. Multiple, comparative heat treatment and aging schedules for controlling the microstructures and mechanical properties of laser powder bed fusion fabricated AlSi10Mg alloy. *J. Mater. Res. Technol.* **2021**, *13*, 669–685. https://doi.org/10.1016/j.jmrt.2021.04.062

[237] Chen, B.; Moon, S.K.; Yao, X.; Bi, G.; Shen, J.; Umeda, J.; Kondoh, K. Strength and strain hardening of selective laser melted AlSi10Mg alloy. *Scripta Mater.* **2017**, *141*, 45–49. https://doi.org/10.1016/j.scriptamat.2017.07.025

[238] de Menezes, J.T.O.; Castrodeza, E.M.; Patriarca, L.; Casati, R. Effect of heat treatments and loading orientation on the tensile properties and fracture toughness of AlSi7Mg alloy produced by Laser Powder Bed Fusion. *Int. J. Fract.* **2022**, *235*, 145–157. https://doi.org/10.1007/s10704-022-00631-5

[239] Yildirim, M.; Özyürek, D. The effects of Mg amount on the microstructure and mechanical properties of Al-Si-Mg alloys. *Mater. Des.* **2013**, *51*, 767–774. https://doi.org/10.1016/j.matdes.2013.04.089

[240] Yap, Y.C.; Chua, C.K.; Dong, Z.L.; Liu, Z.H.; Zhang, D.Q.; Loh, L.E.; Sing, S.L. Review of selective laser melting: Materials and applications. *Appl. Phys. Rev.* **2015**, *2*, 041101. https://doi.org/10.1063/1.4935926

[241] Louvis, E.; Fox, P.; Sutcliffe, C.J. Selective laser melting of aluminium components. *J. Mater. Process. Technol.* **2011**, *211(12)*, 275–284. https://doi.org/10.1016/j.jmatprotec.2010.09.019

[242] Majeed, A.; Lv, J.; Zhang, Y.; Muzamil, M.; Waqas, A. An investigation into the influence of processing parameters on the surface quality of AlSi10Mg parts by SLM process. In *Proceedings of the 16th International Bhurban Conference on Applied Sciences and Technology* (IBCAST), Islamabad, Pakistan, **2019**. https://doi.org/10.1109/IBCAST.2019.8667175

[243] Prashanth, K.G.; Scudino, S.; Maity, T.; Das, J.; Eckert, J. Is the energy density a reliable parameter for materials synthesis by selective laser melting? *Mater. Res. Lett.* **2017**, *5*, 386–390. https://doi.org/10.1080/21663831.2017.1299808

References

[244] Larossa, N.O.; Wang, W.; Read, N.; Loretto, M.H.; Evans, C.; Carr, J.; Tradowsky, U.; et al. Linking microstructure and processing defects to mechanical properties of selectively laser melted AlSi10Mg alloy. *Theor. Appl. Fract. Mec.* **2018**, *98*, 123–133. https://doi.org/10.1016/j.tafmec.2018.09.011

[245] Yadroitsev, I.; Yadroitsava, I.; Bertrand, P.; Smurov, I. Factor analysis of selective laser melting process parameters and geometrical characteristics of synthesized single tracks. *Rapid Prototyp. J.* **2012**, *18*, 201–208. https://doi.org/10.1108/13552541211218117

[246] Heany, D.F.; Mueller, T.W.; Davies, P.A. Mechanical properties of metal injection moulded 316L stainless steel using both prealloy and master alloy techniques. *Powder Metall.* **2021**, *47*, 367–373. https://doi.org/10.1179/003258904225020855

[247] Sufiiarov, V.Sh.; Popovich, A.A.; Borisov, E.V.; Polozov, I.A.; Masaylo, D.V.; Orlov, A.V. The Effect of Layer Thickness at Selective Laser Melting. *Procedia Eng.* **2017**, *174*, 126–134. https://doi.org/10.1016/j.proeng.2017.01.179

[248] Nguyen, Q.B.; Luu, D.N.; Nai, S.M.L.; Zhu, Z.; Chen, Z.; Wei, J. The role of powder layer thickness on the quality of SLM printed parts. *Arch. Civ. Mec. Eng.* **2018**, *18(3)*, 948–955. https://doi.org/10.1016/j.acme.2018.01.015

[249] Li, F.; Wang, Z.; Zeng, X. Microstructure and mechanical properties of Ti6Al4V alloy fabricated by multi-laser beam selective laser melting. *Mater. Lett.* **2017**, *199*, 79–83. https://doi.org/10.1016/j.matlet.2017.04.050

[250] Masoomi, M.; Thomposon, S.M.; Shamsaei, N. Quality part production via multi-laser additive manufacturing. *Manuf. Lett.* **2017**, *13*, 15–20. https://doi.org/10.1016/j.mfglet.2017.05.003

[251] Liu, B.; Li, B.-Q.; Li, Z.; Bai, P.; Wang, Y.; Kuai, Z. Numerical investigation on heat transfer of multi-laser process during selective laser melting of AlSi10Mg. *Results Phys.* **2019**, *12*, 454–459. https://doi.org/10.1016/j.rinp.2018.11.075

[252] Buchbinder, D. Selective Laser Melting von Aluminiumgusslegierungen; Shaker Verlag: Berlin, Germany, **2013**.

[253] Read, N.; Wang, W.; Essa, K.; Attallah, M.M. Selective laser melting of AlSi10Mg alloy: Process optimization and mechanical properties development. *Mater. Des.* **2015**, *65*, 417–424. https://doi.org/10.1016/j.matdes.2014.09.044

[254] Zyguła, K.; Nosek, B.; Pasiowiec, H.; Szysiak, N. Mechanical properties and microstructure of AlSi10Mg alloy obtained by casting and SLM technique. *World Sci. News.* **2018**, *104*, 462–472.

[255] Cerri, E.; Ghio, E. Effect of Distance along the Build Axis on Mechanical Properties and Microstructure in AlSi10Mg SLM Alloy. *Mater. Sci. Forum.* **2021**, *1016*, 309–314. https://doi.org/10.4028/www.scientific.net/MSF.1016.309

[256] Visser, R.; van Huis, M.A.; Jansen, J.; Zandbergen, H.W.; Marioara, C.D.; Andersen, S.J. The crystal structure of the β′ phase in Al-Mg-Si alloys. *Acta Mater.* **2007**, *55(11)*, 3815–3823. https://doi.org/10.1016/j.actamat.2007.02.032

[257] Ghio, E.; Cerri, E. Aging response in Selective Laser Melted AlSi10Mg Alloy as Function of Distance from the Substrate Plate. *Mater. Sci. Forum.* **2021**, *1016*, 476–480. https://doi.org/10.4028/www.scientific.net/MSF.1016.476

[258] Li, Y.; Gu, D. Parametric analysis of thermal behavior during selective laser melting additive manufacturing of aluminum alloy powder. *Mater. Des.* **2014**, *63*, 856–867. https://doi.org/10.1016/j.matdes.2014.07.006

[259] Lingda, X.; Guoli, Z.; Gaoyang, M.; Chunming, W.; Ping, J. A phase-field simulation of columnar-to-equiaxed transition in the entire laser welding molten pool. *J. Alloys Compd.* **2021**, *858*, 157669. https://doi.org/10.1016/j.jallcom.2020.157669

[260] Hadadzadeh, A.; Amirkhiz, B.; Li, J.; Mohammadi, M. Columnar to equiaxed transition during direct metal laser sintering of AlSi10Mg alloy: Effect of building direction. *Addit. Manuf.* **2018**, *23*, 121–131. https://doi.org/10.1016/j.addma.2018.08.001

[261] Maamoun, A.H.; Xue, Y.F.; Elbestawi, M.A.; Veldhuis, S.C. The Effect of Selective Laser Melting Process Parameters on the Microstructure and Mechanical Properties of Al6061 and AlSi10Mg Alloy. *Materials.* **2019**, *12(1)*, 12. https://doi.org/10.3390/ma12010012

[262] Delahaye, J.; Tchuindjang, T.J.; Lecomte-Beckers, J.; Rigo, O.; Habraken, A.M.; Mertens, A. Influence of Si precipitates on fracture mechanisms of AlSi10Mg parts processed by Selective Laser Melting. *Acta Mater.* **2019**, *175*, 160–170. https://doi.org/10.1016/j.actamat.2019.06.013

[263] Qin, H.; Dong, Q.; Fallah, V.; Daymond, M.R. Rapid Solidification and Non-Equilibrium Phase Constitution in Laser Powder Bed Fusion (LPBF) of AlSi10Mg Alloy: Analysis of Nano-Precipitates, Eutectic Phases, and Hardness Evolution. *Metall. Mater. Trans. A.* **2020**, *51*, 448–468. https://doi.org/10.1007/s11661-019-05505-5

[264] Kou, S. Welding Metallurgy; Wiley: Hoboken, NJ, USA, **2003**.

[265] Wang, K.; Wang, D.; Han, F. Effect of crystalline grain structures on the mechanical properties of twinning-induced plasticity steel. *Acta. Mech. Sin.* **2016**, *32*, 181–187. https://doi.org/10.1007/s10409-015-0513-7

[266] Drar, H.; Svensson, I.L. Improvement of tensile properties of Al-Si alloy through directional solidification. *Mater. Lett.* **2007**, *61(2)*, 392–396. https://doi.org/10.1016/j.matlet.2006.04.112

[267] Matyjia, H.; Giessen, B.; Grant, N. The effect of cooling rate on the dendrite spacing in splat-cooled aluminium alloys. *J. Inst. Metals.* **1968**, *96*, 30–32.

[268] Liu, B.; Li, B.-Q.; Li, Z. Selective laser remelting of an additive layer manufacturing process on AlSi10Mg. *Results Phys.* **2019**, *12*, 982–988. https://doi.org/10.1016/j.rinp.2018.12.018

[269] Hyer, H.; Zhou, L.; Park, S.; Gottsfritz, G.; Benson, G.; Tolentino, B.; McWilliams, B.; et al. Understanding the Laser Powder Bed Fusion of AlSi10Mg Alloy. *Metallogr. Microstruct. Anal.* **2020**, *9*, 484–502. https://doi.org/10.1007/s13632-020-00659-w

[270] Garmendia, X.; Chalker, J.; Bilton, M.; Sutcliffe, C.J.; Chalker, P.R. Microstructure and mechanical properties of Cu-modified AlSi10Mg fabricated by Laser-Powder Bed Fusion. *Materialia.* **2020**, *9*, 100590. https://doi.org/10.1016/j.mtla.2020.100590

[271] Andani, M.T.; Dehghani, R.; Karamooz-Ravari, M.R.; Mirzaeifar, R.; Ni, J. Spatter formation in selective laser melting process using multi-laser technology. *Mater. Des.* **2017**, *131*, 460–469. https://doi.org/10.1016/j.matdes.2017.06.040

[272] Galy, C.; Le Guen, E.; Lacoste, E.; Arvieu, C. Main defects observed in aluminium alloy parts produced by SLM: From causes to consequences. *Addit. Manuf.* **2018**, *22*, 165–175. https://doi.org/10.1016/j.addma.2018.05.005

[273] Chen, J.; Hou, W.; Wang, X.; Chu, S.; Yang, Z. Microstructure, porosity and mechanical properties of selective laser melted AlSi10Mg. *Chin. J. Aeronaut.* **2020**, *33*, 2043–2054. https://doi.org/10.1016/j.cja.2019.08.017

[274] Giovagnoli, M.; Tocci, M.; Fortini, A.; Merlin, M.; Ferroni, M.; Migliori, A.; Pola, A. Effect of different heat-treatment routes on the impact properties of an additively manufactured AlSi10Mg alloy. *Mater. Sci. Eng. A.* **2021**, *802*, 140671. https://doi.org/10.1016/j.msea.2020.140671

[275] Wang, L.F.; Sun, J.; Yu, X.L.; Shi, Y.; Zhu, X.G.; Cheng, L.Y.; Liang, H.H.; Yan, B.; Guo, L.J. Enhancement in mechanical properties of selectively laser-melted AlSi10Mg aluminum alloys by T6-like heat treatment. *Mater. Sci. Eng. A.* **2018**, *734*, 299–310. https://doi.org/10.1016/j.msea.2018.07.103

[276] Wang, L.; Jiang, X.; Gou, M.; Zhu, X.; Yan, B. Characterization of structural properties for AlSi10Mg alloys fabricated by selective laser melting. *Mater. Sci. Technol.* **2017**, *33*, 2274–2282. https://doi.org/10.1080/02670836.2017.1398513

[277] Wang, L.; Jiang, X.; Zhu, Y.; Ding, Z.; Zhu, X.; Sun, J.; Yan, B. Investigation of Performance and Residual Stress Generation of AlSi10Mg Processed by Selective Laser Melting. *Adv. Mater. Sci. Eng.* **2018**, *2018*, 1–12. https://doi.org/10.1155/2018/7814039

[278] Tomus, D.; Tian, Y.; Rometsch, P.A.; Heilmaier, M.; Wu, X. Influence of post heat treatments on anisotropy of mechanical behaviour and microstructure of Hastelloy-X parts produced by selective laser melting. *Mater. Sci. Eng. A.* **2016**, *667*, 42–53. https://doi.org/10.1016/j.msea.2016.04.086

[279] Yakout, M.; Elbestawi, M.A.; Veldhuis, S.C. A study of the relationship between thermal expansion and residual stress in selective laser melting of Ti-6Al-4V. *J. Manuf. Process.* **2020**, *52*, 181–192. https://doi.org/10.1016/j.jmapro.2020.01.039

[280] Hadadzedeh, A.; Baxter, C.; Amirkhiz, B.S.; Mohammadi, M. Strengthening mechanisms in direct metal laser sintered AlSi10Mg: Comparison between virgin and recycled powders. *Addit. Manuf.* **2018**, *23*, 108–120. https://doi.org/10.1016/j.addma.2018.07.014

[281] Zhang, X.; Huang, L.; Zhang, B.; Chen, Y.Z.; Liu, F. Microstructural evolution and strengthening mechanism of an Al-Si-Mg alloy processed by high-pressure torsion with different heat treatments. *Mater. Sci. Eng. A.* **2020**, *794*, 139932. https://doi.org/10.1016/j.msea.2020.139932

REFERENCES

[282] Li, Z.; Li, Z.; Tan, Z.; Xiong, D.; Guo, Q. Stress relaxation and the cellular structure-dependence of plastic deformation in additively manufactured AlSi10Mg alloys. *Int. J. Plast.* **2020**, *127*, 102640. https://doi.org/10.1016/j.ijplas.2019.12.003

[283] Ryen, Ø.; Holmedal, B.; Nijs, O.; Sjölander, E.; Ekström, H. Strengthening mechanisms in solid solution aluminum alloy. *Metall. Mater. Trans.* **2006**, *37*, 1999–2006. https://doi.org/10.1007/s11661-006-0142-7

[284] Starink, M.J.; Wang, S.C. A model for the yield strength of overaged Al-Zn-Mg-Cu alloys. *Acta Mater.* **2003**, *51(17)*, 5131–5150. https://doi.org/10.1016/s1359-6454(03)00363-X

[285] ASTM Standard E646: Standard Test Method for Tensile Strain-Hardening Exponents (N-Values) Of Metallic Sheet Materials; ADMET: West Conshohocken, PA, USA, **2000**.

[286] Wang, Z.; Xie, M.; Li, Y.; Zhang, W.; Yang, C.; Kollo, L.; Eckert, J.; Prashanth, K.G. Premature failure of an additively manufactured material. *NPG Asia Mater*. **2020**, *12*, 30. https://doi.org/10.1038/s41427-020-0212-0

[287] Sjögren, T.; Svensson, I.L. The Effect of Graphite Fraction and Morphology on the Plastic Deformation Behavior of Cast Irons. *Metall. Mater. Trans.* **2007**, *38*, 840–847. https://doi.org/10.1007/s11661-007-9115-8

[288] Pierre, V.; Anthony, B.; Lore, T.; Brecht, V.; Kim, V. Heat treatment optimization via thermo-physical characterization of AlSi7Mg and AlSi10Mg manufactured by laser powder bed fusion (LPBF). In *Proceedings of the EUROPM 2018 Congress*, Bilbao, Spain, **2018**.

[289] Bharath, C.; Shamanth, V.; Hemanth, K. Studies on mechanical behaviour of AlSi10Mg alloy produced by Selective Laser Melting and A360 alloy by die casting. *Mater. Today Proc.* **2021**, *45*, 78–81. https://doi.org/10.1016/j.matpr.2020.10.095

[290] Liu, J.; Wei, Q.; Bi, Y. Deformation hardening behaviuor of deformed aluminium alloys. *Phy. Tesing Chem. Ana. Part A Phys. Test.* **2008**, *44*, 4–6. https://doi.org/10.3969/j.issn.1001-4012.2008.01.003

[291] Zhao, L.; Macías, J.G.S.; Ding, L.; Idrissi, H.; Simar, A. Damage mechanisms in selective laser melted AlSi10Mg under as built and different post-treatment conditions. *Mater. Sci. Eng. A.* **2019**, *764*, 138210. https://doi.org/10.1016/j.msea.2019.138210

[292] Tang, M.; Pistorius, P. Oxides, porosity and fatigue performance of AlSi10Mg parts produced by selective laser melting. *Int. J. Fatigue*. **2017**, *94*, 192–201. https://doi.org/10.1016/j.ijfatigue.2016.06.002

[293] Drouzy, M.; Jacob, S.; Richard, M. Interpretation of tensile results by means of quality index and probable yield strength. *AFS Int. Cast Metals Int.* vol. 5, pp. 43–50, **1980**.

[294] Mertens, A.; Delahaye, J.; Dedry, O.; Vertruyen, B.; Tchuindjang, J.T.; Habraken, A. Microstructure and Properties of SLM AlSi10Mg: Understanding the Influence of Local Thermal History. *Proc. Manuf.* **2020**, *47*, 1089–1095. https://doi.org/10.1016/j.promfg.2020.04.121

[295] Cabrini, M.; Calignano, F.; Fino, P.; Lorenzi, S.; Lorusso, M.; Manfredi, D.: Testa, C.; Pastore, T.M. Corrosion Behavior of Heat-Treated AlSi10Mg Manufactured by Laser Powder Bed Fusion. *Materials.* **2018**, *11(7)*, 1051. https://doi.org/10.3390/ma11071051

[296] Cao, X.; Campbell, J. Morphology of β-Al5FeSi Phase in Al-Si Cast Alloys. *Mater. Trans.* **2006**, *47(5)*, 1303–1312. https://doi.org/10.2320/matertrans.47.1303

[297] Wang, X.J.; Zhang, L.C.; Fang, M.H.; Sercombe, T.B. The Effect of Atmosphere on the Structure and Properties of a Selective Laser Melted Al-12Si Alloy. *Mater. Sci. Eng. A.* **2014**, *597*, 370–375. https://doi.org/10.1016/j.msea.2014.01.012

[298] Tang, M.; Pistorius, P.; Beuth, J. Geometric model to predict porosity of part produced in powder bed system, in Materials Science & Technology conference and exhibition, Columbus, Ohio, USA, **2015**.

[299] Anderson, I.E.; White, E.M.H.; Dehoff, R. Feedstock powder processing research needs for additive manufacturing development. *Curr. Opin. Solid State Mater. Sci.* **2018**, *22(1)*, 8–15. https://doi.org/10.1016/j.cossms.2018.01.002

[300] Shi, Y.; Yang, K.; Kairy, S.K.; Palm, F.; Wu, X.; Rometsch, P.A. Effect of platform temperature on porosity, microstructure and mechanical properties of an Al-Mg-Cu-Zn alloy fabricated by selective laser melting. *Mater. Sci. Eng. A.* **2018**, *732*, 41–52. https://doi.org/10.1016/j.msea.2018.06.049

[301] Tiwari, J.K.; Mandal, A.; Sathish, N.; Agrawal, A.K.; Srivastava, A.K. Investigation of porosity, microstructure and mechanical properties of additively manufactured graphene reinforced AlSi10Mg composite. *Addit. Manuf.* ***2020***, *33*, 101095. https://doi.org/10.1016/j.addma.2020.101095

[302] Damon, J.; Dietrich, S.; Vollert, F.; Gibmeier, J.; Schulze, V. Process dependent porosity and influence of shot penning on porosity morphology regarding selective laser melted AlSi10Mg parts. *Addit. Manuf.* **2018**, *20*, 77–89. https://doi.org/10.1016/j.addma.2018.01.001

[303] Xu, Z.; Wen, W.; Zhai, T. Effect of Pore Position in Depth on Stress/Strain Concentration and Fatigue Crack Initiation. *Metall. Mater. Trans.* **2018**, *43*, 2763–2770. https://doi.org/10.1007/s11661-011-0947-x

[304] Davis, T.; Healy, D.; Bubeck, A.; Walker, R. Stress concentrations around voids in three dimensions: The roots of failure. *JSG.* **2017**, *102*, 193–207. https://doi.org/10.1016/j.jsg.2017.07.013

[305] Singla, A.K.; Banerjee, M.; Sharma, A.; Singh, J.; Bansal, A.; Gupta, M.; Khanna, N.; Shahi, A.; et al. Selective laser melting of Ti6Al4V alloy: Process parameters, defects and post-treatments. *J. Manuf. Process.* **2021**, *64*, 161–187. https://doi.org/10.1016/j.jmapro.2021.01.009

[306] Rakesh, C.h; Priyanka, N.; Jayaganthan, R.; Vasa, N.J. Effect of build atmosphere on the mechanical properties of AlSi10Mg produced by selective Laser melting. *Mater. Today: Commun.* **2018**, *5(9)*, 17231–17238. https://doi.org/10.1016/j.matpr.2018.04.133

[307] Xiong, Z.H.; Liu, S.L.; Li, S.F.; Shi, Y.; Yang, Y.F.; Misra, R.D.K. Role of melt pool boundary condition in determining the mechanical properties of selective laser melting AlSi10Mg alloy. *Mater. Sci. Eng. A.* **2019**, *740–741*, 148–156. https://doi.org/10.1016/j.msea.2018.10.083

[308] Bai, Y.; Yang, Y.; Xiao, Z.; Zhang, M.; Wang, D. Process optimization and mechanical property evolution of AlSiMg0.75 selective laser melting. *Mater. Des.* **2018**, *140*, 275–266. https://doi.org/10.1016/j.matdes.2017.11.045

[309] Uriati, F.; Betta, F.; Ferro, P.; Rosso, S.; Savio, G.; Concheri, G.; Meneghello, R. High Density AlSi10Mg Aluminium Alloy Specimens Obtained by Selective Laser Melting, in *International Conference on Design, Simulation, Manufacturing: The Innovation Exchange*, Modena, Italy, **2019**.

[310] Chaijaruwanich, A.; Lee, P.D.; Dashwood, R.; Youssef, Y.M.; Nagaumi, H. Evolution of pore morphology and distribution during the homogenization of direct chill cast Al-Mg alloys. *Acta Mater.* **2007**, *55(1)*, 285–293. https://doi.org/10.1016/j.actamat.2006.08.023

[311] Gu, J.; Yang, S.; Gao, M.; Bai, J.; Zhai, Y.; Ding, J. Micropore evolution in additively manufactured aluminium alloys under heat treatment and inter-layer rolling. *Mater. Des.* **2020**, *186*, 108228. https://doi.org/10.1016/j.matdes.2019.108288

[312] Teng, X.; Zhang, G.; Liang, J.; Li, H.; Liu, Q.; Cui, Y.; Cui, T.; Jiang, L. Parameter optimization and microhardness experiment of AlSi10Mg alloy prepared by selective laser melting. *Mater. Res.* **2019**, *6*, 086592. https://doi.org/10.1088/2053-1591/ab18d0

[313] Hastie, J.C.; Koeblin, J.; Kartal, M.E.; Attallah, M.M.; Martinez, R. Evolution of internal pores within AlSi10Mg manufactured by laser powder bed fusion under tension: As-built and heat treated conditions. *Mater. Des.* **2021**, *204*, 109645. https://doi.org/10.1016/j.matdes.2021.109645

[314] Froes, F.; Boyer, R.; Dutta, B. Introduction to aerospace materials requirements and the role of additive manufacturing. In *Additive Manufacturing for Aero-space Industry*, 1st ed.; Froes, F., Boyer, R., Eds.; Elsevier: Amsterdam, The Netherlands, **2017**, pp. *1–6*. https://doi.org/10.1016/B978-0-12-814062-8.00001-7

[315] Rugg, S.; Dixon, M.; Burrows, J. High-temperature application of titanium alloys in gas turbines. Material life cycle opportunities and threats—An industrial perspective. *Mater. High Temp.* **2016**, *233*, 536–541. https://doi.org/10.1080/09603409.2016.1184423

[316] Singh, P.; Pungotra, H.; Kalsi, N.S. On the characteristics of titanium alloys for the aircraft applications. *Mater. Today Proc.* **2017**, *4(8)*, 8971–8982. https://doi.org/10.1016/j.matpr.2017.07.249

[317] Gurrapa, I. Characterization of titanium alloy Ti-6Al-4V for chemical, marine and industrial applications. *Mater. Charact.* **2003**, *51(2–3)*, 131–139. https://doi.org/10.1016/j.matchar.2003.10.006

[318] Liu, Z.; He, B.; Lyu, T.; Zou, Y. A Review on Additive Manufacturing of Titanium Alloys for Aerospace Applications: Direct Energy Deposition and Beyond Ti-6Al-4V. *JOM.* **2017**, *73*, 1804–1818. https://doi.org/10.1007/s11837-021-04670-6

[319] Inagaki, I.; Takechi, T.; Shirai, Y.; Ariyasu, N. Application and Features of Titanium for the Aerospace Industry. *Nippon Steel Sumimoto Met. Tech. Rep.* **2014**, *106*, 22–27.

[320] Allen, J. *An Investigation into the Comparative Costs of Additive Manufacturing vs. Machine From Solid Aero Engine Parts*; Rolls-Royce PLC Derby: Derbyshire, UK, **2006**.

REFERENCES

[321] Ahmed, M.; Savvakin, D.G.; Ivasishin, O.M.; Pereloma, E.V. The effect of ageing on microstructure and mechanical properties of powder Ti-5Al-5Mo-5V-1Cr-1Fe alloy. *Mater. Sci. Eng. A.* **2014**, *605*, 89–97. https://doi.org/10.1016/j.msea.2014.03.030

[322] Sun, H.; Chu, X.; Liu, Z.; Gisele, A.; Zou, Y. Selective Laser Melting of Maraging Steels Using Recycled Powders: A Comprehensive Microstructural and Mechanical Investigation. *Metall. Mater. Trans. A.* **2021**, *52*, 1714–1722. https://doi.org/10.1007/s11661-021-06180-1

[323] Watson, J.K.; Tamiger, K.M.B. A decision-support model for selective additive manufacturing versus subtractive manufacturing based on energy consumption. *J. Clean. Prod.* **2018**, *176*, 1316–1322. https://doi.org/10.1016/j.jclepro.2015.12.009

[324] Gibbons, D.W.; Serfontein, J.-P.L.; van der Merwe, A.F. Mapping the path to certification of metal laser powder bed fusion for aerospace applications. *Rapid Prototyp. J.* **2021**, *27*, 355–361. https://doi.org/10.1108/RPJ-07-2020-0154

[325] He, Y.; Montgomery, C.; Beuth, J.; Webler, B. Melt pool geometry and microstructure of Ti6Al4V with B additions processed by selective laser melting additive manufacturing. *Mater. Des.* **2019**, *183*, 108126. https://doi.org/10.1016/j.matdes.2019.108126

[326] Karayazig, K.; Elwany, A.; Tapia, G.; Franco, B.; Johnson, L.; Ma, J.; Karaman, I.; Arróyane, R. Numerical and experimental analysis of heat distribution in the laser powder bed fusion of Ti-6Al-4V. *IISE Trans.* **2019**, *51*, 136–152. https://doi.org/10.1080/24725854.2018.1461964

[327] Boyer, R., Welsch, G., Colling, E.W., **1994**. *Materials Properties: Handbook*; ASM International: Gaug Country, OH USA.

[328] ASTM F3001-14: Standard Specification for Additive Manufacturing Titanium -6 Aluminium -4 Vanadium ELI (Extra Low Interstitial) with Powder Bed Fusion; West Conshohocken, PA, USA, **2013.**

[329] Saboori, A.; Gallo, D.; Biamino, S.; Fino, P.; Lombardi, M. An Overview of Additive Manufacturing of Titanium Components by Direct Energy Deposition: Microstructure and Mechanical Properties. *Appl. Sci.* **2017**, *7(9)*, 883. https://doi.org/10.3390/app7090883

[330] Bontha, S.; Klinbeil, N.W.; Kobryn, P.A.; Frase, H.L. Thermal process maps for predicting solidification microstructure in laser fabrication of thin-wall structures. *J. Mater. Process. Technol.* **2016**, *178(1–3)*, 135–142. https://doi.org/10.1016/j.jmatprotec.2006.03.155

[331] Barriobero-Vila, P.; Gussone, J.; Haubrick, J.; Sandlöbes, S.; Da Silva, J.; Cloentes, P.; et al. Inducing Stable α + β Microstructure during Selective Laser Melting of Ti-6Al-4V Using Intensified Intrinsic Heat Treatment. *Materials.* **2017**, *10(3)*, 268. https://doi.org/10.3390/ma10030268

[332] Xu, W.; Brandt, M.; Sun, S.; Elambasseril, J.; Liu, Q.; Latham, K.; Xia, K.; Qian, M. Additive manufacturing of strong and ductile Ti-6Al-4V by selective laser melting via in situ martensite decomposition. *Acta Mater.* **2015**, *14*, 74–84. https://doi.org/10.1016/j.actamat.2014.11.028

[333] Kaschel, F.R.; Vijayaraghavan, R.K.; Shmeliov, A.; McCharty, E.K.; Canavan, M.; et al. Mechanism of stress relaxation and phase transformation in additively manufactured Ti-6Al-4V via *in-situ* high temperature XRD and TEM analyses. *Acta Mater.* **2020**, *188*, 720–732. https://doi.org/10.1016/j.actamat.2020.02.056

[334] Xing, L.-L.; Zhang, W.-J.; Zhao, C.-C.; Gao, W.-Q.; Zhen, Z.-J.; Liu, W. Influence of Powder Bed Temperature on the Microstructure Mechanical Properties of Ti-6Al-4V Alloy Fabricated via Laser Powder Bed Fusion. *Materials.* **2021**, *14(9)*, 2278. https://doi.org/10.3390/ma14092278

[335] Illarinov, A.G.; Stepanov, S.I.; Demakov, S.L. Effect of Thermomechanical Treatment Parameters on Structure, Phase Composition and Mechanical Properties of Ti-3Al-5Mo-4.5V Titanium Alloy. In *Proceedings of the IOP Conference Series: Materials Science and Engineering*, Chelyabinsk, Russian Federation, 22–24 September **2020**. https://doi.org/10.1088/1757-899X/969/1/012085

[336] Haar, G.M.T.; Becker, T.H. Selective Laser Melting Produced Ti-6Al-4V: Post-Process Heat Treatments to Achieve Superior Tensile Properties. *Materials.* **2018**, *11(1)*, 146. https://doi.org/10.3390/ma11010146

[337] Sabban, R.; Bahl, S.; Chatterjee, K.; Suwas, S. Globularization using heat treatment in additively manufactured Ti-6Al-4V for high strength and toughness. *Acta Mater.* **2019**, *162*, 239–254. https://doi.org/10.1016/j.actamat.2018.09.064

[338] Muhammad, M.; Pegeus, J.W.; Shamsei, N.; Haghshenas, M. Effect of heat treatments on microstructure/small-scale properties of additive manufactured Ti-6Al-4V. *Int. J. Manuf. Technol.* **2019**, *103*, 4161–4172. https://doi.org/10.1007/s00170-019-03789-w

[339] Huang, Q.; Liu, X.; Yang, X.; Zhang, R.; Shen, Z.; Feng, Q. Specific heat treatment of selective laser melted Ti-6Al-4V for biomedical applications. *Front. Mater. Sci.* **2015**, *9*, 373–381. https://doi.org/10.1007/s11706-015-0315-7

[340] Lekoadi, P.; Tlotleng, M.; Annan, K.; Maledi, N.; Masina, B. Evaluation of Heat Treatment Parameters on Microstructure and Hardness Properties of High-Speed Selective Laser Melted Ti6Al4V. *Metals* **2021**, *11*, 255. https://doi.org/10.3390/met11020255

[341] Jaber, H.; Kónya, J.; Kulcsár, K.; Kovács, T. Effects of Annealing and Solution Treatments on the Microstructure and Mechanical Properties of Ti6Al4V Manufactured by Selective Laser Melted. *Materials* **2022**, *15*, 1978. https://doi.org/10.3390/ma15051978

[342] Liu, S.; Shin, Y.C. Additive manufacturing of Ti6Al4V alloy: A review. *Mater. Des.* **2019**, *164*, 107552. https://doi.org/10.1016/j.matdes.2018.107552

[343] Bai, H.; Deng, H.; Chen, L.; Liu, X.; Qin, X.; Zhang, D.; Liu, T.; Cui, X. Effect of Heat Treatment on the Microstructure and Mechanical Properties of Selective Laser-Melted Ti64 and Ti-5Al-5Mo-5V-1Cr-1Fe. *Metals.* **2021**, *11(4)*, 534–545. Https://doi.org/10.3390/met11040534

[344] Tennant, R. Mechanical Surface Finishing in the Aerospace Industry. *Aircr. Eng. Aerosp. Technol.* **1992**, *64*, 4–14. https://doi.org/10.1108/eb037216

[345] Bower, K.; Murray, S.; Reinhart, A.; Nieto, A. Corrosion resistance of selective laser melted Ti-6Al-4V alloy in salt fog environment. *Res. Mater.* **2020**, *8*, 100122. https://doi.org/10.1016/j.rinma.2020.100122

[346] Croll, S.G. Surface roughness profile and its effect on coating adhesion and corrosion protection: A review. *Prog. Org. Coat.* **2020**, *148*,105847. https://doi.org/10.1016/j.porgcoat.2020.105847

[347] Günter, J.; Krewerth, D.; Lippmann, T.; Leuders, S.; Tröster, T.; Weidne, A.; Biermann, H.; Niendorf, T. Fatigue life of additively manufactured Ti-6Al-4V in the very high cycle fatigue regime. *Int. J. Fatigue* **2017**, *94*, 236–245. https://doi.org/10.1016/j.ijfatigue.2016.05.018

[348] Zhang, H.; Dong, D.; Su, S.; Chen, A. Experimental study of effect of post processing on fracture toughness and fatigue crack growth performance of selective laser melting Ti-6Al-4V. *Chin. J. Aeronaut*. **2019**, *32(10),* 2383–2393. https://doi.org/10.1016/j.cja.2018.12.007

[349] Dhansay, N.M.; Tait, R.; Becker, T. Fatigue and Fracture Toughness of Ti-6Al-4V Titanium Alloy Manufactured by Selective Laser Melting. *Adv. Mater. Res.* **2014**, *1019*, 248–253. https://doi.org/10.4028/www.scientific.net/AMR.1019.248

[350] Gallaraga, H.; Lados, D.A.; Dehoff, R.R.; Kirka, M.M.; Nandwana, P. Effect of the microstructure and porosity of Ti-6Al-4V ELI alloy fabricated by electron beam melting (EBM). *Addit. Manuf.* **2016**, *10*, 47–57. https://doi.org/10.1016/j.addma.2016.02.003

[351] Tiley, J.; Searles, T.; Lee, E.; Kar, S.; Banerjee, R.; Russ, J.; Fraser, H. Quantification of microstructural features in α/β titanium alloys. *Mater. Sci. Eng. A* **2004**, *372*, 191–198. https://doi.org/10.1016/j.msea.2003.12.008

[352] Eshawish, N.; Malinov, S.; Sha, W.; Wallas, P. Microstructure and Mechanical Properties of Ti-6Al-4V Manufactured by Selective Laser Melting after Stress Relieving, Hot Isostatic Pressing Treatment, and Post-Heat Treatment. *J. Mater. Eng. Perform.* **2021**, *30*, 5290–5296. https://doi.org/10.1007/s11665-021-05753-w

[353] Vilaro, T.; Colin, C.; Bartout, J.D. As-Fabricated and Heat-Treated Microstructures of the Ti-6Al-4V Alloy Processed by Selective Laser Melting. *Metall. Mater. Trans. A.* **2001**, *42*, 3190–3199. https://doi.org/10.1007/s11661-011-0731-y

[354] Qiao, Y.; Xu, D.; Wang, S.; Ma, Y.; Chen, J.; Wnag, Y.; Zhou, H. Corrosion and Tensile Behaviors of Ti-6Al-2V-1Mo-1Fe and Ti-6Al-4V Titanium Alloys. *Metals.* **2019**, *9(11)*, 1213. https://doi.org/10.3390/met9111213

[355] Cao, S.; Chen, Z.; Lim, C.V.S.; Yang, K.; Jia, Q.; Jarvis, T.; Tomus, D.; Wu, X. Defect, Microstructure, and Mechanical Property of Ti-6Al-4V Alloy Fabricated by High-Power Selective Laser Melting. *JOM* **2017**, *96*, 2684–2692. https://doi.org/10.1007/s11837-017-2581-6

[356] Seth, P.; Jha, J.S.; Alankar, A.; Mishra, S.K. Alpha-case Formation in Ti-6Al-4V in a Different Oxidizing Environment and Its Effect on Tensile and Fatigue Crack Growth Behavior. *Oxid. Met.* **2022**, *97*, 77–95. https://doi.org/10.1007/s11085-021-10079-y

[357] Nie, B.; Zhao, Z.; Chen, D.; Liu, S.; Liu, M.; Zhang, J.; Liang, F. Effect of Basketweave Microstructure on Very High Cycle Fatigue Behavior of TC21 Titanium Alloy. *Metals* **2018**, *8(6)*, 401. https://doi.org/10.3390/met8060401

References

[358] Chicos, L.-A.; Zaharia, S.M.; Lancea, C.; Pop, M.A.; Cañadas, I.; Rodríguez, J.; Galindo, J. Concentrated solar energy used for heat treatment of Ti6Al4V alloy manufactured by selective laser melting. *Solar Energy* **2018**, *173*, 76–88. https://doi.org/10.1016/j.solener.2018.07.069

[359] Zhao, X.-A.; So, F.; Nicolet, N.-A. $TiAl_3$ formation by furnace annealing of Ti/Al bilayers and the effects of impurities. *J. Appl. Phys.* **1988**, *63*, 2600–2607. https://doi.org/10.1063/1.340981

[360] Ohnuma, I.; Fujita, Y.; Mitsui, H.; Ishikawa, K.; Kainuma, R.; Ishida, K. Phase equilibria in the Ti-Al binary system. *Acta Mater.* **2000**, *48(12)*, 3113–3123. https://doi.org/10.1016/S1359-6454(00)00118-X

[361] Antonysamy, A.A.; Meyer, J.; Pragnell, P.B. Effect of build geometry on the β-grain structure and texture in additive manufacturing of Ti-6Al-4V by selective electron beam melting. *Mater. Charact.* **2013**, *84*, 153–168. https://doi.org/10.1016/j.matchar.2013.07.012

[362] Wang, T.; Zhou, Y.Y.; Zhang, S.Q.; Tang, H.B.; Wang, H.M. Grain morphology evolution behavior of titanium alloy components during laser melting deposition additive manufacturing. *J. Alloys Compd.* **2015**, *632*, 505–513. https://doi.org/10.1016/j.jallcom.2015.01.256

[363] Qi, M.; Huang, S.; Ma, Y.; Youssef, S.; Zhang, R.; Qiu, J.; Lei, J.; Yang, R. Columnar to equiaxed transition during β heat treatment in a near β alloy by laser additive manufacture. *J. Mater. Res. Technol.* **2021**, *13*, 1159–1168. https://doi.org/10.1016/j.jmrt.2021.05.057

[364] Sui, Q.; Li, P.; Wang, K.; Yin, X.; Liu, L.; Zhang, Y.; Zhang, Q.; Wang, S.; Wang, L. Effect of Build Orientation on the Corrosion Behavior and Mechanical Properties of Selective Laser Melted Ti-6Al-4V. *Metals* **2019**, *9(9)*, 976. https://doi.org/10.3390/met9090976

[365] Salsi, E.; Chiumenti, M.; Cervera, M. Modeling of Microstructure Evolution of Ti6Al4V for Additive Manufacturing. *Metals* **2018**, *8(8)*, 633. https://doi.org/10.3390/met8080633

[366] Hartunian, P.; Eshraghi, M. Effect of Build Orientation on the Microstructure and Mechanical Properties of Selective Laser-Melted Ti-6Al-4V Alloy. *J. Manuf. Mater. Process.* **2018**, *2(4)*, 69. https://doi.org/10.3390/jmmp2040069

[367] Bartsch, K.; Hergoz, D.; Bossen, B. Emmelmann, C. Material modelling of Ti-6Al-4V processed by laser powder bed fusion for application for application in macro-scale process simulation. *Mater. Sci. Eng. A* **2021**, *814*, 141237. https://doi.org/10.1016/j.msea.2021.141237

[368] Wu, S.Q.; Lu, Y.J.; Gan, Y.L.; Huang, T.T.; Zhao, C.Q.; Lin, J.J.; Guo, S.; Lin, J.X. Microstructural evolution and microhardness of selective-laser-melted Ti-6Al-4V alloy after post heat treatments. *J. Alloys Compd.* **2016**, *672*, 643–652. https://doi.org/10.1016/j.jallcom.2016.02.183

[369] Jha, J.S.; Toppo, S.P.; Singh, R.; Tewari, A.; Mishra, S.K. Deformation behavior of Ti-6Al-4V microstructures under uniaxial loading: Equiaxed Vs. transformed-β microstructures. *Mater. Charact.* **2021**, *171*, 110780. https://doi.org/10.1016/j.matchar.2020.110780

[370] ASTM F2924-12, Standard Specification for Additive Manufacturing Titanium -6 Aluminium -4 Vanadium with Powder Bed Fusion, West Conshohooken, PA, USA, **2013**.

[371] Ji, Y.; Heo, T.W.; Zhang, F.; Chen, L. Theoretical Assessment on the Phase Transformation Kinetic Pathways of Multi-Component Alloys: Application to Ti-6Al-4V. *J. Phase Equilibria Diffus.* **2016**, *37*, 53–64. https://doi.org/10.1007/s11669-015-0436-9

[372] Sallica-Leva, E.; Caram, R.; Jardini, A.L.; Fogagnolo, J.B. Ductility improvement due to martensite α' decomposition in porous Ti-6Al-4V parts produced by selective laser melting for orthopedic implants. *J. Mech. Behav. Biomed. Mater.* **2016**, *54*, 149–158. https://doi.org/10.1016/j.jmbbm.2015.09.020

[373] Cao, S.; Chu, R.; Zhou, X.; Yang, K.; Jia, Q.; Lim, C.S.V.; Huang, A.; Wu, X. Role of martensite decomposition in tensile properties of selective laser melted Ti-6Al-4V. *J. Alloys Compd.* **2018**, *744*, 357–363. https://doi.org/10.1016/j.jallcom.2018.02.111

[374] Sieniawski, J.; Ziaja, W.; Kubiac, K.; Motyka, M. Microstructure and Mechanical Properties of High-Strength Two-Phase Titanium Alloys. In *Titanium Alloys—Advances in Properties Control*; Sieniawski, J., Ziaja, W., eds.; IntechOpen: London, UK, **2013**. https://doi.org/10.5772/56197

[375] Gallaraga, H.; Warren, R.J.; Lados, D.A.; Dehoff, R.R.; Kirka, M.M.; Nandwana, P. Effects of heat treatments on microstructure and properties od Ti-6Al-4V ELI alloys fabricated by electron beam melting (EBM). *Mater. Sci. Eng. A* **2017**, *685*, 417–428. https://doi.org/10.1016/j.msea.2017.01.019

[376] Guo, Z.; Malinov, S.; Sha, W. Modelling beta transus temperature of titanium alloys using artificial neural network. *Comput. Mater. Sci.* **2005**, *32(1)*, 1–12. https://doi.org/10.1016/j.commatsci.2004.05.004

[377] Kolachev, B.A.; Egorova, Y.B.; Belova, S.B. Relation between the temperature of the $\alpha + \beta \rightarrow \beta$ transformation of commercial titanium alloys and their chemical composition. *Met. Sci. Heat Treat.* **2008**, *50*, 367–372. https://doi.org/10.1007/s11041-008-9061-0

[378] Bagehorn, S.; Wehr, J.; Maier, H.J. Application of mechanical surface finishing processes for roughness reduction and fatigue improvement of additively manufactured Ti-6Al-4V parts. *Int. J. Fatigue.* **2017**, *102*, 135–142. https://doi.org/10.1016/j.ijfatigue.2017.05.008

[379] Aboulkhair, N.T.; Simonelli, M.; Parry, L.; Ashcroft, I.; Tuck, C.; Hague, R. 3D printing of Aluminium Alloys: Additive Manufacturing of Aluminium alloys using selective laser melting. *Prog. Mater. Sci.* **2019**, *106*, 100578. https://doi.org/10.1016/j.pmatsci.2019.100578

[380] Hergoz, D.; Seyda, V.; Wycisk, E.; Emmelmann, C. Additive manufacturing of metals. *Acta Mater.* **2016**, *117*, 371-392. https://doi.org/10.1016/j.actamat.2016.07.019

[381] Hebert, R.J. Viewpoint: metallurgical aspects of powder bed metal additive manufacturing. *J. Mater. Sci.* **2016**, *51*, 1165–1175. https://doi.org/10.1007/s10853-015-9479-x

[382] DebRoy, T.; Wei, H.L.; Zuback, J.S.; Mukherjee, T.; Elmer, J.W.; Milewski, J.O.; Beese, A.M.; et al. Additive manufacturing of metallic components – Process, structure and properties. *Prog. Mater. Sci.* **2018**, *92*, 112–224. https://doi.org/10.1016/j.pmatsci.2017.10.001

[383] Rosenthal, I.; Shneck, R.; Stern, A. Heat treatment effect on the mechanical properties and fracture mechanisms in AlSi10Mg fabricated by additive manufacturing selective laser melting process. *Mater. Sci. Eng. A.* **2018**, *729*, 310-322. https://doi.org/10.1016/j.msea.2018.05.074

[384] Trevisan, F.; Calignano, F.; Lorusso, M.; Pakkanen, J.; Aversa, A.; Ambrosio, E.P.; Lombardi, M.; et al. On the Selective Laser Melting (SLM) of the AlSi10Mg Alloy: Process, Microstructure, and Mechanical Proeprties. *Materials*. **2017**, *10(1)*, 76. https://doi.org/10.3390/ma10010076

[385] Wu, J.; Wang, X.Q.; Wang, W.; Attallah, M.M.; Loretto, M.H. Microstructure and strength of selective laser metled AlSi10Mg. *Acta Mater.* **2016**, *117*, 311–320. https://doi.org/10.1016/j.actamat.2016.07.012

[386] Takata, N.; Kodaira, H.; Suzuki, A.; Kobashi, M. Size dependence of microstructure of AlSi10Mg alloy fabricated by selective laser melting. *Mater. Charact.* **2018**, *143*, 18–26. https://doi.org/10.1016/j.matchar.2017.11.052

[387] Fusanová, M.; Dvorský, D.; Michalcová, A.; Vojtěch, D. Changes in the microstructure and mechanical properties of additively manufactured AlSi10Mg alloy after exposure to elevated temperatures. *Mater. Charact.* **2018,** *137*, 119–126. https://doi.org/10.1016/j.matchar.2018.01.028

[388] Uzan, N.E.; Shneck, R.; Yeheskel, O.; Frange, N. Fatigue of AlSi10Mg specimens fabricated by additive manufacturing selective laser (AM-SLM). *Mater. Sci. Eng. A.* **2017**, *704*, 229–237. https://doi.org/10.1016/j.msea.2017.08.027

[389] Cerri, E.; Ghio, E. AlSi10Mg alloy produced by Selective Laser Melting: Relationships between Vickers microhardness, Rockwell hardness and mechanical properties. *Metall. Ita.* **2020**, *7–8*, 5–17.

[390] Paoletti, C.; Santecchia, E.; Cabibbo, M.; Cerri, E.; Spigrelli, S. Modeling the creep behavior of an AlSi10Mg alloy produced by additive manufacturing. *Mater. Sci. Eng. A.* **2021**, *799*, 140138. https://doi.org/10.1016/j.msea.2020.140138

[391] Spigarelli, S. Constitutive equations in creep of Mg-Al alloys. *Mater. Sci. Eng. A.* **2008**, *492(1–2)*, 153–160. https://doi.org/10.1016/j.msea.2008.03.007

[392] Paoletti, C.; Regev, M.; Spigarelli, S. Model of Creep in Aluminium Alloys Strengthened by Rod-Shaped Particles: Al-Cu-Mg Age-Hardenable Alloys. *Metals*. **2018**, *8(11)*, 930. https://doi.org/10.3390/met8110930

[393] Nix, W.D.; Ilschner, B. *Mechanisms Controlling Creep of Single Phase Metals and Alloys*; Haasen, P., Gerold, V., Kostorz, G.; Pergamon, Aachen, Germany, *3*, 1503–1530, **1979**. https://doi.org/10.1016/B978-1-4832-8412-5.50243-5

[394] Meier, M.; Blum, W. Modeling high temperature creep of academic and industrial materials using the composite model. *Mater. Sci. Eng. A.* **1993**, *164(1–3)*, 290–294. https://doi.org/10.1016/0921-5093(93)90680-D

[395] Orowan, E. *Dislocations in Metals*; Cohen, M.; The Institute of Metals Division, the American Institute of Mining and Metallurgical Engineers: New York, NY, USA, **1954**.

[396] Spigarelli, S.; Sandström, R. Basic creep modelling of Aluminium. *Mater. Sci. Eng. A.* **2018**, *711*, 343–349. https://doi.org/10.1016/j.msea.2017.11.053

References

[397] Spigarelli, S.; Evangelista, E.; Cucchieri, S. Analysis of the creep response of an Al-17Si-4Cu-0.5Mg alloy. *Mater. Sci. Eng. A.* **2004**, *387–389*, 702–705. https://doi.org/10.1016/j.msea.2004.06.043

[398] Uzan, N.E.; Shneck, R.; Yeheskel, O.; Frange, N. High-temperature mechanical properties of AlSi10Mg specimens fabricated by additive manufacturing using selective laser melting technologies (AM-SLM). *Addit. Manuf.* **2018**, *24*, 257–263. https://doi.org/10.1016/j.addma.2018.09.033

[399] Toschi, S. Optimization of A354 Al-Si-Cu Alloy Heat Treatment: Effect on Microstructure, Hardness, and Tensile Properties of Peak Aged and Overaged Alloy. *Metals*. **2018**, *8(11)*, 961. https://doi.org/10.3390/met8110961

[400] Salleh, M.S.; Omar, M.Z.; Syarif, J.; Alhawari, K.S.; Mohammed, M.N. Microstructure and mechanical properties of thixoformed A319 aluminium alloy. *Mater. Des.* **2014**, *64(142–152)*, 142. https://doi.org/10.1016/j.matdes.2014.07.014

[401] Buffington, F.S.; Cohen, M. Self-Diffusion in Alpha Iron Under Uniaxial Compressive Stress. *JOM*. **1952**, *4*, 859–860. https://doi.org/10.1007/BF03398152

[402] Sandström, R. Basic model for primary and secondary creep in copper. *Acta Mater.* **2012**, *60*, 314–322. https://doi.org/10.1016/j.actamat.2011.09.052

[403] Sandström, R. Influence of phosphorus on the tensile stress strain curves in copper. *J. Nucl. Mater.* **2016**, *470*, 290–296. https://doi.org/10.1016/j.jnucmat.2015.12.024

[404] Sandström, R. The role of cell structure during creep of cold worked copper. *Mater. Sci. Eng. A.* **2016**, *674*, 318–327. https://doi.org/10.1016/j.msea.2016.08.004

[405] Busby, J.T.; Hash, M.C.; Was, G.S. The relationship between hardness and yield stress in irradiated austenitic and ferritic steels. *J. Nucl. Mater.* **2005**, *336(2–3)*, 267–278. https://doi.org/10.1016/j.jnucmat.2004.09.024

[406] Rosenthal, I.; Stern, A.; Frage, N. Strain rate sensitivity and fracture mechanism of AlSi10Mg parts produced by Selective Laser Melting. *Mater. Sci. Eng. A.* **2017**, *682*, 509–517. https://doi.org/10.1016/j.msea.2016.11.070

[407] ASTM E140-12bel, Standard Hardness Conversion Tables for Metals Relationship Among Brinell Hardness, Vickers Hardness, Rockwell Hardness, Superficial Hardness, Knoop Hardness, Scleroscope Hardness, and Leeb Hardness, ASTM International. Wets Conshohoken, PA, USA, **2013**.

[408] Li, J.; Li, F.; Ma, X.; Wang, Q.; Dong, J.; Yuan, Z. A strain-dependent ductile damage model and its application in the variation of fracture toughness by micro-indentation. *Mater. Des.* **2015**, *67*, 623–630. https://doi.org/10.1016/j.matdes.2014.11.010

[409] Cahoon, J. An improved equation relating hardness to ultimate strength. *Metall Trans. A.* **1972**, *3(11)*, 3040. https://doi.org/10.1007/BF02652880

[410] Moteff, J.; Bhargava, R.K.; McCullough, W.L. Correlation of the hot-hardness with the tensile strength of 304 stainless steel to temperature of 1200°C. *Metall. Trans.* **1975**, *6*, 1107–1104. https://doi.org/10.1007/BF02661365

[411] Pintadue, G.; Hoechele, A.R.; Cipriano, G.L. Relation between strain hardening exponent of metals and residual profiles of deep spherical indentation. *Mater. Sci. Technol.* **2012**, *28*, 1051–1054. https://doi.org/10.1179/1743284711Y.0000000107

[412] Krishna, S.C.; Gangwar, N.K.; Jha, A.K.; Pant, B. On the Prediction of Strength from Hardness for Copper Alloys. *J. Mater.* **2013**, *2013*, 6. https://doi.org/10.1155/2013/352578

[413] Rometsch, P.A.; Schaffer, G.B. An age hardening model for Al-7Si-Mg casting alloys. *Mater. Sci. Eng. A.* **2002**, *325 (1–2)*, 424–434. https://doi.org/10.1016/S0921-5093(01)01479-4

[414] Gokuldoss, P.K. Work hardening in selective laser melted Al-12Si alloy. *Mater. Des. Process. Comm.* **2019**, 1e46. https://doi.org/10.1002/mdp2.46

[415] Kim, J.-Y.; Lee, K.-W.; Lee, J.-S.; Kwon, D. Determination of tensile properties by instrumented indentation technique: Representative stress and strain approach. *Surf. Coat. Technol.* **2006**, *201(7)*, 4278–4283. https://doi.org/10.1016/j.surfcoat.2006.08.054